GEOLOGY, $^{40}AR/^{39}AR$ GEOCHRONOLOGY, AND FLUID INCLUSION STUDY OF THE SOLTON SARY MESOTHERMAL GOLD DISTRICT, KYRGYZSTAN

By
Vladimir Olegovich Ispolatov

Submitted in Partial Fulfillment of the Requirements
for the Degree of Doctor of Philosophy in Earth and Environmental
Science with Dissertation in Geology

September 2001

Department of Earth and Environmental Science
New Mexico Institute of Mining and Technology
Socorro, New Mexico

ABSTRACT

This study of the Solton Sary gold district (Kyrgyzstan) generated new data contributing to a better understanding of metallogeny of the southern flank of the Paleozoic Kazakztan-Tien Shan orogen. This area represents one of the richest mineral provinces of Eurasia as it hosts a number of world-class mesothermal gold deposits and large gold-bearing porphyry systems, and possesses a high potential for new discoveries. Results presented here confront the traditional view that the gold mineralization of the area is entirely related to the Carboniferous-Permian plate convergence and collision between the Kazakstan-Tien Shan and Tarim-Karakum plates.

The Solton Sary district is underlain by a largely volcanogenic greenstone succession of Cambrian-Ordovician age. Gold-bearing quartz veins and stockworks are hosted by a suite of hypabyssal sills of alkalic (shoshonitic) lamprophyres and syenite porphyries. Virtually indistinguishable trace element patterns and mineral chemistry of the two rock types imply their comagmatic origin.

Fluid inclusion microthermometry and bulk trapped volatile analyses suggest that gold was transported by low saline (≤ 6 wt % NaCl equiv) aqueous-carbonic ($X_{CO_2} \geq 0.1$) fluids and deposited due to sulfur loss during pressure-controlled fluid unmixing. The most likely temperature of mineralization was 350°C, and apparent fluid pressures fluctuated from 1-1.7 kbar to 3-3.5 kbar probably reflecting pressure cycling under the fault-valve mechanism. The diagnostic bulk trapped volatile signature of mineralized quartz comprises CO_2 and SO_2 contents that are consistently higher than those of quartz from barren veins.

A detailed $^{40}Ar/^{39}Ar$ geochronologic study revealed that in spite of the close spatial association between intrusions and auriferous lodes there was a significant time gap between magmatism and mineralization. The intrusions were emplaced at ca. 455-430 Ma (Late Ordovician- Early Silurian), and the gold bearing veins were formed at ca. 395-390 Ma (Early Devonian). This precludes a genetic relationship between the spatially associated intrusions and mineralization, implying a remote, metamorphic or deep magmatic (granitic) fluid source typical of mesothermal gold systems in general.

The alkalic magmatism and mineralization of the Solton Sary district are interpreted to be broadly related to the Late Ordovician-Silurian collisional tectonism caused by transpressional convergence of the North and Median Tien Shan terranes. The intrusions were likely emplaced during the initiation of the collisional event, whereas the mineralization corresponded to its latest stages. The delayed timing of mineralization could reflect a delayed reheating of tectonically thickened crust.

The Devonian age of the Solton Sary mesothermal gold mineralization and its apparent link to the Early Paleozoic tectonic cycle show that the economically important hydrothermal activity at the southern flank of the Kazakstan-Tien Shan orogen was not restricted to Late Paleozoic-Mesozoic. Additional, yet unrevealed, potential may exist within the area, since some Early Paleozoic systems could have been overlooked by previous exploration. At least some of the largest mesothermal systems that are currently interpreted as being Late Paleozoic-Mesozoic in age could result from superimposed Early Paleozoic and Late Paleozoic-Mesozoic mineralizing events.

ACKNOWLEDGMENTS

I would like to express my gratitude to my academic and research advisor, Dr. David Norman and graduate committee members, Drs. Matthew Heizler, Nelia Dunbar, Laurel Goodwin, and Kent Condie for sharing their expertise in various analytical techniques, for providing invaluable help with data collection and interpretation, and for reviewing numerous versions of this manuscript.

I wish to thank Dr. Edward Bloomstein (formerly of Santa Fe Pacific Gold) who suggested this study of the Solton Sary district and provided extensive organizational support during the initial stages of the project. I also thank Dr. Joseph Kowalik of Newmont, whose support allowed the continuation of the project after Santa Fe Pacific Gold was taken over by Newmont in 1997. Stimulating geologic discussions with Drs. Edward Bloomstein and Joseph Kowalik are gratefully acknowledged.

Geologists of the Solton Sary Joint Venture, namely Drs. Boris Trifonov, Slava Pomazkov, Viktor Matveenko, Oleg Rozzhivin, and Irek Shaidullin are thanked for providing logistical support in the field and sharing their knowledge of the Solton Sary district. Special thanks go to Lisa Peters and Richard Esser (New Mexico Geochronology Research Laboratory, NMGRL) for their expertise and help with $^{40}Ar/^{39}Ar$ analyses, data reduction, and sample preparation. Patricia Frisch and Jean Wardell are thanked for proof reading and constructive criticism of this and other manuscripts.

Financial support for this study came from several sources. NMGRL provided four years of research assistantship and allowed an unlimited use of $^{40}Ar/^{39}Ar$ laboratory facilities. Santa Fe Pacific Gold Kyrgyzstan and Newmont Kyrgyzstan Gold Ltd.

provided summer employment in 1997 and 1998, funded sample shipping and part of $^{40}Ar/^{39}Ar$ analyses. Additional support was received from Geological Society of America (GSA Student Research Grant 6256-98), Society of Economic Geologists (SEG McKinstry Grant-1998), New Mexico Institute of Mining and Technology, and New Mexico Bureau of Mines and Geology.

TABLE OF CONTENTS

LIST OF FIGURES viii

LIST OF TABLES xiv

CHAPTER 1. INTRODUCTION 1

Mesothermal gold deposits: geologic characteristics 1

Alternative model: intrusion-related gold deposits 5

Priorities for future research 6

Objective and scope of the study 7

CHAPTER 2. BACKGROUND 10

Geographic setting 10

History of discovery and exploration 10

Previous studies of geology 12

Geodynamic setting 13

Regional tectonic setting 16

Geologic setting 19

Summary of major tectonic events 19

Timing of gold mineralization 23

CHAPTER 3. GEOLOGY OF THE SOLTON SARY DISTRICT 25

Introduction 25

Stratigraphy 28

Stratigraphic section 31

Detrital modes and geochemistry 36

Provenance types and tectonic setting 39

Intrusive rocks 42

Structure and faults 42

Mesothermal gold mineralization 43

District-scale distribution 43

Mineralized zones 44

Hydrothermal alteration 45

Gold mineralization 51
Hydrothermal occurrences outside mineralized zones 53
CHAPTER 4. ALKALIC MAGMATISM 55
Field geology 55
Petrography 57
Lamprophyres 57
Syenite porphyries 61
Mineral chemistry 64
Electron microprobe analytical techniques 64
Mica 65
Felsdspar 69
Amphibole, apatite, and magnetite 85
Implications of petrographic and mineralogical data 85
Geochemistry 90
Discussion of geochemical data 104
Relationships between rock types, and magma source 104
Implications for gold mineralization 106
Tectonic setting 106
Summary 111
CHAPTER 5. OBSERVATIONS ON DEFORMATION STYLES 113
Introduction 113
Deformation within the intrusive belt 113
Composition control on deformation styles 114
Deformation at sill contacts 117
Quartz vein fabrics 118
Relationships between the deformation and hydrothermal alteration 120
Results of microstructural studies 121
Discussion 125
Factors controlling deformation styles 125
Metamorphic conditions 128

Displacements modes 129
Implications for the morphology of mineralized zones 130
Summary 131
CHAPTER 6. FLUID INCLUSION STUDY 132
Introduction 132
Analytical techniques 133
Results of fluid inclusions microthermometry 134
Results of trapped volatile analysis 142
Relative timing and relationships between fluid types 151
Pressure-temperature estimates 153
Implications of microthermometry data 157
Aqueous-carbonic fluids in auriferous quartz 157
Saline fluids in auriferous quartz 159
Sulfuric species in auriferous fluids 161
Origin of auriferous fluids: CO_2/CH_4-N_2/Ar systematics 167
Possible alternatives to the mesothermal model 170
Saline fluids in propylitic veins 172
Summary 175
CHAPTER 7. ^{40}AR/^{39}AR STUDY 177
^{40}Ar/^{39}Ar methodology 177
Sample selection 177
Sample preparation 179
^{40}Ar/^{39}Ar age dating method 180
^{40}Ar/^{39}Ar analytical technique 181
Age assignment and error estimate 183
^{40}Ar/^{39}Ar results (phyllosilicates and amphiboles) 184
Incremental heating analyses 184
UV laser in situ ablation analyses 197
Discussion 214
^{40}Ar/^{39}Ar dating of magmatic biotites 214
^{40}Ar/^{39}Ar dating of hydrothermal muscovites 219

Geologic implications of step heating and UV laser in situ ablation results 221
$^{40}Ar/^{39}Ar$ K-feldspar thermochronology 223
Multiple diffusion domain model 223
Data collection 224
Results of $^{40}Ar/^{39}Ar$ step heating experiments 225
Correction for Cl-correlated excess ^{40}Ar 232
Thermochronologic modeling 234
Modeling results 236
Geologic implications 252
Summary of $^{40}Ar/^{39}Ar$ data 257
CHAPTER 8. SYNTHESIS AND CONCLUSION 261
Synthesis 261
Tectonic setting of mineralization 261
Relationship with magmatism, and association with potassic intrusions 262
Fluid characteristics 264
Post-mineralization history 265
Implications for the Tien Shan metallogeny 265
Application of the UV laser in situ ablation $^{40}Ar/^{39}Ar$ method for dating mesothermal mineralization 267
Conclusions 268
REFERENCES 271
APPENDIX A. RESULTS OF CHEMICAL ANALYSES A-1
APPENDIX B. ELECTRON MICROPROBE DATA B-1
APPENDIX C. FLUID INCLUSION DATA C-1
APPENDIX D. $^{40}AR/^{39}AR$ DATA D-1

LIST OF FIGURES

Fig. 2.1. Location of the Solton Sary district in Kyrgyz Republic. 11

Fig 2.2. Simplified tectonic map of Kazakstan-Tien Shan folded system 14

Fig 2.3. Paleotectonic reconstruction of Kazakstan-Tien Shan orogen by Sengor and Natal'in (1996 a, b) and Sengor et al. (1993). 15

Fig. 2.4. Major tectonic divisions of North-Median Tien Shan junction 17

Fig. 2.5. Simplified geologic map of the Solton Sary area..................................20

Fig. 2.6. Compiled chronology of major regional geologic events......................21

Fig. 3.1. Generalized geologic map of the Solton Sary district. 26

Fig. 3.2. Geologic map of the Altyntor open pit. 29

Fig. 3.3. Generalized stratigraphic column of the Solton Sary district and correlation to the regional stratigraphic model. 30

Fig. 3.4. Variation of thickness (meters) of Lower-Middle Ordovician turbiditic units. 35

Fig. 3.5. Composition and provenance types of clastic rocks of the Solton Sary district. 38

Fig. 3.6. Primitive mantle-normalized plots for samples of clastic rocks and basalts lCm. 40

Fig. 3.7. Zoning of hydrothermal assemblages: measured cross-section and generalized model. 46

Fig. 4.1. Measured cross sections of the Solton Sary intrusive belt......................56

Fig. 4.2. Photomicrographs of lamprophyres. 58

Fig. 4.3. Backscattered electron images of lamprophyres...................................59

Fig. 4.4. Inclusions in lamprophyres. 62

Fig. 4.5. Photomicrographs depicting two textural varieties of syenite porphyries. 63

Fig. 4.6. Composition of unzoned micas from lamprophyres and syenite porphyries. 70

Fig. 4.7. Variation of mg#, TiO_2, and Al_2O_3 in magmatic micas. 71

Fig. 4.8. Composition of micas from lamprophyre 49-113.7 and syenite porphyry 49-129.2. 74

Fig. 4.9. Backscattered electron images of zoned mica phenocrysts from lamprophyre 49-113.7 and measured crystal-scale variation of mg#. 75

Fig. 4.10. Ternary plots of feldspars from syenite porphyries, lamprophyres and a leucocratic segregation (ocellum) hosted in lamprophyres....77

Fig. 4.11. Variation of BaO in feldspars from lamprophyres and syenite porphyries. 78

Fig. 4.12. Backscattered electron images of zoned K-feldspar phenocrysts. 79

Fig. 4.13. Zoning of K-feldspar phenocrysts as revealed by electron microprobe line scans for Ba. 80

Fig. 4.14. Postmagmatic albitization of a zoned K-feldspar phenocryst....82

Fig. 4.15. Classification diagrams showing the range of compositions of lamprophyres and syenite porphyries....94

Fig. 4.16. Cr, Co, Ni contents and mg# of the Solton Sary potassic rocks compared to corresponding values of primary magmas....96

Fig. 4.17. Major oxide versus silica variation diagrams. 97

Fig. 4.18. Selected trace element (ppm) versus silica (wt percent) variation diagrams....98

Fig. 4.19. Primitive mantle normalized Cu, Au, Pd, and Ni plots of the Solton Sary potassic rocks. 101

Fig. 4.20. Chondrite-normalized rare earth element plots of the Solton Sary potassic rocks. 102

Fig. 4.21. Primitive mantle normalized incompatible element plots of the Solton Sary potassic rocks. 103

Fig. 4.22. Major oxides and trace elements of the Solton Sary lamprophyres normalized by corresponding values of "average" calc-alkaline lamprophyre tabulated by Rock (1991)....105

Fig. 4.23. Discrimination routine by Müller and Groves (1997) applied to the Solton Sary potassic rocks. 109

Fig. 5.1. Photomicrographs of deformed lamprophyres....115

Fig. 5.2. Photomicrographs of deformed syenite porphyries....116

Fig. 5.3. Mylonites from contacts of syenite sills. 119

Fig. 5.4. Photomicrographs of mylonite from the South Kumbel fault zone, sample 643-8, plane polarized light. 123

Fig. 5.5. Photomicrographs of mylonite with quartz veinlets, sample 537....126

Fig. 6.1. Photomicrographs of fluid inclusions....135

Fig. 6.2. Histogram of melting temperature of the carbonic phase in type 1 and type 2 inclusions. 136

Fig. 6.3. Histogram of homogenization temperatures of the carbonic phase 136

Fig. 6.4. Histograms of melting temperatures. 137

Fig. 6.5. Estimated salinities....138

Fig. 6.6. Histogram of total homogenization temperature for type 2, 3, 4, and 5 inclusions....138

Fig. 6.7. Distribution of mole percentages of H_2O in CO_2 produced by quadrupole mass spectrometer analysis of mineralized and barren quartz samples. 144

Fig. 6.8. Relationship between CO_2/CH_4 and N_2/Ar ratios in volatiles trapped in auriferous and barren quartz veins of the Solton Sary district. 145

Fig. 6.9. Sulfur-bearing species in auriferous and barren veins of the Solton Sary district. All histograms show log values. 146

Fig. 6.10. Ternary plot depicting major non-aqueous volatile species. 148

Fig. 6.11. H_2O-CO_2-(H_2S+SO_2)*10000 ternary plot emphasizing diagnostic bulk chemical signatures of fluids trapped in auriferous and barren veins. 150

Fig. 6.12. Isochore plot for type 1 and type 2 fluid inclusions from sample 664-1, and a plot assessing consequences of possible systematic errors 154

Fig. 6.13. Variation of sulfuric species versus CO_2 based on bulk trapped volatile analyses of auriferous quartz from the Solton Sary district. 164

Fig. 7.1. $^{40}Ar/^{39}Ar$ age spectra for biotites 55-62.7 and 57-174.1 185

Fig. 7.2. $^{40}Ar/^{39}Ar$ age spectra for biotites 76-179.9 and 57-166.2 186

Fig. 7.3. $^{40}Ar/^{39}Ar$ age spectra for biotites 58-58.3, 56-158, and 58-110.2, and zoned biotites 49-129.2 and 49-113.7 187

Fig. 7.4. $^{40}Ar/^{39}Ar$ age spectra for amphiboles 397 and TR6A. 188

Fig. 7.5. $^{40}Ar/^{39}Ar$ age spectra for biotite and hornblende 700-2 188

Fig. 7.6. $^{40}Ar/^{39}Ar$ age spectra for fine-grained hydrothermal micas: sericites 59-85.5 and 62-115.2, and fuchsite 59-85.5 189

Fig. 7.7. $^{40}Ar/^{39}Ar$ age spectra for coarse muscovites from mineralized zones: AD2, AD2A, 547, and 601. 190

Fig. 7.8. $^{40}Ar/^{39}Ar$ age spectra for coarse muscovites from propilitic vein (532), and barren quartz veins stratigraphically below (617) and above (659) the mineralized zone. 191

Fig. 7.9. $^{40}Ar/^{39}Ar$ age spectra for hydrothermal biotites 57-157.5-1 and 2 192

Fig. 7.10$^{40}Ar/^{39}Ar$ age spectra for fuchsites 669-3 and 675-2. 192

Fig. 7.11. Results of the in situ ablation $^{40}Ar/^{39}Ar$ analysis of zoned biotite 49-113.7-1 198

Fig. 7.12. Results of the in-situ ablation $^{40}Ar/^{39}Ar$ analysis of zoned biotite 49-113.7-2 199

Fig. 7.13. Results of the in situ ablation $^{40}Ar/^{39}Ar$ analysis of zoned biotite 49-129.2. 200

Fig. 7.14. Results of the in situ ablation $^{40}Ar/^{39}Ar$ analysis of biotite 57-166.2-1 201

Fig. 7.15. Results of the in situ ablation $^{40}Ar/^{39}Ar$ analysis of biotite 57-166.2-2. 202

Fig. 7.16. Systematic variation of the Cl/K ratio in mica phenocrysts from lamprophyres and syenite porphyries. 203

Fig. 7.17. Results of the in situ ablation $^{40}Ar/^{39}Ar$ analysis of muscovite 601-1. 205

Fig. 7.18. Results of the in situ ablation $^{40}Ar/^{39}Ar$ analysis of muscovite 601-2. 206

Fig. 7.19. Results of the in situ ablation $^{40}Ar/^{39}Ar$ analysis of muscovite AD2A. 207

Fig. 7.20. Results of the in situ ablation $^{40}Ar/^{39}Ar$ analysis of muscovite 532. 208

Fig. 7.21. Results of the in situ ablation $^{40}Ar/^{39}Ar$ analysis of muscovite 547 (traverse 1). 209

Fig. 7.22. Results of the in situ ablation $^{40}Ar/^{39}Ar$ analysis of muscovite 547 (traverse 2). 210

Fig. 7.23. $^{40}Ar/^{39}Ar$ age spectra for K-feldspars 57-174.1 and A23. 226

Fig. 7.24. $^{40}Ar/^{39}Ar$ age spectra for K-feldspars 57-166.2 and 49-129.2. 227

Fig. 7.25. $^{40}Ar/^{39}Ar$ age spectra for K-feldspars 664-1 and 626-1. 228

Fig. 7.26. $^{40}Ar/^{39}Ar$ age spectra for K-feldspars 676-2, 700-1, and 700-2. 229

Fig. 7.27. Results of thermochronologic modeling. 238

Fig. 7.28. Contours of thermal histories allowing reheating. 247

Fig. 7.29. Model thermal histories requiring monotonic cooling. 249

Fig. 7.30. Combined thermal histories for six K-feldspar samples. 253

Fig. 7.31. Summary of $^{40}Ar/^{39}Ar$ geochronologic and thermochronologic data for the Solton Sary district and correlation with regional geologic events. 258

Fig. A.1. Detection limits for CODE 4B and CODE 4B OPTION 2 analytical packages of Activation Laboratories Ltd....................................... A-17

Fig. A.2. Detection limits for the CODE 4-Lithoresearch analytical package of Activation Laboratories Ltd. A-18

Fig. A.3. A brief description for the CODE 4-Lithoresearch analytical package of the Activation Laboratories Ltd. A-19

LIST OF TABLES

Table 3.1. Composition of clastic rocks of the Solton Sary district 37

Table 3.2. Representative electron microprobe analyses of hydrothermal carbonates 49

Table 3.3. Representative electron microprobe analyses of hydrothermal biotite 50

Table 3.4. Representative electron microprobe analyses of white micas from auriferous quartz veins and QSCP alteration 52

Table 4.1. Representative electron microprobe analyses of groundmass mica 66

Table 4.2. Representative electron microprobe analyses of mica from mafic enclaves 67

Table 4.3. Representative electron microprobe analyses of unzoned mica phenocrysts 68

Table 4.4. Representative electron microprobe analyses of zoned mica phenocrysts and megacrysts 72

Table 4.5. Representative electron microprobe analyses of K-feldspar and plagioclase phenocrysts 76

Table 4.6. Representative electron microprobe analyses of K-feldspar from groundmass and leucocratic segregation 83

Table 4.7. Representative electron microprobe analyses of plagioclase from groundmass and leucocratic felsic segregation 84

Table 4.8. Representative electron microprobe analyses of amphibole 86

Table 4.9. Electron microprobe analyses of apatite 87

Table 4.10. Electron microprobe analyses of magnetite 87

Table 4.11. Major element abundances in intrusive rocks of the Solton Sary district 91

Table 4.12. Platinum group element abundances 91

Table 4.13. Trace element abundances in intrusive rocks of the Solton Sary district 92

Table 6.1. Representative quadrupole mass spectrometer analyses of trapped volatiles 143

Table 7.1. Samples analyzed by the $^{40}Ar/^{39}Ar$ method 178

Table 7.2. Summary of $^{40}Ar/^{39}Ar$ step heating results 193

Table 7.3. K-feldspar Ar kinetic parameters used for MDD modeling 237

Table A.1. Activation Laboratories Ltd. report on major and selected trace element analyses by fusion-ICP method A-3

Table A.2. Activation Laboratories Ltd. report on trace element analyses by the fusion-ICP/MS method A-4

Table A.3. A revised version of the report placed in Table A.2 .... A-8

Table A.4. Activation Laboratories Ltd. report on major and trace element analyses by fusion-ICP and fusion-ICP-MS methods A-12

Table A.5. Activation Laboratories Ltd. Report on analyses for platinum group elements by Fire Assay-ICP-MS A-16

Table B.1. Electron microprobe analyses of zoned biotite phenocrysts B-2

Table B.2. Electron microprobe analyses of unzoned biotite phenocrysts B-8

Table B.3. Electron microprobe analyses of groundmass biotite B-20

Table B.4. Electron microprobe analyses of biotite from mafic enclaves B-27

Table B.5. Electron microprobe analyses of K-feldspar phenocrysts B-30

Table B.6. Electron microprobe analyses of plagioclase phenocrysts B-36

Table B.7. Electron microprobe analyses of groundmass K-feldspar B-37

Table B.8. Electron microprobe analyses of groundmass plagioclase B-39

Table B.9. Electron microprobe analyses of amphibole from lamprophyres B-40

Table B.10. Electron microprobe analyses of hydrothermal white mica B-43

Table B.11. Electron microprobe analyses of hydrothermal biotite B-54

Table B.12. Electron microprobe analyses of hydrothermal feldspar..............B-57

Table B.13. Electron microprobe analyses of hydrothermal carbonate B-58

Table B.14. Electron microprobe analyses of feldspars from granitoids B-59

Table B.15. Electron microprobe analyses of hornblende from Ordovician granites B-61

Table B.16. Electron microprobe analyses of biotite from Ordovician granites B-61

Table B.17. Summary of SRM analyses (amphiboles) B-62

Table B.18. Summary of SRM analyses (biotite) B-62

Table B. 19. Summary of SRM analyses (feldspars) B-62

Table C.1. Summary of samples characterized by fluid inclusion microthermometry and bulk trapped volatile analysis C-2

Table C.2. Microthermometric data for type 1 fluid inclusions C-3

Table C.3. Microthermometric data for type 2 fluid inclusions C-4

Table C.4. Microthermometric data for type 3 fluid inclusions C-5

Table C.5. Microthermometric data for type 4 fluid inclusions C-6

Table C.6. Microthermometric data for type 5 fluid inclusions C-6

Table C.7. Trapped volatile analyses C-7

Table D.1. $^{40}Ar/^{39}Ar$ data for step heating analyses... D-2

Table D.2. Results of UV laser in situ ablation analyses D-13

Table D.3. Results of step heating analyses of K-feldspars used for MDD modeling D-18

Table D.4. Results of step heating analyses of K-feldspar..............................D-23

CHAPTER 1

INTRODUCTION

Mesothermal deposits represent one of the most important sources of gold. Economic interest in mesothermal deposits can be explained by three factors. First, this type of mineralization includes a number of truly giant systems, with gold reserves of hundreds to thousands of tons. Second, many medium and small mesothermal deposits are characterized by exceptionally high grades and relatively inexpensive extraction techniques, which makes them economically attractive in spite of their low tonnage. And finally, scattered mesothermal veins with coarse gold often serve as a source for vast placer provinces (e. g., Northeast Russia, Alaska).

Mesothermal gold deposits: geologic characteristics

Mesothermal gold deposits (also known as “lode gold” and “orogenic gold” deposits) are epigenetic systems that comprise structurally controlled auriferous quartz veins and zones of vein silicification (e. g., Hodgson, 1993; Kerrich, 1993; McCuaig and Kerrich, 1998; Groves, 1993; Groves et al., 1998). The gold-silver ratio varies from 10 to 1, and averages about 5. Mineralization is accompanied by elevated As, Sb, Te, W, Mo, and Bi (Kerrich, 1993; McCuaig and Kerrich, 1998; Groves, 1993; Groves et al., 1998). The most common host rocks are greenstone volcanics, turbidites, banded iron formation (BIF), and granitoids. Syn-mineralization alteration typically overprints regional metamorphic parageneses and involves addition of CO_2, H_2O, S, K, and large ion lithophile elements (LILE) (e. g., McCuaig and Kerrich, 1998). Trapped auriferous fluids are low saline (3-7 wt % NaCl equiv), CO_2(±CH_4)-rich (mole fraction of CO_2 typically within the 0.1 to 0.25 range) and commonly show evidence for carbonic phase unmixing (Ridley and Diamond, 2000). Bisulfide complexes are believed to be the main gold-transporting agents. Interaction with host rocks (e. g., sulfidation) and phase separaton that result in H_2S loss are the most important mechanisms of gold precipitation (e. g., Mikucki, 1998).

Mesothermal deposits differ from other gold mineralization classes, such as Carlin-type, epithermal, and gold-bearing porphyry in geodynamic setting and depth of formation. The latter types of deposits form largely within the uppermost 2-5 km of crust, typically under an extensional tectonic regime, and are not coeval with regional metamorphism (Groves et al., 1998; McCuaig and Kerrich, 1998). In contrast, mesothermal systems are synmetamorphic, synkinematic, and form over a broad depth range. Metamorphic conditions vary from sub-greenschist to granulite facies (Mueller and Groves, 1991; Groves, 1993; Groves et al., 1998; McCuaig and Kerrich, 1998) but most typically correspond to the greenschist facies, in the vicinity of the seismic-aseismic transition (T~300-350°C and P~1-3 kbar, Ho et al., 1992; Ridley and Diamond, 2000). Unlike epithermal and porphyry gold deposits, mesothermal vein systems are vertically extensive and exhibit very subtle or no vertical zoning (McCuaig and Kerrich, 1998).

Geodynamically, mesothermal systems tend to form at convergent plate margins in accretionary or collisional orogens under predominantly transpressional regimes (e. g., Wyman and Kerrich, 1988a, b; Kerrich and Wyman, 1990; Barley and Groves; 1992; Groves et al., 1998; Goldfarb et al., 1998). It is proposed that strictly accretionary (also, "Cordilleran-type," "external," "peripheral," "Turkic-type," Murphy and Nance, 1991 and 1992; Sengör et al., 1996a, b; Kerrich and Cassidy, 1994) orogens where allochtonous terrranes are added to one another, or to pre-existing continental margins are generally more favorable environments than typical collisional, continent-continent ("internal," Murphy and Nance, 1991 and 1992) orogens, such as Alpine-Himalayan or Appalachian (e. g., Kerrich and Cassidy, 1994; McCuaig and Kerrich, 1998). Goldfarb et al. (1991) show that a shift from near orthogonal subduction to more transcurrent convergence may trigger mass fluid release and mineralization. The association with convergent, particularly accretionary, tectonism explains the global temporal correlation of major mesothermal gold provinces with perioids of intense accretionary orogenesis and continental crust growth (Barley and Groves, 1992; Kerrich et al., 2000).

Within the orogens, mineralization generally postdates Trondhjemite-tonalite-granodiorite (TTG) magmatism, predates or broadly overlaps with the emplacement of post-tectonic granites, and is often temporally and spatially associated with small lamprophyre intrusions (e. g., Kerrich and Cassidy, 1994; Bierlein and Crowe, 2000). Some earlier studies proposed a genetic link between the lamprophyres and gold lodes (e. g., Rock and Groves, 1988a, b). Later, it was recognized that this spatial association is instead paragenetic: the emplacement of lamprophyric magmas and fluid flow is controlled by the same terrain boundary structures (e. g., Kerrich and Wyman, 1990). Although there are epithermal and porphyry deposits genetically related to lamprophyric magmas, it is not the case with "classic" mesothermal systems. Lamprophyres associated with mesothermal lodes do not show intrinsic gold enrichment, precluding the possibility of genetic relations (e. g., Wyman and Kerrich, 1989; Müller and Groves, 1997).

Many significant mesothermal gold districts are spatially associated with predominantly terrestrial alluvial-fluvial, coarse clastic successions that are distributed along major faults and unconformably overlie older volcanogenic or turbiditic rocks (Hodgson, 1993; Robert and Poulsen, 2001). In the Archean Southern Abitibi Province (Canada), accumulation of such a succession (Timiskaming-type sediments) was accompanied by alkalic magmatism (Corfu, 1993). Hodgson (2000) emphasized the temporal correlation of Abitibi Province mineralization with the "Timiskaming-type event".

The geochronology of mesothermal deposits is somewhat problematic because of their complex post-mineralization history. $^{40}Ar/^{39}Ar$ dates often fall out of regional geodynamic context and tend to be systematically younger than U/Pb and Sm-Nd ages. This is attributed to partial resetting of $^{40}Ar/^{39}Ar$ systematics during slow cooling or later hydrothermal events (e. g., Kerrich and Cassidy, 1994; Hagemann and Cassidy, 2000). At the same time, $^{40}Ar/^{39}Ar$ dating still is, and probably will remain, the most frequently used geochronological tool, as minerals suitable for precise U/Pb dating (e. g., zircon) are relatively uncommon in mesothermal systems. The newly developed Re-Os method that is potentially capable of dating ore minerals is also considered highly promising (Hagemann and Cassidy, 2000).

Most recent genetic models agree that mesothermal deposits are generated by extensive, crustal-scale hydrothermal systems. Invariably, models imply generation of large volumes of fluid, and distal (at least several kilometers), channeled fluid transport along major faults or deformation zones (e. g., Groves, 1993; Groves et al., 1998; McCuaig and Kerrich., 1998; Ridley and Diamond, 2000; Hagemann and Cassidy, 2000).

The deep, non-meteoric nature of the fluid is agreed upon, but the exact source is unclear. Two most commonly proposed fluid sources are deeply crystallizing granitoids and metamorphic devolatilization at the greenschist-amphibolite facies transition (e. g., Groves, 1993; Ridley and Diamond, 2000; McCuaig and Kerrich, 1998). McCuaig and Kerrich (1998) speculate on the possibility for the mixing of heterogeneously sourced fluids, such as those derived from devolatilization of subcreted material, mantle degassing, and mid-crustal greenstone devolatilization.

Alternative model: intrusion-related gold deposits

A recently introduced class of intrusion-related gold deposits unites mineralized systems that are associated with and genetically related to I-type granites (Thompson et al., 1999; Thompson and Newberry, 2000; Lang et al., 2000; Baker, 2000). These deposits are either hosted by parent intrusions, or occur up to 1-3 km from them (Thompson et al., 1999). In general, the depth of formation is relatively shallow (<2 to 5 km) but there are examples of deeper systems (Thompson and Newberry, 2000). Mineralization styles and fluid inclusion signatures of intrusion-related gold deposits are often indistinguishable from those of mesothermal systems (Sillitoe and Thompson, 1998). Two types of mineralization may co-exist within the same metallogenic provinces, and some large deposits (e. g., Muruntau, Uzbekistan) are claimed to belong to mesothermal or intrusion-related types by different researchers (e. g., Groves et al., 1998; Thompson and Newberry, 2000).

A fundamental difference between these two models is the relationship of the mineralization and fluid source, and hence, factors controlling the distribution of mineralization in a given terrain. In the mesothermal model, the source is distal and equivocal, and the distribution of mineralization is largely controlled by regional discontinuities that serve as fluid conduits. Under the intrusion-related model, specific intrusions or intrusive complexes control the distribution of gold deposits. It is apparent that both mesothermal proper and intrusion-related gold deposits exist. Distinction between the two types is critical at all stages of the exploration process, from regional target prioritization to detailed exploration, because it defines the fundamental control of mineralization by a particular intrusive complex or regional fault structure-fluid conduit (Sillitoe and Thompson, 1998). As many seemingly diagnostic characteristics of mesothermal and intrusion-related types tend to converge, the broadest possible spectrum of geologic criteria has to be employed to define the genesis of mineralization. The surest way to establish whether a given mineralized system is intrusion-related is to identify a spatially and temporally correlated intrusive suite that is geochemically capable of providing both fluids and gold. For cases of spatial association between gold lodes and intrusions, the significance of this association and a possibility of their genetic link need to be evaluated.

Priorities for future research

Trends and priorities for future research of mesothermal gold deposits are discussed in several recent overviews (e. g., Hagemann and Cassidy, 2000; Partington and

Williams, 2000; Bierlein and Crowe, 2000). Most authors emphasize the need for a better understanding of the geodynamic setting of mineralization, relationships to magmatism, fluid sources, and detailed, reliable geochronology. Studies of individual mesothermal systems should attempt to define the timing of mineralization in the geologic evolution of host terrains.

Also, analysis of contemporary genetic models shows that they rely heavily on detailed data from few well-studied provinces (e. g., the Archean Yilgarn Craton in Australia and the Abitibi Subprovince, Canada; the Paleozoic Tasman foldbelt in Southeast Australia, and the Meso-Cenozoic provinces of Alaska). Information on some regions with long historic gold production, significant explored reserves, and high potential for future discoveries is either completely absent or very fragmental. Gold provinces of the Former Soviet Union, such as Tien Shan (Central Asia) and Russian Northeast are only two examples. Genetic models cannot be truly comprehensive without incorporating data on metallogenically important, but yet poorly characterized areas.

Objective and scope of the study

This study focuses on the Solton Sary mesothermal gold district that is hosted in the Kazakstan-North Tien Shan orogen, one of the largest and most mineral-rich Phanerozoic accretionary orogens. It attempts to determine the origin of the mineralized system, with an emphasis on timing of mineralization, its relationship to magmatism and regional tectonic events, composition and source of mineralizing fluids. The study is intended to improve the understanding of metallogeny and tectonic evolution of the Kazakstan-North Tien Shan orogen, and to advance the knowledge of the genesis and tectonic setting of mesothermal gold systems in general.

Chapter 2 provides a regional geologic background emphasizing the nature of the host terrain and its Paleozoic geodynamic evolution. Available regional tectonic models are in many aspects contradictory. The chapter outlines major tectonic events that are universally recognized (although sometimes interpreted differently) and are essential for understanding the tectonic setting of mineralization. Chapter 3 describes the geology of the ore district and is based primarily on original observations conducted during two seasons of fieldwork and the results of petrographic studies. Chapter 4 focuses on the petrology and geochemistry of intrusive rocks that host the bulk of the mineralization. The objectives of this chapter include characterizing the main rock varieties, determining their geochemical and petrological affinities, tectonic setting, and possible relationships with the mineralization. Chapter 5 summarizes field and petrographic observations of deformation styles and results of a pilot microstructural study of oriented thin sections. This chapter investigates the relative timing of hydrothermal alteration and deformation, variations in deformation styles, and attempts to provide independent constraints on general metamorphic conditions of mineralization. Chapter 6 reports and discusses results of microthermometric studies of fluid inclusions and bulk trapped volatile (quadrupole mass spectrometer) analysis. These studies permitted to infer the chemical composition of auriferous fluids and the most probable mechanism of gold deposition, and to estimate general pressure-temperature conditions. Chapter 7 reports the results of $^{40}Ar/^{39}Ar$ geochronological and thermochronological studies. In addition to conventional step heating analyses that returned complex age spectra indicative of post-crystallization ^{40}Ar loss, high-resolution UV laser in situ analysis of hydrothermal and magmatic micas was used in order to retrieve meaningful data on the timing of magmatism and mineralization. Results of thermochronological studies of K-feldspar are used to constrain the post-mineralization thermal history of the district. Chapter 8 synthesizes all available data and presents conclusions on the nature and tectonic setting of mineralization.

CHAPTER 2

BACKGROUND

Geographic setting

The mesothermal Solton Sary gold district is located in the Kyrgyz Republic (Fig. 2.1). Geographically, the area corresponds to the southern slope of the Kapka-Tash Range of the Tien Shan mountain system. The elevation is 3000-3500 m above sea level. Significant portions of the district, including areas of gold mineralization, are covered by a thin regolith veneer.

History of discovery and exploration

Quartz veins with visible gold were first encountered in this district in the 1940s; however, only limited exploration was conducted until the mid 1960s. From 1964 to1967, an extensive exploration program was implemented by a geologic expedition subordinate to the Ministry of Geology of the USSR. Mineralized zones were uncovered and sampled in surface trenches, core holes and exploratory adits. The delineated reserves did not attract immediate economic interest and the district was abandoned. From 1988 to 1993, a larger area that included the Solton Sary district was mapped at 1:50,000 scale as a part of a nationwide state geologic mapping program. This extensive project must have included more detailed mapping within the Solton Sary district, but as with other government-funded geologic projects of the Soviet period, the results are not accessible. In 1991, the Soviet Union was dissolved, and Kyrgyzstan (Kyrgyz Republic) obtained

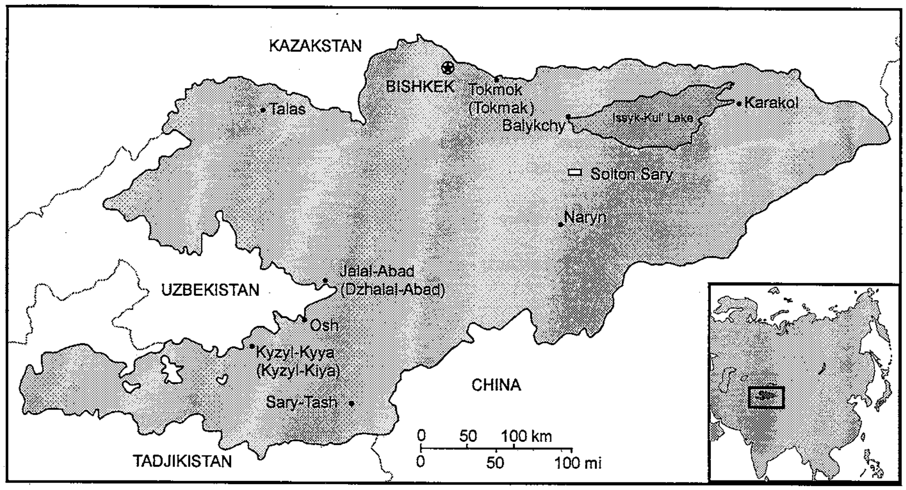

Fig. 2.1. Location of the Solton Sary district in Kyrgyz Republic.

independence. Between 1991 and 1996, Kyrgyz government geologic and gold-mining agencies conducted drilling and trenching throughout the Solton Sary district. During the period of 1994 to1996, small-scale experimental mining was attempted from the Altyntor open pit at the district's eastern flank. Judging from the fact that the operation at the Altyntor pit was shut down in 1997, these first production attempts were not particularly successful. In 1996, a US-based mining company, Santa Fe Pacific Gold, formed a joint venture with the Kyrgyz government gold mining agency, Kyrgyzaltyn, and launched an extensive exploration program that included surface mapping, trenching, core and reverse circulation drilling. In 1997, Santa Fe Pacific Gold was taken over by Newmont, and further exploration in 1997, 1998, and 1999 was continued by the Newmont Kyrgyzstan-Kyrgyzaltyn joint venture. The materials for this work were collected during summer field seasons of 1997 and 1998.

Previous studies of geology

As stated previously, the Solton Sary area has been mapped at 1: 50,000 scale, but original geologic maps and reports are not accessible. Mikolaichuk et al. (1997) summarize some results of the most recent 1:50,000 mapping (1988-1993). This publication focuses on the regional stratigraphy and geochronology of granitoids with implications for Late Precambrian-Early Paleozoic geodynamics. Kheraskova et al. (1997) present a description of regional stratigraphy and paleotectonic interpretation. Lomize et al. (1997) report results of field mapping and geochemical studies of ophiolite complexes and some arc volcanics of the Kyrgyz-Terskei zone. This paper contains major and trace element data for Cambrian basalts that comprise the lowermost stratigraphic unit of the Solton Sary district. None of the three mentioned publications directly focuses on the mesothermal gold system of the Solton Sary district. However, they provide important background information on regional stratigraphy and the chronology of Early Paleozoic tectonic events. Most geodynamic data from Mikolaichuk et al. (1997) and Lomize et al. (1997) are summarized in this chapter. Stratigraphic models reported by Mikolaichuk et al. (1997) and Kheraskova et al. (1997) are employed to constrain geologic ages of stratified units of the Solton Sary district.

Geodynamic setting

A detailed description of the regional tectonics and geologic evolution of the area is found in Zonenshain et al. (1990), Sengör et al. (1993), Sengör and Natal'in (1996a, b). The Solton Sary district is located at the southern flank of the Kazakstan-Tien Shan Paleozoic orogenic system. This triangular-shaped orogen consists of a tectonic collage of elongate fragments of Precambrian crystalline basement and unusually large Paleozoic subduction-accretion complexes (Fig. 2.2) (Sengör et al., 1993; Sengör and Natal'in, 1996a, b). The assemblage is intruded by Paleozoic granitoids and is overlain by subaerial volcanics in places (e. g., Sengör and Natal'in 1996a, b). Sengör with co-authors (Sengör et al., 1993; Sengör and Natal'in, 1996a, b) suggest that this Paleozoic tectonic collage resulted from the evolution of a single island arc (Kipchak arc, Sengör and Natal'in, 1996). The tectonic units are interpreted as segments of initially linear arc that were "stacked," mainly through strike slip tectonics (Fig. 2.3). Alternative views

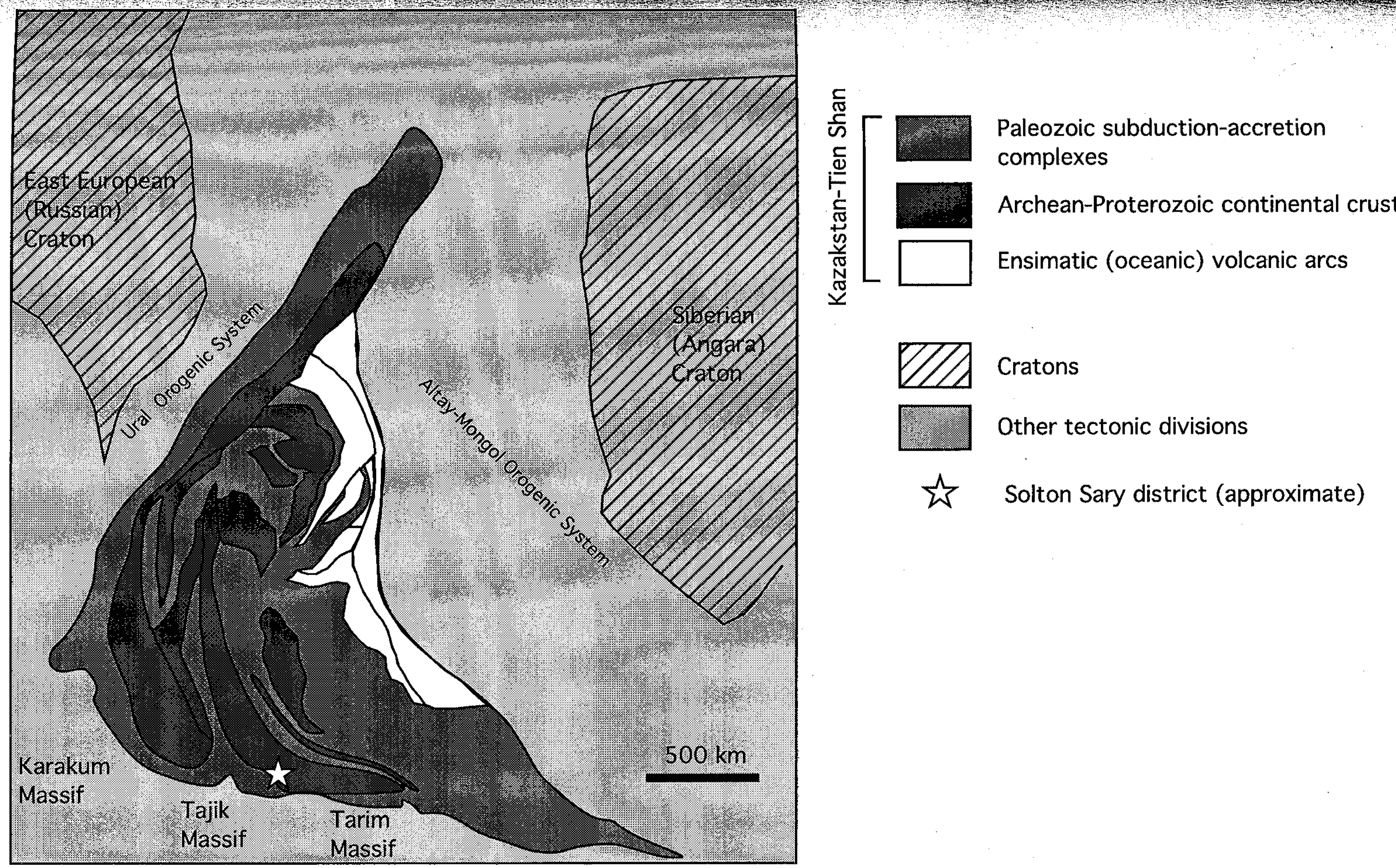

Fig 2.2. Simplified tectonic map of Kazakstan-Tien Shan folded system (after Sengör and Natal'in, 1996 a, b).

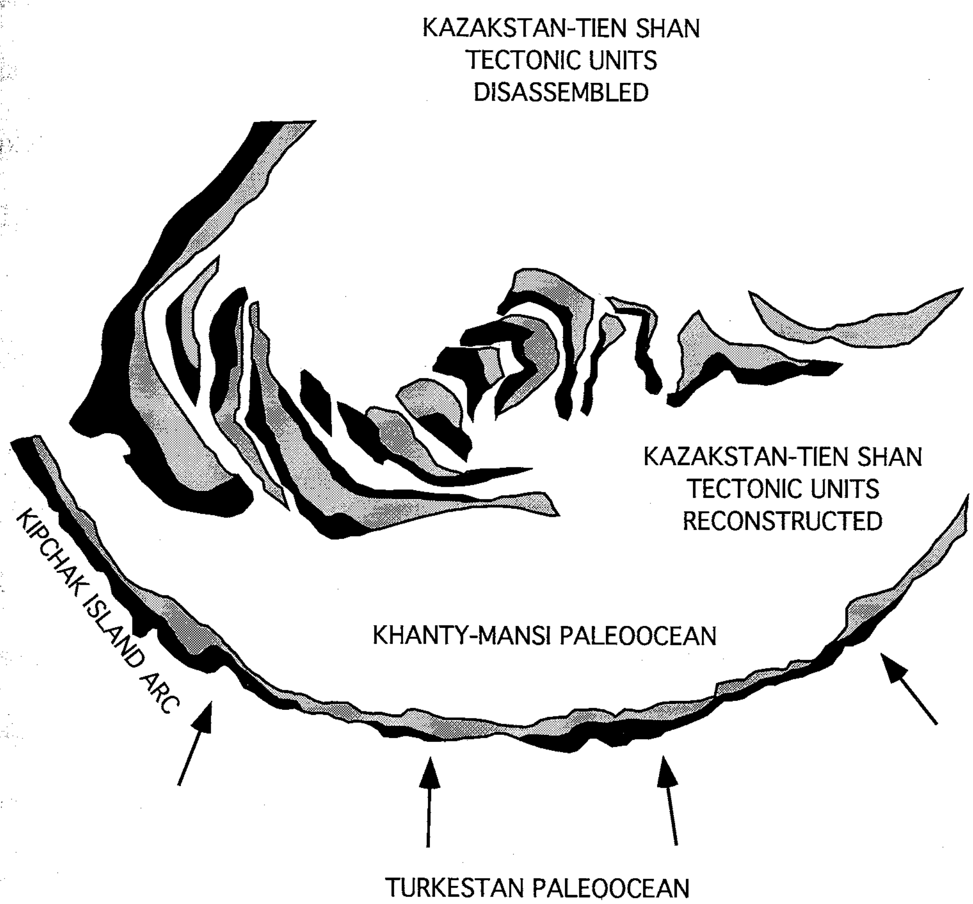

Fig 2.3. Paleotectonic reconstruction of Kazakstan-Tien Shan orogen after Sengör and Natal'in (1996 a, b) and Sengör et al. (1993). Black-subduction-accretion complexes, gray-fragments of Precambrian continental crust, arrows-direction of subduction.

imply more complex, multi-stage amalgamation of independent microcontinental terranes and island arcs at the active margin of a paleoocean (e. g., Zonenshain et al. 1990; Mossakovsky et al. 1993). In spite of differences in details, there is general agreement that throughout most of the Paleozoic, the Kazakstan-Tien Shan orogen was gradually assembled and deformed at the convergent margin of a paleooceanic basin. This regime lasted until the Late Paleozoic, when the basin was closed and the Kazakstan-Tien Shan plate collided with the Tarim-Karakum and Tadjik continental masses (Zonenshain et al., 1990). The present alpine topography is a result of the Cenozoic India-Asia collision.

Regional tectonic setting

On a smaller scale, the Solton Sary district is situated at the southern flank of the Kyrgyz-Teskei zone (Mikolaichuk et al., 1997; Lomize et al., 1997) that constitutes the southern margin of the North Tien Shan block (or microcontinent) (Fig. 2.4). The stratigraphy of the Kyrgyz-Terskei zone comprises Upper Proterozoic rift-related volcanics and passive margin carbonates and clastics that are overlain by Cambrian-Ordovician, largely arc-related volcanogenic successions, with subordinate olistostromes and turbidites as well as scattered ophiolites (Lomize et al., 1997; Mikolaichuk et al., 1997). Stratified units are deformed and intruded by vast, predominantly Ordovician granitoid batholiths (Mikolaichuk et al., 1997).

To the north, the Kyrgyz-Terskei zone is flanked by the Proterozoic Issyk-Kul' crystalline massif (Mikolaichuk et al., 1997) that is also a part of the North Tien Shan microcontinent. In the south, the Kyrgyz Terskei zone and the North Tien Shan as a

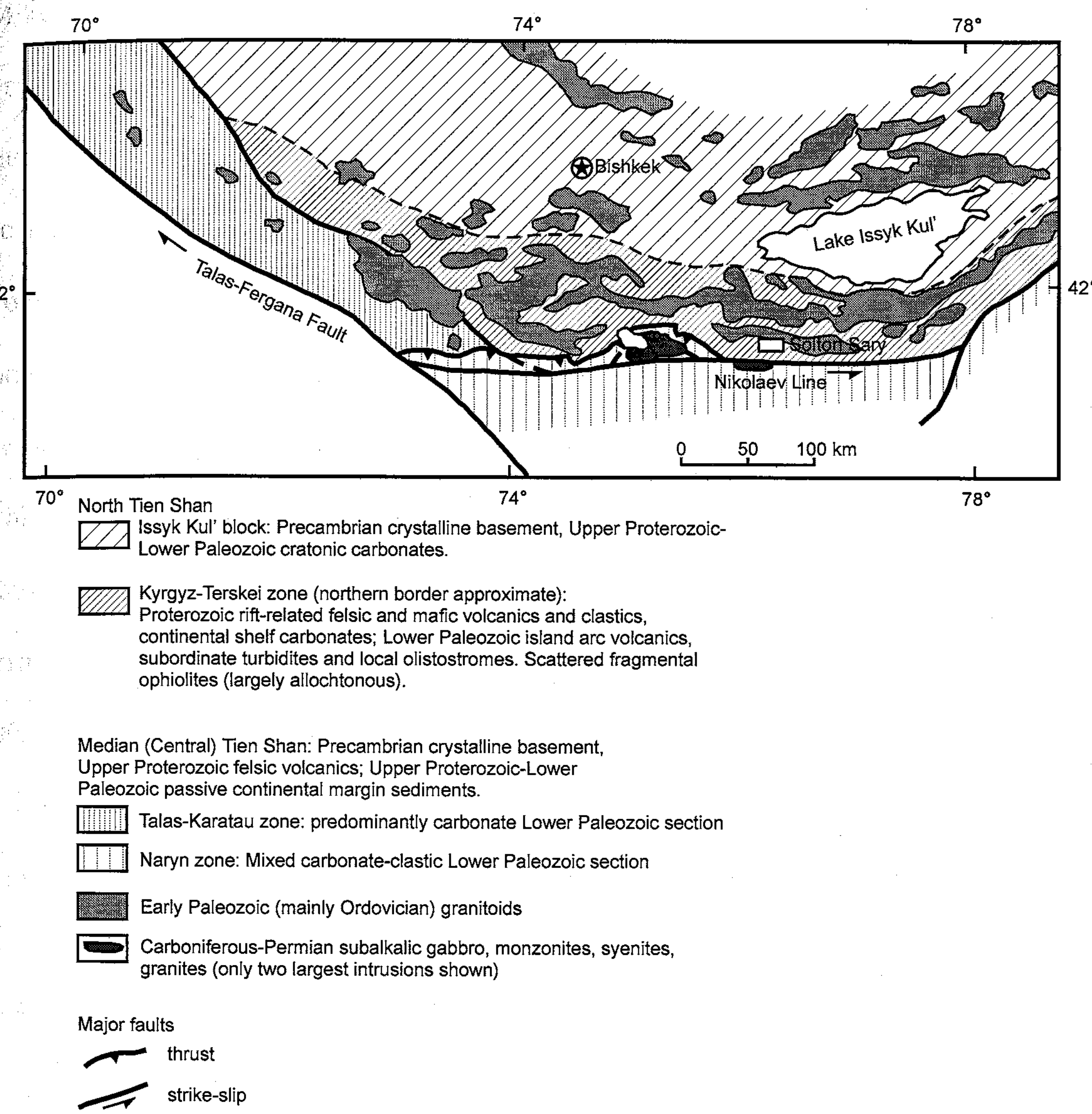

Fig. 2.4. Major tectonic divisions of North-Median Tien Shan junction (based on Proterozoic-Early Paleozoic stratigraphy). Compiled from Lomize et al. (1997) and Mikolaichuk et al. (1997).

whole border on the Median (Central) Tien Shan block (microcontinent) that is characterized by essentially non-volcanogenic Lower Paleozoic stratigraphy (Mikolaichuk et al., 1997; Lomize et al., 1997). The Naryn zone of the Median Tien Shan is situated immediately to the south of the Solton Sary district and comprises mainly clastic Lower Paleozoic sediments. The Talas-Karatau zone of the Median Tien Shan, located about 150 km to the west possesses a distinctive, predominantly carbonate Upper Proterozoic-Lower Paleozoic stratigraphic section (Mikolaichuk et al., 1997; Makarychev and Ges', 1981). The southern border of the North Tien Shan corresponds to a major regional strike-slip fault known as the Nikolaev Line (e. g., Solov'ev, 1995; Mikolaichuk et al., 1997; Kudrin et al., 1990). In addition to separating blocks with contrasting stratigraphic sections, it is also marked by a chain of relatively small Carboniferous-Permian intrusions of subalkalic gabbro, monzonites, syenites, and granites (Solov'yev, 1995).

Mikolaichuk et al. (1997), Lomize et al. (1997), and Makarychev and Ges' (1981) explain stratigraphic differences between the North and Median Tien Shan blocks by the existence of a paleooceanic basin between the two. This basin had a convergent margin with the North Tien Shan and passive with the Median Tien Shan. It was closed sometime in Late Ordovician-Silurian when the two blocks collided. This collision resulted in the termination of marine sedimentation, deformation, and emplacement of thrust sheets from the Talas-Karatau zone over the Kyrgyz-Terskei zone (Mikolaichuk et al., 1997). Some of the granitoids hosted in the Kyrgyz-Terskei zone may be related to this collision rather than to subduction. Sengör with co-authors (e. g., Sengör and Natal'in, 1996a, b) recognize the Late-Ordovician-Silurian tectonic event, although they interpret it differently. According to their interpretation, during this period, the Kipchak volcanic arc experienced longitudinal shortening. The segments of the arc were displaced in strike-slip fashion and "stacked" to form the Kazakstan-Tien Shan tectonic collage. As a result of Late Ordovician-Silurian collisional tectonism, the Kazakstan-Tien Shan orogen emerged as a coherent tectonic unit (e. g., Zonenshain et al., 1990).

Geologic setting

The simplified geologic map adapted from Mikolaichuk et al. (1997) illustrates the geologic setting of the Solton Sary district (Fig. 2.5). Solton Sary is situated immediately to the south of the Ordovician batholith belt and about 5-7 km north of the Nikolaev Line (a strike-slip fault between the North Tien Shan and Median Tien Shan). The district corresponds to the northern limb of a syncline that consists mainly of Cambrian-Ordovician volcanogenic and clastic rocks. The core of the structure comprises carbonate rocks that are most likely allochtonous and were derived from the Talas-Karatau zone. Devonian-Carboniferous terrestrial clastic rocks top the section.

Summary of major tectonic events

Figure 2.6 summarizes the chronology of Paleozoic-Early Mesozoic tectonic events that are potentially important for reconstructing the tectonic setting and post-mineralization history of the Solton Sary district. In spite of uncertainties due to a lack of precise geochronologic data, two major tectonic cycles can be outlined. The first comprises Cambrian-Ordovician arc evolution that ended by Late Ordovician-Silurian

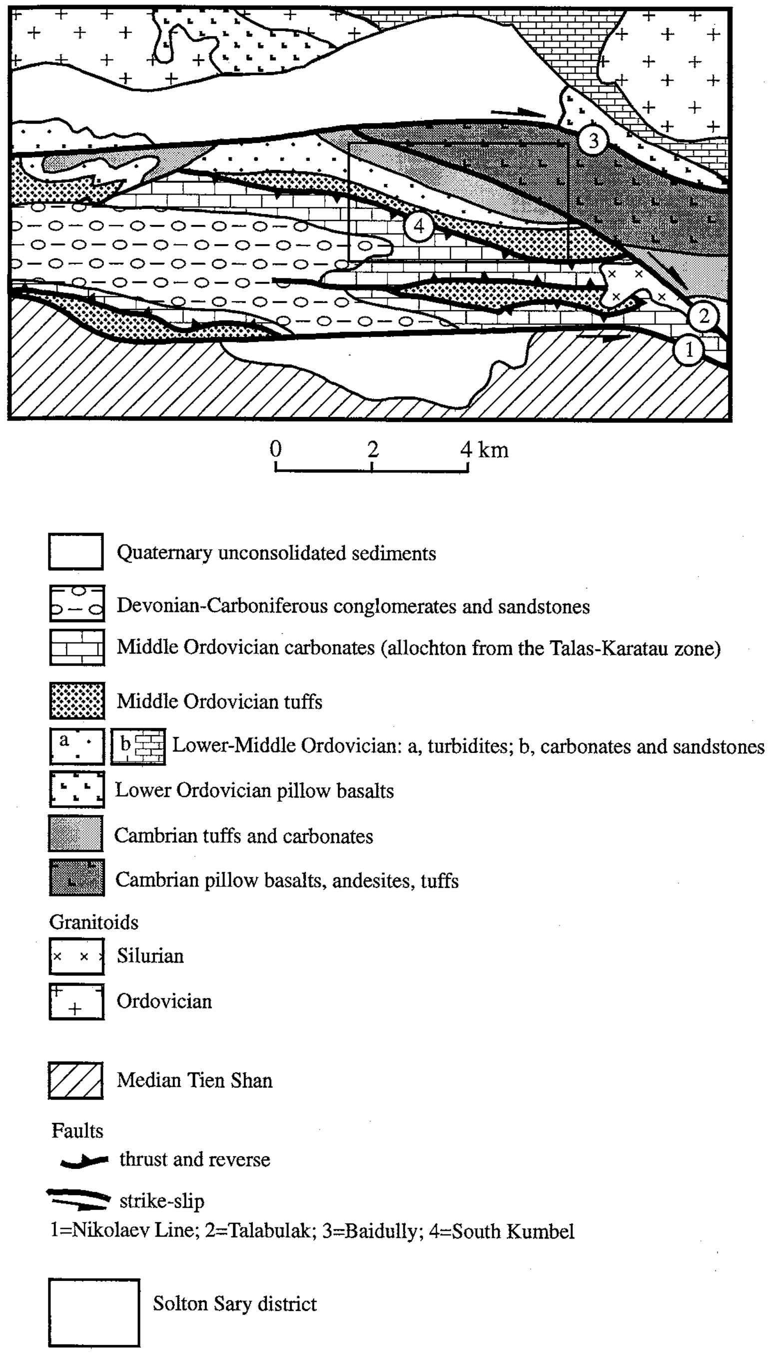

Fig. 2.5. Simplified geologic map of the Solton Sary area. Adapted from Mikolaichuk et al. (1997).

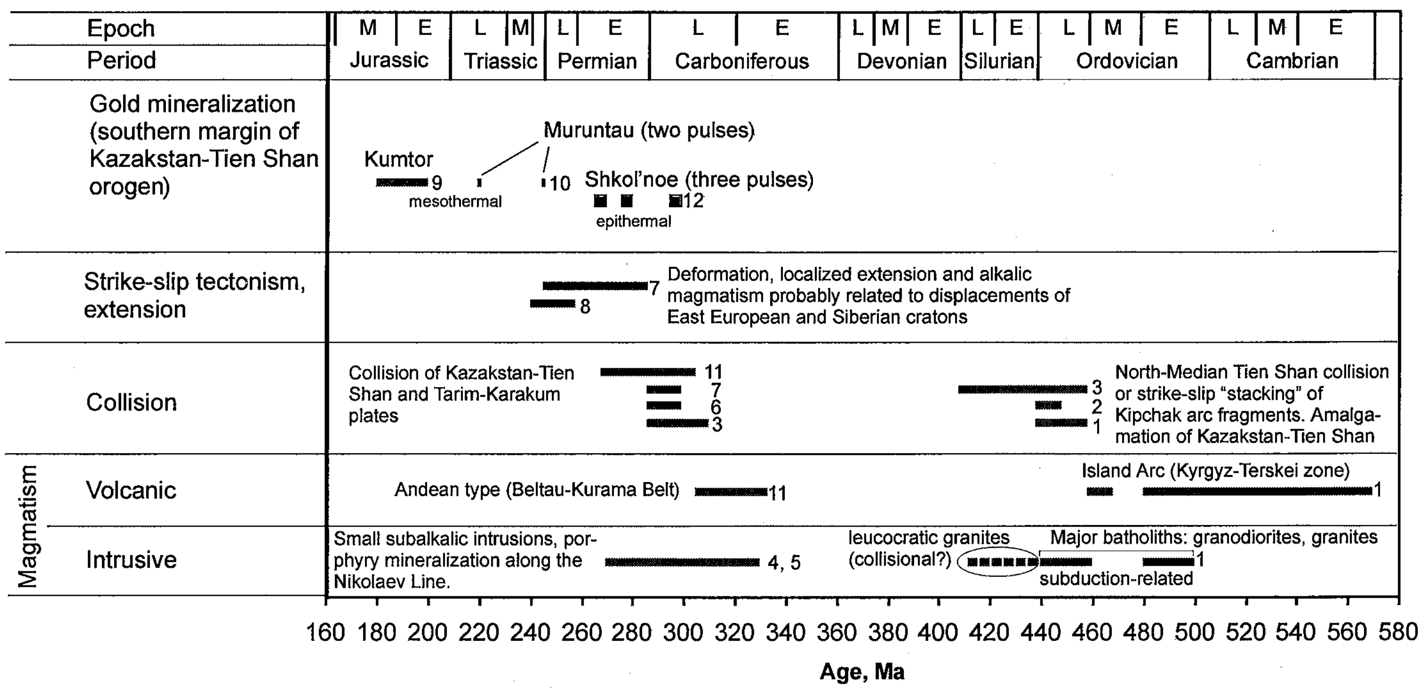

1, Mikolaichuk et al. (1997); 2, Lomize et al.(1997); 3, Sengör and Natal'in (1996a,b); 4 Kudrin et al. (1990); 5, Solov'yev (1995); 6, Burtman et al.(1998); 7, Bazhenov and Burtman (1997); 8, Allen et al. (1995); 9, Nikonorov (1993); 10, Wilde at al. (2001); 11, Zonenshain et al.(1990); 12, Moralev and Shatagin (1999).

Fig. 2.6. Compiled chronology of major geologic events. (Focuses on events experienced by the Kyrgyz-Terskei zone and several adjacent tectonic units). Epochs: E=early, M=middle, L=late.

collisional tectonism and formation of the Kazakstan-Tien Shan collage. It is unclear if this tectonic activity terminated in the Silurian or extended into the beginning of the Devonian.

The second cycle started some time in the Devonian and lasted to the Late Carboniferous-Early Permian. It involved subduction of oceanic crust under margins of the newly assembled Kazakstan-Tien Shan plate (Sengör et al., 1993; Sengör and Natal'in., 1996a, b; Zonenshain et al., 1990). To the west of the Solton Sary area (in present day coordinates), subduction-related, Andean-style volcanism was particularly intense during the Serpukhovian-Bashkirian time of the Carboniferous (ca. 330-310 Ma), when the vast Valerianovsky and Beltau-Kurama volcanic belts were formed (Zonenshain et al., 1990). Subduction ended in the Late Carboniferous-Permian when the Kazakstan Tien Shan collided with the Tarim-Karakum and Tadjik landmasses (e. g., Zonenshain et al., 1990). The collision resulted in deformation, faulting and reactivation of older structures. The subalkalic plutons clustering along the Nikolaev line may be a product of subduction volcanism (Solomovich, personal communication), and some of the intrusions may be related to the collision. In Permian-Triassic time the region experienced additional deformation, localized extension and alkalic magmatism that were likely caused by displacements or rotations of East European (Russian) and Siberian cratons (e. g., Allen et al., 1995).

Timing of gold mineralization

The southern flank of the Kazakhstan-Tien Shan orogenic system and portions of the Paleozoic Tarim, Karakum and Tadjik microcontinents adjacent to the south constitute one of the richest metallogenic provinces of Eurasia. The province comprises a number of world-class mesothermal gold deposits (e. g., Muruntau, Zarmitan, Kumtor), large gold-bearing molybdenum, tungsten, and copper porphyry systems, and several high and low sulfidation epithermal gold deposits (e. g., Anonymous, 1997; Berger et al., 1994; Drew et al, 1996; Kudrin et al., 1995; Moralev and Shatagin, 1999). Relationships between gold mineralization and major regional tectonic events are not fully understood. The largest gold deposits are believed to be broadly related to the Carbonifeous-Permian plate convergence (e. g., Berger et al., 1994). Indeed, epithermal and porphyry systems that are associated with Carboniferous-Permian intrusions and volcanics are likely to be genetically linked to the Late Paleozoic subduction or collisional magmatism. Even though reliable radiometric age determinations are extremely rare, geologic relationships constrain the timing of mineralization, at least to a "period-epoch" scale.

Simple extrapolation of these temporal relationships to mesothermal systems is problematic. For mesothermal deposits, fluid sources are not readily apparent and links to mapped or geophysically detected magmatic centers are somewhat speculative. The direct geologic relationship (e. g., "stratigraphic" ages of host rocks affected by alteration) often provide only loose time constraints. Very few radiometric dates are available and most of them fail to unequivocally constrain the mineralization age.

Recently, Wilde et al. (2001) reported new $^{40}Ar/^{39}Ar$ dates for the mesothermal Muruntau deposit (the largest in Eurasia) and concluded that there were two mineralizing episodes at ca. 220 and 245 Ma. However, $^{40}Ar/^{39}Ar$ results are rather complex, and the suggested interpretation is not unique. The two sericite age spectra that were presented to constrain the timing of hydrothermal activity show ^{40}Ar loss and oldest step ages of ca. 250 Ma. A 25 m.y. difference in reported "plateau" ages may reflect post-crystallization isotopic resetting of variable intensity, rather than the episodic occurrence of mineralizing events. The bulk of Muruntau mineralization is hosted in Cambrian-Ordovician turbidites, and the youngest rocks affected by hydrothermal processes are Devonian carbonates (Drew et al., 1996).

Geochronologic information available for the second largest gold deposit of Tien Shan, Kumtor, includes "radiometric age of sericite 180-210 Ma" and "age of lead from auriferous pyrite 200-280 Ma," as reported by Nikonorov (1993). The youngest host rocks affected by mineralization at Kumtor are Early Carboniferous in age.

Even though the assumption of a Late Carboniferous-Early Permian age for most economically significant gold deposits of the Tien Shan province appears geologically feasible, it still needs to be constrained by high-quality geochronologic data. Without systematic geochronologic studies, it would not be possible to generate a reliable metallogenic model for the region.

CHAPTER 3

GEOLOGY OF THE SOLTON SARY DISTRICT

Introduction

This largely descriptive chapter introduces the geology of the Solton Sary district and provides background for more specialized chapters that focus on the geochemistry of intrusive rocks, deformation styles, $^{40}Ar/^{39}Ar$ geochronology, and fluid inclusion studies. The primary focus is on geologic features that are essential for interpretation of the analytical data. The chapter summarizes original field observations and relevant petrographic and electron microprobe data.

The stratigraphy was studied by measuring a detailed section in the central portion of the district where outcrops are most representative. After stratigraphic units were defined, they were traced to the poorer exposed flanks of the district. Intrusive rocks were studied and sampled in natural outcrops, exploration trenches and drill core. Most information on the internal structure of the intrusive belt was collected by measuring detailed sections in outcrops and trenches. Drill core was less informative, but provided better, unweathered, samples for petrographic, geochemical and geochronologic studies.

Mineralization of the Solton Sary district is poorly exposed. Old exploratory underground workings are currently inaccessible. The economically valuable mineralized zones were delineated by core drilling in the central-west portion of the district (Buchuk area, Fig. 3.1). The advantage of the drill core is the availability of assay data and the possibility to correlate geologic observations and gold grades. However, only limited information on the structural setting of the mineralization and the morphology of

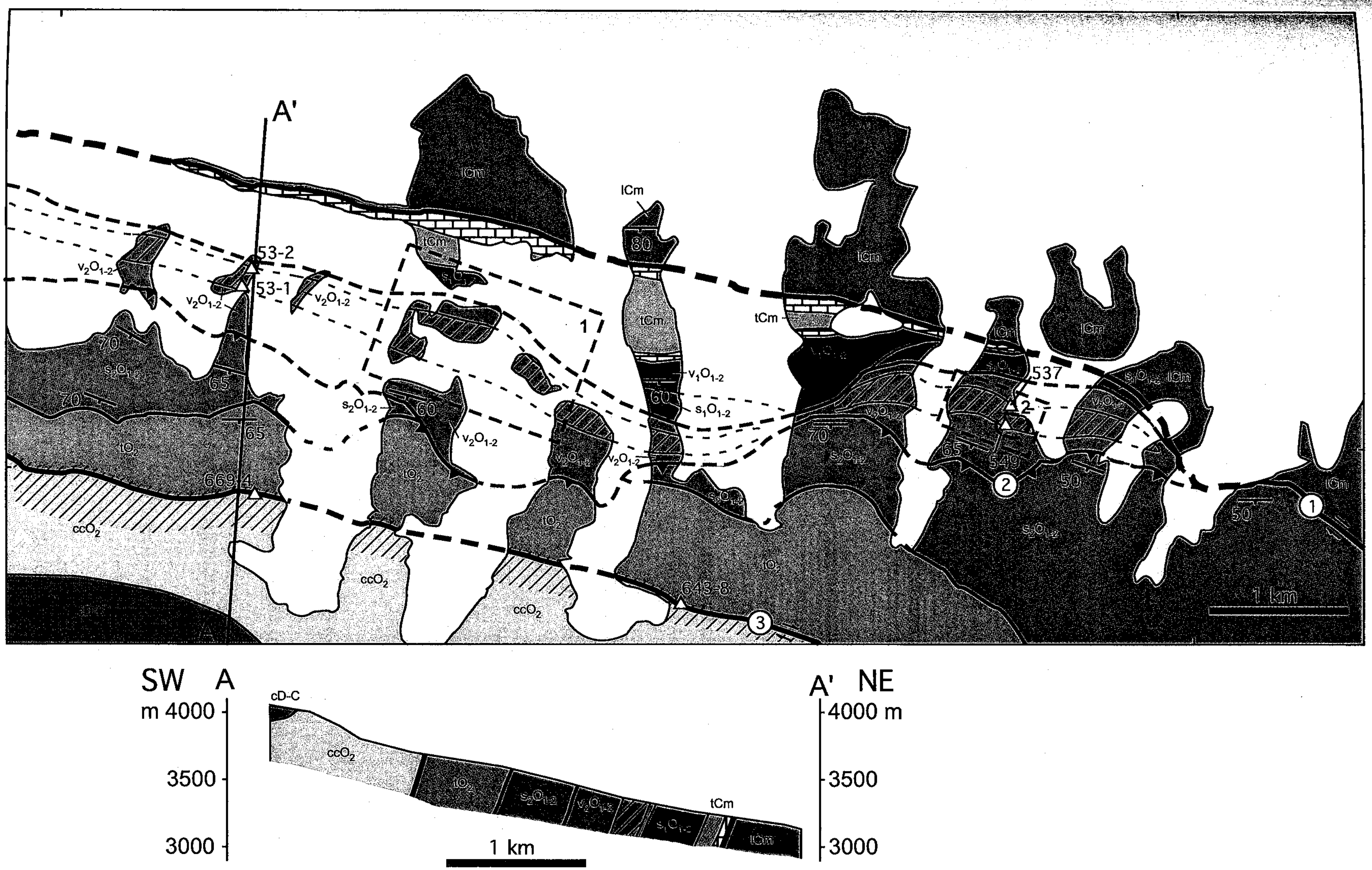

Fig. 3.1. Generalized geologic map of the Solton Sary district. See next page for the legend.

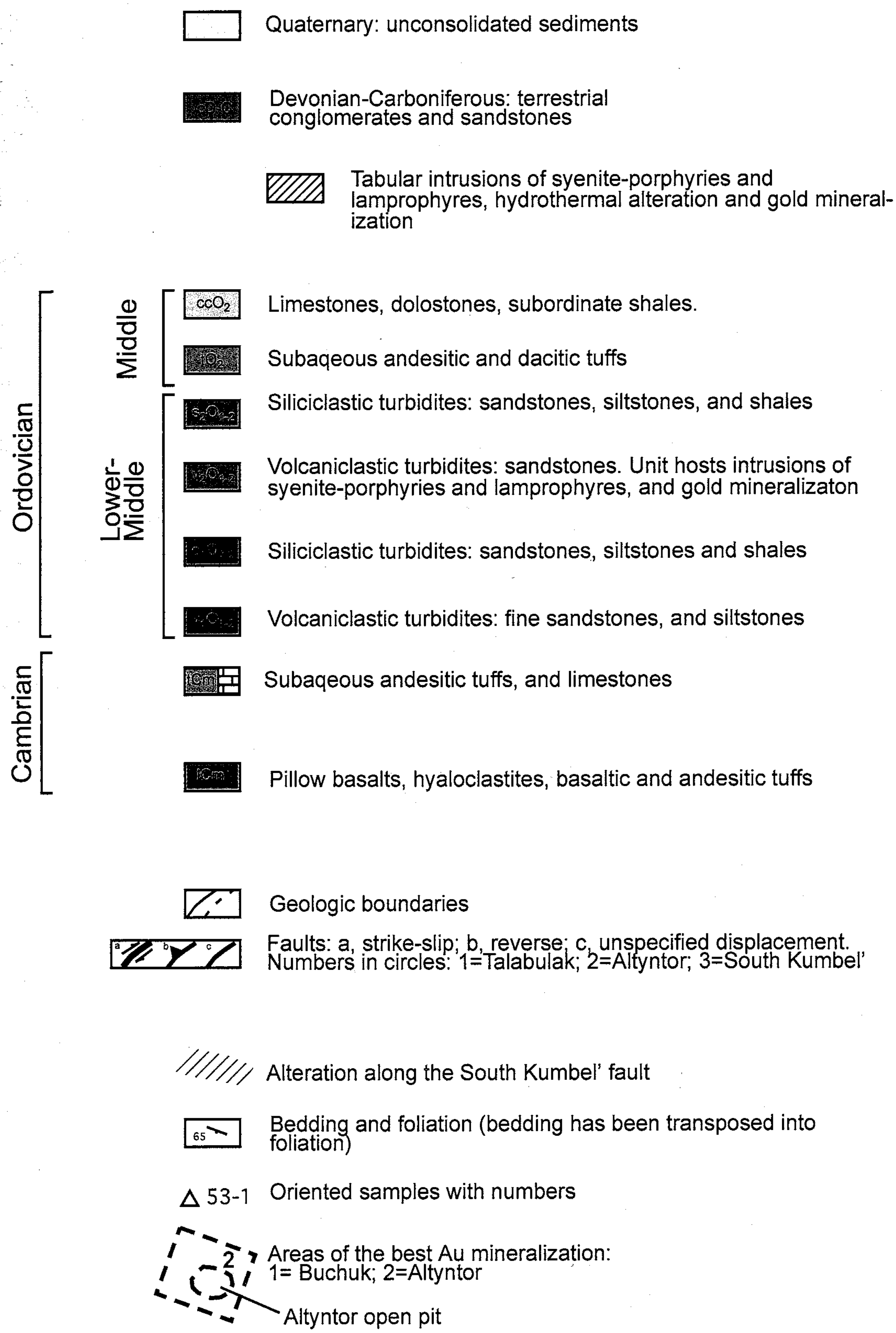

Fig. 3.1. (Continued from previous page). Legend for the generalized geologic map of the Solton Sary district.

auriferous zones can be derived from the core. Representative outcrops of mineralization are confined to the small Altyntor open pit on the eastern flank of the district (Figs. 3.1 and 3.2). Mineralized zones uncovered in the pit are smaller than the best zones delineated by drilling. Detailed assay data are not available, however high gold grades are confirmed by frequent occurrences of visible gold. The data on the Solton Sary mineralization were collected mainly through the detailed (1:5,000 scale) mapping of the Altyntor open pit, and logging drill core from one drilling profile in the central part of the district. The observed and sampled mineralized zones may not be the largest, but they possess high gold grades and reasonable volumetric parameters and thus are representative of the mesothermal mineralization of the Solton Sary district. Geologic maps that are based on fieldwork results are presented in Figures 3.1 and 3.2. A description of the geology follows.

Stratigraphy

The stratigraphic model of the Solton Sary district was developed during the summer of 1998. It is generally compatible with the pre-existing stratigraphic scheme (Mikolaichuk et al., 1997; Kheraskova et al., 1997) that was used by Soviet and Kyrgyzstani geologists for 1:50,000 geologic mapping and broad regional correlations (Fig. 3.3). The new stratigraphic model was designed for district-scale mapping and based mainly on compositional criteria. A primary focus was placed on the ore-hosting Early-Middle Ordovician turbiditic succession that was split into four units. These units are distinguished by contrasting proportions of clastic quartz and feldspar, and the

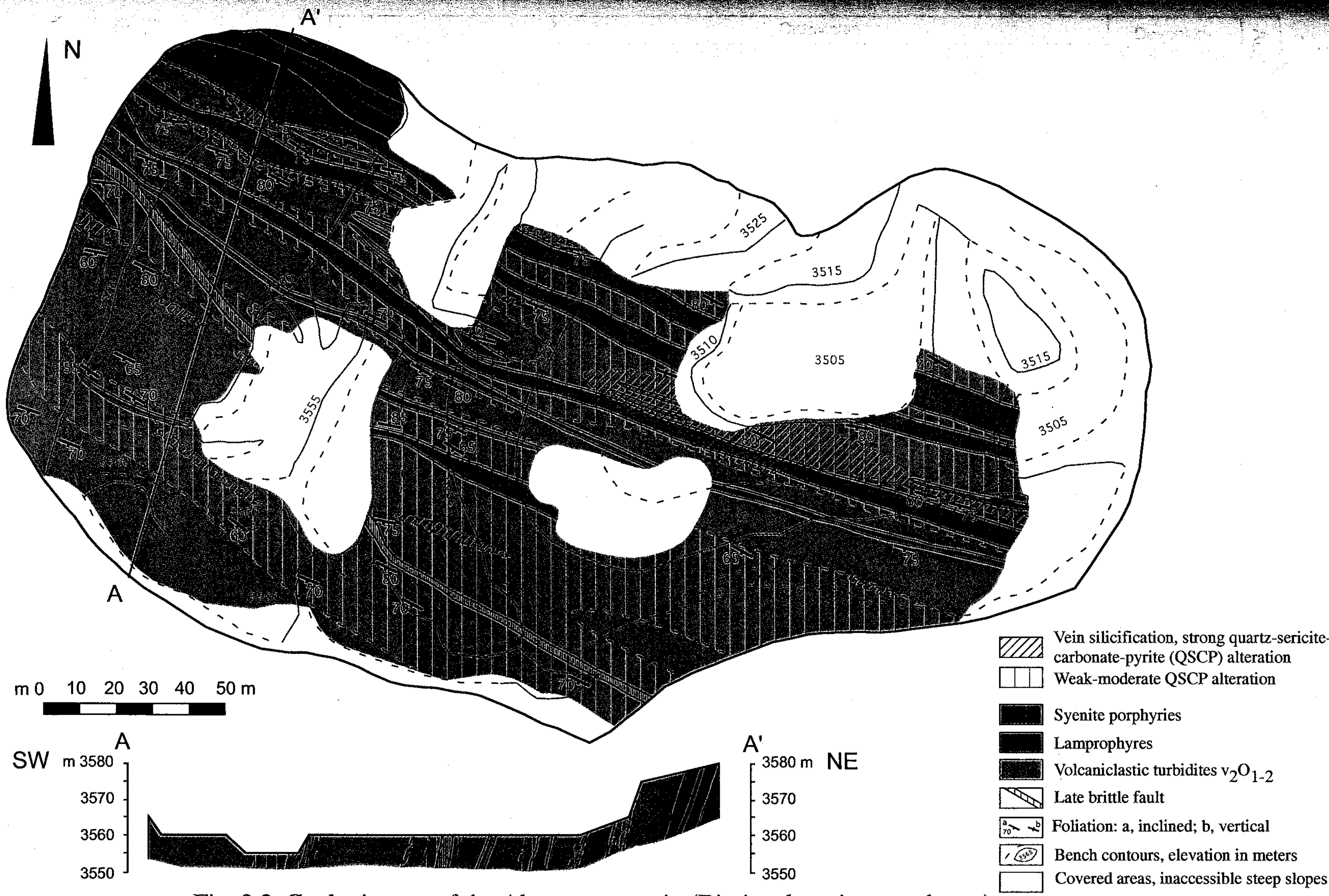

Fig. 3.2. Geologic map of the Altyntor open pit. (Biotite alteration not shown).

Age		Maximum thickness (m)		Description	Map unit	Symbol	Units of Mikolaichuk et al. (1997) and Kheraskova et al. (1997)
Devonian-Carboniferous		> 5000[1]		Massive and thickly bedded pebble conglomerates and subquartzose feldspatholitic sandstones. Pebbles: underlying limestones (in the bottom portion), cherts, quartz, sandstones, granitoids, and volcanics.	cD-C	● (grey)	Koktaiskaja suite
Ordovician	Middle	1000		Limestones, dolostones, subordinate shales in the bottom portion.	ccO_2		Karagyrskaja suite
Ordovician	Middle	780		Massive to medium bedded crystal and lithic-crystal tuffs of andesitic and dacitic composition. The upper part consists predominantly of pelitic ash tuffs.	tO_2	■ (grey)	Dzhakshinskaja suite
Ordovician	Lower-Middle	800		Siliciclastic turbidites: thinly bedded fine to medium quartzose and semiquartzose feldspathic sandstones with subordinate siltstones and shales. Gradational bedding.	s_2O_{1-2}	●	Dzholdzhilginskaja suite
Ordovician	Lower-Middle	850		Volcanicalstic turbidites: massive to medium-bedded crystal-rich coarse tuffaceous arkose and lithic arkose sandstones with subordinate siltstones and shales. Gradational bedding. Increasing proportion of siltstones and shales in the upper part.	v_2O_{1-2}	○	Dzholdzhilginskaja suite
Ordovician	Lower-Middle	660		Siliciclastic turbidites: thinly to medium-bedded fine subarkose sandstones, subordinate siltstones and shales. Gradational bedding.	s_1O_{1-2}	◐	Dzholdzhilginskaja suite
Ordovician	Lower-Middle	450		Volcaniclastic turbidites: thinly bedded fine lithic arkose sandstones and siltstones. Gradational bedding. Upward increase in quartzose component.	v_1O_{1-2}	◆ (grey)	Dzholdzhilginskaja suite
Cambrian		615		Massive to medium-bedded crystal and lithic-crystal subaqueous andesitic (?) tuffs, limestones, lenses of tuffaceous conglomerates. Layer of coarse quartzose sandstones in the base.	tCm	▲	Techarskaja suite
Cambrian		>3000		Subaqeous massive and pillow basalts, basaltic andesites, andesites. Subordinate hyaloclastites, lapilli and agglomerate tuffs. Upward increase in a relative proportion of pyroclastic rocks.	lCm		Soltonsarinskaja suite Bel'tepshinskaja suite

[1] including adjacent areas, based on unpublished data compiled by Newmont Kyrgyzstan Gold Ltd. Thickness within the district does not exceed 700-800 m.

Faults (mapped and inferred)

Angular unconformity

Approximate stratigraphic setting of gold mineralization

Fig. 3.3. Generalized stratigraphic column of the Solton Sary district and correlation to the regional stratigraphic model (Mikolaichuk et al., 1997; Kheraskova et al., 1997). Symbols correspond to Figure 3.5.

boundaries between them can be identified and traced not only in outcrops, but also in talus, drill core, and reverse circulation drill cuttings. All stratigraphic units are metamorphosed to greenschist facies. However, this regional metamorphism had little effect on primary textures, which still can be identified and interpreted. It permitted the classification of the stratified rocks in primary, pre-metamorphism terms. Geologic ages are compiled from Mikolaichuk et al. (1997), Kheraskova et al. (1997) and Lomize et al. (1997). Some of these ages are supported by local fossil findings, but most are based on correlations with paleontologically characterized stratigraphic divisions of adjacent areas. Reported maximum thickness values are based on measurements within the area that is shown on the geologic map (Fig. 3.1), unless otherwise noted.

Stratigraphic section

The section begins with Cambrian massive and pillow lavas, hyaloclastites, and subordinate lapilli and agglomerate tuffs (Fig. 3.3, lCm) of basaltic, basaltic-andesitic, and andesitic composition. The bottom portion of the unit consists almost entirely of pillow basalts, whereas the upper part contains significant amounts of tuffs. The pillow lavas are grayish-green aphyric or porphyritic with phenocrysts (0.5-1 mm) of plagioclase, and chlorite - epidote pseudomorphs after mafic minerals. The individual pillows are about 0.4-0.8 m long and 0.3-0.4 m thick. Numerous vesicles (1-3 mm) are filled with carbonate, and less commonly by quartz and chlorite. Agglomerate tuffs consist of round, elliptic and flattened volcanic bombs 10-30 cm, up to 50 cm, set in a matrix of altered ash and lapilli. The thickness of the lCm exceeds 3 km, and its base is not exposed within the ore district.

The lowermost, primarily extrusive unit is overlain by a predominantly pyroclastic package, tCm. It comprises Cambrian subaqueous crystal and crystal-lithic, likely andesitic tuffs, tuffaceous conglomerates, and limestones. A 9 m thick layer of quartzose sandstones with carbonate cement marks the bottom of the unit. The tuffs are green massive to medium-bedded rocks. Clastic material consists of angular fragments (0.2-1.5 mm) of plagioclase, volcanic rocks, with sparse quartz and altered mafic minerals. The clasts are enclosed in a matrix of chlorite and epidote, likely representing fine ash that was altered during the greenschist facies metamorphism. Volcaniclastic conglomerates that form 5 to 10 m thick beds consist of rounded fragments of volcanics and granitoids and, less commonly, of limestones and clastic sedimentary rocks. Layers of limestones have thicknesses of 5 to 90 m, and most of them are laterally discontinous. Mikolaichuk et al. (1997) and Kheraskova et al. (1997) report findings of Early Cambrian (Botomian) fossils in the limestones. The maximum thickness of the tCm within the Solton Sary district is 615 m.

Following the tCm, there are Lower-Middle Ordovician turbidites that include two siliciclastic (s_1O_{1-2} and s_2O_{1-2}) and two volcaniclastic (v_1O_{1-2} and v_2O_{1-2}) units. The suggested age of the turbidites is Late Arrhenigian-Llanvirnian (Mikolaichuk et al., 1997). The lower volcaniclastic turbidites (v_1O_{1-2}) comprise grayish-green, thinly bedded, fine tuffaceous arkose sandstones and siltstones. In addition to plagioclase and fragments of volcanics, they contain a significant amount of subrounded quartz that tends to increase upwards. The maximum thickness of the v_1O_{1-2} within the ore district is 450 m.

Lower siliciclastic turbidites (s_1O_{1-2}) overly the v_1O_{1-2}. The unit comprises gray and greenish-gray medium to thinly bedded fine subarkose sandstones, siltstones, and shales. The sandstones consist predominantly of quartz with largely subordinate K-feldspar and plagioclase, and contain accessory zircon and tourmaline. The upper part of the unit is strongly sheared. The maximum observed thickness of the s_1O_{1-2} is 660 m.

The upper volcaniclastic turbiditic unit (v_2O_{1-2}) hosts the gold mineralization of the Solton Sary district. The unit comprises grayish-green massive and medium-bedded coarse tuffaceous arkose and lithic arkose sandstones with smaller amount of siltstones and shales that tend to become more abundant in the upper portion of the unit. The sandstones consist mainly of angular to subrounded plagioclase and quartz, and contain lensoid or flaky fragments (0.5-2 cm) of microcrystalline devitrified volcanic glass, most likely altered pumice. Originally tuffaceous matrix is replaced by metamorphogenic chlorite, epidote, and carbonate, sometimes with sericite. Both the bottom and the top contacts of the unit are tectonic surfaces. Near the contacts, the rocks are strongly sheared and in places show porphyroclastic textures with rather sparse (5-10%) clasts of quartz and plagioclase set in a foliated fine-grained matrix of chlorite, quartz, sericite, and carbonate. The maximum thickness of the upper volcaniclastic turbidites is 850 m.

Upper siliciclastic turbidites (s_2O_{1-2}) comprise gray and greenish-gray, thinly bedded, fine to medium-grained quartzose and semiquartzose feldspathic sandstones, with less abundant siltstones and shales. Lithologically, the rocks are similar to those of the lower siliciclastic unit (s_1O_{1-2}). Maximum thickness of the unit is 800 m. It is laterally discontinuous, and is absent in the central portion of the district.

The Lower-Middle Ordovician turbidites are overlain by Middle Ordovician (Llandeilan, according to Mikolaichuk et al., 1997) andesitic-dacitic tuffs (tO_2). These are green massive and medium-bedded crystal and crystal-lithic tuffs consisting of plagioclase, porphyritic and aphyric volcanics, subordinate quartz, and chlorite and epidote-altered mafic minerals. The clasts are set in a fine ash matrix completely replaced by epidote, chlorite and carbonate. In the lower part of the unit, crystal-rich rocks are predominant, whereas the upper portion contains mostly fine ash tuffs. The maximum thickness is 780 m.

Following the tO_2 tuffs, there are Middle Ordovician limestones and dolostones (cO_2), that are bounded by the South Kumbel fault (Fig. 3.1) and have a maximum thickness of about 1000 m. The carbonate rocks contain subordinate siltstones and shales in their lower part.

The section is capped by Devonian-Carboniferous terrestrial conglomerates and sandstones (cD-C) overlying Middle Ordovician carbonates and tuffs with angular unconformity. The coarse clasts consist of underlying limestones, volcanics, granitoids, sandstones, chert, and quartz. The sand-size fraction comprises fragments of quartz, K-feldspar, plagioclase, volcanic and sedimentary rocks. The detrital grains are overgrown and cemented by chlorite and sericite, sometimes with quartz and carbonate. The thickness of the unit within the ore district is not more than 1000 m, but within adjacent areas it exceeds 5000 m (unpublished data compiled by Newmont Kyrgyzstan).

Most of the stratigraphic units, particularly the Lower-Middle Ordovician turbidites, exhibit highly variable thicknesses (Fig. 3.4). The ore-hosting volcaniclastic unit (v_2O_{1-2}) reaches maximum thickness of 650-660 m within the eastern and western portions of the

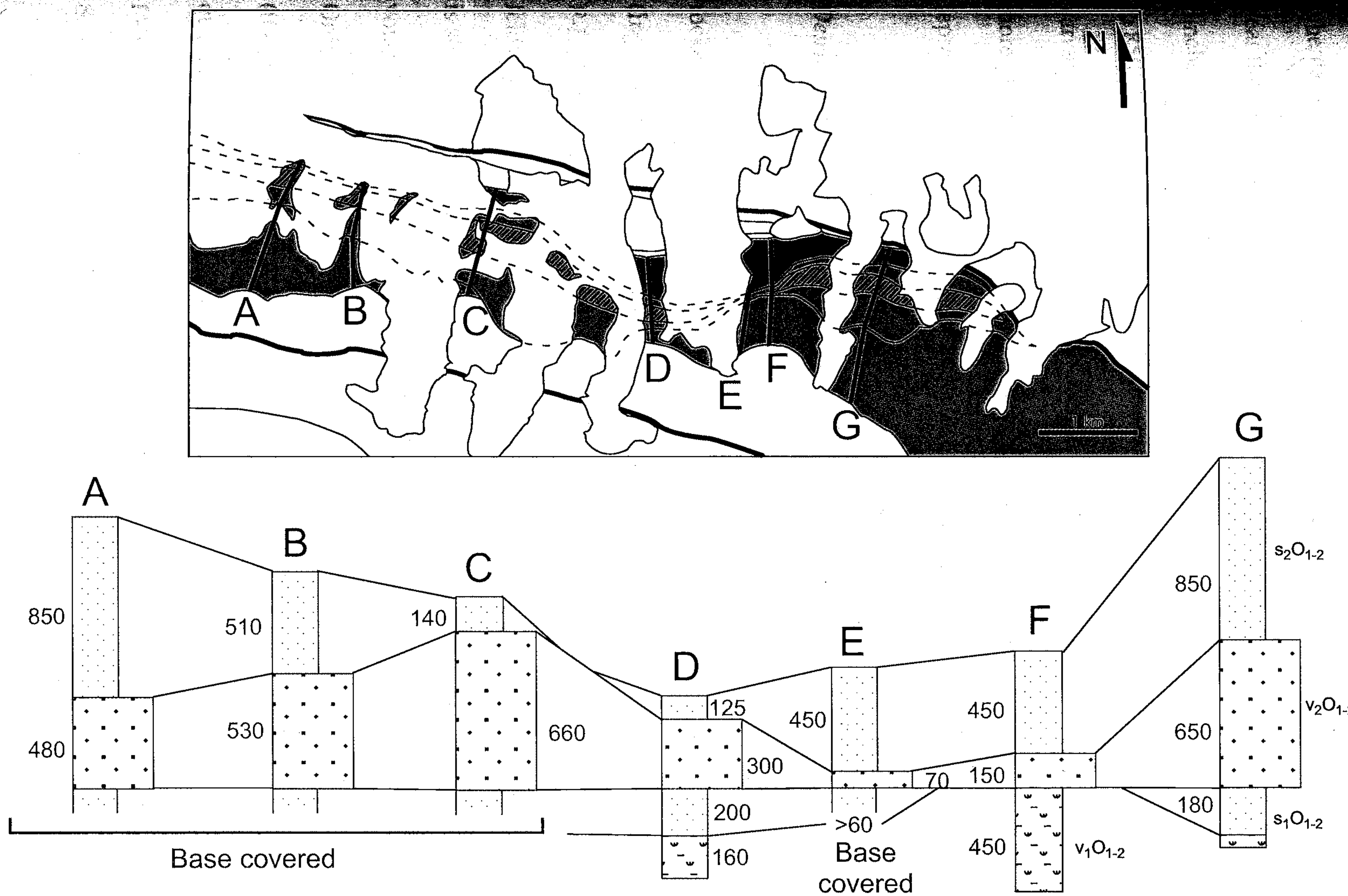

Fig. 3.4. Variation of thickness (meters) of Lower-Middle Ordovician turbiditic units.

district roughly corresponding to Buchuk and Altyntor areas (sections C and G, Fig. 3.4), whereas in the middle (section E, Fig. 3.4) it is only 70 m thick. It tapers out completely near the eastern border of the ore district (Fig. 3.1). The upper siliciclastic unit (s_2O_{1-2}) pinches out in the middle of the Solton Sary trend (sections C and D, Fig. 3.4) and swells to 850 m at its eastern and western terminations (sections A and G, Fig. 3.4). Such strong variations over short distances are unlikely to reflect irregularities of deposition, and are more probably related to later tectonism. Laterally impersistent stratigraphic units represent fault-bounded stratiform tectonic blocks (slices) rather than undisturbed strata.

Detrital modes and geochemistry

To provide an unbiased characterization of the composition of pyroclastic and detrital rocks, a total of 29 thin sections were point-counted using the Gazzi-Dickinson method (Ingersoll et el., 1984; Dickinson, 1985). The counts were recalculated and plotted on Qt-F-L (Total Quartz-Feldspar-Lithic fragments) and Qt-P-K (Plagioclase-Total Quartz-K-feldspar) ternary diagrams (Table 3.1; Fig. 3.5). In Cambrian tuffs (tCm), clastic material is strongly dominated by plagioclase along with aphyric and less commonly porphyritic volcanics. Quartz is much less abundant, and K-feldspar is absent. Lower-Middle Ordovician volcaniclastic sandstones (v_1O_{1-2} and v_2O_{1-2}) and Middle Ordovician tuffs (tO_2) have a similar detrital assemblage, but with a distinctly higher relative proportion of quartz. In siliciclastic sandstones, the total content of feldspar grains does not exceed 21 percent. Plagioclase is commonly accompanied by "scotch plaid" twinned microcline. Sandstones from the Devonian-Carboniferous terrestrial clastic succession (cD-C)

Table 3.1. Composition of clastic rocks of the Solton Sary district

Sample	Unit	Rock	N	Qt-F-L Qt%	Qt-F-L F%	Qt-F-L L%	Qt-K-P Qt%	Qt-K-P K%	Qt-K-P P%	Qm-K-P Qm%	Qm-K-P K%	Qm-K-P P%	%matrix	Lv/L	P/F
643-3	tO_2	tuff	650	32.0	57.7	10.3	35.7	0.7	63.6	18.2	0.9	80.9	48.6	1.00	0.99
643-1	tO_2	tuff	440	30.4	65.5	4.2	31.7	0.0	68.3	14.9	0.0	85.1	28.9	0.92	1.00
643-7	tO_2	tuff	456	1.4	65.6	33.0	2.1	2.1	95.8	1.3	2.1	96.6	22.8	1.00	0.98
663-1	tO_2	tuff	353	20.6	44.9	34.6	31.4	3.3	65.2	35.9	3.6	69.9	9.1	0.97	0.95
642-6	v_2O_{1-2}	sandstone	450	35.2	52.4	12.4	40.1	0.4	59.5	30.9	0.4	68.7	31.8	0.89	0.99
IIR6-6	v_2O_{1-2}	sandstone	480	35.2	58.0	6.8	37.8	1.4	60.8	30.7	1.6	67.7	35.0	0.62	0.98
663-3	v_2O_{1-2}	sandstone	500	42.0	42.6	15.4	49.7	1.0	49.3	34.1	1.3	64.6	27.2	0.91	0.98
665	v_2O_{1-2}	sandstone	500	37.8	54.3	7.8	41.0	3.0	55.9	29.5	3.6	66.9	23.6	0.86	0.95
650-1	v_2O_{1-2}	sandstone	600	29.1	56.9	14.0	33.9	0.0	66.1	27.7	0.0	72.3	50.0	1.00	1.00
642-3	v_2O_{1-2}	sandstone	600	46.5	48.5	5.0	48.9	0.0	51.1	41.8	0.0	58.2	43.0	0.94	1.00
642-4	v_2O_{1-2}	sandstone	600	46.7	48.9	4.4	48.8	0.7	50.5	45.2	0.7	54.1	47.2	1.00	0.99
642-2	v_2O_{1-2}	sandstone	550	36.4	59.3	4.3	38.1	0.7	61.2	33.7	0.7	65.6	45.1	1.00	0.99
639-4	s_1O_{1-2}	sandstone	500	77.5	20.5	2.0	79.1	12.2	8.7	73.4	15.5	11.1	29.8	1.00	0.42
639-2	V_1O_{1-2}	sandstone	799	28.0	39.0	32.9	41.8	8.2	50.0	38.5	8.7	52.9	58.2	0.99	0.86
663	S_2O_{1-2}	sandstone	395	80.5	16.1	3.4	83.3	7.7	9.0	77.6	10.3	12.1	18.2	1.00	0.54
642-5	S_2O_{1-2}	sandstone	498	92.7	7.1	0.3	92.9	2.2	4.9	89.4	3.3	7.3	26.1	0.00	0.69
674-1	S_2O_{1-2}	sandstone	500	87.3	11.1	1.5	88.7	7.0	4.3	84.1	9.9	6.0	33.6	1.00	0.38
651	S_2O_{1-2}	sandstone	498	87.8	11.3	0.9	88.6	3.5	7.9	84.5	4.8	10.7	30.9	1.00	0.69
651-2	S_2O_{1-2}	sandstone	400	90.4	9.6	0.0	90.4	0.0	9.6	87.9	0.0	12.1	22.3	N/A	1.00
636	tCm	sandstone	500	94.2	5.5	0.3	94.5	0.0	5.5	91.7	0.0	8.3	34.2	1.00	1.00
638-10	tCm	tuff	500	0.6	48.6	50.8	1.2	0.0	98.8	0.0	0.0	100.0	33.4	1.00	1.00
638-7	tCm	tuff	421	0.3	63.6	36.1	0.5	0.0	99.5	0.5	0.0	99.5	23.0	1.00	1.00
639	tCm	tuff	444	0.3	67.0	32.7	0.4	0.4	99.1	0.0	0.4	99.6	23.0	1.00	1.00
638-8	tCm	tuff	460	9.9	69.4	20.7	12.5	0.0	87.5	11.8	0.0	89.5	25.4	1.00	1.00
638-2	tCm	tuff	429	0.0	52.5	47.5	0.0	0.0	100.0	0.0	0.0	100.0	25.4	1.00	1.00
676-3	cD-C	sandstone	327	47.2	27.0	25.7	63.6	25.9	10.5	118.7	28.1	11.4	6.1	0.52	0.29
675-3	cD-C	sandstone	350	48.6	30.7	20.7	61.3	28.7	10.0	58.8	30.6	10.6	6.0	0.22	0.26
676	cD-C	sandstone	350	52.5	30.4	17.2	63.3	27.8	8.9	60.6	29.9	9.6	6.9	0.45	0.24
676-4	cD-C	sandstone	350	43.9	28.7	27.5	60.5	32.9	6.6	56.8	36.0	7.2	4.3	0.47	0.17

Qm-monocrystalline quartz, Qt=total quartz, P=plagioclase, K=K-feldspar, F=plagioclase+K-feldspar, Lv=volcanic lithic fragments, L=all lithic fragments.

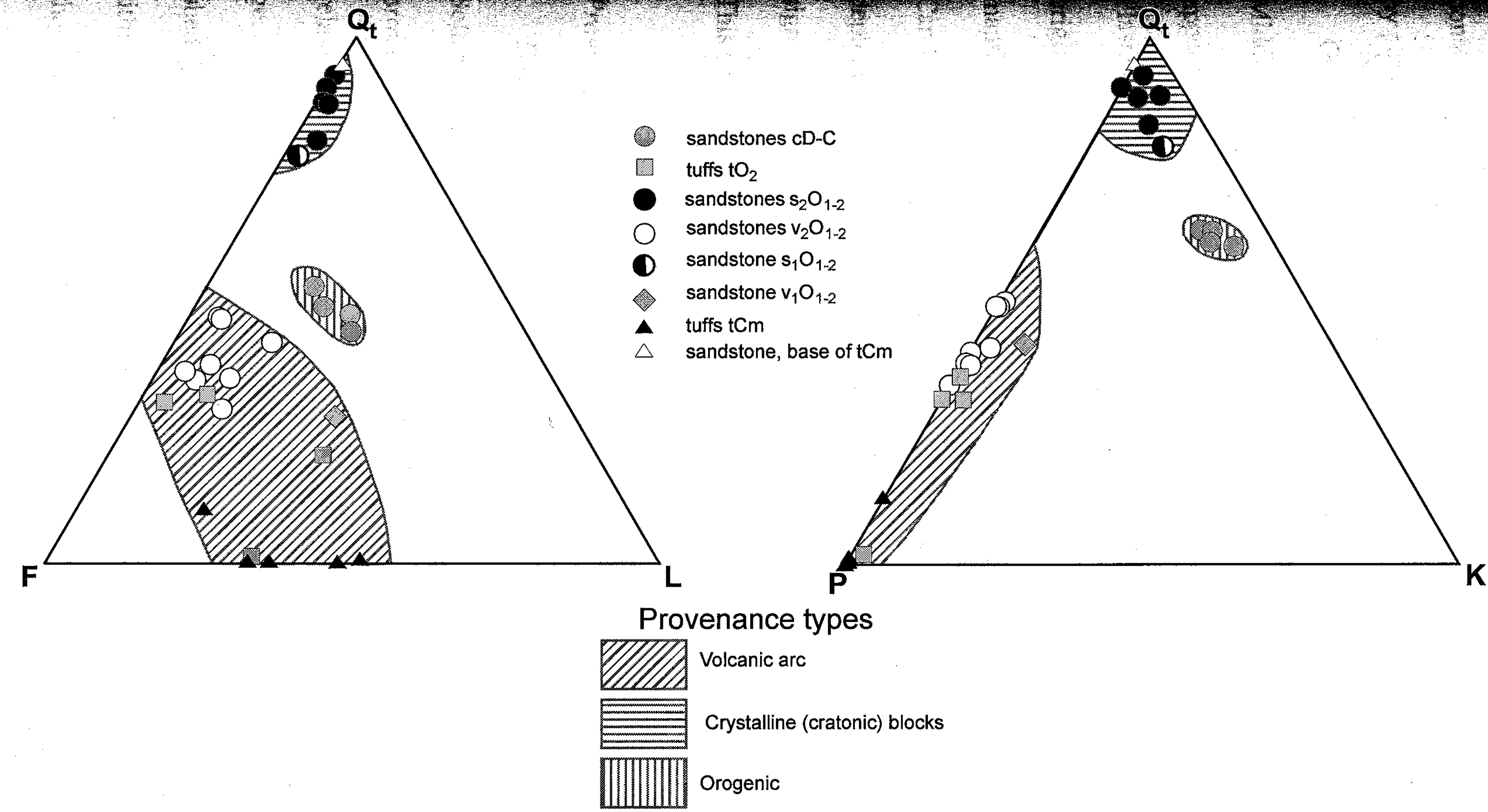

Fig. 3.5. Composition and provenance types of clastic rocks of the Solton Sary district (see Table 3.1 for the data). Q_t-total quartz, F-feldspars (plagioclase+K-feldspar), L-lithic fragments, P-plagioclase, K-K-feldspar.

contain abundant fragments of sedimentary rocks and volcanics. Feldspars are dominated by perthitic K-feldspars likely of granitic origin.

Geochemical data are limited to five samples: one is of Cambrian tuffs (tCm), one of Middle Ordovician tuffs (tO_2) and three from ore-hosting Lower-Middle Ordovician upper volcaniclastic turbidites (v_2O_{1-2}). Samples were analyzed by Inductively Coupled Plasma Mass Spectrometry (ICP-MS) at Actlabs Skyline in Tucson, Arizona. The original analytical report is presented in Appendix A. Figure 3.6A shows primitive mantle normalized plots of incompatible elements for these five samples. Data for Cambrian basalts lCm (Fig. 3.6B) are from Lomize et al. (1997). All samples exhibit depletion in Nb, Ta, and Ti that is indicative of an arc setting. Incompatible element signatures of tuffs (tCm and tO_2) and volcaniclastic turbidites (v_2O_{1-2}) are very similar. This suggests that all three units could have been derived from one volcanic source.

Provenance types and tectonic setting

The results of the petrographic study permit the classification of clastic rocks of the Solton Sary district into three compositional groups, each representing a distinct provenance type. Plagioclase-rich pyroclastic and volcaniclastic sedimentary rocks are related to arc volcanism, and this affinity is additionally confirmed by trace element geochemical data. The quartzose material of siliciclastic turbidites is likely to have been shed from some crystalline, craton-type source. Mixed composition and abundance of lithic fragments typical for the Devonian-Carboniferous terrestrial clastic rocks suggest their most probable orogenic affinity. Fragments of volcanic rocks indicate the erosional recycling of the Early Paleozoic volcanic arc and perhaps the occurrence of minor syn-

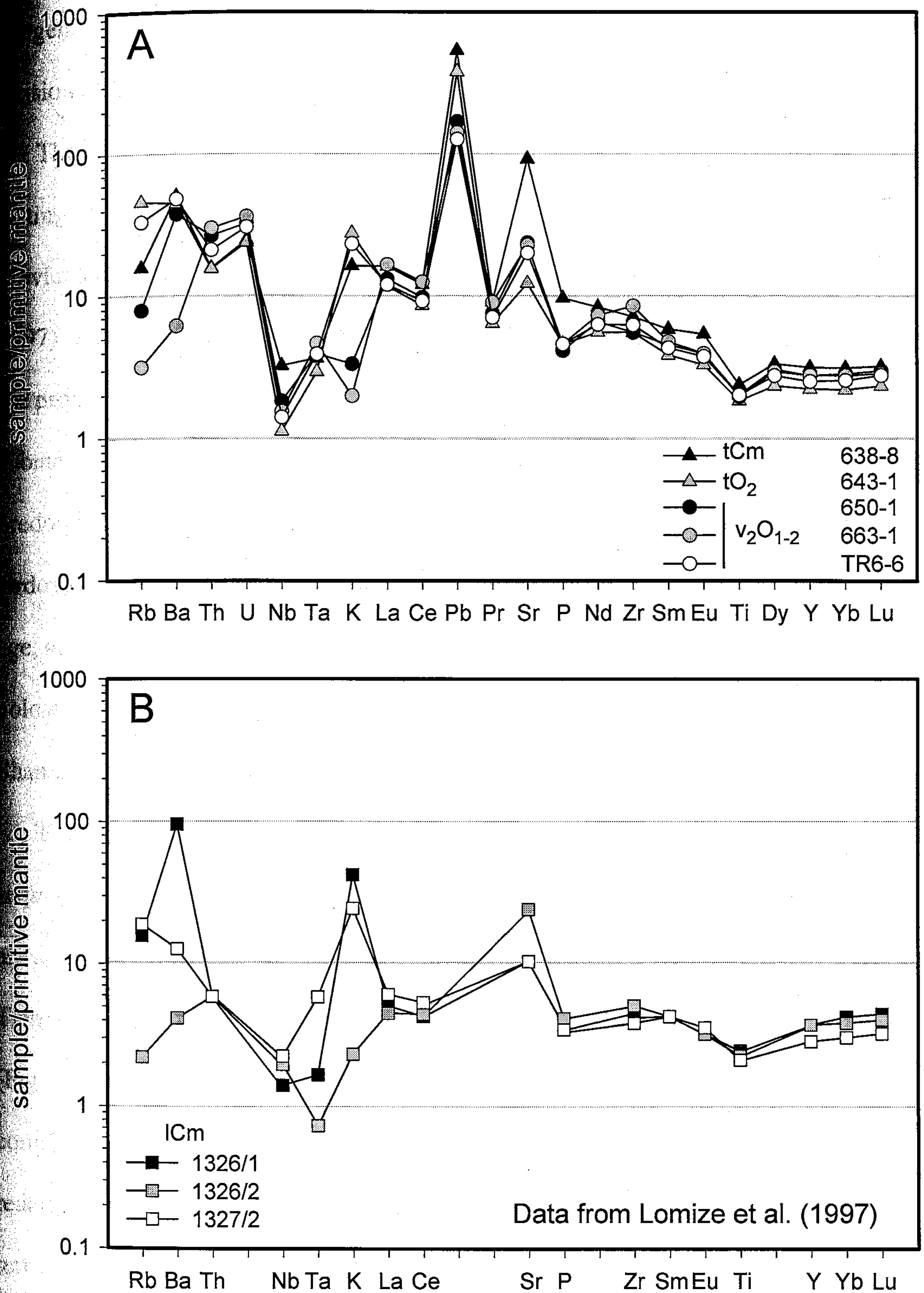

Fig. 3.6. Primitive mantle-normalized plots for samples of clastic rocks (A) and basalts lCm (B). Analytical data are listed in Appendix A. Normalizing factors are from Sun and McDonough (1989).

orogenic volcanism. The abundance of granitic K-feldspar grains suggests unroofing and erosion of Paleozoic subduction-related batholiths.

The stratigraphic assemblage of the Solton Sary district indicates a volcanic arc setting during the Cambrian-Middle Ordovician time. This is in full agreement with previous regional tectonic reconstructions (e. g., Mikolaichuk et al, 1997; Lomize et al., 1997). The occurrence of quartz-rich siliciclastic rocks throughout the section indicates the proximity of an uplifted crystalline block. The volcanism evolved from voluminous submarine eruptions of chiefly mafic lavas (Cambrian) to a more sporadic activity of predominantly intermediate to moderately felsic stratovolcanoes (Cambrian-Middle Ordovician). The latest stratified volcanics within the area presumably have Llandeilan age, according to the stratigraphic model of Mikolaichuk et al. (1997). Termination of arc volcanism is interpreted as related to the collision between the North and Median Tien Shan blocks (e. g., Lomize et al., 1997).

The origin of the Middle Ordovician carbonates that overlie the largely volcanogenic sequence is not completely clear. On the geologic map in Mikolaichuk et al. (1997), they are shown as an allochton that was derived from the Talas-Karatau zone of the Median Tien Shan block during the North-Median Tien Shan collision in the Late Ordovician (Fig. 2.5). The onset of terrestrial clastic sedimentation (Devonian-Carboniferous conglomerates) reflects an orogenic event that was probably accompanied by the reactivation of major regional faults. Chapter 7 discusses a possible older age for these terrestrial sediments.

Intrusive rocks

Lower-Middle Ordovician upper volcaniclastic turbidites (v_2O_{1-2}) host a series of concordant planar intrusions of lamprophyres and syenite porphyries. In plan view, the intrusions are arranged into a linear trend of general northwest-southeast orientation (Fig. 3.1). The syenites and lamprophyres are petrographically and geochemically different from all stratified units. Composition and probable timing of emplacement of these intrusions are considered in detail in Chapters 4 and 7.

Structure and faults

Volcanogenic and siliciclastic rocks are, to a variable extent, affected by deformation, exhibiting a tectonic foliation that is generally parallel to the original bedding and dips steeply (~ 60-80°) south-southwest. The structural framework comprises the dextral Talabulak strike-slip fault, the Altyntor reverse fault and South Kumbel fault (Fig. 3.1). Mikolaichuk et al. (1997) depict the latter as a thrust or reverse fault that emplaced allochtonous Middle Ordovician carbonates (ccO_2) over the underlying, largely volcanogenic succession (Fig. 2.5). The microstructural analysis of this study suggests predominantly dextral strike-slip displacements. The nature of the South Kumbel fault and the timing of tectonism are further discussed in chapters 5 and 7.

Mesothermal gold mineralization

District-scale distribution

Mesothermal gold mineralization is spatially associated with the swarm of concordant syenite and lamprophyre intrusions that are hosted in Lower-Middle Ordovician upper volcaniclastic turbidites (v_2O_{1-2}). Due to this spatial association, the occurrences of gold mineralization are confined to a relatively narrow trend that is generally parallel to the structural grain (Fig. 3.1). On the eastern flank, the gold-bearing trend terminates as the fault-bounded ore hosting volcaniclastic turbidites pinch out. In the west, the unconsolidated sediments cover the potentially mineralized trend and its geologic limits are undefined. In the central portion of the district, where the upper volcaniclastic turbidites are only ~70 m thick, there is a hiatus in the intrusive belt and mineralized trend. The intrusions and mineralization may be truncated by post-mineralization displacements along the Altyntor fault that bounds upper volcaniclastic turbidites from the south. Unfortunately, this area is poorly exposed and direct observations of the relationship between mineralization and faults are not possible.

The distribution of gold mineralization along the strike of the trend is not uniform. Most economically attractive mineralized zones of the Solton Sary district have been delineated within the Buchuk area that roughly corresponds to the west-central portion of the mineralized trend, the Altyntor area in the east ranks second (Fig 3.1). Other portions of the mineralized trend are characterized by sporadic and relatively small occurrences of gold mineralization, although sometimes with high grades.

Mineralized zones

Gold mineralization occurs within steeply dipping zones of vein silicification. Many of the observed zones are spatially associated with the sheared contacts of syenite sills. Three modes of quartz veining are observed. The most typical are steeply dipping quartz veins (5-30 cm thick) and swarms of thinner veinlets concordant to the wall rock foliation. These veins and veinlets commonly occur at syenite sill contacts, and in most cases are enveloped by mylonites. In addition to quartz, veins contain sericite, muscovite, carbonate, and less abundant K-feldspar and albite. Many veins exhibit macroscopically distinct lamination. Bands of quartz are separated by millimiter-thick discontinuous streaks of green sericite-rich material that probably represent slivers of host mylonites detached form vein walls during incremental vein reopening. Gradation of veins into veinlet swarms is common. Overall, the morphology of the concordant, steeply dipping veins permits them to be classified as fault-fill veins (cf. Robert and Poulsen, 2001).

Concordant veins at sheared contacts of competent syenite sills are commonly flanked by zones of stockwork veining. These typically consist of relatively thin (0.3-2 cm thick) variably oriented quartz veinlets hosted by fractured sill endocontacts. These stockwork zones appear to have an overall near tabular shape and be oriented subparallel to the sill contacts.

An array of subparallel shallowly dipping extensional veins hosted in a syenite sill and oriented at high angles (70-90°) to the sill contact was observed at one locality within the northwestern part of the Altyntor open pit. The individual veins are 1-4 cm thick and are spaced 10-20 cm apart. This array fringes a subvertical concordant vein of banded quartz hosted by sheared contact of the sill. The 1-3 cm thick extension veinlets were also observed in the drill core, but overall, this type of quartz veining appears generally insignificant.

Mineralized zones may comprise a combination of steeply dipping concordant veins and adjacent portions of fractured host rocks with variably oriented quartz veinlets. The largest mineralized zone observed during geologic mapping of the Altyntor open pit is 7-15 m wide and about 100 m long (Fig. 3.2). It is concordant with wall rocks and strikes northwest-southeast with a steep southwest dip. The silicification zone is hosted in altered metasedimentary rocks and syenite porphyries. At the northwestern flank, the zone consists of at least four steeply dipping veinlet swarms bearing rich macroscopically visible gold mineralization. These veinlet suites are 0.25-0.5 m thick and are separated by areas of altered rocks 1-3 m wide, with less abundant quartz veining. Individual veinlets are 0.5-10 cm thick. At the southeastern flank, the thickness of the auriferous zone decreases. There, the zone consists of two veins (15-25 cm) hosted in altered sandstones approximately 1.5 m apart.

As the most recent exploration data are not accessible, the parameters of ore bodies and average gold grades are not discussed here. In 1997, core holes drilled in Buchuk area intersected intervals with grades exceeding 10 g/t over several meters. Based on these results and observations in the Altyntor open pit, it appears realistic to expect ore bodies with average grades on the order of 5-10 g/t, or even higher.

Hydrothermal alteration

A simplified model of alteration zoning is presented in Figure 3.7. The background epigenetic mineral assemblage consists of chlorite, carbonate, epidote, and albite. This

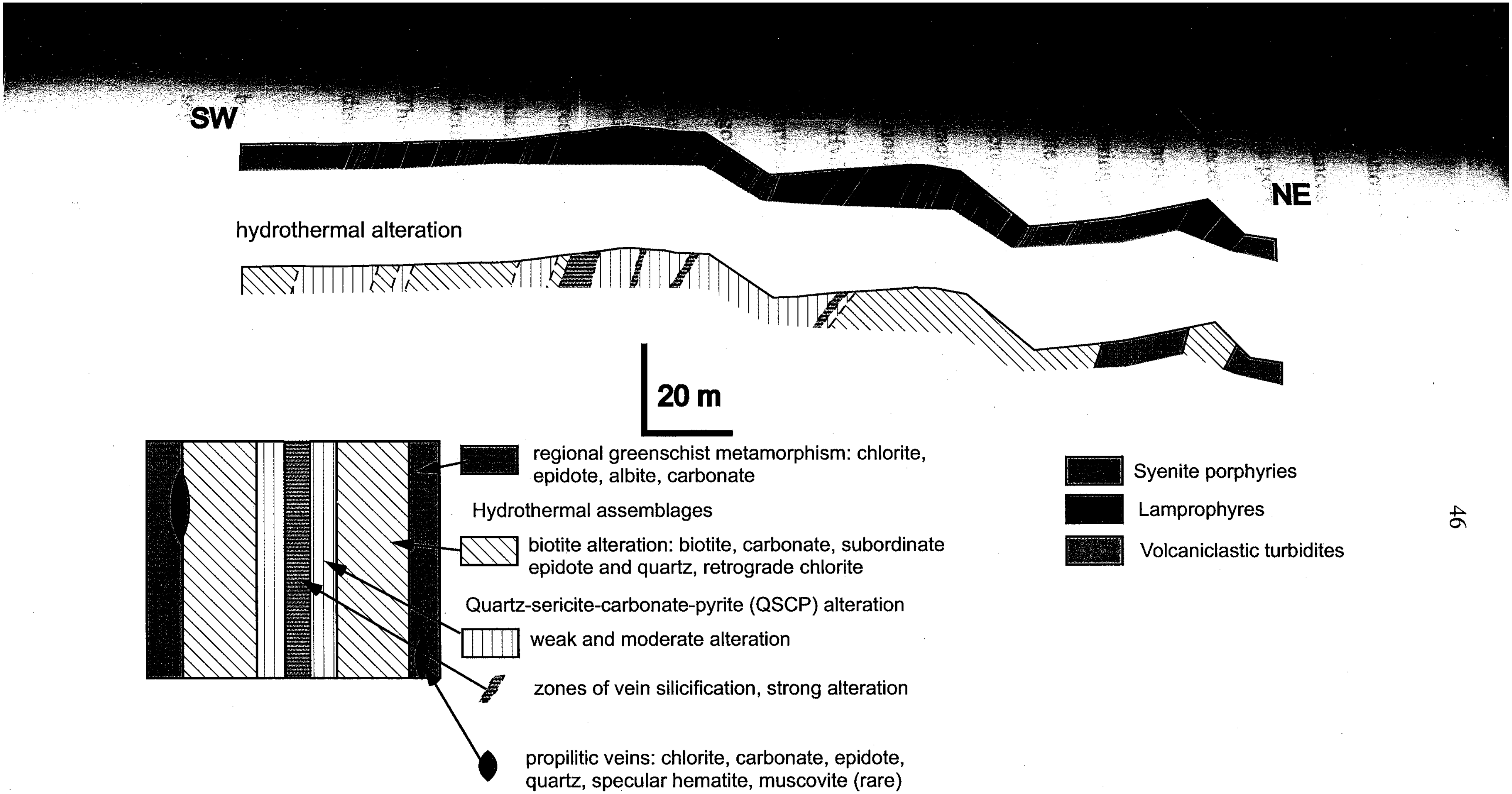

Fig. 3.7. Zoning of hydrothermal assemblages: measured cross-section and generalized model. See Figure 4.1 for the cross section location.

association is characteristic for regional greenschist facies metamorphism. The abundances of these epigenetic minerals are much higher in stratified volcanics than in syenite porphyries and lamprophyres. The matrix of volcanic rocks is completely replaced by epigenetic epidote, chlorite, and carbonate. In the intrusive rocks, the epigenetic component is largely limited to smaller amounts of carbonate and epidote occurring as clots in the groundmass. At flanks of the intrusive belt, lamprophyres and syenite porphyries commonly host barren quartz veins with variable amounts of chlorite, carbonate, epidote, specular hematite, and rarely muscovite and pyrite. Based on the characteristic mineralogy, these veins are defined as propylitic veins (Fig. 3.7). Monomineral veinlets of epidote, hematite, and carbonate are also common.

Hydrothermal alteration comprises two major assemblages: biotite alteration and quartz-sericite-carbonate-pyrite (QSCP) alteration. Biotite alteration is distal with regards to gold-bearing mineralized zones (Fig. 3.7). Macroscopic identification of biotitic alteration is difficult mainly because of the relatively low content of epigenetic minerals and their very small grain sizes. In places, however, the alteration can be detected by the presence of thin and discontinuous streaks of epigenetic biotite and, in rare cases, by a characteristic brownish tint of altered rocks. Due to the generally cryptic nature of biotitization, geometric parameters of alteration halos are somewhat difficult to estimate. The biotitization appears to broadly coincide with the intrusive belt, and is probably discontinuous along and across the strike.

Microscopic studies show that epigenetic brown biotite (10-100 μm) is accompanied by carbonate and forms streaks, discontinuous veinlets, lenticular and lensoid segregations, and irregular clots in the groundmass. Carbonate and biotite fill microfractures in K-feldspar phenocrysts, or, less commonly, replace K-feldspar selectively following zoning patterns. Complete replacement of K-feldspar phenocrysts is relatively rare. In addition to biotite and carbonate, the alteration assemblage comprises much less abundant epidote and quartz. Biotite is commonly replaced by later retrograde chlorite or by white mica related to the QSCP alteration. Opaque minerals vary from sample to sample and include hematite, magnetite, pyrite, and chalcopyrite. The overall content of epigenetic minerals varies from 5 to 20 percent, and in rare cases exceeds 20-30 percent. Electron microprobe analysis of two samples showed essentially pure calcitic composition of carbonate (Table 3.2). Analyses of epigenetic biotites from a syenite porphyry and sandstone revealed that the sandstone-hosted biotite has distinctly higher Mg content (Table 3.3). This may reflect the existence of two discrete populations or a broad compositional range, possibly controlled by host rock geochemistry, or by the distance to major mineralized zones (cf. Neall and Phillips, 1986). Biotite-altered rocks exhibit consistently low gold grades. Copper contents may locally reach 1000 ppm due to abundant chalcopyrite.

Proximal alteration is represented by a quartz-sericite-carbonate-pyrite (QSCP) assemblage. The QSCP alteration halos are enclosed within discontinuous envelopes of biotite alteration. The intensity of the QSCP alteration appears to be largely controlled by the distance to vein silicification zones, and by the intensity of shearing. A typical mode of occurrence comprises relatively large areas of weakly altered rocks and narrow zones of strong alteration (Fig. 3.7). In the Altyntor open pit at the eastern flank of the Solton Sary district, weak and moderate QSCP alteration occurs as southeast-trending bands up

Table 3.2. Representative electron microprobe analyses of hydrothermal carbonates

probe run id	cc-579-1[4]	cc-579-2[4]	cc-579-3[4]	cc-579-9	cc-59-708-1	cc-59-708-9[4]	cc-59-708-10[4]	cc-59-708-11[4]	cc-59-708-12[4]	cc-59-708-13	cc-59-708-20
sample	579[3]	579	579	579	59-70.8[3]	59-70.8	59-70.8	59-70.8	59-70.8	59-70.8	59-70.8
assemblage	QSCP[1]	QSCP	QSCP	QSCP	QSCP	QSCP	QSCP	QSCP	QSCP	QSCP	QSCP
wt%											
$MgCO_3$	21.33	17.75	23.72	30.05	28.24	28.22	28.92	27.05	27.41	27.26	18.15
$CaCO_3$	50.59	49.1	49.17	50.98	52.65	51.73	50.62	50.82	51.64	51.36	51.34
$MnCO_3$	1.68	1.93	1.57	0.94	0.26	1.24	0.9	1.15	1.15	1.04	1.24
$FeCO_3$	25.89	30.82	24.28	17.73	19.25	18.35	19.74	20.77	21.47	22.02	30.52
$SrCO_3$	0.3	0.06	0.21	0.82	0.78	0.36	0.31	0.13	0.09	0.23	0.11
$BaCO_3$	0.04	0.04	0	0.01	0	0	0	0	0	0.01	0
Total	99.83	99.7	98.95	100.53	101.18	99.9	100.49	99.92	101.76	101.92	101.36

probe run id	cc49-113-1	cc49-113-4	cc49-1132	ccA23-2	ccA23-3	ccA23-4	ccA23-6	ccA23-7
sample	49-113.7	49-113.7	49-113.7	A23	A23	A23	A23	A23
assemblage	bt[2]	bt	bt	bt	bt	bt	bt	bt
wt%								
$MgCO_3$	0.1	0.48	0.14	1.11	1.04	0.87	0.92	0.9
$CaCO_3$	99.29	98.39	100.08	95.98	93.65	94.88	96.2	96.09
$MnCO_3$	0.52	1.11	0.71	2.3	2.01	1.98	2.23	2.13
$FeCO_3$	0.14	0.22	0.15	1.68	1.64	1.53	1.62	1.27
$SrCO_3$	0.22	0.25	0.22	0.53	0.74	0.66	0.62	0.48
$BaCO_3$	0.04	0	0	0	0	0	0.04	0.01
Total	100.31	100.45	101.3	101.6	99.08	99.92	101.63	100.88

[1]quartz-sericite-carbonate-pyrite alteration;
[2]biotite alteration;
[3]samples 579 and 59-70.8: 1-1.5 cm thick quartz veinlets enclosed in strongly altered syenite porphyry;
[4]grains intimately associated with gold particles.

Table 3.3. Representative electron microprobe analyses of hydrothermal biotite

probe run id	btA23-13	btA23-14	btA23-2	btA23-3	btA23-4	btA23-6	btA23-7	biot57-15675-1	biot57-15675-2	biot57-15675-3	biot57-15675-4	biot57-15675-5
sample	A23	A23	A23	A23	A23	A23	A23	57-156.75	57-156.75	57-156.75	57-156.75	57-156.75
host rock	syenite	syenite	syenite	syenite	syenite	syenite	syenite	sandstone	sandstone	sandstone	sandstone	sandstone
SiO_2	38.47	39.20	38.74	39.53	37.92	37.43	37.17	39.08	39.44	40.89	40.03	38.62
TiO_2	2.33	2.36	2.16	2.03	2.18	1.99	1.70	1.26	1.33	1.22	1.34	1.32
Al_2O_3	14.00	13.42	13.55	13.11	13.33	13.83	13.84	14.50	13.91	13.87	14.69	14.59
Cr_2O_3	0.00	0.00	0.04	0.04	0.10	0.02	0.06	0.00	0.00	0.00	0.01	0.00
MgO	14.57	15.11	14.71	15.18	14.17	14.04	14.25	18.28	18.87	18.81	18.29	18.27
CaO	0.01	0.03	0.03	0.03	0.03	0.01	0.03	0.02	0.04	0.06	0.14	0.04
MnO	0.12	0.15	0.17	0.11	0.11	0.08	0.04	0.00	0.01	0.00	0.00	0.00
FeO	15.26	14.92	16.00	14.94	16.24	16.45	16.48	11.43	10.92	10.99	11.41	11.43
BaO	0.00	0.00	0.00	0.00	0.00	0.00	0.00	0.00	0.00	0.00	0.00	0.00
Na_2O	0.06	0.05	0.07	0.05	0.03	0.09	0.07	0.06	0.04	0.03	0.05	0.03
K_2O	10.03	10.04	9.94	9.82	10.11	10.12	10.15	9.56	9.78	9.56	9.63	9.80
F	2.22	2.56	2.44	2.87	2.25	2.34	2.44	1.58	1.59	1.70	1.46	1.49
Cl	0.00	0.00	0.01	0.00	0.01	0.00	0.01	0.03	0.03	0.01	0.01	0.01
	97.07	97.84	97.86	97.71	96.48	96.40	96.24	95.78	95.95	97.14	97.05	95.59
"-O=F,Cl"	0.93	1.08	1.03	1.21	0.95	0.99	1.03	0.67	0.68	0.72	0.62	0.63
Total	96.14	96.76	96.83	96.50	95.53	95.41	95.21	95.11	95.27	96.42	96.43	94.97
Number of ions on the basis of 24 O, F, Cl												
Si	6.165	6.217	6.178	6.265	6.163	6.097	6.071	6.204	6.244	6.361	6.259	6.159
Al	2.644	2.508	2.547	2.449	2.553	2.655	2.664	2.712	2.596	2.544	2.706	2.741
Ti	0.281	0.282	0.259	0.242	0.266	0.244	0.209	0.151	0.158	0.143	0.158	0.158
Cr	0.000	0.000	0.005	0.005	0.013	0.003	0.008	0.000	0.000	0.000	0.001	0.000
Mg	3.481	3.572	3.497	3.587	3.433	3.410	3.470	4.326	4.453	4.364	4.262	4.343
Ca	0.002	0.005	0.005	0.005	0.005	0.002	0.005	0.003	0.007	0.010	0.023	0.007
Mn	0.016	0.020	0.023	0.015	0.015	0.011	0.006	0.000	0.002	0.000	0.000	0.000
$Fe^2(t)$	2.045	1.979	2.134	1.980	2.207	2.241	2.251	1.517	1.445	1.430	1.492	1.524
Ba	0.000	0.000	0.000	0.000	0.000	0.000	0.000	0.000	0.000	0.000	0.000	0.000
Na	0.019	0.015	0.022	0.015	0.009	0.028	0.022	0.017	0.013	0.008	0.014	0.011
K	2.050	2.031	2.022	1.985	2.096	2.103	2.115	1.937	1.975	1.898	1.921	1.994
F	1.125	1.284	1.230	1.438	1.156	1.205	1.260	0.792	0.798	0.838	0.723	0.749
Cl	0.000	0.000	0.003	0.000	0.003	0.000	0.003	0.007	0.007	0.002	0.003	0.003
Sum	17.829	17.913	17.925	17.986	17.920	17.998	18.084	17.665	17.697	17.597	17.561	17.690
mg#	0.630	0.644	0.621	0.644	0.609	0.603	0.607	0.740	0.755	0.753	0.741	0.740

mg# = Mg/(Mg+ Fe^2(t)); A complete listing of hydrothermal biotite analyses is presented in Appendix B.

60 m wide. These bands are generally concordant with the strike of host rocks and are separated by areas of weak biotite alteration or by unaltered metasediments.

Macroscopically, weakly QSCP-altered rocks are distinguishable by their characteristic bleached appearance, the presence of disseminated pyrite, and generally good preservation of primary (magmatic and clastic) feldspar. Strong alteration occurs as relatively narrow envelopes around zones of vein silicification and shear zones. The most prominent macroscopic feature of strong QSCP alteration is sericitization of feldspars.

Microscopic observations confirm that volumetrically extensive bleach zones comprise predominantly weak to moderate QSCP alteration. Sericite and carbonate form lenses, veinlets and irregular clots in the groundmass, and muscovite replaces biotite. Pyrite occurs as scattered cubic grains and could be partially related to the sulfidation of accessory magnetite. Locally present bright green fuchsite (Table 3.4) may have formed after primary magmatic Cr-rich biotite. Quartz forms veins and veinlets that contain streaks and segregations of muscovite, sericite and ankerite (Tables 3.2 and 3.4). K-feldspar and albite occur along the walls of the veins and sometimes as scattered grains in their central portions. In moderately altered rocks, replacement of K-feldspar phenocrysts is insignificant and is represented by sericitization and carbonatization along fractures. In the immediate proximity of quartz veins, the alteration is stronger, and feldspars may be replaced by sericite and carbonate, sometimes with subordinate quartz.

Gold mineralization

Gold mineralization occurs in quartz veinlets and veins that are surrounded by envelopes of QSCP alteration. Gold particles are generally anhedral and have sizes of 10

Table 3.4. Representative electron microprobe analyses of white micas from auriferous quartz veins and QSCP alteration

probe run id	src-579-1	src-579-2	src-579-3	src-579-5	src-59-708-6	src-59-708-2	src-59-708-4	src-59-708-8	mu601-1	mu601-2	mu547-1	mu547-10	fchs59-855-2	fchs59-855-3
sample	579	579	579	579	59-70.8	59-70.8	59-70.8	59-70.8	601	601	547	547	59-85.5	59-85.5
mineral	sericite	sericite	sericite	sericite	sericite	sericite	sericite	sericite	muscovite	muscovite	muscovite	muscovite	fuchsite	fuchsite
SiO_2	52.18	51.19	51.98	51.38	52.61	52.31	52.21	52.47	47.44	45.77	46.22	45.20	49.05	49.64
TiO_2	0.00	0.06	0.53	1.07	0.05	0.08	0.05	0.45	0.22	0.36	0.06	0.02	0.70	0.52
Al_2O_3	35.30	37.07	32.08	31.81	32.71	33.09	32.60	30.15	33.92	34.30	34.11	32.56	30.24	30.46
Cr_2O_3	0.00	0.02	0.50	0.79	0.00	0.00	0.00	0.06	0.00	0.01	0.00	0.00	1.63	1.56
MgO	0.79	0.68	2.56	2.23	2.68	2.41	2.72	2.78	0.98	0.64	1.27	1.23	2.68	2.53
CaO	0.16	0.09	0.01	0.07	0.04	0.02	0.01	0.13	0.02	0.01	0.02	0.01	0.02	0.02
MnO	0.00	0.00	0.00	0.00	0.00	0.00	0.00	0.00	0.00	0.00	0.00	0.00	0.00	0.00
FeO	1.07	0.76	2.42	2.60	1.68	1.32	2.05	3.69	3.09	2.59	2.33	2.94	1.94	1.93
BaO	0.04	0.02	0.60	0.78	0.61	0.33	0.74	0.39	1.06	1.19	2.69	3.32	0.59	0.55
Na_2O	0.04	0.03	0.08	0.04	0.05	0.03	0.04	0.02	0.57	0.60	0.12	0.28	0.13	0.14
K_2O	7.71	6.73	6.07	5.81	7.15	7.40	7.34	6.65	9.49	9.76	9.64	9.68	8.95	9.60
F	0.22	0.13	0.56	0.49	0.73	0.55	0.52	0.53	0.23	0.18	0.03	0.23	0.54	0.80
Cl	0.02	0.00	0.00	0.00	0.00	0.00	0.01	0.00	0.00	0.00	0.00	0.01	0.00	0.01
	97.53	96.78	97.39	97.07	98.31	97.54	98.29	97.32	97.01	95.42	96.48	95.48	96.47	97.75
-O=F,Cl	0.10	0.05	0.24	0.21	0.31	0.23	0.22	0.22	0.10	0.08	0.01	0.10	0.23	0.34
Total	97.43	96.73	97.15	96.86	98.00	97.31	98.07	97.10	96.91	95.34	96.47	95.38	96.24	97.41
Number of ions on the basis of 24 O, F, Cl														
Si	7.183	7.048	7.212	7.172	7.233	7.228	7.212	7.338	6.833	6.721	6.762	6.763	7.045	7.053
Al	5.727	6.015	5.245	5.233	5.300	5.388	5.307	4.969	5.759	5.937	5.881	5.741	5.118	5.101
Ti	0.000	0.006	0.055	0.112	0.005	0.008	0.005	0.047	0.024	0.040	0.007	0.002	0.075	0.056
Cr	0.000	0.002	0.055	0.087	0.000	0.000	0.000	0.007	0.000	0.002	0.000	0.000	0.185	0.175
Mg	0.162	0.140	0.530	0.464	0.549	0.496	0.560	0.580	0.210	0.141	0.276	0.275	0.575	0.535
Ca	0.024	0.013	0.001	0.010	0.006	0.003	0.001	0.019	0.003	0.002	0.003	0.001	0.002	0.003
Mn	0.000	0.000	0.000	0.000	0.000	0.000	0.000	0.000	0.000	0.000	0.000	0.000	0.000	0.000
Fe^2(t)	0.123	0.088	0.281	0.303	0.193	0.153	0.237	0.432	0.372	0.318	0.285	0.368	0.233	0.229
Ba	0.002	0.001	0.033	0.043	0.033	0.018	0.040	0.021	0.060	0.069	0.154	0.194	0.033	0.030
Na	0.011	0.008	0.022	0.011	0.013	0.008	0.011	0.005	0.158	0.170	0.034	0.082	0.037	0.038
K	1.354	1.182	1.074	1.034	1.254	1.304	1.293	1.186	1.744	1.828	1.799	1.848	1.640	1.739
F	0.096	0.057	0.246	0.216	0.317	0.240	0.227	0.234	0.105	0.085	0.012	0.106	0.244	0.361
Cl	0.005	0.000	0.000	0.000	0.000	0.000	0.002	0.000	0.000	0.000	0.000	0.003	0.000	0.001
Sum	14.686	14.560	14.753	14.687	14.904	14.846	14.896	14.840	15.267	15.311	15.213	15.384	15.188	15.323

A complete listing of hydrothermal white mica analyses is presented in Appendix B.

microns to 10 millimeters. In quartz veins, gold is accompanied by pyrite and chalcopyrite and occurs principally within streaks of green sericite, with or without ankerite. These streaks are often hosted by brittle fractures. In some cases, gold is found fractures in large (~ 5 mm) pyrite crystals. The most abundant sulfides are pyrite and chalcopyrite. Arsenopyrite is found occasionally, galena and brownish-gray semi-transparent sphalerite are relatively rare. In places, sulfides are replaced by supergene hematite and iron hydroxides. The observed distribution of visible gold in the Altyntor pit and comparison of alteration and silicification patterns in drill core with gold assays show that most of the gold is likely to occur within quartz veins rather than in altered wall rocks. In relatively thick veins (10 cm and thicker), visible gold tends to occur closer to the vein margins.

Hydrothermal occurrences outside mineralized zones

Products of hydrothermal activity are not restricted to the swarm of alkalic intrusions. A broad (up to ~ 200 m wide) halo of chlorite-fuchsite-carbonate alteration is spatially associated with the South Kumbel fault. In places, the altered rocks contain sparse pyrite dissemination and host quartz veins that contain magnetite, or less commonly, pyrite. Both altered rocks and quartz veins are barren with regards to gold mineralization. Chapter 5 considers chlorite-fuchsite-carbonate rocks of South Kumbel faults in more detail. In addition to the alteration and quartz veining along the South Kumbel fault, there are barren quartz veins that occur in virtually all stratigraphic units of the district. These veins may contain chlorite, hematite, carbonate, and rarely muscovite. Apart from the ence of epidote, these veins appear generally similar to the propilitic veins at flanks of intrusive belt. The relative timing of the barren vein formation and mesothermal gold mineralization is unclear from field observations due to the absence of crosscutting relationships.

CHAPTER 4

ALKALIC MAGMATISM

Field geology

Most plutonic rocks of the Solton Sary district occur within a discontinuous 200-400 m wide, 5000 m long, west-northwest striking belt that is hosted in Lower-Middle Ordovician upper volcaniclastic turbidites (v_2O_{1-2}). The intrusions (sills) are concordant with host rocks, dip steeply south-southwest, and are composed of hypabyssal lamprophyres and syenite porphyries (Fig. 4.1). Cross-sections measured over the most representative outcrops of the intrusive belt revealed up to 35 individual bodies, most of which appear discontinuous along the strike. Volumetrically predominant syenite porphyries form 0.5 to 150 m thick and 100 m to 1 km long sills. The lamprophyric sills are 1 to 50 m thick and 100 m to 1 km long. They exhibit essentially tabular shapes with strong variations in thickness over short distances, typical of lamprophyric intrusions in general (Rock, 1991). Intrusives lack chilled margins and exocontact thermal halos; their marginal portions are commonly sheared. The relative timing of the emplacement of individual bodies is unclear due to a lack of unequivocal crosscutting relationships. The intrusive belt defines a linear positive magnetic anomaly that typically comprises two near-parallel highs separated by a relative low.

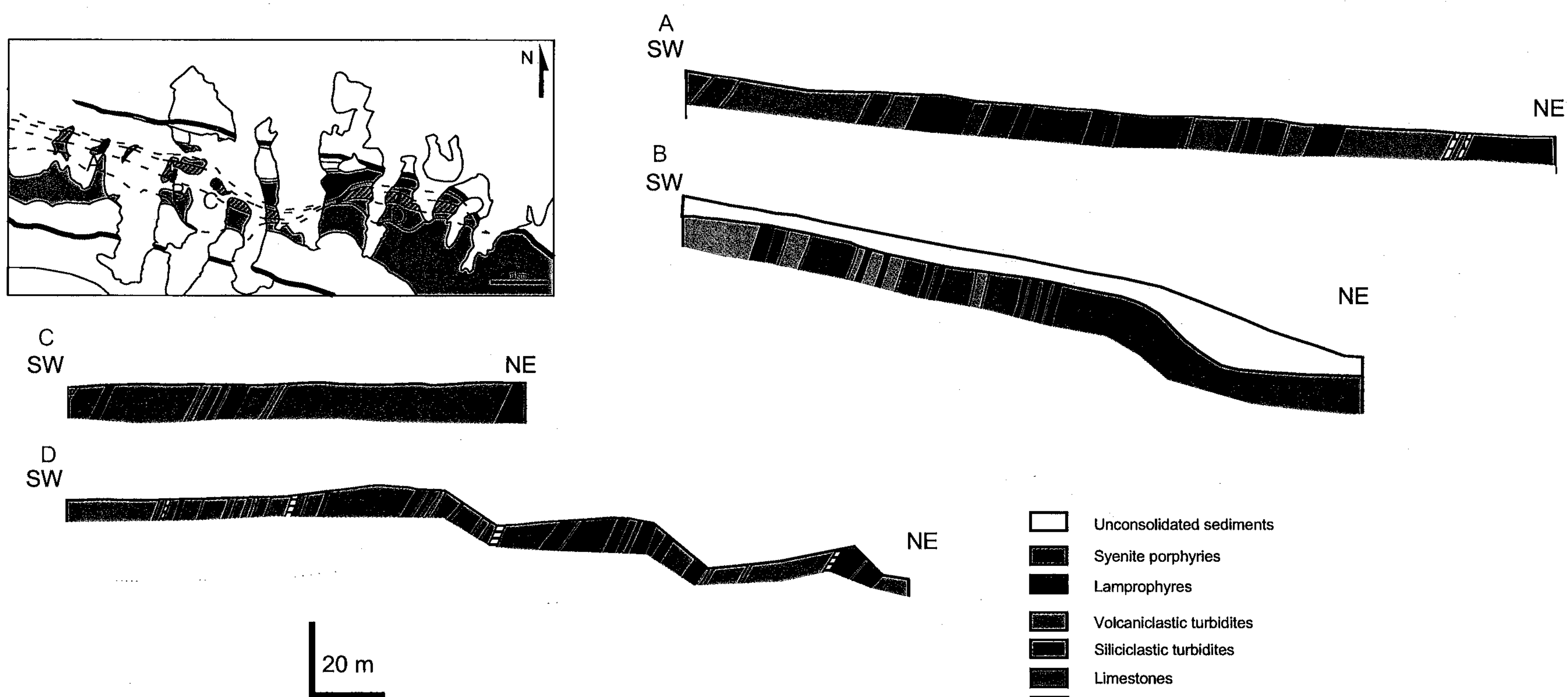

Fig. 4.1. Measured cross sections of the Solton Sary intrusive belt (slightly generalized).

Petrography

Lamprophyres

The unaltered lamprophyre is a dark gray, fine-grained, porphyritic rock. Phenocrysts (0.5-2 mm) constitute 30-40 percent of the rock volume. They are randomly oriented, or less commonly flow-aligned. Subhedral to euhedral (battlemented and pseudohexagonal) mica and amphibole are the most abundant phenocryst phases. Following the nomenclature developed by Rock (1991), the lamprophyres of the Solton Sary district can be classified into mica lamprophyres (minettes) that contain only mica phenocrysts (Fig. 4.2A, B; Fig. 4.3A), and amphibole lamprophyres, where amphibole is a predominant phenocryst phase, whereas mica phenocrysts are either subordinate or completely absent (Fig.4.2C, D; Fig. 4.3B, C, D).

Mica phenocrysts are of two types: uniform green to greenish brown (Fig. 4.2A) and optically zoned with pale green cores and deep green rims (Fig 4.2E). Relative proportions of uniformly colored and zoned micas are difficult to quantitatively evaluate by petrographic observations. This is because the optical zoning of a given mica phenocryst is not apparent unless the plane of a thin section intersects the very innermost portion of a crystal. However, it is clear that the zoned micas are generally subordinate, and their proportion varies from sample to sample. Some lamprophyres tend to be relatively enriched in zoned mica crystals, others contain only uniformly colored micas. In addition to rather fine phenocrysts, zoned mica forms very coarse, round-shaped to pseudohexagonal megacrysts, with diameters varying from 3 mm to 4 cm, and averaging about 0.5-1.5 cm. The content of these megacrysts normally does not exceed 1-3 percent. Mica phenocrysts and megacrysts commonly contain acicular sagenitic rutile and may be

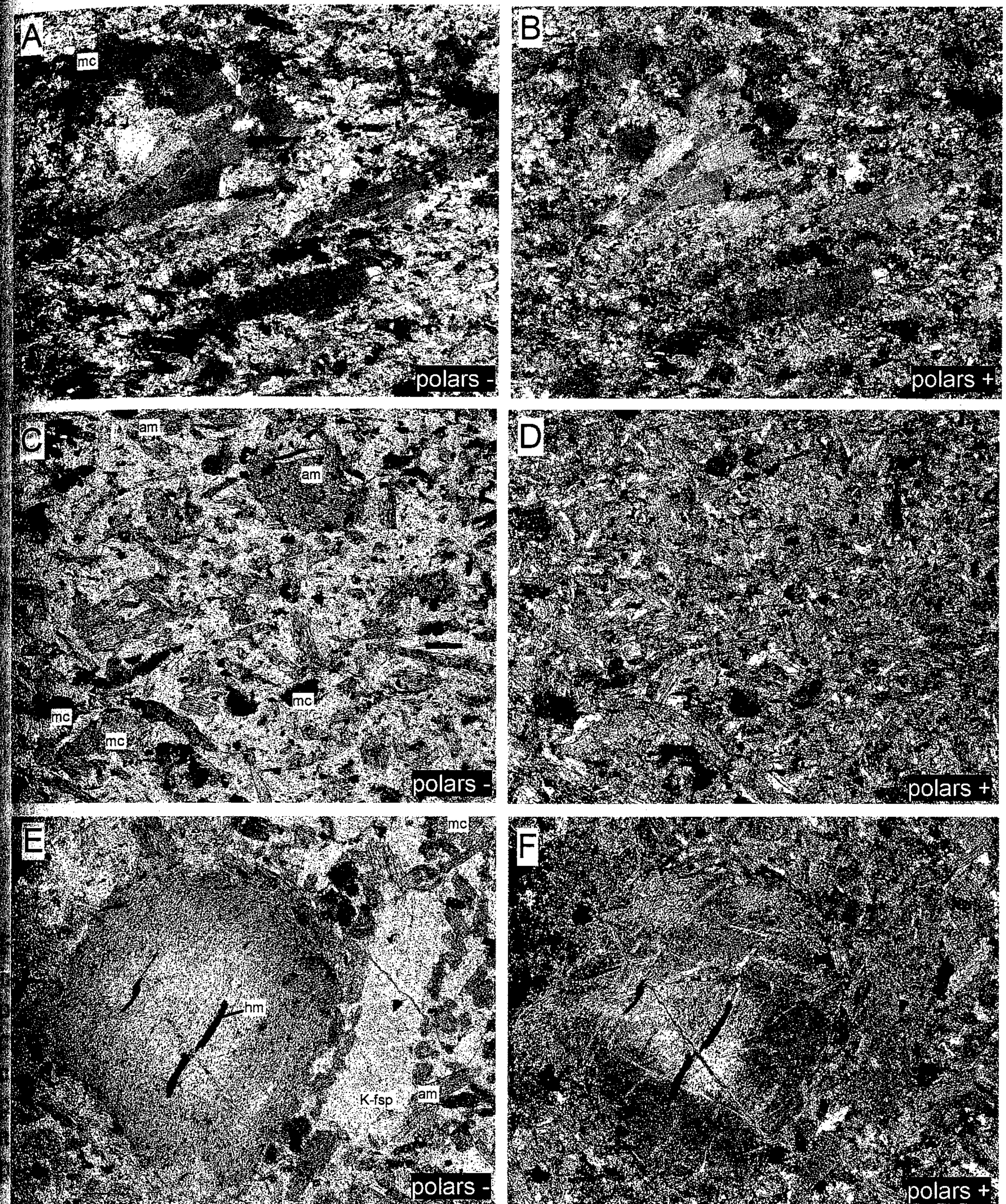

Fig. 4.2. Photomicrographs of lamprophyres (A+B, C+D, and E+F depict the same fields of view in plane-polarized light on the left and cross-polarized light on the right). A and B, mica lamprophyre with flow-aligned greenish-brown mica phenocrysts. C and D, amphibole-bearing lamprophyre with randomly oriented phenocrysts of green amphibole and dark green mica in a groundmass consisting mainly of prismatic K-feldspar crystals. E, F, optically zoned mica phenocryst, atypically coarse K-feldspar crystals, and smaller crystals of unzoned mica and amphibole. Field of view is approximately 3 mm. Mineral symbols: am = amphibole, K-fsp = K-feldspar; mc = mica; hm = secondary hematite.

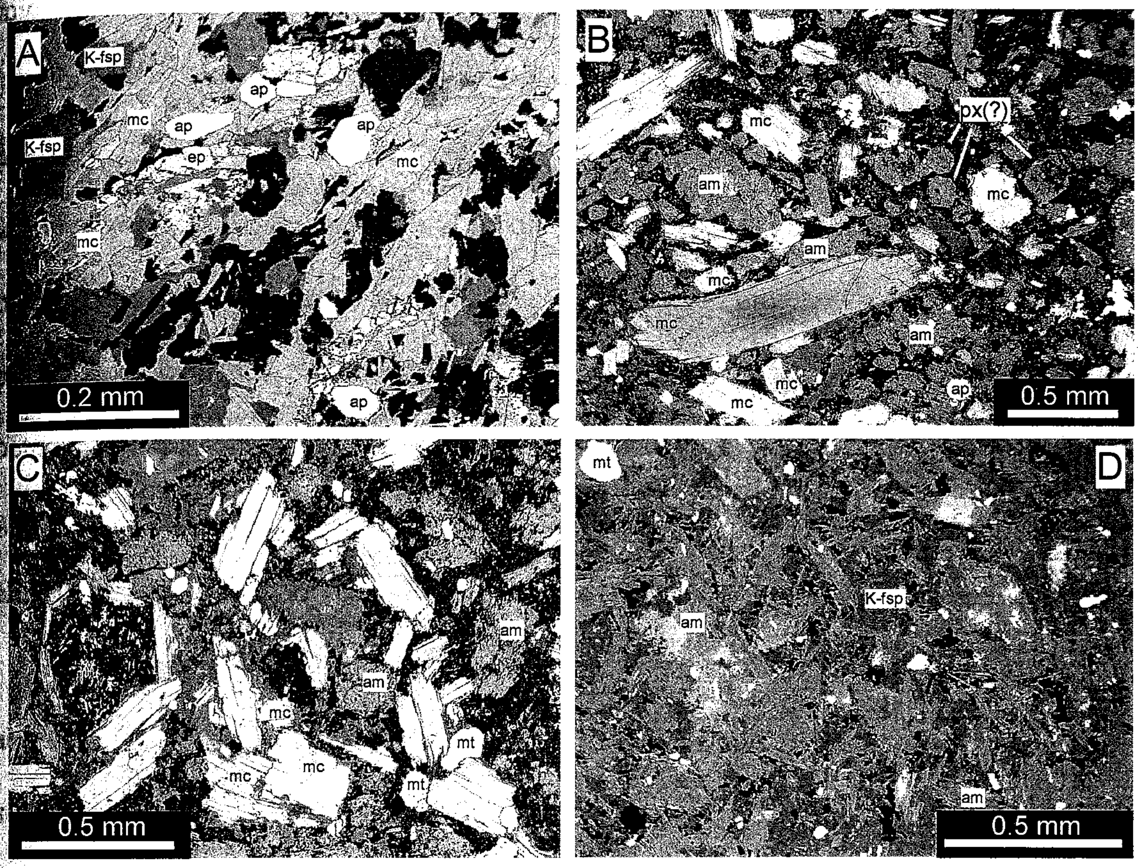

Fig. 4.3. Backscattered electron images of lamprophyres. A, fine grained mica lamprophyre with abundant euhedral apatite. B, amphibole lamprophyre with phenocrysts of mica and amphibole. Some amphibole crystals have rounded and pseudo-octagonal cross sections and probably represent pseudomorphs after pyroxene. C, unzoned, slightly chloritized micas in amphibole-bearing lamprophyre. D, fine-grained lamprophyre with phenocrysts of amphibole and K-feldspar matrix. Mineral symbols: am = amphibole, ap = apatite, ep = secondary epidote, mc = mica, mt = magnetite, K-fsp = K-feldspar; px(?) = presumed pseudomorphs of amphibole after pyroxene.

weakly chloritized. Films of secondary hematite occur along cleavage planes of some mica crystals.

Phenocrysts of green amphibole are optically uniform (Fig. 4.2C) and distinctly pleochroic. In most cases, these are subhedral prismatic crystals with "splintery" terminations and rhomb-shaped or pseudohexagonal cross-sections. Pyroxene phenocrysts were not directly identified, but their original presence is suggested by petrographic evidence. Some lamprophyres contain phenocrysts with equant or pseudo-octagonal cross-sections that are typical of pyroxenes (Fig. 4.3B). These pyroxene-like grains consist either of monocrystalline green amphibole, or of amphibole-carbonate-chlorite aggregates, and most likely represent pseudomorphs after pyroxene phenocrysts.

The groundmass of the lamprophyres consists mainly of K-feldspar, with less abundant plagioclase, biotite, and amphibole. K-feldspar and plagioclase occur as subhedral, prismatic, 0.2-0.3 mm long crystals that are often arranged in radiating, fan-shaped intergrowths. Finer (0.03-0.05 mm) subequant anhedral feldspars are less common. Plagioclase and K-feldspar show ambiguous reaction relationships. In some cases, plagioclase forms replacement rims surrounding K-feldspar cores. In other cases, plagioclase cores are mantled by K-feldspar. Groundmass biotite and amphibole vary from 0.05 to 0.3 mm in length. Accessory phases such as apatite, titanite, and magnetite normally occur as fine (0.05-0.2 mm) euhedral grains scattered in the groundmass. In some lamprophyres, apatite and titanite form microphenocrysts up to 0.7 mm long. In addition to unequivocally primary phases, the groundmass of lamprophyres contains relatively abundant carbonate and epidote of likely epigenetic origin.

Most lamprophyres carry dark angular or lens-shaped mafic enclaves (2 mm to 5 cm long) that consist predominantly of fine-grained mica, rarely of amphibole, with variable amounts of feldspar, apatite, magnetite, and secondary epidote, chlorite, and carbonate (Fig.4.4A, B). Less abundant are rounded leucocratic segregations (ocelli, cf. Rock, 1991), 0.5 to 20 cm in diameter (Fig. 4.4C, D). These segregations differ from host lamprophyres by a lower color index and, in most cases, by a larger grain size. They are composed of relatively coarse (0.7-5 mm) anhedral K-feldspar and subordinate plagioclase, with smaller amounts of amphibole and/or biotite, accessory apatite, and, sometimes, epigenetic carbonate and chlorite. Similar to the groundmass of host lamprophyres, many anhedral plagioclase grains of the leucocratic segregations are overgrown by irregular K-feldspar rims.

Syenite porphyries

The syenite porphyries are brownish-pinkish-gray to dark-gray rocks with euhedral and subhedral phenocrysts (0.5-4 mm, up to 1 cm) of K-feldspar and largely subordinate plagioclase. The amount of feldspar phenocrysts varies from less than 5 percent to 50 percent and averages about 25-30 percent. In most cases, the relative proportion of plagioclase among feldspar phenocrysts does not exceed 20 percent. Some rocks contain mostly euhedral, long prismatic (length to width ratio 4-10) feldspar phenocrysts that are flow-aligned (Fig. 4.5A, B); other rocks are massive and comprise predominantly subequant and short prismatic (length to width ratio 1-2) feldspars (Fig. 4.5C). In addition to the feldspars, some syenite porphyries contain up to 20 percent phenocrysts (0.5-1 mm) of optically uniform green to greenish brown mica (Fig. 4.5, A and B). Zoned mica

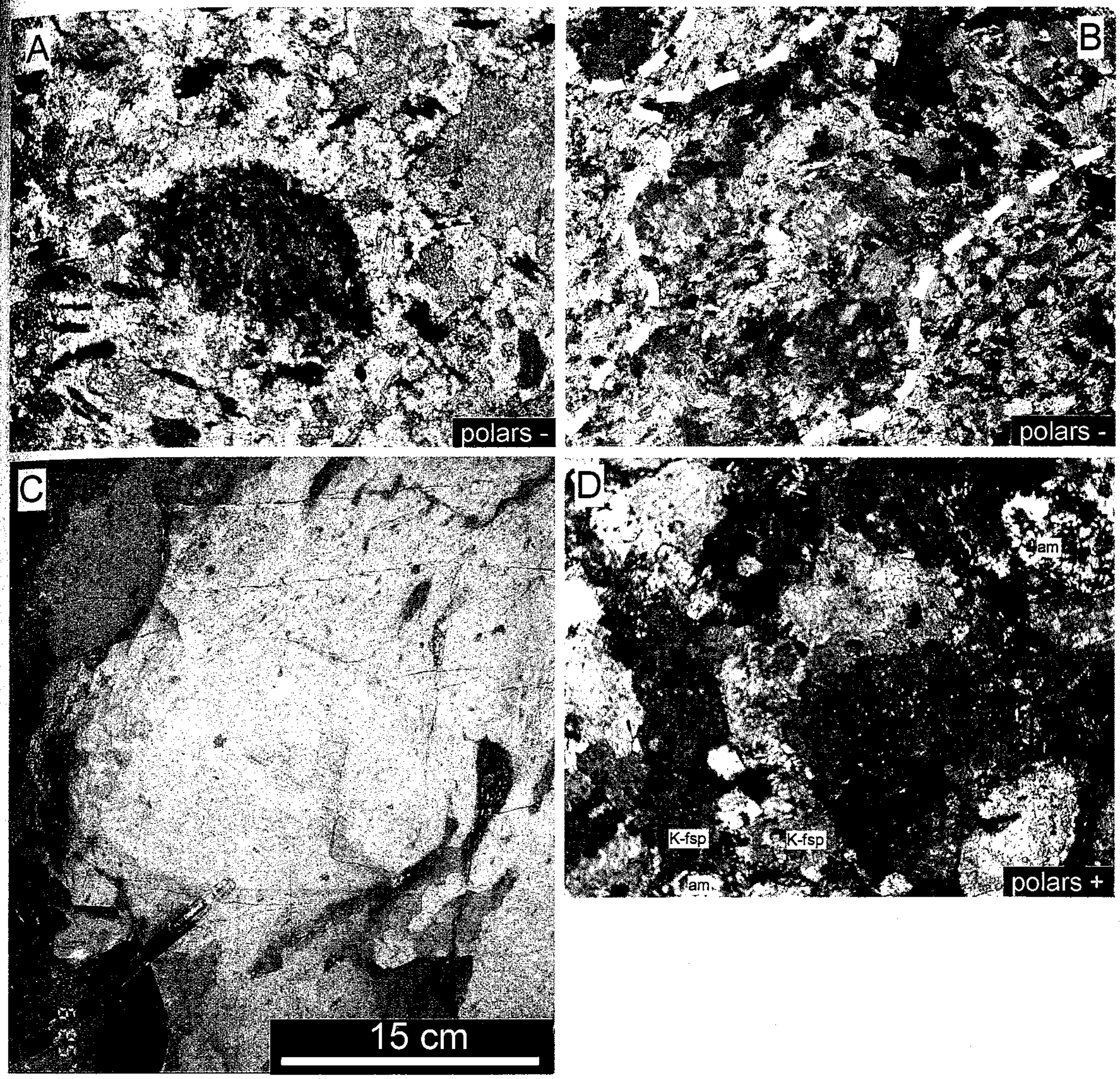

Fig. 4.4. Inclusions in lamprophyres. A and B, photomicrographs of mica-rich mafic enclaves (dashed lines on B highlight boundaries of enclaves). C, leucocratic segregation (ocellum). D, photomicrograph of a leucocratic ocellum similar to the one shown in C. The rock consists predominantly of anhedral K-feldspar (K-fsp) with subordinate plagioclase and amphibole (am). Field of view is approximately 3 mm for all photomicrographs.

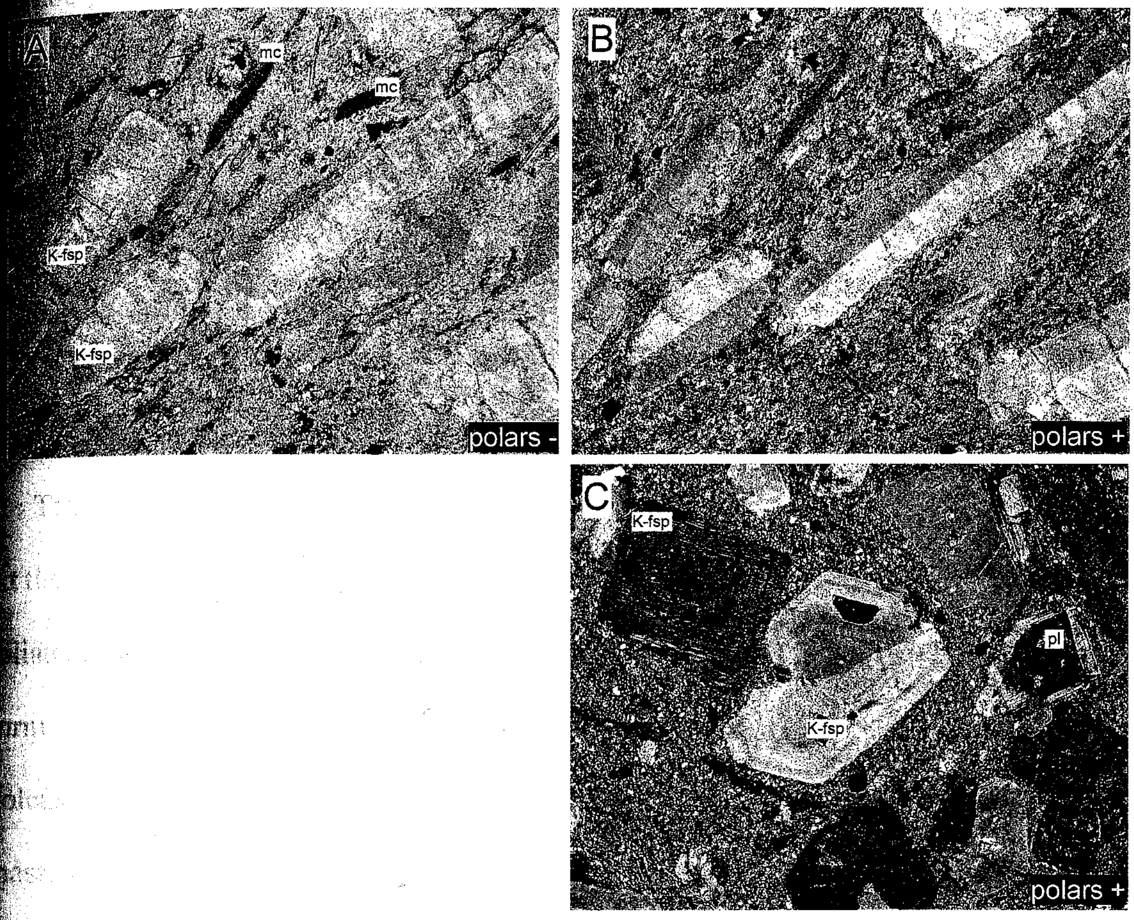

Fig. 4.5. Photomicrographs depicting two textural varieties of syenite porphyries (A and B depict the same field of view in plane-polarized and cross-polarized light). A and B, mica-bearing syenite porphyry with flow-aligned phenocrysts of long prismatic K-feldspar and mica. C, massive leucocratic syenite porphyry with subequant and short prismatic phenocrysts of K-feldspar and plagioclase. Field of view approximately 3 mm. Mineral symbols: K-fsp = K-feldspar; mc = mica; pl = plagioclase.

phenocrysts and megacrysts are relatively rare. The groundmass is composed of microgranular, anhedral, equant plagioclase, K-feldspar, and quartz (0.005-0.02 mm), often with fine mica (0.05-0.1 mm). In some varieties, K-feldspar and plagioclase of the groundmass form subhedral aligned microlites up to 0.1 mm long. Most common accessory minerals are apatite and magnetite; titanite, zircon, and allanite are less abundant. Syenite porphyries contain mica-rich mafic enclaves similar to those found in the lamprophyres.

Textures and phenocryst assemblages of syenite porphyries exhibit spatial variations. At the margins of the intrusive belt, syenite porphyries are represented mostly by flow-foliated, sparsely porphyritic (phenocrysts up to 15-20%) mica-bearing varieties. These form relatively thin sills that intercalate with sills of lamprophyres and remnants of host volcanicalstic sandstones. The core of the intrusive belt comprises mainly thick bodies of massive, feldspar-rich, leucocratic syenite porphyries.

Mineral chemistry

Electron microprobe analytical techniques

Chemical compositions of magmatic and hydrothermal minerals were determined with the Cameca SX-100 electron microprobe at New Mexico Institute of Mining and Technology. Analyses were conducted on polished thin sections and mounted mineral separates. Two analytical techniques were employed: the quantitative electron microprobe analysis and the line scan method. The quantitative analysis was conducted on magmatic feldspar, biotite, amphibole, apatite, and magnetite, and on hydrothermal feldspar, white mica, biotite, and carbonate. The beam current and acceleration voltage were set at 20 nA and 15 kV, respectively, with the exception of carbonate analyses, during which the beam current was lowered to 10 nA. The optimum beam diameters were 10 μm for feldspar and apatite, 1 μm for amphibole, 5 μm for mica, and 20 μm for carbonate. For fine-grained groundmass feldspar, the beam diameter was set at 1 μm and 5 μm. Some fine-grained hydrothermal white micas and carbonates were analyzed with 1 μm and 5 μm beam diameters, respectively. In order to monitor the accuracy and precision, mineral standard reference materials (SRM) were analyzed during each session. The results of the SRM analyses are summarized in Appendix B. Analytical errors reported in this chapter are assigned approximately equal to one standard deviation of replicate SRM analyses.

The line scan method was used to investigate the compositional zoning of K-feldspar phenocrysts. The obtained line scans characterize relative variations of Ba, K, Si, and Na along linear traverses. The results are expressed as uncorrected counts per second (cps) and do not provide quantitative concentration values.

Mica

Magmatic micas of the Solton Sary lamprophyres and syenite porphyries can be classified into four morphological types: 1) fine grained mica of the groundmass, 2) fine grained mica of mafic enclaves, 3) phenocrysts without apparent zoning, and 4) distinctly zoned phenocrysts and megacrysts. The first three populations comprise uniformly colored green to greenish-brown crystals that differ only by size and mode of occurrence. Electron microprobe analyses confirm their chemical uniformity (Tables 4.1, 4.2, and 4.3). Virtually all unzoned micas, independent of their morphological type, plot within

Table 4.1: Representative electron microprobe analyses of [illegible]

run ID	biot397-4	biot49-1137gr-1	biot49-1137gr-2	biot56-158gr-1	biot58-583gr-1	biotTR223-1	biotTR223-2	biot49-1292gr-1	biot49-1292gr-2	bio-55_62.7-2	bio-55_62.7-3	biot57-1662gr-2	biot57-1741gr-1	biot58-110gr-1	[illegible]
sample	397	49-113.7	49-113.7	56-158.0	58-58.3	TR223	TR223	49-129.2	49-129.2	55-62.7	55-62.7	57-166.2	57-174.1	58-110.2	658
rock type	L	L	L	L	L	L	L	SP	SP	SP	SP	SP	SP	SP	SP
SiO_2	36.63	35.34	36.99	35.96	37.41	37.01	38.09	36.40	37.30	38.77	39.12	38.39	36.61	37.74	38.28
TiO_2	1.23	1.84	1.34	2.33	1.86	1.34	1.25	2.03	2.95	1.22	1.34	1.88	2.52	1.93	1.77
Al_2O_3	15.24	15.06	14.49	15.97	15.50	15.09	14.99	14.31	13.68	15.23	15.08	14.68	14.30	14.70	14.73
Cr_2O_3	0.12	0.04	0.02	0.11	0.07	0.01	0.03	0.17	0.02	0.00	0.22	0.02	0.00	0.04	0.02
MgO	12.74	13.06	13.67	12.37	13.89	13.32	13.47	14.45	14.33	13.09	13.47	13.78	12.33	13.86	12.91
CaO	0.01	0.29	0.04	0.00	0.03	0.01	0.00	0.02	0.03	0.04	0.04	0.00	0.05	0.04	0.01
MnO	0.18	0.14	0.12	0.00	0.02	0.17	0.24	0.00	0.00	0.25	0.18	0.01	0.00	0.00	0.16
FeO	19.45	18.53	18.06	17.84	16.32	17.70	17.59	17.09	15.99	17.76	17.54	16.55	17.81	17.03	18.13
BaO	0.43	0.97	0.00	0.76	0.43	0.00	0.03	0.00	0.55	0.00	0.00	0.00	1.04	0.00	0.00
Na_2O	0.03	0.05	0.04	0.03	0.04	0.04	0.00	0.05	0.09	0.07	0.01	0.04	0.07	0.06	0.03
K_2O	9.65	8.94	9.86	9.67	9.83	9.77	9.39	9.99	9.87	8.40	7.91	9.98	9.39	9.63	9.66
F	0.44	0.61	0.82	0.86	0.46	0.31	0.27	2.77	2.95	0.55	0.50	1.07	1.07	0.73	0.69
Cl	0.03	0.08	0.10	0.03	0.04	0.00	0.00	0.05	0.05	0.04	0.03	0.04	0.07	0.05	0.01
	96.17	94.96	95.56	95.92	95.90	94.77	95.36	97.32	97.80	95.41	95.43	96.43	95.24	95.81	96.41
-O=F, Cl	0.19	0.28	0.37	0.37	0.20	0.13	0.11	1.18	1.25	0.24	0.22	0.46	0.46	0.32	0.30
Total	95.98	94.68	95.19	95.55	95.70	94.64	95.25	96.14	96.55	95.17	95.21	95.97	94.78	95.49	96.11
Number of ions on the basis of 24 O, F, Cl															
Si	6.076	5.945	6.123	5.952	6.118	6.156	6.260	5.902	5.996	6.319	6.345	6.221	6.109	6.173	6.244
Al	2.980	2.985	2.828	3.114	2.987	2.958	2.904	2.733	2.591	2.926	2.882	2.804	2.813	2.833	2.832
Ti	0.153	0.232	0.167	0.290	0.229	0.168	0.155	0.247	0.356	0.150	0.164	0.229	0.316	0.237	0.217
Cr	0.015	0.006	0.003	0.014	0.009	0.001	0.004	0.021	0.002	0.000	0.028	0.002	0.000	0.006	0.002
Mg	3.151	3.274	3.373	3.051	3.388	3.302	3.300	3.492	3.434	3.182	3.256	3.329	3.067	3.379	3.139
Ca	0.002	0.053	0.007	0.001	0.006	0.002	0.001	0.003	0.006	0.006	0.007	0.000	0.008	0.007	0.002
Mn	0.025	0.020	0.017	0.000	0.003	0.023	0.034	0.000	0.000	0.034	0.024	0.002	0.000	0.000	0.023
$Fe^2(t)$	2.698	2.606	2.500	2.468	2.232	2.462	2.418	2.317	2.149	2.420	2.379	2.243	2.485	2.328	2.473
Ba	0.028	0.064	0.000	0.049	0.027	0.000	0.002	0.000	0.035	0.000	0.000	0.000	0.068	0.000	0.000
Na	0.010	0.016	0.013	0.009	0.013	0.012	0.001	0.017	0.026	0.021	0.002	0.012	0.023	0.018	0.010
K	2.043	1.919	2.082	2.041	2.051	2.074	1.969	2.067	2.024	1.747	1.635	2.063	1.999	2.008	2.011
F	0.229	0.324	0.431	0.450	0.240	0.165	0.139	1.420	1.500	0.284	0.256	0.547	0.563	0.375	0.358
Cl	0.008	0.024	0.027	0.008	0.010	0.001	0.001	0.014	0.013	0.010	0.007	0.011	0.018	0.015	0.003
Sum	17.418	17.468	17.571	17.448	17.312	17.322	17.186	18.233	18.133	17.099	16.987	17.464	17.470	17.379	17.313
mg#	0.54	0.56	0.57	0.55	0.60	0.57	0.58	0.60	0.62	0.57	0.58	0.60	0.55	0.59	0.56

Abbreviations:L = lamprophyre; SP = syenite porphyry; mg# = Mg/(Mg+ Fe^2(t)). A complete listing of mica analyses is presented in Appendix B. Precision of analyses (wt%) based on replicate analyses of standard reference material (SRM) Biotite-3 (S. Kuehner, pers. comm..): SiO_2 (±0.4), TiO_2 (±0.05), Al_2O_3 (±0.2), MgO (±0.10), MnO (± 0.05), FeO (±0.3), Na_2O (±0.1), K_2O (±0.3), F (±0.3). Results of SRM Biotite-3 analyses are summarized in Appendix B

Table 4.2. Representative electron-microprobe analyses of mica from mafic enclaves

run ID	biot56-158e-1	biot56-158e-2	biot664-4e-1	biot664-4e-2	biot49-1292e-3	biot49-1292e-4	biot55-627e-1	biot55-627e-4	biot57-1662e-1	biot57-1662e-2	biot57-1741e-1	biot57-1741e-2	biot58-1102e-1	biot58-1102e-2
sample	56-158.0	56-158.0	664-4	664-4	49-129.2	49-129.2	55-62.7	55-62.7	57-166.2	57-166.2	57-174.1	57-174.1	58-110.2	58-110.2
rock type	L	L	L	L	SP	SP	SP	SP	SP	SP	SP	SP	SP	SP
SiO_2	36.98	38.35	35.79	37.20	35.98	36.34	35.17	35.88	38.04	35.86	38.18	37.22	36.28	37.68
TiO_2	1.86	1.88	1.34	1.17	2.13	2.10	1.03	1.08	0.81	2.13	1.81	1.92	2.04	2.03
Al_2O_3	14.57	14.35	15.31	15.42	14.02	14.12	16.12	16.16	14.71	15.70	14.04	14.86	15.10	14.81
Cr_2O_3	0.60	0.62	0.13	0.07	0.07	0.10	0.29	0.26	1.13	0.04	0.40	0.32	0.07	0.05
MgO	14.51	14.60	13.17	13.35	14.24	13.94	12.50	12.54	13.50	11.93	14.13	12.88	12.93	13.71
CaO	0.01	0.03	0.02	0.05	0.03	0.05	0.04	0.02	0.03	0.03	0.06	0.06	0.02	0.00
MnO	0.04	0.00	0.20	0.16	0.01	0.06	0.23	0.16	0.02	0.00	0.07	0.04	0.08	0.03
FeO	16.21	15.97	18.29	18.35	17.28	17.26	18.69	19.19	16.89	19.07	17.05	18.09	18.37	17.08
BaO	0.00	0.00	0.60	0.07	0.23	0.69	0.33	0.34	0.39	1.13	0.07	0.17	0.00	0.00
Na_2O	0.05	0.03	0.06	0.09	0.03	0.05	0.06	0.04	0.05	0.03	0.04	0.05	0.04	0.05
K_2O	9.20	9.54	9.55	9.38	9.65	9.54	9.66	8.70	9.16	9.30	9.50	9.35	9.69	9.60
F	1.40	1.31	0.31	0.31	2.22	2.00	0.44	0.40	0.64	0.62	1.30	0.98	0.56	0.68
Cl	0.01	0.02	0.04	0.05	0.04	0.06	0.06	0.07	0.02	0.06	0.04	0.05	0.05	0.04
	95.44	96.70	94.80	95.66	95.93	96.32	94.60	94.85	95.37	95.90	96.69	95.99	95.23	95.76
-O=F, Cl	0.59	0.56	0.14	0.14	0.94	0.86	0.20	0.19	0.27	0.27	0.55	0.42	0.25	0.29
Total	94.85	96.15	94.66	95.52	94.98	95.46	94.40	94.67	95.10	95.62	96.14	95.56	94.98	95.46
Number of ions on the basis of 24 O, F, Cl														
Si	6.054	6.178	6.014	6.133	5.932	5.979	5.931	5.997	6.253	5.980	6.190	6.115	6.035	6.165
Al	2.812	2.724	3.031	2.997	2.725	2.738	3.203	3.184	2.849	3.086	2.682	2.878	2.959	2.855
Ti	0.230	0.228	0.169	0.146	0.264	0.259	0.131	0.136	0.100	0.267	0.220	0.237	0.255	0.250
Cr	0.077	0.079	0.017	0.009	0.009	0.013	0.038	0.035	0.146	0.005	0.051	0.042	0.009	0.006
Mg	3.541	3.507	3.300	3.282	3.499	3.421	3.142	3.126	3.309	2.966	3.416	3.156	3.207	3.344
Ca	0.002	0.004	0.004	0.009	0.005	0.010	0.007	0.004	0.005	0.006	0.011	0.011	0.003	0.000
Mn	0.005	0.000	0.029	0.022	0.002	0.009	0.033	0.023	0.003	0.000	0.010	0.005	0.012	0.005
$Fe^2(t)$	2.218	2.151	2.569	2.530	2.382	2.375	2.636	2.682	2.321	2.659	2.312	2.485	2.555	2.338
Ba	0.000	0.000	0.040	0.004	0.015	0.044	0.022	0.022	0.025	0.074	0.004	0.011	0.000	0.000
Na	0.017	0.010	0.020	0.028	0.011	0.016	0.021	0.014	0.016	0.010	0.014	0.016	0.013	0.017
K	1.921	1.961	2.048	1.972	2.030	2.003	2.077	1.854	1.921	1.977	1.965	1.961	2.057	2.004
F	0.726	0.669	0.163	0.160	1.155	1.042	0.235	0.214	0.334	0.324	0.665	0.507	0.296	0.350
Cl	0.002	0.004	0.012	0.013	0.011	0.016	0.016	0.019	0.005	0.017	0.010	0.013	0.015	0.010
Sum	17.605	17.515	17.415	17.305	18.041	17.925	17.492	17.308	17.287	17.371	17.549	17.436	17.416	17.344
mg#	0.61	0.62	0.56	0.56	0.59	0.59	0.54	0.54	0.59	0.53	0.60	0.56	0.56	0.59

Abbreviations: L = lamprophyre; SP = syenite porphyry; mg# = Mg/(Mg+ Fe^2(t)). A complete listing of mica analyses is presented in Appendix B. Estimated precisions are listed in footnotes for Table 4.1.

Table 4.3. Representative electron microprobe analyses of unzoned mica phenocrysts

run ID	bio-56_158-1	bio-56_158-10	bio-58_583-12	bio-58_583-14	bt-76-179.9-10	bt-76-179.9-11	bio-55_62.7-13	bio-55_62.7-14	bio-57_1741-10	bio-57_1741-4	bio-58_110-2	bio-58_110-4	57-166.2-11	57-166.2-10
sample	56-158.0	56-158.0	58-58.3	58-58.3	76-179.9	76-179.9	55-62.7	55-62.7	57-174.1	57-174.1	58-110.2	58-110.2	57-166.2	57-166.2
rock type	L	L	L	L	L	L	SP	SP	SP	SP	SP	SP	SP	SP
SiO_2	38.42	38.83	37.79	37.71	36.06	37.00	39.02	37.90	37.85	37.50	37.82	37.51	39.25	34.86
TiO_2	2.83	2.14	2.45	1.91	2.29	2.05	1.69	1.54	2.31	3.88	3.27	2.24	1.72	2.32
Al_2O_3	15.95	15.62	16.93	16.45	15.96	16.15	15.96	16.45	15.89	15.17	15.34	15.76	14.67	16.20
Cr_2O_3	0.12	1.12	0.02	0.10	0.11	0.24	0.04	0.04	0.03	0.02	0.13	0.68	0.39	0.04
MgO	12.18	13.49	13.40	13.78	11.85	12.89	13.09	12.17	13.01	12.15	12.72	14.93	13.70	11.43
CaO	0.02	0.00	0.05	0.01	0.04	0.01	0.01	0.01	0.05	0.02	0.02	0.03	0.02	0.08
MnO	0.00	0.00	0.09	0.05	0.00	0.04	0.17	0.21	0.02	0.01	0.03	0.04	0.07	0.12
FeO	17.64	16.47	16.21	16.64	18.50	17.33	17.92	18.59	17.90	18.33	17.50	17.64	16.11	18.73
NiO	n.a.	n.a.	n.a.	n.a.	0.02	0.03	n.a.	n.a.	n.a.	n.a.	n.a.	n.a.	0.03	0.01
BaO	1.17	0.52	0.91	0.64	0.92	0.07	0.00	0.05	0.13	0.00	0.29	0.05	0.28	1.63
Na_2O	0.04	0.00	0.03	0.00	0.06	0.04	0.03	0.00	0.00	0.00	0.05	0.02	0.13	0.09
K_2O	7.03	7.06	7.79	8.67	9.37	10.10	6.88	7.37	8.58	7.38	7.78	7.16	9.80	9.20
F	0.00	1.15	0.00	0.36	0.60	0.63	0.00	0.32	0.00	0.80	0.58	0.00	0.66	0.00
Cl	0.03	0.02	0.04	0.04	0.08	0.05	0.05	0.05	0.07	0.05	0.05	0.05	0.04	0.06
	95.43	96.42	95.72	96.35	95.88	96.63	94.85	94.70	95.83	95.31	95.56	96.11	96.86	94.75
-O=F, Cl	0.01	0.49	0.01	0.16	0.28	0.28	0.01	0.15	0.02	0.35	0.26	0.01	0.29	0.01
Total	95.42	95.93	95.71	96.19	95.60	96.35	94.84	94.55	95.81	94.96	95.30	96.09	96.58	94.74
Number of ions on the basis of 24 O, F, Cl														
Si	6.257	6.202	6.117	6.099	5.988	6.030	6.330	6.214	6.166	6.115	6.152	6.052	6.321	5.916
Al	3.061	2.941	3.230	3.136	3.123	3.103	3.051	3.179	3.052	2.916	2.940	2.997	2.784	3.240
Ti	0.347	0.258	0.298	0.232	0.286	0.251	0.207	0.190	0.283	0.476	0.401	0.271	0.209	0.296
Cr	0.015	0.142	0.003	0.013	0.014	0.031	0.005	0.005	0.004	0.003	0.017	0.086	0.049	0.005
Mg	2.958	3.213	3.233	3.323	2.934	3.132	3.165	2.975	3.161	2.955	3.084	3.590	3.289	2.892
Ca	0.003	0.000	0.009	0.002	0.007	0.002	0.002	0.001	0.009	0.003	0.003	0.004	0.003	0.015
Mn	0.000	0.000	0.012	0.007	0.001	0.005	0.023	0.029	0.002	0.001	0.004	0.006	0.010	0.017
$Fe^2(t)$	2.402	2.199	2.194	2.251	2.569	2.362	2.431	2.549	2.439	2.500	2.380	2.379	2.169	2.658
Ni	-	-	-	-	0.003	0.004	-	-	-	-	-	-	0.004	0.001
Ba	0.075	0.033	0.058	0.041	0.060	0.004	0.000	0.003	0.008	0.000	0.018	0.003	0.018	0.108
Na	0.013	0.000	0.009	0.000	0.021	0.014	0.009	0.000	0.000	0.000	0.015	0.005	0.040	0.029
K	1.461	1.438	1.608	1.788	1.983	2.100	1.424	1.541	1.783	1.534	1.614	1.473	2.013	1.992
F	0.000	0.581	0.000	0.183	0.317	0.325	0.000	0.163	0.000	0.410	0.299	0.000	0.334	0.000
Cl	0.008	0.006	0.012	0.011	0.024	0.014	0.013	0.014	0.018	0.015	0.014	0.014	0.010	0.017
Sum	16.599	17.012	16.783	17.085	17.329	17.378	16.659	16.864	16.924	16.929	16.940	16.882	17.253	17.185
mg#	0.55	0.59	0.60	0.60	0.53	0.57	0.57	0.54	0.56	0.54	0.56	0.60	0.60	0.52

Abbreviations: L = lamprophyre, SP = syenite porphyry, n.a .= not analyzed, mg# = Mg/(Mg+ Fe^2(t)). A completete listing of mica analyses is presented in Appendix B. Estimated precisions are listed in footnotes for Table 4.1.

the biotite field on the Fe-Mg-Al diagram (Fig. 4.6, cf. Rock, 1991). The data points form a tight cluster, with no evidence for chemically distinct populations (Figs. 4.6 and 4.7). For most of the unzoned biotites, magnesium number (mg#), calculated as atomic ratio $Mg/(Mg+Fe^{+2}_{total})$ varies from 0.52 to 0.64, Al_2O_3 and TiO_2 values range from 14 to 16.5, and from 1 to 2.5 weight percent, respectively (Fig. 4.7).

Optically zoned micas form phenocrysts (1-2 mm) and megacrysts (0.3-4 cm) with pale-green cores and deep-green rims. The chemical compositions of these zoned micas vary on the scale of a single crystal (Table 4.4, Figs 4.8 and 4.9). Pale cores of the crystals have phlogopitic composition, are strongly enriched in Mg, and have lower Al and Ti compared to fine biotite in the groundmass (Fig. 4.7). Mg numbers of the colored rims tend to be intermediate between those of the cores and of fine groundmass mica (Fig. 4.7).

Feldspar

K-feldspar phenocrysts of the syenite porphyries contain more than 80 percent orthoclase component and are Ba-rich (Table 4.5, Figs. 4.10 and 4.11). BaO content varies from ~0.3 to ~6 percent defining a characteristic oscillatory zoning of the phenocrysts (Fig. 4.12). Zoned phenocrysts consist of discrete 20-500 micron-wide concentric growth bands separated by sharp euhedral, or slightly wavy boundaries. The adjacent bands are either concordant or discordant, with clear indications of resorption (Fig 4.12B). Most of these relatively coarse bands are in turn finely zoned and show an outward decrease in Ba content, followed by a sharp increase corresponding to the beginning of each new band (Fig. 4.13).

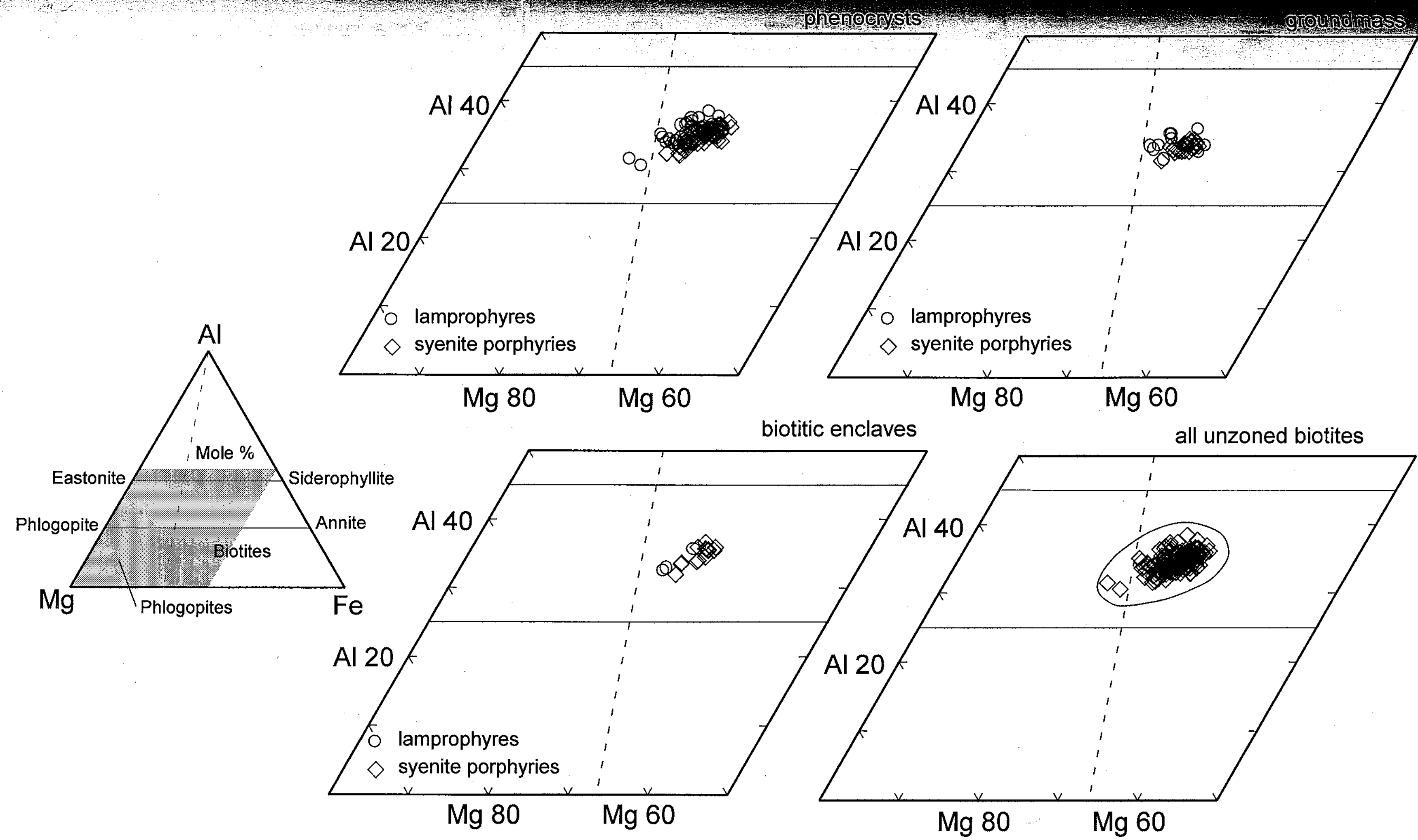

Fig. 4.6. Composition of unzoned micas from lamprophyres and syenite porphyries. All plots represent enlargements of the shaded area on the Mg-Al-Fe triangular diagram. Fields on the Mg-Al-Fe triangle as defined by Rock (1991). Compositional range represented by analytical errors is smaller than the symbol size.

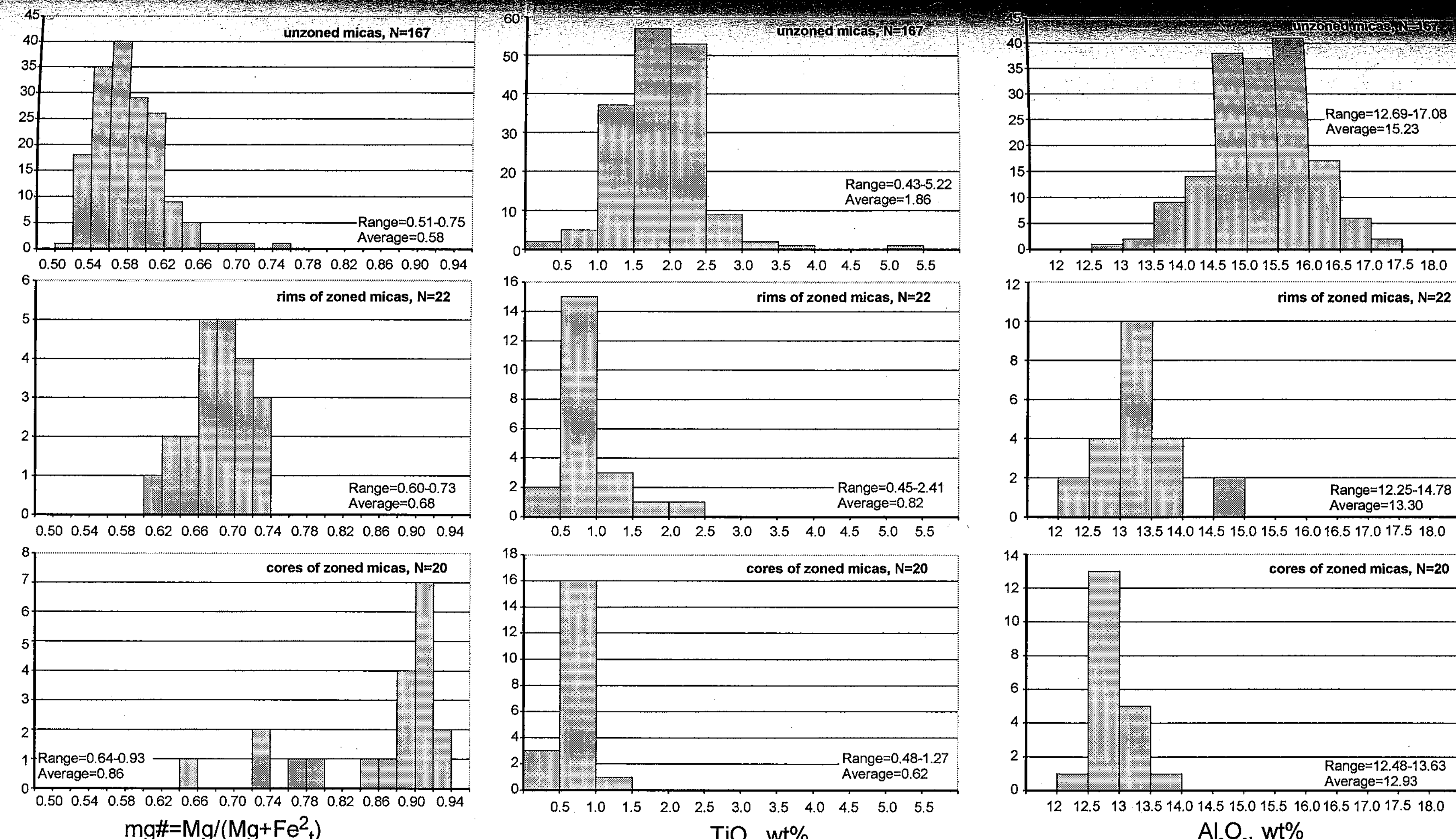

Fig. 4.7. Variation of mg#, TiO_2, and Al_2O_3 in magmatic micas. Vertical axes depict number of analyses. Estimated uncertainties: mg# ±0.4, TiO_2 ±0.05 wt %, and Al_2O_3 ±0.2 wt %.

Table 4.4. Representative electron microprobe analyses of zoned mica phenocrysts and megacrysts (continued on the next page)

run ID	bio-49_113.7-3	bio-49_113.7-38	bio-49_113.7-32	bio-49_113.7-25	bio-49_113.7-10	bio-49_113.7-12	bio-49_113.7-9	bio-49_113.7-1	bio-49_113.7-5	bio-49_113.7-8	bio-49_113.7-39	bio-49_113.7-21	bio-49_113.7-7
sample	49-113.7	49-113.7	49-113.7	49-113.7	49-113.7	49-113.7	49-113.7	49-113.7	49-113.7	49-113.7	49-113.7	49-113.7	49-113.7
rock type	L	L	L	L	L	L	L	L	L	L	L	L	L
zone	core	core	core	core	core	core	rim	rim	rim	rim	rim	rim	rim
SiO_2	42.29	42.37	42.68	42.14	42.34	42.84	41.68	41.30	41.38	41.53	39.65	40.94	40.66
TiO_2	0.64	0.77	0.66	0.52	0.52	0.58	0.53	0.68	0.47	0.45	1.21	0.67	0.63
Al_2O_3	12.58	12.90	12.48	12.88	12.81	13.14	13.01	13.32	13.46	12.96	14.78	13.94	13.34
Cr_2O_3	0.52	0.07	0.20	0.49	1.00	1.18	0.91	0.49	1.21	0.99	0.11	0.46	0.87
MgO	23.59	23.58	24.35	23.94	24.29	24.15	18.85	16.73	18.26	18.13	15.88	15.54	16.21
CaO	0.02	0.06	0.00	0.01	0.02	0.03	0.03	0.01	0.01	0.02	0.03	0.02	0.04
MnO	0.05	0.04	0.00	0.00	0.02	0.02	0.14	0.15	0.08	0.07	0.15	0.09	0.15
FeO	5.65	6.50	4.71	5.34	4.39	4.33	12.65	14.57	12.32	13.57	15.24	15.86	15.13
BaO	0.22	0.22	0.29	0.22	0.15	0.23	0.18	0.19	0.20	0.16	0.29	0.16	0.17
Na_2O	0.07	0.06	0.00	0.00	0.00	0.08	0.02	0.03	0.00	0.00	0.00	0.03	0.17
K_2O	7.88	7.72	7.67	7.85	8.01	7.90	7.62	6.74	6.93	7.43	7.26	6.64	7.58
F	1.52	1.71	1.79	1.76	1.38	0.96	0.00	1.11	1.06	0.91	0.86	1.05	0.96
Cl	0.01	0.02	0.00	0.02	0.00	0.01	0.02	0.00	0.01	0.02	0.04	0.03	0.03
	95.03	96.03	94.82	95.15	94.91	95.44	95.63	95.30	95.38	96.23	95.50	95.44	95.95
-O=F, Cl	0.64	0.73	0.75	0.75	0.58	0.41	0.00	0.47	0.45	0.39	0.37	0.45	0.41
Total	94.39	95.31	94.06	94.40	94.33	95.03	95.62	94.83	94.94	95.84	95.13	94.99	95.54
					Number of ions on the basis of 24 O, F, Cl								
Si	6.509	6.466	6.536	6.464	6.491	6.525	6.580	6.558	6.513	6.535	6.340	6.523	6.484
Ti	2.282	2.320	2.252	2.329	2.315	2.358	2.420	2.492	2.497	2.404	2.784	2.618	2.507
Al	0.074	0.089	0.075	0.059	0.060	0.066	0.063	0.081	0.055	0.053	0.146	0.080	0.076
Cr	0.064	0.008	0.024	0.059	0.121	0.141	0.113	0.061	0.151	0.123	0.014	0.058	0.110
Mg	5.413	5.364	5.560	5.474	5.551	5.483	4.436	3.960	4.284	4.253	3.785	3.692	3.855
Ca	0.004	0.010	0.000	0.002	0.003	0.005	0.005	0.001	0.001	0.004	0.005	0.004	0.008
Mn	0.007	0.006	0.000	0.000	0.003	0.003	0.018	0.020	0.011	0.009	0.021	0.012	0.020
Fe	0.727	0.830	0.604	0.685	0.563	0.551	1.670	1.934	1.622	1.785	2.037	2.114	2.018
Ba	0.013	0.013	0.017	0.013	0.009	0.014	0.011	0.012	0.013	0.010	0.018	0.010	0.011
Na	0.021	0.019	0.000	0.000	0.000	0.022	0.006	0.008	0.000	0.000	0.000	0.008	0.053
K	1.548	1.503	1.498	1.535	1.566	1.534	1.534	1.365	1.391	1.490	1.481	1.350	1.541
F	0.737	0.827	0.867	0.854	0.668	0.464	0.000	0.556	0.526	0.451	0.436	0.527	0.482
Cl	0.003	0.006	0.001	0.005	0.001	0.002	0.004	0.000	0.003	0.005	0.012	0.009	0.008
Sum	17.399	17.459	17.434	17.479	17.348	17.170	16.861	17.049	17.068	17.122	17.079	17.006	17.173
mg#	0.88	0.87	0.90	0.89	0.91	0.91	0.73	0.67	0.73	0.70	0.65	0.64	0.66

Table 4.4 (Continued)

run ID	bio-49_1292-7	bio-49_1292-32	bio-49_1292-17	bio-49_1292-4	bio-49_1292-3	bio-49_1292-15	bio-49_1292-24	bio-49_1292-29	bio-49_1292-28	bio-49_1292-18	bio-49_1292-19	bio-49_1292-23	bio-49_1292-26
sample	49-129.2	49-129.2	49-129.2	49-129.2	49-129.2	49-129.2	49-129.2	49-129.2	49-129.2	49-129.2	49-129.2	49-129.2	49-129.2
rock type	SP	SP	SP	SP	SP	SP	SP	SP	SP	SP	SP	SP	SP
zone	core	core	core	core	core	core	core	core	core	rim	rim	rim	rim
SiO_2	40.54	40.71	42.52	41.34	42.16	41.67	42.52	41.90	41.75	41.23	40.51	40.96	40.59
TiO_2	1.27	0.55	0.63	0.48	0.54	0.65	0.55	0.68	0.73	0.53	1.48	0.68	1.50
Al_2O_3	13.63	12.77	12.59	12.95	13.16	12.67	12.93	12.80	13.15	12.29	13.02	12.99	13.58
Cr_2O_3	0.42	0.74	0.73	0.71	0.74	0.68	0.58	0.13	0.18	0.72	0.67	0.61	0.17
MgO	15.87	24.72	24.88	20.13	25.39	27.92	24.81	26.84	23.96	18.37	16.09	16.89	16.37
CaO	0.02	0.01	0.00	0.06	0.00	0.00	0.01	0.04	0.01	0.01	0.01	0.03	0.02
MnO	0.00	0.01	0.07	0.01	0.01	0.02	0.00	0.04	0.03	0.04	0.04	0.00	0.00
FeO	15.03	4.45	3.81	10.30	4.40	3.89	4.35	4.88	5.07	12.61	14.43	14.02	15.00
BaO	0.18	0.16	0.20	0.25	0.23	0.14	0.26	0.28	0.26	0.19	0.10	0.18	0.28
Na_2O	0.07	0.03	0.08	0.06	0.17	0.00	0.14	0.08	0.05	0.04	0.00	0.00	0.00
K_2O	8.58	10.63	8.60	8.44	9.55	8.66	8.49	8.57	8.78	7.34	7.80	7.70	8.03
F	3.16	0.00	3.39	2.55	3.47	0.00	3.27	2.92	2.89	2.42	0.00	3.21	2.65
Cl	0.04	0.02	0.00	0.03	0.00	0.01	0.01	0.01	0.03	0.01	0.02	0.02	0.02
	98.80	94.80	97.52	97.29	99.84	96.30	97.92	99.15	96.88	95.80	94.17	97.27	98.22
-O=F, Cl	1.34	0.00	1.43	1.08	1.46	0.00	1.38	1.23	1.22	1.02	0.01	1.36	1.12
Total	97.46	94.79	96.09	96.20	98.37	96.30	96.54	97.92	95.66	94.78	94.16	95.92	97.10
Number of ions on the basis of 24 O, F, Cl													
Si	6.298	6.379	6.359	6.384	6.221	6.330	6.343	6.206	6.326	6.491	6.561	6.399	6.323
Ti	2.495	2.358	2.220	2.356	2.289	2.267	2.274	2.235	2.348	2.280	2.485	2.392	2.493
Al	0.149	0.064	0.071	0.056	0.059	0.074	0.062	0.076	0.083	0.063	0.180	0.080	0.176
Cr	0.052	0.092	0.087	0.087	0.087	0.081	0.068	0.015	0.022	0.089	0.086	0.075	0.021
Mg	3.677	5.774	5.547	4.635	5.585	6.323	5.518	5.926	5.413	4.313	3.885	3.934	3.802
Ca	0.004	0.001	0.000	0.009	0.000	0.000	0.001	0.007	0.001	0.002	0.002	0.005	0.004
Mn	0.000	0.001	0.009	0.001	0.001	0.003	0.000	0.005	0.003	0.005	0.005	0.000	0.000
Fe	1.952	0.583	0.476	1.330	0.543	0.494	0.543	0.605	0.643	1.660	1.955	1.831	1.953
Ba	0.011	0.010	0.012	0.015	0.014	0.008	0.015	0.016	0.015	0.012	0.006	0.011	0.017
Na	0.021	0.008	0.024	0.017	0.047	0.000	0.039	0.022	0.015	0.013	0.000	0.000	0.000
K	1.700	2.125	1.641	1.663	1.798	1.679	1.615	1.618	1.697	1.474	1.611	1.533	1.596
F	1.550	0.000	1.604	1.247	1.621	0.000	1.544	1.365	1.385	1.203	0.000	1.583	1.305
Cl	0.010	0.005	0.000	0.007	0.001	0.002	0.002	0.002	0.006	0.002	0.007	0.006	0.006
Sum	17.920	17.401	18.051	17.806	18.265	17.262	18.024	18.097	17.958	17.607	16.782	17.849	17.697
mg#	0.65	0.91	0.92	0.78	0.91	0.93	0.91	0.91	0.89	0.72	0.67	0.68	0.66

Abbreviations: L = lamprophyre, SP = syenite porphyry, mg# = Mg/(Mg+ Fe^2(t)). A completete listing of mica analyses is presented in Appendix B. Estimated precisions are listed in footnotes for Table 4.1.

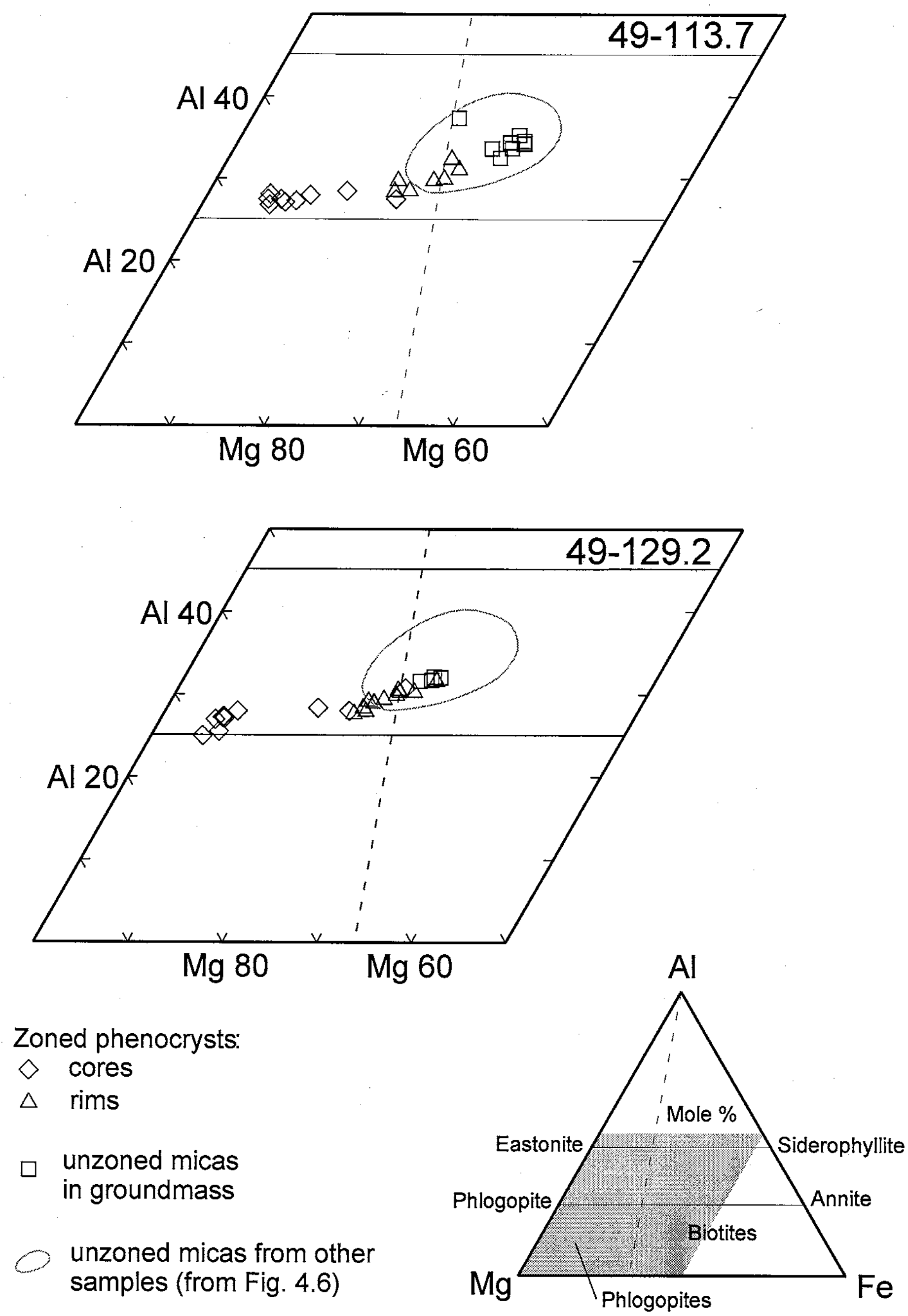

Fig. 4.8. Composition of micas from lamprophyre 49-113.7 and syenite porphyry 49-129.2. Plots represent enlargements of the shaded area on the Mg-Al-Fe triangular diagram. Fields on the Mg-Al-Fe triangle as defined by Rock (1991). Cores of zoned phenocrysts have phlogopitic compositions and are distinct from groundmass micas from the same samples, as well as from unzoned micas of all morphological types from other samples. Compositional range represented by analytical errors is smaller than the symbol size.

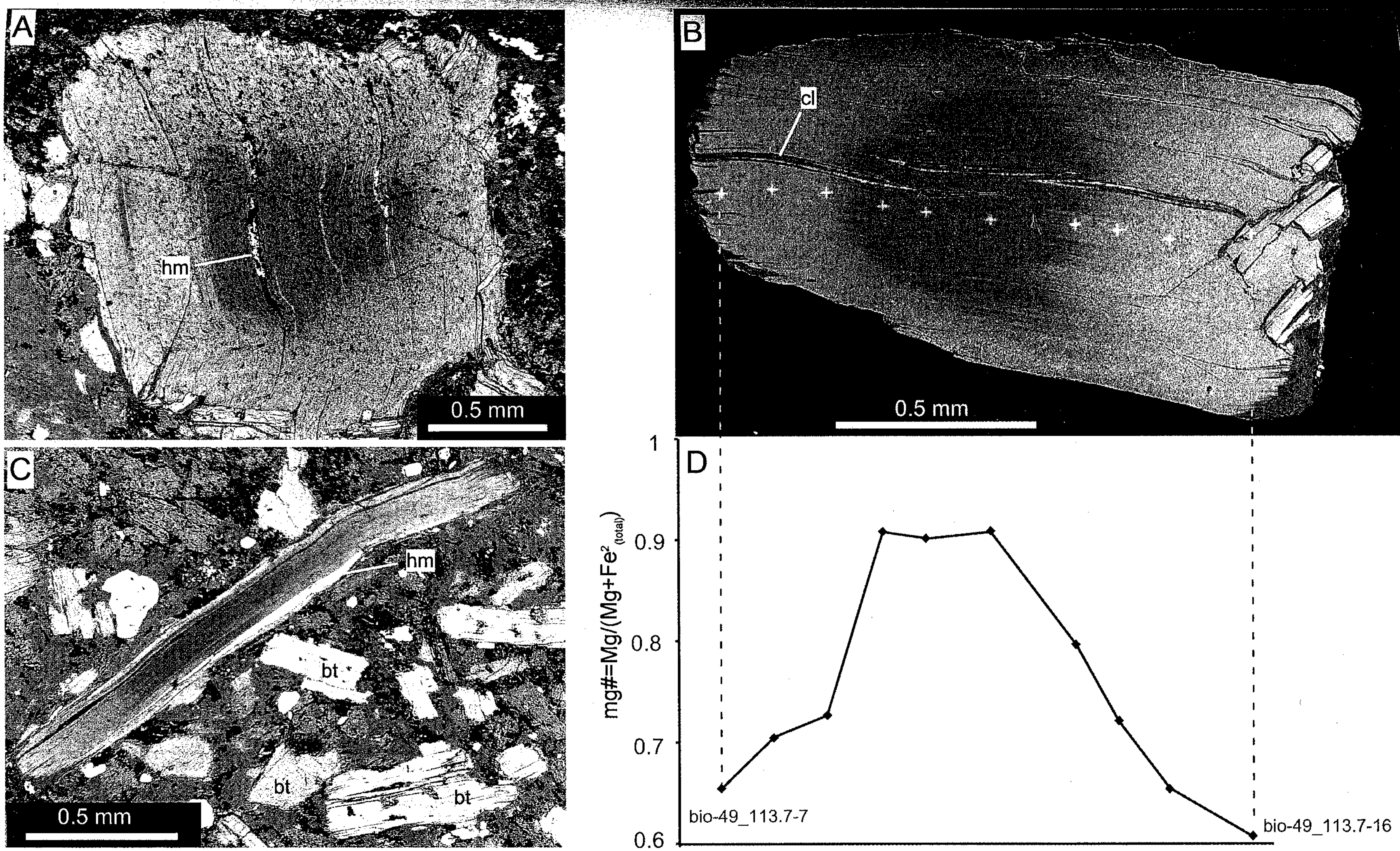

Fig. 4.9. Backscattered electron images of zoned mica phenocrysts from lamprophyre 49-113.7 (A-C) and measured crystal-scale variation of mg# (D). Mg-rich cores of the phenocrysts appear dark-gray on the backscattered electron images. Symbols: bt = unzoned mica, hm = secondary hematite (bright streaks along cleavage planes), and cl = secondary chlorite.

Table 4.5. Representative electron microprobe analyses of K-feldspar and plagioclase phenocrysts

run ID	ksp-491292-6	ksp-491292-2	ksp55627-3	ksp55627-6	fsp57-166.2-14	fsp57-166.2-26	fsp57-166.2-22a	fsp57-166.2-20	ksp-571741-6	ksp-571741-2	kspA23-7	kspA23-4	kspA23-5	plA23-5	plA23-3
sample	49-129.2	49-129.2	55-62.7	55-62.7	57-166.2	57-166.2	57-166.2	57-166.2	57-174.1	57-174.1	A23	A23	A23	A23	A23
rock type	SP	SP	SP	SP	SP	SP	SP	SP	SP	SP	SP	SP	SP	SP	SP
SiO_2	63.38	63.28	61.47	58.91	63.23	62.52	61.42	59.03	63.92	61.07	63.72	61.51	61.90	68.14	67.42
Al_2O_3	19.39	19.54	20.22	20.69	19.46	19.58	19.82	20.64	19.46	19.98	19.15	19.64	19.79	19.96	20.19
CaO	0.04	0.16	0.32	0.17	0.16	0.22	0.21	0.25	0.33	0.23	0.00	0.00	0.00	0.16	0.43
FeO	0.14	0.13	0.11	0.18	0.09	0.10	0.14	0.15	0.17	0.15	0.00	0.32	0.26	0.00	0.05
SrO	0.64	0.58	0.79	0.61	0.66	0.49	0.88	0.93	0.35	0.73	0.07	0.28	0.32	0.05	0.16
BaO	0.70	1.21	2.56	6.46	0.36	1.12	2.27	5.52	0.32	3.29	0.97	3.46	3.51	0.02	0.02
Na_2O	0.75	0.94	1.30	0.44	0.97	0.78	0.82	1.08	1.84	0.61	0.32	0.78	0.66	11.33	11.22
K_2O	15.39	15.04	13.56	12.88	15.07	14.96	14.38	12.54	14.17	14.27	16.32	14.25	14.53	0.09	0.13
Total	100.44	100.88	100.32	100.35	100.00	99.77	99.94	100.13	100.55	100.33	100.54	100.24	100.98	99.74	99.61
Number of ions on the basis of 32 O. All Fe recalculated as Fe^{3+}.															
Si	11.760	11.721	11.534	11.332	11.748	11.697	11.584	11.328	11.758	11.542	11.825	11.611	11.611	11.926	11.846
Al	4.241	4.268	4.473	4.693	4.263	4.318	4.408	4.669	4.220	4.452	4.189	4.371	4.377	4.119	4.182
Fe	0.022	0.020	0.017	0.030	0.014	0.015	0.023	0.023	0.026	0.024	0.000	0.050	0.041	0.000	0.007
Ca	0.008	0.032	0.064	0.035	0.031	0.045	0.042	0.052	0.065	0.046	0.000	0.000	0.000	0.030	0.081
Sr	0.069	0.062	0.086	0.068	0.071	0.053	0.096	0.103	0.037	0.080	0.007	0.030	0.035	0.005	0.016
Ba	0.051	0.088	0.188	0.487	0.026	0.082	0.167	0.415	0.023	0.244	0.071	0.256	0.258	0.001	0.001
Na	0.269	0.338	0.471	0.164	0.349	0.283	0.300	0.400	0.655	0.225	0.113	0.286	0.241	3.845	3.822
K	3.644	3.554	3.246	3.162	3.572	3.571	3.460	3.071	3.325	3.440	3.863	3.432	3.476	0.020	0.029
Sum	20.065	20.081	20.080	19.970	20.074	20.063	20.080	20.061	20.109	20.052	20.068	20.037	20.039	19.947	19.985
Ab	0.069	0.086	0.125	0.049	0.088	0.072	0.079	0.114	0.162	0.061	0.029	0.077	0.065	0.987	0.972
An	0.002	0.008	0.017	0.010	0.008	0.012	0.011	0.015	0.016	0.012	0.000	0.000	0.000	0.008	0.021
Or	0.929	0.906	0.858	0.941	0.904	0.916	0.910	0.872	0.822	0.927	0.971	0.923	0.935	0.005	0.007

Abbreviations: L = lamprophyre; SP = syenite porphyry. Feldspar end-members calculated as recommended by Deer et al. (1992). A complete listing of feldspar analyses is presented in Appendix B. Precision of analyses (wt%) based on replicate analyses of standard reference materials (SRM) UCB 374 MAD-10 Orthoclase and UCB 301 Cazadero Albite (Donovan, pers. comm.): SiO_2 (±0.4), Al_2O_3 (±0.1), FeO (±0.04), Na_2O in K-feldspar (±0.03), Na_2O in albite (± 0.2), K_2O in K-feldspar (±0.1). Results of SRM Orthoclase and Albite analyses are summarized in Appendix B. Uncertainty in BaO at a level of 4 wt%, based on counting statistics is ±0.04 wt%.

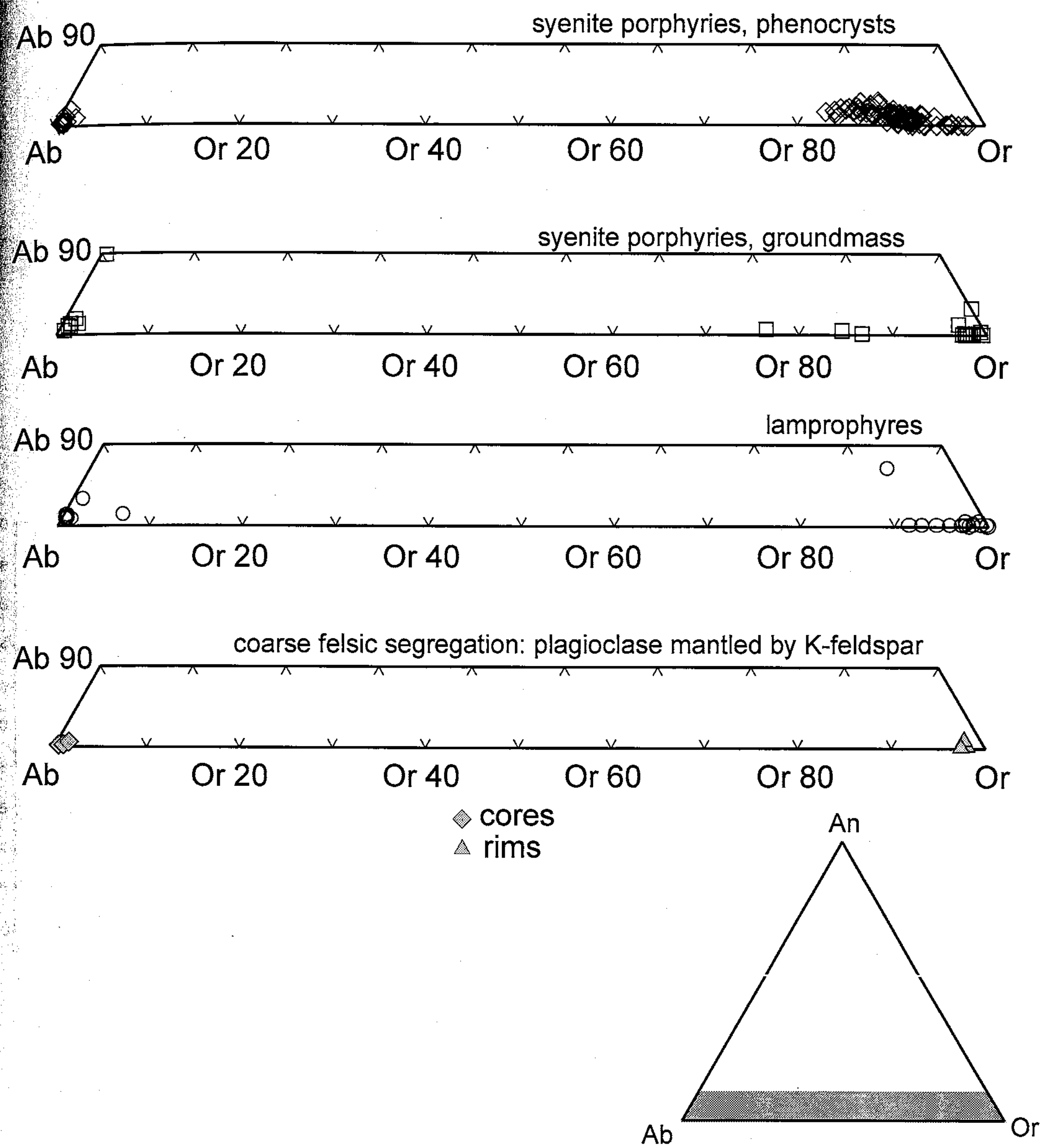

Fig. 4.10. Ternary plots of feldspars from syenite porphyries, lamprophyres and a leucocratic segregation (ocellum) hosted in lamprophyres. Feldspar end members calculated according to Deer et al. (1992). Plots correspond to the shaded bottom portion of the Ab-An-Or triangle. Compositional range represented by analytical errors is comparable to the symbol size.

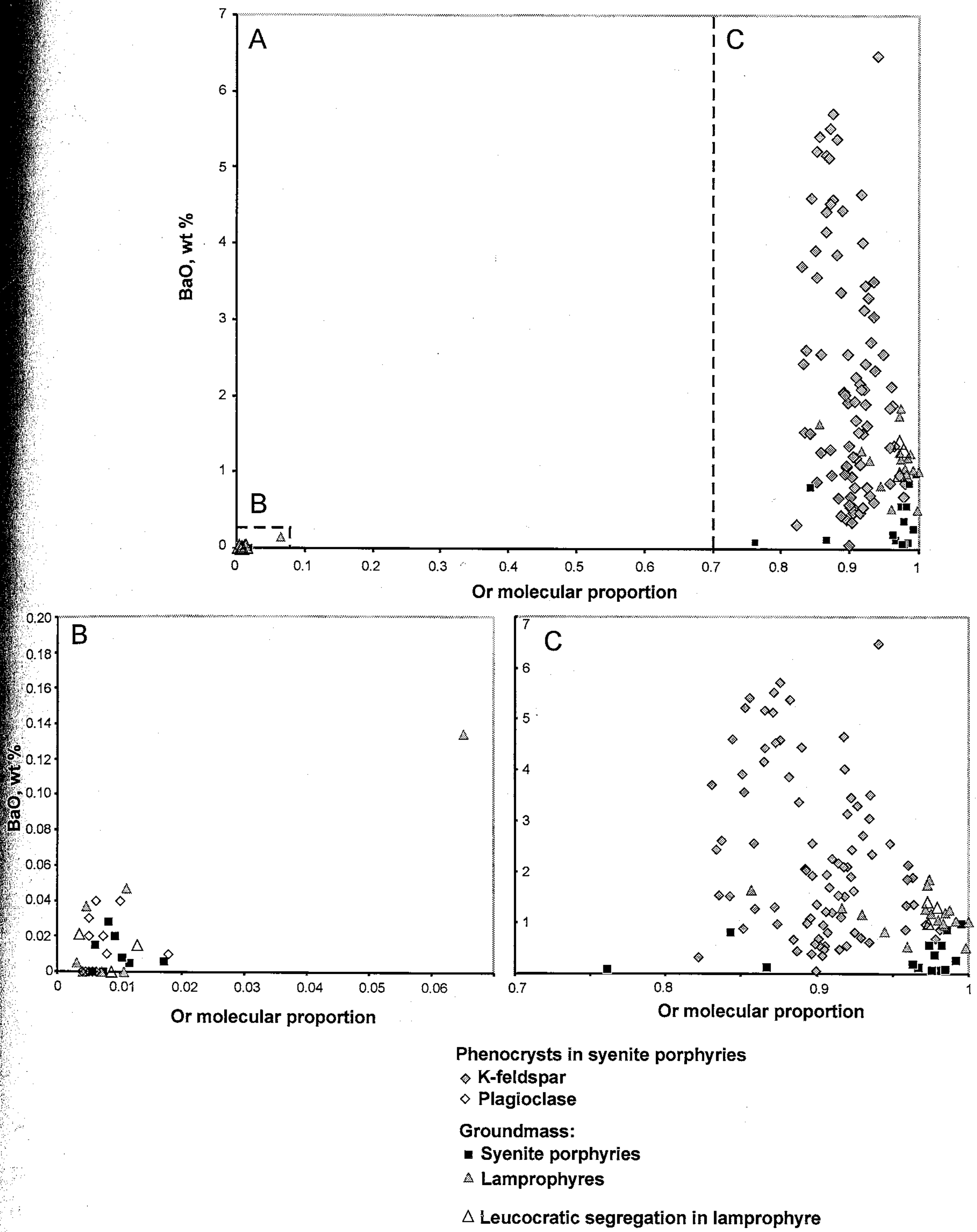

Fig. 4.11. Variation of BaO in feldspars from lamprophyres and syenite porphyries. Graphs B and C are enlarged areas from the graph A. Analytical error for BaO is about ±0.04 wt %.

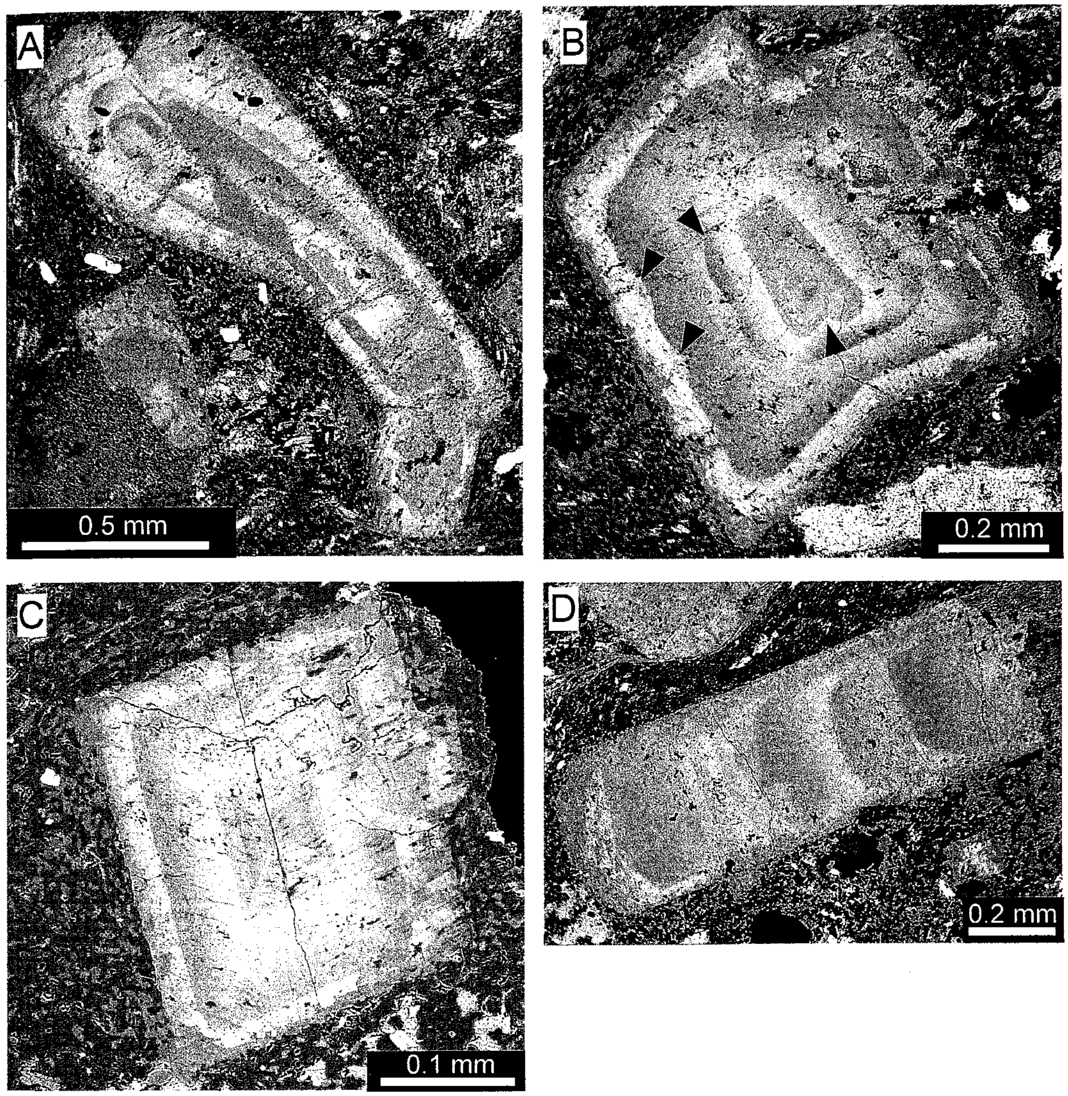

Fig. 4.12. Backscattered electron images of zoned K-feldspar phenocrysts. Lighter zones have higher Ba content. A, twinned K-feldspar phenocryst; B, discordant zoning indicative of repeated resorption (resorption boundaries marked with arrows); C, euhedral sector zoning; D, zoning developed along the faster growing face of an elongate crystal.

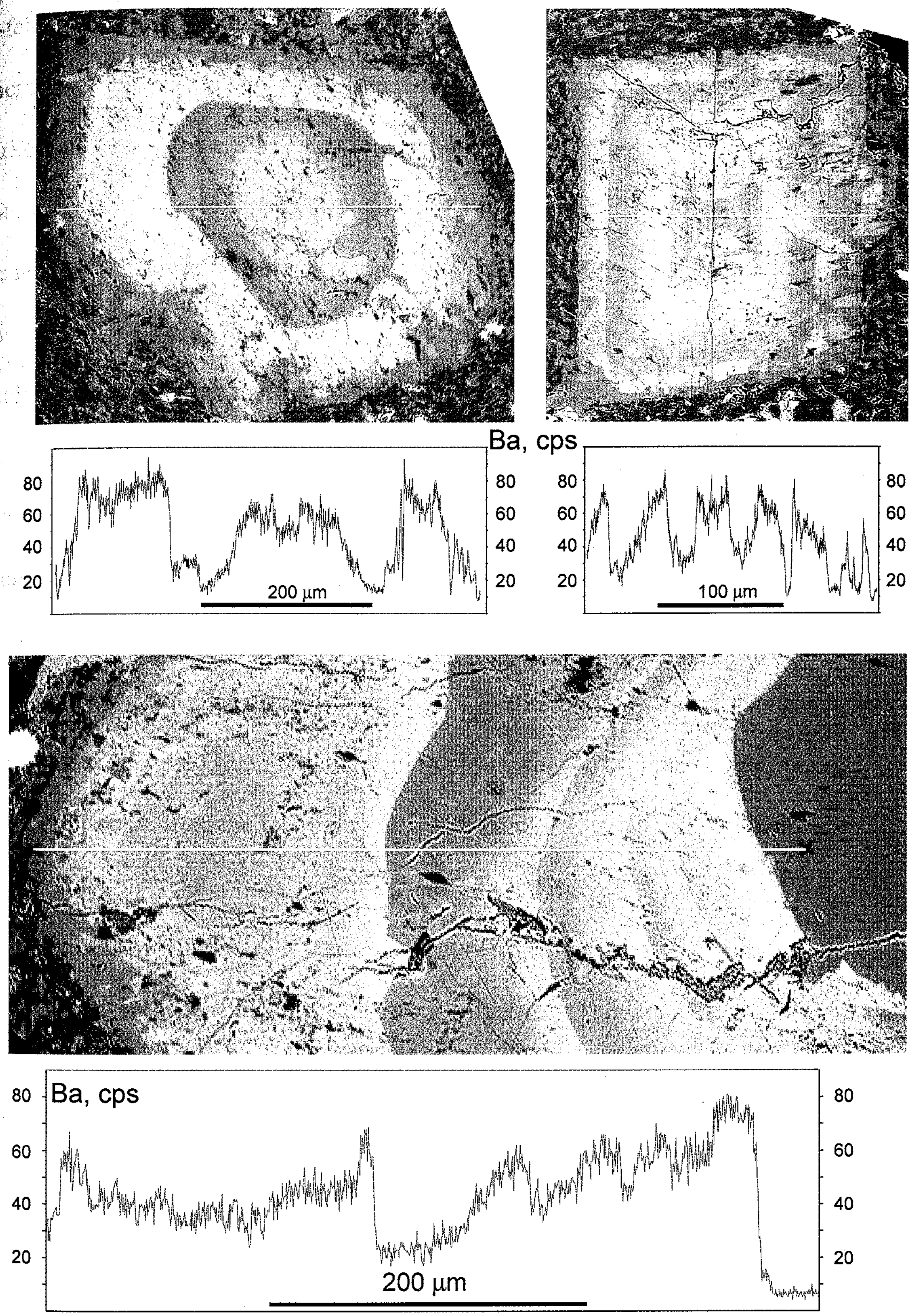

Fig. 4.13. Zoning of K-feldspar phenocrysts as revealed by electron microprobe line scans for Ba. Phenocrysts consist of sharply bounded compositional bands that are finely zoned and, in most cases, have an outward decrease in Ba content. White lines show locations of the line scans. Vertical axes depict counts per second (cps).

K-feldspar phenocrysts contain very small irregular inclusions of albite (Fig. 4.14). These micron-size albitic speckles are distinguished on backscattered electron images by their darker tone and correspond to sharp K lows and Na highs on electron microprobe line scan graphs (Fig. 4.14). The inclusions are typically arranged in discontinuous trains that are near parallel to brittle microfractures crosscutting feldspars. This preferred orientation, along with rather irregular shapes, suggests that the albite inclusions are more likely products of superimposed metasomatism rather than exsolution features (perthites).

K-feldspars of the groundmass of lamprophyres and syenite porphyries are typically unzoned. They are commonly enriched in Ba but not as strongly as the phenocrysts (Table 4.6, Fig. 4.11). The groundmass K-feldspars of syenite porphyries show BaO contents below 1 percent. K-feldspars of lamprophyres are characterized by somewhat intermediate BaO values (0.4-2 percent, Fig. 4.11). K-feldspars from a coarse-grained leucocratic segregation enclosed in a lamprophyric sill (TR6-e) are compositionally indistinguishable from the feldspars of the host lamprophyre (TR6A, Table 4.6).

All analyzed plagioclases, including phenocrysts from the syenite porphyries, fine grains from the groundmass of syenite porphyries and lamprophyres, and coarse plagioclase from leucocratic segregation are composed of almost pure albite (Tables 4.5 and 4.7, Figs 4.10 and 4.11). Albite plagioclase of the Solton Sary intrusive rocks could be of three origins: 1) replacement of originally more calcic plagioclase, 2) replacement of primary K-feldspar, and 3) primary magmatic. The first origin of albite appears the most probable (Rock, 1991). The albitization of groundmass K-feldspar is difficult to identify due to small grain sizes. This process could have taken place but was probably volumetrically insignificant, similar to rather weak “speckle” albitization of K-feldspar

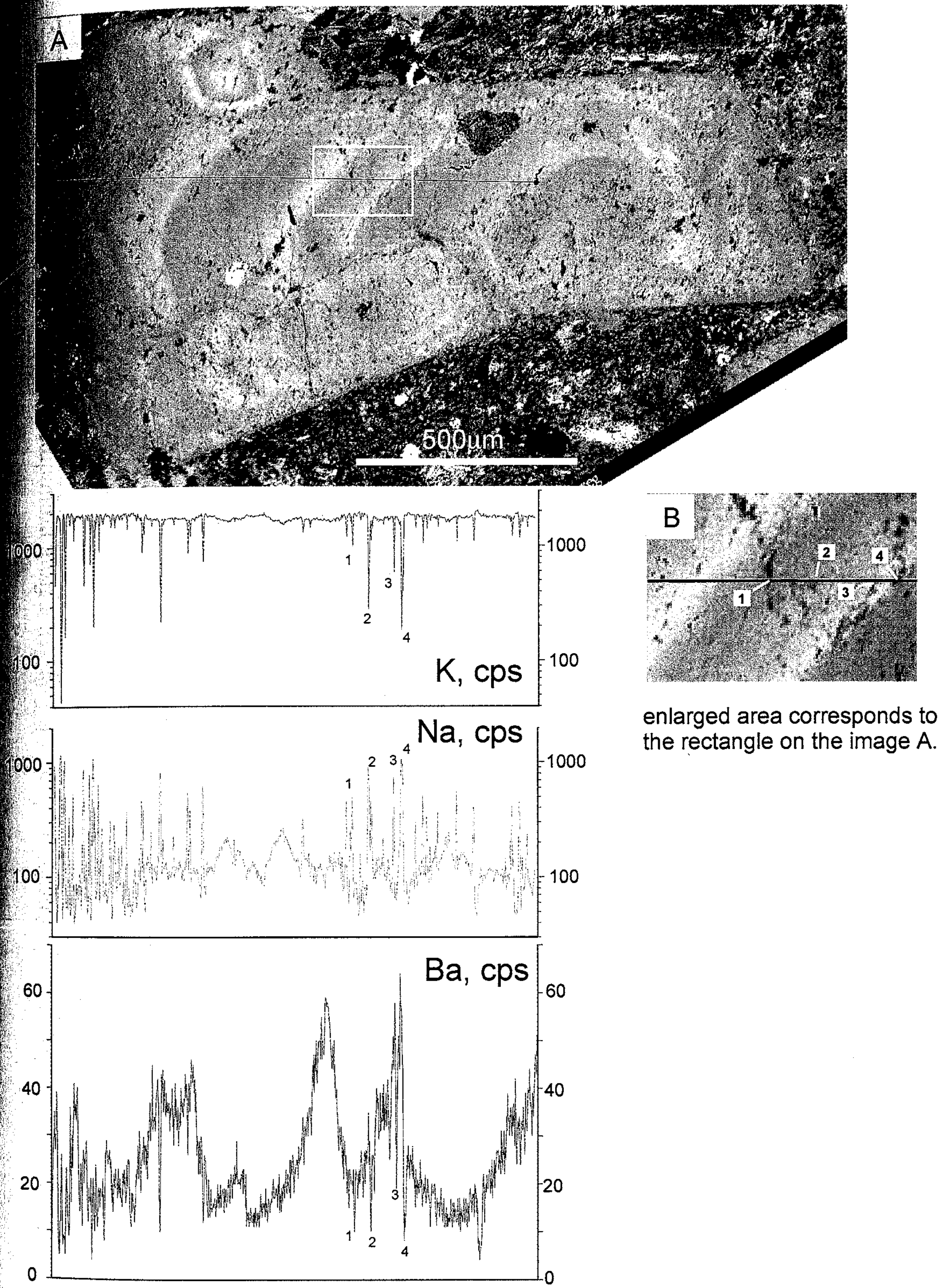

Fig. 4.14. Postmagmatic albitization of a zoned K-feldspar phenocryst. 5-20 μm-size albitized areas appear as small dark gray specks on backscattered electron images (A and B), and correspond to sharp Na highs and K and Ba lows and on electron microprobe line scan graphs. All graphs depict counts per second (cps), Na and K graphs are on logarithmic scale.

Table 4.6. Representative electron microprobe analyses of K-feldspar from groundmass and leucocratic segregation

run ID	fsp397gr-1	fsp49-1137gr-2	fsp56-158gr-1	fspTR223gr-8	fspTR6-3	fsp49-1292gr-1	fsp55-627gr-1	fsp57-1662gr-2	fsp57-1662gr-3	fsp57-1741gr-3	fsp658gr-2	fsp658gr-4	fspTR6en-2	fspTR6en-3
sample	397	49-113.7	56-158.0	TR223	TR6A	49-129.2	55-62.7	57-166.2	57-166.2	57-174.1	658	658	TR6A	TR6A
rock type	L	L	L	L	L	SP	SP	SP	SP	SP	SP	SP	O	O
SiO_2	64.81	63.42	64.05	63.28	63.91	64.99	64.51	64.71	64.61	63.64	64.45	64.63	63.04	63.35
Al_2O_3	19.07	19.23	19.20	19.14	19.19	18.63	18.85	18.85	18.74	18.45	19.13	18.95	19.15	19.35
CaO	0.03	0.03	0.03	0.04	0.05	0.04	0.00	0.03	0.03	0.65	0.00	0.01	0.05	0.19
FeO	0.05	0.07	0.13	0.20	0.23	0.43	0.13	0.10	0.14	0.21	0.04	0.10	0.00	0.11
SrO	0.05	0.14	0.10	0.03	0.04	0.00	0.05	0.00	0.01	0.01	0.05	0.01	0.07	0.05
BaO	0.52	1.27	0.83	1.16	1.00	0.07	0.36	0.09	0.13	0.13	0.87	0.56	1.31	1.40
Na_2O	0.00	0.29	0.59	0.79	0.16	0.22	0.25	0.16	1.56	0.00	0.16	0.19	0.20	0.20
K_2O	16.77	15.95	15.83	16.47	16.45	16.93	16.66	16.80	15.57	16.03	16.34	16.65	16.34	16.15
Total	101.30	100.42	100.76	101.11	101.01	101.31	100.82	100.74	100.78	99.12	101.03	101.11	100.16	100.79
Number of ions on the basis of 32 O. All Fe recalculated as Fe^{3+}.														
Si	11.894	11.799	11.827	11.743	11.812	11.914	11.894	11.913	11.878	11.898	11.872	11.890	11.785	11.763
Al	4.126	4.218	4.179	4.187	4.182	4.026	4.097	4.091	4.061	4.067	4.154	4.111	4.221	4.236
Fe	0.008	0.011	0.020	0.031	0.035	0.066	0.019	0.016	0.022	0.033	0.006	0.016	0.000	0.017
Ca	0.006	0.006	0.007	0.008	0.009	0.008	0.000	0.006	0.005	0.131	0.000	0.003	0.009	0.038
Sr	0.005	0.016	0.011	0.003	0.004	0.000	0.005	0.000	0.001	0.001	0.005	0.001	0.007	0.005
Ba	0.037	0.093	0.060	0.084	0.072	0.005	0.026	0.006	0.009	0.009	0.063	0.040	0.096	0.102
Na	0.000	0.105	0.211	0.286	0.057	0.079	0.090	0.055	0.556	0.000	0.056	0.068	0.074	0.070
K	3.926	3.786	3.730	3.899	3.877	3.960	3.920	3.947	3.652	3.824	3.839	3.906	3.897	3.826
Sum	20.002	20.032	20.044	20.241	20.048	20.059	20.053	20.034	20.184	19.964	19.996	20.034	20.090	20.058
Ab	0.000	0.027	0.054	0.068	0.015	0.019	0.023	0.014	0.132	0.000	0.014	0.017	0.018	0.018
An	0.002	0.002	0.002	0.002	0.002	0.002	0.000	0.002	0.001	0.033	0.000	0.001	0.002	0.010
Or	0.998	0.972	0.945	0.930	0.983	0.979	0.977	0.985	0.867	0.967	0.986	0.982	0.979	0.972

Abbreviations: L = lamprophyre, SP = syenite porphyry, O = leucocratic segregation (ocellum) in lamprophyre. A complete listing of feldspar analyses is presented in Appendix B. Estimated precisions are listed in footnotes for Table 4.5.

Table 4.7. Representative electron microprobe analyses of plagioclase from groundmass and leucocratic felsic segregation

run ID	fsp397gr-8	fspTR223gr-1	fspTR223gr-1	fspTR6-7	fspTR6-5	fsp55-627gr-4	fsp55-627gr-3	fsp57-1662gr-6	fsp658gr-6	fspTR6en-6	fspTR6en-7
sample	397	TR223	TR223	TR6A	TR6A	55-62.7	55-62.7	57-166.2	658	TR6A	TR6A
rock type	L	L	L	L	L	SP	SP	SP	SP	O	O
SiO_2	67.52	68.74	68.74	68.61	68.56	68.53	68.18	65.93	68.79	69.03	67.94
Al_2O_3	20.96	20.29	20.29	20.26	20.33	20.26	20.17	19.21	20.12	20.22	20.11
CaO	0.71	0.24	0.24	0.18	0.18	0.30	0.25	2.18	0.26	0.05	0.13
FeO	0.21	0.20	0.20	0.23	0.12	0.19	0.22	0.13	0.05	0.05	0.04
SrO	0.23	0.06	0.06	0.03	0.02	0.08	0.07	0.07	0.08	0.03	0.00
BaO	0.05	0.00	0.00	0.04	0.00	0.01	0.03	0.00	0.02	0.00	0.02
Na_2O	11.46	10.04	10.04	11.65	11.69	11.69	9.91	10.93	10.25	11.92	11.71
K_2O	0.20	0.06	0.06	0.08	0.19	0.32	0.13	0.11	0.15	0.16	0.23
Total	101.33	99.64	99.64	101.07	101.08	101.38	98.95	98.54	99.71	101.45	100.18
	Number of ions on the basis of 32 O. All Fe recalculated as Fe^{3+}.										
Si	11.710	11.975	11.975	11.874	11.867	11.852	11.968	11.785	11.991	11.901	11.871
Al	4.285	4.168	4.168	4.133	4.148	4.131	4.173	4.047	4.135	4.109	4.142
Fe	0.030	0.030	0.030	0.033	0.017	0.028	0.032	0.019	0.007	0.007	0.006
Ca	0.131	0.045	0.045	0.034	0.034	0.055	0.046	0.417	0.049	0.010	0.024
Sr	0.023	0.006	0.006	0.003	0.002	0.008	0.007	0.007	0.008	0.003	0.000
Ba	0.003	0.000	0.000	0.003	0.000	0.000	0.002	0.000	0.001	0.000	0.001
Na	3.854	3.390	3.390	3.909	3.923	3.918	3.374	3.787	3.464	3.985	3.969
K	0.045	0.014	0.014	0.019	0.043	0.069	0.029	0.024	0.033	0.035	0.052
Sum	20.082	19.628	19.628	20.007	20.033	20.062	19.631	20.087	19.687	20.051	20.065
Ab	0.956	0.983	0.983	0.987	0.981	0.969	0.978	0.896	0.977	0.989	0.981
An	0.033	0.013	0.013	0.009	0.008	0.014	0.013	0.099	0.014	0.002	0.006
Or	0.011	0.004	0.004	0.005	0.011	0.017	0.008	0.006	0.009	0.009	0.013

Abbreviations: L = lamprophyre, SP = syenite porphyry, O = leucocratic segregation (ocellum) in lamprophyre. Feldspar end-members calculated as recommended by Deer et al. (1992).
A complete listing of feldspar analyses is presented in Appendix B. Estimated precisions are listed in footnotes for Table 4.5.

phenocrysts. The possibility for occurrence of primary, magmatic albite appears improbable but should not be completely excluded (cf. Rock, 1991).

Amphibole, apatite, and magnetite

Green, distinctly pleochroic amphiboles, including apparent pseudomorphs after pyroxenes, have actinolite compositions (Table 4.8, cf. Yavuz, 1999). As suggested by Rock (1991, Fig. 4.4 therein), the actinolitic amphiboles with SiO_2 exceeding ca. 51.25 percent and TiO_2 below 0.75-1.25 percent are likely to be secondary. The actinolites of the Solton Sary lamprophyres probably represent pseudomorphs after original magmatic amphiboles and possibly pyroxenes. Apatite of the Solton Sary intrusive rocks is characterized by a relatively high F content (3-4%), and magnetite is Ti-poor (Tables 4.9 and 4.10).

Implications of petrographic and mineralogical data

Petrographic and electron microprobe studies show that the lamprophyres and syenite porphyries of the Solton Sary district share many common features. Major and accessory mineral assemblages are quite similar, as are chemical compositions of the minerals. This strongly supports close genetic relations between the lamprophyres and syenite porphyries.

Several textural and mineralogical characteristics of the Solton Sary intrusive rocks are recognized as universally typical for Precambrian and Phanerozoic potassic rocks, particularly for calc-alkaline lamprophyres, including those of greenstone-hosted

Table 4.8. Representative electron microprobe analyses of amphibole

run ID	amph397-1	amph397-3	amph397-5	amphTR6-1	amphTR6-2	hbl49-1137gr-1	hbl49-1137gr-2	amphTR6e-3	amphTR6e-4	px(?)49-113-3	px(?)49-113-4
sample	397	397	397	TR6A	TR6A	49-113.7	49-113.7	TR6A	TR6A	49-113.7	49-113.7
rock type	L	L	L	L	L	L	L	O	O	L	L
SiO_2	54.15	54.11	52.59	54.37	52.90	54.80	55.27	55.17	54.78	55.23	53.69
TiO_2	0.04	0.03	0.03	0.02	0.05	0.04	0.03	0.03	0.02	0.04	0.06
Al_2O_3	1.46	1.78	2.41	1.28	2.75	1.32	1.42	0.69	0.39	1.27	2.25
MgO	16.84	15.92	15.62	16.71	15.36	16.64	16.04	15.16	13.77	17.49	15.71
CaO	12.35	12.19	11.94	12.66	12.34	12.92	12.49	12.59	12.47	13.03	12.60
MnO	0.26	0.31	0.27	0.31	0.32	0.27	0.27	0.29	0.22	0.19	0.25
FeO	12.32	12.89	13.74	12.28	13.46	11.69	12.10	14.27	16.32	9.54	11.85
Na_2O	0.30	0.40	0.48	0.12	0.25	0.21	0.24	0.06	0.04	0.21	0.39
K_2O	0.09	0.20	0.18	0.04	0.11	0.09	0.09	0.04	0.03	0.07	0.17
Total	97.81	97.83	97.26	97.79	97.54	97.98	97.95	98.30	98.04	97.07	96.97
Number of ions on the basis of 23 O (H_2O-free). All Fe calculated as Fe^{2+}.											
Si	7.777	7.790	7.664	7.807	7.667	7.833	7.894	7.933	7.971	7.881	7.768
Al	0.246	0.301	0.413	0.216	0.470	0.222	0.239	0.116	0.067	0.214	0.384
Ti	0.004	0.003	0.003	0.002	0.005	0.004	0.004	0.003	0.002	0.004	0.007
Mg	3.605	3.418	3.392	3.577	3.319	3.547	3.416	3.250	2.988	3.721	3.388
Ca	1.900	1.880	1.863	1.947	1.916	1.978	1.911	1.940	1.945	1.992	1.953
Mn	0.032	0.037	0.033	0.037	0.039	0.032	0.032	0.036	0.027	0.023	0.031
Fe^{2+}	1.480	1.552	1.674	1.475	1.631	1.397	1.445	1.716	1.985	1.138	1.434
Na	0.085	0.111	0.134	0.034	0.071	0.059	0.067	0.016	0.010	0.058	0.109
K	0.017	0.037	0.034	0.008	0.020	0.016	0.017	0.007	0.005	0.013	0.031
Cation distribution (cf. Yavuz, 1999)											
$Si_{(T)}$	7.777	7.790	7.664	7.807	7.667	7.833	7.894	7.933	7.971	7.881	7.768
$Al_{(T)}$	0.223	0.210	0.336	0.193	0.333	0.167	0.106	0.067	0.029	0.119	0.232
$Al_{(C)}$	0.024	0.092	0.077	0.023	0.138	0.055	0.133	0.049	0.038	0.094	0.151
$Ti_{(C)}$	0.004	0.003	0.003	0.002	0.005	0.004	0.004	0.003	0.002	0.004	0.007
$Mg_{(C)}$	3.605	3.418	3.392	3.577	3.319	3.547	3.416	3.250	2.988	3.721	3.388
$Fe^{2+}_{(C)}$	1.367	1.488	1.527	1.398	1.539	1.394	1.445	1.697	1.972	1.138	1.434
$Mn_{(C)}$	0.000	0.000	0.000	0.000	0.000	0.000	0.003	0.000	0.000	0.042	0.020
$Fe^{2+}_{(B)}$	0.113	0.064	0.146	0.077	0.092	0.003	0.000	0.019	0.013	0.000	0.000
$Mn_{(B)}$	0.032	0.037	0.033	0.037	0.039	0.032	0.029	0.036	0.027	0.000	0.011
$Ca_{(B)}$	1.900	1.880	1.863	1.947	1.916	1.978	1.911	1.940	1.945	1.992	1.953
$Na_{(B)}$	0.000	0.018	0.000	0.000	0.000	0.000	0.059	0.006	0.010	0.008	0.036
$Na_{(A)}$	0.085	0.093	0.134	0.034	0.071	0.059	0.008	0.010	0.000	0.050	0.073
$K_{(A)}$	0.017	0.037	0.034	0.008	0.020	0.016	0.017	0.007	0.005	0.013	0.031
T	8	8	8	8	8	8	8	8	8	8	8
C	5	5	5	5	5	5	5	5	5	5	5
B	2.044	2.000	2.042	2.062	2.047	2.014	2.000	2.000	1.996	2.000	2.000
A	0.101	0.130	0.168	0.042	0.090	0.075	0.025	0.017	0.005	0.063	0.104
Sum	15.146	15.130	15.210	15.104	15.138	15.089	15.025	15.017	15.001	15.063	15.104
mg#	0.709	0.688	0.670	0.708	0.671	0.717	0.703	0.654	0.601	0.766	0.703

Abbreviations: L = lamprophyre; O = leucocratic leucocratic segregation (ocellum). Analyses px(?)49-113-3 and px(?)49-113-4 were performed on apparent pseudomorphs after pyroxene. A complete listing of amphibole analyses is presented in Appendix B. Precision of analyses (wt%) based on replicate analyses of standard reference material (SRM) Kakanui USNM 143965 Hornblende (Jarosewich et al., 1980): SiO_2 (±0.35), TiO_2 (±0.1), Al_2O_3 (±0.1), MgO (±0.3), CaO (±0.2), MnO (± 0.02), FeO (±0.3), Na_2O (±0.1), K_2O (±0.05). Results of SRM analyses are summarized in Appendix B.

Table 4.9. Electron microprobe analyses of apatite

run ID	apTR223-2rim	apTR223-1	apTR6lamp-2	apTR6lamp-1	ap397-3	ap397-2	ap397-1	ap49-1292-2	ap49-1292	ap57-1662-2	ap57-1662-1	ap57-1741-2	ap57-1741-1
sample	TR223	TR223	TR6A	TR6A	397	397	397	49-129.2	49-129.2	57-166.2	57-166.2	57-174.1	57-174.1
rock type	L	L	L	L	L	L	L	SP	SP	SP	SP	SP	SP
P_2O_5	41.31	39.69	39.23	40.23	39.26	39.50	40.28	38.87	39.71	40.37	40.88	39.78	40.54
SiO_2	0.03	0.73	0.73	0.42	0.77	0.72	0.19	2.23	0.46	0.48	0.16	0.64	0.55
SO_2	0.02	0.41	0.51	0.35	0.74	0.51	0.29	0.38	0.45	0.32	0.21	0.43	0.23
CaO	56.44	54.76	55.38	54.67	54.93	54.57	55.24	52.29	54.65	55.15	53.94	54.65	54.62
MnO	0.02	0.03	0.02	0.03	0.06	0.05	0.03	0.03	0.01	0.06	0.03	0.06	0.04
FeO	0.34	0.37	0.13	0.26	0.26	0.32	0.18	0.19	0.11	0.11	0.11	0.14	0.26
SrO	0.30	0.44	0.67	0.20	0.67	0.36	0.61	0.65	0.48	0.39	0.38	0.13	0.21
F	1.83	2.94	4.05	3.89	4.18	3.76	4.27	4.42	4.77	4.02	4.03	4.51	4.54
Cl	0.00	0.10	0.02	0.00	0.02	0.02	0.03	0.02	0.02	0.02	0.03	0.03	0.03
	100.28	99.48	100.74	100.04	100.89	99.82	101.12	99.06	100.64	100.92	99.77	100.37	101.02
-O=F,Cl	0.77	1.26	1.71	1.64	1.76	1.59	1.80	1.86	2.01	1.70	1.70	1.91	1.92
Total	99.51	98.22	99.03	98.40	99.13	98.23	99.32	97.20	98.63	99.22	98.07	98.46	99.10

Abbreviations: L = lamprophyre, SP = syenite porphyry.

Table 4.10. Electron microprobe analyses of magnetite

run ID	mag397-2	mag397-3	mag397-1	mag49-1137-4	mag49-1137-2	mag49-1137-3	mag49-1292-2	mag49-1292-1	mag55-627-1	mag55-627e-1	mag57-1662-1	mag57-1662-2	mag57-1741-1	mag57-1741-2	mag658-1
sample	397	397	397	49-113.7	49-113.7	49-113.7	49-129.2	49-129.2	55-62.7	55-62.7	57-166.2	57-166.2	57-174.1	57-174.1	658
rock name	L	L	L	L	L	L	SP	SP	SP	SP	SP	SP	SP	SP	SP
SiO_2	0.06	0.06	0.03	0.05	0.15	0.26	0.05	0.08	0.06	0.08	0.27	0.09	0.05	0.07	0.03
TiO_2	0.10	0.01	0.05	0.03	0.00	0.00	0.05	0.20	0.00	0.01	0.50	0.02	0.01	0.06	0.02
Al_2O_3	0.03	0.00	0.03	0.02	0.00	0.00	0.01	0.00	0.01	0.02	0.12	0.01	0.00	0.01	0.12
Cr_2O_3	0.28	0.15	0.21	0.03	0.01	0.02	0.25	0.15	0.01	0.68	0.00	0.15	0.09	0.00	0.01
Fe_2O_3	69.39	69.45	69.19	67.00	69.86	70.01	69.81	69.53	67.56	69.26	65.70	69.32	69.91	67.14	66.90
MgO	0.02	0.03	0.00	0.03	0.00	0.00	0.00	0.01	0.00	0.01	0.11	0.00	0.00	0.00	0.01
CaO	0.07	0.04	0.00	0.04	0.04	0.00	0.02	0.00	0.03	0.02	0.00	0.02	0.00	0.14	0.01
MnO	0.00	0.00	0.00	0.00	0.00	0.01	0.00	0.00	0.02	0.00	0.00	0.00	0.00	0.00	0.00
FeO	31.52	31.27	31.34	30.17	31.43	31.50	31.61	31.68	30.39	31.49	30.34	31.29	31.51	30.31	30.19
Total	101.46	101.01	100.85	97.37	101.48	101.80	101.80	101.64	98.08	101.55	97.04	100.88	101.57	97.71	97.29

Abbreviations: L = lamprophyre, SP = syenite porphyry.

mesothermal gold provinces of the Yilgarn Block (Australia) and Abitibi Subprovince (Canada). The most diagnostic features include the presence of chemically distinct mica populations, sharp optical and compositional zoning of micas, Ba-enrichment of K-feldspars, and the presence of mafic enclaves and essentially feldspathic leucocratic segregations (e. g., Bachinski and Simpson, 1984; Rock, 1984; Rock, 1991; Sheppard and Taylor, 1992; Müller et al., 1993; Wyman and Kerrich, 1993).

Variation in mica composition could indicate that magmas of the Solton Sary intrusive suite were generated at mantle depths and underwent significant evolution prior to their final emplacement. The phlogopitic cores of zoned micas from Solton Sary intrusive rocks have mg# and Al_2O_3 contents similar to those of phlogopites from diverse lamprophyres (Bachinski and Simpson, 1984; Rock, 1991). The TiO_2 contents of the Solton Sary phlogopites are lower than typical values of lamprophyric micas, and are comparable to those of phlogopites from kimberlites and mantle xenoliths (Bachinski and Simpson, 1984). Bachinski and Simpson (1984) summarize the results of high-pressure experiments and studies of the equilibration conditions of phlogopites in potassic and ultrapotassic rocks. They conclude that Mg-rich micas from lamprophyres may crystallize at temperatures of up to ~1250°C and pressures of ~40 kbar, which broadly corresponds to the upper mantle. Pale-green phlogopite from the Solton Sary intrusions is compositionally comparable to the described micas and probably formed under similar conditions, perhaps representing one of the earliest mineral phases in the Solton Sary intrusive rocks. Unzoned biotite phenocrysts and fine biotites from the groundmass and mafic enclaves are compositionally indistinguishable and have higher TiO_2 and Al_2O_3 contents, and lower mg#, compared to phlogopite cores. This chemical uniformity may ly similar conditions of formation for all three morphological types of unzoned micas. solubility in phlogopite is believed to increase with increasing oxygen fugacity, and possibly, with decreasing pressure (Arima and Edgar, 1981). The unzoned micas of the Solton Sary intrusive rocks could have crystallized in relatively shallow-level magma chambers and perhaps, at least partially, after final emplacement.

Zoning of coarse K-feldspar crystals supports their primary magmatic (i.e. phenocrystic) origin. Fine euhedral oscillatory zoning is diagnostic for crystallization from melt, and is not found in metamorphogenic feldspars (Smith and Brown, 1988, p. 489). Zonation of K-feldspar phenocrysts can be described as a sequence of compositionally distinct growth bands that show outwardly decreasing Ba contents and are separated by sharp boundaries, sometimes with clear resorption features. LeCheminant et al. (1987) describe similar zoning for fine groundmass K-feldspars in Precambrian lamprophyres from central Keewatin (Canada). The authors conclude that the growth of K-feldspar crystals was rapid and occurred after the emplacement of intrusions. Resorption and repeated renewal of crystal growth are attributed to movements of magma within the crystallizing intrusive bodies. K-feldspar phenocrysts of the Solton Sary syenite porphyries are relatively coarse and unlikely to have been formed entirely after the emplacement of the sills. More probably, the formation of the phenocrysts involved period(s) of residence in magma chamber(s) where crystal growth was disrupted by repeated inputs of Ba-rich magmas. This episodic input of melts could have been controlled by movements along deep-seated faults that served as conduits for ascending magmas.

Geochemistry

A total of 16 samples - 7 syenite porphyries, 8 lamprophyres and 1 mica-rich mafic enclave - were analyzed for major oxides and trace elements. Concentrations of major oxides and trace elements were determined by Inductively Coupled Plasma-Optical Emission Spectroscopy (ICP), and Inductively Coupled Plasma-Mass Spectrometry (ICP-MS), respectively. For both methods, analytical routines included lithium metaborate/tetraborate fusion in order to ensure a complete digestion of sample material. Five of these samples were additionally analyzed for Au, Pt, and Pd by Fire Assay with ICP-MS finish. All analyses were performed at Activation Laboratories Ltd. (Ancaster, Ontario, Canada). Analytical results are summarized in Tables 4.11, 4.12, and 4.13; laboratory reports and information on detection limits are included in Appendix A. Results returned by lamprophyre 76-179.9 are excluded from further consideration due to a high loss on ignition value (LOI=10.75, Table 4.11), which suggests significant post-emplacement alteration.

On the total alkali-silica (TAS) and SiO_2 versus K_2O plots, the lamprophyres and syenite porphyries form rather diffuse clusters (Fig. 4.15, Table 4.11). As chemical compositions of major mineral phases are fairly consistent, the irregular silica-alkali patterns must be due to variable proportions of mineral constituents. An overall phenocryst abundance, relative proportions of biotite, amphibole, and feldspar phenocrysts, and percentages of K-feldspar, albite, and quartz in the groundmass appear to largely control the alkali-silica balance of the rocks. The variability of these compositional parameters is the most probable reason for somewhat irregular alkali-silica

Table 4.11. Major element abundances in intrusive rocks of the Solton Sary district

Sample	55-62.7	57-174.1	515-sp	57-166.2	49-129.2	A23	658	1966	49-113.7	TR6	60-74.8	76-179.9	664-4	613	397	515-x
Rock type	SP	SP	SP	SP	SP	SP	SP	L	L	L	L	L	L	L	L	E
Phenocrysts	Bt, Kfsp Kfsp>Bt	Bt, Kfsp Kfsp>Bt	Bt, Kfsp Kfsp>Bt	Bt, Kfsp Kfsp>Bt	Bt, Kfsp Kfsp>Bt	Kfsp, Pl Kfsp>Pl	Bt, Kfsp Kfsp>Bt	Bt	Bt, Phl, Amph Amph>(Bt+Phl)	Amph	Bt	Bt	Bt, Phl, Amph Amph>(Bt+Phl)	Bt, Amph Bt>Amph	Bt, Phl, Amph Amph>(Bt+Phl)	Bt
wt %																
SiO_2	55.86	59.95	55.96	60.98	55.95	65.00	58.70	49.17	48.81	51.13	51.75	46.20	49.94	47.58	51.07	49.75
Al_2O_3	16.80	14.57	15.45	14.98	13.58	15.30	14.24	12.69	11.90	12.71	15.06	11.55	12.60	14.45	13.01	12.72
Fe_2O_3	6.02	4.36	7.11	4.15	5.24	2.97	4.54	8.73	9.66	8.79	7.86	8.15	9.33	10.43	8.92	10.77
MnO	0.08	0.05	0.07	0.04	0.08	0.05	0.10	0.19	0.12	0.16	0.16	0.13	0.16	0.12	0.11	0.14
MgO	3.15	2.21	2.83	2.68	2.79	0.74	2.85	5.52	7.74	6.47	3.64	6.73	7.06	6.34	6.04	7.79
CaO	2.94	3.50	4.00	3.23	4.56	1.98	4.06	8.04	6.64	8.35	6.56	7.64	8.94	6.27	6.39	5.60
Na_2O	3.62	4.16	3.28	3.94	2.86	4.09	4.44	1.69	2.31	2.17	2.77	2.46	3.53	2.02	2.53	2.37
K_2O	7.17	5.59	6.42	5.96	7.58	6.73	4.34	5.67	4.01	5.22	6.57	5.07	2.83	6.50	6.16	3.42
TiO_2	0.40	0.41	0.47	0.38	0.53	0.31	0.34	0.62	0.60	0.64	0.59	0.65	0.68	0.75	0.67	0.49
P_2O_5	0.24	0.32	0.31	0.27	0.42	0.15	0.22	0.56	0.60	0.57	0.35	0.57	0.50	0.72	0.79	0.26
LOI	1.91	4.23	3.59	3.47	6.34	2.03	4.24	5.92	6.67	3.04	5.34	10.75	4.38	4.17	3.64	5.34
Total	98.18	99.36	99.48	100.10	99.93	99.36	98.08	98.80	99.06	99.25	100.66	99.91	99.96	99.33	99.34	98.65
$mg\#^1$	0.65	0.65	0.59	0.70	0.66	0.47	0.69	0.69	0.74	0.73	0.63	0.75	0.73	0.69	0.71	0.72
$mg\#^2$	0.55	0.54	0.48	0.60	0.55	0.37	0.59	0.60	0.65	0.63	0.52	0.66	0.64	0.59	0.61	0.63

Abbreviations: rock type, SP = syenite porphyry, L = lamprophyre, E = mica-rich mafic enclave in syenite porphyry; phenocrysts: Bt=unzoned biotite; Phl=zoned mica with phlogopitic core; Amph=amphibole; Kfsp=K-feldspar, Pl=plagioclase.

[1 and 2] magnesium number calculated as $mg\# = Mg/(Mg+Fe^2)$ where [1] $Fe^3/(Fe^2+Fe^3)=0.45$ (Rock, 1991) and [2] $Fe^2/(Fe^2+Fe^3)=0.85$ (Müller and Groves, 1997).

A complete laboratory report is presented in Appendix A.

Table 4.12. Platinum group element abundances

sample	515-x	613	TR6	49-113.7	57-166.2
rock type	E	L	L	L	SP
ppb					
Pd	8.8	9.4	5.5	6.8	2.1
Pt	7.6	10	5.9	7.3	1.2
Au	4	7	5	10	4

A complete laboratory report is presented in Appendix A.

Table 4.13. Trace element abundances (ppm) in intrusive rocks of the Solton Sary district (continued on the next page)

Sample	55-62.7	57-174.1	515-sp	57-166.2	49-129.2	A23	658
Rock type	SP	SP	SP	SP	SP	SP	SP
Sc	13	11	16	11	13	5	13
V	140	81	152	78	93	38	84
Cr	99	78	69	130	83	33	92
Co	11	8	11	6	8	3	13
Ni	31	40	30	42	39	64	46
Cu	18	17	17	32	22	n.d.	17
Zn	49	29	20	21	45	27	41
Ga	18	18	16	18	18	21	17
Ge	1.5	1.5	1.2	1.3	1.4	1.3	1.3
As	36	9	16	7	27	17	n.d.
Rb	267	203	210	208	191	238	149
Sr	1344	728	557	705	849	550	489
Y	22	23	22	22	29	24	24
Zr	179	229	161	241	252	304	170
Nb	11.9	15.4	10.9	15.7	18.3	25.2	16.9
Mo	2.2	3.3	1.6	3.8	3.4	0.3	0.5
Sn	1.7	2.1	1.4	2.8	2.2	2.4	1.6
Sb	2.95	9.18	8.34	4.17	7.71	1.52	0.70
Cs	17.8	5.9	5.8	8.4	2.4	2.5	6.9
Ba	3457	2489	5331	2466	2933	4502	5227
La	59.0	57.9	55.4	60.3	63.1	64.9	49.9
Ce	132.1	132.3	124.5	143.5	145.4	149.4	113.6
Pr	11.84	11.95	11.21	13.21	13.09	13.51	10.23
Nd	41.0	42.0	40.1	46.6	46.9	46.1	36.0
Sm	7.30	7.39	7.37	8.42	8.49	7.89	6.58
Eu	1.775	1.652	1.821	1.890	1.882	1.852	1.547
Gd	5.20	5.28	5.21	5.95	6.08	5.54	4.88
Tb	0.74	0.78	0.75	0.82	0.88	0.80	0.73
Dy	3.62	3.74	3.68	4.11	4.49	3.92	3.74
Ho	0.70	0.70	0.68	0.77	0.85	0.73	0.72
Er	1.97	2.00	1.96	2.24	2.50	2.19	2.07
Tm	0.275	0.291	0.282	0.329	0.357	0.317	0.308
Yb	1.90	2.01	1.87	2.21	2.44	2.18	2.10
Lu	0.309	0.324	0.314	0.368	0.403	0.361	0.335
Hf	4.1	5.8	3.8	6.6	6.2	7.9	4.7
Ta	0.51	0.80	0.50	0.92	0.90	1.22	0.94
W	7.8	6.7	4.8	13.3	24.2	6.7	2.7
Tl	3.02	2.99	2.84	2.58	2.09	2.34	1.60
Pb	25	25	10	14	28	27	21
Be	6	6	6	6	8	6	6
Bi	1.61	0.25	0.50	0.14	0.57	0.81	0.90
Th	26.6	26.9	22.5	32.7	27.5	35.0	24.9
U	12.08	8.02	8.28	8.91	5.96	11.88	6.68
La/Yb(n)	22.32	20.72	21.21	19.60	18.58	21.33	17.02
Eu/Eu*	0.88	0.81	0.90	0.82	0.80	0.86	0.84

Table 4.13 (Continued)

Sample	1966	49-113.7	TR6	60-74.8	76-179.9	664-4	613	397	515-x
Rock type	L	L	L	L	L	L	L	L	E
Sc	28	31	31	22	26	33	26	29	34
V	189	211	204	191	188	220	242	193	248
Cr	118	395	249	111	339	268	225	172	797
Co	22	27	32	19	26	29	32	18	17
Ni	77	92	78	44	82	82	78	78	109
Cu	69	112	85	11	71	15	89	29	132
Zn	63	70	79	94	81	55	34	65	57
Ga	14	14	15	17	14	16	17	15	20
Ge	1.2	1.6	1.5	1.7	1.3	1.9	1.6	1.6	1.6
As	5	24	20	14	31	16	28	27	10
Rb	215	210	143	247	297	147	321	225	318
Sr	895	481	645	1683	1030	893	723	674	854
Y	21	18	20	24	19	20	27	21	17
Zr	109	109	123	166	121	109	151	148	75
Nb	8.4	7.1	8.7	11.4	9.1	7.8	12.6	10.4	3.5
Mo	n.d.	4.0	0.3	1.1	0.9	1.1	2.6	0.4	0.2
Sn	1.47	1.5	1.6	1.9	1.5	1.6	2.3	1.8	2.1
Sb	1.10	3.76	4.42	5.48	2.66	6.62	2.92	6.29	7.49
Cs	9.8	13.2	6.3	17.6	19.5	13.5	18.3	11.0	18.3
Ba	2666	2234	2263	2267	2386	2487	3010	3889	3504
La	50.5	48.1	40.1	58.9	50.0	34.4	69.7	45.8	47.5
Ce	121.1	109.3	95.8	133.9	116.4	83.0	153.6	110.0	89.3
Pr	11.44	10.10	9.15	12.47	11.00	8.01	14.04	10.41	8.16
Nd	42.4	37.0	34.6	45.5	40.5	30.2	51.3	39.3	29.8
Sm	8.23	7.02	6.67	8.37	7.47	5.90	9.41	7.24	5.67
Eu	1.901	1.605	1.521	1.907	1.711	1.389	2.090	1.729	1.609
Gd	5.75	4.92	4.78	5.94	5.29	4.38	6.71	5.04	4.16
Tb	0.79	0.65	0.67	0.82	0.72	0.65	0.96	0.72	0.59
Dy	3.73	3.14	3.37	4.11	3.42	3.28	4.76	3.53	2.97
Ho	0.69	0.56	0.64	0.76	0.60	0.63	0.88	0.68	0.54
Er	1.86	1.59	1.81	2.17	1.71	1.83	2.44	1.93	1.48
Tm	0.248	0.219	0.253	0.301	0.219	0.255	0.328	0.268	0.204
Yb	1.67	1.42	1.69	1.92	1.43	1.67	2.16	1.83	1.37
Lu	0.262	0.233	0.271	0.315	0.229	0.275	0.334	0.281	0.231
Hf	2.9	2.6	3.0	3.9	3.1	2.8	3.9	3.6	2.1
Ta	0.41	0.31	0.42	0.48	0.42	0.35	0.53	0.48	0.12
W	1.4	15.2	2.0	5.0	3.4	7.9	3.9	11.8	3.6
Tl	1.93	1.60	1.68	3.48	4.35	2.08	2.75	3.11	6.56
Pb	25	14	21	21	21	12	11	22	10
Be	5	4	5	5	6	4	8	5	10
Bi	0.17	0.40	0.36	0.60	0.19	1.09	1.32	0.40	0.36
Th	16.2	17.7	15.2	22.7	17.4	12.9	21.1	18.0	7.1
U	4.60	5.50	4.33	6.37	5.13	3.23	7.67	4.53	3.89
La/Yb(n)	21.62	24.39	16.99	22.06	25.08	14.75	23.17	17.96	24.95
Eu/Eu*	0.85	0.83	0.82	0.83	0.83	0.84	0.80	0.87	1.01

Abbreviations: SP = syenite porphyry, L = lamprophyre, E = mica-rich mafic enclave in syenite porphyry, n.d. = not detected. Ag and In abundances of all samples are below detection limits;
La/Yb(n), Eu/Eu* calculated for chondrite-normalized values, with normalizing factors from Sun and McDonough (1989); $Eu/Eu^*=Eu_n/(Sm^*Gd)^{0.5}$. A complete laboratory report is presented in Appendix A.

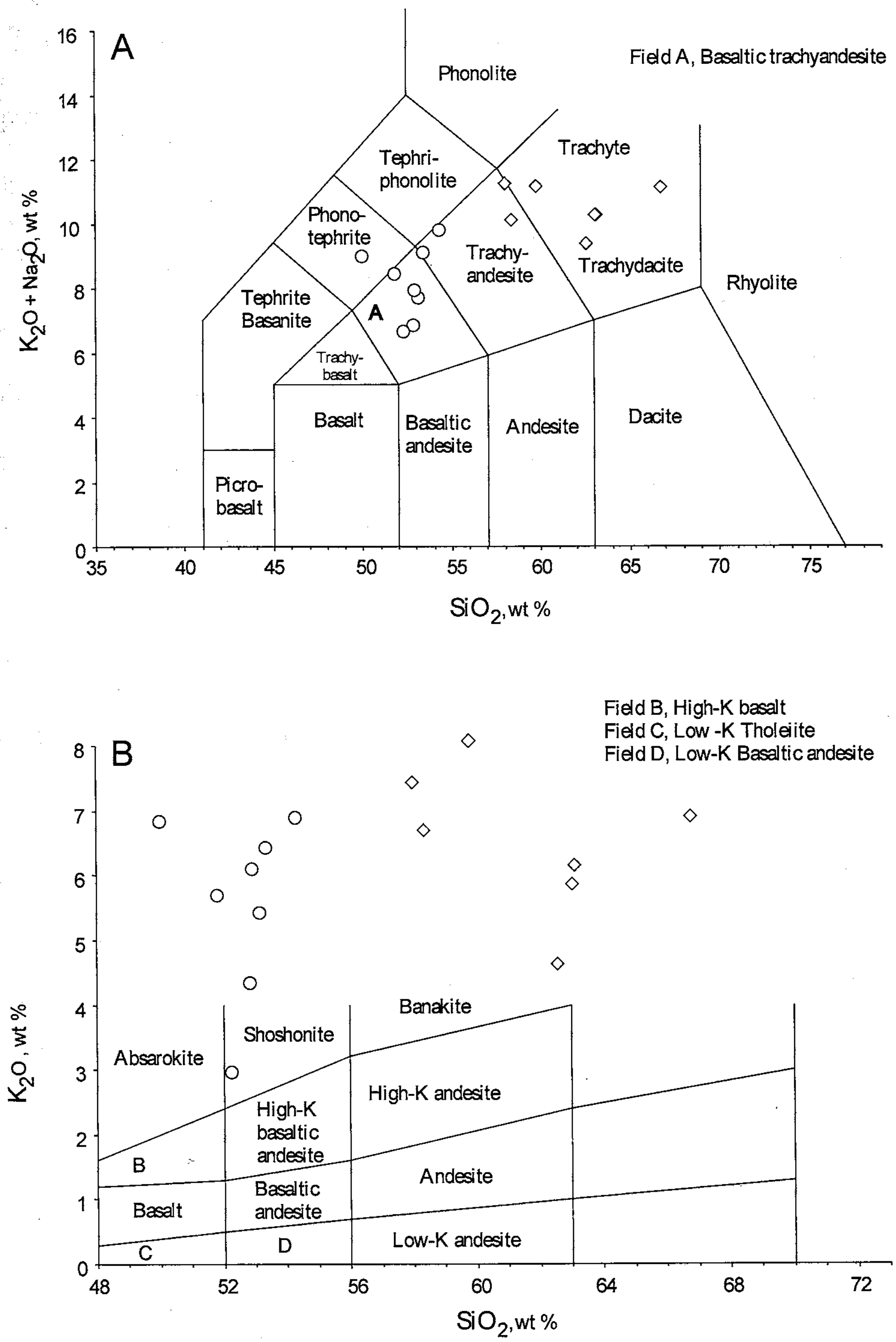

Fig. 4.15. Classification diagrams showing the range of compositions of lamprophyres (circles) and syenite porphyries (diamonds). A, total alkali-silica (TAS) diagram (Le Bas et al., 1986); B, K_2O-SiO_2 diagram (Peccerillo and Taylor, 1976). All analyzes normalized to 100 percent on a volatile free basis.

patterns. The significance of the apparent compositional gaps in SiO_2 cannot be evaluated due to a relatively small number of samples. The SiO_2 content of lamprophyres varies from 49 to 54 percent, total alkali range from 6 to 9 percent (recalculated volatile-free). Compared to the lamprophyres, the syenite porphyries are more silicic (SiO_2=58-66%) and in most cases have higher total alkali content (8-10%). K_2O/Na_2O ratios of both rock types vary from 0.8 to 3.4 and with the exception of one sample exceed unity. This allows the syenite porphyries and lamprophyres of the Solton Sary district to be classified as potassic igneous rocks (cf. Müller and Groves, 1997). The chemical and petrographic composition of the Solton Sary lamprophyres suggests their affinity to the calc-alkaline or shoshonitic suite of lamprophyres (Rock, 1991; Müller and Groves, 1997). Magnesium numbers (mg#) calculated as mole percent $Mg/(Fe^{2+}+Mg)$, with $Fe^{3+}/(Fe^{2+}+Fe^{3+})=0.45$ (Rock, 1991) are 0.62 to 0.74 for lamprophyres and 0.47 to 0.69 for syenite porphyries (Table 4.11). Contents of compatible elements (Cr, Ni, Co, Sc, Table 4.13) and mg# of some amphibole-bearing lamprophyres are close to the values expected for primary magmas (i. e. undifferentiated melts that are still in equilibrium with mantle source, cf. Rock, 1991; Fig. 4.16). Biotite lamprophyres and syenite porphyries apparently represent more evolved compositions.

Variation diagrams of most major oxides show somewhat linear trends complicated by a significant scatter of individual data points (Fig. 4.17). MnO, MgO, TiO_2, Fe_2O_3, P_2O_5, and CaO decrease with increasing SiO_2, Na_2O increases, and the variation of K_2O (Fig. 4.15) is rather irregular. Trace elements plotted against SiO_2 show increasing (e. g. Nb, Ta, Zr, Th, and U, Fig. 4.18) or decreasing (Cr, V, Co, Sc, and Ni) linear trends. Rare

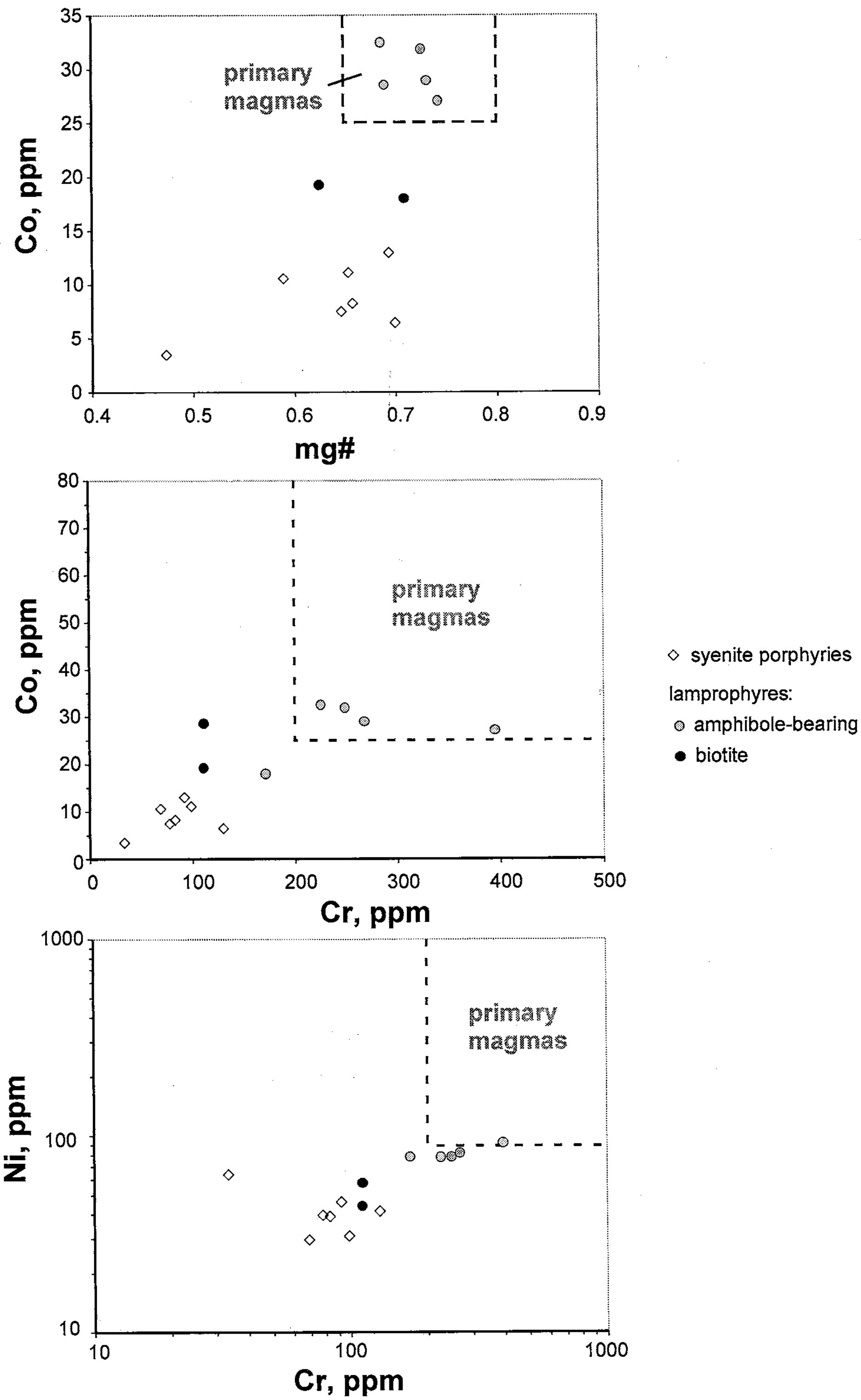

Fig. 4.16. Cr, Co, Ni contents and mg# of the Solton Sary potassic rocks compared to corresponding values of primary magmas (i.e. mg# 0.65-0.8, Cr 200-500 ppm, Co 25-80 ppm, and Ni 90-700 ppm, as defined by Rock (1991)). Mg# calculated as a mole percent ratio Mg/(Mg+Fe^2), with Fe^3/(Fe^3+Fe^2) = 0.45. Analytical data are in Tables 4.11 and 4.13.

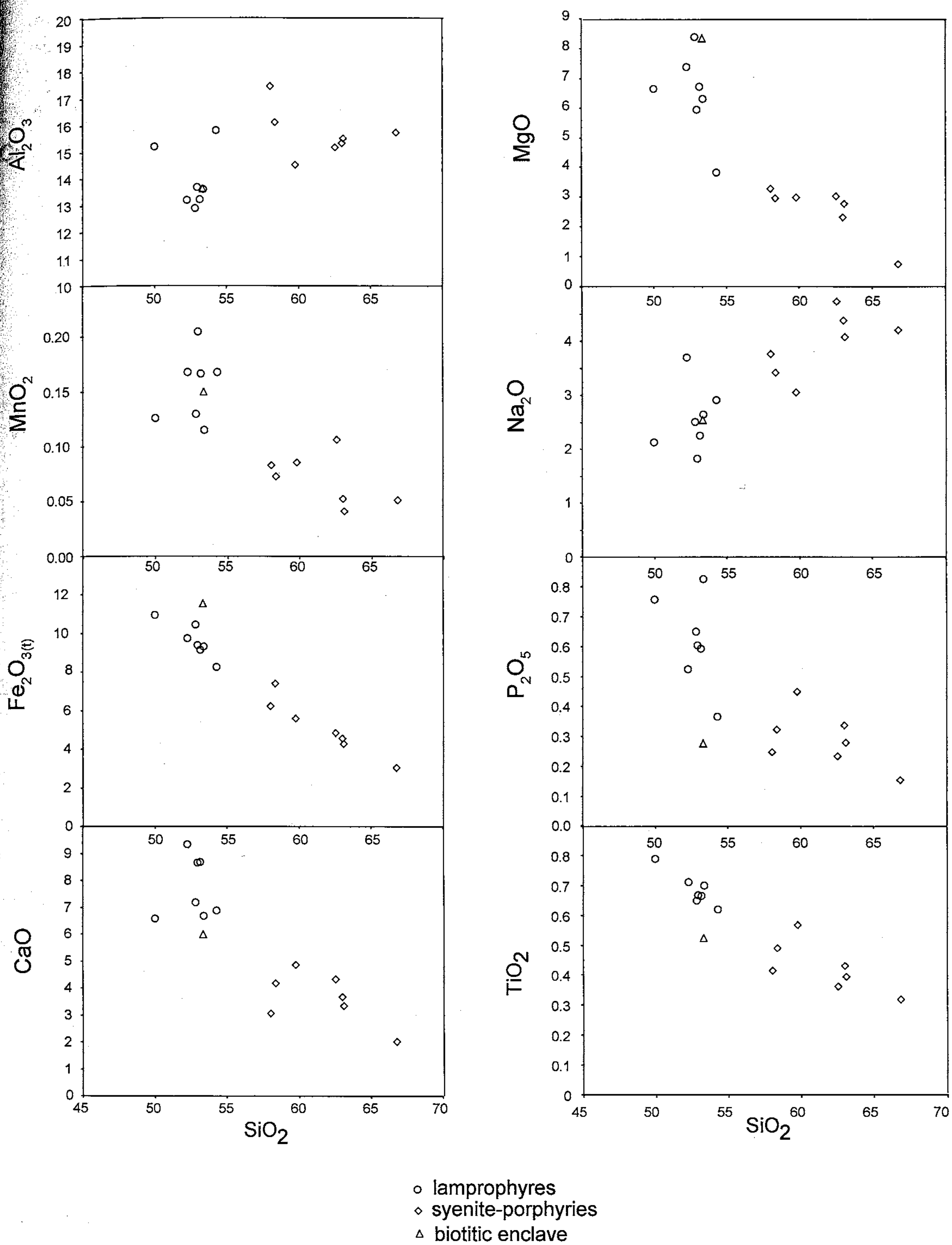

Fig. 4.17. Major oxide versus silica variation diagrams. All analyses are recalculated to 100 percent on a volatile free basis. Analytical data are presented in Table 4.11.

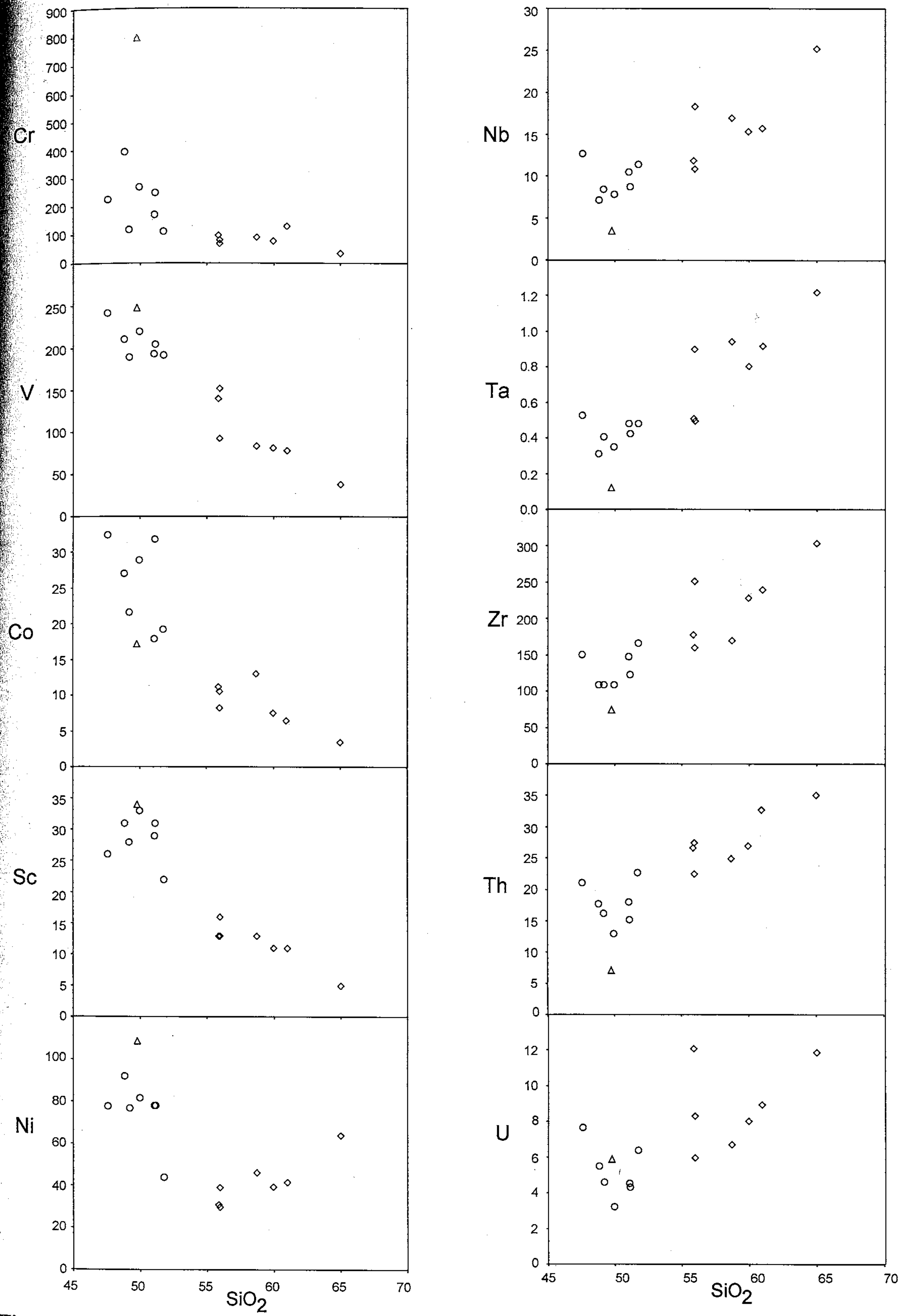

Fig. 4.18. Selected trace element (ppm) versus silica (wt percent) variation diagrams. Data are from Tables 4.11 and 4.13. Continued on the next page.

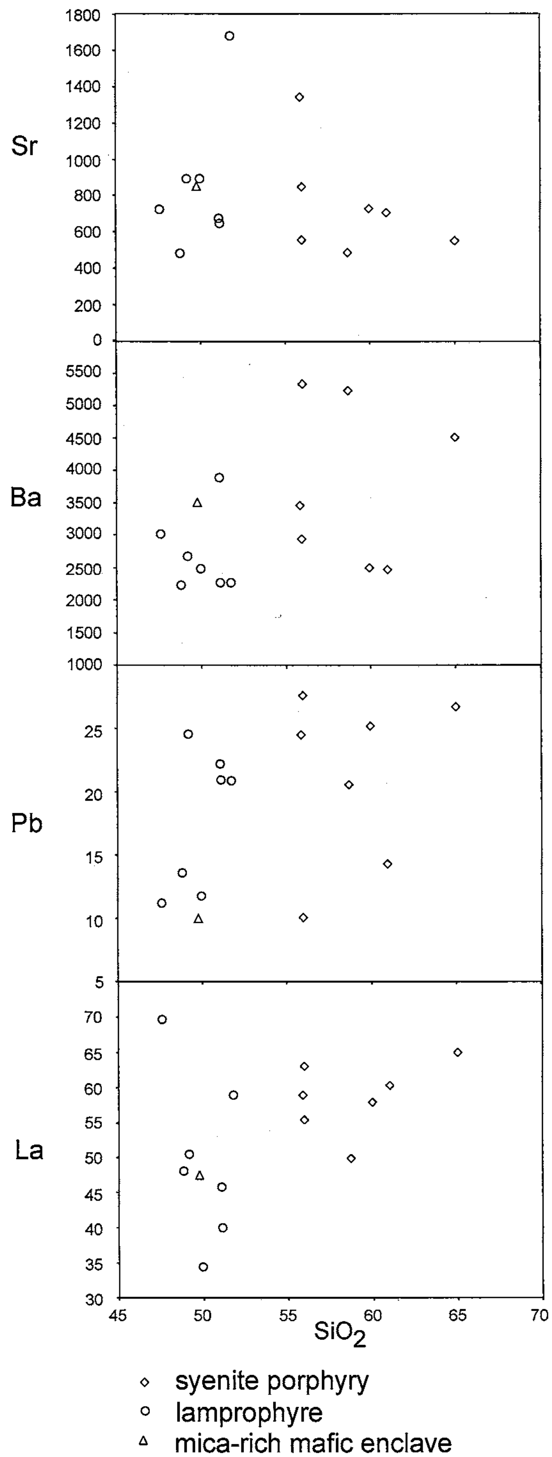

Fig. 4.18. Continued from previous page.

earth elements (REE; e. g., La, Fig. 4.18) and most of large ion lithophile elements (LILE, e. g., Pb, Sr, Ba, Fig. 4.18) show irregular variations.

Abundances of platinum-group elements in five samples of the Solton Sary intrusive rocks are listed in Table 4.12. Syenite porphyries and lamprophyres are slightly enriched in Au compared to the primitive mantle values from Brügmann et al. (1987). However, these elevated Au values tend to be decoupled from Cu and Pd on the primitive mantle normalized plot (Fig. 4.19), suggesting the likelihood of the epigenetic nature of this relatively weak gold enrichment (cf. Müller and Groves, 1997).

Normalized REE plots of syenite porphyries and lamprophyres are similar, with only subtle rock-type related differences (Fig. 4.20). Both rock varieties are significantly enriched in light rare earth elements (LREE), with chondrite-normalized La/Yb ratios (La/Yb_n) ranging from ~15 to ~24 for lamprophyres and from ~17 to ~22 for syenite porphyries (Table 4.13). All samples possess a weak negative Eu anomaly (Table 4.13). Lamprophyres tend to have slightly lower REE, and particularly LREE values, and stronger variations between individual samples.

Plots of primitive mantle-normalized incompatible elements (spidergrams) of lamprophyres and syenite porphyries show strong enrichment in LILE (e. g., K, Rb, Sr, Ba, Pb), including sharp positive Pb spikes, and negative Ta-Nb-Ti (TNT) and Zr anomalies (Fig. 4.21). Syenite porphyries are depleted in P and tend to have higher Zr values compared to the well defined Zr lows of lamprophyres. Such P and Zr patterns of the more evolved syenite porphyries are unlikely to be representative of magma source but are probably related to the fractionation of apatite and zircon.

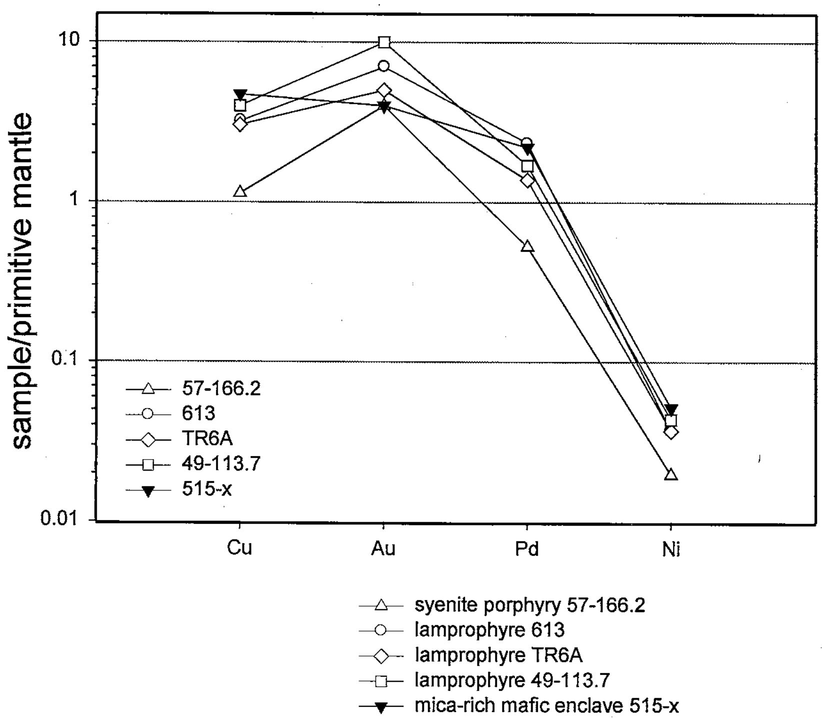

Fig. 4.19. Primitive mantle normalized Cu, Au, Pd, and Ni plots of the Solton Sary potassic rocks. Normalizing factors are from Brügmann et al. (1987).

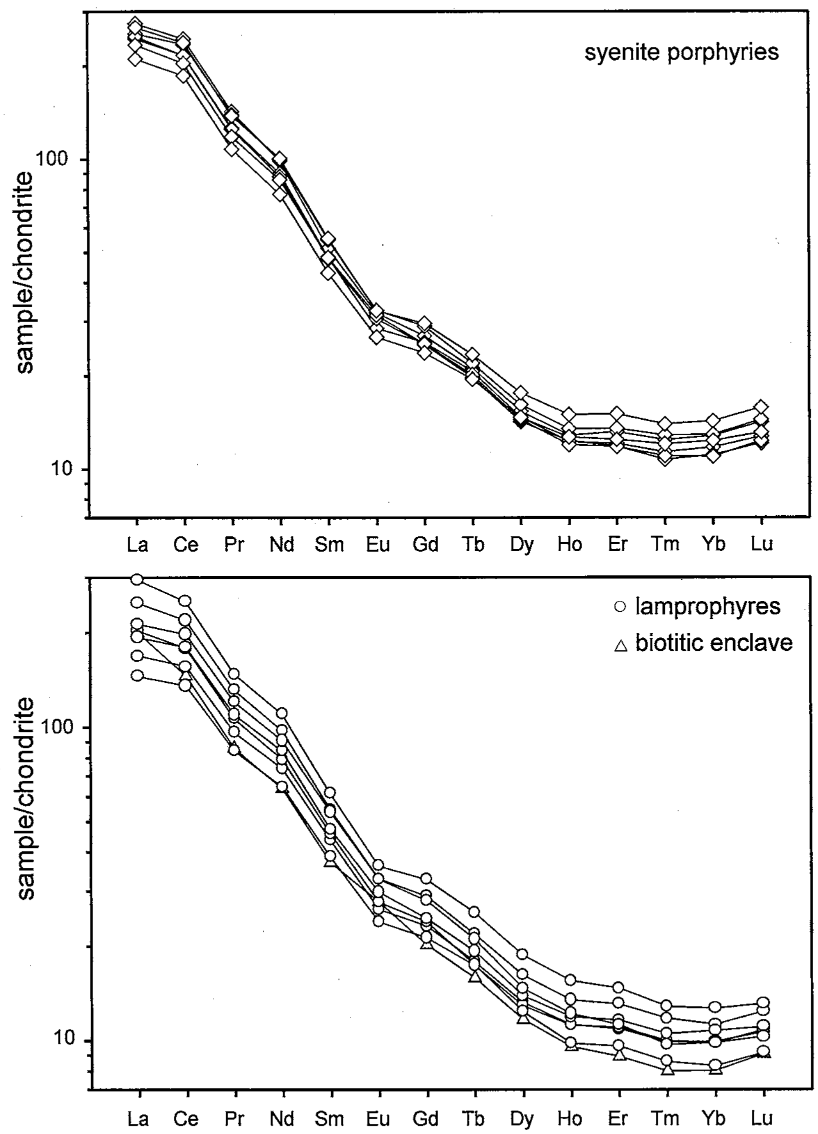

Fig. 4.20. Chondrite-normalized rare earth element plots of the Solton Sary potassic rocks. Normalizing factors are from Sun and McDonough (1989).

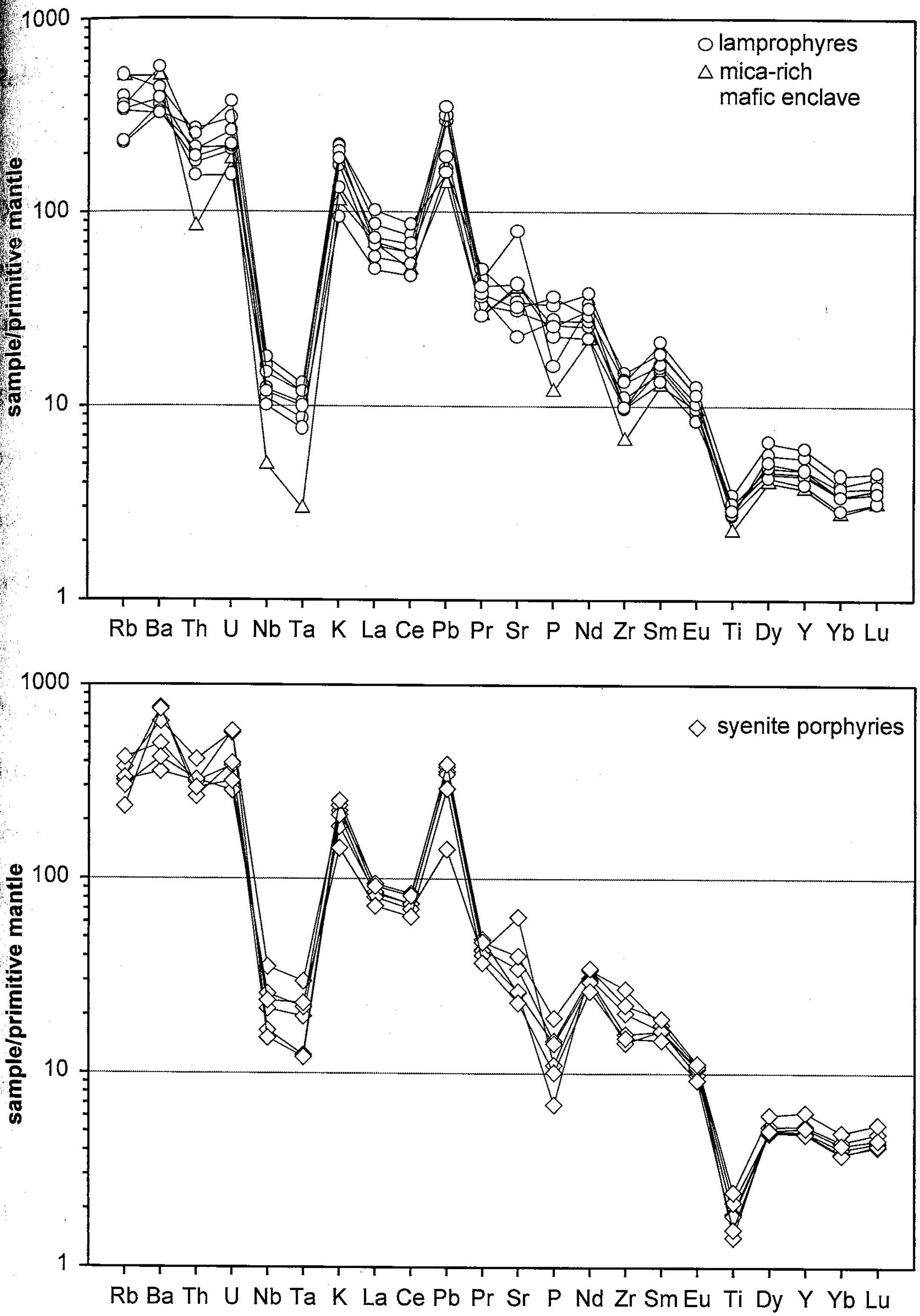

Fig. 4.21. Primitive mantle normalized incompatible element plots (spidergrams) of the Solton Sary potassic rocks. Normalizing factors are from Sun and McDonough (1989).

Discussion of geochemical data

Relationships between rock types, and magma source

Similarities in chondrite-normalized REE plots and spidergrams, as well as the systematic variation of major oxides and compatible elements, support a comagmatic origin of the syenite porphyries and lamprophyres. Rowins et al. (1993), Fowler and Henney (1996), and Leat et al. (1988) show that leucocratic alkalic rocks may be generated from lamprophyric parental magmas through fractional crystallization of pyroxene, mica, and feldspars, perhaps with minor crustal assimilation. Although no numerical modeling was attempted in this study, the scenario involving fractional crystallization appears to be generally applicable to the Solton Sary intrusive suite. The compositional variation of the Solton Sary intrusive rocks could be the result of the fractional crystallization principally of mica, amphibole, and possibly K-feldspar. This differentiation process was probably complicated by repeated mixing of related but compositionally differing magma batches and remobilization of crystal cumulates. Amphibole-bearing lamprophyres with zoned micas show chemical signatures resembling those of primary magmas (Fig. 4.8) and are likely to be compositionally closest to the parental melt. Leucocratic syenite porphyries represent the most evolved magmas. Major oxide and trace element abundances of the Solton Sary lamprophyres are very close to the "average" composition of calc-alkaline lamprophyres reported by Rock (1991). Differences comprise slightly lower values of TiO_2 and most of the compatible trace elements, and higher K, Rb, Ba, Sr, Th, and U in the Solton Sary intrusions (Fig. 4.22). The Solton Sary lamprophyres have major oxide compositions of basaltic trachyandesite or shoshonite, compatible trace element contents comparable to those of

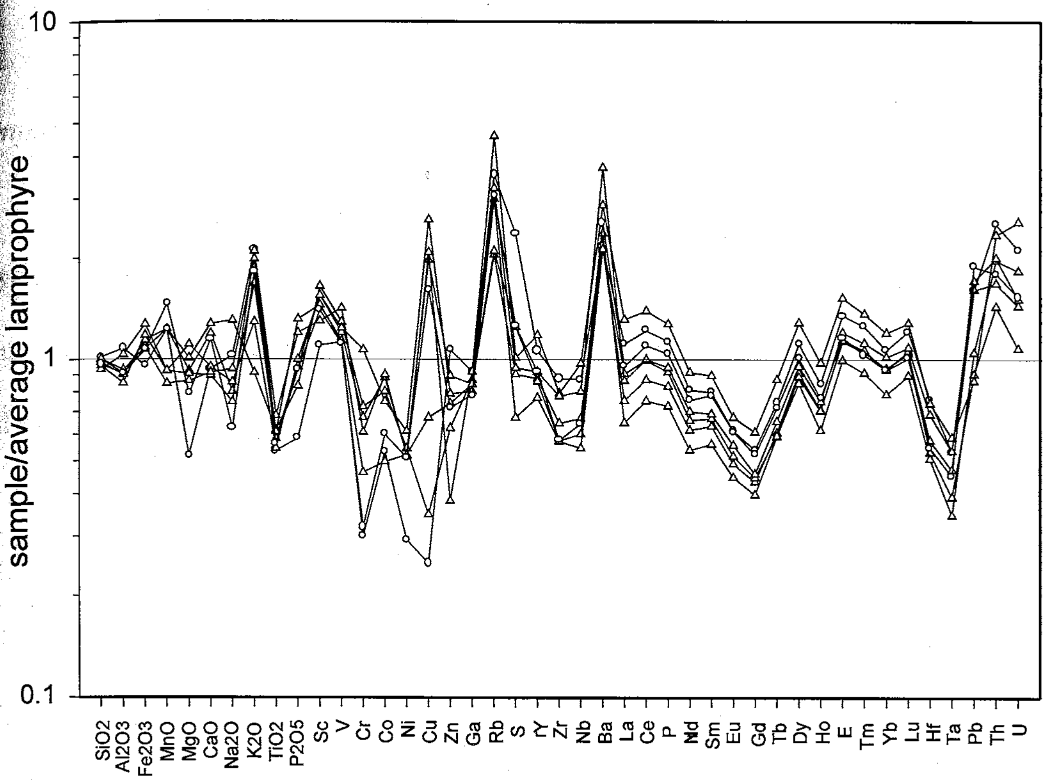

Fig. 4.22. Major oxides and trace elements of the Solton Sary lamprophyres normalized by corresponding values of "average" calc-alkaline lamprophyre tabulated by Rock (1991).

primary magmas, strong enrichment in LREE and LILE, and relative depletion in Nb, Ta, and Ti. These features are typical for calc-alkaline lamprophyres in general (Rock, 1991; Wyman and Kerrich, 1993). They are interpreted as indicative of partial melting of the upper mantle that has been metasomatically enriched in LILE and LREE by fluids and/or melts (e. g., Sheppard and Taylor, 1992; Wyman and Kerrich, 1993; Müller and Groves, 1997).

Implications for gold mineralization

The absence of distinct intrinsic gold enrichment of the Solton Sary lamprophyres and syenite porpyries implies that, in spite of the close spatial association, the mesothermal mineralization is unlikely to be genetically related to this potassic intrusive complex. Moreover, the intrusions are unlikely to have served as major contributors of gold during the superimposed hydrothermal events due to their relatively small volume (cf. Taylor et al., 1994).

Tectonic setting

Trace element patterns of the lamprophyres and syenite porphyries provide information on the possible tectonic setting of the potassic magmatism. Negative Eu anomalies are common for arc-related igneous rocks, and presumably indicate the involvement of subducted sediments in magma generation (e. g., McLennan and Taylor, 1981; Sun and McDonough, 1989). However, Eu lows can be generated by plagioclase fractionation or by albitization of primary magmatic plagioclase (Taylor et al., 1994). An extreme Na-rich composition of plagioclase in syenite porphyries and lamprophyres implies a rather high probability for metasomatic albitization. Thus, the Eu anomalies alone are not particularly reliable geodynamic indicators. Ta-Nb-Ti lows (TNT) are characteristic of virtually all calc-alkaline lamprophyres (Rock, 1991). This geochemical signature is traditionally regarded as a subduction tracer, but is recognized as not absolutely diagnostic for potassic rocks (Rock, 1991, Müller and Groves, 1997). For this rock type, TNT anomalies are not unique to subduction settings (e. g., Sheppard and Taylor, 1992) and some arc-related potassic rocks do not bear the TNT signatures (e. g., Rock, 1991).

In order to further constrain the tectonic setting of the potassic magmatism, the discrimination routine by Müller and Groves (1997) was applied to the geochemical data from the Solton Sary intrusive suite. This procedure was designed specifically for potassic igneous rocks because traditional geochemical discrimination methods (e. g., Pearce and Cann, 1973; Pearce and Norry, 1979; Wood et al., 1979) were found to be unsuitable for this rock type. The procedure is based on the multigroup linear discriminant analysis of geochemical data representing Cenozoic potassic igneous rocks from known tectonic settings. These settings include initial oceanic arc, late oceanic arc, intra-plate, continental arc, and post-collisional arc. Post-collisional arcs are situated within the marginal portions of collided continental plates that could have hosted subduction-related (i.e. continental arc) magmatism prior to the collision. Post-collisional magmatism occurs after the convergence of two continental plates terminates the subduction, and can be broadly associated with an uplift-related extensional tectonic regime (Müller and Groves, 1997).

The discrimination has the following steps: First, the data set is screened in order to sort out highly evolved, cumulate, and hydrothermally altered samples. After that, the selected results are plotted on a set of hierarchical discrimination diagrams. The initial step of the discrimination procedure separates most distinct tectonic settings (i.e. within plate, ocean arcs, continental and post-collisional arcs). The later steps target more subtle differences (e. g., continental arc versus post-collisional arc; initial oceanic arc versus late oceanic arc). The routine permits most of the tectonic settings to be constrained using two element sets. The results of the application of the discrimination routine to the Solton Sary samples are shown in Figure 4.23. Screening criteria used in this study (Fig. 4.23A) are similar to those of Müller and Groves (1997), except for the loss on ignition (LOI) cut-off value that was raised to 7 percent from the originally suggested 5 percent. Seven lamprophyre samples passed the screening. Two discrimination systems were used. The first included TiO_2/Al_2O_3 versus Zr/Al_2O_3 and Zr/TiO_2 versus Ce/P_2O_5 biaxial plots (Fig. 4.23B and C). The second system employed two triangular plots: Hf*10-TiO_2/100-La and Ce/P_2O_5-Zr*3-Nb*50 (Fig. 23D and E). The initial steps (Fig. 4.23B and D) confidently sorted out intraplate and oceanic arc settings. Further results were somewhat ambiguous. The Ce/P_2O_5 versus Zr/TiO_2 diagram indicates the continental arc setting for the Solton Sary lamprophyres and the Ce/P_2O_5-Zr*3-Nb*50 diagram was unable to discriminate between the post-collisional arc and continental arc settings.

In spite of the potential drawbacks of individual geodynamic indicators, Eu and TNT patterns and results of geochemical discrimination are consistent in supporting the arc setting of the potassic magmatism. The inferred tectonic setting (magmatic arc underlained by continental crust) is in good agreement with the regional geology and

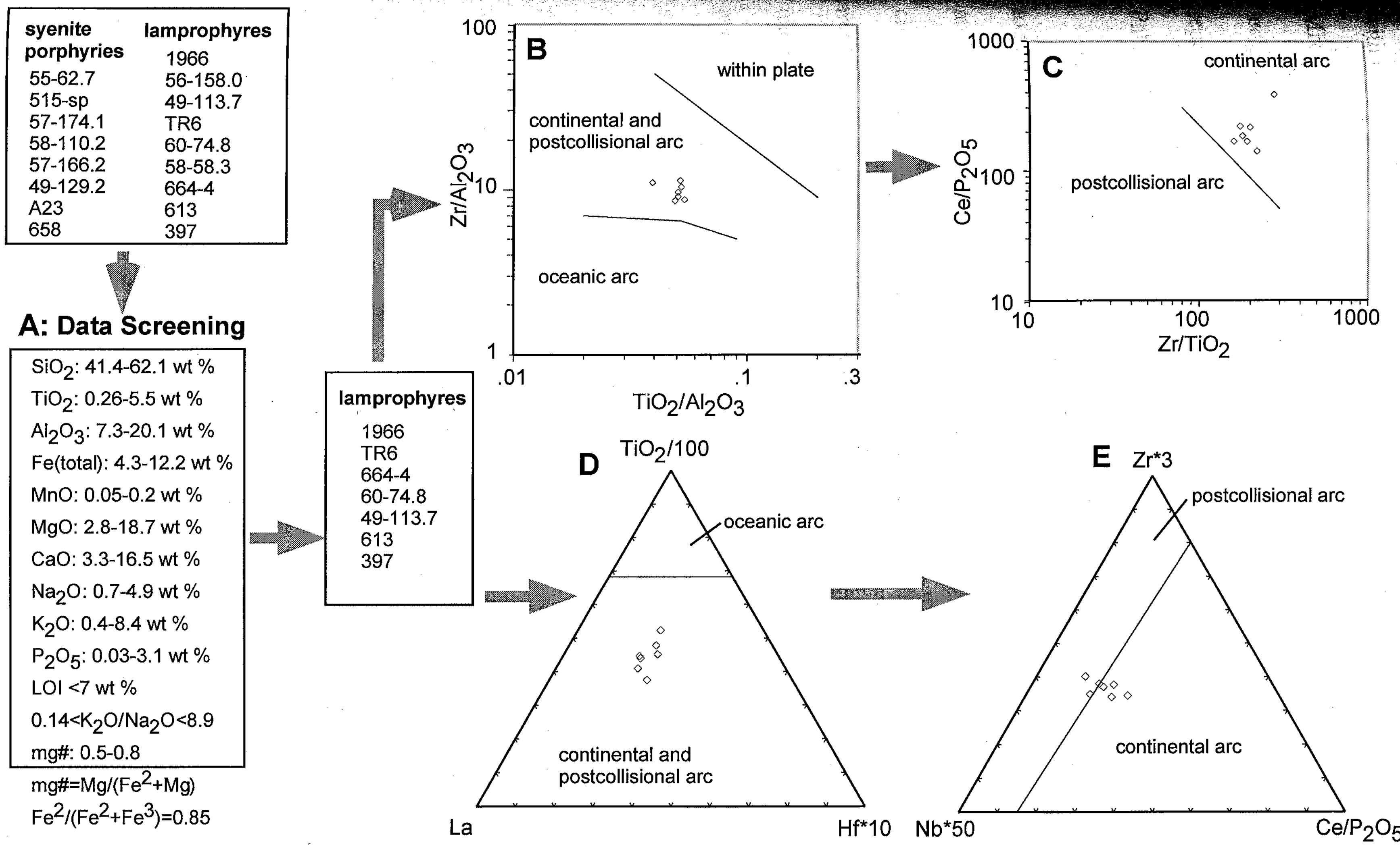

Fig. 4.23. Discrimination routine by Mü ller and Groves (1997) applied to the Solton Sary potassic rocks. LOI filter is set at 7 wt % instead of recommended 5 wt percent. Trace elements and major oxides are in ppm and wt percent, respectively. In the diagram D, $TiO_2/100$ is calculated in ppm. See text for additional explanations.

with most geodynamic models (e. g., Sengör and Natal'in, 1996a, b; Sengör et al. 1993; Mikolaichuk et al., 1997; and Lomize et al., 1997). According to these models, the tectonostratigraphic unit that hosts the Solton Sary district (Kyrgyz-Terskei zone), represented a magmatic arc on continental crust basement during the latest Early Paleozoic.

The fact that the discrimination procedure by Müller and Groves (1997) was unable to positively discriminate between the post-collisional arc and continental arc can be attributed to the general similarity of the two tectonic settings. Both environments are characterized by the concurrent or recent subduction of oceanic lithosphere, by fluid and/or melt-induced metasomatic enrichment of the upper mantle in LILE and LREE, and possibly by the interaction of the ascending melts with thick continental crust (Müller and Groves, 1997). After the collision, the magmas would still originate in a mantle source area that was previously modified by subduction processes. Such melts are expected to inherit, at least partially, the geochemistry of the subduction zone. Perhaps due to these factors, geochemical signatures of potassic rocks from two tectonic settings show only subtle differences (e. g., slightly higher Ce/P ratio in the post-collisional arc), most of which still lack reliable theoretical explanations (Müller and Groves, 1997). Therefore the authors of the discrimination routine emphasize the high probability of overlaps between the potassic rocks from continental and post-collisional arcs.

Trace element signatures ultimately reflect the chemistry of the magma source rather than the tectonic regime in which the melt was generated. It is recognized that even in arc settings, potassic magmatism is usually not a product of "steady-state" subduction but is associated with some anomalous tectonic episodes such as plate boundary rearrangements due to oblique convergence (Müller and Groves, 1997). At terrane boundaries, shoshonitic lamprophyres are typically associated with major strike-slip tectonism under transpressive regimes of oblique subduction and/or collision (e. g., Wyman and Kerrich, 1988a, b; Kerrich and Wyman, 1990; Rock and Groves, 1988a, b). The lamprophyres of the Solton Sary district differ petrologically and geochemically from arc volcanics and granitoids and thus are unlikely to be a product of simple arc volcanism. More probably, the emplacement of alkalic magmas was related to activation of regional strike-slip faults during plate collision. This interpretation appears feasible especially considering the location of the Solton Sary near a terrane-dividing fault, the Nikolaev Line.

Summary

Syenite porphyries and lamprophyres of the Solton Sary gold district represent a single magmatic system. A close genetic relationship between the two rock varieties is supported by the likeness of mineral assemblages, compositional similarity of individual mineral phases, and by virtually indistinguishable trace element patterns. The syenite porphyries and lamprophyres may be related by the fractional crystallization principally of mica, amphibole, and, possibly, K-feldspar that was complicated by mixing of discrete batches of differentiated magma during its ascent to the surface. Mafic lamprophyres with phenocrysts of amphibole and zoned, phlogopite-cored micas are compositionally closest to the primary magmas, whereas generally more leucocratic, feldspar-phyric, syenite porphyries represent more evolved melts.

prophyres of the Solton Sary gold district belong to the calc-alkaline ric) suite. Their whole-rock chemical composition, petrographic assemblage, osition of major mineral phases are similar or closely comparable to those for shoshonitic lamprophyres from various localities, including world-class nal gold districts. Geochemical signatures of the Solton Sary potassic rocks are t with their setting within the Early Paleozoic magmatic arc. The occurrence of magmatism at the margin of the North Tien Shan plate is likely to be related to a event. Lamprophyres and syenite porphyries show only slight and likely ic enrichment in gold. This makes the genetic relationship between the ation and potassic magmatism highly unlikely.

CHAPTER 5

OBSERVATIONS ON DEFORMATION STYLES

Introduction

This chapter summarizes observations that were made during field and petrographic studies of mineralization and host rocks of the Solton Sary gold district, with primary attention to the intrusive belt that hosts auriferous mineralized zones. It attempts to establish links between the observed deformation patterns, petrography of host rocks, composition and intensity of hydrothermal alteration, and the structure of the district. Understanding these relations is essential for future exploration within the Solton Sary area, especially for the assessment of geometric parameters of the mineralization (i. e. thickness and orientation of the mineralized zones). By providing information on prevailing metamorphic conditions, the observations on deformation styles supplement fluid inclusion and thermochronologic data in constraining the pressure-temperature environment during the mineralizing event.

Deformation within the intrusive belt

Alkalic intrusive rocks and gold-bearing mineralized zones of the Solton-Sary gold trend were affected by shearing. Deformational features vary from brittle fractures with slickensides to a macroscopically ductile, penetrative foliation with local development of mylonites. The distribution of deformation styles is not random but appears to be controlled by two major factors: rock composition (original lithology, as well as the composition and intensity of alteration) and the existence of inherited, pre-tectonic discontinuities.

Composition control on deformation styles

Deformed lamprophyres usually exhibit a well developed penetrative foliation defined by the orientation of individual mica grains (including both fine-grained biotite in the matrix and relatively large biotite phenocrysts), subparallel biotite-rich bands, lenticular to lensoid carbonate segregations, and flattened mafic enclaves (Fig. 5.1A, B). Microstructures include bending, kinking, and dynamic recrystallization of mica phenocrysts (Fig.5.1C) as well as development of mica "fish". In spite of this generally predominantly ductile deformation style, some thick lamprophyric sills still contain weakly foliated domains in their central parts. Within these, deformation also produced fracturing with slickensides. Thin veinlets of hydrothermal minerals (carbonate, epidote, quartz, biotite and hematite) are developed along some fractures. Locally, these veinlets crosscut foliation and show syn to post-alteration displacement along fracture surfaces.

Deformational features in syenite porphyries vary significantly and appear to largely depend on the amount of K-feldspar and, to a lesser extent, mica phenocrysts. Sparsely porphyritic, mica-bearing varieties commonly show a well developed foliation that is defined by the alignment of porphyroclasts formed after phenocrysts and by mica-rich cleavage domains in the matrix. Biotite porphyroclasts are normally kinked and bent. Most feldspar porphyroclasts are fractured, and in cases of stronger deformation attain characteristic lensoid or ovoid shapes (Fig.5.2). In the matrix, the foliation is marked by moderately to well developed cleavage domains defined by wavy bands and lenses of

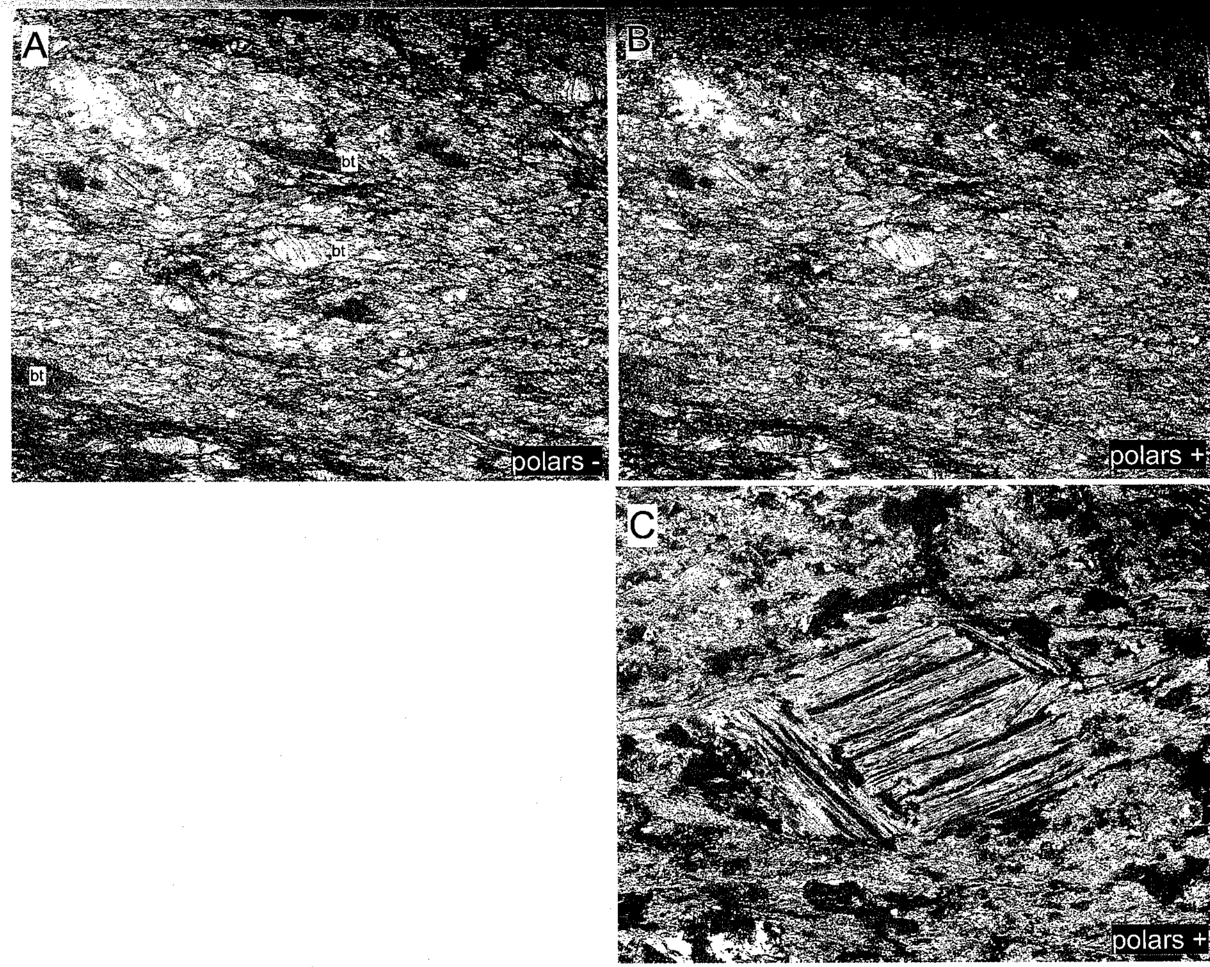

Fig. 5.1. Photomicrographs of deformed lamprophyres (A+B show the same field of view in plane-polarized light on the left and cross-polarized light on the right). Photos A and B depict a general view of a typical sheared lamprophyre. Continuous foliation is defined mainly by the orientation of biotite crystals (bt), most of which are kinked, bent, and partially chloritized. C shows a deformed and muscovite-altered biotite porphyroclast. Field of view 2.5 mm (A and B), and 1 mm (C).

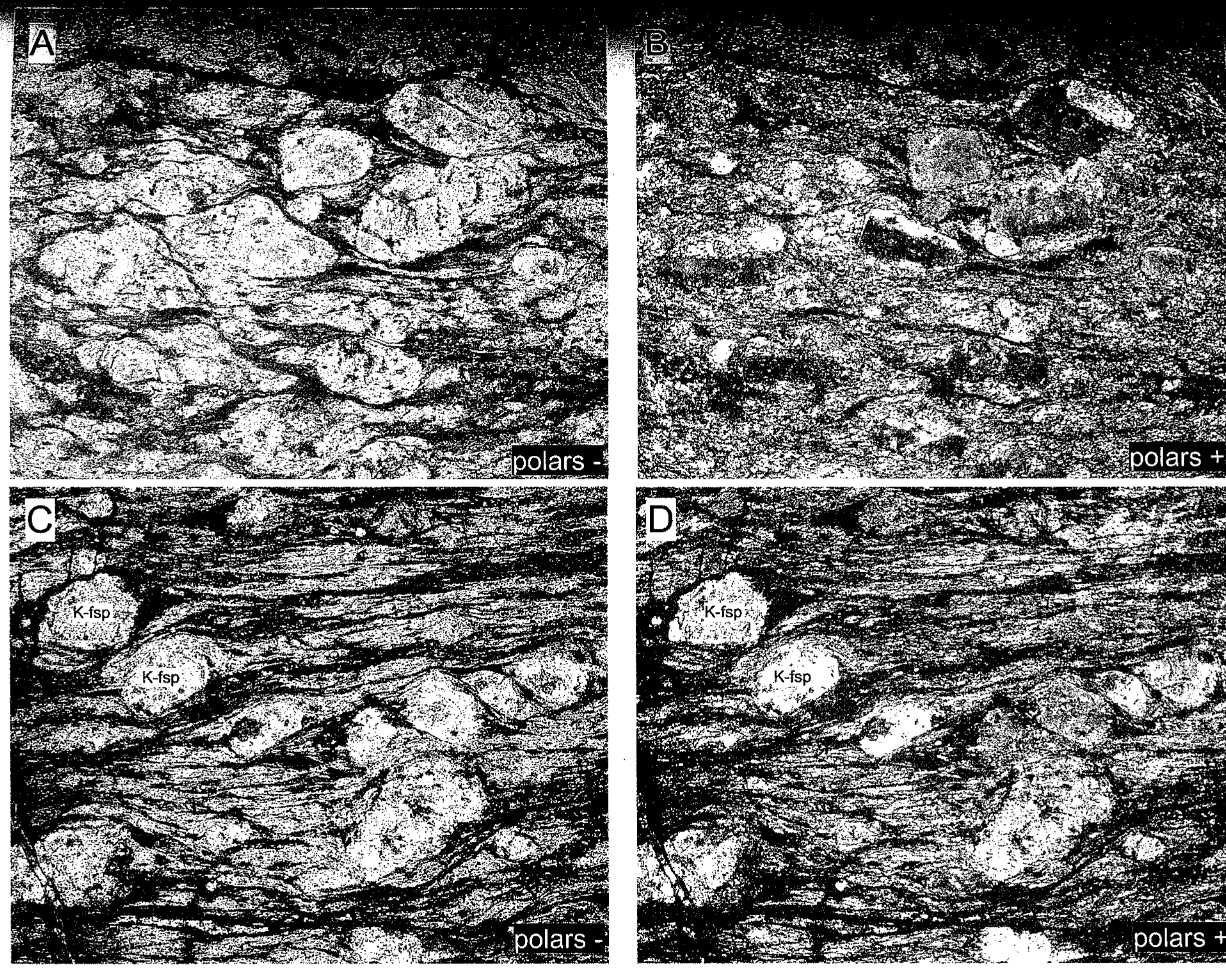

Fig. 5.2. Photomicrographs of deformed syenite porphyries. A + B and C + D depict the same fields of view in plane-polarized light (left) and cross-polarized light (right). The foliation is marked mainly by cleavage domains that are defined by bands and streaks enriched in fine secondary biotite (dark streaks on A and C). Porphyroclasts are represented by rounded and ovoid K-feldspar (K-fsp). Field of view in each photomicrograph approximately 2.5 mm.

fine-grained, likely epigenetic, biotite. These usually wrap around feldspar grains and create the characteristic pseudo-gneissic appearance of the rocks (Fig.5.2). In spite of the generally brittle behavior of feldspar phenocrysts, the overall style of deformation of the sparsely porphyritic mica-bearing syenites is predominantly ductile rather than brittle. There are, however, cases of brittle fracturing with the formation of veinlets of secondary biotite, carbonate, hematite and pyrite. In places, such veinlets crosscut foliation.

Massive leucocratic syenite porphyries, that usually lack biotite and are enriched with short prismatic feldspar phenocrysts, appear to be unfavorable for the development of tectonic foliation. The most typical deformation features include relatively weak cataclastic fracturing of phenocrysts, and formation of tension gashes and discrete shear fractures with slickensides. Hydrothermal minerals (mainly quartz, sericite, and carbonate) deposited in the fractures are usually affected by shearing. Quartz exhibits undulose extinction, development of subgrains and dynamic recrystallization.

Deformation at sill contacts

The most prominent discontinuities within the intrusive belt are the contacts between the sills. These are usually marked by shear zones composed of mylonites with thicknesses varying from 1-2 cm to more than 1.0 m. Within these zones, even the most competent rocks, the leucocratic syenite porphyries, experienced intense ductile deformation and strong quartz-sericite-carbonate pyrite (QSCP) alteration. Aposyenitic mylonite is a fine-grained rock consisting almost entirely of epigenetic minerals. It contains euhedral cubic and stretched, pseudo-prismatic pyrite, sparse quartz -sericite pseudomorphs after lensoid K-feldspar porphyroclasts, and, rarely, muscovite fish perhaps formed by deformation and replacement of magmatic biotite). The matrix is composed primarily of sericite with segregations of carbonate and discontinuous lenses of quartz (Fig. 5.3). These lenses either comprise aligned, elongate, fine grains or, less commonly, recovered granoblastic aggregates (Fig. 5.3F). Strain shadows of massive granoblastic quartz and strain fringes of fibrous quartz are found near pyrite grains. Commonly, they contain muscovite at their outer rims adjacent to sericite-altered wallrocks. The foliation is defined by the orientation of sericite flakes, porphyroclast pseudomorphs, strain shadows, quartz lenses, and veinlets. In places, relatively thick (~0.5-1 m) mylonite zones host concordant quartz veins and swarms of quartz veinlets. Transitions from mylonites to weakly deformed syenites are abrupt (on the order of 1-3 cm), but, in places, contacts of thick sills are marked by a series of mylonite zones separated by domains of fractured syenites with abundant quartz veinlets. Within syenite sills, the most extensive cataclasis is usually found close to the contacts and rarely in the central parts of the bodies.

In less competent sills of lamprophyre and sparsely porphyritic mica-bearing syenite, contrasts between the deformation styles of different parts of a single intrusion are not so strong. However, the cases where the relict non-foliated rocks are found in the internal parts of thick lamprophyric sills suggest that there could be a continuous decrease in strain from the contacts of the bodies to their central parts.

Quartz vein fabrics

As mentioned in Chapter 3, vein silicification occurs as concordant steeply dipping veins and veinlet swarms, syenite-hosted stockworks of variably oriented veinlets and

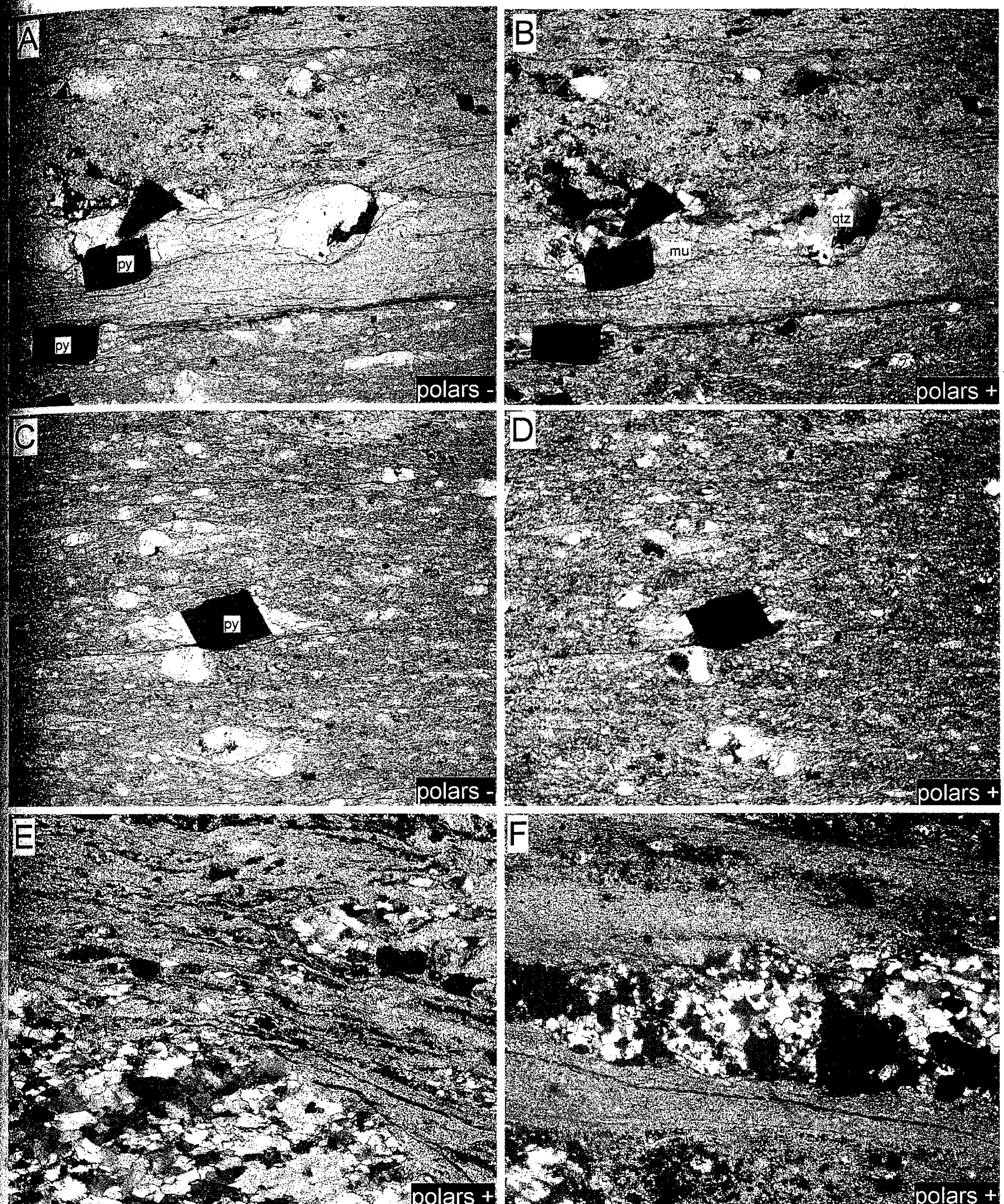

Fig. 5.3. Mylonites from contacts of syenite sills. Photos A + B, C + D depict the same fields of view in plane-polarized light (left) and cross-polarized light (right) . Matrix of mylonites consists almost entirely of sericite and encloses segregations and veinlets of quartz, stretched pyrite grains (py), commonly accompanied by quartz (qtz) and muscovite (mu). Some quartz segregations may represent pseudomorphs after magmatic phases. Photos E and F (cross-polarized light) show textures of quartz veinlets. E: continuous foliation defined by grain preferred orientation inclined to foliation outside the veinlet; F, recovered polygonal aggregate. Field of view in each photograph is 2.5 mm.

relatively uncommon arrays of extensional veins. Most typical are mylonite-hosted concordant quartz veins at contacts of syenite sills. The microscopic fabrics of these quartz veins reflect dynamic recrystallization of variable intensity. Veins (especially those that are relatively thick) may comprise an inequigranular assemblage of old and new grains with undulose extinction and deformation lamellae. In cases of stronger recrystallization, veins consist predominantly of new, uniformly sized grains with a continuous foliation defined by the preferred orientation of the grains (Fig. 5.3E). In virtually all cases, quartz hosts healed microfractures with trails of fluid inclusions. Common sericite streaks are oriented subparallel to vein contacts. Relatively rare, coarse-grained (1-3 mm) muscovite is inferred to have deformed by basal-plane sliding combined with kinking and bending.

Relationships between the deformation and hydrothermal alteration

The relative timing of deformation and hydrothermal activity is constrained by observed relationships between deformation-induced fabrics and alteration assemblages. In deformed hydrothermally altered rocks, deformation fabrics are defined by the orientation of hydrothermal biotite, sericite, muscovite, carbonate, and quartz, implying that the fabric generation could not have predated the hydrothermal activity. Also, all observed quartz veins are to a variable extent deformed, suggesting the improbability of any significant post-kinematic hydrothermal precipitation. Widespread pyrite-cored pressure fringes consisting of fibrous quartz with sericite and muscovite or, less commonly, biotite, represent the direct evidence for the syn-deformational crystallization of major hydrothermal phases.

As mentioned in Chapter 3, the intensity of the hydrothermal alteration correlates the intensity of shearing. The QSCP alteration appears to be the strongest within lonite zones located at contacts of syenite sills. The QSCP alteration resulted in lacement of mechanically strong phases (K-feldspar and plagioclase) by less mpetent (sericite and carbonate) minerals, and thus must have assisted ductile formation. Fracturing and cataclasis of K-feldspar phenocrysts, i.e. the phase that is the st resistant against the OSCP alteration, facilitated the virtually complete replacement the syenite protolith by hydrothermal minerals.

Results of microstructural studies

Microstructural studies of oriented thin sections were done to establish the general pattern of tectonic movements within the Solton Sary district. Oriented samples were collected from the South Kumbel fault zone and from the swarm of ore-hosting intrusions. The location of the samples is shown on the geologic map (Fig. 3.1).

South Kumbel fault separates middle Ordovician tuffs (tO_2) from carbonates (ccO_2). The fault is accompanied by a ~ 200 m wide halo of chlorite-fuchsite-carbonate alteration. Mylonites from the axial zone of the fault consist entirely of epigenetic chlorite, fuchsite, carbonate, with subordinate quartz and pyrite. Two samples of mylonites, 669-4 and 643-8, were collected from two localities along the strike of the fault, about 2.5 km apart. Macroscopically, the mylonites show a well developed foliation or, in some cases, lineation. Sample 643-8 was collected from an outcrop with a macroscopically visible lineation plunging at about 30° to the west-northwest (275-280°).

This sample was characterized by two thin sections: one oriented parallel to the lineation and perpendicular to the foliation and the second oriented perpendicular to the lineation and nearly parallel to the foliation. At the microscopic scale, the deformation fabric of the sample 643-8 appears to be defined mainly by the orientation of linear, rod-shaped, domains that are enriched in chlorite, fuchsite, and quartz and enclosed in an essentially carbonate matrix. Observations on the thin section oriented parallel to the lineation revealed the presence of a predominantly planar foliation (C) and shear bands (C'-foliation) that displace the chlorite-rich domains. The orientation of the shear bands indicates an apparent sinistral shear sense (Fig. 5.4). Considering the orientation of the thin section and the plunge of the lineation, this translates into a dextral strike-slip displacement with a normal shear component in geographic coordinates. The thin section oriented perpendicular to the lineation does not reveal any shear sense indicators, suggesting that the lineation is roughly parallel to the transport direction.

Sample 669-4 was collected from a mylonite that did not exhibit a macroscopically distinct lineation. With respect to the foliation, thin sections are oriented parallel to the strike and perpendicular to the dip, and parallel to the dip and perpendicular to the strike. The thin section parallel to the strike shows a planar foliation defined by chlorite-rich bands set in a matrix of carbonate and subordinate quartz. This is accompanied by somewhat poorly defined shear bands (C’), the orientation of which implies dextral strike-slip displacement in geographic coordinates. The thin section oriented perpendicular to the foliation strike does not show unequivocal kinematic indicators, indicating that the deformation was dominated by strike-slip shear.

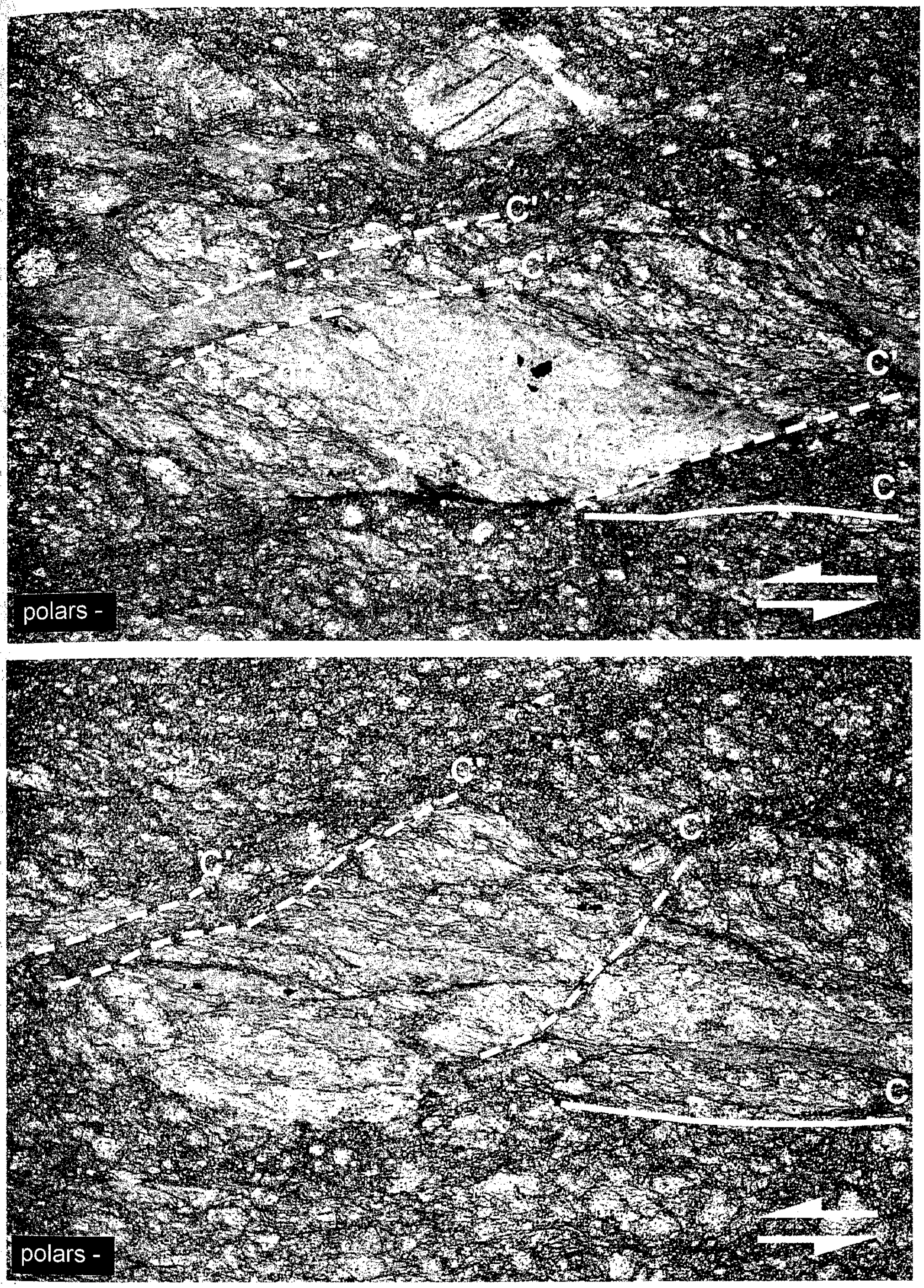

Fig. 5.4. Photomicrographs of mylonite from the South Kumbel fault zone, sample 643-8, plane polarized light. Thin section is oriented parallel to lineation and perpendicular to foliation. Lensoid domains of chlorite (chl), fuchsite and quartz, (qtz) are set in essentially carbonate matrix. The combination of C' (shear bands) and C foliation defines an apparent sinistral sense of shear that corresponds to dextral sense of shear in geographic coordinates.

Four other samples were collected from the swarm of alkalic intrusions that hosts the mesothermal mineralization and related alteration halos. Western and eastern segments of the intrusive belt were characterized by two pairs of samples, each pair comprised oriented slabs from the northern and southern flanks of the belt. All samples are mylonites that developed in alkalic intrusive rocks simultaneously with the QSCP alteration. A tectonic lineation was not macroscopically detectable at any of the four localities. Each sample was characterized by two thin sections: one oriented parallel to the foliation strike and perpendicular to the dip, and second cut parallel to the foliation dip and perpendicular to the strike.

Samples from the southern flank of the intrusive swarm (53-1 and 549) show a well-developed main foliation (C) defined by the orientation of mica-rich cleavage domains, individual mica flakes, and quartz-carbonate pseudomorphs after magmatic feldspars. Maximum asymmetry is observed in thin sections oriented parallel to the strike of the foliation. In these thin sections, the C' and S foliation systems are defined, respectively, by shear bands and the orientation of mica fish. In addition to these, pyrite-cored quartz-muscovite fringes are present in sample 53-1. The kinematic indicators support a sinistral (in geographic coordinates) dominantly strike-slip shear sense. In thin sections oriented perpedicular to the foliation strike, shear sense indicators are less developed and, in case of sample 53-1, are equivocal. This sample shows two sets of poorly defined shear bands that imply mutually opposite shear directions. Temporal relationships between the two sets of shear bands are unclear. In sample 549, shear bands suggest a sinistral sense of shear that corresponds to the reverse fault mode (south-side-up) in geographic coordinates. Overall, the results of the microstructural studies of oriented thin sections from the southern flank of the intrusive belt imply predominantly sinistral strike-slip displacements with variably oriented dip-slip components.

Samples 53-2 and 537 from the northern flank of the intrusive belt reveal a well defined C-foliation marked by compositional banding and the orientation of mica flakes. Sample 53-2 from the western part of the intrusive belt does not exhibit shear sense indicators, implying predominantly coaxial deformation, or possibly, very high strain. The sample from the east (537) represents essentially sericitic mylonite with quartz veinlets (Fig. 5.5). Kinematic indicators are observed in both thin sections but appear better defined in the direction parallel to the foliation strike. In addition to intercalation of sericite streaks and quartz veinlets defining a C-foliation, an oblique S-foliation defined by the orientation of elongate quartz grains and rather poorly developed shear bands (C' foliation) are apparent in both thin sections (Fig. 5.5). The inferred sense of shear is dextral strike-slip, with a normal shear (north-side-up) component.

Discussion

Factors controlling deformation styles

Deformational patterns observed in the intrusive belt of the Solton-Sary gold district are in many ways similar to those reported for granitoid complexes deformed under the greenschist facies metamorphic conditions (Vernon and Flood, 1988; Paterson et. al., 1989). In spite of the existence of some pre-tectonic fabrics such as a locally developed magmatic flow alignment of K-feldspar phenocrysts, the foliation found in igneous rocks of the Solton Sary gold district was formed by solid-state deformation. The latter was heterogeneous. Paterson et al. (1989) suggest that the most important factors controlling

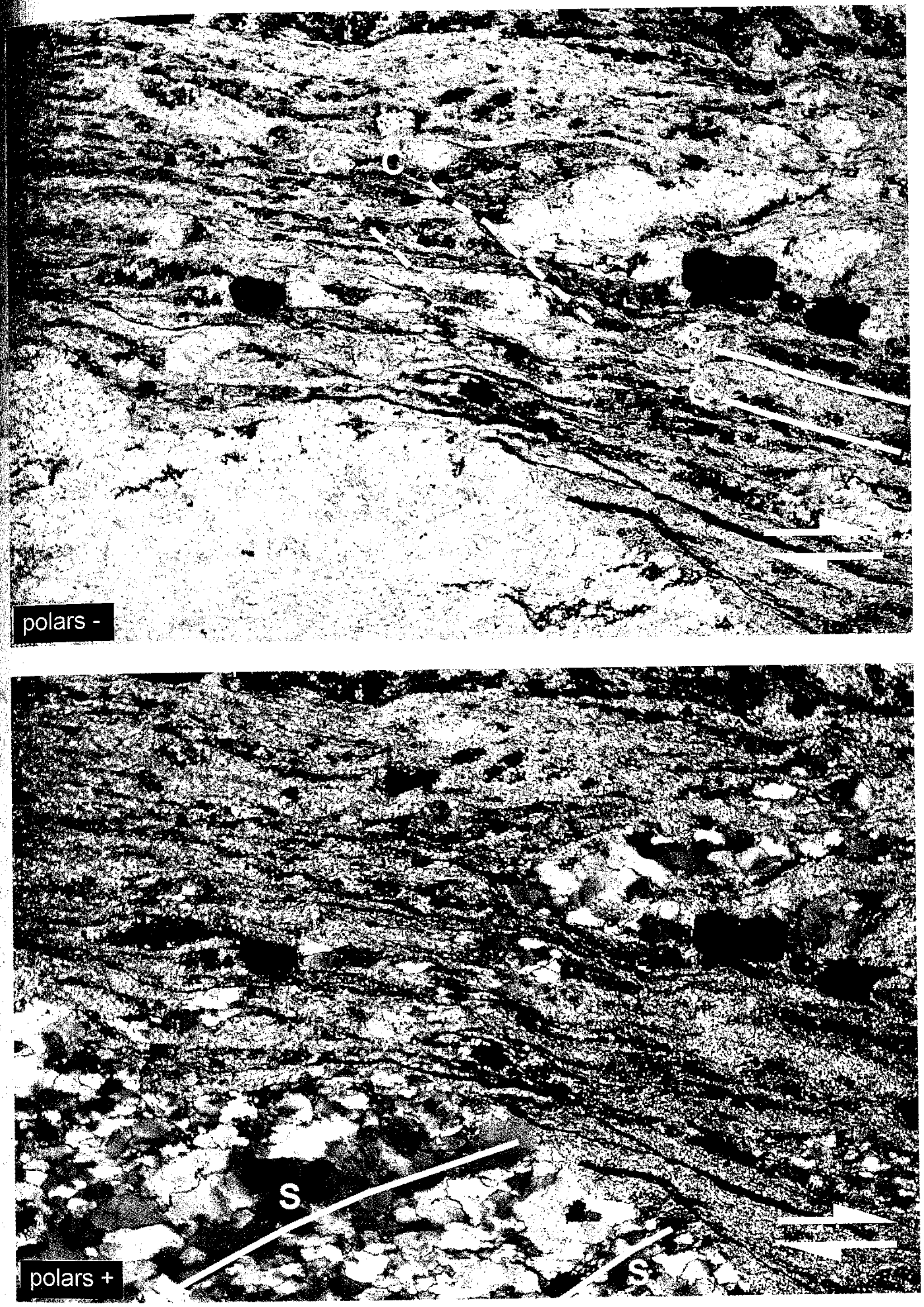

Fig. 5.5. Photomicrographs of mylonite with quartz veinlets, sample 537. Photos depict the same field of view in plane-polarized light (top) and cross-polarized light (bottom). The thin section is parallel to the strike and perpendicular to the dip of the foliation. A combination of a well defined C foliation (compositional banding), distinct S foliation (elongation of quartz grains) and poorly defined C' foliation (barely distinct shear bands) suggests dextral sense of shear.

intensity and distribution of deformation in granitoid intrusions are the proportions of ductile (quartz and micas) versus brittle (feldspars) minerals, and the existence of early formed, inherited tectonic surfaces or foliations. These relations are generally applicable to porphyritic intrusive rocks of the Solton-Sary intrusive belt. Here, the proportion of mica and the percentage of feldspar phenocrysts appear to be the two primary compositional factors controlling deformation styles. The abundance of mica enhances plastic deformation. The mica-rich lamprophyres are therefore the least competent rocks among the Solton-Sary intrusive suite. Similar observations are reported by Perring et al., (1989) for lamprophyres of the Kambalda gold district in western Australia. The increase in feldspar phenocryst content produces an opposite effect. The more phenocryst-rich varieties of syenites tend to respond in a more brittle fashion to imposed strain, resulting in the development of predominantly cataclastic deformation features.

As with cases described by Paterson et al. (1989), the ductile deformation developed preferentially along pre-existing mechanical discontinuities. These were sill contacts. The shearing was most intensive at the contacts that resulted in localization of mylonites along sill margins. The deformation was initially concentrated at the contacts and subsequently advanced into inner portions of the intrusions. The distribution of deformational patterns within individual intrusions is largely dependent on their mechanical properties, which are controlled by rock composition. Lamprophyres show a relatively continuous distribution of strain and thus gradual transitions from strongly foliated to locally unfoliated rocks. In leucocratic syenite porphyries, most of the strain is concentrated within relatively thin discrete mylonite zones at sill contacts, whereas the interiors of the bodies show only weak brittle deformation. Transitions from the contact mylonitic zones to relatively undisturbed cores are either abrupt or marked by cataclastic domains.

The observations on the relationships between the deformation and hydrothermal alteration suggest the syn-kinematic nature of the hydrothermal activity. Although possibilies for additional pre- and post-mineralization deformation cannot be ruled out, the majority of deformation definitely occurred during the mineralization. The spatial coincidence of the maximum hydrothermal alteration, quartz veining, and strong shearing implies that the shear zones located mainly at contacts of competent syenite sills focused fluid flow during the mineralization. Within these zones, progressive alteration diminished rock competency promoting ductile deformation. Conversely, tectonic fracturing and fragmentation of K-feldspar phenocrysts assisted more efficient replacement of this relatively resistant phase by hydrothermal minerals. Occasional brittle fracturing of endocontact portions of syenite sills could have additionally enhanced permeability and fluid focusing.

Metamorphic conditions

Deformation styles provide information on metamorphic conditions. The observed patterns vary from brittle cataclasis to the development of ductile mylonitic fabrics and strongly depend on the protolith composition (particularly, the proportion of coarse feldspar). In all observed cases, coarse K-feldspar exhibits brittle deformation. On the contrary, quartz was deformed predominantly by dynamic recrystallization. Variations in quartz fabrics (i.e. relatively weakly recrystallized to completely recrystallized aggregates with penetrative foliation) may be due to variable timing of vein emplacement and/or strain partitioning. Healed microfractures in quartz could reflect episodes of elevated strain rate.

The combination of generally plastic behavior of quartz and brittle deformation of feldspar is characteristic of greenschist facies conditions, particularly for the zone of the seismic-aseismic transition (e. g., Sibson, 2001; Sibson et al., 1988; Passchier and Trouw, 1996). The most probable temperature conditions for this transition in quartzofeldspathic rocks is 300-450°C (e. g., Scholz, 1988; Passchier and Trouw, 1996).

Displacement modes

The results of the microstructural study suggest the overall predominance of oblique strike-slip shear, the existence of a local coaxial component to the deformation, and, consequently, the likelihood of a syn-mineralization transpressional regime. The number of observations is insufficient to interpret the discrepancy between sinistral and dextral shear modes that were revealed respectively for southern and northern flanks of the intrusive belt. Most likely this is the result of repeated reactivations and contrasting displacements along individual faults. Strike-slip shear was accompanied by variably oriented dip-slip movements. The inconsistency of apparent dip-slip displacements may reflect the diachronism of the latter. Altenatively, it could have resulted from complex strain partitioning during the same (likely protracted) transpressional event (cf. Goodwin and Williams, 1996). As there is no evidence unequivocally supporting the occurrence of multiple discrete tectonic events, the second explanation appears more viable.

The results of the microstructural study of tectonites from the South Kumbel fault differ from the interpretation by Kyrgyzstani and Russian geologists, who interpret it as a thrust or reverse fault emplaced during the North-Median Tien Shan collision (Fig. 2.5; Mikolaichuk et al., 1997, Fig. 5 therein). The difference, however, is not fundamental. The fault may indeed have initiated as a thrust in the Late Ordovician-Silurian, and the strike-slip displacements may have occurred later, perhaps after additional compression and regional folding.

Implications for the morphology of mineralized zones

Deformation styles and sense of shear define the morphology and orientation of mineralized quartz veins and zones of vein silicification. Mapping of the Altyntor open pit at the eastern flank of the district and re-logging the drill core from its central portion show that most of the veins and vein swarms are concordant with foliation, and are generally enveloped by mylonites. At the contacts of competent syenite sills, the concordant veins may be flanked by relatively narrow zones of brittle fracturing and stockwork silicification, or, less commonly, by shallowly dipping extensional veinlets hosted in syenites. The predominantly concordant vein orientation and their close association with mylonites at sill margins are consistent with the observed deformation patterns and with the assumption that most of the strain was probably accommodated by shear zones at sill contacts. Consequently, concordant steeply dipping zones of vein silicification should be considered as the most probable target for future exploration at the flanks of the district.

Summary

The deformation patterns within the intrusive belt of the Solton-Sary district vary from brittle (cataclastic) to ductile (mylonitic). They are controlled primarily by rock composition (percentage of feldspar and mica phenocrysts), by existence of inherited discontinuities (sill contacts) and, to a minor extent, by the intensity of hydrothermal alteration. Hydrothermal activity was syncronous with the deformation. Alteration processes favored development of foliation by replacing mechanically strong phases (feldspar) by relatively weak phases (sericite, carbonate, quartz). Ductile deformation promoted the hydrothermal alteration through grain-size reduction of resistant feldspar phenocrysts. The brittle behavior of feldspar and ductile of quartz suggests that during the hydrothermal activity the system resided at greenschist metamorphic conditions, more specifically at the zone of seismic-aseismic transition, at temperatures between 300° and 450°C. The deformation resulted from predominantly strike-slip tectonism that was probably related to a regional transpressive regime.

CHAPTER 6

FLUID INCLUSION STUDY

Introduction

Eighteen standard doubly-polished 0.3-0.5 mm thick wafers were prepared for the fluid inclusion study. Petrographic examination revealed strong shearing, especially in samples from mineralized zones. Dynamic recrystallization with grain-size reduction made quartz of most samples barely suitable for the study. Overall, fluid inclusions are abundant, but most of them are too small for microthermometric measurements. Sufficiently large inclusions were identified only within relatively small areas of weaker deformation in overall strongly sheared material. In several samples, fluid inclusions were found to be better preserved when hosted in quartz grains and aggregates completely enclosed in pyrite and chalcopyrite. Apparently, sulfides acted as stronger phases during the deformation and partially shielded enclosed gangue material. A total of nine samples, seven from auriferous mineralized zones and two from barren propylitic veins, were selected for microthermometric analyses. For samples with identified native gold, attempts were made to conduct measurements close to gold particles. However, unlike the case described by Robert and Kelly (1987), it was not possible to identify inclusions hosted by exactly the same microfractures as gold grains. Fluid inclusion gas chemistry analysis was conducted on 17 samples. The analysis was intended to a) provide information on volatiles undetectable by microthermometry but essential for understanding ore genesis, and b) help evaluate if the thermometric data derived from subjectively chosen (i. e. the largest) fluid inclusions are representative of the entire fluid inclusion population of a given sample. In the case of strongly sheared quartz of the lion Sary district, this was particularly important because the bulk of trapped volatiles must be confined to very small inclusions that cannot be analyzed by microthermometric methods. For samples with visible gold, gold grains intergrown with vein quartz were selected for bulk trapped volatile analysis.

Analytical techniques

Microthermometric measurements were conducted on a Linkam THMG600 stage. The stage was calibrated at –56.6°C (melting point of CO_2) and 0.0°C (melting point of pure H_2O ice) using synthetic fluid inclusion standards, and at 395°C by melting K_2CrO_4. Analytical procedures followed those described by Shepherd et al. (1985). Thermometric data were reduced using MacFlinCor software (Brown and Hagemann, 1995).

The bulk composition of trapped volatiles was analyzed with Balzers QME 125 quadrupole mass spectrometer. The analysis employed a crush-fast-scan method similar to that described by Moore et al. (2000). Samples (mass 0.2-0.3 g) were placed in a vacuum chamber and gases were extracted in a series of short crushing motions of a threaded steel piston. Each crush generated a burst of volatiles that were pumped into the mass spectrometer and measured in fast scan mode. Measured species included H_2O, CO_2, H_2, He, CH_4, N_2, H_2S, Ar, SO_2, and hydrocarbons (C_{2-7}). Six to 18 crushes were performed on each individual sample; 1 to 3 analyses per sample usually failed due to the system overload.

Results of fluid inclusion microthermometry

Microthermometric data are listed in Appendix C and summarized in Figures 6.2 to 6. Five types of fluid inclusions were identified based on their composition, morphology, thermometric properties, and the host hydrothermal assemblage. Types 1-4 are present in auriferous mineralized zones and type 5 occurs only in propylitic veins.

Type 1 comprises carbonic inclusions that lack a microscopically distinct aqueous phase. These inclusions appear to be the most abundant in the Solton Sary auriferous quartz. Most of the measured carbonic inclusions have sizes of 3-5 μm. They exhibit euhedral subequant (perhaps dipyramidal) or rounded, droplet-like shapes (Fig. 6.1A), a random distribution, and are interpreted as primary. Secondary, fracture-controlled non-aqueous carbonic inclusions are far less abundant and their thermometric properties do not differ from those of primary inclusions. A vast majority of type 1 inclusions exhibits first melting at –56.9° to –56.5°C (Fig. 6.2) indicating their relatively pure CO_2 composition. However, in two samples, 587 and especially in 585, non-aqueous-carbonic inclusions showed a significant depression of $TmCO_2$ (–58.2° to –61.2°C) and typical sluggish meniscus inversion during melting suggesting the probable presence of dissolved CH_4 (Shepherd et al., 1985). Mole fraction of CH_4 (X_{CH_4}) in type 1 inclusions from sample 585 estimated using the diagram from Thiéry et al. (1994; built into the MacFlinCor program) varies from 0.05 to 0.20. Type 1 inclusions homogenize to liquid from ca. –4°C to about +30°C, with most of observed homogenization temperatures clustering at 12° to 22°C and 24° to 30°C (Fig. 6.3). Bulk density ranges from 0.65 to 0.8 g/cm^3 for most measured inclusions.

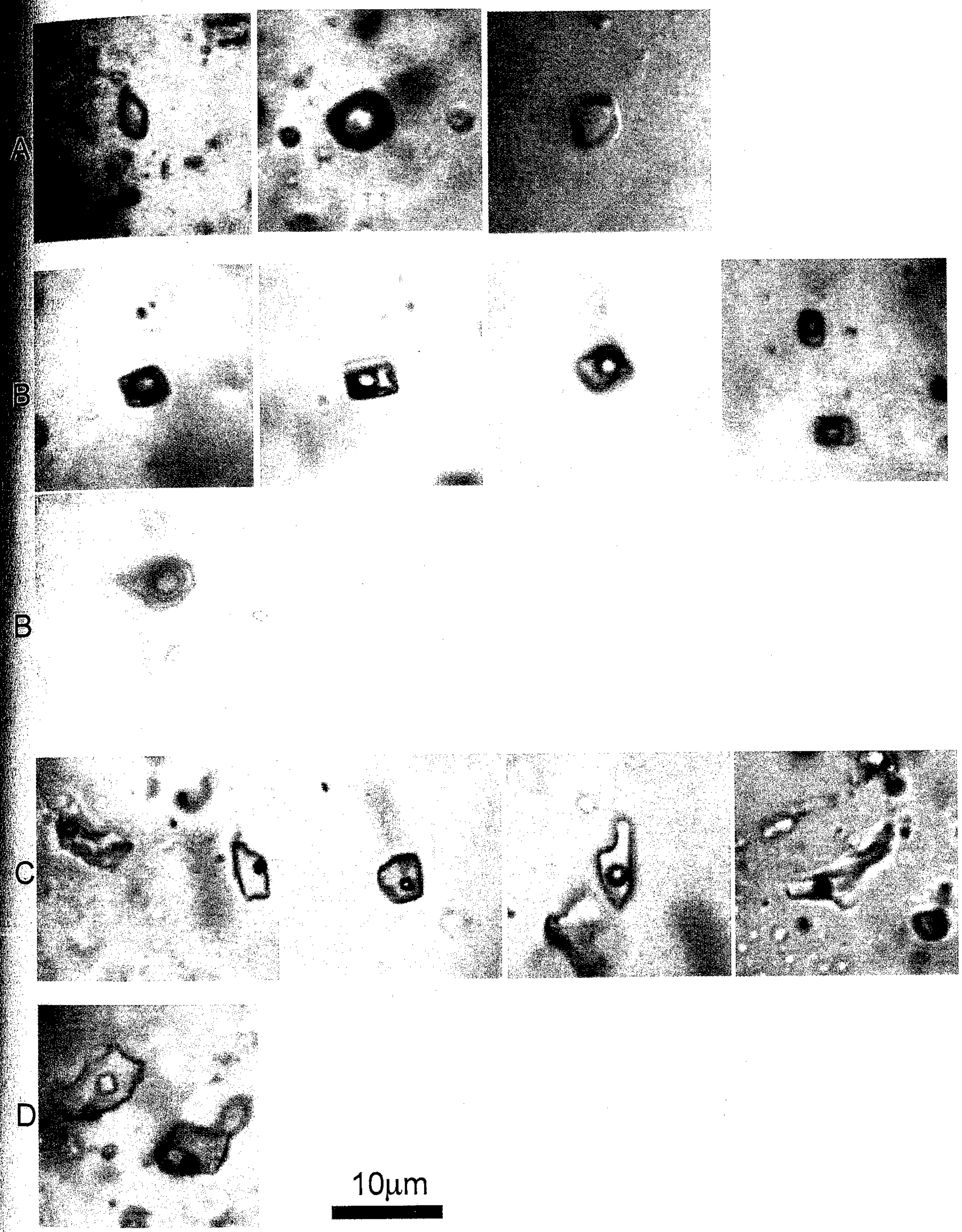

Fig. 6.1. Photomicrographs of fluid inclusions: A, type 1; B, type 2; C, type 3; and D, type 4.

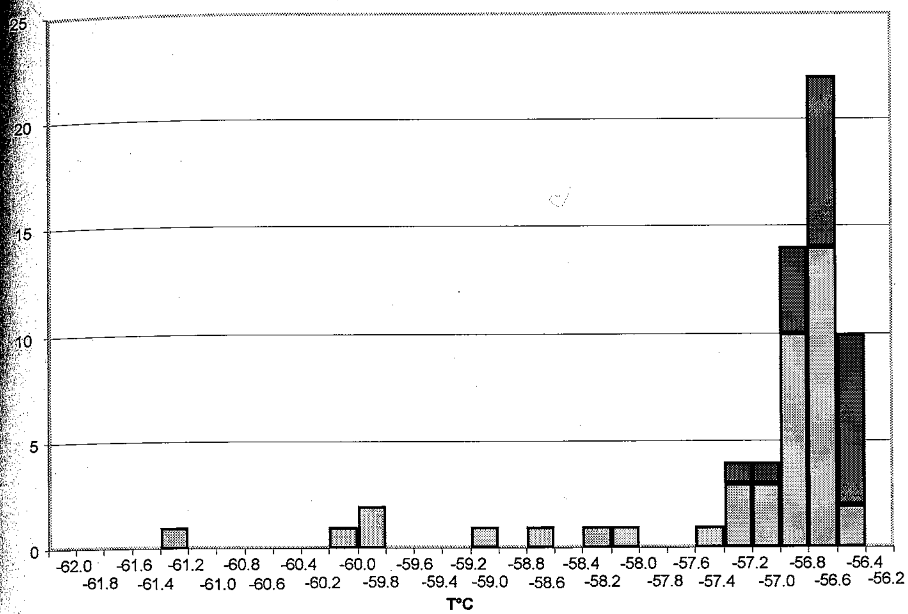

Fig. 6.2. Histogram of melting temperature of the carbonic phase in type 1 (gray) and type 2 (dark gray) inclusions.

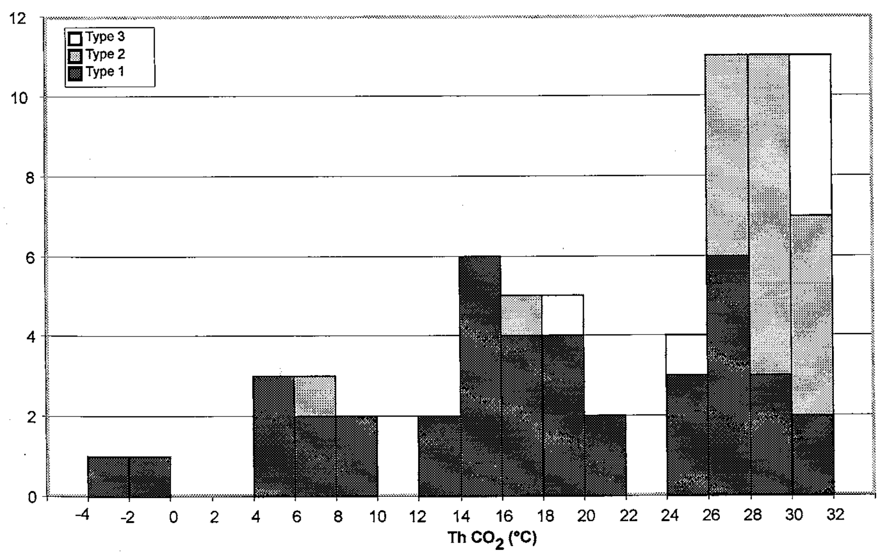

Fig. 6.3. Histogram of homogenization (V-L) temperatures of the carbonic phase

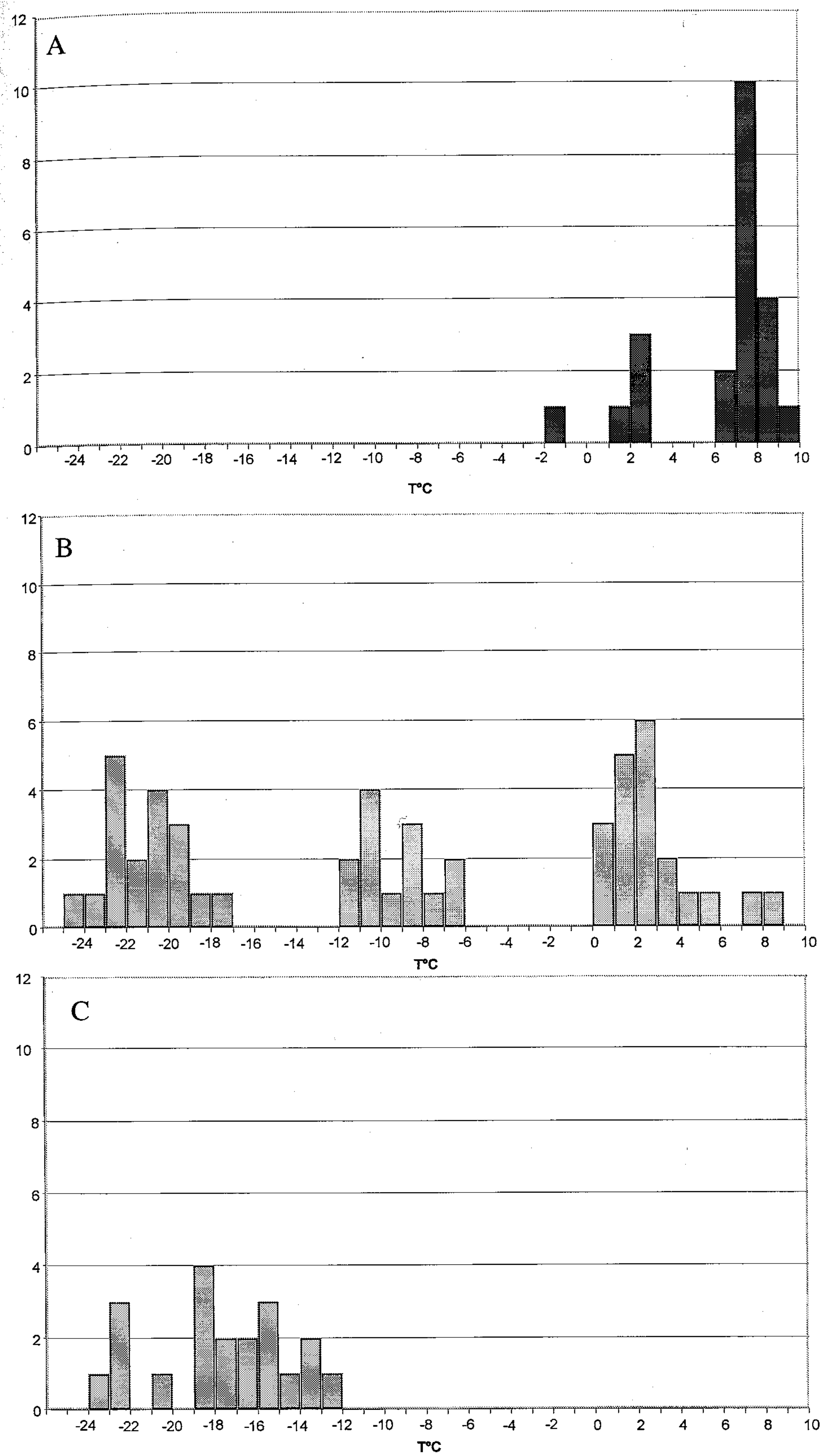

Fig. 6.4. Histograms of melting temperatures: A-clathrate in type 2 inclusions, B-clathrate (gray) and ice (dark gray) in type 3 inclusions, and C-ice in type 5 inclusions.

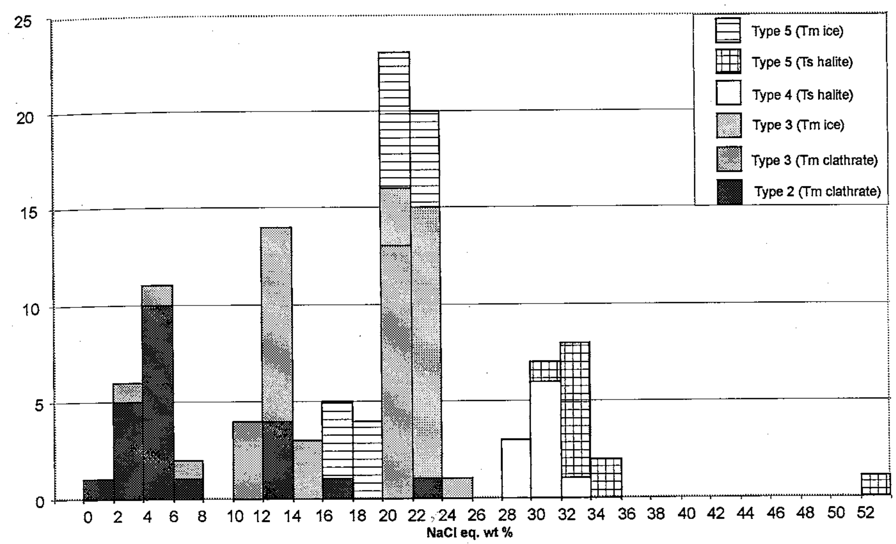

Fig. 6.5. Estimated salinities (the legend depicts measured parameters that were used for salinity estimates).

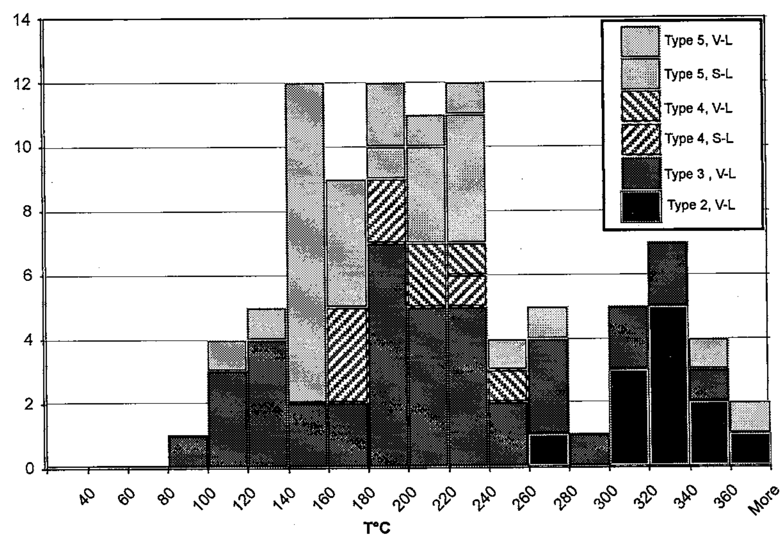

Fig. 6.6. Histogram of total homogenization temperatures for type 2, 3, 4, and 5 inclusions.

Type 2 unites primary aqueous-carbonic fluid inclusions (3-7 μm), most of which are documented in one sample (663-2, n=21), where they are hosted by quartz completely enclosed in chalcopyrite. Another 6 inclusions were identified in sample 587- In other samples, measurable inclusions of this type are virtually absent. Type 2 inclusions are typically euhedral, with rectangular to almost square, sometimes slightly skewed contours (Fig. 6.1, B). In fewer cases, the outlines of the inclusions constitute irregular polygons with sharp corners. Such a geometry could be related to the natural decrepitaion of originally euhedral inclusions (Shepherd et al., 1985) that perhaps was shortly followed by fluid re-trapping and re-sealing. In most of the inclusions, the aqueous phase strongly predominates. Volumetric proportions of the carbonic phase range from 0.20 to 0.32, averaging about 0.25 for most euhedral inclusions. In only two measured inclusions, the carbonic phase clearly exceeds aqueous, possibly due to a partial leakage. The inclusions typically generate a CO_2 bubble at ca. –56.8° to –56.5°C (Fig. 6.2) and form an envelope of liquid CO_2 simultaneously with the clathrate melting at about 7-9°C (sample 663-2), or in fewer cases at 1.9-2.5°C (sample 587-2, Fig. 6.4). The most frequently observed clathrate dissociation temperatures (i.e. ~ 7-9°C, Fig. 6.4A) imply salinities of 1.8 to 6.4 wt percent NaCl equiv (Fig. 6.5). The carbonic phase homogenizes into liquid at ca. 26-30°C (Fig. 6.3). Estimated CO_2 mole fraction values (X_{CO_2}) vary from 0.05 to 0.15, but most commonly are in the 0.07-0.1 range. Temperatures of the total homogenization to aqueous phase span from 269° to 355°C (Fig. 6.6; one inclusion returned 386°C, but partial leakage was suspected). Commonly, the inclusions decrepitate prior to total homogenization. The consistency of volume proportions of the carbonic phase and similarities in the homogenization behavior (no aqueous to carbonic phase homogenization has been observed) implies a homogeneous entrapment of fluids.

Type 3 comprises secondary inclusions (3-10 μm) hosted by healed microcracks. They are generally flat, have irregular outlines and a degree of fill normally exceeding 9 (Fig. 6.1C). Low temperature behavior of the type 3 inclusions is somewhat complex. Melting of the carbonic phase at –60.0° to 56.6°C is not observed. Final melting of ice occurs between –23° and –18°C. After the disappearance of the ice, the vapor bubble usually remains static due to the presence of invisible clathrate. Clathrate dissociation is normally accompanied by steady "back and forth" shifts of the bubble that are followed by its unrestricted random movement. Observed temperatures of clathrate dissociation vary from about –10° to +8°C and average about –1.9°C (Fig. 6.4). Sometimes, the vapor bubble is invisible at low temperatures and suddenly appears ("pops out") during ice or clathrate melting (-22° to -3°C). Several inclusions did not show any evidence of clathration. An envelope of liquid CO_2 surrounding the vapor bubble has been positively identified in six inclusions. Apart from few outliers, most salinity estimates (based on ice and clathrate melting) fall into a broad range from ca. 10 to 24 wt percent NaCl equiv (Fig. 6.5). Observed ice melting temperatures below the H_2O-NaCl eutectic point (-20.8°C) indicates the presence of cations other than Na^+, probably Ca^{2+} (Shepherd et al., 1985). Total homogenization to liquid occurs from 97° to 350°C with most values clustering between 160° and 240°C (Fig. 6.6). Partial leakage during heating experiments was observed in several cases.

Type 4 fluid inclusions are morphologically indistinguishable from the type 3 and commonly occur within the same fracture trails. The main compositional difference is the presence of a daughter halite crystal (Fig 6.1D) that is either present at room temperature or is generated by freezing and re-melting. Halite dissolution temperatures vary from 155° to 222°C, indicating salinities of 29 to 33 wt percent NaCl equiv (Fig. 6.5). Vapor to liquid homogenization often occurs prior to the halite dissolution. Secondary aqueous inclusions of types 3 and 4 are probably closely related and belong to the same population. This population is characterized by variable salinities that are typically higher than those of type 2 inclusions. The amount of carbonic phase present in type 3 and 4 inclusions must be also variable, since some of the inclusions show melting of ice and no clathration, others generate clathrate, and few contain a visible liquid carbonic phase. This inconsistency in compositions and homogenization temperatures implies a high probability of heterogeneous trapping (Diamond, 2001; Van den Kerkhof and Hein, 2001).

Fluid inclusions of type 5 occur in quartz and carbonate of barren propylitic veins. These are secondary flat anhedral inclusions 3-15 mm long hosted in healed fractures. The degree of fill normally exceeds 0.9, with no detectable carbonic component. Some inclusions lack a vapor bubble at room temperatures and it appears only after freezing and re-melting. Some of the type 5 inclusions (sample TR223) contain daughter halite crystals that dissolve mostly at 200-250°C (Fig. 6.6). Vapor homogenizes to liquid prior to the halite dissolution, at 94-193°C. Inclusions without daughter halite show ice melting at –23° to –12°C (Fig. 6.4) and homogenization to liquid at 105° to 240°C (Fig. 6.6). Salinities estimated from ice melting and halite dissolution cluster at 16 to 24 and 30 to 36 wt percent NaCl equiv, respectively (Fig. 6.5).

Results of trapped volatile analysis

Representative results of bulk analyses of trapped volatiles are presented in Table 6.1, and a complete listing of analytical data is placed in Appendix C. Overall, the results are compatible with the microthermometric data. In mineralized quartz, trapped volatiles are strongly dominated by CO_2 and H_2O. The cumulative mole percentage of the two species normally exceeds 95, and their relative proportions show broad variations, both for individual samples and the entire population (Fig. 6.7). The CO_2 concentrations vary from 2 to 65 mole percent and tend to cluster between 15 and 35 mole percent. Three other relatively abundant species include CH_4, N_2 and Ar. The N_2/Ar ratio in virtually all cases exceeds 100 and the CO_2/CH_4 ratio is normally higher than 4 (Fig. 6.8). According to Norman and Moore (1999) and Moore et al. (2000), such values are characteristic of fluids of deep crustal or magmatic origin, and are atypical for meteoric waters. H_2S percentages are generally low and are below detection for about half of the analyses. Where H_2S is detected, measured values range from $1*10^{-5}$ to $9*10^{-4}$ mole percent. In contrast, SO_2 is detected in virtually all crush analyses. The measured contents are generally higher (ca. $5*10^{-4}$ to $2.5*10^{-3}$ mol %). Combined SO_2 and H_2S values (cf. Landis and Hofstra, 1991) show a distribution that is similar to SO_2 (Fig. 6.9). High concentrations of CO_2 and strong variability of the CO_2/H_2O ratio are consistent with the presence of multiple populations of fluid inclusions that differ mainly by CO_2/H_2O proportions. Based on microscopic observations of the relative abundance of fluid inclusions, carbonic inclusions (type 1) and secondary aqueous inclusions (types 3 and 4) are likely to be the main contributors of the bulk compositional balance of trapped

Table 6.1. Representative quadrupole mass spectrometer analyses of trapped volatiles

Sample	mineral	Crush	Counts	H_2	He	CH_4	H_2O	N_2	O_2	H_2S	Ar	CnHm	CO_2	SO_2	Total-H_2O	CO_2/CH_4	N_2/Ar
									Auriferous								
57-11.3	quartz	6520B	402253.9	0.07	0.001742	0.11	82.18	0.57	0.00	0.000000	0.002624	0.05	17.01	0.00070	17.82	150.60	218.30
57-11.3	quartz	6520J	198771.2	0.23	0.003849	1.79	69.20	1.04	0.00	0.000148	0.004276	0.13	27.60	0.00130	30.80	15.41	242.57
579	quartz	6505D	23285.3	3.40	0.010628	1.21	49.40	1.16	0.00	0.000315	0.002491	0.04	44.78	0.00000	50.60	37.07	464.55
579	quartz	6505E	30732.47	2.44	0.006020	1.33	62.56	1.18	0.00	0.000105	0.003813	0.04	32.44	0.00123	37.44	24.46	310.66
579	quartz	6505F	67703.29	1.01	0.006969	0.97	64.58	1.16	0.00	0.000000	0.005890	0.08	32.19	0.00126	35.42	33.19	196.29
585	quartz	6506A	9825.142	4.40	0.000525	2.57	80.11	1.79	0.00	0.000000	0.002981	0.00	11.12	0.00183	19.89	4.33	600.80
585	quartz	6506E	59247.02	0.75	0.003280	2.82	82.43	1.67	0.00	0.000000	0.002214	0.05	12.27	0.00042	17.57	4.35	756.49
585	quartz	6506G	16562.34	2.48	0.002097	3.80	76.79	2.31	0.00	0.000150	0.000548	0.08	14.53	0.00000	23.21	3.83	4226.52
587-2	quartz	6507B	34612.54	1.49	0.017376	1.77	59.92	3.54	0.02	0.000000	0.008783	0.24	32.99	0.00245	40.08	18.65	402.82
587-2	quartz	6507D	56332.19	0.61	0.007331	0.67	47.71	0.69	0.00	0.000093	0.003539	0.14	50.16	0.00166	52.29	74.92	195.07
59-70.8	quartz	6522B	59076.93	0.47	0.001975	0.59	75.44	0.21	0.00	0.000000	0.001699	0.04	23.24	0.00103	24.56	39.38	122.86
59-70.8	quartz	6522F	46086.06	0.29	0.002408	0.22	66.38	0.54	0.02	0.000000	0.005310	0.09	32.46	0.00124	33.62	148.51	101.15
59-89.1	quartz	6523B	45349.35	0.20	0.004237	0.17	85.48	0.04	0.00	0.000000	0.000489	0.04	14.08	0.00019	14.52	85.03	82.97
59-89.1	quartz	6523F	8253.264	0.36	0.000024	0.14	81.39	0.13	0.00	0.000277	0.000000	0.04	17.94	0.00079	18.61	132.43	-
61-72.15	quartz	6517A	10980.49	0.59	0.000401	0.28	80.11	0.71	0.00	0.000218	0.004084	0.05	18.26	0.00107	19.89	65.89	173.11
61-72.15	quartz	6517E	77856.69	0.14	0.004114	0.17	57.47	0.36	0.00	0.000000	0.001117	0.11	41.73	0.00161	42.53	241.05	318.56
60-152.5	quartz	6524A	4772.42	0.64	0.000000	0.42	72.16	1.12	0.00	0.000000	0.001578	0.06	25.60	0.00147	27.84	61.61	710.83
60-152.5	quartz	6524B	47112.09	0.27	0.001854	0.83	69.48	1.82	0.05	0.000000	0.005740	0.10	27.45	0.00119	30.52	33.26	317.00
61-199.6	quartz	6521H	65856.92	0.24	0.006453	1.09	40.83	0.17	0.00	0.000293	0.001745	0.18	57.49	0.00251	59.17	52.88	96.98
Altyntor	quartz	6465C	227454.7	0.06	0.001531	0.29	87.25	0.32	0.01	0.000015	0.001898	0.04	12.03	0.00055	12.75	41.89	169.41
Altyntor	quartz	6465D	216533	0.06	0.001729	0.36	82.84	0.34	0.01	0.000000	0.002236	0.05	16.33	0.00073	17.16	44.74	153.96
Altyntor	quartz	6465E	365903.5	0.05	0.001527	0.34	85.10	0.35	0.01	0.000000	0.001949	0.04	14.12	0.00069	14.90	41.34	179.23
									Barren								
669-2	Quartz	6519I	214806.1	0.11	0.000000	0.06	95.69	1.21	0.02	0.000000	0.002879	0.01	2.89	0.00011	4.31	46.39	420.81
669-2	Quartz	6519L	82351.73	0.18	0.000000	0.36	95.61	1.29	0.02	0.000000	0.003753	0.02	2.51	0.00000	4.39	6.89	342.97
TR 6-2	Quartz	6516F	37045.52	0.30	0.000000	0.11	96.80	1.27	0.01	0.000043	0.002362	0.01	1.49	0.00023	3.20	13.28	537.92
TR 6-2	Quartz	6516G	30264.68	0.38	0.000000	0.16	97.07	1.00	0.00	0.000187	0.001390	0.01	1.38	0.00000	2.93	8.77	720.47
TR223	Quartz	6518	10217.08	0.53	0.003621	0.70	96.61	1.40	0.00	0.000625	0.003190	0.06	0.69	0.00036	3.39	0.98	438.35
TR223	Quartz	6518F	34778.89	0.38	0.003551	1.38	95.28	1.83	0.01	0.000000	0.003991	0.10	1.01	0.00000	4.72	0.73	459.74
659	Quartz	6319l	1493988	0.00	0.036380	0.34	96.03	1.58	0.00	0.000000	0.002435	0.00	2.00	0.00005	3.98	5.87	650.66
659	Quartz	6319m	3063698	0.00	0.013738	0.24	97.21	0.94	0.00	0.000015	0.001189	0.00	1.59	0.00008	2.79	6.70	792.10
TR223-s	Quartz	6320b	1549477	0.00	0.030666	0.04	99.54	0.19	0.00	0.000000	0.000549	0.00	0.19	0.00002	0.46	4.60	351.12
TR223-s	K-spar	6321a	199098	0.00	0.226225	0.11	98.55	0.76	0.05	0.000064	0.005307	0.00	0.28	0.00005	1.45	2.50	143.67

For samples 579, 585, and Altyntor: analyzed material comprized quartz intergrown with native gold

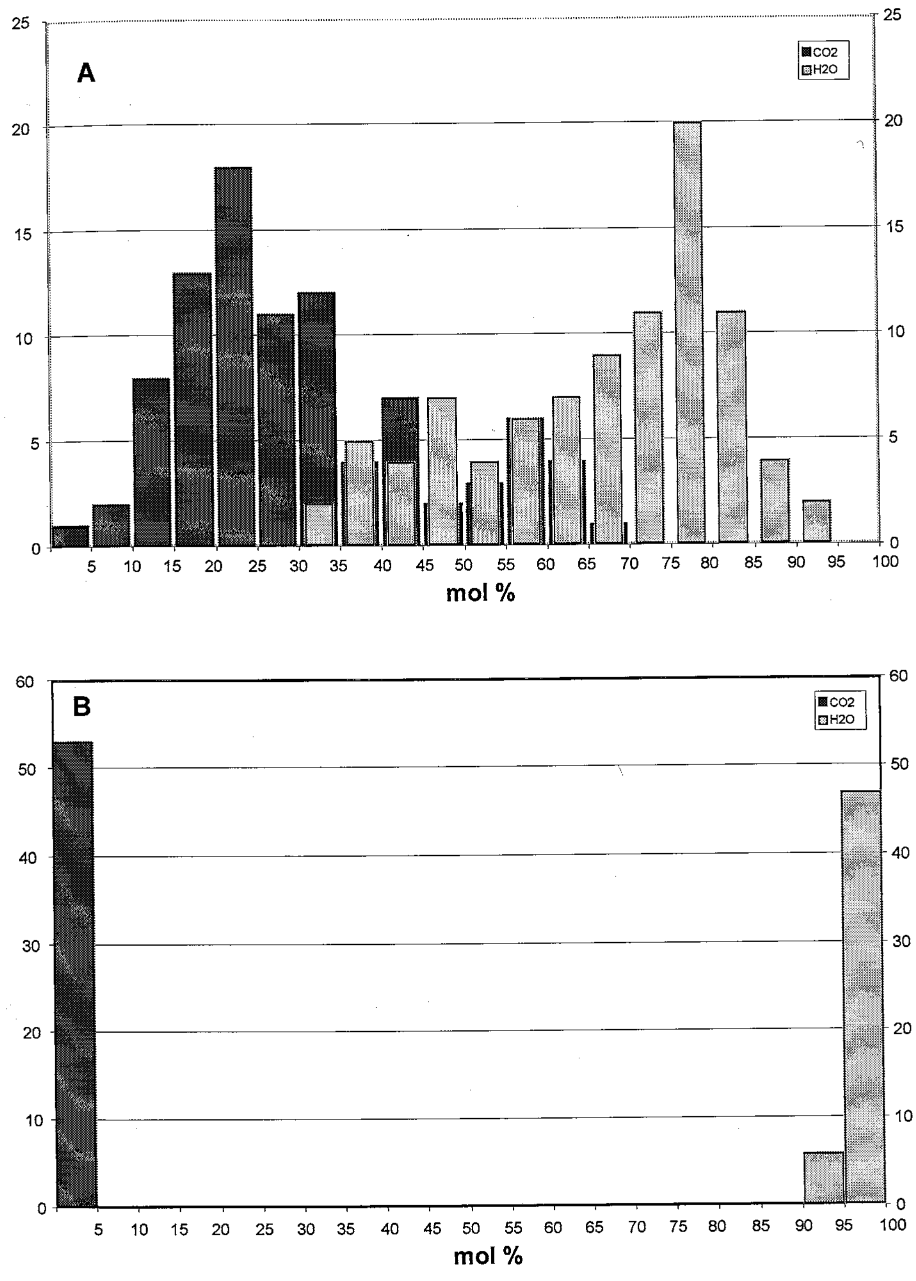

Fig. 6.7. Distribution of mole percentages of H_2O (gray) in CO_2 (dark gray) produced by quadrupole mass spectrometer analysis of mineralized (A) and barren (B) quartz samples.

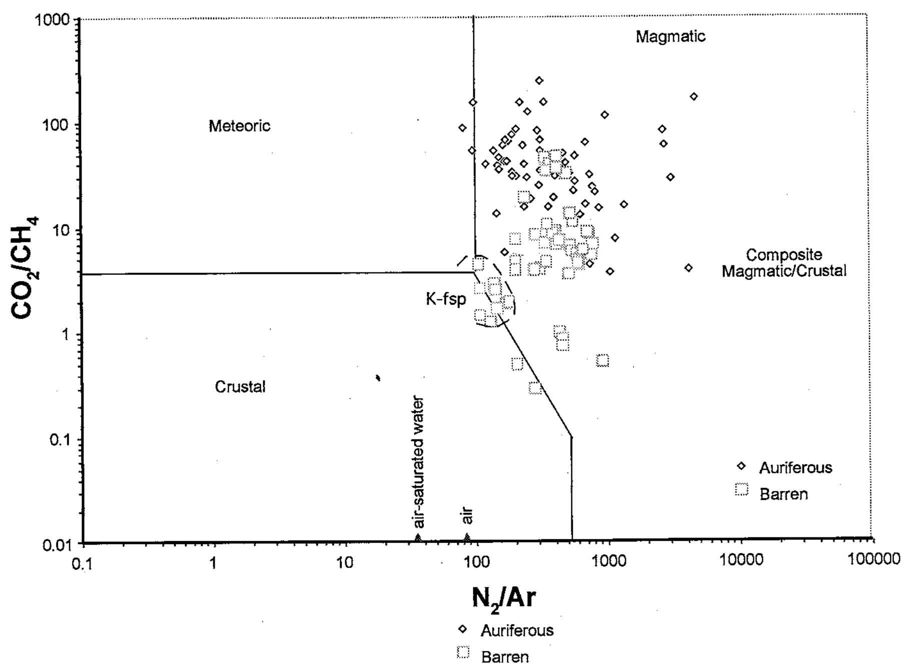

Fig. 6.8. Relationship between CO_2/CH_4 and N_2/Ar ratios in volatiles trapped in auriferous and barren quartz veins of the Solton Sary district. All analyses are of quartz, except for K-feldspar TR223-S (marked K-fsp). Field boundaries and N_2/Ar values for air and air-saturated water are after Norman and Moore (1999) and Moore et al. (2000).

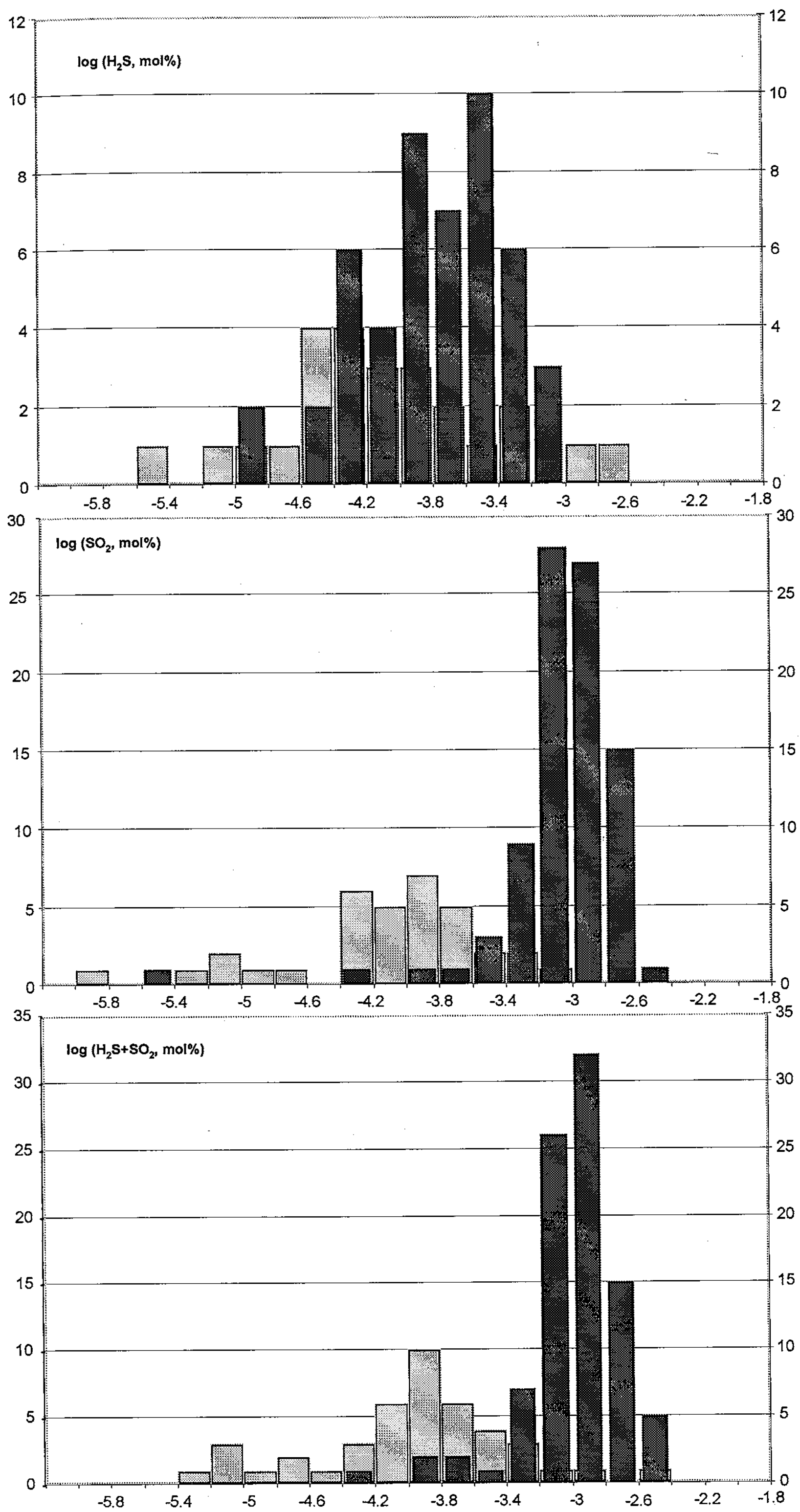

Fig. 6.9. Sulfur-bearing species in auriferous (dark gray) and barren (gray) veins of the Solton Sary district. All histograms show log values.

volatiles. Primary aqueous-carbonic inclusions (type 2) appear relatively sparse during the microscopic studies. However, smaller, microscopically unidentifiable, inclusions of this type may be present in much higher abundance and, consequently, influence the bulk quadrupole mass spectrometer results. No significant difference has been noticed between the results produced by quartz intergrown with gold and quartz without visible gold mineralization. Thus, in spite of the fact that gold is commonly hosted by discordant microfractures, there is no evidence for the preservation of any special "auriferous" fluids that are compositionally distinct from fluids trapped by the bulk of the quartz in mineralized zones.

Unmineralized samples represent a) propylitic veins (TR223, TR6-2, also characterized by microthermometric measurements), b) a barren K-feldspar-quartz vein hosted by unaltered syenite-porphyry (TR223-s), c) quartz vein in the hanging wall of the South Kumbel fault (669-2), and d) barren quartz vein hosted in Middle Ordovician tuffs (tO_2) stratigraphically above the mineralized trend (659). All samples return consistently high H_2O concentrations, typically exceeding 95 mole percent (Fig. 6.7). Unlike quartz from mineralized zones, where the gas assemblage is overwhelmingly dominated by CO_2, in barren veins, concentrations of CO_2, N_2 and CH_4 are somewhat comparable (Fig. 6.10), although CH_4 contents tend to be lower (CO_2: ~ 0.15-4, average 1.5 mol %; N_2 ~ 0.15-3, average 1.19 mol %; and CH_4 ~ 0.02-3.6, average 0.36 mol %). The highest CO_2 contents, reaching 2-4 mole percent, are produced by quartz from barren veins hosted in the South Kumbel faults zone and in Middle Ordovician tuffs (samples 669-2 and 659). The CO_2 values of propylitic veins are slightly lower. Contents of sulfuric species, especially SO_2 as well as combined H_2S and SO_2 tend to be lower than corresponding

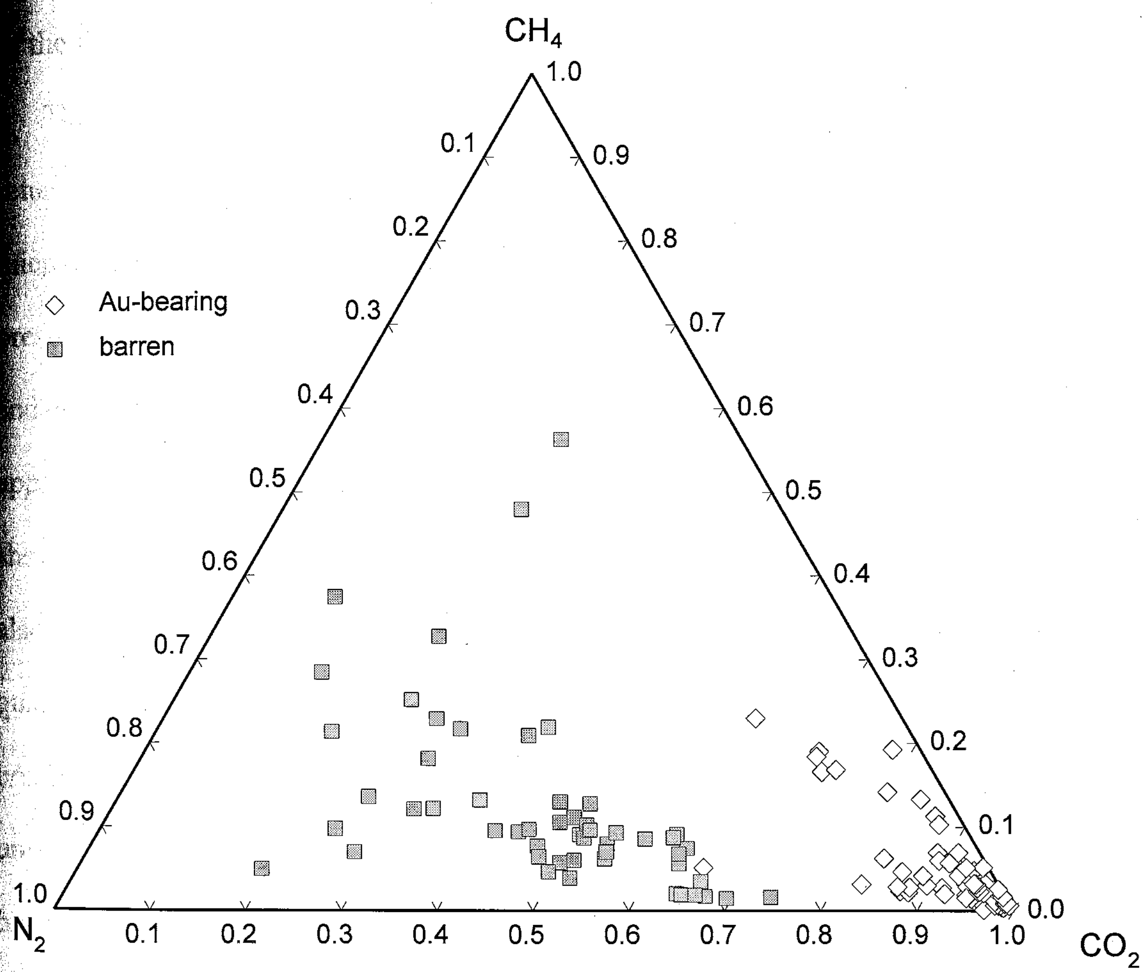

Fig. 6.10. Ternary plot depicting major non-aqueous volatile species. In auriferous quartz, they are strongly dominated by CO_2, in barren quartz three species are present in comparable amounts.

values of mineralized quartz (Fig. 6.9). The N_2/Ar ratios of barren quartz are virtually indistinguishable from those of mineralized material. K-feldspar TR223-s has a somewhat higher Ar concentration compared to other samples, probably because of in-situ build-up of radiogenic ^{40}Ar. The CO_2/CH_4 ratios of some barren quartz samples tend to be lower than corresponding values of auriferous quartz, primarily due to lower CO_2 content. The N_2/Ar versus CO_2/CH_4 plot (Fig. 6.8) implies a deep, non-meteoric origin of the fluids trapped in barren veins.

The consistency of H_2O values and of relative proportions of major volatile species returned by quartz from propylitic veins (TR223, TR6-2) confirms the validity of microscopic observations that identified type 5 as the only population of fluid inclusions present in the propylitic quartz. The occurrence of some microscopically undetectable and compositionally different fluid inclusions appears unlikely, otherwise it would be apparent from the gas analyses. Since the microscopically uncharacterized samples also show consistent concentrations of major volatiles, the trapped fluids in these samples are also likely to have uniform compositions. In contrast with analyses of the mineralized quartz that represent, in a strict sense, a mixture of compositionally differing fluids, fast-crush-scan data obtained from the unmineralized quartz characterizes a single, rather uniform fluid. Overall, major differences between fluids trapped in mineralized and barren quartz include higher CO_2 content with broad variations of relative proportions of H_2O and CO_2, and generally higher H_2S+SO_2 mole percent (Fig 6.11).

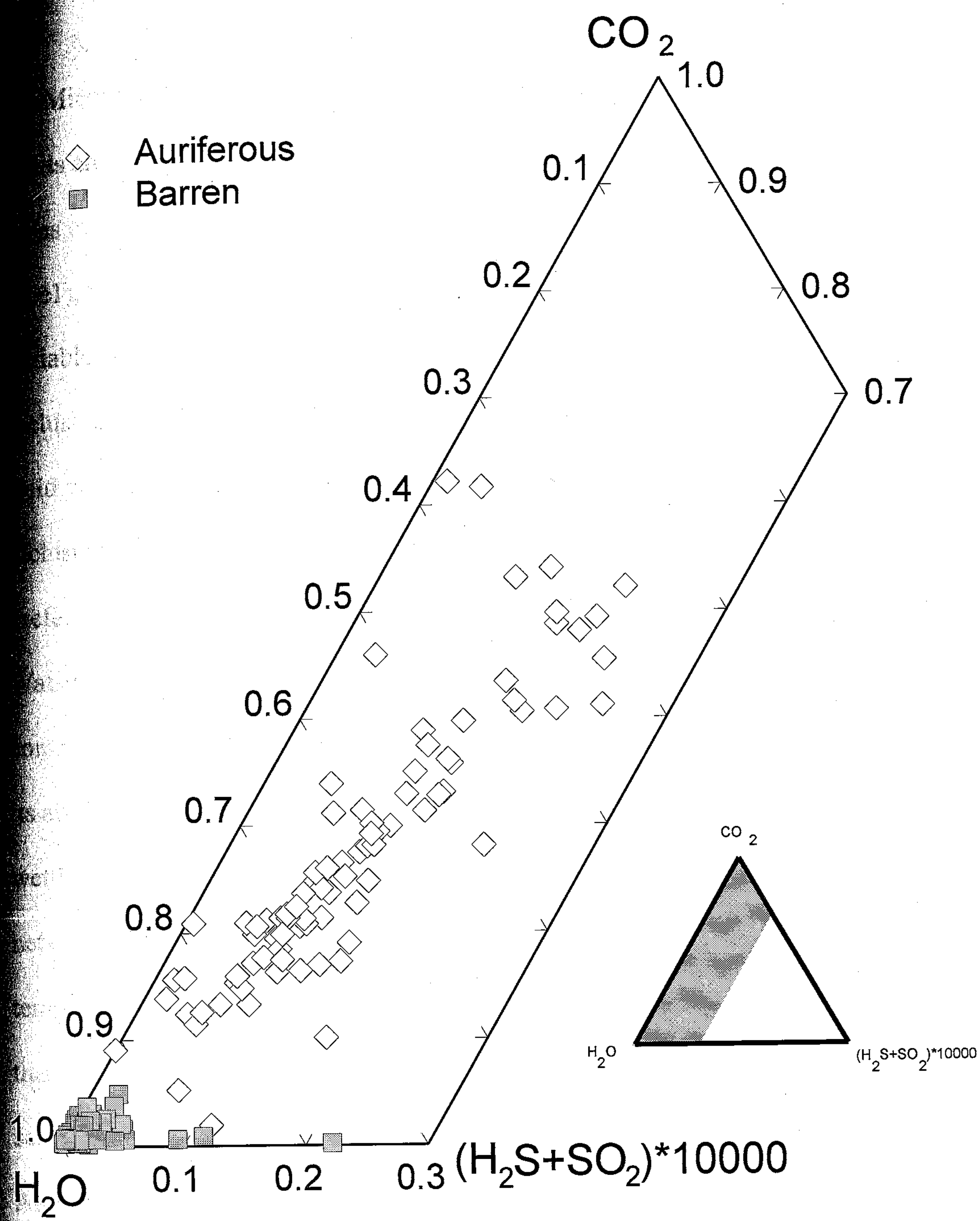

Fig. 6.11. H_2O-CO_2-(H_2S+SO_2)*10000 ternary plot emphasizing diagnostic bulk chemical signatures of fluids trapped in auriferous and barren veins. Fluids from auriferous veins are enriched in CO_2, show broad variations of H_2O-CO_2 proportions and generally have a higher content of sulfuric species.

Relative timing and relationships between fluid types

Microthermometric data and the results of gas analyses indicate that four types of fluids are present in quartz veins of the Solton Sary district. In auriferous quartz, three types of fluids are preserved. These include the non-aqueous carbonic fluid (inclusions of type 1), the low saline aqueous-carbonic fluid (type 2), and the saline aqueous fluid with variable contents of the carbonic component (types 3 and 4). Primary euhedral fluid inclusions of type 1 and 2 probably originated from a parent low saline aqueous-carbonic fluid through phase separation processes. The predominance of carbonic (type 1) fluid inclusions over sparse aqueous-carbonic (type 2) inclusions is probably due to preferential trapping of carbonic phase after fluid unmixing (cf. Xu and Pollard, 1999). Watson and Brenan (1987) show that such selective entrapment can be explained by contrasting wetting properties of H_2O and CO_2. The wetting angle >60° of CO_2 inhibits its ability to migrate, and makes it to stay in isolated pore spaces, whereas H_2O has wetting angle <60°, tends to wet grain edges, and is more likely to form interconnected networks and escape (Watson and Brenan, 1987). Although estimated pressures and temperatures of the Solton Sary mineralization (see next section) are significantly lower than 10 kbar and 950-1150°C (experimental settings of Watson and Brenan, 1987), this selective entrapment mechanism appears generally applicable to the Solton Sary system. An alternative explanation for the predominance of carbonic inclusions implies poor preservation of type 2 inclusions during deformation. At present, there is no evidence to confirm or disapprove this possibility.

Types 3 and 4 inclusions are hosted in crosscutting fractures and thus must have generally postdated the randomly distributed euhedral primary carbonic and aqueous-carbonic inclusions of types 1 and 2. However, the fact that many of the type 3 or 4 inclusions still contain a microscopically detectable carbonic phase suggests that saline aqueous fluids partially overlapped in time with carbonic-rich fluids during the late stages of hydrothermal activity. Aqueous brines could represent a product of multiple phase separation events and thus be ultimately related to parent low-saline, carbonic rich-fluids (e.g., Robert and Kelly, 1987). Alternatively, they could have resulted from an infiltration of a separate saline and non-carbonic aqueous fluid. In this case, the presence of the carbonic phase in fluid inclusions could reflect mixing (possibly largely mechanical) with carbonic-rich fluids that were still present in the system. A heterogeneous entrapment could explain the observed compositional variability of type 3 and 4 fluid inclusions. Overall, the fluid inclusion data show that carbonic-rich fluids were predominant early in the evolution of the hydrothermal system, and saline aqueous fluids prevailed during later stages of the hydrothermal activity. There was apparently no significant time gap between periods of dominance of two fluid types.

A compositionally distinct low-carbonic brine is found in propylitic veins where it represents the only trapped fluid. The assemblage of non-aqueous volatiles of this brine is generally similar to those of fluids trapped in barren syn-metamorphic veins outside the mineralized trend. No gold or gold-bearing sulfides have been found in propylitic veins, and thus the low-carbonic saline aqueous fluids (type 5) cannot be directly related to the gold mineralization.

Pressure-temperature estimates

To constrain P-T conditions of the mineralization and to further clarify relationships between aqueous-carbonic and carbonic fluids, isochore modeling was performed on fluid inclusions of type 1 and 2. These populations have the best-documented and rather consistent thermometric properties that permit the reliable identification of major molecular components of contained fluids. In addition, volume proportions of the carbonic phase in type 2 inclusions can be estimated with reasonably good precision due to their relatively simple euhedral geometric shapes. Total homogenization temperatures of type 2 inclusions provide a minimum constraint for trapping temperatures, and no independent geothermometric data are available. However, according to the most recent overviews (e. g. Hagemann and Cassidy, 2000; Bierlein and Crowe 2000; Ridley and Diamond, 2000; Partington and Williams 2000) temperatures higher than 350°C are relatively uncommon for this type of mineralization. Consequently, the highest homogenization temperatures of type 2 inclusions (ca. 350°C) likely represent a reasonably good approximation of the trapping temperature. Isochores calculated in MacFlinCor using the method of Kerrick and Jacobs (1981) are shown in Fig. 6.12A. Measured total homogenization temperatures (275-355°C) of type 2 inclusions correspond to pressures of 2.5-3.5 kbar. Pressure estimated for ca. 350°C ranges from 3 to 3.5 kbar. Assuming that the fluid pressure approximates lithostatic values, this translates to a depth of 10-11.5 km (lithostatic conditions, pressure gradient 33 m/MPa or 3.3 km/kbar, cf. Brown and Hagemann, 1995). Isochores of type 1 inclusions show a significant vertical spread. Pressures estimated for the temperature range of 300-

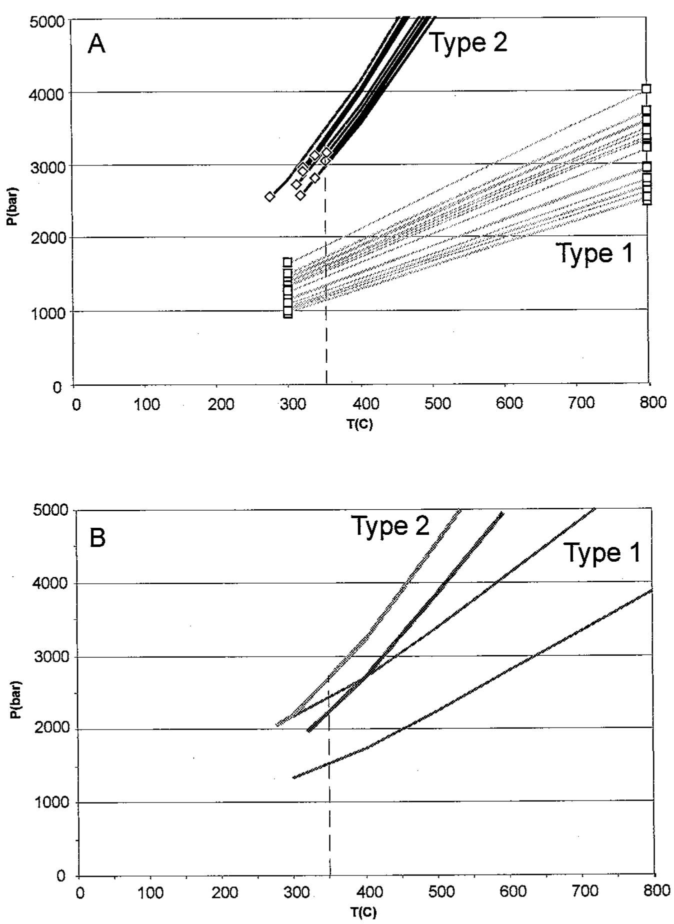

Fig. 6.12. (A) Isochore plot for type 1 and type 2 fluid inclusions from sample 664-1, and (B) a plot assessing consequences of possible systematic errors such as underestimation of the volume of the carbonic phase in type 2 inclusions by 10 percent and underestimation of bulk density of type 1 inclusions due to a presence of 20 volume percent of unidentified aqueous phase. Vertical dashed lines correspond to the presumed trapping temperature. See text for additional explanations.

350°C tend to cluster within the1-1.7 kbar interval, i.e. significantly lower than those of type 2 inclusions.

Prior to proceeding to the geologic interpretation of the P-T model, it has to be assessed for potential inaccuracies. For aqueous-carbonic inclusions, the largest errors in isochore calculations originate from estimated volumetric proportions of carbonic and vapor phases (e. g., Brown and Hagemann, 1995). For each type 2 inclusion used for the isochore modeling, a total volume and a volume of contained carbonic phase were modeled as a cylinder and a rotation ellipsoid, respectively, with radii and altitudes derived from photomicrographs. A simple visual comparison of the calculation results with charts in Shepherd et al. (1985) shows that the overestimation of proportions of the carbonic phase is unlikely, but some underestimation is possible. To evaluate the worst potential effect of such an underestimation, the uppermost and the lowermost lines of the isochore swarm were recalculated with the volume of carbonic phase increased by 10 percent (a larger underestimation appears highly improbable). The addition of 10 volume percent to the carbonic phase causes a ~ 0.75 kbar decrease in pressure values resulting in values of ca. 2.25-2.75 kbar for temperatures of about 350°C (Fig. 12B). This pressure range corresponds to a depth of ca. 7.5-9 km if the fluid pressure is assumed to approximate the lithostatic load. As for the type 1 inclusions, the greatest error can originate from underestimating the bulk density due to the presence of a microscopically unidentifiable aqueous film wetting the walls of fluid inclusions. The volume fraction of this "cryptic" aqueous fluid is unlikely to exceed 20 percent because it would become visible if the volume was greater. A recalculation assuming the presence of 20 percent aqueous fluid with salinities similar to those of type 2 inclusions raises estimated pressures for about 0.5 kbar. For 350°C, the recalculated pressures range from ca. 1.5 to 2.5 kbar (Fig. 12, B). As is evident from Figure 6.12, the most pessimistic assessment of potential systematic errors reduces but does not eliminate completely differences in estimated trapping pressures between the type 1 and type 2 fluid inclusions.

The apparent pressure gap probably reflects real fluctuations of the trapping pressure and implies that (assuming no post-entrapment modification) coexisting aqueous-carbonic (type 2) and pure carbonic (type 1) inclusions are unlikely to represent end-members of a simple one-step phase separation event. In the case of the latter, the isochores of type 1 and type 2 inclusions must intersect at temperatures equal to or exceeding the total homogenization temperature of type 2 inclusions. The pattern produced by the Solton Sary fluid inclusions is almost identical to the one reported for reverse fault-hosted veins of the mesothermal Val d'Or district (Robert et al., 1995, Figure 11 therein). Sibson et al. (1988), Boullier and Robert (1992) and Robert et al. (1995) explain fluctuations of the trapping pressure by a cyclic fault-valve model. The model implies generally lithostatic conditions, with the fluid pressure building up within a fault conduit under an impermeable seal. When the fluid pressure exceeds the ambient lithostatic pressure the fault will fail. The seismogenic fault failure causes an abrupt pressure drop that promotes the separation of the carbonic phase and deposition of carbonate and quartz. Precipitating minerals seal fluid pathways, and the pressure starts to increase again. Wilkinson and Johnston (1996) and Cole et al. (2000) apply similar models to strike-slip-dominated systems. The association of carbonic and aqueous-carbonic fluid inclusions (types 1 and 2) in the mineralized quartz of the Solton Sary district probably represents a fragmental record of the fault-valve mechanism. Under the fault-valve model, type 2 inclusions of the Solton Sary district are likely to have been trapped under "background", near-lithostatic conditions. Type 1 inclusions contain gases that are interpreted to have been separated and trapped during pressure drops related to fault failures. Since pressure drops can differ in amplitude, the same batch of CO_2-rich but predominantly aqueous fluid can undergo several stages of unmixing of the carbonic phase. Not surpisingly, it is not always possible to identify and correlate the end members of each separation event. The fault-valve model fits well with the geology of the Solton Sary district, where most of gold-bearing veins are either hosted by or associated with shear zones, and syn-mineralization, predominantly strike-slip tectonism is documented. Assuming that apparent trapping pressures of type 2 inclusions approximate the lithostatic pressure and considering potential inaccuracies of the isochore modeling, the most probable depth of mineralization appears to be in a range of 9-12 km. This inferred depth interval is in agreement with the non-meteoric N_2/Ar signature of fluids and deformation styles of auriferous veins and host rocks. However, these depths represent a rather crude estimate that has to be used with a great caution as it heavily relies on phase volume fractions that have to be approximated and cannot be precisely measured.

Implications of microthermometry data

Aqueous-carbonic fluids in aurieferous quartz

The presence of low saline aqueous-carbonic and predominantly carbonic inclusions in the mineralized quartz of the Solton Sary district is consistent with results of numerous studies of mesothermal gold systems of various ages and locations (e. g., Robert and Kelly, 1987; Ho et al., 1992, So and Yun, 1997; Hagemann and Cassidy, 2000; Ridley

Diamond, 2000). This association is commonly interpreted as a result of unmixing of originally homogeneous, predominantly aqueous, CO_2-rich fluid (e. g., Ridley and Diamond, 2000; Diamond 2001). Apart from few exceptions (e. g., Schmidt Mumm et al., 1997), most authors regard this fluid as responsible for gold transport, with hydrosulfide complexes being the main gold transporting agent (Ridley et al., 1996; Mikucki, 1998; Mikucki and Ridley, 1993; Ridley and Diamond, 2000; Phillips and Powell, 1993; Hagemann and Cassidy, 2000). The origin of the parent aqueous-carbonic fluid is still debated. The two most common interpretations are 1) deep metamorphic and 2) magmatic (granitic) sources (e. g., Phillips and Powell, 1993; Ho et al., 1992; Ridley and Diamond, 2000). There is general agreement that fluids are channelled and travel over long distances along structurally controlled conduits from source areas to mineralization sites (e. g., Ridley et al., 1996; Mikucki, 1998). The H_2S loss due to sulfidation of host rocks is considered to be a leading mechanism of gold deposition (e. g., Ho et al., 1992; Phillips and Powell, 1993; Ridley et al., 1996; Hagemann and Cassidy, 2000). Phase separation and fluid mixing may also be effective precipitation mechanisms, especially for deposits where gold occurs within quartz veins rather than in altered wall rocks (e. g., Ridley et al., 1996; Mikucki, 1998). According to the compilation by Ridley and Diamond (2000), the most frequently reported salinity values of auriferous fluids range from 3 to 7 wt percent NaCl equiv, and CO_2 mole fractions cluster at 0.1 to 0.25. Aqueous-carbonic fluids trapped in the Solton Sary type 2 inclusions are compositionally close to this range. Somewhat lower mole percentages of CO_2 ($X_{CO_2} \sim 0.07$-0.10) can be explained by a partial unmixing of the carbonic phase prior to the entrapment. Based on geologic similarity of the Solton Sary district to typical greenstone-hosted mesothermal gold deposits, it appears feasible that gold at Solton Sary was transported and deposited by low-moderate saline aqueous-carbonic fluid. Type 1 and 2 inclusions preserve products of unmixing of this parental fluid. Thus, CO_2 content and salinity of type 2 inclusions can be used to estimate minimum CO_2 mole percentage and maximum salinity of the parental gold-bearing fluid. The observed CO_2 contents in type 2 fluid inclusions (excluding cases of suspected leakage) suggest that the X_{CO_2} of the original fluid likely exceeded 0.1. The salinity of the parental fluid most probably was below 4-6 wt percent NaCl equiv. As gold at the Solton Sary occurs mostly within veins, the phase separation is likely to be the most important mechanism for gold deposition (e. g., Ridley et al., 1996; Mikucki, 1998; Hagemann and Cassidy, 2000), although the precipitation of gold due to fluid mixing could also have taken place.

Saline fluids in auriferous quartz

Saline aqueous fluid inclusions are not as widespread as carbonic, but are not uncommon in mesothermal systems (e. g., Parnell et al., 2000; Wilkinson et al., 1999; Murphy and Roberts, 1997; Robert and Kelly, 1987; Boullier et al., 1998; Ho et al., 1992). The origin of these fluids and their role in gold mineralization are not completely clear (Ho et al., 1992). The three most common interpretations are summarized below.

a) Saline aqueous fluids are genetically related to the mesothermal mineralization. These fluids are products of unmixing of originally low saline ore-bearing aqueous-carbonic fluid (Robert and Kelly, 1987; Mishra and Panigrahi, 1999).

b) Aqueous saline fluids found in secondary inclusions are supergene brines that clearly postdated the mineralization (Boullier et al., 1998; Murphy and Roberts, 1997).

their role is largely limited to resetting the isotopic systems of syn-mineralization phases (Boullier et al., 1998).

c) Aqueous saline fluids are low-temperature basinal brines that modified the pre-existing mesothermal mineralization by remobilizing and redepositing gold (Wilkinson et al., 1999; Parnell et al., 2000).

Available data are insufficient to firmly establish the origin of the saline fluids trapped in secondary inclusions within the mineralized quartz of the Solton Sary district. The absence of a significant time gap between carbonic-rich and aqueous saline fluids and the robust non-meteoric N_2/Ar signature of the mineralized quartz rule out the much later timing of saline fluids and their meteoric (*sensu strictu*) nature. The generation of hypersaline brines from originally low saline fluids through multiple phase separations cannot be completely ruled out but appears generally improbable because of very strong salinity differences and relatively low efficiency of phase separation process as a mechanism of salinity increase. The aqueous brines are most likely external with regards to the mesothermal system and are probably related to saline aqueous fluids in propylitic veins. The variably carbonic brines trapped in secondary inclusions in mineralized quartz (types 3 and 4) may have resulted from mixing of low carbonic "propylitic" brines and low saline aqueous-carbonic fluids. Propylitic veins are barren, and thus the saline aqueous fluids are unlikely to have transported gold. The mixing of barren and auriferous fluids could have contributed to the mineralization process by triggering the gold deposition, but there is no direct evidence supporting this.

Sulfuric species in auriferous fluids

Results of the bulk quadrupole mass spectrometer gas analysis provide independent information on important trace volatiles. This section focuses on sulfuric species that are essential for the gold transport. In mesothermal systems, gold is transported mainly as reduced-sulfur complexes $AuHS^0$ and $Au(HS)_2^-$ (e. g., Mikucki, 1998), and the transporting capacity depends on the abundance of H_2S in the fluid. Only about half (49 of 92) of crush-fast-scan analyses of auriferous quartz of the Solton Sary district detected the presence of H_2S. Measured H_2S contents (~ $n*10^{-4}$ mole percent) are barely distinguishable from those of barren quartz and are overall low, especially compared to the values reported by Landis and Hofstra (1991) for mesothermal deposits of Alaska (~ 0.02-0.8 mole percent). At the same time, virtually all analyses (87 of 92) of auriferous quartz detected measurable quantities of SO_2. When both species are detected, the SO_2/H_2S ratio normally exceeds unity and in many cases exceeds 10.

Published data on directly measured abundances of sulfuric species in mesothermal systems are sparse. Landis and Hofstra (1991) report 0.25-0.99 mole percent of SO_2 in volatiles trapped in sphalerite of Alaskan mesothermal systems. Quartz from the same deposits does not reportedly contain detectable SO_2. Yonaka (1996) presents data for auriferous quartz of Southern Ghana mesothermal mineralization, where SO_2 contents in the order of 10^{-3} mole percent are typical. In both cases, SO_2 is accompanied by comparable amounts of H_2S. Fundamentally, the proportion of H_2S and SO_2 (or SO_4^{2-}) indicates the redox state of a system (e. g., Ohmoto and Rye, 1979). Mikucki and Ridley (1993) conduct thermodynamic analysis based on fluid inclusion, stable isotope and alteration mineralogy data from Archean mesothernmal deposits and identify reduced and oxidized systems, i.e. with fluids dominated by sulfide and sulfate species, respectively. Although vein and alteration mineralogy is not always diagnostic of redox conditions, the oxidized systems commonly comprise hematite (±magnetite) and sulfates in their vein and alteration assemblages (Mikucki and Ridley, 1993; Cameron and Hattori, 1987). In case of the Solton Sary district, old Soviet exploration reports mention the presence of relatively sparse barite. Hematite replacing pyrite was observed in some veins during this study but was interpreted as supergene. The most typical mineralogic assemblage of veins and proximal alteration of the Solton Sary district are not clearly diagnostic of an oxidized system. This makes the apparent predominance of SO_2 in crush-fast-scan analyses to appear somewhat suspicious. The generally low H_2S and total sulfur contents also require explanation. These imply a need for a more detailed consideration of trapped volatile analysis results.

The crush-fast-scan quadrupole mass spectrometer analysis is a bulk technique. In case of auriferous quartz of the Solton Sary district, the analysis characterizes a mixture of heterogeneous fluids. Two major molecular components of this mixture, H_2O and CO_2 add up to constitute 95-99 mole percent for most of the analyses. Compared to H_2O and CO_2 all other species are essentially trace constituents. The CO_2 is derived mainly from carbonic (type 1) inclusions, whereas secondary aqueous inclusions (types 3 and 4) contribute most of the H_2O. Role of primary aqueous-carbonic inclusions (type 2) is likely insignificant, because of their low abundance. Even though the bulk CO_2/H_2O proportion of trapped volatiles is close to that of a "typical" mesothermal fluid, in reality it reflects not more than the relative abundance of carbonic inclusions that preserve volatiles derived from original ore bearing fluid, and secondary aqueous inclusions filled chiefly with external brines. Similarly, none of the measured trace volatile mole percentages directly represents auriferous fluid chemistry. However, it is possible to approximate the bulk volatile chemistry as a mixing system, where CO_2 and H_2O components are assumed to be "ore-related" and "barren", respectively, and to examine the relationships of trace volatiles with CO_2 and H_2O. This can provide information on a possible affinity of a given volatile component to auriferous or barren fluids. Figure 6.13 illustrates the application of this approach to sulfuric species trapped in auriferous quartz of the Solton Sary district. The SO_2 tends to be positively correlated to CO_2 implying a high probability of residence in carbonic fluid inclusions and consequently, a derivation from auriferous fluids during phase separation. The H_2S versus CO_2 plot does not show positive correlation. The CO_2-rich crushes return consistently low H_2S contents (ca. 1-2*10^{-4} mole percent). For the CO_2-poor crushes, the H_2S values vary from ca. 0.5*10^{-4} to 9*10^{-4} mole percent and broadly overlap with the lowest measured SO_2 values. These H_2S variations may be due to occasional contribution from overall volumetrically insignifcant type 2 inclusions.

These patterns show that phase separation likely resulted in major sulfur depletion of the auriferous fluid, because sulfur, presently occurring chiefly as SO_2 tends to be associated with the carbonic phase. Drummond and Ohmoto (1985) and Bowers (1991) show that rates of phase separation decrease in the order: H_2-CH_4-CO_2-H_2S-SO_2. Low, but still detectable H_2S values that tend to be higher in H_2O-rich analyses rule out the possibility for a complete absence of H_2S in the fluid. Since H_2S was present, it had to unmix from the aqueous solution more efficiently than SO_2, and be associated with the

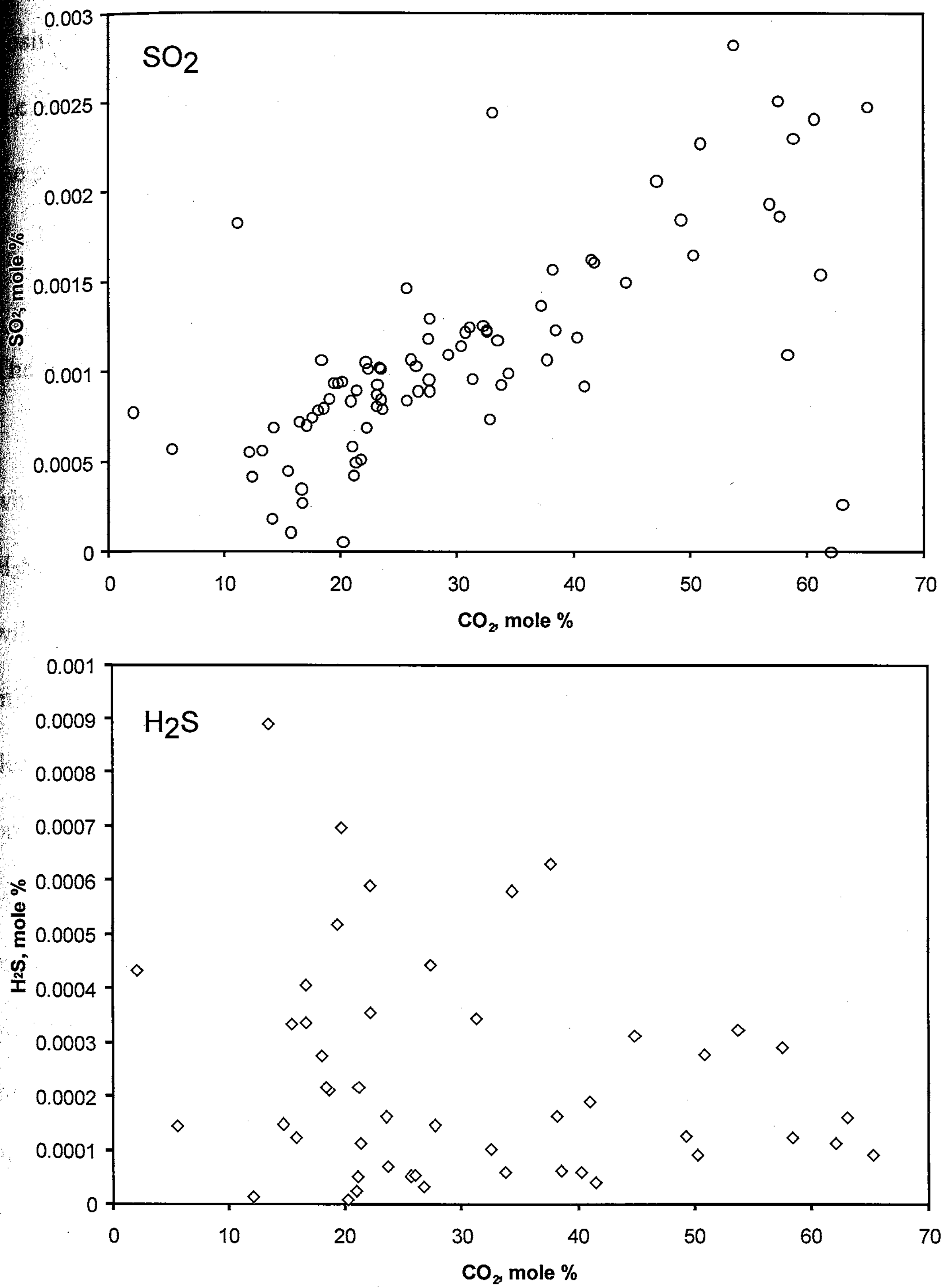

Fig. 6.13. Variation of sulfuric species versus CO_2 based on bulk trapped volatile analyses of auriferous quartz from the Solton Sary district. Results with zero values omitted. Note different scales of the graphs.

carbonic-rich fraction of the fluid that is trapped in type 1 inclusions. The absence of positive correlation between H_2S and CO_2 implies either modification of H_2S into SO_2 (i.e. oxidation) or "selective" loss of H_2S from the carbonic fluid during or shortly after the phase separation.

The oxidation of H_2S with formation of SO_2 can be expressed by the reaction:

$$H_2S+2H_2O=3H_2+SO_2$$

The proportion of H_2S and SO_2 can be expressed as:

$$fSO_2/fH_2S=K/(fH_2)^3$$

where K is the equilibrium constant and fH_2, fSO_2, and fH_2S are fugacities of H_2, SO_2, and H_2S. The decrease in pressure and, correspondingly, in fugacities of all gaseous species will result in an increase of the SO_2/H_2S ratio, i.e. will favor the oxidation. The increase in fSO_2/fH_2S ratio equals to the third power of the pressure decrease, i.e. the two-fold decrease in pressure results in 8-fold increase of the fSO_2/fH_2S ratio, and the three-fold pressure drop increases the fSO_2/fH_2S ratio 27 times. In addition to this effect, the sufficiently severe pressure drops would cause early H_2 separation, shifting the equilibrium to the right (i.e. increasing the oxidation efficiency). These relationships show that the oxidation of H_2S to SO_2 could have accompanied phase separation, although it is unclear whether this process was capable of converting all H_2S into SO_2. If the oxidation was only partial, it must have left some residual H_2S correlated to CO_2, which is not the case. Perhaps, the residual H_2S is present in concentrations that are too low to be quantitatively detected by the quadrupole mass spectrometer.

An alternative interpretation implies a possibility of the H_2S loss sometime between the phase separation and the entrapment of carbonic fluid inclusions. At present, there is no well-constrained explanation for the loss of H_2S and preservation of SO_2. It may be due to different solubilities of the two sulfuric species in the CO_2-dominated fluid. If so, the solubility of H_2S must be lower than that of SO_2, but there is no experimental data to confirm or disapprove it. Overall, the scenario involving the oxidation of H_2S appears more realistic. In any case, the observed incoherent behavior of H_2S and SO_2 implies that low measured H_2S concentrations probably underestimate the original H_2S content of the auriferous fluid.

Although the fast crush scan analyses of auriferous quartz of the Solton Sary district do not provide direct quantitative information on the concentration of sulfuric species in auriferous fluids, they still have important implications. The occurrence of SO_2 in carbonic inclusions that most likely originated from unmixing of the presumably auriferous, aqueous-carbonic fluid indicate: a) the overall sulfur enrichment of the parent aqueous-carbonic fluid, and b) the removal of sulfur from the solution during phase separations. The sulfur enrichment of aqueous-carbonic fluid directly supports its probable gold-transporting role that would otherwise be supported only by analogy with other mesothermal systems. The fact that the fluid unmixing resulted in partitioning of sulfuric species into the carbonic phase and, consequently, in reduction of sulfur concentration in the aqueous fraction confirms that phase separation could be, and most likely was the efficient mechanism of gold precipitation.

Origin of auriferous fluids: CO_2/CH_4-N_2/Ar systematics

As mentioned earlier, the mesothermal model implies a remote fluid source of a still debated nature. The two most prominent hypotheses suggest metamorphic devolatilization and devolatilization of felsic magmas (Ridley and Diamond, 2000). Phillips et al. (1987), Powell et al. (1991), and Phillips and Powell (1993) propose the devolatilization of greenschist-metamorphosed (i.e. hydrated and carbonated) mafic volcanics and greywacke as the leading mechanism for generatiing low saline aqueos-carbonic fluids. Under this scenario, the most extensive fluid release occurs presumably at the greenschist-amphibolite facies boundary around 480°±20°C, 3-5 kbar (Phillips and Powell, 1993). Cambrian-Ordovician largely volcanogenic greenstone sequences predominate within the Solton Sary area and the Kyrgyz-Terskei zone in general and comprise a viable fluid source under the metamorphic devolatilization model. As can be judged from the composition of type 1 and type 2 fluid inclusions, the chemistry of the auriferous fluids of the Solton Sary district agrees with the metamorphic fluid source.

This agreement, however, does not preclude the possibility for the magmatic origin of the fluids. Granitoid magmas are considered capable of producing chemically similar low saline aqueous-carbonic fluids (Cameron and Hattori, 1987; Ridley and Diamond, 2000). In addition to non-distinguishing fluid chemistry, the fundamental aspect of mesothermal model, the distal fluid transport, diminishes the importance of traditional geologic and geochronologic criteria. Even the absence of correlative granitoids in the proximity of mineralization cannot rule out the occurrence of such intrusions at depth (Ridley and Diamond, 2000), especially if deeper amphibolite metamorphism is assumed.

In this context, the results of bulk trapped volatile analyses need to be evaluated as a potential diagnostic tool. The CO_2/CH_4 and N_2/Ar ratios have been used to distinguish between magmatic, meteoric, and "crustal" fluid sources for active geothermal systems, epithermal and Carlin-type gold mineralization (e. g., Moore et al., 2000; Blamey, 2000; Groff, 1996). Meteoric sources are characterized by N_2/Ar ratios clustering between those of air (84) and air-saturated water (36), and CO_2/CH_4 ratios exceeding 4 (Moore et al., 2000). "Crustal" fluids (i.e. those "not involved in meteorological cycle", Moore et al., 2000) are relatively enriched in methane (CO_2/CH_4 <4). Their N_2/Ar ratios generally approximate meteoric values but may reach about 525 due to the N_2 enrichment through plant degrading (Moore et al., 2000). Apparently, this chemistry characterises supergene fluids, such as sedimentary basin brines, rather than hypogene crustal (i.e. metamorphogenic) fluids. Chemical signatures of magmatic gases are largely based on direct measurements at active volcanoes and comprise variable but usually very high (up to the order of thousands) CO_2/CH_4 and N_2/Ar ratios (Moore et al., 2000).

These geochemical criteria have been proven diagnostic for relatively shallow hydrothermal systems in predominantly extensional tectonic settings where potential fluid sources are indeed largely limited to meteoric, shallow magmatic, and variably evolved basinal. The application of the CO_2/CH_4 and N_2/Ar discrimination system to more deep syn-kinematic mesothermal mineralization requires caution. The disrcrimination of meteoric waters from assorted deeply sourced fluids appears still appropriate. Meteoric waters, if not modified by prolonged interaction with wallrocks, are likely to retain their characteristically low N_2/Ar ratios and thus can be identified based on their volatile signatures. Interpreting sources of hypogene fluids is somewhat problematic. In short, elevated CO_2/CH_4 and N_2/Ar ratios are probably not unique to magma-derived fluids and can be linked to various metamorphic processes, fluid-rock interactions, and heterogeneous fluid mixing. The CO_2 rich fluids can be produced by metamorphic devolatilization of carbonate-bearing sedimentary rocks and metavolcanics and these fluids are likely to have high CO_2/CH_4 ratios. The relative proportion of CO_2 tends to increase with increasing metamorphic grade (e. g., Crawford, 1981; Landis and Hofstra, 1991). Consequently, the relative abundance of carbonic species is not particularly source-specific. The N_2/Ar ratio is more difficult to evaluate because of scarsity of representative data on Ar contents in trapped fluids. However, elevated N_2 concentrations are quite common and not always clearly related to magmatism. High N_2 contents (e. g., up to 8 mole percent) in fluid inclusions are reported for mesothermal systems of Central Iberian Zone in Spain (e. g. Murphy and Roberts, 1997; Dee and Roberts, 1993). Elevated N_2 is attributed to the NH_4^+ that was released from mica and feldspar of metapelitic host rocks during metamorphism. Yonaka (1996) reports N_2 values up to 25 mole percent and N_2/Ar ratios corresponding to the "magmatic" range (i.e. hundreds) for granite-hosted mesothermal systems in Ghana. However, the author interprets high N_2 concentrations as related to interaction with "organic-rich metasediments", not to magmatic origin of fluids. The N_2-rich fluid inclusions occur within high-pressure shear zones (eclogite and high-pressure granulite facies), where N_2 presumably originated as NH_4^+ derived from mica and feldspar of the protolith (Andersen et al., 1993). This source is a very probable contributor of N_2 to mesothermal fluids, because upper portions of major transcrustal shear zones commonly serve as fluid conduits for mesothermal systems.

The CO_2/CH_4 versus N_2/Ar plots of the Solton Sary data clearly imply the non-meteoric fluid origin. Although data points cluster within the magmatic field (Fig. 6.8), classifying fluids as magmatic appears excessive. For deep syn-kinematic hydrothermal systems, high CO_2/CH_4 and N_2/Ar ratios are not strictly unique to magmatic fluids. Thus, the assignment of magmatic origin to the Solton Sary fluids based entirely on this geochemical feature is not justified. It appears more appropriate to recognize that fluid inclusion and bulk trapped volatile analysis data from the Solton Sary mineralized quartz indicate deep non-mereoric origin of the fluids but are not conclusive for specifying metamorphic or magmatic source.

Possible alternatives to the mesothermal model

Although fluid inclusion characteristics of the Solton Sary mineralization are in good agreement with the mesothermal model, an alternative interpretation needs to be considered. Fluid inclusion assemblages similar to the one of Solton Sary are regarded as characteristic for a recently introduced class of intrusion-related gold deposits (Sillitoe and Thompson, 1998; Thompson et al., 1999; Thompson and Newberry, 2000; Lang et al., 2000; Baker, 2000). In contrast with typical mesothermal systems, with remote and somewhat uncertain (metamorphic or magmatic) fluid source, the intrusion-related gold deposits are genetically linked to specific plutonic complexes. In most cases, parent intrusions comprise relatively reduced I-type granitoids (Sillitoe and Thompson, 1998). Mineralization may be hosted by the intrusions or concentrate up to 1-3 km from them, but even in cases of spatial separation parent plutonic suites can be viably identified.

deposits show consistent geochemical signatures (Au-Bi-Te-As), form over a wide range of depths, down to 5-6 km, and exhibit a variety of mineralization styles, commonly quite similar to those of mesothermal systems (Thompson and Newberry, 2000; Lang et al., 1999). Detailed published fluid inclusion data from this type of mineralization are relatively rare (e. g., Cole et al., 2000). As shown in several overview papers, CO_2-bearing fluids are present in most deposits (Thompson and Newberry, 2000; Lang et al., 1999). Not universally present, but still common, are aqueous saline fluids that are more typical for relatively shallow systems (pressures ~0.5-1.5 kbar, Lang et al., 1999). However, brines also occur in some deeper systems (pressure > 1.5 kbar) where they appear to postdate higher temperature carbonic fluids. This presumably reflects a progression of volatile exsolution from cooling magma (Lang et al., 1999; Thompson and Newberry, 2000). The paragenesis of carbonic and aqueous saline inclusions, especially at trapping pressures below ~1.5 kbar is normally attributed to phase separation from a homogeneous magmatic fluid (Lang et al., 1999; Marsh et al, 2000; Rombach and Newberry, 2000). However, a possibility for mixing of a primary magmatic fluid with externally derived (meteoric or connate) fluids is suggested by Sillitoe and Thompson (1998). The fact that data from Solton Sary match with both models is not surprising considering that the reported parameters of fluid inclusions from intrusion-related deposits overlap with those of typical mesothermal systems (cf. Sillitoe and Thompson, 1998; Thompson et al., 1999). The processes of fluid evolution, with a leading role of immiscibility also appear similar. Consequently, the composition of fluid inclusions cannot be used as a sole diagnostic feature to classify a particular system into mesothermal or intrusion-related type. More essential for classifying a particular deposit intrusion-related is the possibility of identifying a potential "parent" magmatic complex and to establish spatial, temporal, and geochemical links between the magmatism and mineralization. In spite of the very close spatial association of the Solton Sary district with the alkalic intrusion complex, there are two features that make close genetic relations somewhat suspicious. First, the intrusions do not show intrinsic gold enrichment. Second, there is a controversy between the textural appearance of the igneous rocks, fluid inclusion data and mineralization styles. The textures of lamprophyres and syenite porphyries imply their hypabyssal origin, fluid inclusion data and mineralization styles (including deformation processes and patterns) suggest greenschist facies metamorphic conditions. The fact that magma emplacement and hydrothermal activity apparently took place under different conditions implies a high probability of time gap between the two events. Thus, even apart from the geochronologic data that will be discussed in the next chapter, a genetic link between the mineralization of the Solton Sary district and alkalic intrusions appears highly improbable. No other magmatic complex suitable as a fluid source can be identified, and thus, a mesothermal model, with remote fluid transport and a deep, metamorphic or magmatic fluid source, is more appropriate for the Solton Sary mineralization.

Saline fluids in propylitic veins

The CO_2/CH_4– N_2/Ar systematics of saline, non-carbonic brines hosted in propylitic veins imply their non-meteoric nature. More specific source interpretation based on CO_2/CH_4-N_2/Ar signatures appears excessive for reasons outlined earlier in the connection with auriferous quartz data. High salinity of the fluids is consistent with the magmatic source, but no clearly correlative intrusive suite can be identified. Besides, the pervasive nature of barren quartz veining implies the regional spread of these fluids, which is difficult to explain by a magmatic source.

Aqueous brines are not uncommon for low-grade metamorphic terrains. However, high salinity is not linked to metamorphic processes but is rather attributed to dissolution of salts in evaporitic sequences, observed or hypothetical (Crawford, 1981). Greenschist facies metamorphism results in consumption, not generation, of fluids, because anhydrous phases are replaced by hydrous. Thus, in situ metamorphic production of fluids during the greenschist facies metamorphism is not a possibility, whereas fluids generated at higher metamorphic grades are expected to be CO_2-rich and low saline. Preservation of residual pore fluids (in case of Solton Sary, evolved seawater) would explain high salinity, but is somewhat problematic, because these fluids are likely to have been expelled at temperatures lower than homogenization temperatures of type 5 inclusions (ca. 200-250°C).

Interestinlgy, very similar saline aqueous fluids trapped in veins with virtually identical, essentially propylitic, mineral assemblages are documented at Archean mesothermal gold systems (Noranda and Val d'Or districts) of the southeastern Abitibi subprovince (Boullier et al., 1998), and at Archean Eye Dashwa Lakes granitoid pluton within the Wabigoon subprovince (Kerrich and Kamineni, 1988). These two areas are roughly 700 km apart and correspond to eastern and western portions of the Superior Province of the Canadian Shield, respectively. At Donalda mine (Noranda district) calcite-chlorite-epidote-quartz veins that host inclusions with aqueous brines clearly date the mineralization (Boullier et al., 1998). At the Eye Dashwa Lakes pluton, the dote-quartz-chlorite veins with variable amounts of muscovite have an age of 2650±15 a ($^{40}Ar/^{39}Ar$, muscovite; Kerrich and Kamineni, 1988) that virtually overlaps with the ming mesothermal gold mineralization of the Superior Province (ca. 2710-2670 Ma, rrich and Cassidy, 1994). Kerrrich and Kamineni (1988) interpret the brines as chean marine waters that infiltrated and evolved chemically during the cooling of the luton. Kerrich and Kamineni (1988) and Boullier et al. (1998) emphasize the analogy of rapped fluids to enigmatic brines that are presently encountered in several areas of the Canadian Shield at depths below 1 km (Fritz and Frape, 1982).

The brines trapped in secondary inclusions of barren propylitic veins of the Solton Sary district could represent highly evolved marine waters that completely lost their original supergene N_2/Ar signature. The mechanism of their emplacement is unclear because prevalent lithostatic conditions appear unfavorable for simple pervasive downward infiltration of large volumes of fluid. Perhaps residual marine pore fluids responsible for greenschist alteration of stratified volcanics comprise at least some fraction of the brines. Independently of the origin of highly saline barren fluids, they are likely to have temporally overlapped with focused flow of aqueous-carbonic mineralizing fluids. Secondary, variably saline inclusions in mineralized quartz may indicate single or multiple incursions of external barren brines and mixing of these brines with low saline aqueous-carbonic fluids. Most probably, these events correspond to the final stages of mineralization.

Summary

The fluid inclusion study revealed that three types of fluids are trapped within the mineralized quartz of the Solton Sary mesothermal gold district. These are predominantly carbonic (inclusions of type 1), low saline aqueous-carbonic (inclusions of type 2) and saline aqueous, variably carbonic (inclusions of type 3 and 4). Fluid inclusions in barren propylitic veins contain aqueous highly saline brines (type 5 inclusions). Maximum homogenization temperatures of ca. 350°C demonstrated by type 2 inclusions are likely to approximate to the trapping temperature. Trapping pressures estimated for 350°C range from 3 to 3.5 kbars for type 2 inclusions and from 1 to 1.7 kbars for type 1 inclusions. This significant pressure range is interpreted to reflect fluid pressure variations related to a fault-valve regime. The depth of mineralization estimated assuming that maximum fluid pressures approximate lithostatic load and considering potential inaccuracies of phase volume evaluations is in a range of 9-12 km. Similar to other mesothermal systems, aqueous-carbonic (type 2) and predominantly carbonic (type 1) fluids trapped in auriferous quartz of the Solton Sary district were probably derived from a parent auriferous low saline aqueous-carbonic fluid ($X_{CO_2} \geq 0.1$; salinity$\leq$ ~6 wt % NaCl equiv) through tectonically controlled phase separation. The H_2S loss during phase separations has probably served as a leading mechanism of gold precipitation. The probable gold transporting role of the aqueous-carbonic fluid and the importance of phase separation for gold precipitation are additionally supported by results of bulk trapped volatile analysis. The analysis of auriferous quartz revealed the presence of SO_2 likely residing in carbonic (type 1) fluid inclusions. This implies that the aqueous-carbonic fluids were originally enriched in sulfur and thus suitable for transporting gold. Phase separation reduced total sulfur content in the aqueous solution that likely caused the gold deposition. The virtual absence of H_2S in trapped fluids can be explained by its oxidation to SO_2 or, less likely, loss between phase separation and entrapment of fluid inclusions. Bulk chemical analyses of trapped volatiles in auriferous and barren quartz imply a deep, non-meteoric origin of fluids. Aqueous-carbonic auriferous fluids are likely to have been derived from a remote metamorphic or magmatic (granitic) source. The alkalic intrusive suite that hosts auriferous lodes is an unlikely fluid source because it lacks the intrinsic gold enrichment and there is apparent diachronism of magmatism and mineralization. The latter is evident from the hypabyssal textural appearance of intrusive rocks that contrasts with a significant depth of mineralization supported by the fluid inclusion data and mineralization styles. During the waning stages of mesothermal mineralization the system experienced incursions of external brines that were mixing with carbonic-rich fluids. These are non-carbonic, saline aqueous brines with a non-meteoric N_2/Ar ratio. Most likely, these saline fluids represent highly evolved marine waters that lost their original volatile signature through interaction with volcanogenic host rocks.

CHAPTER 7

^{40}AR/^{39}AR STUDY

^{40}Ar/^{39}Ar methodology

Sample selection

The ^{40}Ar/^{39}Ar studies of the Solton Sary district pursued several goals. The primary two were to establish timing of mineralization and alkalic magmatism in order to help in understanding the nature of close spatial relationships between auriferous zones and host intrusions. The two largest groups of samples analyzed in this study included phenocrysts from alkalic intrusive rocks and gangue minerals from mineralized zones and associated alteration (Table 7.1). Phenocrysts included nine biotites (in this chapter, the term "biotite" is applied both to compositionally uniform and zoned micas), four zoned Ba-rich K-feldspars, and two amphiboles. Mineralization was represented by seven white micas (four coarse muscovites, two fine sericites and one fine fuchsite), and one K-feldspar. Three samples were collected from the immediate flanks of the mineralized zones: two biotites from biotitic alteration halo and one coarse muscovite from a barren propylitic vein.

Two muscovite samples represented barren quartz veins that are widespread in the region. These samples were intended to constrain relative timing of economically significant hydrothermal activity and regional-scale fluid migration. Two samples of tectonogenic fuchsite from the South Kumbel fault zone were analyzed in an attempt to characterize the timing of tectonic activity that is likely related to the North-Median Tien Shan collision (Mikolaichuk et al., 1997).

Table 7.1. Samples analyzed by the $^{40}Ar/^{39}Ar$ method

Sample ID	Approximate location	Rock type	Mineral	Step heating analysis, number of aliquots	In-situ UV laser ablation analysis, number of crystals
Phenocrysts from alkalic intrusive rocks of the Solton Sary district					
A23	Solton Sary, east	syenite porphyry	Feldspar	2	
49-113.7	Solton Sary, central part	lamprophyre	Zoned biotite	1	2
49-129.2	Solton Sary, central part	syenite porphyry	Feldspar	2	
49-129.2	Solton Sary, central part	syenite porphyry	Zoned biotite	1	1
55-62.7	Solton Sary, central part	syenite porphyry	Biotite	1	
56-158	Solton Sary, central part	syenite porphyry	Biotite	1	
57-166.2	Solton Sary, central part	syenite porphyry	Biotite	1	2
57-166.2	Solton Sary, central part	syenite porphyry	Feldspar	2	
57-174.1	Solton Sary, central part	syenite porphyry	Biotite	1	
57-174.1	Solton Sary, central part	syenite porphyry	Feldspar	2	
58-58.3	Solton Sary, central part	lamprophyre	Biotite	1	
58-110.2	Solton Sary, central part	syenite porphyry	Biotite	1	
76-179.9	Solton Sary, central part	lamprophyre	Biotite	1	
TR6A	Solton Sary, west	lamprophyre	Amphibole	1	
397	Solton Sary, central part	lamprophyre	Amphibole	1	
Magmatic phases from intrusive rocks other than alkalic rocks of the Solton Sary district					
700-1	north of Solton Sary	Ordovician granite	Feldspar	1	
700-2	north of Solton Sary	Ordovician granite	Feldspar	1	
700-2	north of Solton Sary	Ordovician granite	Biotite	1	
700-2	north of Solton Sary	Ordovician granite	Amphibole	1	
626-1	southeast of Solton Sary	Silurian leucocratic granite	Feldspar	1	
676-2	Solton Sary, southern border	granite clast, conglomerate	Feldspar	1	
Hydrothermal phases from the Au-bearing mineralized zone and alteration halos					
59-85.5	Solton Sary, central part	QSCP alteration	Sericite	1	
59-85.5	Solton Sary, central part	QSCP alteration	Fine fuchsite	1	
62-115.2	Solton Sary, central part	QSCP alteration	Sericite	1	
AD2	Solton Sary, central part	mineralized quartz vein	Muscovite	1	
AD2A	Solton Sary, central part	mineralized quartz vein	Muscovite	1	1
601	Solton Sary, east	mineralized quartz vein	Muscovite	1	2
547	Solton Sary, east	mineralized quartz vein	Muscovite	1	1
664-1	Solton Sary, west	mineralized quartz vein	Feldspar	1	
532	Solton Sary, east	barren propylitic vein	Muscovite	1	1
57-157.5-1	Solton Sary, central part	biotitic alteration	Biotite	1	
57-157.5-2	Solton Sary, central part	biotitic alteration	Biotite	1	
Hydrothermal phases spatially unrelated to Au mineralization					
617	Solton Sary, east	barren quartz vein	Muscovite	1	
659	Solton Sary, east	barren quartz vein	Muscovite	1	
669-3	Solton Sary, south	alteration, fault zone	Fuchsite	2	
675-2	Solton Sary, south	alteration, fault zone	Fuchsite	1	

The main goal of the thermochronologic studies of K-feldspar was to reconstruct temperature conditions during the mineralization and provide data on the post-mineralization tectonic evolution of the area. In addition to four samples from syenite porphyries and one from an auriferous vein, one feldspar sample was collected from a granitic clast in Devonian-Carboniferous conglomerates and three samples represented Ordovician and Silurian granitic intrusions outside the Solton Sary district.

All mineral phases were characterized by quantitative electron microprobe analysis. The results are presented in Appendix B. In addition, a detailed description of phenocrysts from lamprophyres and syenite porphyries is found in Chapter 4 that deals with petrology and geochemistry of the alkalic intrusive rocks.

Sample preparation

For most of the samples, concentrates of monocrystalline grains were obtained. Grain sizes normally ranged from 300 to 850 μm, coarser (1-3 mm) crystals were separated for detailed in situ laser ablation work. Seven fine mica concentrates (sericites 59-85.5 and 62-115.5; fuchsite 59-85.5, 669-3, and 675-2; and biotites 57-157.5-1 and 2 comprised fragments of monomineral aggregates, with individual flakes ranging from 50 to 100 μm. To obtain separates, samples were crushed with a jaw crusher and a disk pulverizer, ultrasonically cleaned with de-ionized water, and concentrated using standard magnetic techniques. Final separates were hand-picked under a binocular microscope. Some concentrates of feldspars and micas were treated with 10 percent HCl to eliminate secondary carbonate.

Separates were loaded in aluminum trays and irradiated for 24 to 100 hours in evacuated quartz tubes in the Ford reactor at the University of Michigan. Fish Canyon tuff sanidine (27.84 Ma relative to 520.4 Ma for Mmhb-1; Samson and Alexander, 1987) was employed as a flux monitor.

$^{40}Ar/^{39}Ar$ age dating method

The theoretical basis and fundamental principles of the $^{40}Ar/^{39}Ar$ technique are presented in detail in McDougall and Harrison (1999) and only the main features are outlined here. The $^{40}Ar/^{39}Ar$ method is a modified version of the K-Ar method, as both techniques employ the radiogenic decay of ^{40}K to ^{40}Ar. The ^{40}Ar formed by the in situ radiogenic decay of ^{40}K is defined as radiogenic ^{40}Ar ($^{40}Ar^*$). Unlike the conventional K-Ar method where measurements of K and Ar are conducted by different methods on separate portions of the sample, the $^{40}Ar/^{39}Ar$ analysis includes measurements of argon isotope ratios on a single sample aliquot. This overcomes sample inhomogenieties and achieves higher analytical precision. Also, samples can be degassed in steps, that allows determining a series of apparent ages for a single sample.

Prior to the analysis, samples are irradiated by fast neutrons in a nuclear reactor in order to convert ^{39}K to ^{39}Ar. The data are collected by in-vacuo degassing of a sample and measuring relative abundances of ^{40}Ar, ^{39}Ar, ^{38}Ar, ^{37}Ar, and ^{36}Ar in a mass spectrometer. The measured values are corrected for isotopic interferences and for the presence of non-radiogenic argon. The $^{40}Ar^*/^{39}Ar_K$ ratio is proportionate to the age of the sample, however a quantitative measure of the neutron-induced ^{39}K to ^{39}Ar conversion is necessary to calculate the apparent age. To determine this quantitative parameter, the J-

The samples of known ages (flux monitors) are irradiated together with unknown samples and subsequently analyzed for argon isotopes. The J-value is calculated from the measured argon isotope ratios of the flux monitors. Once the J-value is determined, the apparent age can be calculated from the $^{40}Ar^{*}/^{39}Ar_{K}$ ratio of the sample.

The $^{40}Ar^{*}$ that is produced throughout the geologic history of a mineral can be lost through thermally driven volume diffusion. In general, the apparent $^{40}Ar/^{39}Ar$ age defines the timing of cooling below the mineral closure temperature, i.e. the temperature below which $^{40}Ar^{*}$ loss can be considered negligible (Dodson, 1973). The closure temperature is controlled by intrinsic diffusion properties of the mineral, and also depends on the cooling rate and grain size. McDougall and Harrison (1999) refer to the most commonly asserted closure temperatures of biotite and muscovite, 300°-350°C and 350°C, respectively. The authors recommend a cautious approach to these "nominal" values. Diffusion parameters and thus closure termperatures may be highly variable depending on composition. For example, closure temperatures of some biotite varieties may reach 450°C (McDougall and Harrison, 1999).

$^{40}Ar/^{39}Ar$ analytical technique

The $^{40}Ar/^{39}Ar$ analyses were conducted at the New Mexico Geochronological Research Laboratory at New Mexico Institute of Mining and Technology. Two analytical methods were employed: the step heating (or incremental heating) technique and the UV-laser in situ ablation method. During the step heating experiments, multi-grain mineral separates were degassed in a series of increments in a double-vacuum molybdenum resistance furnace. Reactive gases were removed during the heating with a SAES GP-50 getter operated at 450°C. After heating, the gas was additionally purified in the second stage of the extraction line with two SAES GP-50 getters (one at 450°C and one at room temperature) and a tungsten filament (at 2000°C). The most commonly used gas extraction schedule included 10 minutes of heating and 5 minutes of second stage clean-up for each step.

For the UV laser in-situ analysis, the irradiated mica crystals were mounted on copper plates with Superglue and placed in a laser vacuum chamber. The argon was extracted by ablating square 100x100 µm, approximately 100 µm deep, pits on the {001} cleavage planes of the mica crystals. The pits were arranged in linear traverses with a distance between the centers of two adjacent pits equal to 120 µm. The ablation was achieved with an SL 454 Nd-YAG laser (wavelength 266 nm). Laser power settings and ablation times largely depended on the analytical limits of the mass spectrometer. First experiments showed that a satisfactory precision of the in situ age determination could be achieved with the ^{40}Ar beam signal to be at least 100 pA. For the Solton Sary samples, a power of 0.09-0.1 W and a blasting time of 20 seconds was typically required. During several analyses, the power of 0.1 W could not be achieved and the laser was fired at 0.075-0.08 W, with an increased ablation time of 25 seconds. The extracted gas was purified for 4 minutes with two SAES GP-50 getters.

For both extraction techniques, isotope measurements were conducted using a MAP 215-50 mass spectrometer equipped with an electron multiplier. Data for masses 40, 39, 38, 37, and 36 were collected in 5 (step heating) or 10 (in situ UV laser ablation) measuring cycles. The measured intensities were extrapolated to the time of the gas admission by applying linear regression of peak height versus time. Each mass intensity was corrected for mass spectrometer baseline and background, and the extraction system blank. Net sensitivity varied from 1.7 x 10^{-16} to 2.3 10^{-16} moles/pA for the furnace extraction line and was about 1.9 x 10^{-16} for the UV laser extraction system. Furnace extraction line blanks were measured at least two times for each sample and typically were about 3000, 25, 3, 4, 8 x 10^{-18} moles for masses 40, 39, 38, 37, and 36, respectively. The UV laser extraction line blank measurements were repeated between every three in-situ analyses. Most typical blank values were about 1500, 9, 2.5, 4, and 8.5 x 10^{-18} moles for masses 40, 39, 38, 37, and 36, respectively.

J-values were determined to a precision of ±0.1% by analyzing 4 single crystals from each of 3 (6-hole tray) or 4 (12-hole tray) radial positions around the irradiation vessel. Correction factors for interfering nuclear reactions were determined by analyzing irradiated K-rich glass and CaF_2. The decay constants and isotope abundances used for age calculations are from Steiger and Jäger (1977).

Age assignment and error estimate

Two types of ages were calculated for samples analyzed by the step heating technique: a plateau age and a total gas age. The plateau age combines apparent ages of subjectively selected contiguous increments assumed to be geologically meaningful. In contrast to one of the original definitions of the plateau age (Fleck et al., 1977), the strict statistical consistency of the individual apparent ages was not required in this study. The plateau ages were calculated as weighted means of apparent ages of individual increments with the inverse of variance used as the weighting factor. Errors of plateau ages were estimated using the method of Taylor (1982). In addition, a mean square of weighted deviates (MSWD) value was calculated for each plateau population. If the MSWD was outside the 95 percent confidence interval for (n-1) degrees of freedom (cf. Mahon, 1996) the error was multiplied by the square root of the MSWD. This method combines sizes of individual step errors and the scatter of apparent step ages.

The total gas age incorporates results of all heating steps, and is a more precise equivalent of the conventional K-Ar age. Total gas ages reported in this paper were calculated by weighting individual apparent ages by the size of the ^{39}Ar signal for each step. Errors of total gas ages were calculated by weighing individual step errors by the corresponding fraction of ^{39}Ar.

In addition to the ages that incorporate results of several heating steps, some individual step ages were used for interpretation in this study. In most cases these ages correspond to the highest or near the highest temperature steps and are referred to as terminal ages or maximum step ages. All age uncertainties are reported at 2σ. Errors of plateau, integrated, and total gas ages include the 0.1 percent error in the J-factor.

$^{40}Ar/^{39}Ar$ results (phyllosilicates and amphiboles)

Incremental heating analyses

The results of the $^{40}Ar/^{39}Ar$ step heating analyses (excluding K-feldspars) are presented in Appendix D (Table D.1), Figures 7.1-7.10, and are summarized in Table 7.2. The K-feldspar analyses are considered in a separate section that is dedicated to thermochronological modeling.

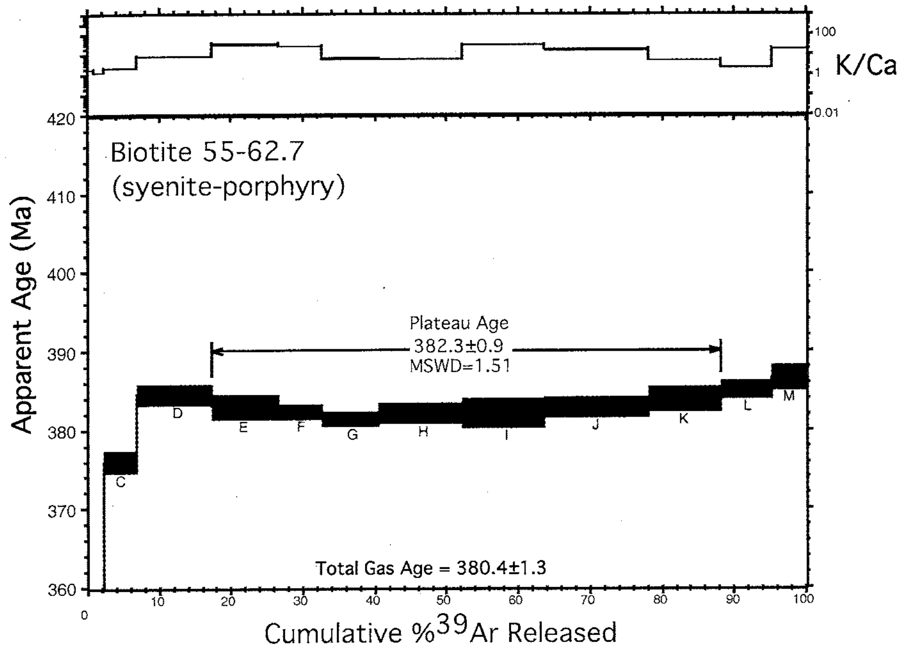

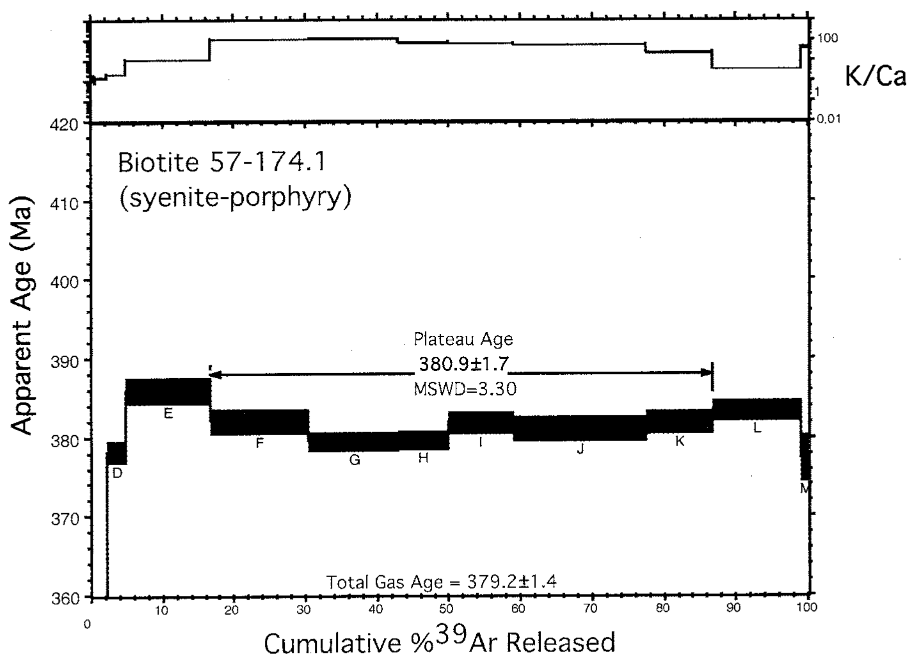

Fig. 7.1. $^{40}Ar/^{39}Ar$ age spectra for biotites 55-62.7 and 57-174.1

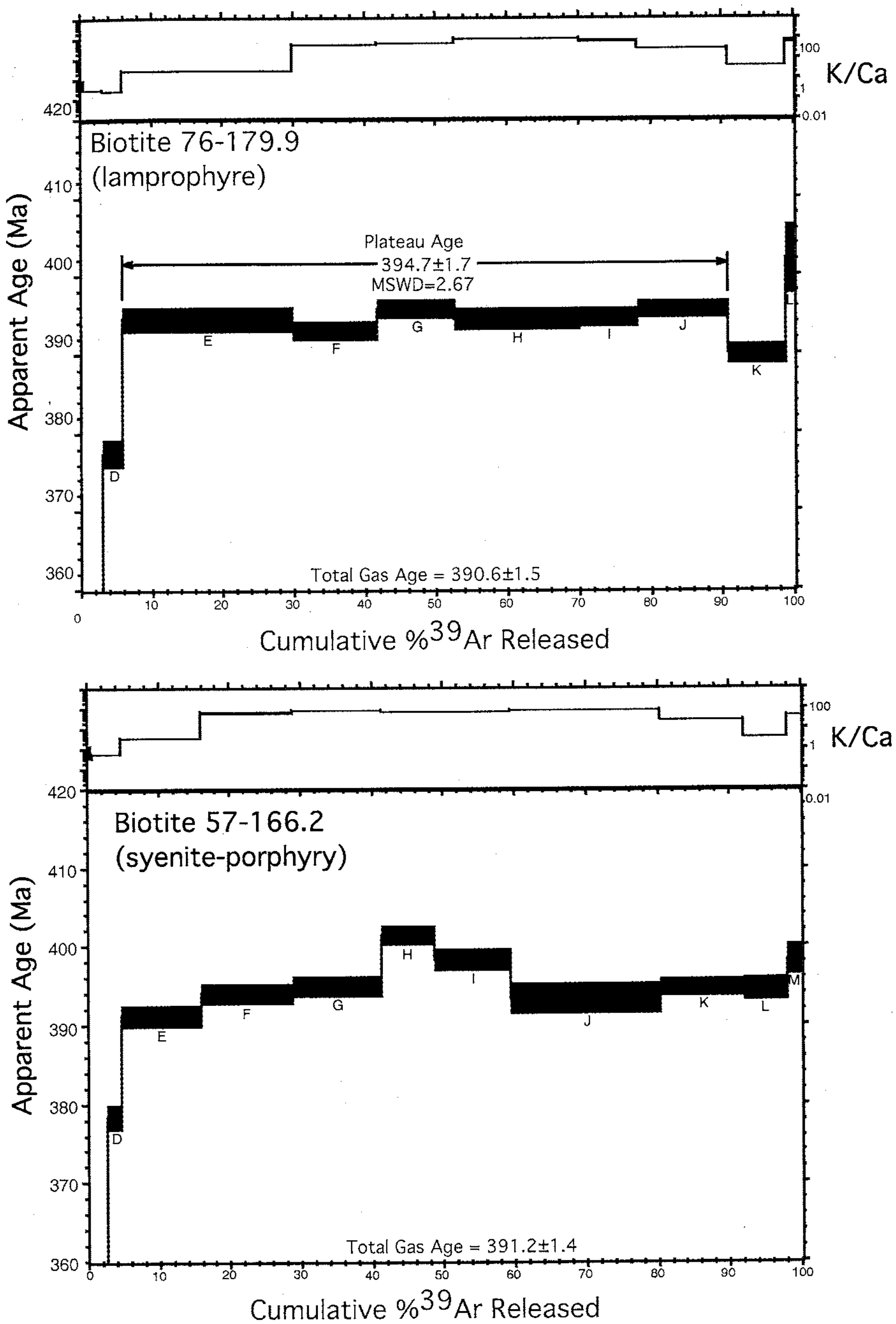

Fig. 7.2. $^{40}Ar/^{39}Ar$ age spectra for biotites 76-179.9 and 57-166.2

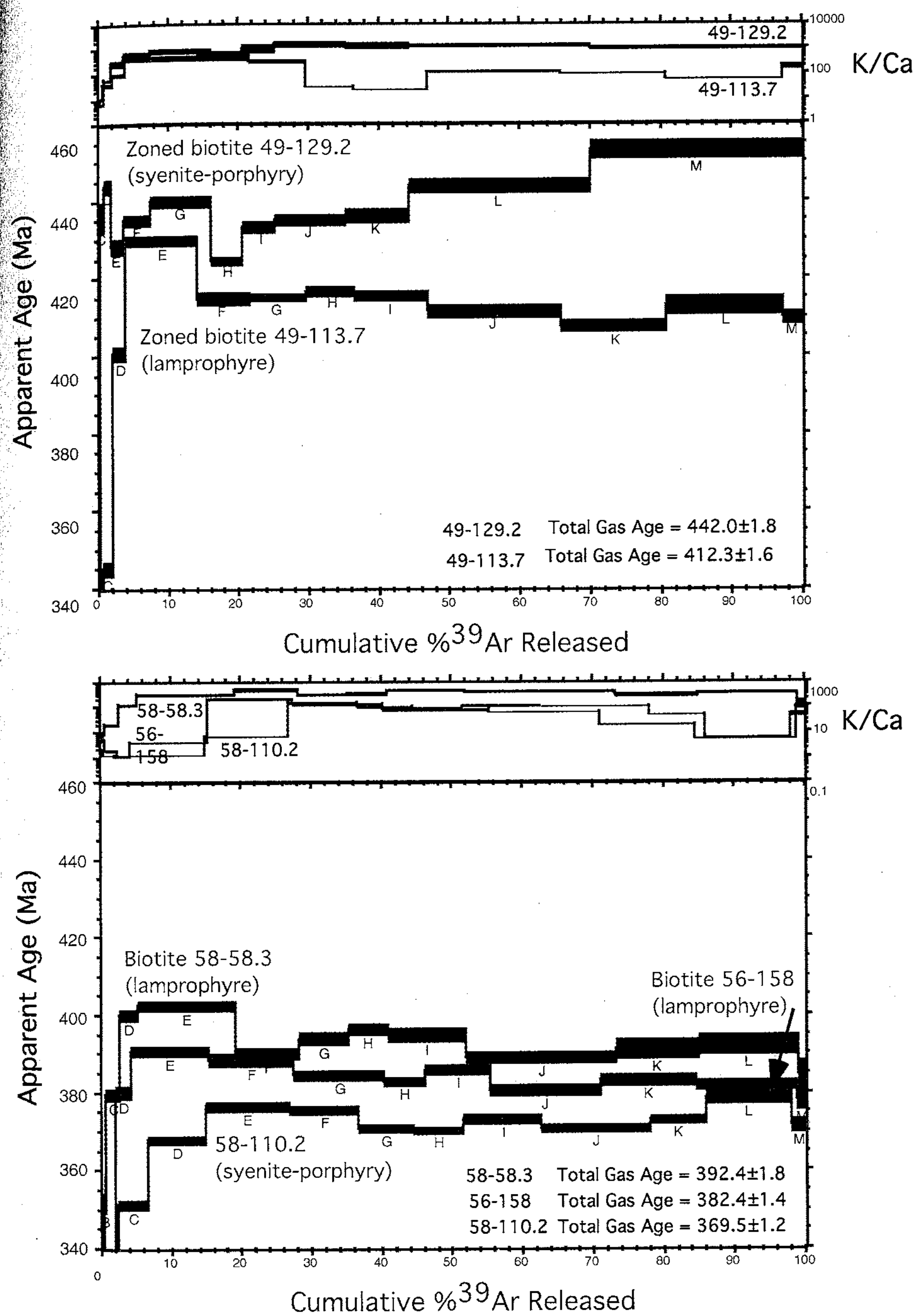

Fig. 7.3. $^{40}Ar/^{39}Ar$ age spectra for biotites 58-58.3, 56-158, and 58-110.2, and zoned biotites 49-129.2 and 49-113.7

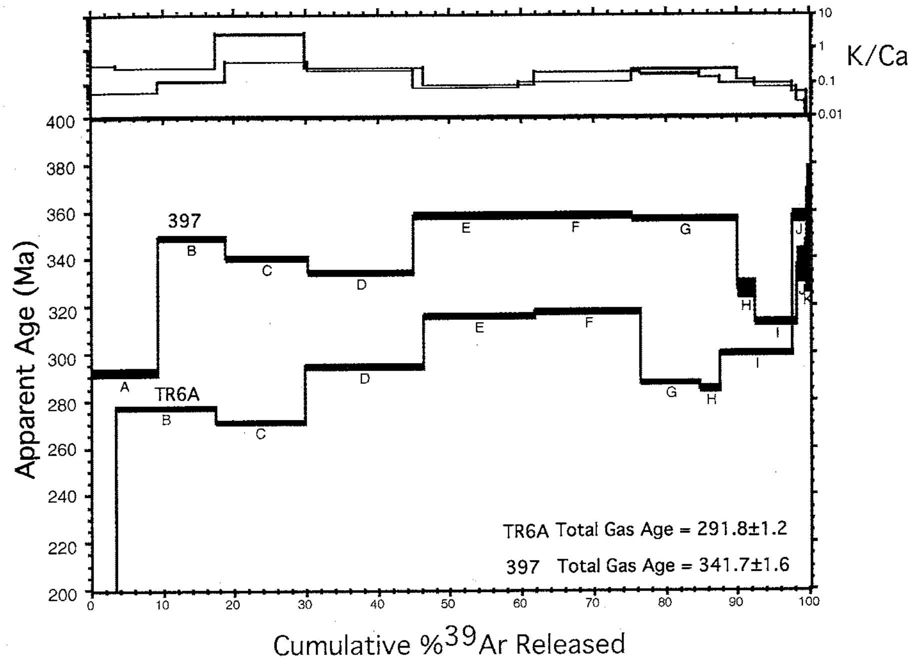

Fig. 7.4. $^{40}Ar/^{39}Ar$ age spectra for amphiboles 397 and TR6A.

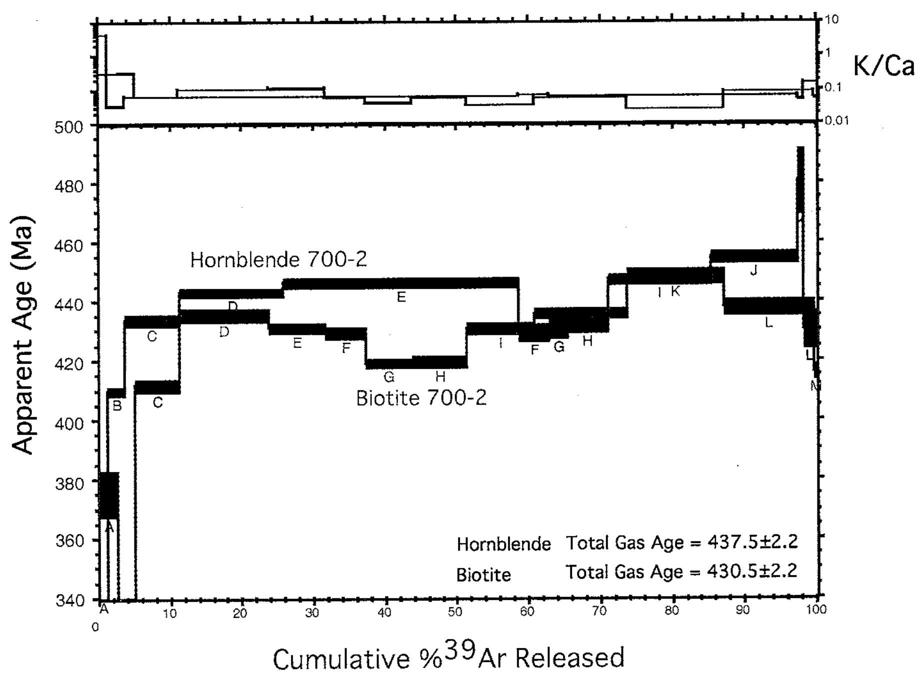

Fig. 7.5. $^{40}Ar/^{39}Ar$ age spectra for biotite and hornblende 700-2

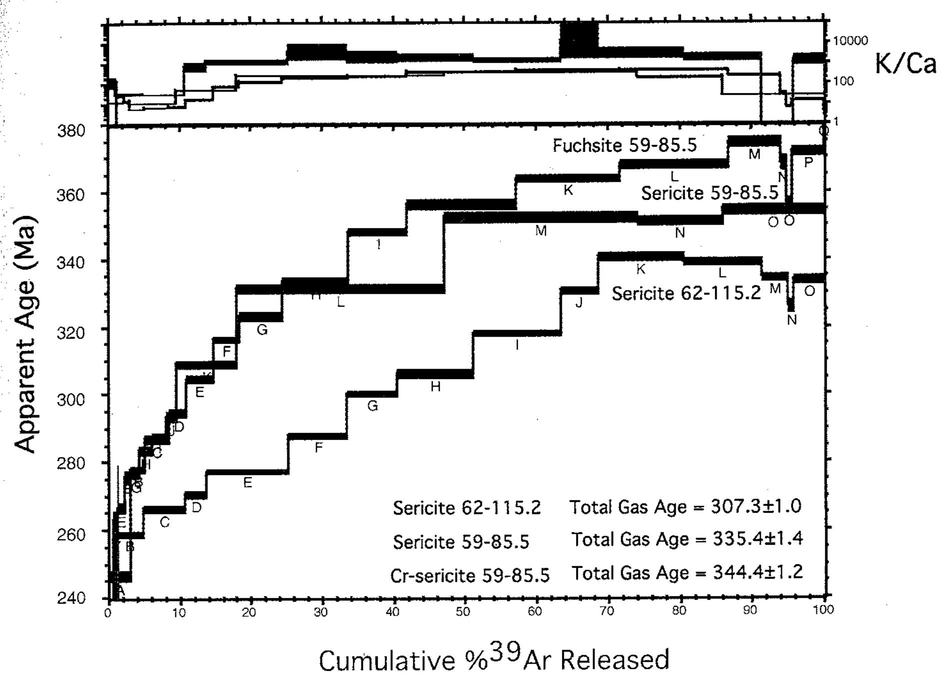

Fig. 7.6. $^{40}Ar/^{39}Ar$ age spectra for fine-grained hydrothermal micas: sericites 59-85.5 and 62-115.2, and fuchsite 59-85.5.

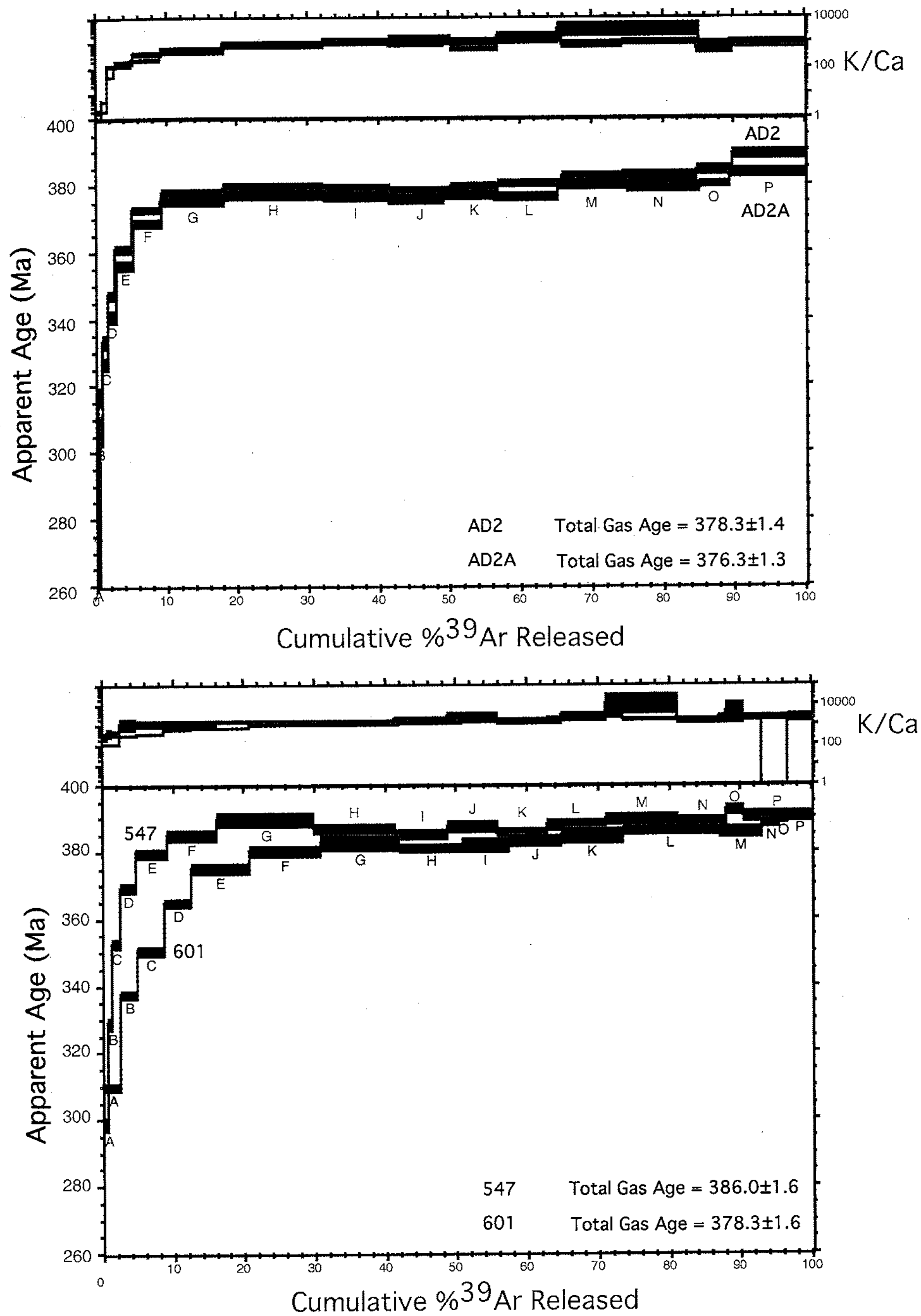

Fig. 7.7. $^{40}Ar/^{39}Ar$ age spectra for coarse muscovites from mineralized zones: AD2, AD2A, 547, and 601.

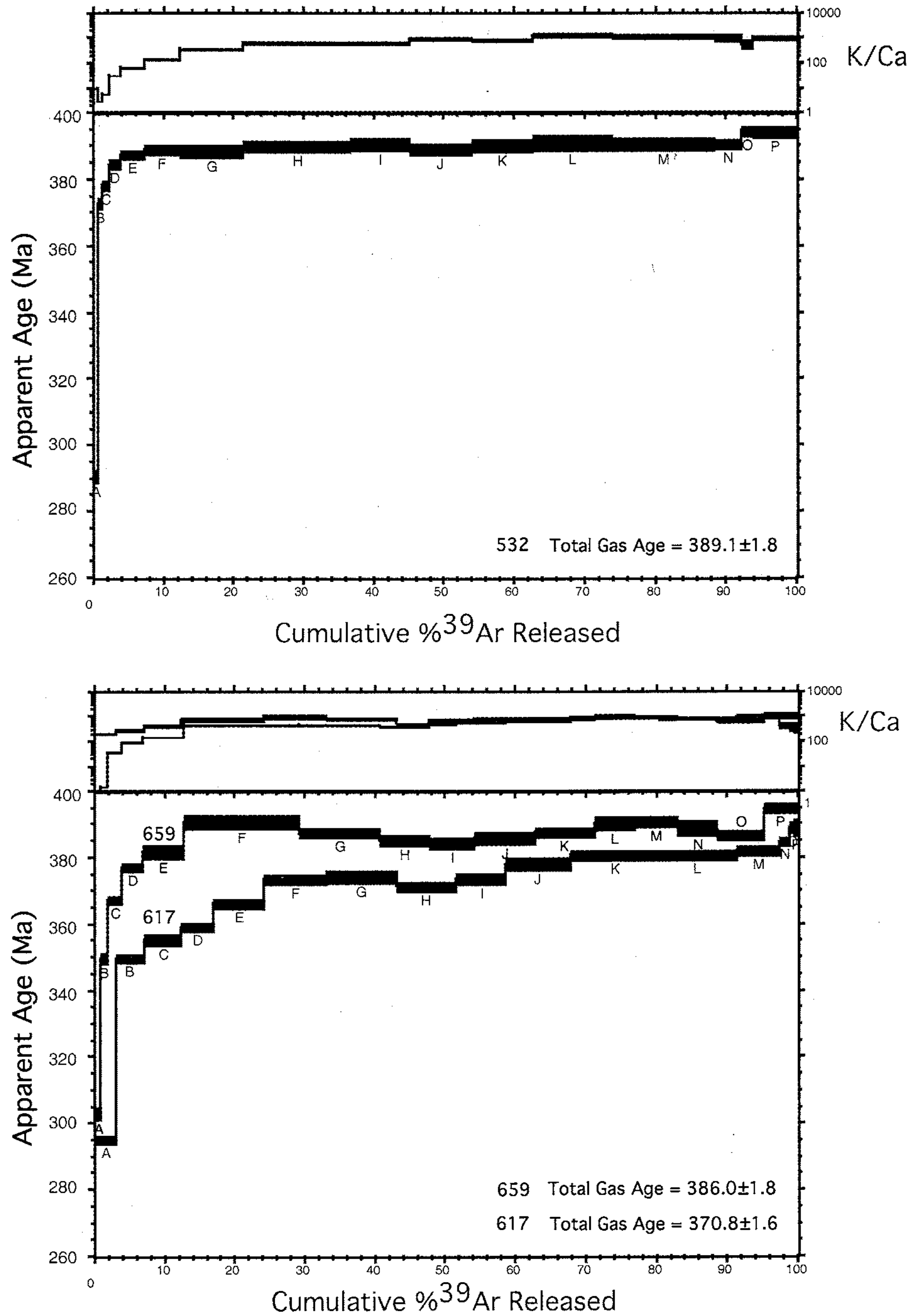

Fig. 7.8. $^{40}Ar/^{39}Ar$ age spectra for coarse muscovites from propilitic vein (532), and barren quartz veins stratigraphically below (617) and above (659) the mineralized zone.

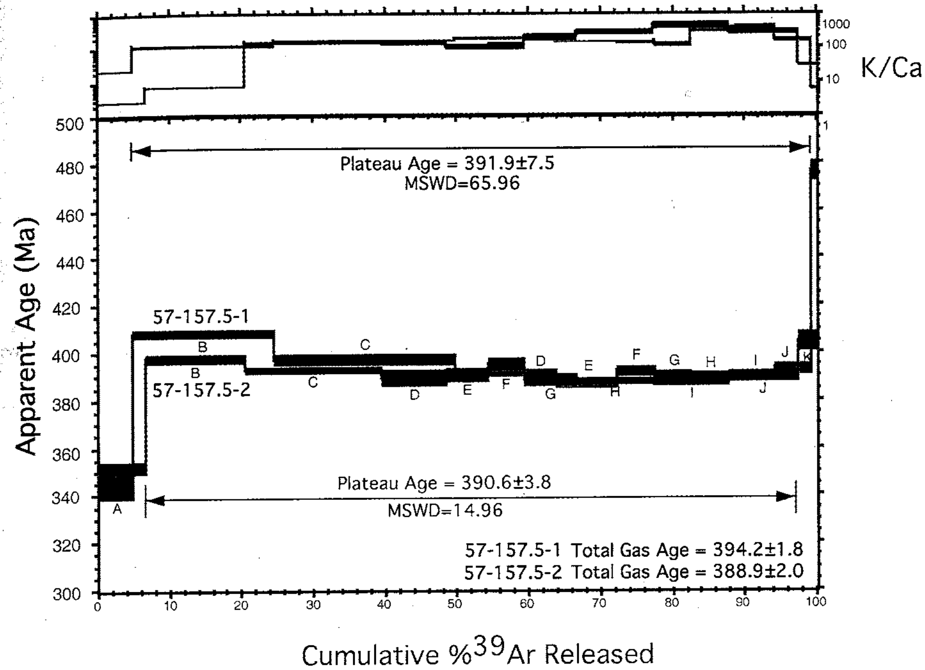

Fig. 7.9. $^{40}Ar/^{39}Ar$ age spectra for hydrothermal biotites 57-157.5-1 and 2.

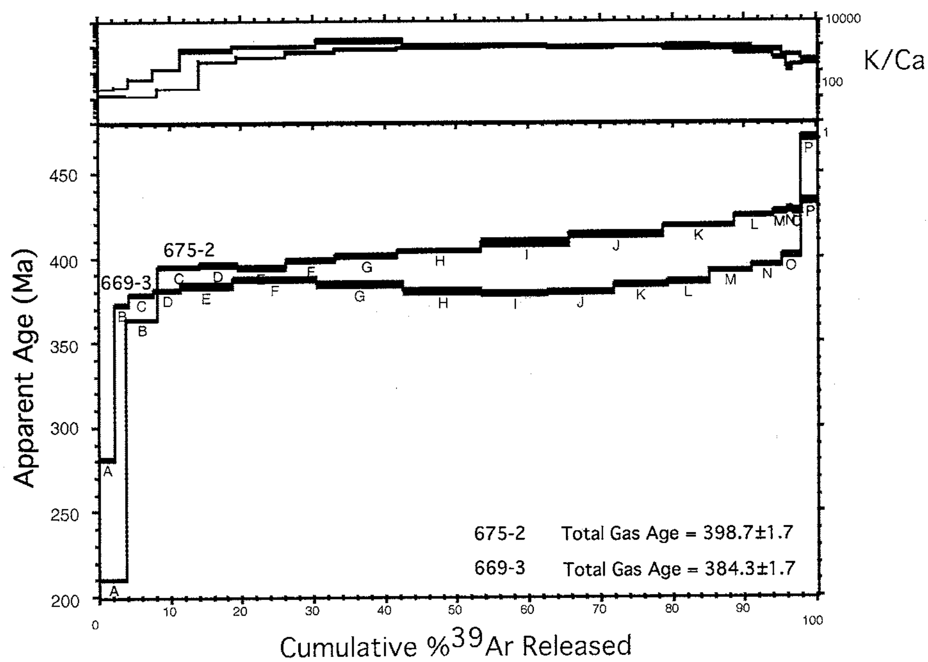

Fig. 7.10. $^{40}Ar/^{39}Ar$ age spectra for fuchsites 669-3 and 675-2.

Table 7.2. Summary of $^{40}Ar/^{39}Ar$ step heating results (phyllosilicates and amphiboles)

Sample ID	Rock type	Mineral	Total Gas Age, Ma		Plateau Age, Ma		Terminal Age[1], Ma	
			Age	±2σ	Age	±2σ	Age	±2σ
	Phenocrysts from alkalic intrusive rocks of the Solton Sary district							
49-113.7	lamprophyre	Zoned biotite	412.3	1.6				
49-129.2	syenite porphyry	Zoned biotite	442.0	1.8				
55-62.7	syenite porphyry	Biotite	380.4	1.3	382.3	0.9		
56-158	syenite porphyry	Biotite	382.4	1.4				
57-166.2	syenite porphyry	Biotite	391.2	1.4				
57-174.1	syenite porphyry	Biotite	379.2	1.4	380.9	1.7		
58-58.3	lamprophyre	Biotite	392.4	1.8				
58-110.2	syenite porphyry	Biotite	369.5	1.2				
76-179.9	lamprophyre	Biotite	390.6	1.5	394.7	1.5		
TR6A	lamprophyre	Amphibole	291.8	1.2				
397	lamprophyre	Amphibole	341.7	1.6				
	Magmatic phases from intrusive rocks other than alkalic rocks of the Solton Sary district							
700-2	Ordovician granite	Biotite	430.5	2.2				
700-2	Ordovician granite	Amphibole	437.5	2.2				
	Hydrothermal phases from the Au-bearing mineralized zone and alteration halos							
59-85.5	QSCP alteration	Sericite	335.4	1.4				
59-85.5	QSCP alteration	Fine fuchsite	344.4	1.2				
62-115.2	QSCP alteration	Sericite	307.3	1.0				
AD2	mineralized quartz vein	Muscovite	378.3	1.4			389.0	1.4
AD2A	mineralized quartz vein	Muscovite	376.3	1.3			383.4	1.5
601	mineralized quartz vein	Muscovite	378.3	1.6			390.4	1.1
547	mineralized quartz vein	Muscovite	386.0	1.6			392.4[2]	1.5
532	barren propylitic vein	Muscovite	389.1	1.8			394.0	1.7
57-157.5-1	biotitic alteration	Biotite	394.2	1.8	391.9	7.5		
57-157.5-2	biotitic alteration	Biotite	388.9	2.0	390.6	3.8		
	Hydrothermal phases spatially unrelated to Au mineralization							
617	barren quartz vein	Muscovite	370.8	1.6			388.9[2]	1.8
659	barren quartz vein	Muscovite	386.0	1.8			394.6	1.6
669-3	alteration, fault zone	Fuchsite	384.3	1.7			401.5[2]	1.8
675-2	alteration, fault zone	Fuchsite	398.7	1.7			433.5[2]	1.8

[1]Presented for selected samples;
[2]Apparent age of step preceding the final step.

Biotites 55-62.7 and 57-174.1, both from syenite-porphyries, returned plateau ages 382.3±0.9 Ma and 380.9±1.7 Ma, respectively (Fig. 7.1). Biotite 76-179.9 from lamprophyre produced a plateau age of 394.7±1.5 Ma (Fig. 7.2). Biotite 57-166.2 (syenite-porphyry) returned a relatively flat spectrum complicated by a "hump" (Fig. 7.2). The total gas age 391.2±1.4 Ma falls into a time interval bracketed by the ages of biotites 55-62.7, 57-174.1 and 76-179.9.

All other mica phenocrysts returned significantly more complex age spectra with rather scattered apparent ages (Fig. 7.3). Total gas ages of biotites 56-158 (382.4±1.4 Ma) and 58-58.3 (392.4±1.8 Ma) are in general agreement with the plateau ages of the other micas mentioned above. Biotite 58-110.2 has a significantly younger total gas age (369.5±1.2 Ma). Total gas ages of zoned biotites 49-113.7 and 49-129.2 are significantly older: 412.3±1.6 Ma, and 442.0±1.8 Ma.

Amphibole phenocrysts from lamprophyres 397 and TR6-A returned irregular age spectra with young and discrepant (relative to micas) total gas ages: 341.7±1.6 Ma and 291.8±1.2 Ma (Fig. 7.4). These amphiboles have actinolite compositions resulted from alteration of original magmatic amphiboles. These complex and erroneously young ages are not meaningful with regards to the timing of magmatism and are not further discussed.

Biotite-amphibole pair 700-2 from an Ordovician granitic batholith produced discordant age spectra with total gas ages of 430.5±2.2 Ma (biotite) and 437.5±2.2 Ma (amphibole) (Fig. 7.5). The anomalously low K/Ca ratio of the biotite reveals its strong secondary chloritization, which presumably contributes to the age spectrum complexity.

Due to the complexity of these data, the ages of biotite and amphibole 700-2 are not considered reliable.

All samples of hydrothermal white micas returned age gradients indicative of post-crystallization ^{40}Ar loss. The age gradients range from ca. 260-300 Ma to ca. 340-390 Ma. The degree of argon loss and maximum step ages are strongly correlated to grain size. Age spectra of fine white micas from mineralized zones (sericites 59-85.5 and 62-115.2, and fine fuchsite 59-85.5) comprise well-defined broad age gradients with poorly developed or completely absent flat portions at high temperatures (Fig. 7.6). Maximum step ages vary from ca. 340 to 375 Ma and are unlikely to reflect true crystallization ages.

Age spectra of coarse muscovites from auriferous quartz veins (Fig. 7.7), propylitic veins and barren quartz veins outside the mineralized zone (Fig. 7.8) differ from age spectra of fine micas. The initial heating steps (ca. 0-20% of released ^{39}Ar) generate steep age gradients that are followed by relatively flat release patterns. These flat portions usually show some increase of apparent ages, and sometimes exhibit a slightly concave geometry. Maximum step ages (terminal ages) of muscovites from mineralized zones are 390.4±1.1 Ma (601), 392.4±1.5 Ma (547); 389.0±1.4 (AD2), and 383.4±1.5 Ma (AD2A). Terminal ages of all other muscovite samples are generally similar: 394±1.7 Ma (532), 394.6±1.6 Ma (659), and 388.9±1.8 Ma (617). The age spectra of coarse muscovites indicate some ^{40}Ar loss that apparently is less severe than that experienced by fine white micas and is unlikely to have significantly affected the most retentive portions of coarse muscovite crystals. Thus, in contrast with fine white micas, high temperature portions of age spectra of muscovites, and especially their maximum step ages could represent reasonably good approximations of crystallization ages.

Hydrothermal biotites 57-157.5-1 and 57-157.5-2 were collected from two different biotite-carbonate veinlets hosted in the same drill core sample. Initial heating steps show young apparent ages (ca. 340-350 Ma) following by a steep rise before falling to relatively flat segments at ca. 390 Ma (Fig. 7.9). Final heating steps show an increase of apparent ages (up to ca. 475 Ma, sample 57-157.5-1) accompanied by a decrease of K/Ca ratios that probably reflects release of excess ^{40}Ar from contaminant mineral phases. Total gas ages are 394.2±1.8 Ma (57-157.5-1) and 388.9±2.0 Ma (57-157.5-2). Plateau ages incorporating all but the initial and final heating steps are indistinguishable for these two samples: 391.9±7.5 Ma (57-157.5-1) and 390.6±3.8 Ma (57-157.5-2).

Fuchsites from syn-tectonic alteration halo of the South Kumbel fault (two aliquots of 669-3 and 675-2) returned complex age spectra that are in some respects similar to the coarse muscovite age spectra (Fig. 7.10). The low temperature age gradients are steep and comprise only two heating steps (about 5-10% of ^{39}Ar). Following this, the age spectra exhibit either a linear, monotonous increase of apparent ages (ca. 395-430 Ma, sample 675-2), or a more complex, upward concave geometry comprising a general apparent age increase from about 380 Ma to about 400 Ma (sample 669-3). Final heating steps of both aliquots of sample 669-3 return anomalously old ages (462 and 471 Ma) that are likely related to excess ^{40}Ar degassing from contaminant phases. The age spectra of these chromium rich tectonogenic micas suggest that they underwent some ^{40}Ar loss, but high temperature step ages (433.5 Ma, sample 675-2; 401 and 408 Ma, two aliquots of 669-3, excluding results of last steps) may provide a minimum estimate for their crystallization age.

UV laser in situ ablation analysis

The UV laser in situ ablation analysis was intended to investigate the crystal-scale distribution of the apparent $^{40}Ar/^{39}Ar$ ages in order to assist the interpretation of the step heating $^{40}Ar/^{39}Ar$ data and to provide additional information on the geologic age of the magmatism and mineralization of the Solton Sary district. The UV laser in situ ablation analysis allows high spatial resolution, but for samples with apparent age of ca. 500-400 Ma, the precision of age determinations is lower compared to the step heating technique. The ablation of a relatively small amount of sample material releases correspondingly small amounts of $^{40}Ar^{*}$. This results in low mass spectrometer analytical signals, less systematic change of peak heights during measuring cycles, and consequently, in less certain time zero extrapolation and relativeliy impresise apparent ages. For similar reasons, results of the UV laser in situ ablation analysis are more sensitive to blank corrections compared to those of step heating technique. In spite of these negative aspects, the method is capable of providing important information on intra-crystalline age zoning that cannot be derived from the step heating data.

The results of the UV laser in situ ablation analyses are presented in Appendix D, Table D.2 and Figures 7.11-7.22. Each figure includes a photomicrograph, an age versus position graph of the in situ ablation analysis, an age spectrum produced by the furnace step heating experiment on a multigrain separate of the same sample, and an age-probability distribution diagram. The latter was originally introduced by Deino and Potts (1992) and is generally used to display a set of single-crystal dates, however in this study, these diagrams are used to illustrate the statistical significance of in situ age populations.

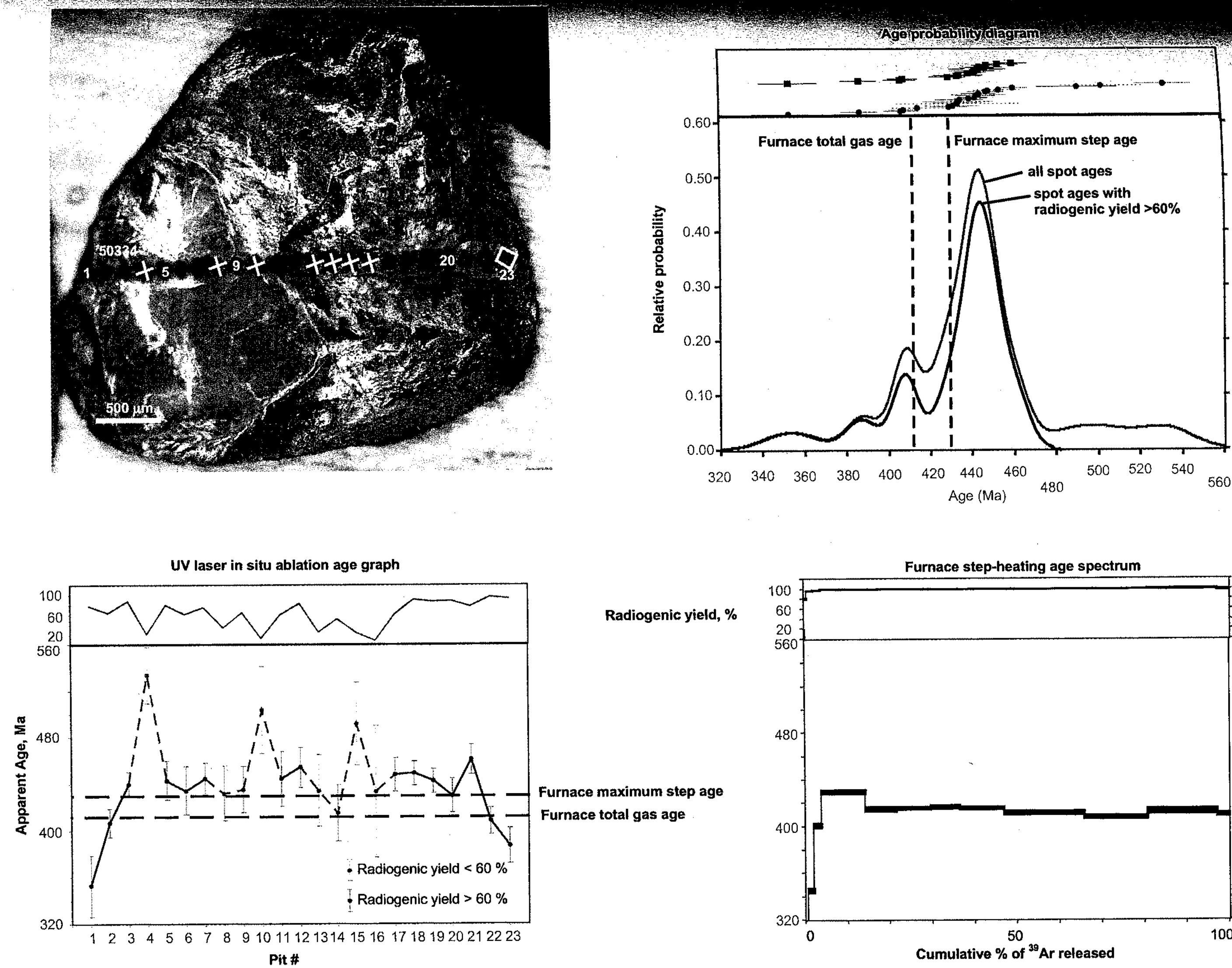

Fig. 7.11. Results of the in situ ablation $^{40}Ar/^{39}Ar$ analysis of zoned biotite 49-113.7-1.

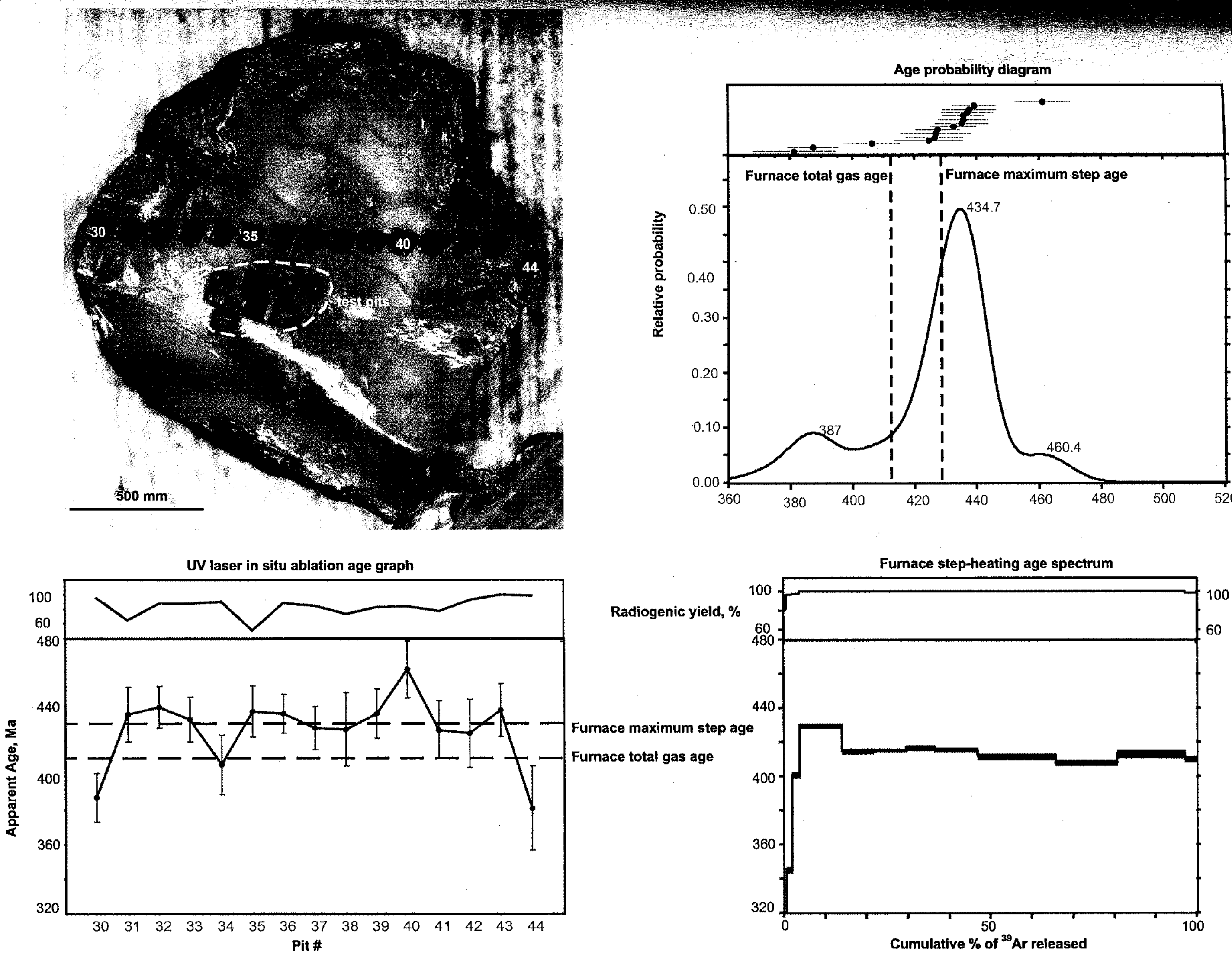

Fig. 7.12. Results of the in-situ ablation $^{40}Ar/^{39}Ar$ analysis of zoned biotite 49-113.7-2.

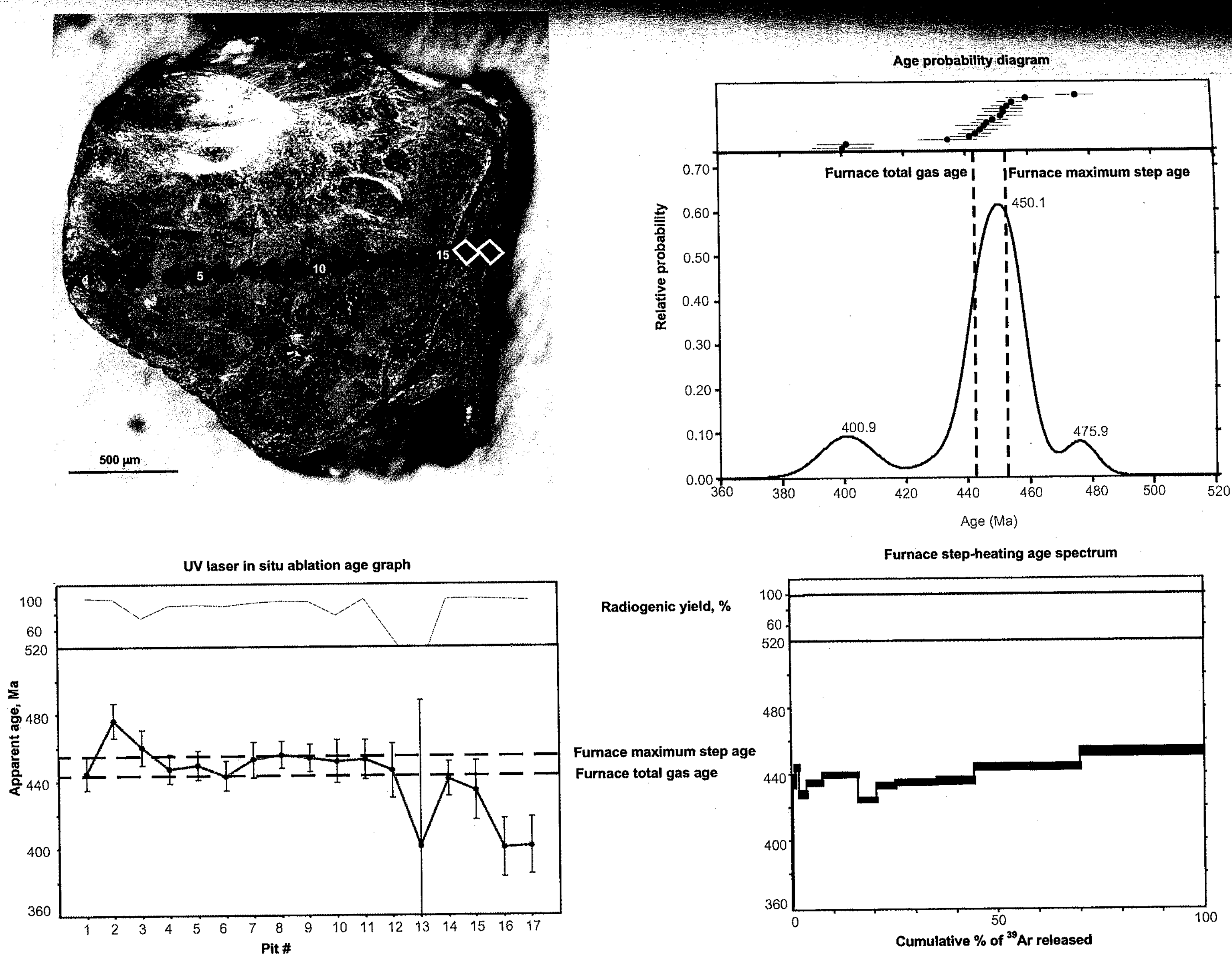

Fig. 7.13. Results of the in situ ablation $^{40}Ar/^{39}Ar$ analysis of zoned biotite 49-129.2.

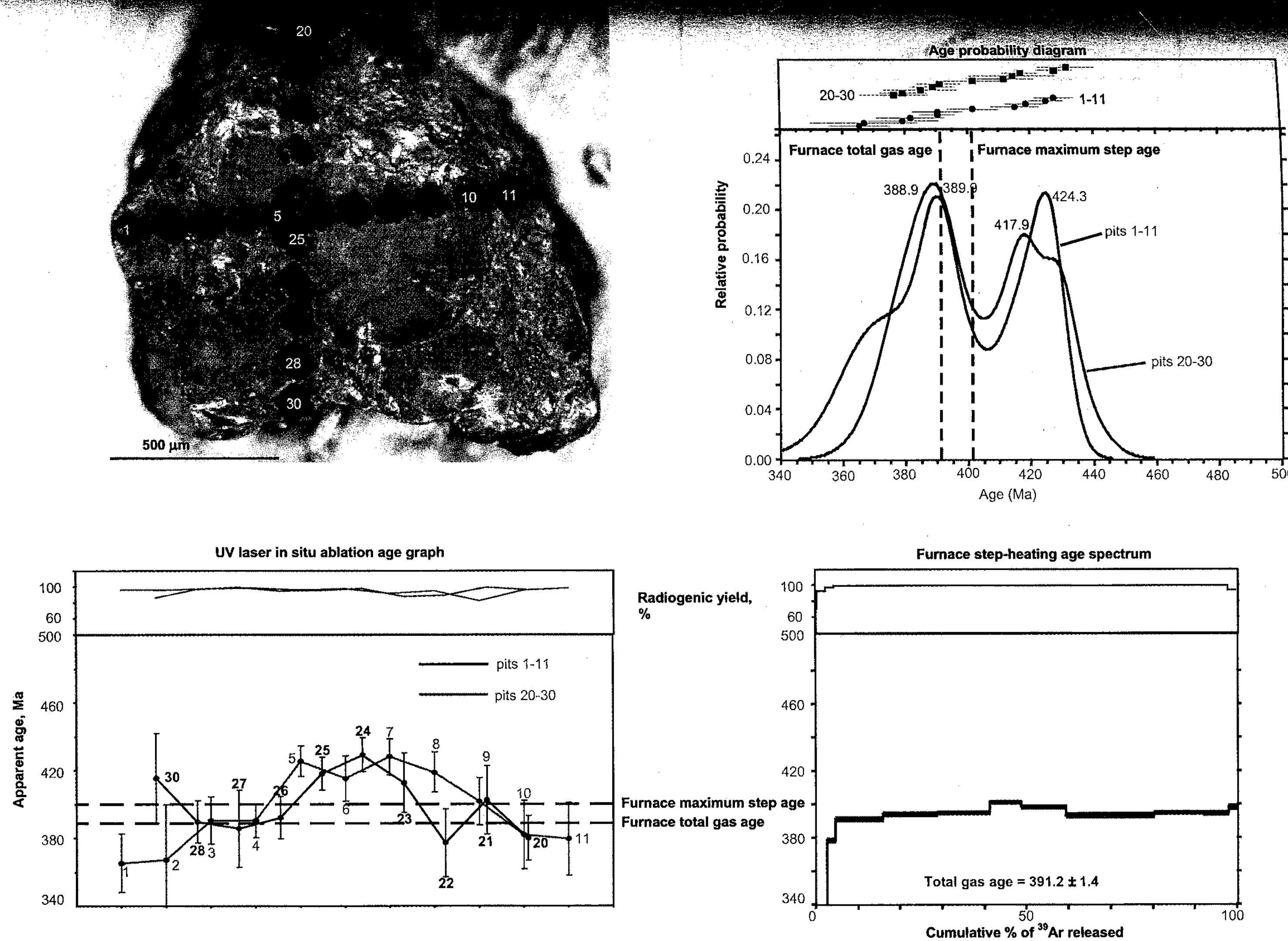

Fig. 7.14. Results of the in situ ablation $^{40}Ar/^{39}Ar$ analysis of biotite 57-166.2-1.

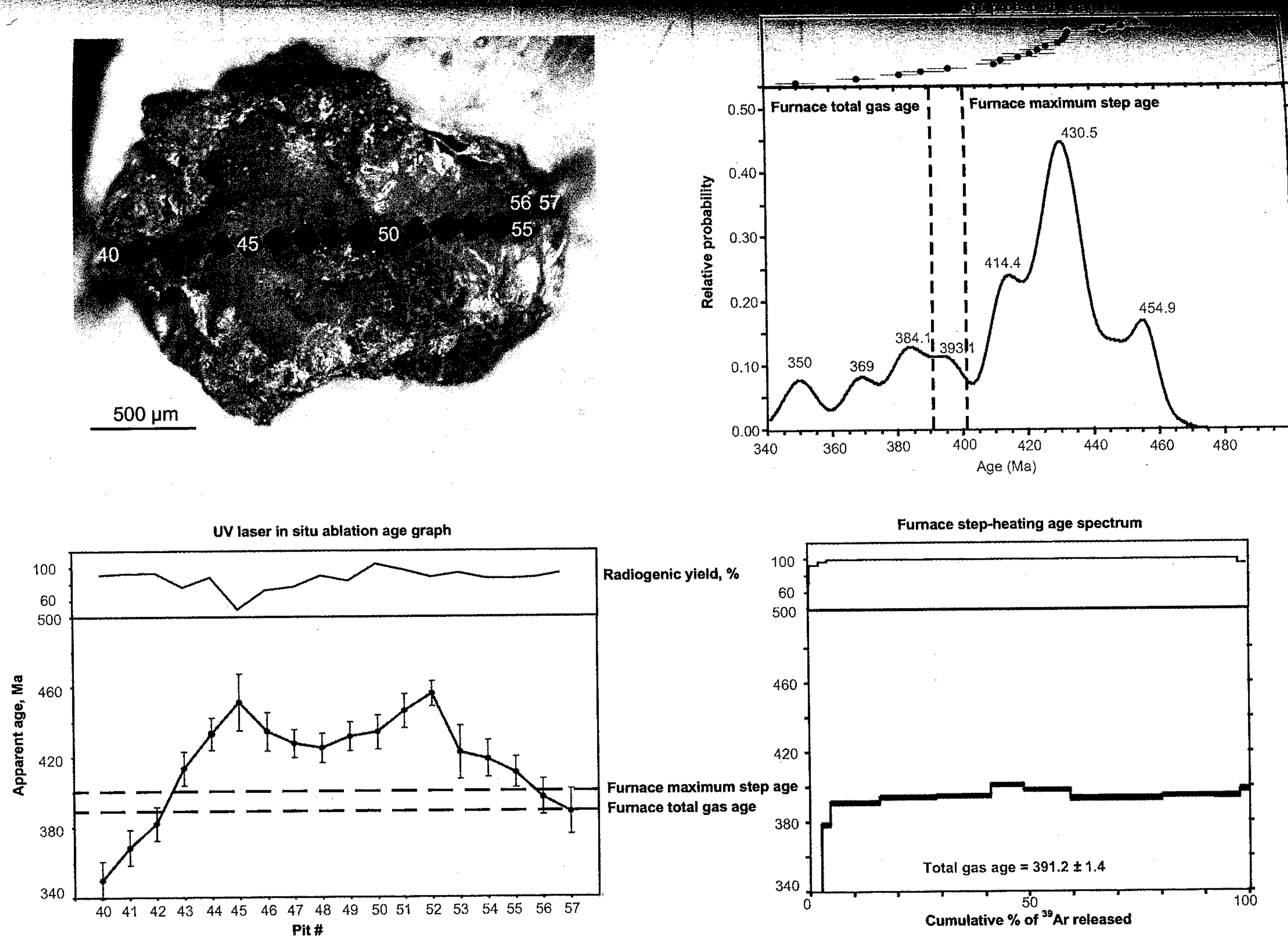

Fig. 7.15. Results of the in situ ablation $^{40}Ar/^{39}Ar$ analysis of biotite 57-166.2-2.

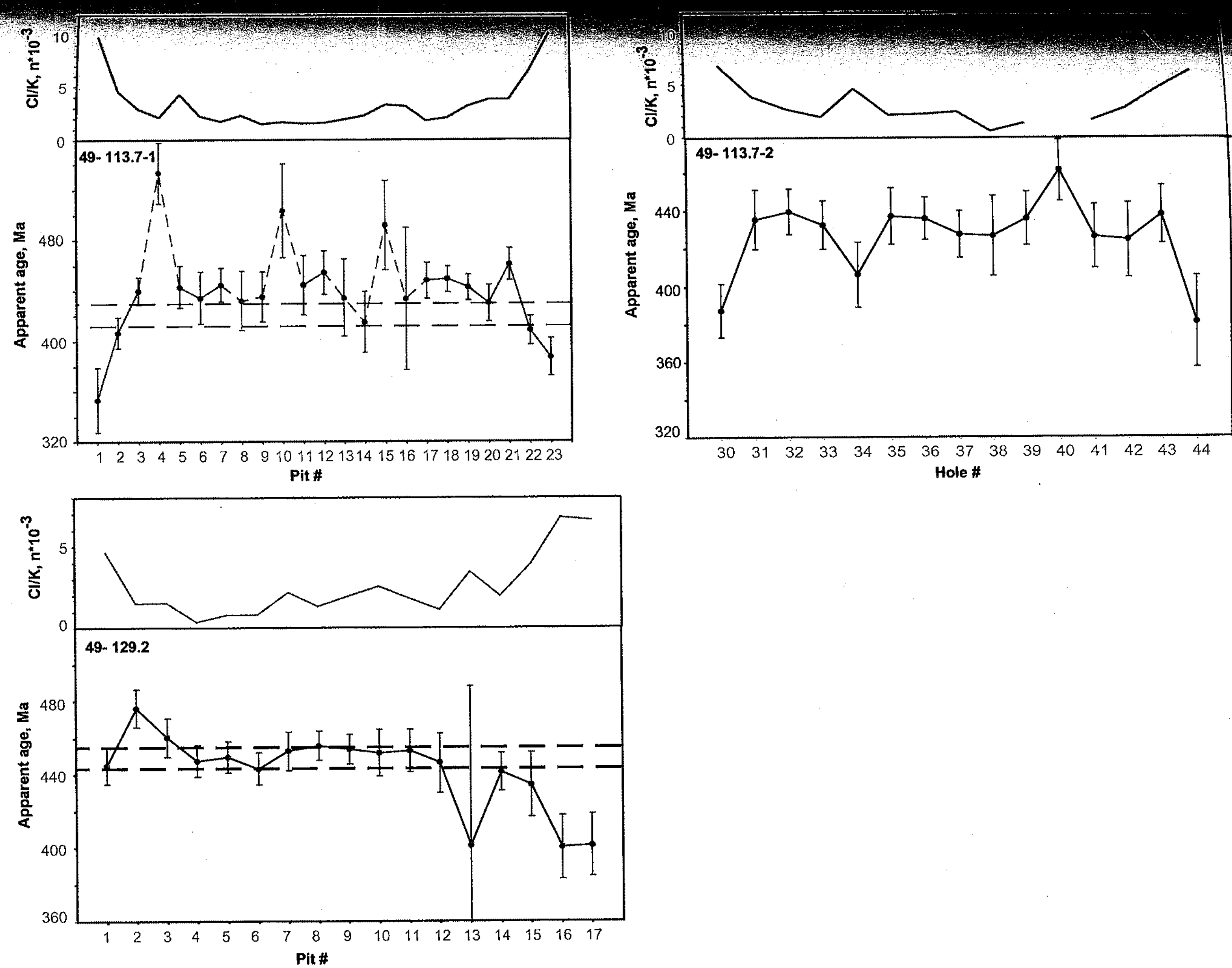

Fig. 7.16. Systematic variation of the Cl/K ratio in mica phenocrysts from lamprophyres and syenite porphyries.

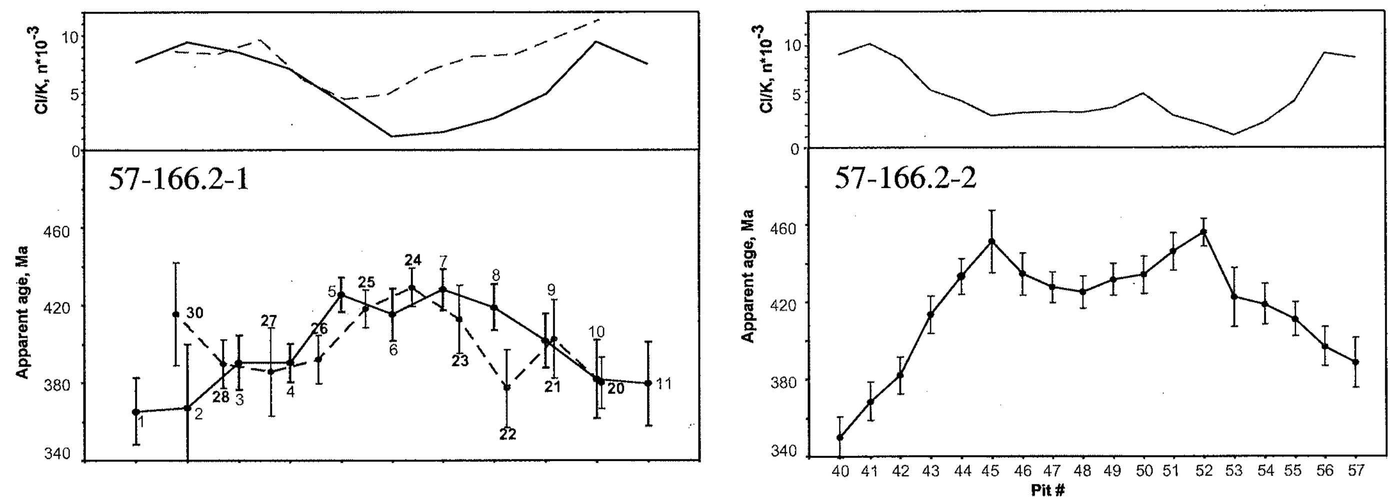

Fig. 7.16. (Continued).

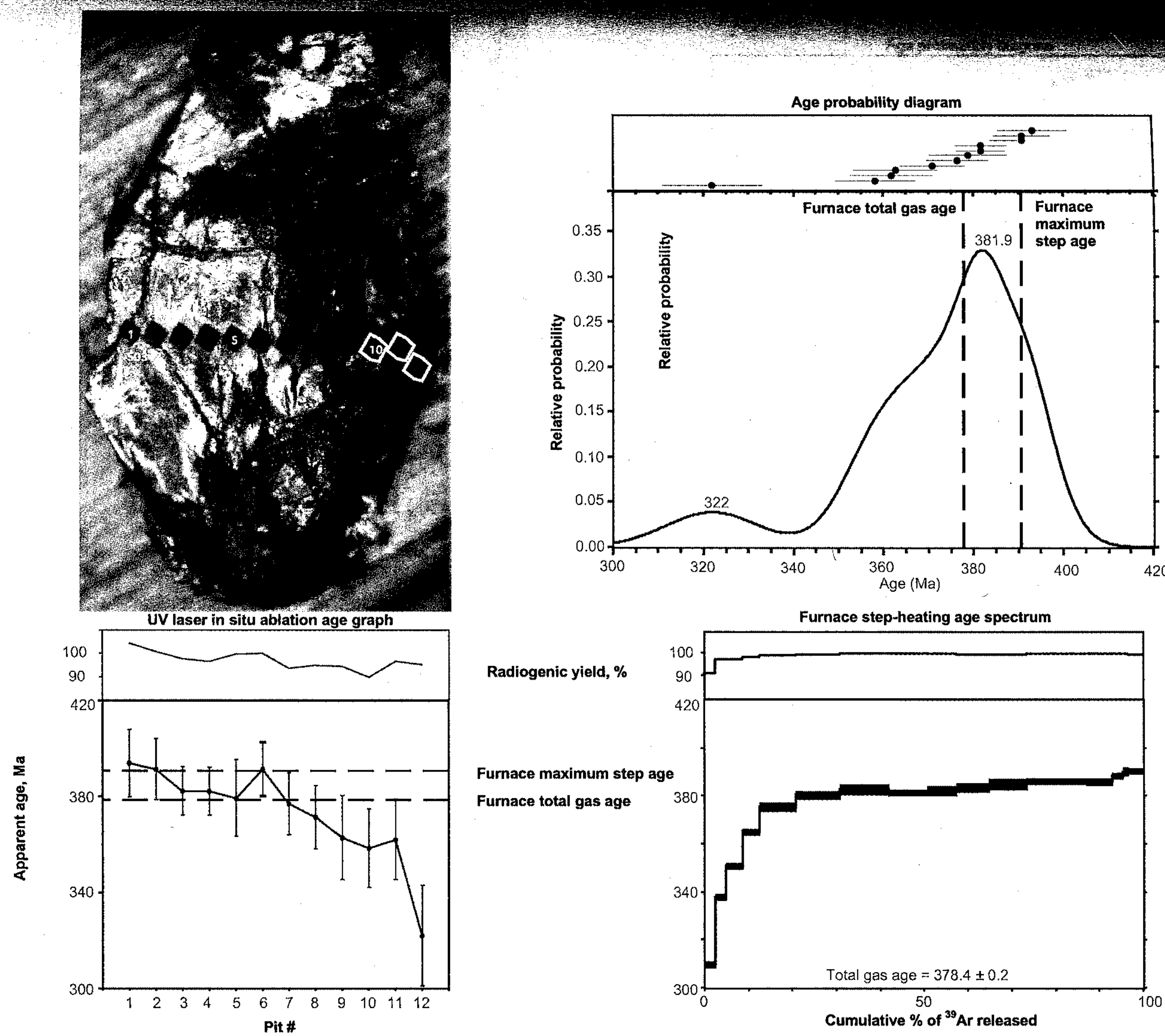

Fig. 7.17. Results of the in situ ablation $^{40}Ar/^{39}Ar$ analysis of muscovite 601-1.

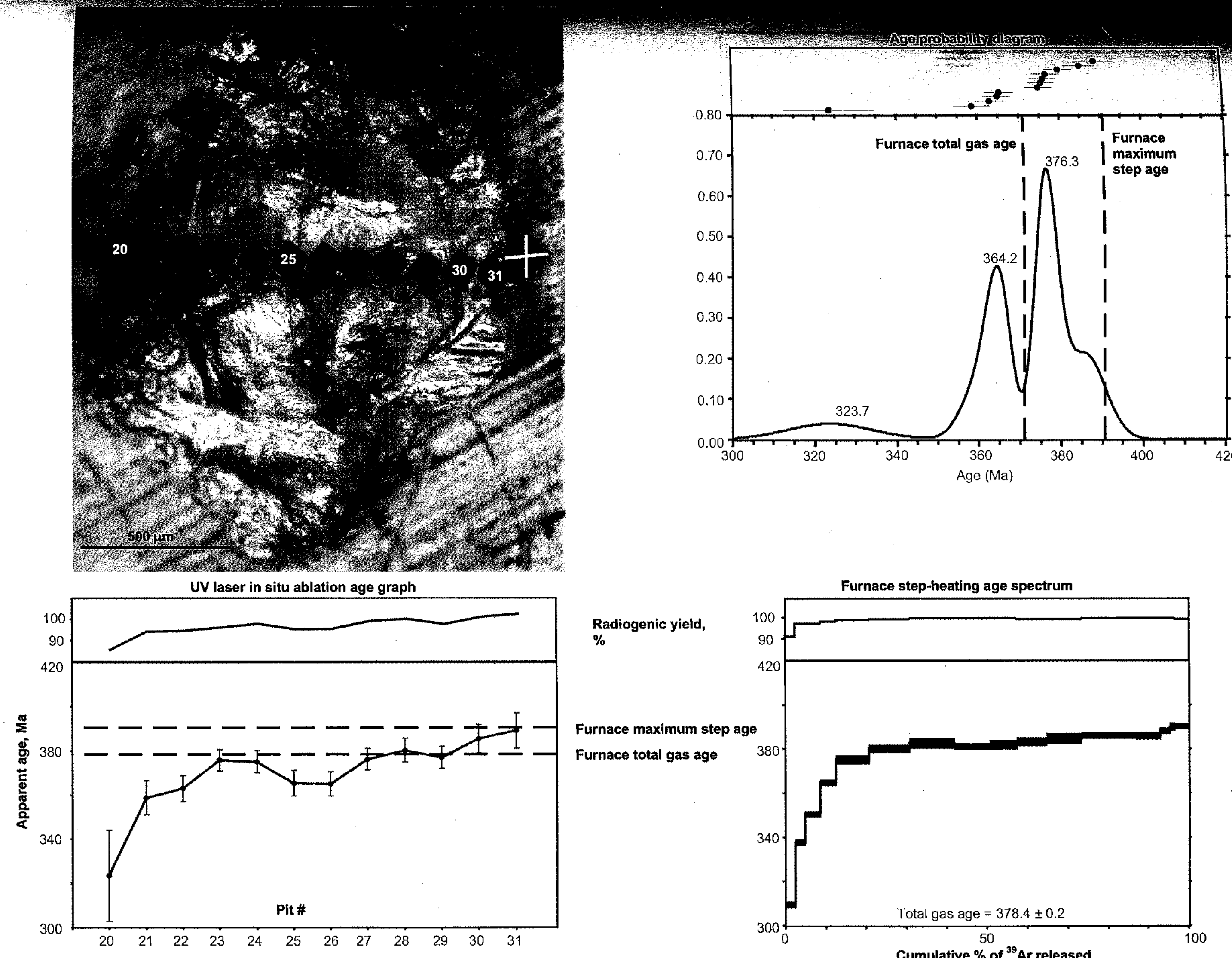

Fig. 7.18. Results of the in situ ablation $^{40}Ar/^{39}Ar$ analysis of muscovite 601-2.

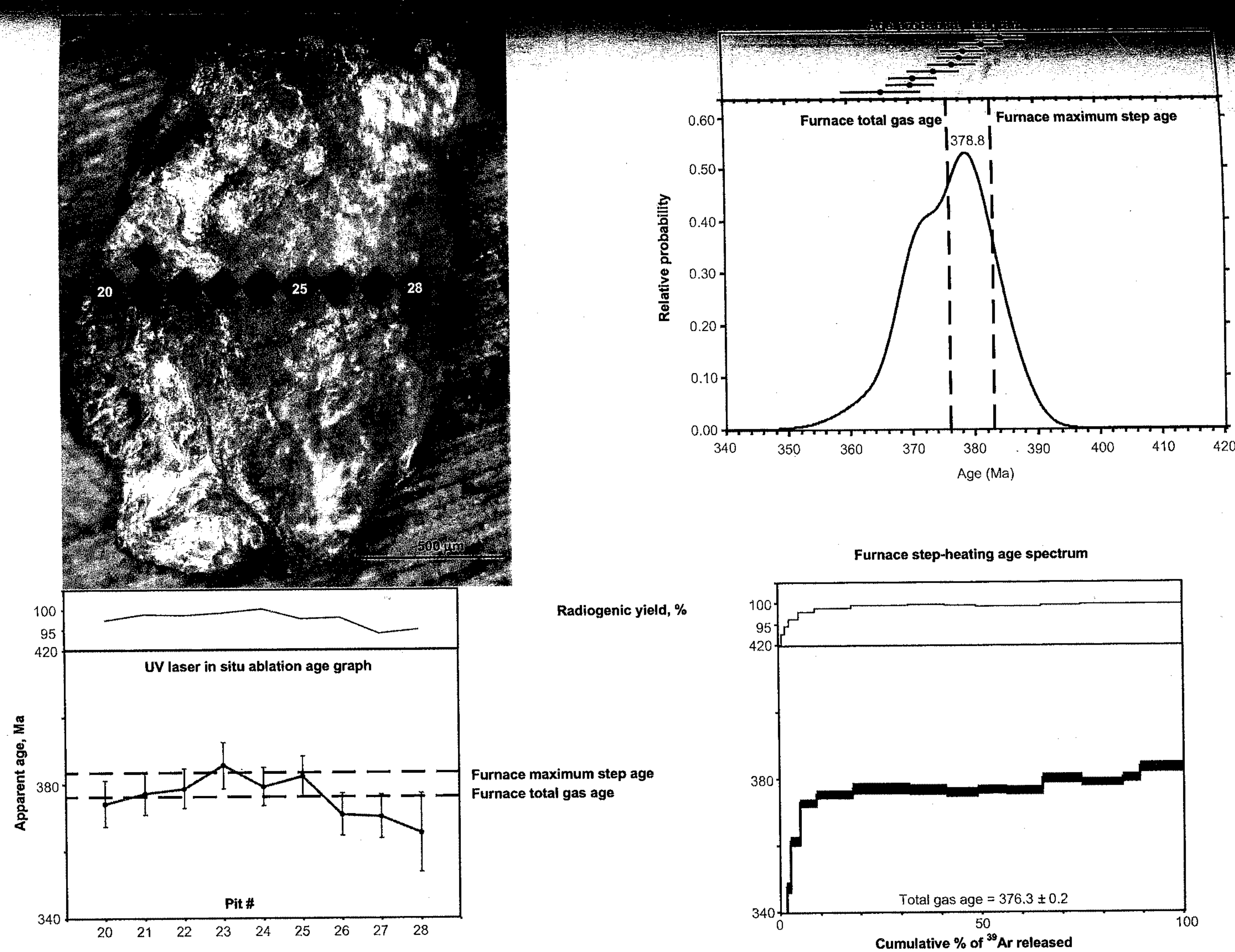

Fig. 7.19. Results of the in situ ablation $^{40}Ar/^{39}Ar$ analysis of muscovite AD2A

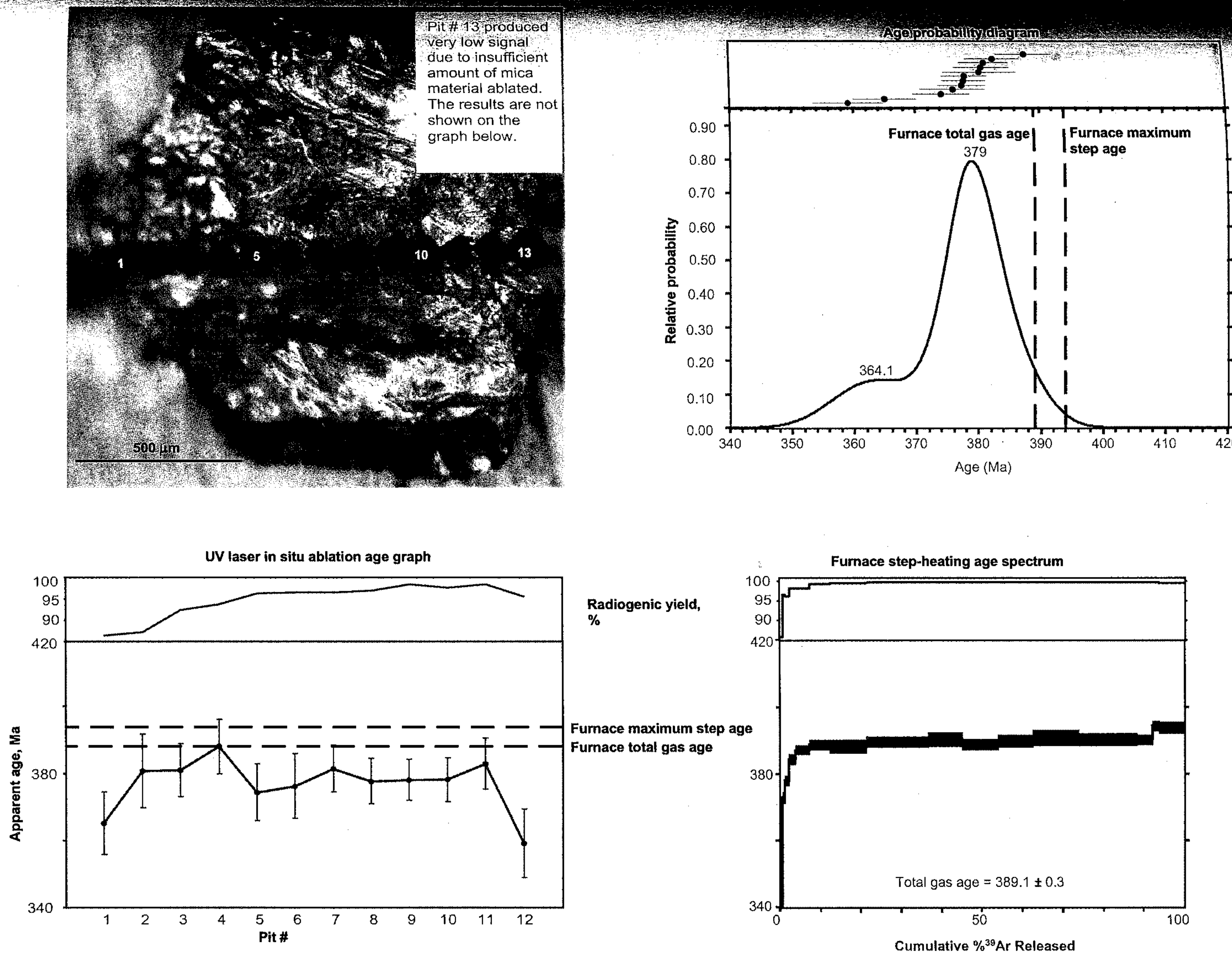

Fig. 7.20. Results of the in situ ablation $^{40}Ar/^{39}Ar$ analysis of muscovite 532.

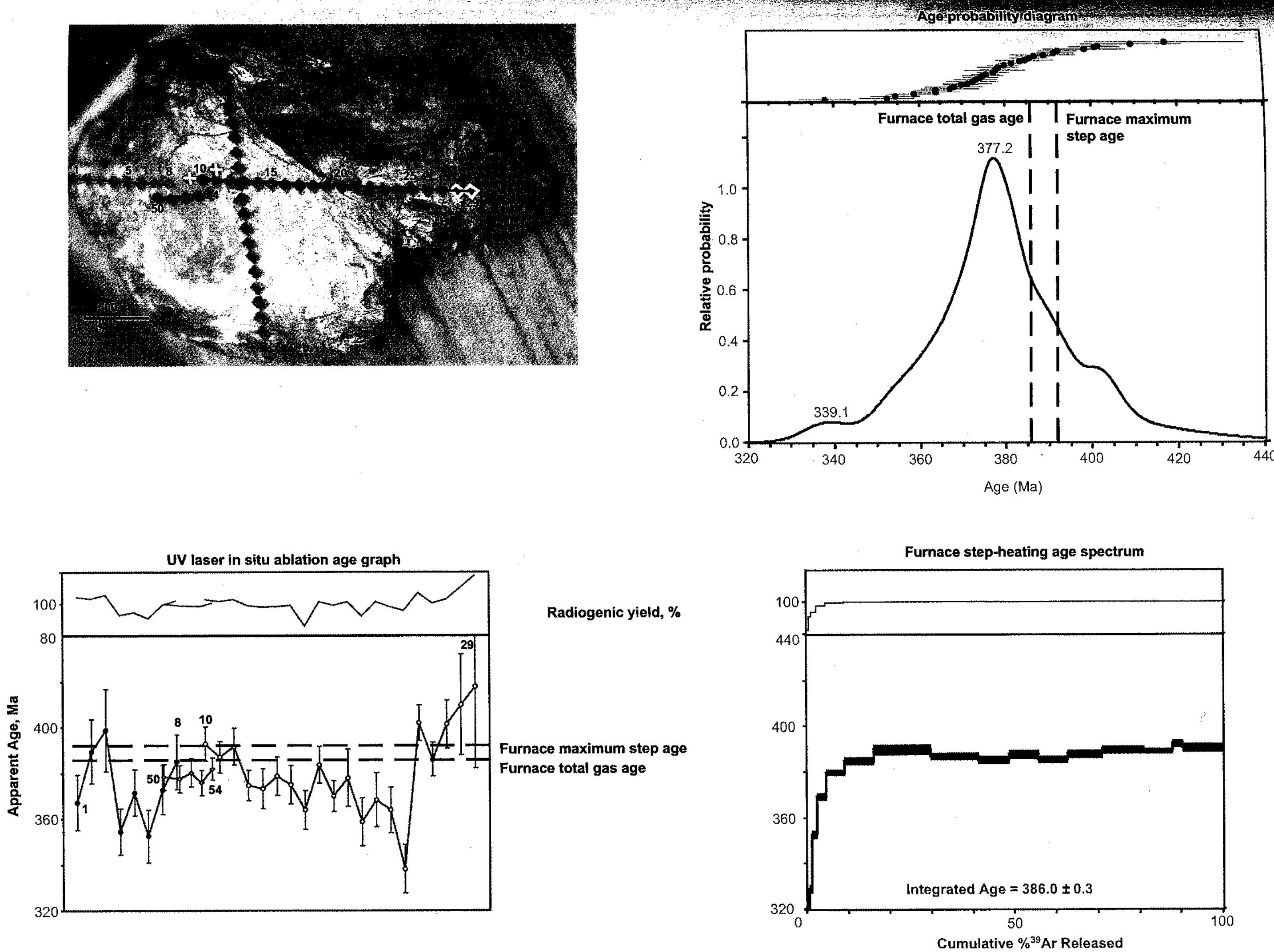

Fig. 7.21. Results of the in situ ablation $^{40}Ar/^{39}Ar$ analysis of muscovite 547 (traverse 1).

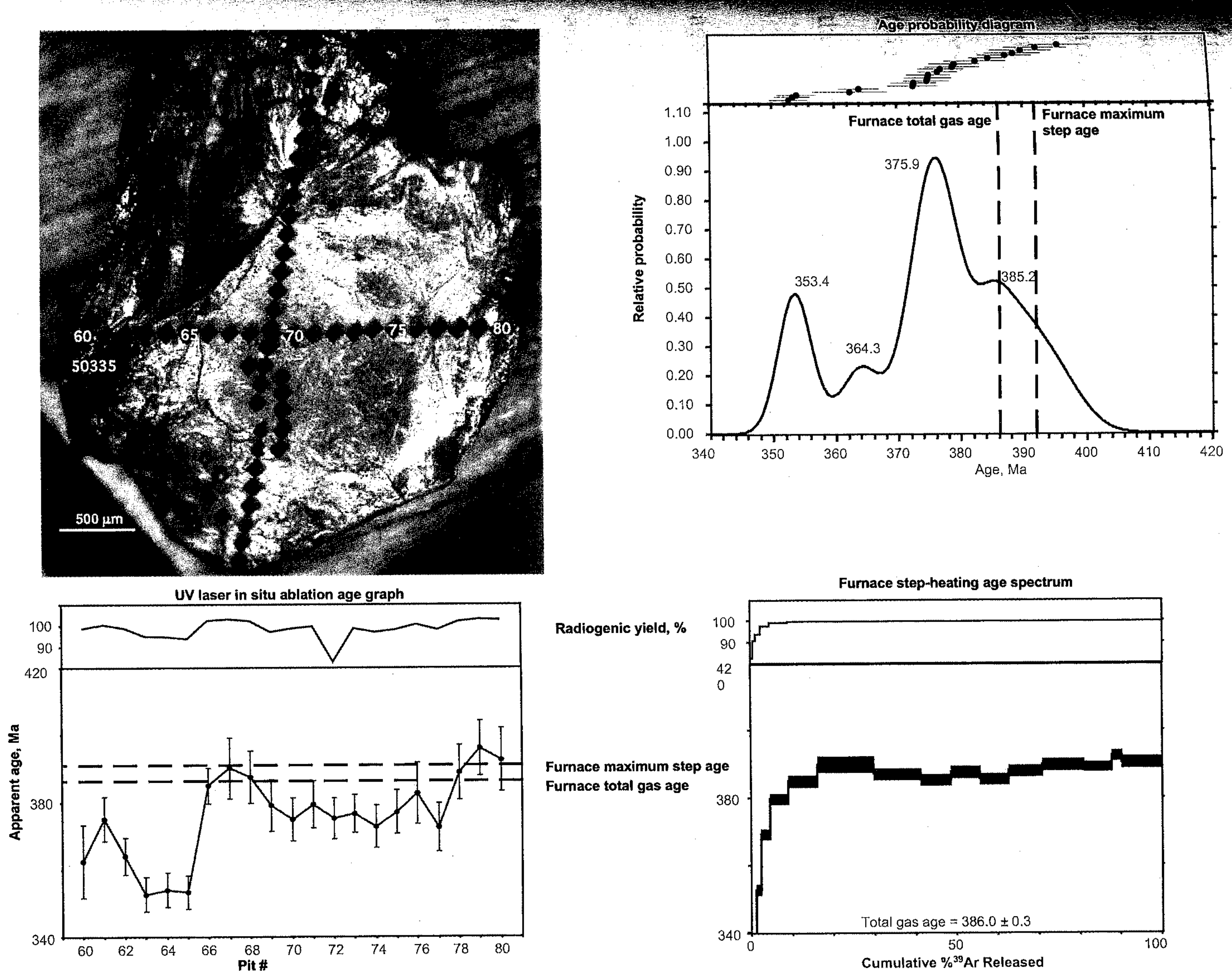

Fig. 7.22. Results of the in situ ablation $^{40}Ar/^{39}Ar$ analysis of muscovite 547 (traverse 2).

Zoned biotites 49-113.7-1 and -2 (Figs. 7.11 and 7.12) produced age profiles with younger apparent ages at the grain margins and older in situ ages in the central portions of the grains, that cluster at about 435 (49-113.7-2) and 440 (49-113.7-1) Ma. There are also several older and minor younger age outliers within crystal cores. In the case of the mica 49-113.7-1, most of the highly uncertain anomalously old ages correlate with low radiogenic yields and are thought to be related to excess ^{40}Ar. "Removal" of apparent ages with radiogenic yields below 60 percent reveals a more concordant age distribution (Fig. 7.11). Most of the in situ ages from the central portion of the crystal are older than the total gas age determined from the step heating analysis.

Zoned biotite 49-129.2 generated an asymmetric age profile, with younger apparent ages (400-401 Ma) on one side of the crystal (Fig. 7.13). Most of the ages from the core and left edge vary from 445 to 455 Ma and overlap within the analytical error. A young and extremely uncertain (401± 87 Ma) age yielded at pit 13 is characterized by a very low radiogenic yield (5.5%) and is unlikely to be meaningful. The laser in situ ablation results are in general agreement with the data of the step heating experiment, where the maximum apparent age and total gas age were 453.1±2.4 Ma and 442±1.8 Ma, respectively.

Biotite 57-166.2-1 was sampled by two nearly perpendicular traverses (Fig. 7.14). Both traverses returned similar age graphs where (except for one, pit 30) younger ages are found near grain margins and older ages broadly correspond to the grain interior. In situ ablation ages from the central part of the grain (pits 5, 6, 7, 8, and 23, 24, 25) vary from 412.2 Ma to 428.6 Ma and overlap within the analytical error. Biotite 57-166.2-2 gave the most precise results (±10-12 Ma) of all in situ analyses. The age profile is characterized by a well-defined gradient from 350 Ma to about 450 Ma that is nearly symmetric about the central part of the grain (Fig. 7.15). The individual ages within the central portion vary from 425 to 456 Ma averaging about 430 Ma. All in situ ages from the central part of the core exceed both the maximum step age and total gas age of the step heating analysis.

In addition to variations of the apparent ages, virtually all biotite samples exhibit a systematic variation of the Cl/K ratio with the highest values corresponding to the rims and the lowest found at the cores of the grains (Fig. 7.16). This zoning creates the effect of negative correlation between the apparent ages and the Cl/K ratio.

Muscovite 601-1 returned in situ ages varying from 322.0 to 393.5 Ma. The youngest age was produced by a deformed grain margin stained by iron oxides (Fig. 7.17). Most of the in situ ages are indistinguishable within the analytical error and overlap with the maximum step age and the total gas age of the furnace step heating analysis. Results from muscovite 601-2 are characterized by lower analytical errors, but otherwise are similar to the data from the muscovite 601-1 (Fig. 7.18). Asymmetric shape of age graphs can be explained by the fact that these anhedral grains represent fragments of larger crystals broken along kink bands or fractures. A monotonic increase of in situ ages from one side of the grain to the other most likely represents margin-to core age increase of grain fragments.

Muscovite AD2A produced a slight age gradient, but virtually all in-situ ages are indistinguishable at the 2σ level (Fig. 7.19). The in-situ ablation ages are similar to the step heating ages.

The age profile produced by muscovite 532 (Fig. 7.20) is characterized by short age gradients at the margins of the grain and a relatively flat distribution for its central part. Most of the in situ ages are indistinguishable at the 2σ level and are younger than the total gas age of the step heating experiment. One in situ age (388.0±8.1 Ma) overlaps with the maximum step age of the incremental heating analysis.

In situ age results returned by muscovite 547 are the most complex (Fig. 7.21). The first traverse consisted of three sections (pits 0-8, 50-54, 10-29) and was oriented parallel to the elongation of the grain. The geometry of the age profile is somewhat complex. Many individual ages are characterized by high uncertainties. The first three pits (1-3) show an increase in the apparent age from 367 Ma to 399 Ma, then there is an abrupt drop to 355 Ma. This is followed by a section (pits 4-8, 50-54, 10-24) where in situ ages vary from 338 Ma to 392 Ma. This part of the graph is slightly convex, complicated by strong fluctuations of the individual ages. The final portion of the profile (pits 25-29) represents an area adjacent to an inclusion of hydrothermal quartz. This part is characterized by anomalously old ages (402-418 Ma), increasing uncertainties and elevated Cl/K values (Appendix D, Table D.2). Most likely, pits 25-29 sampled a mixture of quartz and muscovite. The old ages and high Cl/K ratios can be explained by the release of excess ^{40}Ar and Cl-derived ^{38}Ar from fluid inclusions hosted in quartz. The second profile intersected the grain across its elongation and returned more precise results. The age graph starts with a segment of relatively young ages (ca. 350-360 Ma) that correspond to a kinked margin of the grain (Fig. 7.22). The rest of the traverse produced older ages (ca. 375-390 Ma) and a characteristic concave geometry of the age

About 50 percent of in situ ages overlap with the total gas age, and some of them the maximum step age of the step heating experiment.

The Cl/K ratio varied in muscovites, but in contrast to the biotites, this variation was clearly systematic. In many cases, ^{38}Ar values were below detection limits which oduced apparent negative Cl/K values (Appendix D, Table D.2). The highest values of Cl/K ratio were generated by the traverse 547-1, pits 27-29, and are apparently caused ablation of hydrothermal quartz with Cl -rich fluid inclusions.

Discussion

^{40}Ar/^{39}Ar dating of magmatic biotites

UV laser in situ ablation analysis of magmatic micas from alkalic intrusive rocks revealed systematic crystal-scale variations of apparent ages. In zoned biotites (49-113.7 and 49-129.2), the younger ages occur at the very outer rims (not more than 250 μm from edges) and tend to increase towards the center forming steep age gradients. In situ ages from central portions of the zoned micas are typically internally consistent, except for some anomalously old outliers most of which are characterized by low radiogenic yields. With the exception of mica 49-129.2, the in situ ages of biotite cores are distinctly older than the step heating total gas ages of the same samples. In unzoned micas (57-166.2-1 and 2), edge-center age gradients are better defined and occupy larger areas of the crystals compared to the zoned micas.

The observed crystal-scale zoning of the apparent ages suggests post crystallization ^{40}Ar loss. Biotite 57-166.2-2 shows the strongest effects of this process. The ages from the core of this biotite tend to be younger compared to those of four other mica crystals.

Most of the in situ ages from the cores of the biotites 49-113.7, 49-129.2, and 49-166.2-2 fall in a range of ca. 430-455 Ma. These ages either approximate the timing of magma emplacement and cooling or are anomalously old due to the presence of excess ^{40}Ar. Excess ^{40}Ar can be concentrated in some discrete domains (e. g., inclusions of secondary phases, crystallographic defects) or be distributed throughout the crystal (Pickles et al., 1997). In the first case, the excess ^{40}Ar would produce sporadic anomalously old in situ ages. The "pervasive" excess ^{40}Ar may generate a systematic edge-core decrease of the apparent ages (Pickles et al., 1997) or may be (in a case of complete resetting of the isotopic system) distributed homogeneously and thus be not distinguishable from radiogenic ^{40}Ar.

Anomalous age spikes complicating otherwise concordant age graphs of mica cores (e. g., 49-113.7-1, pits 4, 8, 10, 15; 49-113.7-2, pit 40; 49-129.2, pit 2) are probably related to some excess ^{40}Ar perhaps residing in small pockets of chloritization, hematite coatings, apatite inclusions, or deformation-induced crystal defects. Most of these age anomalies are characterized by low radiogenic yields and due to their discrete nature they can be easily identified and excluded from interpretation. The question of occurrence of "pervasive" excess ^{40}Ar is more complex but is essential for geologic interpretation of the in situ ages from the cores of mica crystals. The UV laser in situ ablation analysis revealed no direct evidence for the post-crystallization excess ^{40}Ar incorporation. Magmatic micas from the Solton Sary district do not show a systematic edge-center age decrease similar to that described by Pickles et al. (1997). The homogeneously distributed excess ^{40}Ar cannot be identified strictly from the ^{40}Ar/^{39}Ar data. Consequently, a probability of its presence has to be evaluated based on a broader spectrum of geologic information including available $^{40}Ar/^{39}Ar$ data on micas from similar magmatic systems elsewhere. Phillips (1991) reports results of the in situ $^{40}Ar/^{39}Ar$ analyses of phlogopite phenocrysts from the Swartruggens kimberlite dike (South Africa). Analyzed phlogopites revealed near concentric age zoning, with a center-edge decrease of in situ ages. The ages found in cores of the crystals exceed the age of kimberlite emplacement that is constrained by the $^{40}Ar/^{39}Ar$ age of groundmass phlogopite, as well as independent geochronologic data. The author interprets older ages of phenocryst cores as related to excess ^{40}Ar that was incorporated into the crystals in the mantle under high Ar partial pressure. The age zoning is attributed to a partial ^{40}Ar loss during the rapid emplacement of the dike. As groundmass phlogopites from the same sample does not appear to contain excess ^{40}Ar, it is concluded that the Ar partial pressure decreased prior to or during the early stages of the dike emplacement. Similar patterns are reported for phlogopites from mantle xenoliths entrapped in kimberlites (Phillips, 1991; Phillips and Onstott, 1988), alnoites, and lamprophyres (Kelley and Wartho, 2000). Cores of phlogopites show ages that significantly exceed ages of intrusions. These ages are interpreted as reflecting the actual timing of mica crystallization during mantle plume events (Kelley and Wartho, 2000) or being caused by excess ^{40}Ar and thus geologically meaningless (Phillips and Onstott, 1988). The younger ages found at grain margins generally agree with the known ages of host intrusions. The age gradients are attributed to a partial ^{40}Ar loss during extremely fast (hours-days) emplacement of magmas. In all cases mentioned above, the raise of magmas from the mantle to the surface causes a net ^{40}Ar loss from phlogopites, and only a very short duration of magmatic events prevents isotopic systems from being completely reset. No evidence for incorporation of excess ^{40}Ar during the late stages of magma emplacement is found, as none of the analyzed phlogopites reveals "reverse" age gradients, and groundmass phlogopites return $^{40}Ar/^{39}Ar$ ages consistent with the age of the magmatism (Phillips, 1991). Based on these facts, it is not unreasonable to assume that excess ^{40}Ar in micas from mantle-derived alkalic rocks is retained under high Ar partial pressures in the mantle and is rapidly lost during magma ascent. In other words, excess ^{40}Ar is a mantle-inherited component that is partially preserved only due to a very fast emplacement of magmas.

Under this assumption, it is unlikely that Solton Sary micas contain a significant fraction of excess ^{40}Ar. Unlike the cases described by Phillips (1991), Phillips and Onstott (1988), and Kelley and Wartho (2000), the emplacement of magmas at Solton Sary was not geologically instantaneous. Phlogopitic micas are overgrown by later biotite rims that compositionally converge with fine groundmass biotite. Even if phlogopites crystallized in the mantle and initially contained excess ^{40}Ar, they definitely experienced a fairly long interaction with the melt at more shallow levels, and their original isotope signatures would have been completely erased. The complete resetting is additionally confirmed by the fact that micas from relatively primitive lamprophyre (49-113.7) and evolved syenite-porphyry (49-129.2) show generally similar in situ $^{40}Ar/^{39}Ar$ ages and age zoning patterns. This would not be expected if the phenocrysts were still preserving inherited excess ^{40}Ar, because micas from syenite porphyries must have resided in the melt longer than micas from lamprophyres. Preservation of mantle-inherited excess ^{40}Ar in mica phenocrysts of the Solton Sary lamprophyres and syenite porphyries is highly unlikely. There is also no evidence for volume diffusion of excess ^{40}Ar during the latest stages of magma emplacement. Thus, the internally concordant in situ ages of the cores of biotite 49-113.7, 49-129.2, and 57-166.2-2 approximate the age of the magmatism. The crystal-scale age gradients are interpreted to be entirely related to the post-emplacement ^{40}Ar loss.

The most probable mechanism for the post-emplacement ^{40}Ar loss that generated near concentric age zoning is volume diffusion under elevated temperatures (cf. Hodges et al., 1994). This mechanism agrees with fluid inclusion data that indicate the depth of 9-12 km for the hydrothermal system that is spatially associated with intrusions but clearly postdated the magmatism. In addition to residing at high temperatures, the magmatic micas probably were exposed to hydrothermal fluids that produced relatively weak, but voluminous pre-mineralization biotite alteration. The systematic variation in Cl content of mica phenocrysts could be an artifact of interaction with these fluids. Phillips (1991) reports an outward decrease of Cl in kimberlitic phlogopites and suggested the ion exchange with hydrothermal fluids as one of possible mechanisms. Onstott et al. (1991) experimentally reproduce the Cl loss from biotite to a pure aqueous hydrothermal fluid. Sisson (1987) reports the increase of Cl contents in magmatic biotites caused by the interaction with Cl-rich metamorphic fluids. Similarly, center to edge Cl concentration gradients in the magmatic micas of the Solton Sary alkalic rocks may have resulted from interaction with Cl-rich hydrothermal solutions. Exposure to hydrothermal fluids could cause some simultaneous non-diffusional ^{40}Ar loss (cf. Kent and McCuaig, 1997) and, more importantly, it could enhance diffusivity of ^{40}Ar by generating additional crystallographic defects suitable for pipe diffusion (Onstott et al., 1991).

Comparison of the age spectra with the UV laser in situ ages shows that the step heating analysis homogenized gas fractions derived from isotopically distinct zones of crystals. UV laser analyses revealed three Ar reservoirs that correspond to a) ages from the cores of the crystals likely approximating the timing of intrusion emplacement and cooling, b) younger ages from crystal margins, and c) anomalously old ages related to excess ^{40}Ar sited in discrete crystallographic defects, areas of alteration, and mineral inclusions. The first two Ar reservoirs are volumetrically predominant and largely control the total Ar balance. The results of step heating experiments tend to underestimate the crystallization age, and are likely grain-size dependent. The shapes of age spectra are not diagnostic. The example of a near concordant age spectrum of strongly zoned boitite 57-166.2 shows that a relatively flat step heating release pattern can be produced by a disturbed isotopic system, and thus the simple geometry of age spectra should not be employed as a universal criterion for reliability. All these factors imply that geologic interpretation of geochronologic data produced by magmatic micas from this study should be based primarily on the UV laser results rather than on step heating data.

$^{40}Ar/^{39}Ar$ dating of hydrothermal muscovites

UV laser in situ ablation analysis of hydrothermal muscovites revealed age zoning patterns that are generally more diverse than those of magmatic micas. Some irregularities of age distribution can be explained by a fragmental nature of analyzed grains and incompleteness of their age profiles with regards to original crystals. For example, muscovite 532 is characterized by subequant geometry that probably closely approximates the original crystal shape. This grain showed relatively simple symmetric age zoning with younger ages found on the margins. In contrast with muscovite 532, muscovites 601 1 and 2 clearly represent crystal fragments. Their asymmetric age graphs are also fragmental but probably still reflect systematic variations of apparent ages from the edge to the center. The original crystals probably had relatively simple concentric age zoning. Ages of anhedral and likely fragmental grain of muscovite AD2A tend to be concentrically zoned but are virtually indistinguishable within the analytical uncertainty.

Zoning of muscovite 547 is rather complex and cannot be explained solely by the fragmental nature of the grain. However, in spite of the apparent irregularities in age variations, most of the ages from the grain interior overlap at 2σ level, and the significantly younger in-situ ages tend to occur at grain margins.

Overall, hydrothermal muscovites of the Solton Sary district show age zoning with the youngest in situ ages found at grain margins. This pattern implies post-crystallization ^{40}Ar loss through volume diffusion. Hodges et al. (1994) and Hames and Bowring (1994) report well-defined concentric age zoning in undeformed muscovites and attributed it to cylindrical volume diffusion of ^{40}Ar (along the {001} cleavage plane) with the effective diffusion dimension approximately equal to the grain size. Muscovites analyzed in this study are variably deformed, with microstructures interpreted as recording predominant sliding along {001} basal planes combined with bending and fracturing. Unlike simple basal plane sliding (Reddy and Potts, 1999), this type of deformation would generate discontinuities in mica layers and can potentially transform the mica crystal into a stack-like aggregate of sheets and lenses with sizes approximately equal to or smaller than the original crystal size. The transformation would result in an overall decrease in ^{40}Ar retentivity, decrease in effective diffusion dimension, deviation of the grain as a whole from the ideal cylinder diffusion pattern, and more complex age zoning. Irregularities of the age distribution in muscovite 547 may be at least partially related to deformation. For ample, the younger ages of muscovite 547 correspond to a strongly deformed marginal portion of the grain and there is a rather abrupt transition to older ages within a relatively undeformed area. This is somewhat similar to the results reported by Hames and Hodges (1993) that show the enhanced ^{40}Ar loss along planar deformation features intersecting the {001} plane of a muscovite porphyroblast. However, more detailed crystal-scale in situ age mapping is necessary to adequately explain the observed age variation of the olton Sary muscovites and assess the importance of deformation-related discontinuities.

Unlike magmatic micas, the UV laser results produced by hydrothermal muscovites are in good agreement with the step heating data. A systematic increase of apparent ages during step heating experiments indicates that areas of crystals with younger $^{40}Ar/^{39}Ar$ ages (largely corresponding to crystal edges) contribute most of the gas during low temperature heating steps. For virtually all analyzed muscovites most of the in situ ages from central portions of the grains overlap with apparent ages from relatively flat portions of age spectra. Maximum in situ ages and maximum step ages of incremental heating experiments agree as well. The consistency of step heating and UV laser data suggest that the oldest step ages of the age spectra are good approximations of the crystallization age of coarse white micas. It is noted that real "geologic" uncertainties of these ages are probably higher than 2σ analytical errors.

Geologic implications of step heating and UV laser in situ ablation results

Most of the in situ ages of the cores of mica phenocrysts (49-129.2, 49-113.7, and 57-166.2-2) fall in a range from ca. 455 to 430 Ma suggesting a Late-Ordovician-Early

Silurian age of the intrusions. The broad spread of ages is unlikely to reflect the real duration of the magmatism but is probably related to post-crystallization disturbance and relatively low precision of in situ analyses. Since the post-crystallization thermal disturbance causes ^{40}Ar loss and thus a decrease in apparent age, it is likely that the age of ca. 455 Ma more closely reflects the timing of magmatism compared to ca. 430 Ma. However, currently available data are insufficient to constrain the age of the intrusions more precisely.

The age of mineralization is constrained by maximum step ages of coarse muscovites from auriferous lodes: 390.4±1.1 Ma (601), 392.4±1.5 Ma (547); 389.0±1.4 (AD2). The younger terminal age of muscovite AD2A, 383.4±1.5 Ma probably reflects more severe ^{40}Ar loss. Alternatively, the multi-grain aliquot analyzed by step heating could have contained a disproportionately high fraction of crystal margin fragments. Considering the uncertainties, the results support the formation of auriferous zones at ca. 395-390 Ma (late Early Devonian). Plateau ages of hydrothermal biotites 391.9±7.5 Ma (57-157.5-1) and 390.6±3.8 Ma (57-157.5-2) fall into the same range, however, it is unclear if these results reflect real crystallization ages or are thermally reset like the coarse magmatic biotites. Regional hydrothermal activity that resulted in the formation of propylitic veins at the flanks of the mineralized system and barren quartz veins elsewhere in the district appears to have broadly overlapped with the mineralizing event. This is based on terminal ages of coarse muscovites 532 (propylitic vein, 394±1.7 Ma), 659 (394.6±1.6 Ma, barren vein, south of mineralized system), and 617 (388.9±1.8 Ma, barren vein, north of the mineralized system).

The terminal age of chromium-rich fuchsite from the alteration along the South Kumbel fault provides a 433.5 Ma (Early Silurian) minimum constraint for the age of tectonism. Mikolaichuk et al. (1997) suggest the allochtonous nature of the limestones that are bound by the fault. The authors relate the tectonic emplacement of the carbonates to the collision of North and Median Tien Shan blocks during the end of the Ordovician. The new result generally agrees with this interpretation and provides a minimum time constraint for the proposed collisional tectonism.

Virtually all analyzed phases experienced post-crystallization ^{40}Ar loss indicating elevated temperatures during and after the mineralizing event. Thermal history of the Solton Sary district is further addressed in the following section that focuses on K-feldspar thermochronology.

$^{40}Ar/^{39}Ar$ K-feldspar thermochronology

Multiple diffusion domain model

Thermochronologic studies were conduced in accordance with the Multiple Diffusion Domain (MDD) model. Principles of the model are described in detail in Lovera et al. (1989, 1991, 1997) and only briefly outlined here. The fundamental assumption of the MDD theory is that the argon loss from K-feldspar is the thermally activated diffusion process that can be adequately reproduced during laboratory in-vacuo heating. The MDD model explains diffusion properties of K-feldspar through the existence of discretely sized non-interacting diffusion domains. The argon concentration at domain boundaries is assumed equal to zero, in other words, as diffusing argon atoms reach domain boundaries they are instantaneously lost from the system. Closure temperatures of the domains differ depending on their sizes (i.e. diffusion length scales). The larger domains have higher closure temperatures (i.e. are more retentive) because argon atoms have to travel longer distances before reaching the diffusion boundary. The existence of variably retentive multiple diffusion domains allows K-feldspar to retain a continuous record of its thermal history. The geometry of the age spectrum and Arrhenius plot ($\log D/r^2$ versus $1/T$) are defined by diffusion parameters of each domain (activation energy (E), and frequency factor (D/r_0^2)) and by domain sizes (r) and volume fractions (f). The shape of the age spectrum additionally depends on the thermal history experienced by the sample. As experimental in vacuo diffusion of ^{39}Ar is assumed to adequately simulate the diffusion of ^{40}Ar in nature, the thermal history of the sample can be recovered based on experimentally derived diffusion parameters and the age spectrum.

Data collection

Data for thermochronologic modeling are collected through $^{40}Ar/^{39}Ar$ step heating experiments that combine determination of apparent ages and observations on thermal diffusion of ^{39}Ar. The results include age spectra and the Arrhenius plots illustrating ^{39}Ar diffusion behavior (Lovera et al., 1997; Quidelleur et al., 1997; Mahon et al., 1998). Heating schedules of these experiments differ from those of conventional incremental heating $^{40}Ar/^{39}Ar$ analyses. In general, K-feldspar analyses are designed to maximize the extraction of Ar prior to the beginning of melting at ca. 1150°C (Lovera et al., 1997). The experiments usually involve more temperature steps, the duration of which varies from minutes to several hours. Unlike conventional incremental heating analyses where temperatures are set to increase monotonically, K-feldspar diffusion experiments include isothermal heating, i.e. two or more contiguous steps at constant temperatures. These are carried out during the initial phases of gas extraction and are intended to improve the resolution of kinetic parameters and to correct age spectra for the presence of excess ^{40}Ar hosted in fluid inclusions (Harrison et al., 1994). For most samples in this study, isothermal pairs were obtained for the first four heating steps at 500°, 550°, 600°, and 650°C (Appendix D, Tables D.3 and D.4). Heating schedules of sample A23 and an additional aliquot of sample 57-166.2 included, respectively, 12 and 9 isothermal duplicates (Appendix D, Tables D.3 and D.4).

Results of $^{40}Ar/^{39}Ar$ step heating experiments

The results of step heating analyses of nine K-feldspar samples are presented in Figures 7.23-7.26, and in Appendix D, Tables D.3 and D.4. K-feldspar phenocrysts from syenite porphyries were represented by four samples: 49-129.2; 57-166.2; 57-174.1, and A23. Each of these was analyzed at least twice. In the case of 49-129.2, 57-166.2, and 57-174.1, the experiments were repeated because the temperature calibration appeared suspicious during the first run. Sample 57-166.2 was additionally re-analyzed (for the 3rd time) with a more detailed low-temperature heating schedule designed specifically to derive diffusion parameters (age spectrum of this analysis is not shown). Sample A23 was initially analyzed with a simplified heating schedule that lacked isothermal duplicates. The objective of this analysis was to crudely estimate the minimum age. A more detailed analysis of A23 was conducted later in order to generate data for thermochronologic modeling. Though not the original intent, the duplicate analyses

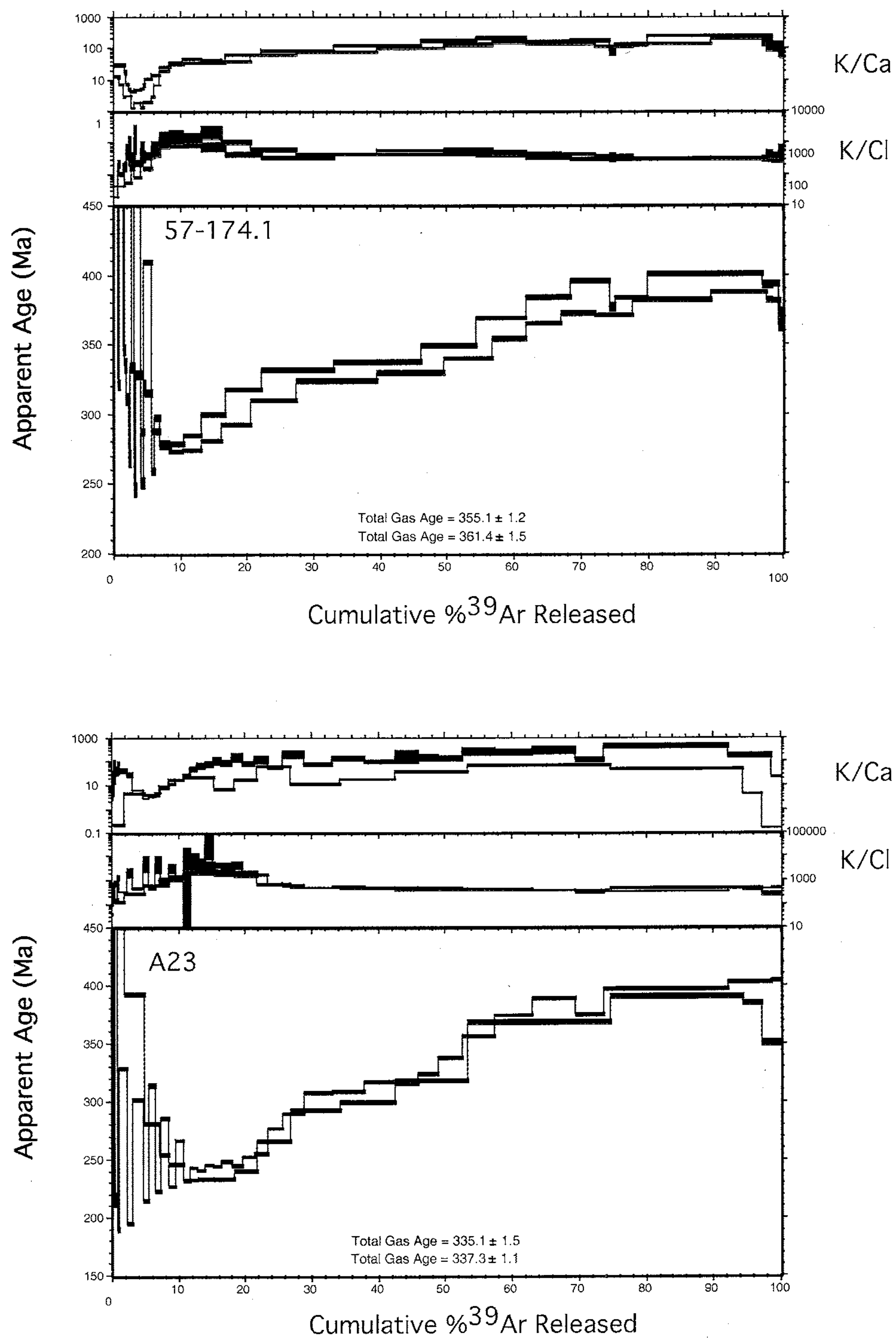

Fig. 7.23. $^{40}Ar/^{39}Ar$ age spectra for K-feldspars 57-174.1 and A23. Data that were used for thermochronologic modeling are shown in black.

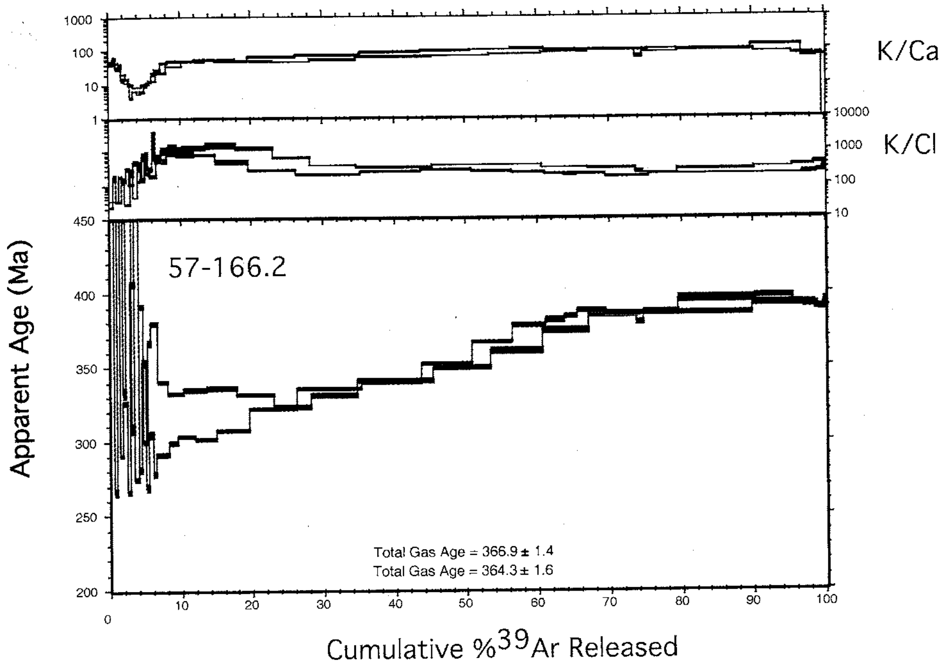

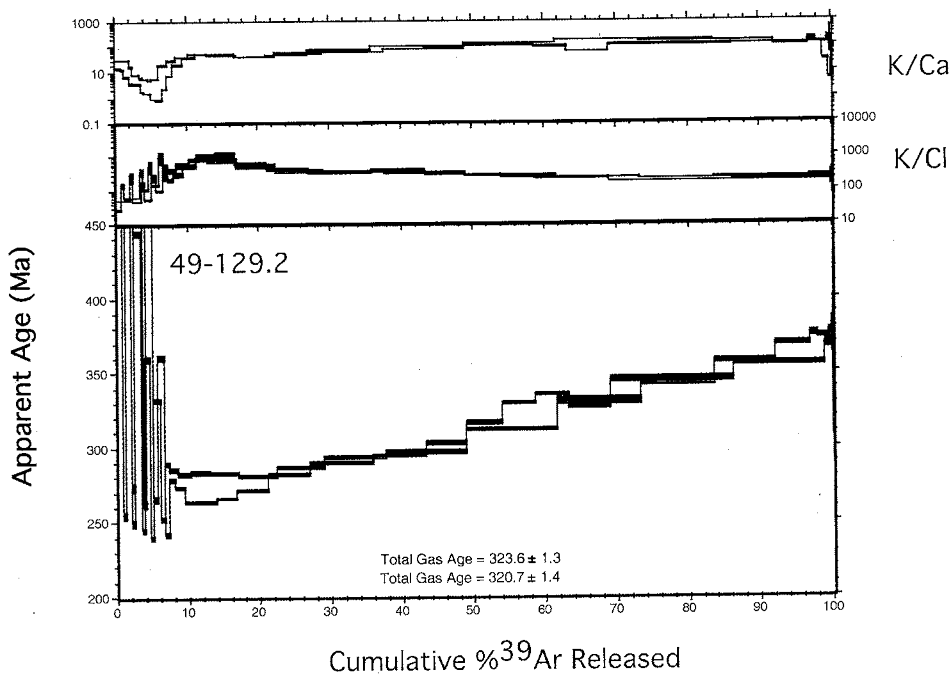

Fig. 7.24. $^{40}Ar/^{39}Ar$ age spectra for K-feldspars 57-166.2 and 49-129.2. Data that were used for thermochronologic modeling are shown in black.

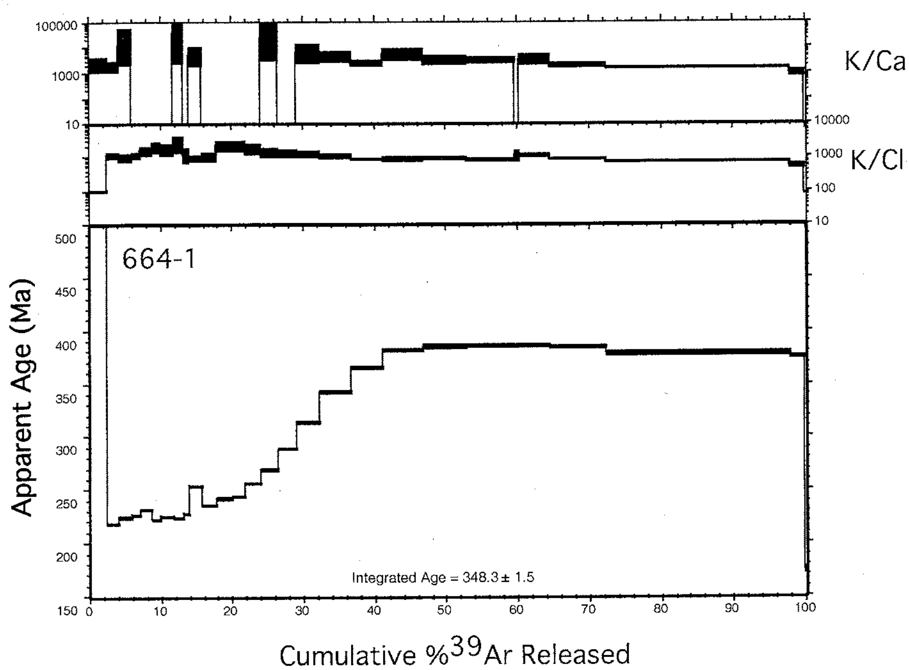

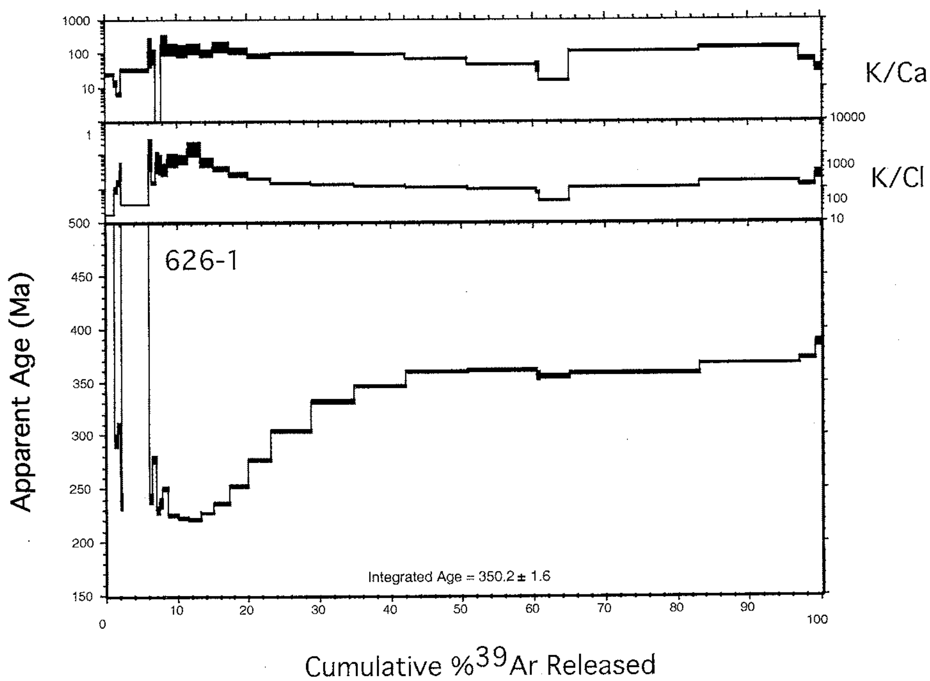

Fig. 7.25. $^{40}Ar/^{39}Ar$ age spectra for K-feldspars 664-1 and 626-1.

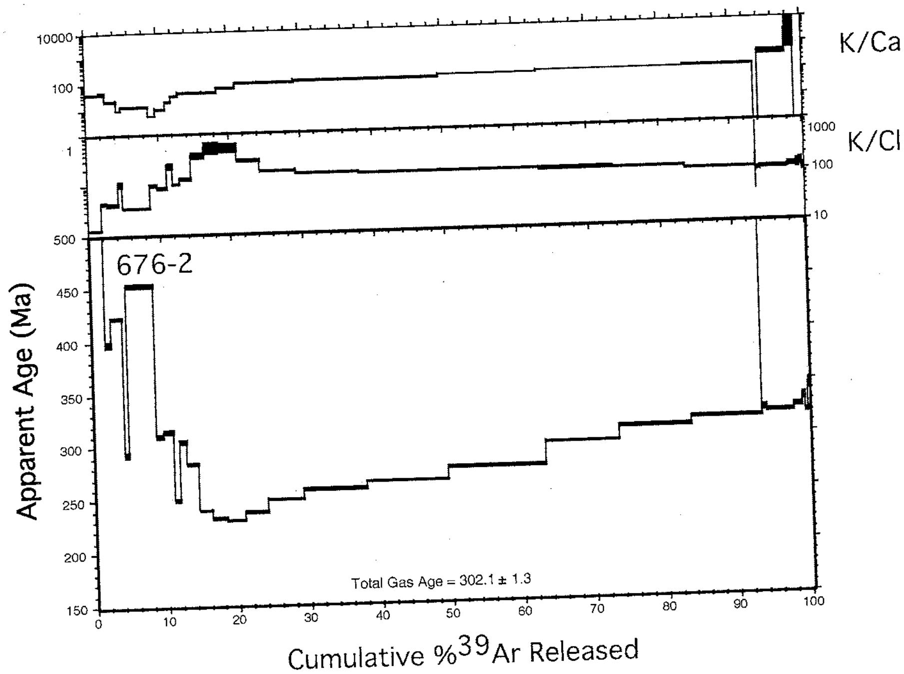

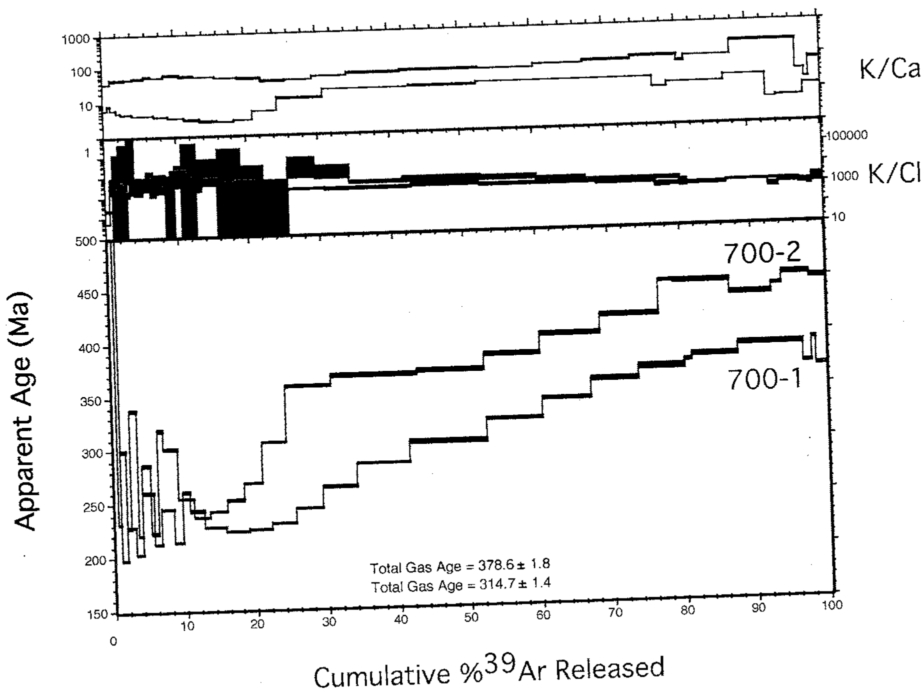

Fig. 7.26. $^{40}Ar/^{39}Ar$ age spectra for K-feldspars 676-2, 700-1, and 700-2.

provided an opportunity to assess the reproducibility of the results and reliability of thermochronologic models.

Age spectra of all analyzed K-feldspar phenocrysts share similar patterns (Figs. 7.23-7.24). The initial set of isothermal pairs generates strong fluctuations of apparent ages. The apparent age of the first isothermal step is consistently older than that returned by a contiguous second isothermal step. The old ages correlate to lower K/Cl ratios and are interpreted as related to excess ^{40}Ar that is released by decrepitating fluid inclusions with saline fluids (cf. Harrison, et al., 1994). Decrepitation of fluid inclusions is largely temperature-controlled and thus most of the inclusions that are likely to decrepitate at a given temperature will decrepitate and release excess ^{40}Ar and Cl-derived ^{38}Ar during the first step of each isothermal pair. The following isothermal step causes less decrepitation and the result is less affected by excess ^{40}Ar. Unlike three other K-feldspar phenocrysts that returned somewhat erratic apparent age fluctuations, sample A23 that was analyzed with more detailed heating schedule produced more systematic age variations during the isothermal heating. Apparent ages of the second isothermal steps define a rather consistent, near monotonic, age gradient (Fig. 7.23).

In addition to fluctuations of ages and Cl/K ratios, initial heating steps of all K-feldspar phenocrysts show a well-defined trough-like decrease in K/Ca ratio. The lowermost part of the K/Ca trough corresponds to temperatures ca. 600-700°C. The K/Ca ratio does not oscillate during isothermal heating, and is not clearly correlated to Cl. Thus, it is unlikely that the decrease in K/Ca is caused by Ca ions present in trapped fluids. Plagioclase inclusions in K-feldspar phenocrysts consist of almost pure albite and could not contribute significant amounts of Ca-derived ^{37}Ar. Therefore, the most probable explanation implies degassing of secondary calcite that could be occurring as coatings in microfractures. Heating beyond the isothermal steps generated a monotonic increase of apparent ages typical of K-feldspars that have experienced diffusional ^{40}Ar loss. The initial ages of these gradients vary from sample to sample: ca. 230 Ma for sample A23, ca. 260-280 Ma for sample 49-129.2; ca. 280 Ma for sample 57-174.1, and 300-330 Ma for sample 57-166.2. Maximum ages of most analyzed K-feldspar phenocrysts are in a range of ~390-405 Ma. K-feldspar 49-129.2 shows younger maximum apparent ages of ca. 375-380 Ma.

Comparison of age spectra from replicate analyses shows only partial reproducibility of release patterns (Figs. 7.23-7.24). Detailed and simplified age spectra of sample A23 agree reasonably well. Two analyses of K-feldspar 57-174.1 generated age spectra with almost identical geometry, however, virtually all apparent ages of run 2 are systematically older (Fig. 7.23). For sample 49-129.2, the two age spectra generally agree except for the low temperature portions immediately after the isothermal heating steps that differ by ca. 20 Ma (Fig. 7.24). Sample 57-166.2 shows even worse reproducibility of the low temperature segment of the age spectrum (Fig. 7.24). This lack of reproducibility for the low temperature apparent ages requires explanation because it can have serious implications for the thermochronologic modeling. Most probably, the low temperature apparent ages are affected by inhomogeneously distributed excess ^{40}Ar that is not completely released during the isothermal duplicates. Sample to sample discrepancies in low temperature apparent ages may also be (at least partially) due to excess ^{40}Ar. Thus, the data derived from K-feldspar phenocrysts, especially from the low temperature portions of the age spectra, has to be treated with great caution. If the excess

^{40}Ar is the main reason for low temperature age discrepancies, then sample A23, that was analyzed with a more detailed heating schedule and returned a better defined age gradient with younger low temperature apparent ages, should be considered as a more reliable sample.

K-feldspar from the mineralized quartz vein 664-1 has a well-defined age gradient (Fig. 7.25). Only the first heating step appears to be significantly affected by excess ^{40}Ar. The age gradient starts at ca. 220 Ma, and the maximum step age is 384 Ma. The remaining four samples (626-1; 676-2; 700-1, and 700-2) returned well-defined age spectra with low temperature segments strongly complicated by excess ^{40}Ar (Figs. 7.25-7.26).

Correction for Cl-correlated excess ^{40}Ar

The fluid inclusion-hosted excess ^{40}Ar disturbs the low temperature segments of age spectra and complicates the assessment of thermal history. Harrison et al. (1994) introduce a quantitative technique for correcting measured ^{40}Ar/^{39}Ar ratios for excess ^{40}Ar through the use of the isothermal heating steps. For each isothermal pair, the differences in ^{40}Ar/^{39}Ar and Cl/K between the two heating steps are calculated and plotted as delta ^{40}Ar/^{39}Ar versus delta Cl/K. If these delta values for several isothermal pairs form a linear array, its slope defines the Cl-correlated excess ^{40}Ar. The excess ^{40}Ar component correlated to Cl is subtracted from total measured non-atmospheric ^{40}Ar to obtain a corrected age. Mahon et al. (1998) show that for sufficiently detailed experiments sensible geometry of age profiles can be estimated directly from results of isothermal heating without correcting for Cl-correlated excess argon. The age spectra that approximate the geometry expected for diffusional ^{40}Ar loss are defined by second and higher heating steps of isothermal sets (the authors use isothermal quadruplicates instead of duplicates).

In this study, the quantitative correction routine of Harrison et al. (1994) was applied to samples 57-166.2, 57-174.1, 49-129.2, 676-2, 626-1, and 700-1. Only ages produced by isothermal steps were corrected (Appendix D, Table D.3). The procedure proved only variably successful. For samples 676-2, 626-1, and 700-1, the corrected low temperature age profiles generally agree with the geometry that would be expected from simple extrapolation of higher temperature portions of the age spectra. In contrast, the correction of age spectra of samples 57-166.2, 57-174.1, and 57-166.2 introduced dramatic changes in their shapes by generating sharp inflections from relatively flat segments at ca. 280-330 Ma to steep age gradients to about 200 Ma. This tendency was particularly strong for samples 57-166.2 and 49-129.2.

For sample 700-2, the isothermal data did not yield a strong linear correlation between excess ^{40}Ar and Cl, and the quantitative correction was omitted. For sample 664-1, only first heating step appeared to be significantly affected by Cl-correlated excess ^{40}Ar (Fig. 7.25). Following isothermal pairs produced some age and Cl/K variations that were relatively small and not clearly systematic as would be expected under the model of Harrison et al. (1994). The geometry of the low temperature segment of the age spectrum excluding the first heating step was assumed to be relatively unaffected by Cl-correlated excess ^{40}Ar, and thus there was no basis for quantitative correction. Sample A23 was analyzed by a much more detailed set of low temperature measurements. The resulting age spectrum shows a presence of Cl-correlated excess ^{40}Ar. However second steps of isothermal pairs (starting with step 5) define a rather consistent age gradient (Fig. 7.23), and the quantitative correction appears unnecessary.

Thermochronologic modeling

Practical application of the MDD model is described by Quidelleur et al. (1997). The E and D_0/r_0^2 are determined from Arrhenius plots by linear regression to low temperature data points. Domain distribution parameters are calculated using an automated routine that varies the domain sizes and volume fractions to achieve the best fit to the fraction of ^{39}Ar released during step heating. After the kinetic parameters are obtained, a model thermal history capable of reproducing the experimentally derived age spectrum is calculated. Two approaches are employed. Either a monotonic cooling model that permits no temperature increase with time, or an unconstrained thermal history can be obtained. The calculated monotonic time-temperature histories are evaluated at the 90 percent confidence interval for both the mean and for the entire set of thermal histories. Solutions for the unrestricted models are treated by contouring the number of model thermal histories that pass through each area unit of time-temperature space.

For most samples analyzed in this study, it was not possible to derive the E from the Arrhenius plots because a linear trend of the initial diffusion coefficients was not established due to simultaneous degassing of multiple diffusion domains. More detailed low temperature step heating of sample A23 and an additional aliquot of sample 57-166.2 produced Arrhenius plots with suitable linear segments and allowed determination of E's. The inferred values of activation energy are 47.7 and 43.9 kcal/mol for samples A23 and 57-166.2, respectively. For all other samples, the E was assigned equal to 43 kcal/mol that is close to 43.8±1.0 kcal/mol reported by Foland (1974). Neither inferred nor postulated activation energy values differ significantly from the 46±6 kcal/mol that characterizes a normally distributed population of activation energies determined by Lovera et al. (1997) for 115 K-feldspar samples from various geologic settings and geographic locations.

Since the model thermal histories are calculated using the automatic routines which minimizes differences between calculated and measured age spectra, features such as excess ^{40}Ar age spectrum discordance that are not completely removed prior to modeling will yield spurious thermal histories. In order to overcome measured age spectra discontinuities, the measured apparent age data were modified for some samples. These modifications were applied to the isothermal step data. The underlying assumption was that results of second isothermal steps reasonably well approximate "true" apparent ages, while the older ages from the first steps are probably still affected by excess ^{40}Ar and are meaningless. To force the model to follow the lower limits of the age spectra, these older apparent ages were interpolated to fall between the younger values from adjacent steps. The uncertainties of the interpolated ages were assigned to overlap with adjacent steps. This correction scheme was applied to samples 700-1, 700-2, and A23. For samples 57-166.2 and 57-174.1 two step ages were modified in order to smooth the sharp bends of age spectra that were introduced by using the Cl-correlated excess ^{40}Ar correction method. For sample 676-2, a clearly erroneous apparent age of step V (1108.9±113.7 Ma) that was probably caused by a system failure, was removed and replaced by the age of a previous step (Fig. 7.26, Appendix D Table D.3). All changes introduced into the experimental and Cl-corrected data are summarized in the last column of Table D.3, Appendix D.

Modeling results

Diffusion and domain distribution parameters are summarized in Table 7.3, the results are graphically displayed in Figures 7.27, 7.28, and 7.29. Results of unconstrained thermal history modeling differ in detail from sample to sample but also exhibit important similarities (Fig. 7.28). The best-defined feature that is shown by virtually all samples except 49-129.2 and 57-166.2 is the thermal peak at ca. 250-225 Ma with temperatures of about 200-250°C. Models for the other two samples exhibit less intensive reheating (ca. 150°C) at about 200 Ma. The earlier thermal history is more loosely constrained and shows significant sample-to-sample variation. However, most of the samples require high temperatures (250-350°C) at 400-375 Ma to model their age spectra. Patterns returned by samples 57-166.2, 49-129.2 and 57-174.1 are largely controlled by sharp inflections of measured age spectra that are presumably influenced by excess ^{40}Ar corrections.

For the most part, the monotonic cooling models are similar (Fig. 7.29). These show gently inclined, slow cooling, or virtually isothermal segments with temperatures 200° to 300°C that are followed by a rapid increase in the cooling rate at ca. 225-200 Ma. The rather broad vertical spread of T-t histories is likely due to model differences in activation energies of the samples. Thermal histories of samples 57-166.2, 57-174.1 and 49-129.2 are anomalous, and, like the unconstrained models, are believed to be inaccurate due to artifacts of excess ^{40}Ar correction.

Table 7.3. K-feldspar Ar kinetic parameters used for MDD modeling

	A23		57-166.2		57-174.1		49-129.2		626-1	
E, kcal/mol	47.7		43.9		43.0		43.0		43.0	
$Log(D_0/r_0)$, s^{-1}	7.0		5.77		5.56		5.8		5.39	
Domain	Log(D/r)	Volume Fraction	Log(D/r)	Volume Fraction	Log(D/r)	Volume Fraction	Log(D/r)	Volume Fraction	Log(D/r)	Volume Fraction
1	10.03	0.011	9.29	0.014	9.22	0.014	9.15	0.016	7.48	0.059
2	9.22	0.024	7.90	0.013	7.66	0.011	7.79	0.020	5.68	0.024
3	8.33	0.027	6.50	0.015	3.66	0.319	6.10	0.020	5.00	0.021
4	7.43	0.028	4.87	0.055	2.77	0.144	3.88	0.371	3.86	0.083
5	6.53	0.032	3.98	0.202	2.27	0.101	2.77	0.257	2.71	0.058
6	4.21	0.300	3.09	0.156	1.16	0.410	2.23	0.221	1.96	0.222
7	3.23	0.091	2.44	0.103			1.80	0.096	0.99	0.533
8	2.20	0.487	1.37	0.442						

	676-2		664-1		700-1		700-2	
E, kcal/mol	43.0		43.0		43.0		43.0	
$Log(D_0/r_0)$, s^{-1}	5.75		6.0		5.3		4.8	
Domain	Log(D/r)	Volume Fraction	Log(D/r)	Volume Fraction	Log(D/r)	Volume Fraction	Log(D/r)	Volume Fraction
1	7.50	0.075	8.51	0.038	7.70	0.036	7.83	0.016
2	6.55	0.022	7.25	0.038	6.29	0.036	6.01	0.059
3	3.78	0.337	6.04	0.074	5.53	0.087	5.42	0.035
4	2.74	0.168	5.16	0.038	3.76	0.208	3.57	0.151
5	1.92	0.398	3.94	0.099	3.72	0.006	3.03	0.143
6	1.75	0.000	2.60	0.084	2.99	0.148	2.15	0.031
7			1.84	0.052	2.22	0.132	2.15	0.203
8			1.00	0.576	1.30	0.347	1.20	0.363

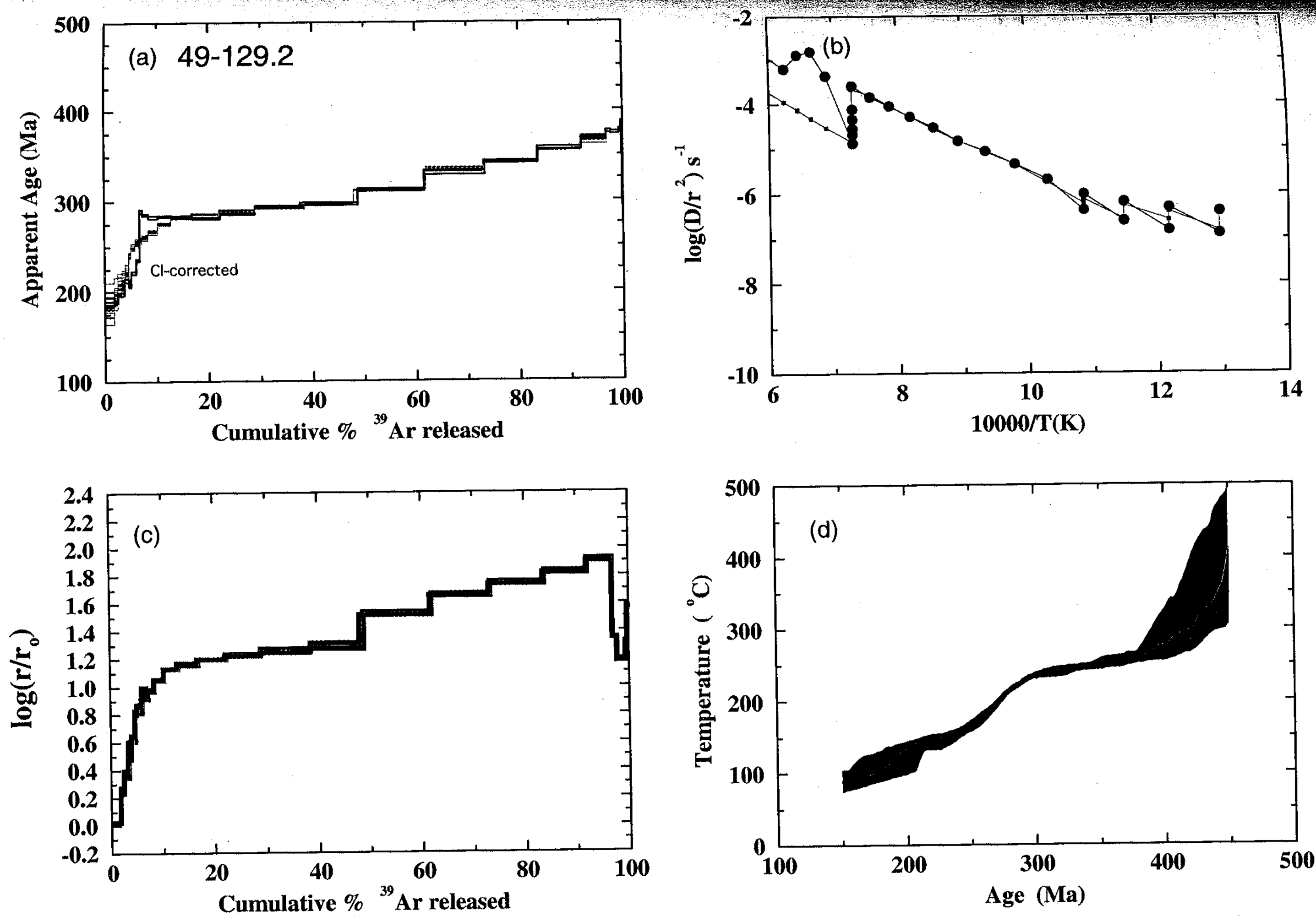

Fig. 7.27. Results of thermochronologic modeling: a, input and model age spectra (corrections applied to experimental age spectra and differences between experimental, Cl-corrected, and input data are specified on graphs; unmodified age spectra are shown in Figs. 23-26); b, experimental and model Arrhenius plots; c, experimental and model $\log(r/r_o)$ versus percent ^{39}Ar plots; d, monotonic cooling history (see Fig. 7.29 for more details). On graphs a, b, and c, model data are shown in red.

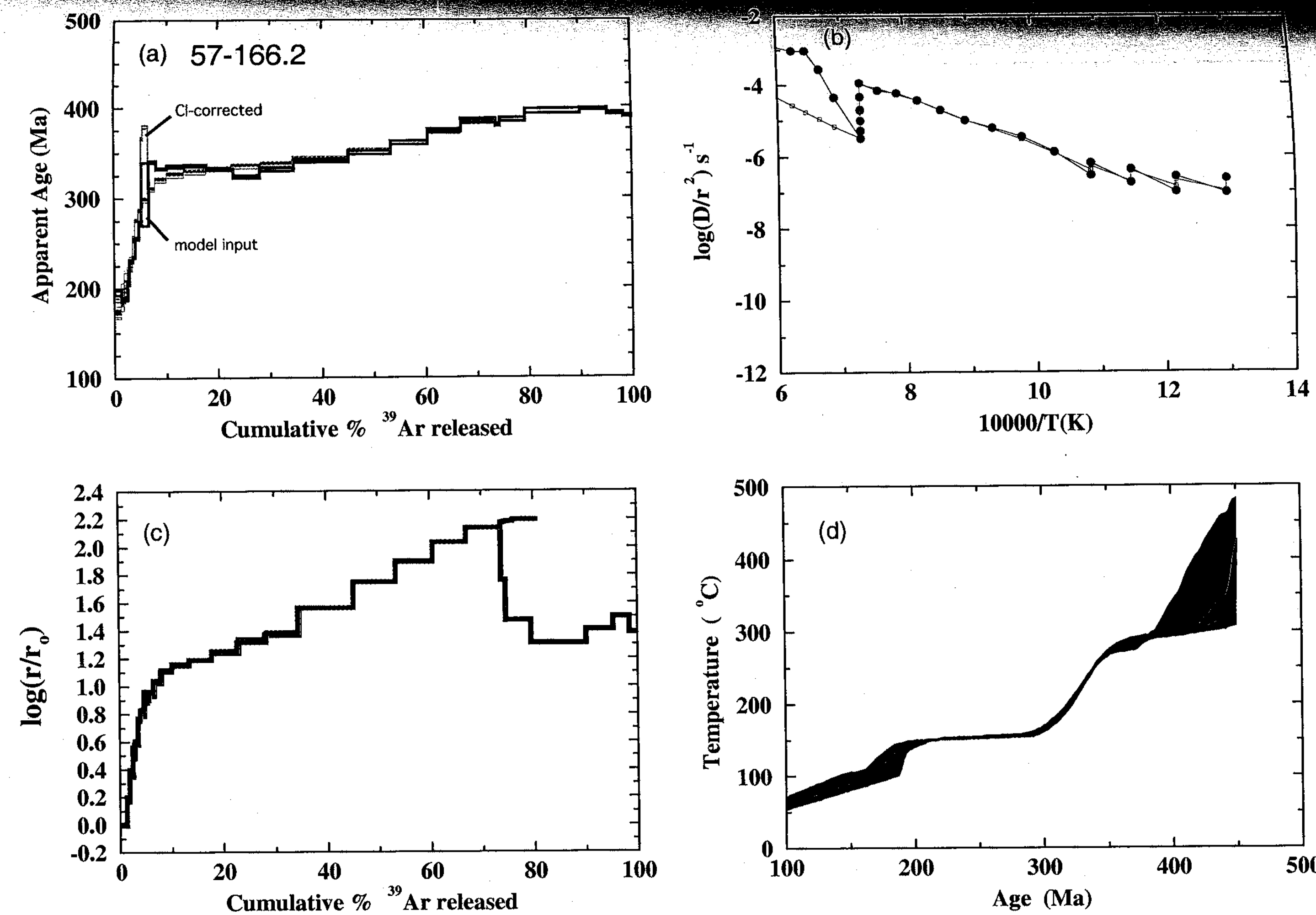

Fig. 7.27. (Continued).

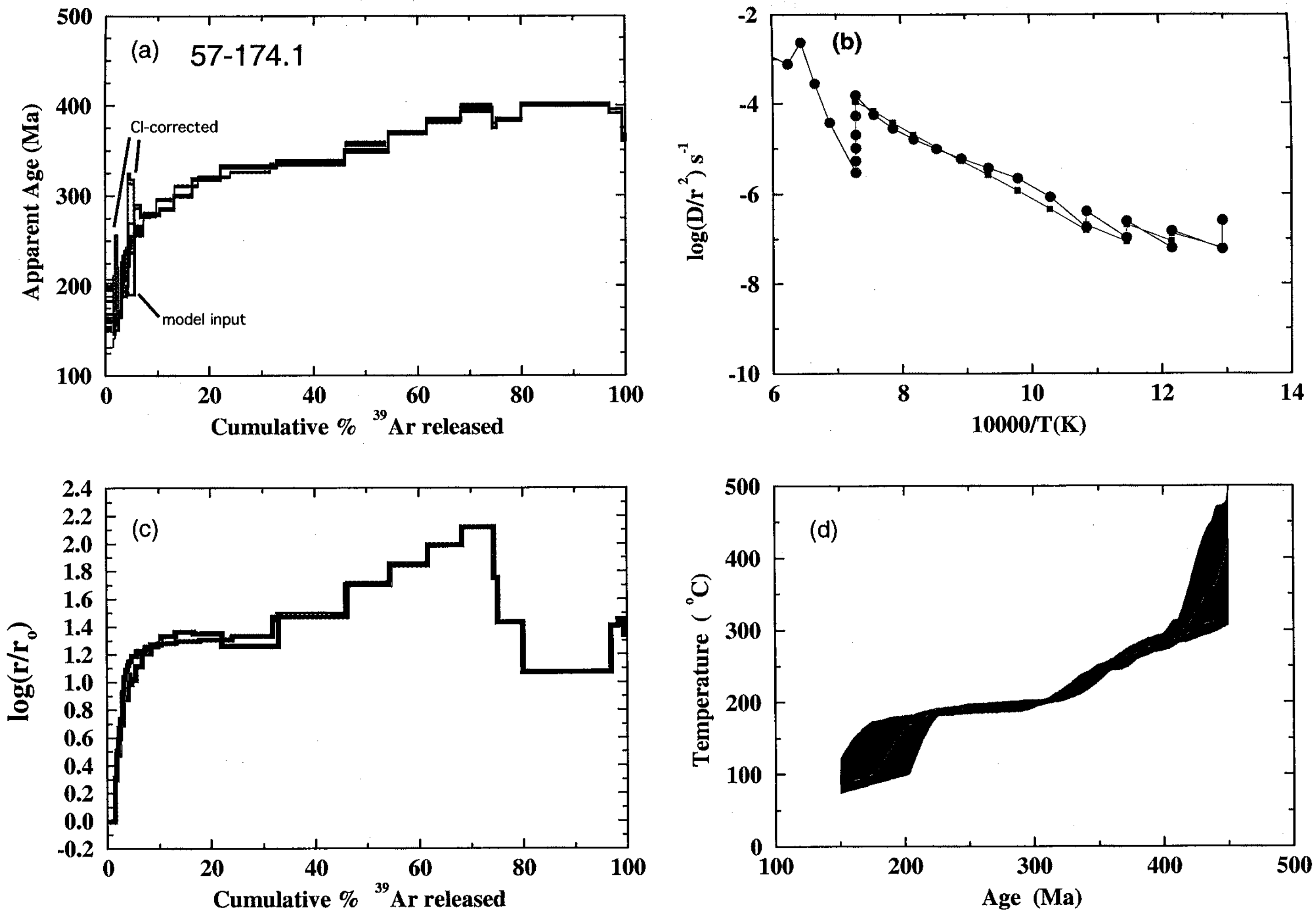

Fig. 7. 27. (Continued).

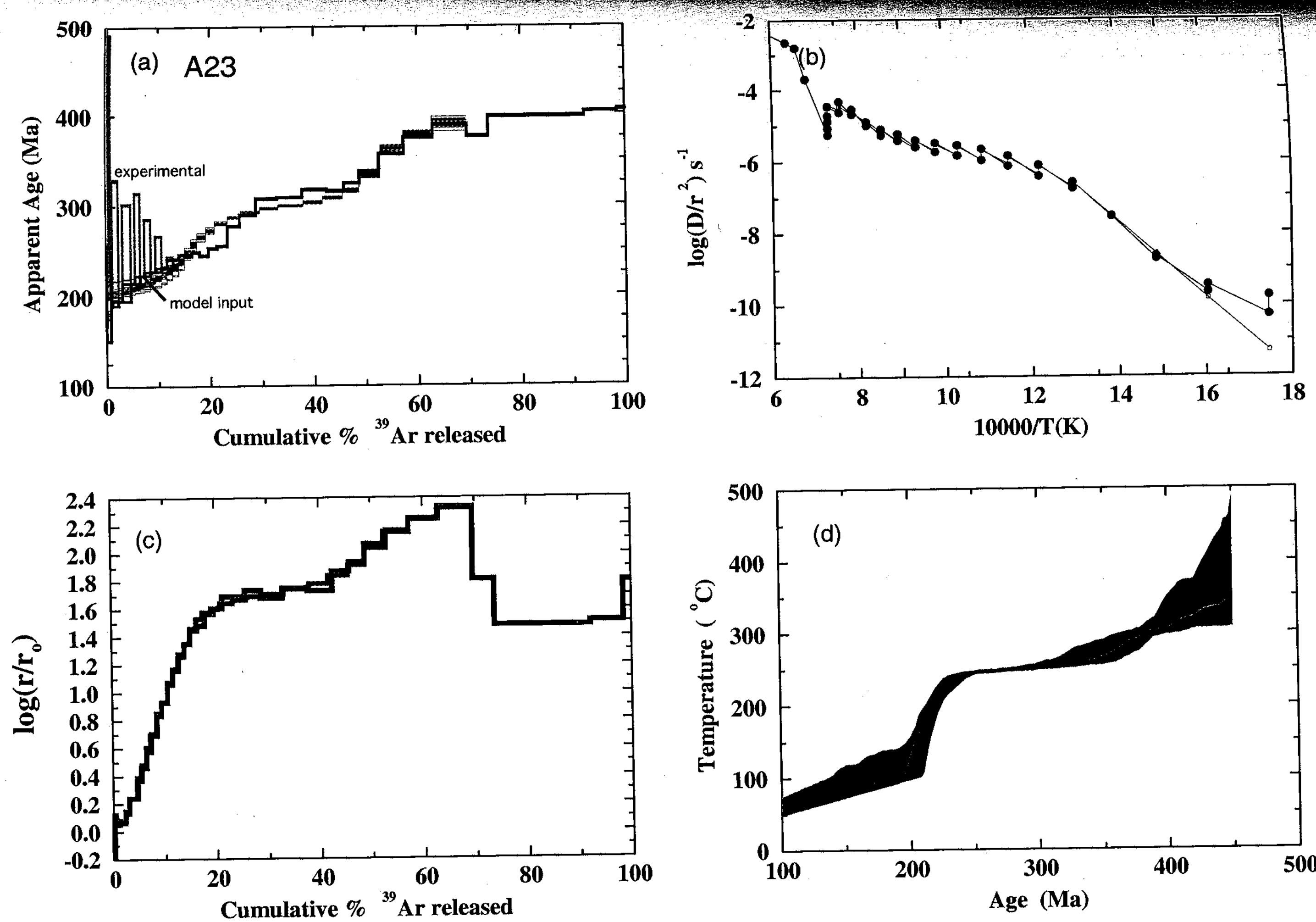

Fig. 7.27. (Continued).

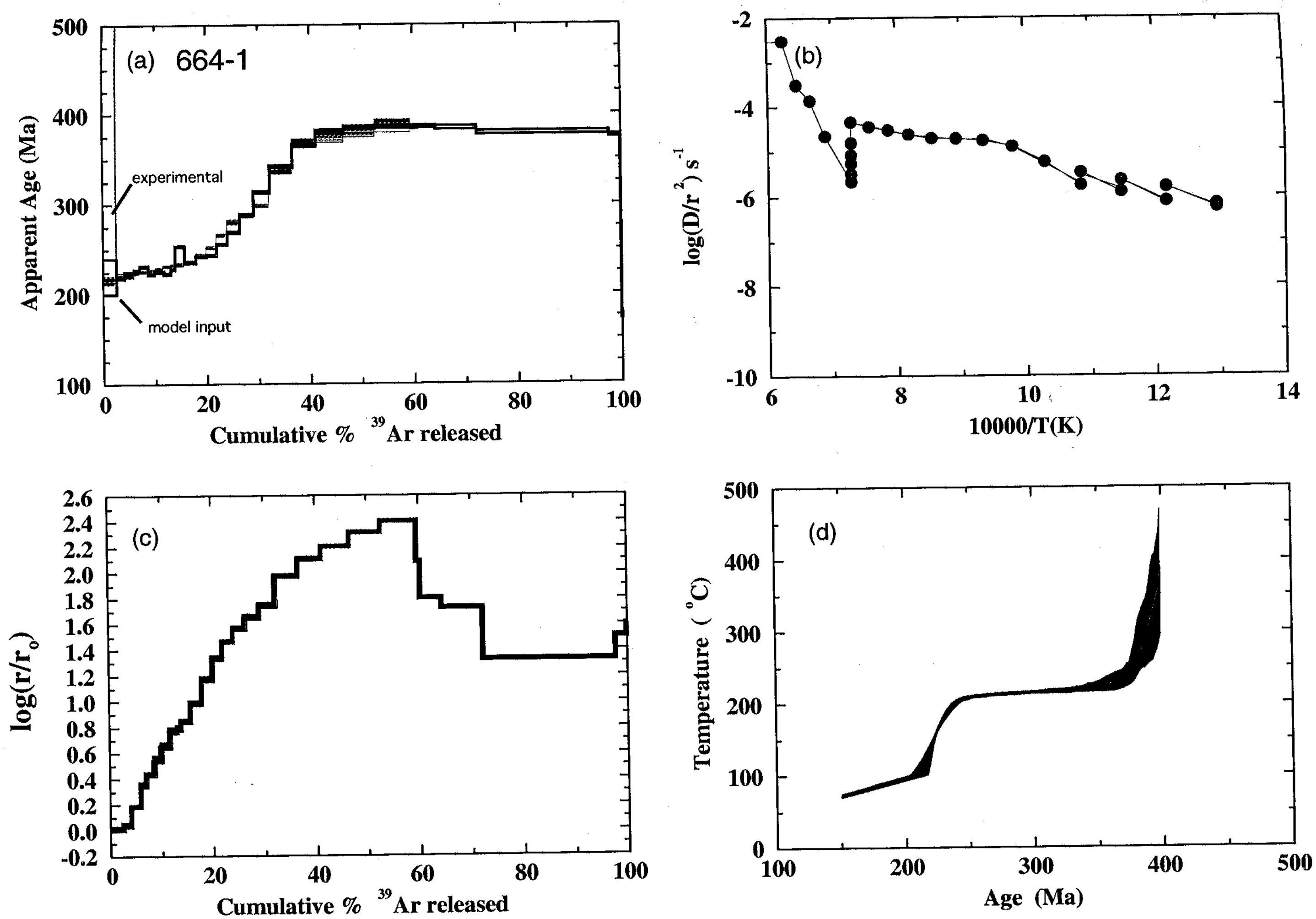

Fig. 7.27. (Continued).

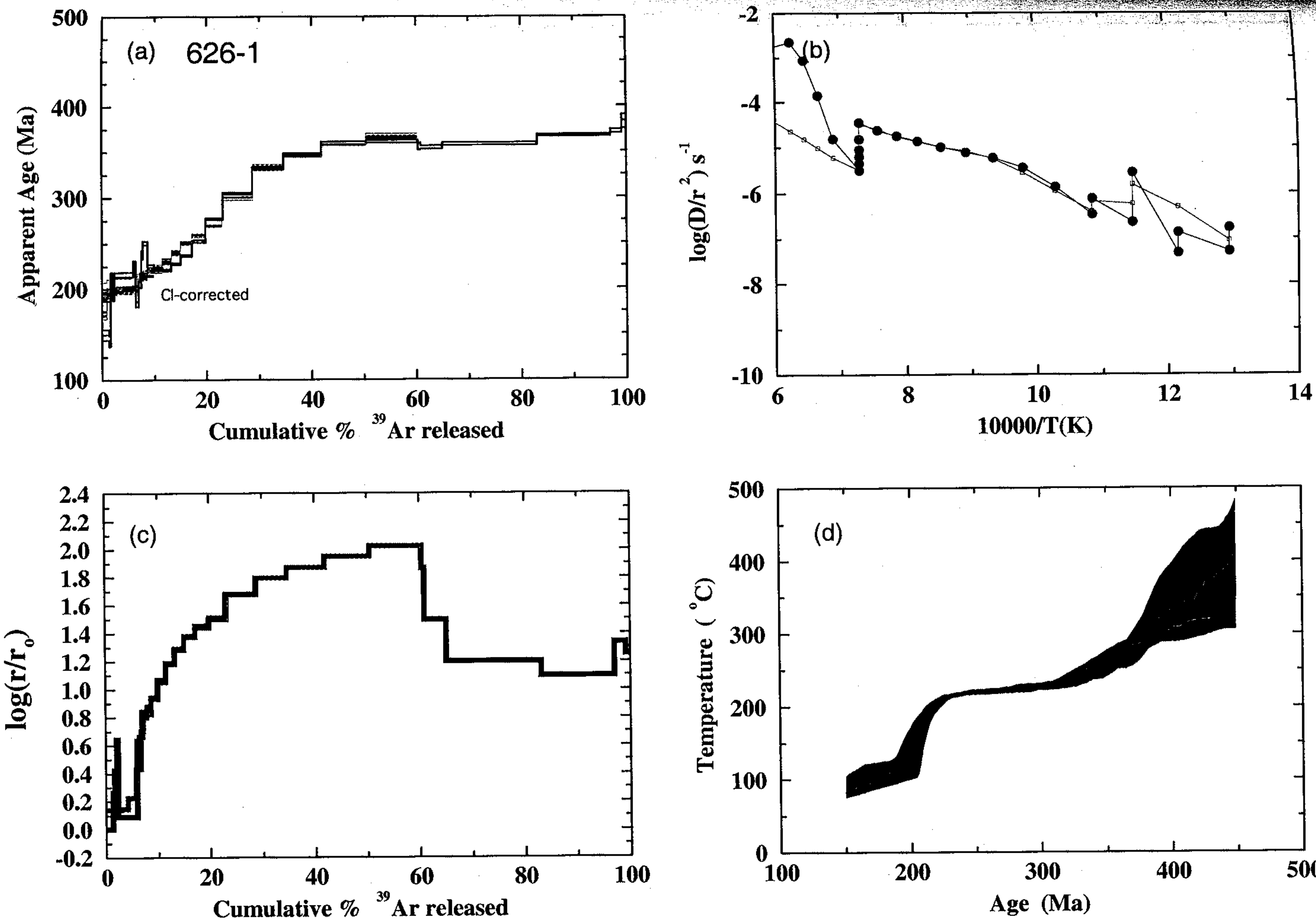

Fig. 7.27. (Continued).

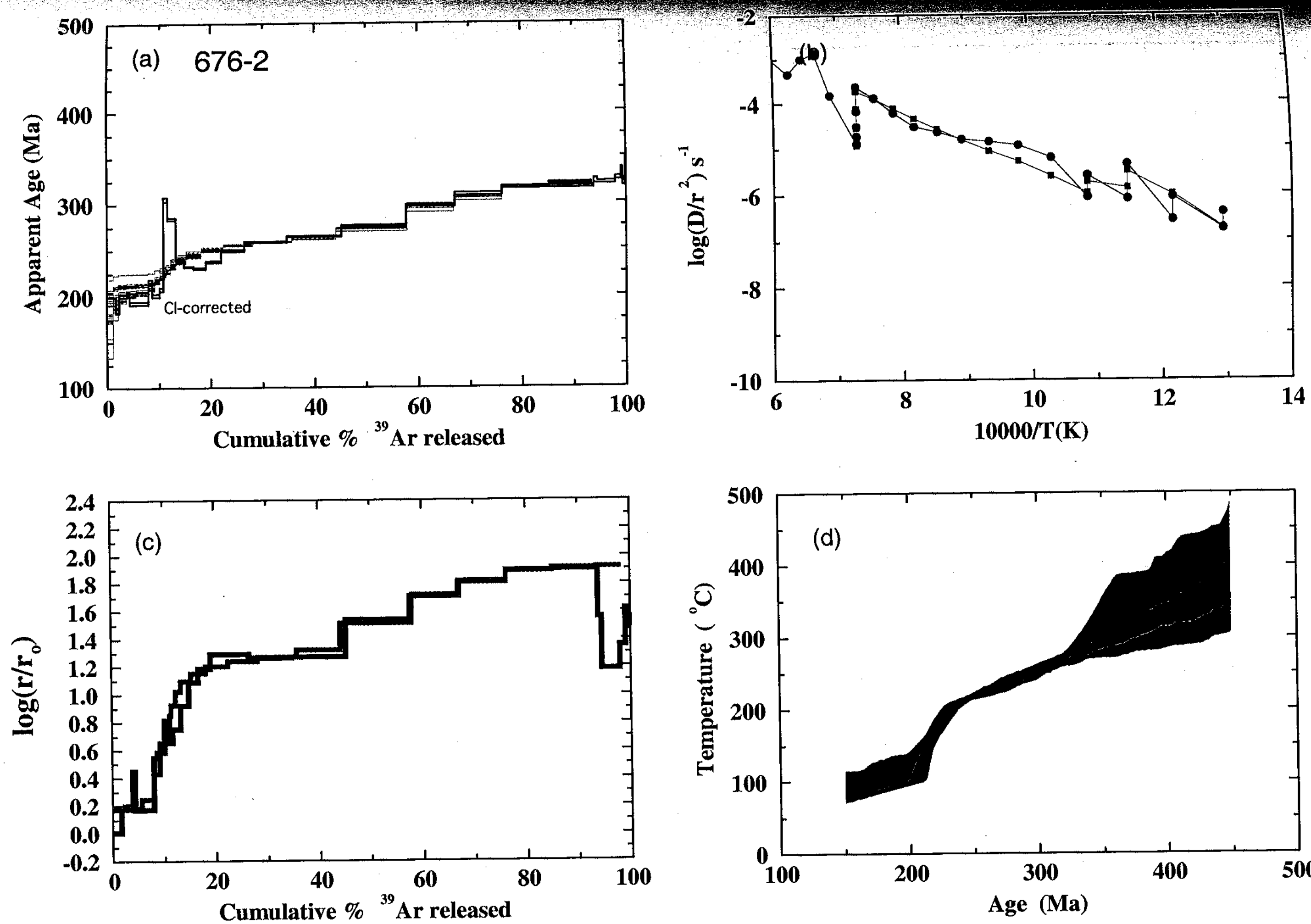

Fig. 7.27. (Continued).

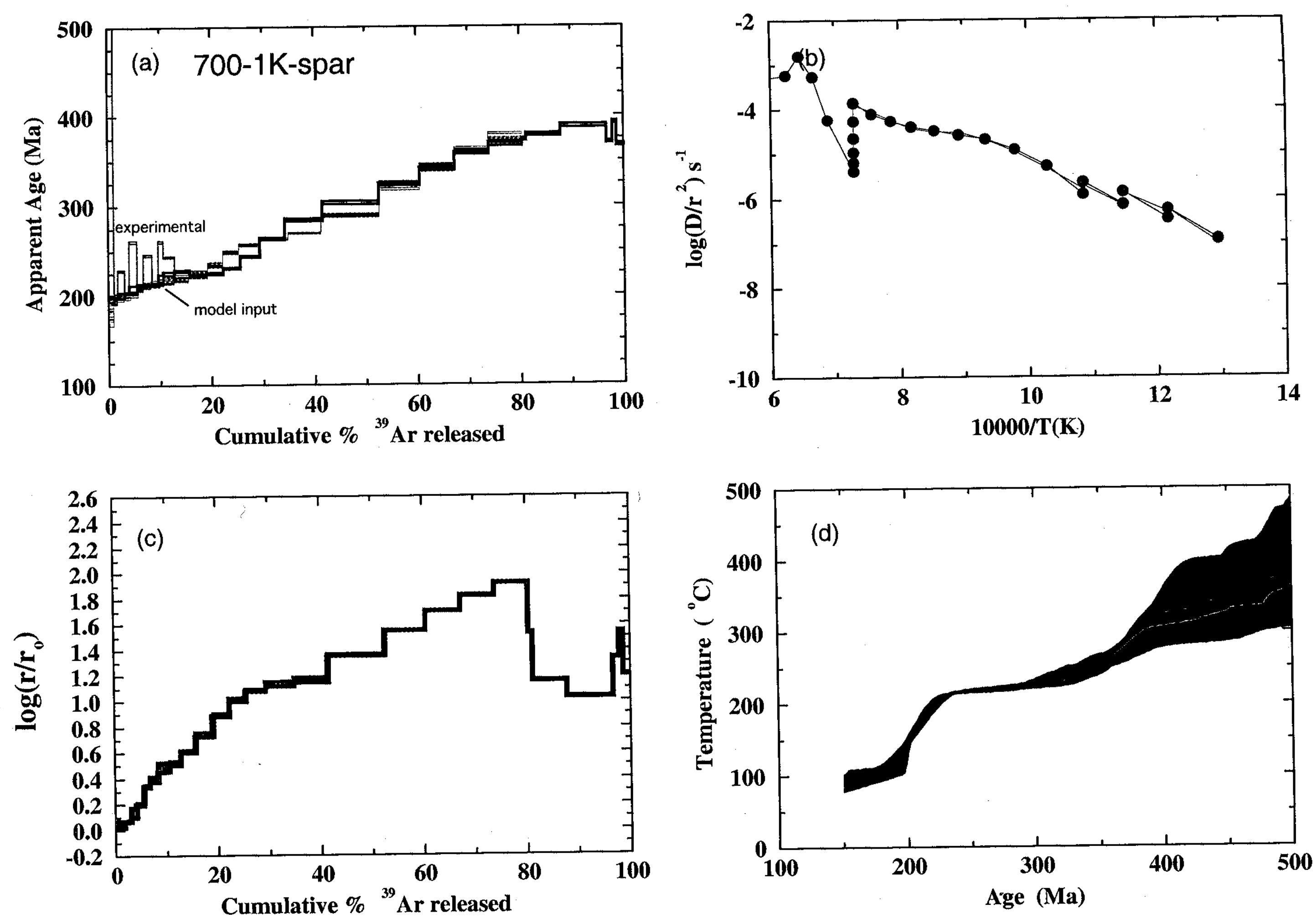

Fig. 7.27. (Continued).

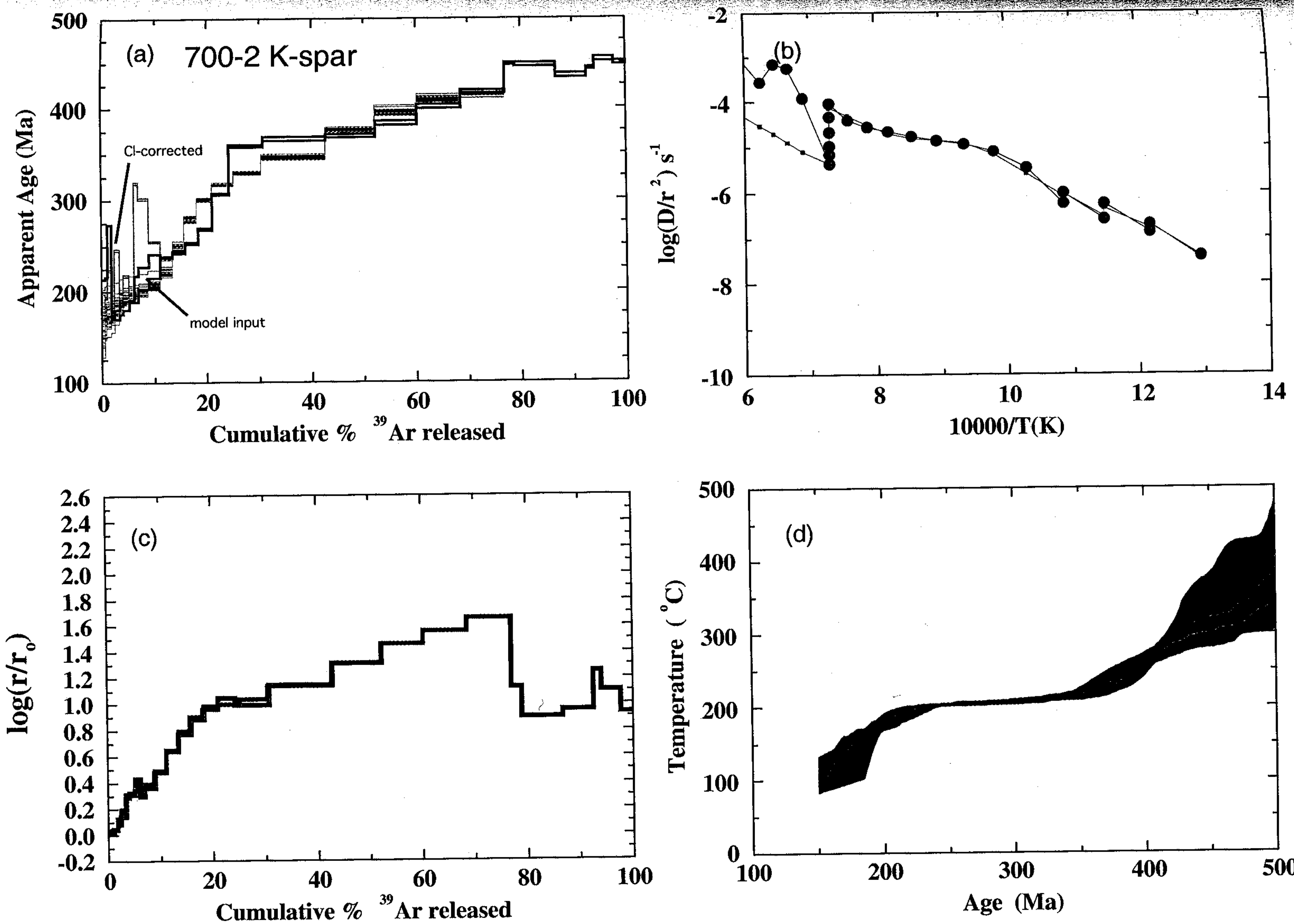

Fig. 7.27. (Continued).

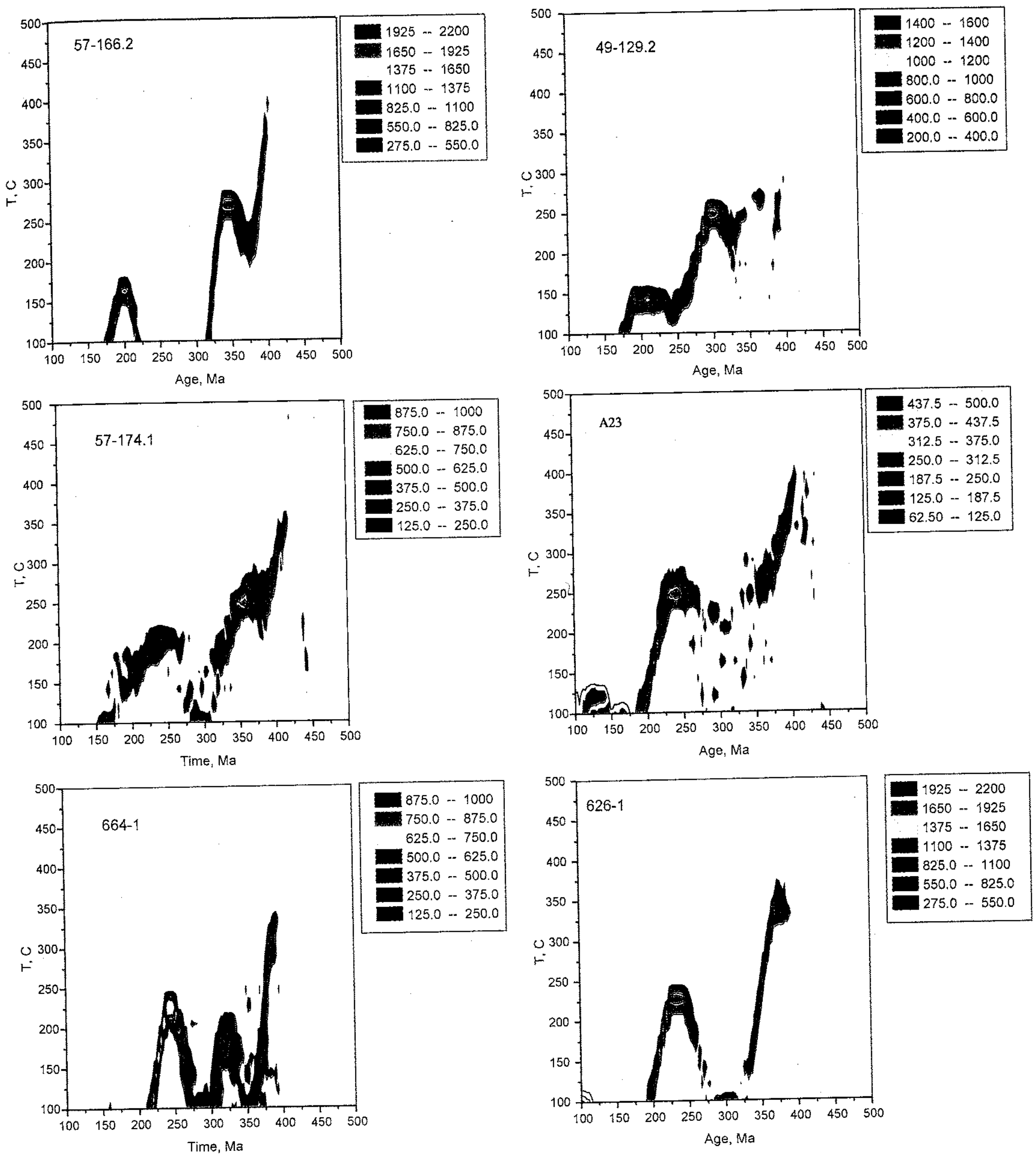

Fig. 7.28. Contours of thermal histories allowing reheating. Continued on the next page.

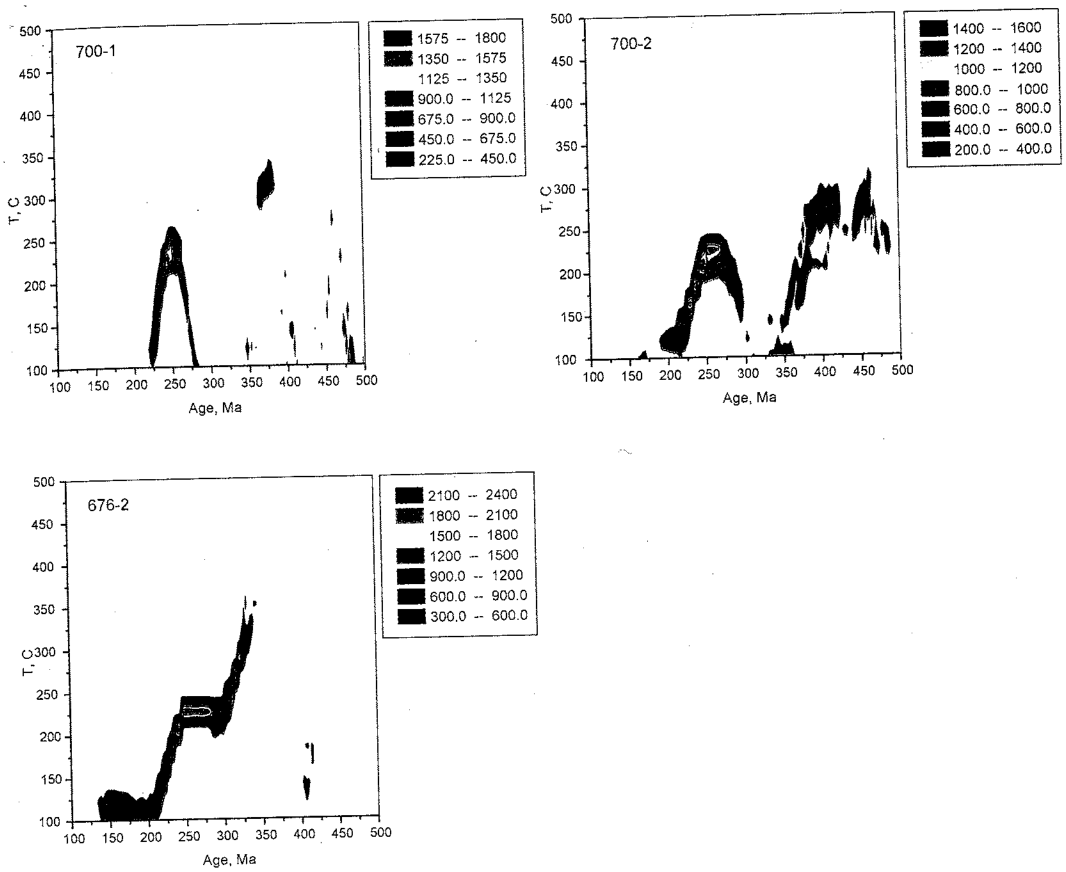

Fig. 7.28. (Continued).

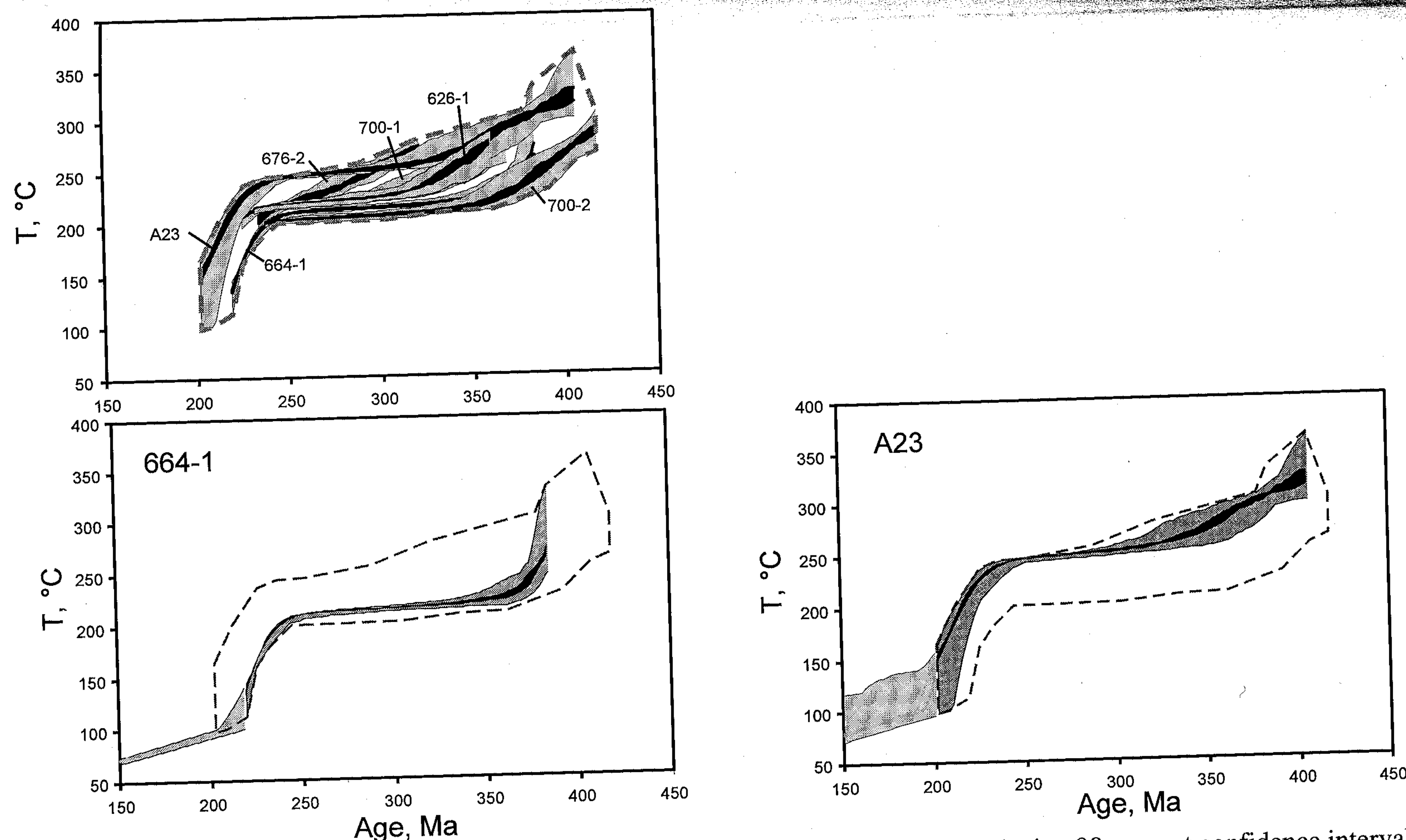

Fig. 7.29. Model thermal histories requiring monotonic cooling. Black and gray contours depict 90 percent confidence intervals for the mean and overall distribution of thermal histories, respectively. Light gray contours correspond to low temperature portions of age spectra that are significantly affected by excess ^{40}Ar. Dashed line shows spread of thermal histories of samples A23, 664-1, 676-2, 626-1, 700-1, and 700-2. Final, "fast cooling" portion of the contour is defined by thermal histories of samples A23 and 664-1(see the graph in the upper row). Continued on next two pages.

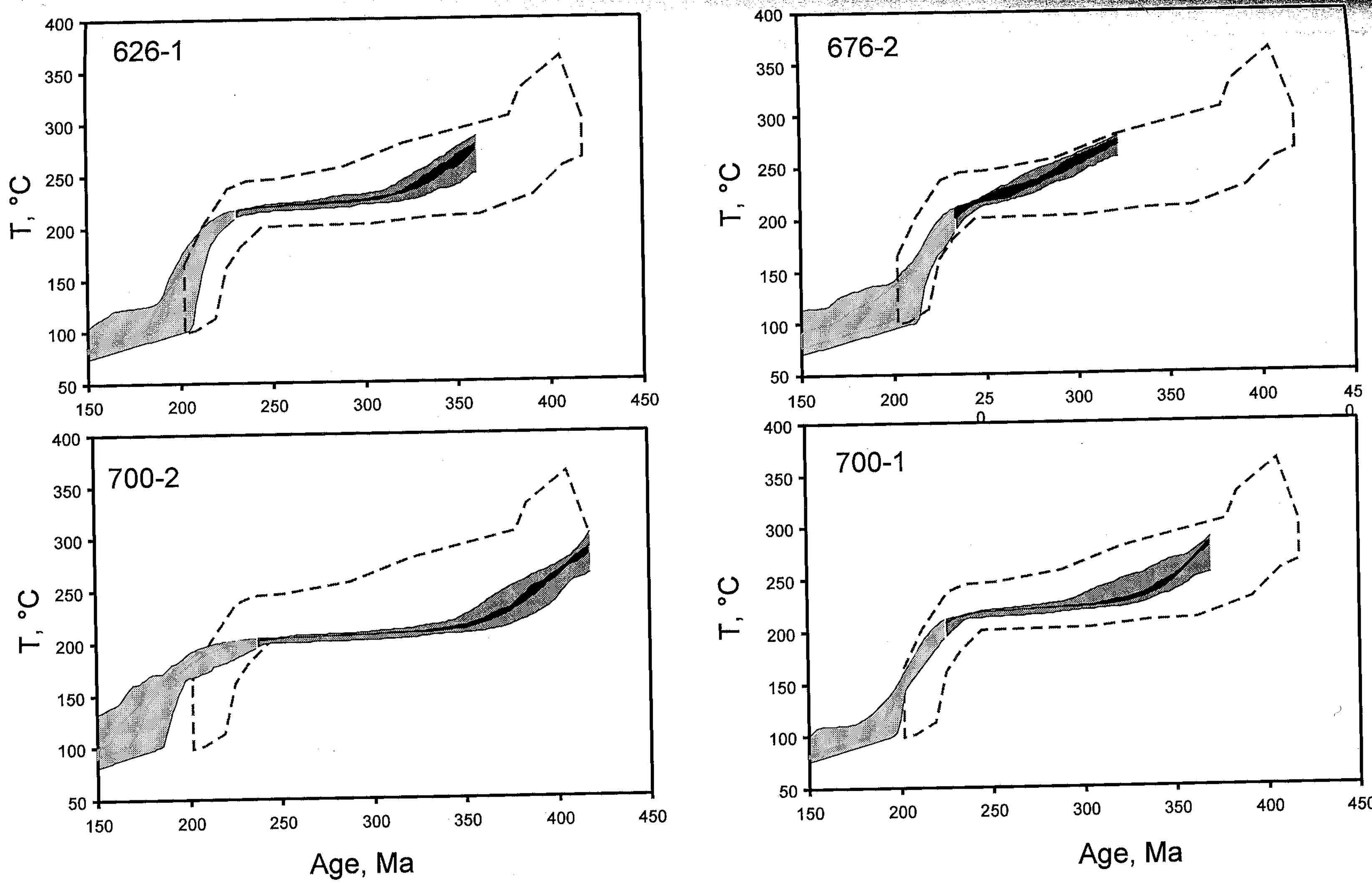

Fig. 7.29. (Continued).

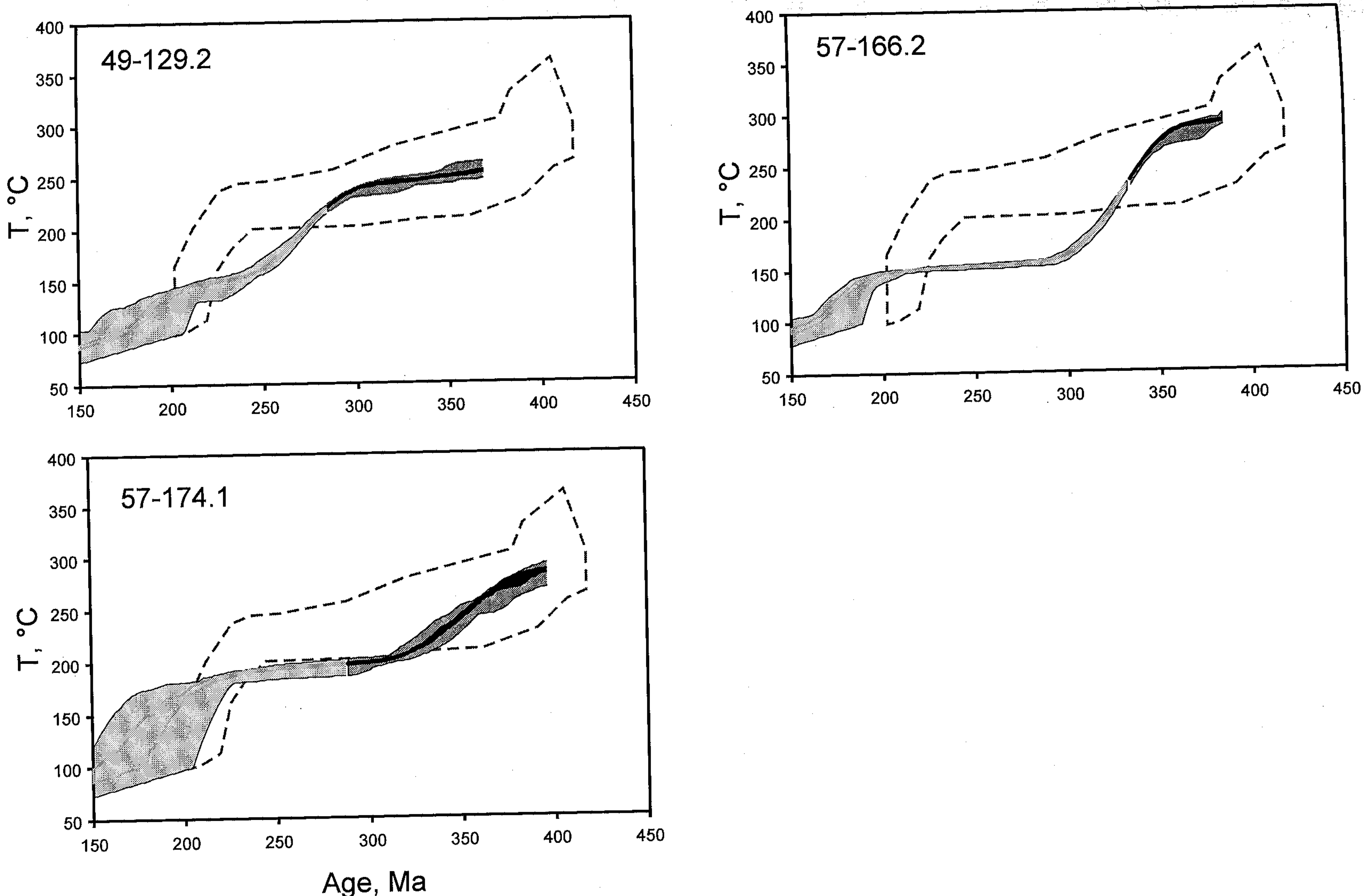

Fig. 7.29. (Continued).

Inconsistent results yielded by K-feldspar phenocrysts from the syenite porphyries need to be addressed. Samples A23, 49-129.2; 57-166.2, and 57-174.1 are chemically similar and occupy essentially the same position with regards to stratigraphy and proximity to the hydrothermal system and major faults. Thus, thermal histories of these samples are expected to be similar. Model thermal histories produced by sample A23 are generally compatible with those of other K-feldspars from within and outside the Solton Sary district, however thermal histories of K-feldspars 49-129.2, 57-166.2, and 57-174.1 are distinctly dissimilar. These thermal histories are likely influenced by artifacts of Cl-correlated excess ^{40}Ar correction and by apparent presence of excess ^{40}Ar that affects the shape of the age spectra beyond the isothermal steps. Unlike the age spectrum of sample A23 where the beginning of age gradient corresponds to ca. 230 Ma, age gradients of the three anomalous K-feldspars start from 270-330 Ma. It is suggested that among four analyzed K-feldspars sample A23 is the most reliable because it was analyzed with a more detailed heating schedule that provided a more accurate age spectrum. Results of K-feldspars 49-129.2, 57-166.2, and 57-174.1 are excluded from further consideration.

Geologic implications

All samples other than 49-129.2, 57-166.2, and 57-174.1 returned geometrically similar t-T graphs, although with rather broad spread of temperatures that probably reflects the inability to accurately determine the E. Combined unrestricted and monotonic cooling models of six K-feldspar samples are presented in Figure 7.30. Prior to addressing geologic implications of these models, it has to be recognized that the combined thermal histories are highly uncertain and unsuitable for truly quantitative,

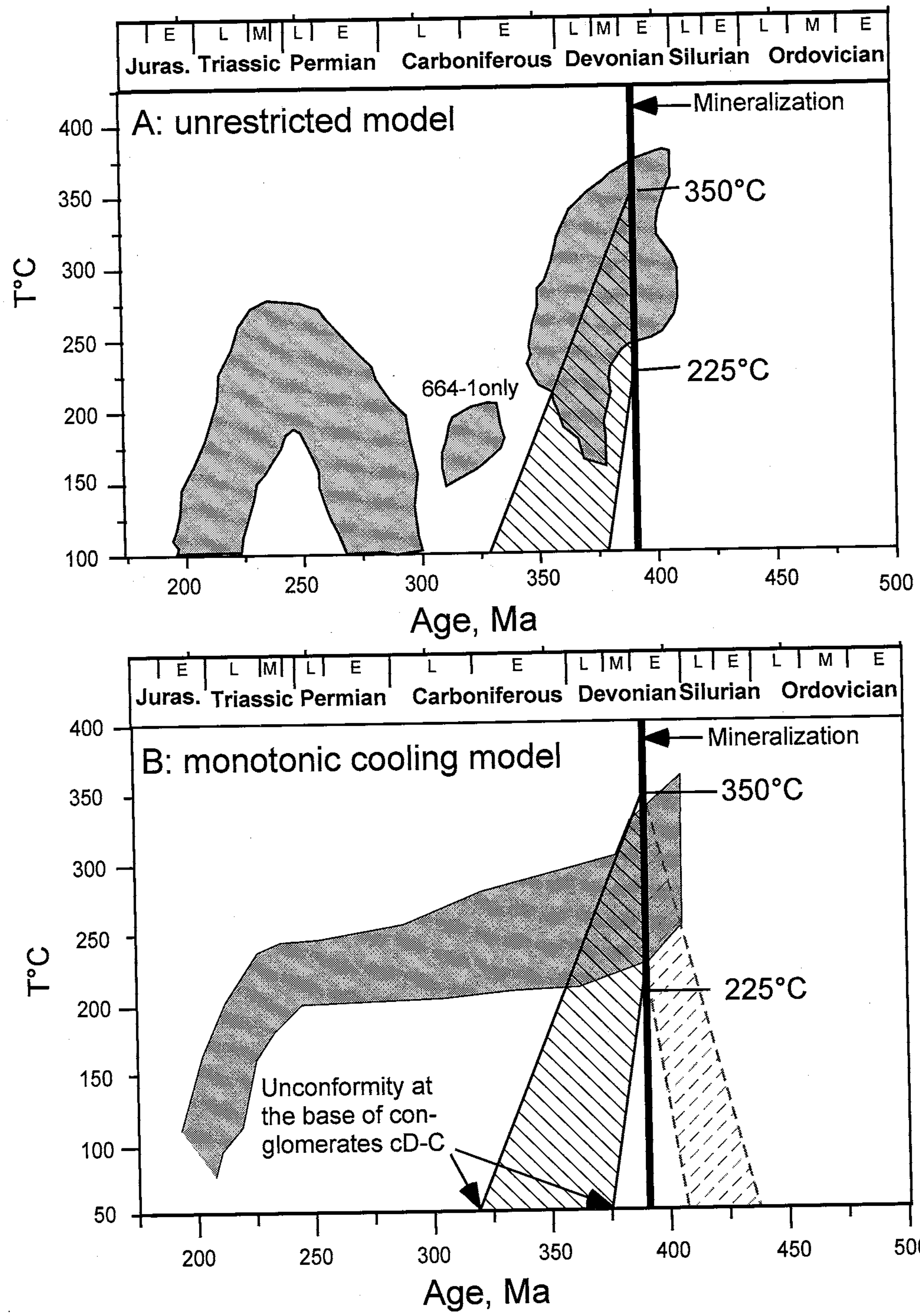

Fig. 7.30. Combined thermal histories for six K-feldspar samples. A, unrestricted models; B, monotonic cooling models. Combined graphs are compiled by overlaying t-T graphs of individual samples and shading between minimum and maximum temperatures (for unrestricted models, only reasonably well constrained portions of graphs are included). Hatched areas depict geologic constraints. Black solid hatch is based on presently accepted stratigraphic scheme that assumes Devonian-Carboniferous age of conglomerates. Gray dashed hatch (only on B plot) assumes Silurian-Devonian age of conglomerates. See text for additional explanations.

"high-resolution", interpretation. The following discussion attempts to test models for general compliance with available geologic constraints and to explain geologically the most prominent features of t-T graphs.

Independent t-T constraints are available only for the earliest portion of post-mineralization history (Fig. 7.30). Fluid inclusion data indicate that during the mineralization (i.e. at ca. 395-390 Ma), the temperature could have varied from 225° to 350°C. The upper limit is based on the most probable fluid temperature. The lower temperature limit is calculated from the minimum estimated paleodepth (9 km) and thermal gradient 25°C/km. The second t-T constraint is much less certain and is defined by the unconformity at the base of Devonian-Carboniferous conglomerates. The exact timing of the initiation of clastic sedimentation is unknown. For simplicity, it is assumed that the deposition started sometime during Late Devonian-Early Carboniferous (i.e. 374-320 Ma). The temperature is assumed equal to 50°C reflecting a paleodepth of 2 km. Geology of the Solton Sary district does not provide direct constraints for the subsequent thermal evolution. Several regional magmatic and tectonic events (Fig. 2.6) may have influenced the thermal history, but their timing and potential thermal effects on the Solton Sary area are uncertain.

Both unconstrained and slow cooling models (Fig 7.30) agree on high temperatures during the mineralization that are consistent with P-T conditions inferred from the fluid inclusion data. Another common feature of the two models is the final cooling after 250 Ma. Apart from these similarities, the two model thermal histories are different. The unconstrained model (Fig 7.30A) shows that the observed ^{40}Ar loss patterns could have resulted from rapid post-mineralization cooling and subsequent reheating with a thermal peak at about 250 Ma. The monotonic cooling model (Fig. 7.30B) involves only insignificant post-mineralization temperature decrease that is followed by a prolonged near isothermal segment prior to the final fast cooling at ca. 225-200 Ma. Geologic implications of two thermochronologic models are discussed below.

The initial phases of the unconstrained model thermal history do not conflict with the geologic evidence. The 9-12 km paleodepth of the hydrothermal system is likely a result of pre-mineralization tectonic burial. This burial probably postdated the alkalic magmatism at ca. 455-430 Ma, as the textures of lamprophyres and syenite porphyries imply the likelihood of shallow emplacement. Post-mineralization cooling could be related to regional uplift and denudation that is marked by the unconformity at the base of Devonian-Carboniferous conglomerates. The modeled timing of maximum cooling is too uncertain, but appears to broadly agree with the equally uncertain geologic age of the unconformity. Deposition of conglomerates took place mainly during Carboniferous, most likely episodically. The thermal regime between the 350 Ma and 300 Ma is unconstrained for most of the samples, except for the K-feldspar 664-1 from a mineralized quartz vein. This sample reveals a probability for elevated temperatures (175°-200°C) at ca. 325 Ma. The significance of this thermal episode is unclear. The elevated temperatures could be a combined effect of a paleodepth and some discrete reheating event such as proximal magmatism, or a localized flux of thermal fluids that re-entered the extinct mesothermal system. Unfortunately, no geologic data are available to support these interpretations. At ca. 300-250 Ma (Late Carboniferous-Permian), the system experienced heating that peaked at 200-275°C by ca. 250 Ma. The interpretation of this thermal event is complicated by high uncertaintlies of the thermochronologic model and regional geochronologic data. The heating could represent a combined effect of burial and increased heat flow. The latter may be related to the final phases of Tarim-Tien Shan collision, or, more probably, to the Permian-Triassic regional tectonism that caused local extension and alkalic magmatism (e. g., Allen et al., 1995, Bazhenov and Burtman, 1997). After the reheating, the area was rapidly cooled, perhaps due to uplift or extensional exhumation.

The monotonic cooling model agrees with 225°-350°C paleotemperatures at ca. 395-390 Ma but is clearly incompatible with the Devonian-Carboniferous age of the unconformity at the base of terrestrial clastic sedimentary rocks. A revision of present stratigraphic scheme is required to viably interpret this thermal history. The large depth of the mineralization and prolonged residence at high temperatures could be due to the burial under the conglomerates the remnants of which cap the stratigraphic section of the Solton Sary district and are presently identified as Devonian-Carboniferous. To accommodate with the monotonic cooling model, these sedimentary rocks are required to be older, perhaps Silurian-Devonian, so the maximum burial could have been achieved by ca. 395 Ma (Early Devonian). If this assumption is accepted, the monotonic cooling model is geologically realistic. The conglomerates could have started to accumulate sometime in Silurian and achieved maximum thickness (i.e. at least 7-8 km) by the time of mineralization (ca. 395 Ma). After the termination of the hydrothermal activity, the system remained deeply buried until ca. 225-200 Ma, when it was uplifted, unroofed, and cooled.

Interestingly, this scenario is not completely unrealistic: the presently accepted Devonian-Carbonifreous age of the conglomerates is poorly constrained. Moreover, Lomize et al. (1997) report the occurrence of Late Ordovician conglomerates in about 70 km northwest of the Solton Sary area. These conglomerates are presumably related to North-Median Tien Shan collision. Similarly, the conglomerates of the Solton Sary area could be older than Devonian, and their deposition could have been triggered by the Late Ordovician -Early Silurian collisional tectonism. It appears reasonable to re-examine the age of the terrestrial clastic sediments of the Solton Sary district. However, the uncertain thermochronologic data alone are insufficient for re-assigning the age of the stratigraphic unit. The unrestricted model that implies post-mineralization uplift and denudation, followed by later burial and reheating is in better agreement with the available geologic evidence.

Summary of $^{40}Ar/^{39}Ar$ data

The $^{40}Ar/^{39}Ar$ data are summarized in Figure 7.31. Alkalic magmatism that resulted in emplacement of lamprophyres and syenite porphyries occurred sometime during 455-430 Ma (Late Ordovician-Early Silurian), and most likely closer to 455 Ma. The emplacement of lamprophyres and syenite porphyries broadly coincided with final stages of arc-related granitoid magmatism (460-440 Ma, Mikolaichuk et al., 1997) and Late Ordovician, presumably post-Caradocian (i.e. 448-438 Ma) collision of North Tien Shan and Median Tien Shan blocks (Lomize et al., 1997; Mikolaichuk et al., 1997). Minimum age estimate for the South Kumbel fault (ca. 430 Ma) supports a possible association of this fault with the North-Median Tien Shan collision.

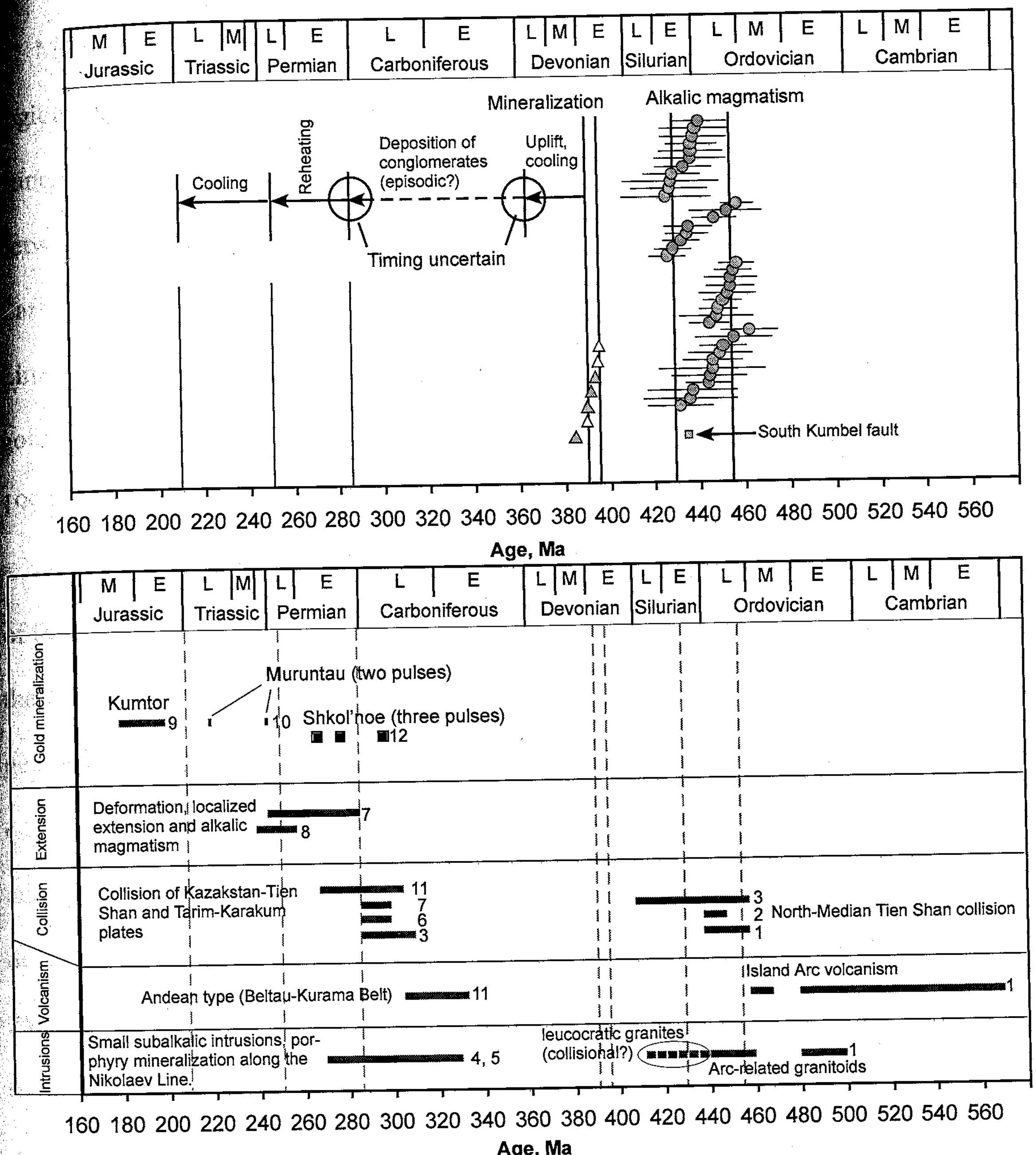

1, Mikolaichuk et al. (1997); 2, Lomize et al.(1997); 3, Sengör and Natal'in (1996a,b); 4 Kudrin et al. (1990); 5, Solov'yev (1995); 6, Burtman et al.(1998); 7, Bazhenov and Burtman (1997); 8, Allen et al. (1995); 9, Nikonorov (1993); 10, Wilde at al. (2001); 11, Zonenshain et al.(1990); 12, Moralev and Shatagin (1999).

$^{40}Ar/^{39}Ar$ step heating terminal ages

△ muscovite from barren quartz veins

▲ muscovite from auriferous quartz veins

▫ fuchsite

$^{40}Ar/^{39}Ar$ UV laser in situ ablation ages

–●– cores of magmatic biotites, 2σ errors

Fig. 7.31. Summary of $^{40}Ar/^{39}Ar$ geochronologic and thermochronologic data for the Solton Sary district and correlation with regional geologic events. Post-mineralization history is based on results of unrestricted thermochronologic modeling (Fig. 7.30A). For more details on regional tectonics see chapter 2 and Figure 2.6.

Mesothermal mineralization was formed at 395-390 Ma, near simultaneously with regionally widespread barren quartz veins. A significant time gap between the mineralization and alkalic magmatism precludes any possibility for genetic relationships between auriferous veins and host intrusions. The mineralization is older than Carboniferous intrusions and associated porphyry systems clustering along the Nikolaev Line (Kudrin et al., 1990; Solov'yev, 1995). It is also older than the giant mesothermal gold systems Kumtor and Muruntau, that have ages of 200-180 Ma (K-Ar, Nikonorov, 1993), and 220 and 245 Ma ($^{40}Ar/^{39}Ar$, Wilde et al., 2001), respectively.

Virtually all analyzed samples experienced post-crystallization ^{40}Ar loss. The results of thermochronologic modeling, although uncertain, do allow a post-mineraliziation thermal history that is capable of explaining the ^{40}Ar loss and is compatible with the geology of the district. At the time of mineralization (ca. 395-390 Ma) the area experienced high temperatures (ca. 250°-375°C) due to the large paleodepth (9-12 km) and hydrothermal activity. This was followed by fast cooling caused by uplift and denudation. Later reheating, with the highest temperatures of 200-275°C reached at ca. 250 Ma (Late Permian), was likely a combined effect of burial under terrestrial clastic sediments and increased heat flow. The latter could be related to the final stages of collision between the Kazakstan-Tien Shan and Tarim-Karakum plates, or more, probably, to the Permian-Triassic tectonic event that involved reactivation of major faults, local extension and alkalic magmatism (e. g., Bazhenov and Burtman, 1997; Allen et al., 1995). The final cooling below ca. 150°C took place in the Triassic, at ca. 225-200 Ma probably due to accelerated uplift or perhaps extensional exhumation. The timing of the cooling broadly corresponds to the reported ages of gold mineralization at two largest mesothermal systems of the region, Muruntau and Kumtor but these ages are too uncertain to support the significance of this temporal association.

CHAPTER 8

SYNTHESIS AND CONCLUSION

Synthesis

Tectonic setting of mineralization

The mesothermal mineralization of the Solton Sary district appears to be broadly related to the final stages of the Early Paleozoic tectonic cycle, more specifically to the collisional tectonism that resulted in the amalgamation of the Kazakstan-Tien Shan orogen in the Late Ordovician-Silurian (Zonenshain et al., 1990; Sengör and Natal'in, 1996a, b). During the Cambrian-Middle Ordovician, the host tectonic unit, Kyrgyz Terskei zone, represented an island arc at the southern (in present day coordinates) margin of the North Tien Shan block. Orogenesis initiated when North Tien Shan converged with the Talas-Karatau zone of the Median Tien Shan terrain (Mikolaichuk et al., 1997; Lomize et al., 1997). The collisional tectonism caused thrusting, folding, strike-slip displacements along regional faults, and probably formation of the synform structure, the north limb of which subsequently hosted gold mineralization. The mantle-sourced potassic magmatism that produced sills of lamprophyres and syenite porphyries at 430-455 Ma is likely to have been triggered by this collision. In addition to the age of the intrusions, the timing of tectonism is directly supported by the terminal age (ca. 430 Ma) of fuchsite from the South Kumbel fault.

Solton Sary is proximal to the terrane boundary fault, the Nikolaev Line. The auriferous quartz veins were formed at 395-390 Ma, i. e. about 40-60 m. y. after the initial collision event. Although the temporal association of collision and mineralization is typically closer, there are cases of 40-50 m.y. time gaps that are explained by delayed internal heating of tectonically thickened crust (e. g., Stüwe, 1998). At Solton Sary, the deformation continued (perhaps episodically) long after the initial collision, and the mineralization was synkinematic. Virtually all mineralized zones are (to variable extent) affected by shearing, and hydrothermal minerals commonly show evidence for syn-deformational crystallization. The deformation resulted from predominantly strike-slip tectonism that was probably related to a regional transpressive regime. Metamorphic conditions corresponded to greenschist facies, more specifically, to the seismic-aseismic transition zone.

Relationship with magmatism and association with potassic intrusions

All mineralized zones are hosted by one stratigraphic unit (upper volcaniclastic turbidites v_2O_{1-2}) and are intimately associated with planar intrusions of potassic lamprophyres and syenite porphyries. The absence of intrinsic gold enrichment in potassic rocks and, more importantly, a 40-60 m. y. time gap between magmatism and mineralization rule out a possibility for genetic relations between the host intrusions and the mesothermal system.

This district-scale control of gold mineralization by planar intrusions is not fully understood, but at least its structural aspect can be addressed. It appears that the intrusive swarm as a whole could act as an efficient fluid conduit. The intrusive suite is a vertically extensive structure that may extend to lower crustal depths and is likely connected to a deep structural network. The upper portion of the intrusive suite that is exposed at the present day erosion level can be approximated as intercalating sheets or lenses of compositionally and rheologically different syenite porphyries and lamprophyres. During formation, competent syenite intrusions, especially thick sills (~10 m and thicker), are expected to behave as stronger bodies in a weaker matrix that would result in a heterogeneous stress distribution (Oliver et al,, 1990). This may generate highly permeable fluid pathways spatially associated with competent bodies, such as strain shadows and dilation zones at exocontacts and/or fracture and breccia zones within the sills (Oliver et al., 1990). As shown by Ojala et al. (1993) and Oliver et al. (1990) this mechanism can operate from sub-greenschist to amphibolite conditions. The predominance of incompetent mica-rich lamprophyres at the flanks of the intrusion belt and of thicker and more competent syenite bodies in its internal portion provides a favorable environment for strongly focused fluid flow isolated from surrounding rocks. This is because the fluid pathways associated with syenite intrusions are being additionally enclosed in an impermeable envelope. Along the strike of the intrusive belt, the areas with thicker syenite intrusions are likely to be more favorable for fluid focusing compared to the portions that comprise equally sized and relatively thin bodies of lamprophyres and syenite porphyries. Also, areas of abrupt tapering of thick lens-shaped syenite bodies are likely to host “pressure shadow” fluid pathways (cf. Oliver et al. 1990). Thus, deformation of the swarm of alkalic intrusions could have generated a vertically extensive fluid conduit for the mesothermal system of the Solton Sary district. If this plumbing system was connected to a potentially auriferous source, it must have been suitable for distal transport of fluids to mineralization sites.

Fluid characteristics

The parental auriferous fluids had low salinity (up to 6 equiv. wt % NaCl) and contained at least 10 mole percent CO_2. Most probable temperature-pressure conditions were ca. 350°C and 3-3.5 kbar, however, fluid pressure episodically dropped down to 1-1.7 kbar under a presumed fault-valve mechanism. These pressure fluctuations promoted phase separation that resulted in loss of sulfuric species and caused gold deposition. Assuming that maximum fluid pressures approximate the lithostatic load and considering potential inaccuracies of fluid inclusion-based pressure reconstructions, the most probable depth of mineralization appears to be in a range of 9-12 km. The fluids show a distinctly non-meteoric N_2/Ar signature. The lack of documented syn-mineralization magmatism within the Solton Sary district does not favor the proximal magmatic source and suggests distal fluid transport. The auriferous fluids could have been generated by metamorphic devolatilization at greenschist-amphibolite facies transition or have been derived from a deep magmatic (granitic) source. Toward the waning stages of hydrothermal activity, there was an incursion of highly saline, low carbonic, aqueous fluids. Within the mesothermal system, aqueous brines were mixing with carbonic-rich fluids, generating secondary fluid inclusions with markedly variable salinities and CO_2 contents. At the flanks of the system, the external low carbonic saline fluids were trapped in secondary inclusions of propylitic veins. The N_2/Ar signature of the brines implies their non-meteoric nature. Most likely, these saline fluids represent highly evolved marine waters that lost their original volatile signature through interaction with volcanogenic host rocks.

Post-mineralization history

Termination of the hydrothermal activity was followed by fast cooling caused by uplift and denudation. Sometime during the latest Devonian-Early Carboniferous, the terrestrial coarse clastic sediments started to accumulate over the unconformity surface. This accumulation probably continued through most of the Carboniferous, perhaps episodically. In Late Carboniferous-Permian, the system experienced reheating, with the thermal peak of 200-275°C achieved at ca. 250 Ma (Late Permian). This thermal event was likely a combined effect of burial and increased heat flow. The latter could be associated with the final stages of collision between the Kazakstan-Tien Shan and Tarim-Karakum plates, or more, probably, be related to the Permian-Triassic tectonism that involved reactivation of major faults, local extension and alkalic magmatism (e. g., Bazhenov and Burtman, 1997; Allen et al., 1995). The final cooling below ca. 150°C took place in the Triassic (at ca. 225-200 Ma) probably due to uplift or extensional exhumation. The exhumation of the Solton Sary also appears to broadly correlate with mesothermal mineralization at Muruntau and Kumtor, but the geochronological data supporting these mineralizing events are not conclusive and the significance of the temporal correlation is uncertain.

Implications for the Tien Shan metallogeny

The Devonian age of the Solton Sary mineralization shows that economically important hydrothermal activity at the southern margin of the Kazakstan-Tien Shan orogen was not restricted to the Late Paleozoic-Mesozoic time. At least some tectonic units of the orogen experienced two cycles of plate convergence, both of which culminated by collisional events with characteristic transpressional tectonism. Apparently, both tectonic cycles generated gold mineralization. As a result, deposits of different ages co-exist within relatively compact areas and commonly cluster along the same regional structures. The Nikolaev Line, the regional strike-slip fault separating the North and Median Tien Shan blocks, is one of these structures. The Devonian mesothermal Solton Sary district, several Carboniferous-Permian gold-bearing porphyry systems and the giant Late Paleozoic-Early Mesozoic mesothermal Kumtor gold deposit are spatially associated with this fault (Kudrin et al., 1990; Ivanov et al., 2000; Abeleira et al., 2000). The metallogenic role of the Nikolaev Line has been recognized earlier (e. g., Kudrin et al., 1990), and systematic exploration has been conducted within the area in Soviet and post-Soviet times. However, some potentially economic Early Paleozoic systems may have been overlooked, as the exploration philosophy was strongly biased towards models applicable only for the Late Paleozoic mineralization (for example, relating the mineralization to Carboniferous-Permian magmatism, e. g., Kudrin et al., 1990). A considerable potential may be remaining, even within the previously explored areas.

The province-scale association of diachronous mineralized systems raises questions about a possibility of repeated mineralizing events occurring at different times at the same deposit. Drew et al. (1996) review hypotheses by Soviet geologists that propose the occurrence of Early Paleozoic mineralization at Muruntau, over which the later hydrothermal events superimpose causing increasing gold concentration. The authors conclude on the unlikelihood of this scenario, however, due to a complexity and fragmental nature of available geochronologic data, the question cannot be considered completely answered. The well-established Devonian age of mesothermal mineralization at Solton Sary shows that a possibility for earlier mineralizing events within Late Paleozoic mesothermal systems is not completely unrealistic and deserves additional attention.

The results of this study imply that the metallogeny of the southern flank of the Kazakstan-Tien Shan orogen cannot be generalized to a single regional mineralizing event. There is a need for comprehensive metallogenic studies supported by precise geochronology that would allow better understanding of the factors controlling the distribution of mineralization and its relationships with major tectonic and magmatic events.

Application of the UV laser in situ ablation $^{40}Ar/^{39}Ar$ method for dating mesothermal mineralization

As mentioned in Chapter 1, the ^{40}Ar/^{39}Ar geochronology of mesothermal gold deposits is generally problematic because of common post-crystallization ^{40}Ar loss. This study illustrates the high potential of the UV laser in situ ablation ^{40}Ar/^{39}Ar technique for dating mesothermal mineralization. Relatively coarse (1-3 mm in diameter) muscovite, fuchsite, biotite, and phlogopite are not uncommon in mesothermal lodes. Even after experiencing some post-crystallization ^{40}Ar loss, the cores of these coarse micas can retain ages approximating the timing of mineralization. In the case of intracrystalline age zoning, the step heating method may produce meaningless "homogenized" ages, whereas the high-resolution in situ laser ablation technique is capable of retrieving meaningful ages from cores of mica crystals. Specifically for the Solton Sary mineralization, the UV laser in situ ablation method provided crucial information for resolving the timing of mineralization and potassic magmatism that would not be possible based solely on the step heating data. The technique appears to be particularly promising for dating Precambrian systems because of greater $^{40}Ar^{*}$ contents and better precision of in situ ages.

Conclusions

The Solton Sary mesothermal gold district is hosted in an Early Paleozoic arc-related volcanogenic succession at the southern flank of the North Tien Shan terrane. The host volcanogenic sequence underwent deformation as a result of a collision with a different tectonostratigraphic terrane, the Median Tien Shan. The Solton Sary district is underlain by Cambrian subaqeous mafic to intermediate lavas and tuffs, Middle Ordovician tuffs and turbidites, and Middle Ordovician likely allochtonous carbonates. Terrestrial conglomerates and sandstones that unconformably cap the section are interpeted to have the Devonian-Carboniferous age. The volcanic rocks are metamorphosed to greenschist facies and dip steeply south-southwest. Intrusive rocks comprise shoshonitic lamprophyres and their more felsic derivatives, syenite-porphyries. Both rock types occur as concordant intrusions that were likely emplaced at shallow levels. The mineralization is spatially associated with the intrusive suite and comprises steeply dipping fault-fill veins and, less commonly, swarms of variably oriented veinlets. Most commonly, the mineralized zones occur at syenite contacts. Hydrothermal alteration includes distal biotite alteration and a proximal quartz-sericite-carbonate-pyrite assemblage. Native gold occurs in quartz veins rather than in altered wall rocks. Mineralization was synkinematic and was emplaced under a predominantly transpressive tectonic regime. Deformation styles of host intrusions and mineralized zones imply greenschsit metamorphic conditions at the seismic-aseismic transition. Gold was deposited from low saline ($\leq$ 6 equiv. wt % NaCl) aqueous-carbonic ($X_{CO_2} \geq 0.1$) fluids at temperatures of about 350°C. Fluid trapping pressures fluctuate from 1-1.7 to 3-3.5 kbar, which probably reflects pressure cycling under the fault-valve mechanism. Phase separation due to pressure drops must have represented the most probable mechanism of gold precipitation. The most likely depth of mineralization is about 9-12 km. Bulk volatile chemistry of the fluids, especially $N_2/Ar > 100$, implies their non-meteoric origin. The fluids could have been generated by metamorphic devolatilization at the greenschist-amphibolite transition or by deep granitic magmatism. The close spatial association of the gold mineralization and potassic intrusions likely reflects the role of the intrusive sequence as a fluid pathway.

$^{40}Ar/^{39}Ar$ dating shows that the lamprophyres and syenites were emplaced at ca. 455-430 Ma and the mineralizing events occurred at 395-390 Ma. The potassic magmatism most likely marked the initiation of the North-Median Tien Shan collision, and the mineralization was formed during the last phases of collisional deformation. The age of ca. 430 Ma of tectonogenic fuchsite provides a direct constraint on the minimum age of the tectonism. After the mineralization was complete, the system experienced cooling due to uplift and denudation. During the Late-Carboniferous-Permian, the area was reheated with the maximum temperature of 200-275°C achieved at ca. 250 Ma. This reheating likely resulted from burial under terrestrial clastic sediments and increased heat flow. The latter could be related to collision between the Kazakstan-Tien Shan and Karakum-Tarim plates or to Permian-Triassic tectonic reactivation caused by re-arrangments of East

European and Siberian cratons. The final cooling at ca. 225-200 Ma reflects uplift or extensional exhumation.

The Solton Sary system represents a reliably documented example of Devonian mesothermal mineralization linked to the Early Paleozoic plate convergence. Thus, contrary to the broadly shared view, gold mineralization at the southern flank of the Kazakstan-Tien Shan orogen was not limited to the Late Paleozoic-Mesozoic time. This deviation from the currently accepted metallogenic interpretation implies a need for further detailed geologic and geochronologic studies of Tien Shan gold deposits that would allow generation of a reliable and more comprehensive regional metallogenic model.

REFERENCES

Abeleira, A., Ansdell, K. M., Thomas, D., Heaman, L., and Melrose, D. L., 2000, Geology and structural evolution of the Kumtor region, Tien Shan, Kyrgyzstan, *in* Bucci, L. A., and Mair, J. L., eds., Gold in 2000. Poster session extended abstracts, Lake Tahoe, Nevada. November 10-11, 2000, p. 41-46.

Allen, M. B., Sengör, A. M. C., and Natal'in, B. A., 1995, Junggar, Turfan and Alakol basins as Late Permian to ?Early Triassic extensional structures in a sinistral shear zone in the Altaid orogenic collage, Central Asia: Journal of the Geological Society, London, v. 152, p. 327-338.

Andersen, T., Austrheim, H., Burke, E. A. J., and Elvevold, S., 1993, N_2 and CO_2 in deep crustal fluids: evidence from the Caledonides of Norway: Chemical Geology, v. 108, p. 113-132.

Anonymous, 1997, Oxus' Central Asian Hopes, Mining Magazine, November 1997, p. 300-305.

Arima, M., and Edgar, A. D., 1981, Substitution mechanisms and solubility of titanium in phlogopites from rocks of probable mantle origin: Contributions to Mineralogy and Petrology, v. 77, p. 288-295.

Bachinski, S. W., and Simpson, E. L., 1984, Ti-phlogopites of the Shaw's Cove minette: a comparison with micas of other lamprophyres, potassic rocks, kimberlites, and mantle xenoliths: American Mineralogist, v. 69, p. 41-56.

Baker, T., 2000, The role of carbon dioxide in intrusion-related gold deposits: Economic Geology Research Unit (James Cook University, School of Earth Sciences) Newsletter. Research 2000 special edition., p. 3.

Barley, M. E., and Groves, D. I., 1992, Supercontinent cycles and the distribution of metal deposits through time: Geology, v. 20, p. 291-294.

Bazhenov, M. L., and Burtman, V. S., 1997, Late Paleozoic Deformations of the Tien Shan: Geotectonika, p. 56-65 (in Russian).

Berger, B. R., Drew, L. J., and Snee, L. W., 1994, An epoch of gold riches: the Late Paleozoic in Uzbekistan, Central Asia: SEG Newsletter, v. 16, p. 1-11.

Bierlein, F. P., and Crowe, D. E., 2000, Phanerozoic orogenic lode gold deposits: Reviews in Economic Geology, v. 13, p. 103-139.

Blamey, N. J. F., 2000, The evolution of hydrothermal fluids at the Pipeline Gold Mine, Lander county, Nevada: Unpub. Ph.D. thesis, New Mexico Institute of Mining and Technology, 183 p.

Boullier, A. M., Firdaous, K., and \ Robert, F., 1998, On the significance of aqueous fluid inclusions in gold-bearing quartz vein deposits from the southeastern Abitibi subprovince (Quebec, Canada): Economic Geology, v. 93, p. 216-223.

Boullier, A. M., and Robert, F., 1992, Paleoseismic events recorded in Archean gold-quartz vein networks, Val d'Or, Abitibi, Quebec, Canada: Journal of Structural Geology, v. 14, p. 161-179.

Bowers, T. S., 1991, The deposition of gold and other metals: Pressure-induced fluid immiscibility and associated stable isotope signatures: Geochimica et Cosmochimica Acta, v. 55, p. 2417-2434.

Brown, P. E., and Hagemann, S. G., 1995, MacFlinCor and its application to fluids in Archean lode-gold deposits: Geochimica et Cosmochimica Acta, v. 59, p. 3943-3952.

Brügmann, G. E., Arndt, N. T., Hofmann, A. F., and Tobschall, H. J., 1987, Noble metal abundances in komatiite suite from Alexo, Ontario and Gorgona Island, Colombia: Geochimica et Cosmochimica Acta, v. 51, p. 2159-2169.

Burtman, V. S., Gurarii, G. Z., Belen'kii, A. V., Ignat'ev, A. V., and Audibert, M., 1998, Turkestan ocean in the Middle Paleozoic: reconstruction using paleomagnetic data for the Tien Shan: Geotectonika, p. 15-26 (in Russian).

Cameron, E. M., and Hattori, K., 1987, Archean gold mineralization and oxidized hydrothermal fluids: Economic Geology, v. 82, p. 1177-1191.

Cole, A., Wilkinson, J. J., Halls, C., and Serenko, T. J., 2000, Geological characteristics, tectonic setting and preliminary interpretation of the Jilau gold-quartz vein deposit, Tajikistan: Mineralium Deposita, v. 35, p. 600-618.

Corfu, F., 1993, The evolution of the Southern Abitibi greenstone belt in light of precise U-Pb geochronology: Economic Geology, v. 88, p. 1323-1340.

Crawford, M. L., 1981, Fluid inclusions in metamorphic rocks-low and medium grade, *in* Hollister, L. S., and Crawford, M. L., eds., Fluid inclusions: applications to petrology; Mineralogical association of Canada short course handbook, volume 6: Calgary, Mineralogical association of Canada, p. 157-181.

Dee, S. J., and Roberts, S., 1993, Late-kinematic gold mineralisation during regional uplift and the role of nitrogen: an example from the La Codosera area, W. Spain: Mineralogical Magazine, v. 57, p. 437-450.

Deer, W. A., Howie, R. A., and Zussman, J., 1992, An introduction to the rock-forming minerals: Harlow, England; New York, Longman Scientific & Technical, John Wiley & Sons, 696 p.

Deino, A., and Potts, R., 1992, Age-probability spectra for examination of single-crystal $^{40}Ar/^{39}Ar$ dating results: examples from Olorgesailie, southern Kenya Rift: Quaternary International, v. 13-14, p. 47-53.

Diamond, L. W., 2001, Review of the systematics of CO_2-H_2O fluid inclusions: Lithos, v. 55, p. 69-99.

Dickinson, W. R., 1985, Interpreting provenance relations from detrital modes of sandstones, *in* Zuffa, G. G., ed., Provenance of arenites: Hingham, Massachusetts, D. Reidel Publishing Company, p. 333-361.

Dodson, M. H., 1973, Closure Temperature in Cooling Geochronological and Petrological Systems: Contributions to Mineralogy and Petrology, v. 40, p. 259-274.

Drew, L. J., Berger, B. R., and Kurbanov, N. K., 1996, Geology and structural evolution of the Muruntau gold deposit, Kyzylkum desert, Uzbekistan: Ore Geology Reviews, v. 11, p. 175-196.

Drummond, S. E., and Ohmoto, H., 1985, Chemical evolution and mineral deposition in boiling hydrothermal systems: Economic Geology, v. 80, p. 126-147.

Fleck, R. J., Sutter, J. F., and Elliot, D. H., 1977, Interpretation of discordant $^{40}Ar/^{39}Ar$ age spectra of Mesozoic tholeiites from Antarctica: Geochimica et Cosmochimica Acta, v. 41, p. 15-32.

Foland, K. A., 1974, ^{40}Ar diffusion in homogeneous orthoclase and an interpretation of Ar diffusion in K-feldspar: Geochimica et Cosmochimica Acta, v. 38, p. 151-166.

Fowler, M. B., and Henney, P. J., 1996, Mixed Caledonian appinite magmas; implications for lamprophyre fractionation and high Ba-Sr granite genesis: Contributions to Mineralogy and Petrology, v. 126, p. 199-215.

Fritz, P., and Frape, S. K., 1982, Saline groundwaters in the Canadian Shield-a first overview: Chemical Geology, v. 36, p. 179-190.

Goldfarb, R. J., Phillips, G. N., and Nokleberg, W. G., 1998, Tectonic setting of synorogenic gold deposits of the Pacific Rim: Ore Geology Reviews, v. 13, p. 185-218.

Goldfarb, R. J., Snee, L. W., Miller, L. D., and Newberry, R. J., 1991, Rapid dewatering of the crust deducted from ages of mesothermal gold deposits: Nature, v. 354, p. 296-298.

Goodwin, L. B., and Williams, P. F., 1996, Deformation path partitioning within a transpressive shear zone, Marble Cove, Newfoundland: Journal of Structural Geology, v. 18, p. 975-990.

Groff, J., 1996, $^{40}Ar/^{39}Ar$ geochronology of gold mineralization and origin of auriferous fluids for the Getchell and Twin Creeks mines, Humboldt County, Nevada: Unpub. Ph.D. thesis, New Mexico Institute of Mining and Technology, 291 p.

Groves, D. I., 1993, The crustal continuum model for late-Archaean lode-gold deposits of the Yilgarn Block, Western Australia: Mineralium Deposita, v. 28, p. 366-374.

Groves, D. I., Goldfarb, R. J., Gebre-Mariam, M., Hagemann, S. G., and Robert, F., 1998, Orogenic gold deposits: A proposed classification in the context of their crustal distribution and relationship to other gold deposit types: Ore Geology Reviews, v. 13, p. 7-27.

Hagemann, S. G., and Cassidy, K. F., 2000, Archean orogenic lode gold deposits: Reviews in Economic Geology, v. 13, p. 9-68.

Hames, W. E., and Bowring, S. A., 1994, An empirical evaluation of the argon diffusion geometry in muscovite: Earth & Planetary Science Letters, v. 124, p. 161-167.

Hames, W. E., and Hodges, K. V., 1993, Laser $^{40}Ar/^{39}Ar$ evaluation of slow cooling and episodic loss of ^{40}Ar from a sample of polymetamorphic muscovite: Science, v. 261, p. 1721-1723.

Harrison, T. M., Grove, M., Heizler, M. T., Lovera, O. M., and Chen, W., 1994, A chlorine disinfectant for excess argon released from K-feldspar during step heating: Earth & Planetary Science Letters, v. 123, p. 95-104.

Ho, S. E., Groves, D. I., McNaughton, N. J., and Mikucki, E. J., 1992, The source of ore fluids and solutes in Archaean lode-gold deposits of Western Australia: Journal of Volcanology and Geothermal Research, v. 50, p. 173-196.

Hodges, K. V., Hames, W. E., and Bowring, S. A., 1994, $^{40}Ar/^{39}Ar$ age gradients in micas from a high-temperature-low- pressure metamorphic terrain: evidence for very slow cooling and implications for the interpretation of age spectra: Geology, v. 22, p. 55-58.

Hodgson, C. J., 1993, Mesothermal gold deposits, *in* Kirkham, R. V., Sinclair, W. D., Thorpe, R. I., and Duke, J. M., eds., Mineral Deposit Modeling: Geological Association of Canada Special Paper 40, p. 635-678.

Hodgson, C. J., 2000, Archean orogenic gold-industry view: Presentation at the SEG sponsored "Gold in 2000" short course, Lake Tahoe, November 2000.

Ingersoll, R. V., Bullard, T. F., Ford, R. L., Grimm, J. P., Pickle, J. D., and Sares, S. W., 1984, The effect of the grain size on detrital modes: a test of the Gazzi-Dickinson point-counting method, Journal of Sedimentary Petrology: Journal of Sedimentary Petrology, v. 54, p. 103-116.

Ivanov, S. M., Ansdell, K. M., and Melrose, D. L., 2000, Ore texture and stable isotope constraints on ore deposition mechanisms at the Kumtor lode gold deposit, *in* Bucci, L. A., and Mair, J. L., eds., Gold in 2000. Poster session extended abstracts, Lake Tahoe, Nevada. November 10-11, 2000, p. 47-52.

Jarosewich, E., Nelen, J. A., and Norberg, J. A., 1980, Reference samples for electron microprobe analyses: Geostandards Newsletter, v. 4, p. 43-47.

Kelley, S. P., and Wartho, J. A., 2000, Rapid kimberlite ascent and the significance of Ar-Ar ages in xenolith phlogopites: Science, v. 289, p. 609-611.

Kent, A. J. R., and McCuaig, T. C., 1997, Disturbed ^{40}Ar-^{39}Ar systematics in hydrothermal biotite and hornblende at the Scotia gold mine, Western Australia: Evidence for argon loss associated with post-mineralization fluid movement: Geochimica et Cosmochimica Acta, v. 61, p. 4655-4669.

Kerrich, R., 1993, Perspectives on genetic models for lode gold deposits: Mineralium Deposita, v. 28, p. 362-365.

Kerrich, R., and Cassidy, K. F., 1994, Temporal relationships of lode gold mineralization to accretion, magmatism, metamorphism and deformation; Archean to present; a review: Ore Geology Reviews, v. 9, p. 263-310.

Kerrich, R., Goldfarb, R. J., Groves, D. I., and Garwin, S., 2000, The geodynamics of world-class gold deposits: characteristics, space-time distribution, and origins: Reviews in Economic Geology, v. 13, p. 501-551.

Kerrich, R., and Kamineni, D. C., 1988, Characteristics and chronology of fracture-fluid infiltration in the Archean , Eye Dashwa Lakes pluton, Superior Province: evidence from H, C, O-isotopes and fluid inclusions: Contributions to Mineralogy and Petrology, v. 99, p. 430-445.

Kerrich, R., and Wyman, D., 1990, Geodynamic setting of mesothermal gold deposits: an association with accretionary tectonic regimes: Geology, v. 18, p. 882-885.

Kerrick, D. M., and Jacobs, G. K., 1981, A modified Redlich-Kwong equation for H_2O, CO_2, and H_2O-CO_2 mixtures at elevated pressures and temperatures: American Journal of Science, v. 281, p. 735-767.

Kheraskova, T. N., Dubinina, S. V., Orlova, A. R., and Seryezhnikova, E. A., 1997, Early Paleozoic accretion complex of northern Tien Shan, *in* Leonov, Y. G., ed., Tectonic and geodynamic phenomena: Moscow, Nauka, p. 221-243 (in Russian).

Kudrin, V. S., Solov'yev, S. G., Stavinsky, V. A., and Karabdin, L. L., 1990, The gold-copper-molybdenum-tungsten ore belt of the Tien Shan: International Geology Review, v. 32, p. 930-941.

Landis, G. P., and Hofstra, A. H., 1991, Fluid inclusion gas chemistry as a potential minerals exploration tool: case studies from Creede, CO, Jerrit Canyon, NV, Coeur d' Alene district, ID and MT, southern Alaska mesothermal veins and mid-continent MVT's: Journal of Geochemical Exploration, v. 42, p. 25-29.

Lang, J. R., Baker, T., Hart, C. J. R., and Mortensen, J. K., 2000, An exploration model for intrusion-related gold systems: SEG Newsletter, v. 40, p. 1-15.

Le Bas, M. J., Le Maitre, R. W., Streckeisen, A., and Zanettin, B., 1986, A chemical classification of volcanic rocks based on the total alkali-silica diagram: Journal of Petrology, v. 27, p. 745-750.

Leat, P. T., Thompson, R. N., Morrison, M. A., Hendry, G. L., and Dickin, A. P., 1988, Silicic magmas derived by fractional crystallization from Miocene minette, Elkhead Mountains, Colorado: Mineralogical Magazine, v. 52, p. 577-585.

LeCheminant, A. N., Miller, A. R., and LeCheminant, G. M., 1987, Early Proterozoic alkaline igneous rocks, District of Keewatin, Canada: petrogenesis and mineralization, *in* Pharaoh, T. C., Beckinsale, R. D., and Rickard, D., eds., Geochemistry and mineralization of Proterozoic volcanic suites (Geological Society Special Publication No 33): Oxford, Boston, Blackwell Scientific Publications, p. 219-240.

Lomize, M. G., Demina, L. I., and Zarshchikov, A. A., 1997, The Kyrgyz-Terskei paleooceanic basin, Tien Shan: Geotektonika, v. 1997, p. 35-55 (in Russian).

Lovera, O. M., Mahon, K. I., Grove, M., and Harrison, T. M., 1997, Systematic analysis of K-feldspar $^{40}Ar/^{39}Ar$ step heating results: I. Significance of activation energy determinations: Geochimica et Cosmochimica Acta, v. 61, p. 3171-3192.

Lovera, O. M., Richter, F. M., and Harrison, T. M., 1989, The $^{40}Ar/^{39}Ar$ thermochronology for slowly cooled samples having a distribution of diffusion domain sizes: Journal of Geophysical Research, v. 94, p. 17917-17935.

Lovera, O. M., Richter, F. M., and Harrison, T. M., 1991, Diffusion domains determined by ^{39}Ar released during step heating: Journal of Geophysical Research, B, Solid Earth and Planets, v. 96, p. 2057-2069.

Mahon, K. I., 1996, The new 'York' regression: application of an improved statistical method of geochemistry: International Geology Review, v. 38, p. 293-303.

Mahon, K. I., Harrison, T. M., and Grove, M., 1998, The thermal and cementation histories of a sandstone petroleum reservoir, Elk Hills, California. Part 1: $^{40}Ar/^{39}Ar$ thermal history results: Chemical Geology, v. 152, p. 227-256.

Makarychev, G. I., and Ges', M. D., 1981, Tectonics of the junction zone between North and Central Tien Shan: Geotectonics, v. 15, p. 327-337.

Marsh, E., Goldfarb, R. J., Hart, C. J. R., and Johnson, C., 2000, Auriferous sheeted quartz veins of the Clear Creek intrusion-related gold deposit, Tintina mineral belt, Yukon, Canada, *in* Bucci, L. A., and Mair, J. L., eds., Gold in 2000. Poster session extended abstracts, Lake Tahoe, Nevada. November 10-11, 2000., p. 53-56.

McCuaig, T. C., and Kerrich, R., 1998, P-T-t-deformation-fluid charcteristics of lode gold deposits: evidence from alteration systematics: Ore Geology Reviews, v. 12, p. 381-453.

McDougall, I., and Harrison, T. M., 1999, Geochronology and thermochronology by the $^{40}Ar/^{39}Ar$ method: New York, Oxford University Press, 269 p.

McLennan, S. M., and Taylor, S. R., 1981, Role of subducted sediments in island arc magmatism: constraints from REE patterns: Earth and Planetary Science Letters, v. 54, p. 423-430.

Mikolaichuk, A. V., Kurenkov, S. A., Degtyarev, K., E., and Rubtsov, V. I., 1997, Northern Tien Shan main stages of geodynamic evolution in the late Precmbrian-early Paleozoic: Geotectonika, v. 1997, p. 16-32 (in Russian).

Mikucki, E. J., 1998, Hydrothermal transport and depositional processes in Archean lode-gold systems: a review: Ore Geology Reviews, v. 13, p. 307-321.

Mikucki, E. J., and Ridley, J. R., 1993, The hydrothermal fluid of Archaean lode-gold deposits at different metamorphic grades: compositional constraints from the ore and wall rock alteration assemblages: Mineralium Deposita, v. 28, p. 469-481.

Mishra, B., and Panigrahi, M. K., 1999, Fluid evolution of the Kolar Gold Field: evidence from fluid inclusion studies: Mineralium Deposita, v. 34, p. 173-181.

Moore, J. N., Powell, T. S., Heizler, M. T., and Norman, D. I., 2000, Mineralization and hydrothermal history of the Tiwi geothermal system, Phillippines: Economic Geology, v. 95, p. 1001-1023.

Moralev, G. V., and Shatagin, K. N., 1999, Rb-Sr study of Au-Ag Shkol'noe deposit (Kurama Mountains, north Tadjikistan): age of mineralization and time scale of hydrothermal processes: Mineralium Deposita, v. 34, p. 405-413.

Mossakovsky, A. A., Ruzhentsev, S. V., Samygin, S. G., and Kheraskova, T. N., 1993, The Cental Asian fold belt: geodynamic evolution and formation history: Geotectonika, v. 6, p. 3-32 (in Russian).

Mueller, A. G., and Groves, D. I., 1991, The classification of Western Australian greenstone-hosted gold deposits according to wallrock-alteration mineral assemblages: Ore Geology Reviews, v. 6, p. 291-331.

Müller, D., and Groves, D. I., 1997, Potassic igneous rocks and associated gold-copper mineralization: Berlin, New York, Springer, 238 p.

Müller, D., Morris, B. J., and Farrand, M. G., 1993, Potassic alkaline lamprophyres with affinities to lamproites from the Karinya Syncline, South Australia: Lithos, v. 30, p. 123-137.

Murphy, J. B., and Nance, R. D., 1991, Superconinent model for the contrasting character of Late Proterozoic orogenic belts: Geology, v. 19, p. 469-472.

Murphy, J. B., and Nance, R. D., 1992, Mountain belts and the supercontinental cycle: Scientific American, v. 266, p. 84-91.

Murphy, P. J., and Roberts, S., 1997, Evolution of a metamorphic fluid and its role in lode gold mineralization in the Central Iberian Zone: Mineralium Deposita, v. 32, p. 459-474.

Neall, F. B., and Phillips, G. N., 1987, Fluid-wall rock interaction in an Archean hydrothermal gold deposit: a thermodynamic model for the Hunt Mine, Kambalda: Economic Geology, v. 82, p. 1679-1694.

Nikonorov, V. V., 1993, A new type of gold mineralization in Kyrgyzstan: Geology of Ore Deposits, v. 35, p. 450-454 (in Russian).

Norman, D. I., and Moore, J. N., 1999, Methane and excess nitrogen and argon in geothermal fluid inclusions: Proceedings of twenty fourth workshop on geothermal reservoir engineering, Stanford University, California, 1999.

Ohmoto, H., and Rye, R. O., 1979, Isotopes of Sulfur and Carbon, *in* Barnes, H. L., ed., Geochemistry of hydrothermal ore deposits (second edition): New York, Chinchester, Brisbane, Toronto, John Wiley & Sons, p. 509-567.

Ojala, V. J., Ridley, J. R., Groves, D. I., and Hall, G. C., 1993, The Granny Smith gold deposit: the role of heterogeneous stress distribution at an irregular granitoid contact in a greenschist facies terrane: Mineralium Deposita, v. 28, p. 409-419.

Oliver, N. H. S., Valenta, R. K., and Wall, V. J., 1990, The effect of heterogeneous stress and strain on metamorphic fluid flow, Mary Kathleen, Australia, and a model for large-scale fluid circulation: Journal of Metamorphic Geology, v. 8, p. 311-331.

Onstott, T. C., Phillips, D., and Pringle-Goodell, L., 1991, Laser microprobe measurement of chlorine and argon zonation in biotite: Chemical Geology, v. 90, p. 145-168.

Parnell, J., Earls, J., Wilkinson, J. J., Hutton, D. H. W., Boyce, A. J., Fallick, A. E., Ellam, R. M., Gleeson, S. A., Moles, N. R., Carey, P. F., and Legg, I., 2000, Regional fluid flow and gold mineralization in the Dalradian of the Sperrin mountains, Northern Ireland: Economic Geology, v. 95, p. 1389-1416.

Partington, G. A., and Williams, P. J., 2000, Proterozoic lode gold and (iron)-copper-gold deposits: a comparison of Australian and global examples: Reviews in Economic Geology, v. 13, p. 69-101.

Passchier, C. W., and Trouw, R. A. J., 1996, Microtectonics: Berlin-Heidelberg, Springer-Verlag, 289 p.

Paterson, S. R., Vernon, R. H., and Tobisch, T., 1989, A review of criteria for the identification of magmatic and tectonic foliations in granitoids: Journal of Structural Geology, v. 11, p. 349-363.

Pearce, J. A., and Cann, J. R., 1973, Tectonic setting of basic volcanic rocks determined using trace element analyses: Earth and Planetary Science Letters, v. 19, p. 290-300.

Pearce, J. A., and Norry, M. J., 1979, Petrogenetic implications of Ti, Zr, Y and Nb variations in volcanic rocks: Contributions to Mineralogy and Petrology, v. 69, p. 33-47.

Peccerillo, A., and Taylor, S. R., 1976, Geochemistry of Eocene calc-alkaline volcanic rocks from the Kostomonon area, northern Turkey: Contributions to Mineralogy and Petrology, v. 28, p. 63-81.

Perring, C. S., Rock, N. M. S., Golding, S. D., and Roberts, D. E., 1989, Criteria for recognition of metamorphosed and altered lamprophyres: a case study from the Archaean of Kambalda, Western Australia: Precambrian Research, v. 43.

Phillips, D., 1991, Argon isotope and halogen chemistry of phlogopite from South African kimberlites; a combined step-heating, laser probe, electron microprobe and TEM study: Chemical Geology; Isotope Geoscience Section, v. 87, p. 71-98.

Phillips, D., and Onstott, T. C., 1988, Argon isotopic zoning in mantle phlogopite: Geology, v. 16, p. 542-546.

Phillips, G. N., Groves, D. I., and Brown, I. J., 1987, Source requirements for the Golden Mile, Kalgoorlie: significance to the metamorphic replacement model for Archean gold deposits: Canadian Journal of Earth Science, v. 24, p. 1643-1651.

Phillips, G. N., and Powell, R., 1993, Link between gold provinces: Economic Geology, v. 88, p. 1084-1098.

Pickles, C. S., Wheeler, J., Kelley, S. P., and Reddy, S. M., 1997, Determination of high spatial resolution argon isotope variations in metamorphic biotites: Geochimica et Cosmochimica Acta, v. 61, p. 3809-3833.

Powell, R., Will, T. M., and Philips, G. N., 1991, Metamorphism in Archean greenstone belts: calculated fluid compositions and implications for gold mineralization: Journal of Metamorphic Geology, v. 9, p. 141-150.

Quidelleur X, Grove M, Lovera O. M, Harrison T. M, Yin, A., and Ryerson F. J, 1997, Thermal evolution and slip history of the Renbu Zedong thrust, southeastern Tibet: Journal of Geophysical Research, v. 102, p. 2659-2679.

Reddy S.M, and Potts G.J, 1999, Constraining absolute deformation ages: The relationship between deformation mechanisms and isotope systematics: Journal of Structural Geology, v. 21, p. 1255-1265.

Ridley, J., Mikucki, E. J., and Groves, D. I., 1996, Archean lode-gold deposits: fluid flow and chemical evolution in vertically extensive hydrothermal systems: Ore Geology Reviews, v. 10, p. 279-293.

Ridley, J. R., and Diamond, L. W., 2000, Fluid chemistry of orogenic lode gold deposits and implications for genetic models: Reviews in Economic Geology, v. 13, p. 141-162.

Robert, F., Boullier, A. M., and Firdaous, K., 1995, Gold-quartz veins in metamorphic terranes and their bearing on the role of fluids in faulting: Journal of Geophysical Research, v. 100, p. 12861-12879.

Robert, F., and Kelly, W. C., 1987, Ore-forming fluids in Archean gold-bearing quartz veins at the Sigma mine, Abitibi greenstone belt, Quebec, Canada: Economic Geology, v. 82, p. 1462-1482.

Robert, F., and Poulsen, K. H., 2001, Vein formation and deformation in greenstone gold deposits: Reviews in Economic Geology, v. 14, p. 111-155.

Rock, N. M. S., 1984, Nature and origin of calc-alkaline lamprophyres: minettes, vogesites, kersantites and spessartites: Transactions of the Royal Society of Edinburgh: Earth Sciences, v. 74, p. 193-227.

Rock, N. M. S., 1991, Lamprophyres: Glazgow, Blackie, 285 p.

Rock, N. M. S., and Groves, D. I., 1988a, Can lamprophyres resolve the genetic controversy over mesothermal gold deposits?: Geology, v. 16, p. 538-541.

Rock, N. M. S., and Groves, D. I., 1988b, Do lamprophyres carry gold as well as diamonds?: Nature, v. 322, p. 253-255.

Rombach, C. S., and Newberry, R. J., 2000, Shotgun deposit: granite porphyry with Au-As mineralization in southwest Alaska, USA, *in* Bucci, L. A., and Mair, J. L., eds., Gold in 2000. Poster session extended abstracts, Lake Tahoe, Nevada. November 10-11, 2000, p. 74-76.

Rowins, S. M., Cameron, E. M., Lalonde, A. E., and Ernst, R. E., 1993, Petrogenesis of the Late Archean syenitic Murdock Creek pluton, Kirkland Lake, Ontario: evidence for extensional tectonic setting: Canadian Mineralogist, v. 31, p. 219-244.

Samson, S. D., and Alexander, C. E., 1987, Calibration of the interlaboratory $^{40}Ar/^{39}Ar$ dating standard, Mmhb-1: Isotope Geoscience, v. 66, p. 27-34.

Schmidt Mumm, A., Oberthür, T., Vetter, U., and Blenkinsop, T. G., 1997, High CO_2 content of fluid inclusions in gold mineralizations in the Ashanti belt, Ghana: a new category of ore forming fluids?: Mineralium Deposita, v. 32, p. 107-118.

Scholz, C. H., 1988, The brittle-plastic transition and the depth of seismic faulting: Geologische Rundschau, v. 77, p. 319-328.

Sengör, A. M. C., and Natal'in, B. A., 1996a, Paleotectonics of Asia, fragments of a synthesis, *in* Yin, A., and Harrison, T. M., eds., The tectonic evolution of Asia. Rubey Colloquium (1994: University of California, Los Angeles): Cambridge, New York, Cambridge University Press, p. 486-540.

Şengör, A. M. C., and Natal'in, B. A., 1996b, Turkic-type orogeny and its role in the making of the continental crust: Annual Review of Earth and Planetary Sciences, v. 24, p. 263-337.

Şengör, A. M. C., Natal'in, B. A., and Burtman, V. S., 1993, Evolution of the Altaid tectonic collage and Palaeozoic crustal growth in Eurasia: Nature, v. 364, p. 299-306.

Shepherd, T. J., Rankin, A. H., and Alderton, D. H. M., 1985, A practical guide to fluid inclusion studies: Glazgow and London, Blackie, 239 p.

Sheppard, S., and Taylor, W. R., 1992, Barium- and LREE-rich, olivine-mica-lamprophyres with affinities to lamproites, Mt. Bundey, Northern Territory, Australia: Lithos, v. 28, p. 303-325.

Sibson, R. H., 2001, Seismogenic framework for hydrothermal transport and ore deposition: Reviews in Economic Geology, v. 14, p. 25-50.

Sibson, R. H., Robert, F., and Poulsen, K. H., 1988, High-angle reverse faults, fluid-pressure cycling, and mesothermal gold-quartz deposits: Geology, v. 16, p. 551-555.

Sillitoe, R. H., and Thompson, J. F. H., 1998, Intrusion-related vein gold deposits: types, tectono-magmatic settings and difficulties of distinction from orogenic gold deposits: Resource Geology, v. 48, p. 237-250.

Sisson, V. B., 1987, Halogen chemistry as an indicator of metamorphic fluid interaction with the Ponder pluton, Coast Plutonic Complex, British Columbia, Canada: Contributions to Mineralogy and Petrology, v. 95, p. 123-131.

Smith, J. V., and Brown, W. L., 1988, Feldspar minerals. Volume 1. Crystal structures, physical, chemical, and microtextural properties: Berlin, Springer-Verlag, 828 p.

So, C. S., and Yun, S. T., 1997, Jurassic mesothermal gold mineralization of the Samhwanghak mine, Youngdong area, Republic of Korea: constraints on hydrothermal fluid chemistry: Economic Geology, v. 92, p. 60-80.

Solov'yev, S. G., 1995, The RE and rare elements in the Sonkul' Gabbro-Monzonite-(Syenite)-Granite complex in Kirgizia: Geochemistry International, v. 32, p. 1-18.

Steiger, R. H., and Jäger, E., 1977, Subcomission on geochronology: Convention on the use of the of the decay constants in geo- and cosmochronology: Earth and Planetary Science Letters, v. 36, p. 359-362.

Stüwe, K., 1998, Tectonic constraints on the timing relationships of metamorphism, fluid production and gold-bearing quartz vein emplacement: Ore Geology Reviews, v. 13, p. 219-228.

Sun, S. S., and McDonough, W. F., 1989, Chemical and isotope systematics of oceanic basalts: implications for mantle composition and processes, *in* Saunders, A. D., and Norry, M. J., eds., Magmatism in the ocean basins (Geological Society Special Publication No 42): Oxford, Boston, Blackwell Scientific Publications, p. 313-345.

Taylor, J. R., 1982, An introduction to error analysis: the study of uncertainties in physical measurements: Mill Valley, California, University Science Books, 270 p.

Taylor, W. R., Rock, N. M. S., Groves, D. I., Perring, C. S., and Golding, S. D., 1994, Geochemistry of Archean shoshonitic lamprophyres from the Yilgarn Block, Western Australia; Au abundance and association with gold mineralization: Applied Geochemistry, v. 9, p. 197-222.

Thiéry, R., Van den Kerkhof, A. M., and Dubessy, F., 1994, VX properties of CH_4-CO_2 and CO_2-N_2 fluid inclusions: Modeling for T<31°C and P<400 bar: European Journal of Mineralogy, v. 6, p. 753-771.

Thompson, J. F. H., and Newberry, R. J., 2000, Gold deposits related to reduced granitic intrusions: Reviews in Economic Geology, v. 13, p. 377-400.

Thompson, J. F. H., Sillitoe, R. H., Baker, T., Lang, J. R., and Mortensen, J. K., 1999, Intrusion-related gold deposits associated with tungsten-tin provinces: Mineralium Deposita, v. 34, p. 323-334.

Van den Kerkhof, A. M., and Hein, U. F., 2001, Fluid inclusion petrography: Lithos, v. 55, p. 27-47.

Vernon, R. H., and Flood, R. H., 1988, Contrasting deformations of S- and I-type granitoids in the Lachlan fold belt, eastern Australia: Tectonophysics, v. 147, p. 127-143.

Watson, B. E., and Brenan, J. M., 1987, Fluids in the lithosphere, 1. Experimentally determined wetting characteristics of H_2O-CO_2 fluids and their implications for fluid transport, host-rock physical properties, and fluid inclusion formation: Earth and Planetary Science Letters, v. 85, p. 497-515.

Wilde, A. R., Layer, P., Mernagh, T., and Foster, J., 2001, The giant Muruntau gold deposit: geologic, geochronologic, and fluid inclusion constraints on ore genesis: Economic Geology, v. 96, p. 633-644.

Wilkinson, J. J., Boyce, A. J., Earls, J., and Fallick, A. E., 1999, Gold remobilization by low-temperature brines: evidence from the Curraghinalt gold deposit, Northern Ireland: Economic Geology, v. 94, p. 289-296.

Wilkinson, J. J., and Johnston, J. D., 1996, Pressure fluctuations, phase separation, and gold precipitation during seismic fracture propagation: Geology, v. 24, p. 395-398.

Wood, D. A., Joron, J. L., and Treuil, M., 1979, A re-appraisal of the use of trace elements to classify and discriminate between magma series erupted in different tectonic settings: Earth and Planetary Science Letters, v. 45, p. 326-336.

Wyman, D., and Kerrich, R., 1988a, Alkaline magmatism, major structures, and gold deposits: implications for greenstone belt gold metallogeny: Economic Geology, v. 83, p. 454-461.

Wyman, D. A., and Kerrich, R., 1988b, Lamprophyres as a source of gold: Nature, v. 332, p. 209-210.

Wyman, D. A., and Kerrich, R., 1989, Archean shoshonitic lamprophyres associated with Superior Province gold deposits: distribution, tectonic setting, noble metal abundance and significance for gold mineralization: Economic Geology Monograph, v. 6, p. 651-667.

Wyman, D. A., and Kerrich, R., 1993, Archean shoshonitic lamprophyres of the Abitibi Subprovince, Canada; petrogenesis, age, and tectonic setting: Journal of Petrology, v. 34, p. 1067-1109.

Xu, G., and Pollard, P. J., 1999, Origin of CO_2-rich fluid inclusions in synorogenic veins from the Eastern Mount Isa Fold Belt, NW Queensland, and their impliations for mineralisation.: Mineralium Deposita, v. 34, p. 395-404.

Yavuz, F., 1999, A revised program for microprobe-derived amphibole analyses using the IMA rules: Computers & Geosciences, v. 25, p. 909-927.

Yonaka, B. E., 1996, Gold-bearing granitoids of southern Ghana, West Africa: Unpub. M.S. thesis, New Mexico Institute of Mining and Technology, 181 p.

Zonenshain, L. P., Kuzmin, M. I., and Natapov, L. M., 1990, Geology of the USSR: a plate-tectonic synthesis: Washington, DC, American Geophysical Union, 242 p.

APPENDIX A

RESULTS OF CHEMICAL ANALYSES

This appendix contains results of chemical analyses conducted by Activation Laboratories Ltd. Table A.1. Tables A.1 to A.5 reproduce original laboratory reports. Samples were submitted in two batches. The first batch that comprised samples of alkalic intrusive rocks was submitted to the Activation Laboratories Ltd. (1428 Sandhill Drive, Ancaster, Ontario, Canada L9G 4V5). Samples were analyzed for major and selected trace elements by the fusion-Inductively Coupled Plasma-Optical Emission Spectroscopy method (fusion-ICP, laboratory code 4B; Table A.1). More detailed determination of trace elements was conducted by the fusion-Inductively Coupled Plasma-Mass Spectrometry method (fusion-ICP-MS, laboratory code 4B, option 2-research). The original report and its revised version are reproduced in Tables A.2 and A.3, respectively. The revision was necessary, because the original report contained an erroneous Sn content for the sample TR6. The revised version differs from the original report only by the corrected Sn value for the sample TR6. Five samples from the first batch were additionally analyzed for platinum group elements by the Fire Assay the ICP MS finish (Table A.5). The second batch included samples of stratified volcanics and was submitted to Actlabs Skyline (a division of Activation Laboratories Ltd., ACTLABS-SKYLINE, 1775 W. Sahuaro Dr., P.O. Box 85670, Tucson, AZ 85754). Samples were analyzed by the 4 Lithoresearch package, in which major and trace elements are determined by fusion-ICP and fusion ICP-MS, respectively. Figures A.1, A.2, and A.3 are scanned fragments from the Activation Laboratories pricelists. Figures A.1 and A.2 contain information on detection limits, and Figure A.3 contains brief description of the methods.

Table A.1. Activation Laboratories Ltd. report on major and selected trace element analyses by a fusion-ICP method (code 4B).

Activation Laboratories Ltd. Work Order No. 16443 Report No. 16221

SAMPLE	SiO2	Al2O3	Fe2O3	MnO	MgO	CaO	Na2O	K2O	TiO2	P2O5	LOI	TOTAL
	%	%	%	%	%	%	%	%	%	%	%	%
397	51.07	13.01	8.92	0.11	6.04	6.39	2.53	6.16	0.67	0.79	3.64	99.34
613	47.58	14.45	10.43	0.12	6.34	6.27	2.02	6.50	0.75	0.72	4.17	99.33
658	58.70	14.24	4.54	0.10	2.85	4.06	4.44	4.34	0.34	0.22	4.24	98.08
49-113.6	48.81	11.90	9.66	0.12	7.74	6.64	2.31	4.01	0.60	0.60	6.67	99.06
49-129.2	55.95	13.58	5.24	0.08	2.79	4.56	2.86	7.58	0.53	0.42	6.34	99.93
515-SP	55.96	15.45	7.11	0.07	2.83	4.00	3.28	6.42	0.47	0.31	3.59	99.48
515-X	49.75	12.72	10.77	0.14	7.79	5.60	2.37	3.42	0.49	0.26	5.34	98.65
55-62.7	55.86	16.80	6.02	0.08	3.15	2.94	3.62	7.17	0.40	0.24	1.91	98.18
57-166.2	60.98	14.98	4.15	0.04	2.68	3.23	3.94	5.96	0.38	0.27	3.47	100.10
57-174.1	59.95	14.57	4.36	0.05	2.21	3.50	4.16	5.59	0.41	0.32	4.23	99.36
60-74.8	51.75	15.06	7.86	0.16	3.64	6.56	2.77	6.57	0.59	0.35	5.34	100.66
664-4	49.94	12.60	9.33	0.16	7.06	8.94	3.53	2.83	0.68	0.50	4.38	99.96
76-179.9	46.20	11.55	8.15	0.13	6.73	7.64	2.46	5.07	0.65	0.57	10.75	99.91
1966	49.17	12.69	8.73	0.19	5.52	8.04	1.69	5.67	0.62	0.56	5.92	98.80
A23	65.00	15.30	2.97	0.05	0.74	1.98	4.09	6.73	0.31	0.15	2.03	99.36
TR223	49.07	12.69	9.06	0.19	5.60	8.28	1.77	6.08	0.62	0.72	6.01	100.07
TR6	51.13	12.71	8.79	0.16	6.47	8.35	2.17	5.22	0.64	0.57	3.04	99.25

SAMPLE	Ba	Sr	Y	Sc	Zr	Be	V
	ppm	ppm	ppm	ppm	ppm	ppm	ppm
397	4269	653	19	29	132	5	201
613	3111	703	25	26	132	8	250
658	5710	473	22	13	156	6	88
49-113.6	2268	466	17	31	97	4	218
49-129.2	3028	830	27	13	229	8	99
515-SP	5529	543	20	16	134	6	157
515-X	3620	820	16	34	56	10	261
55-62.7	3664	1289	21	13	158	6	140
57-166.2	2560	695	20	11	221	6	84
57-174.1	2542	708	21	11	205	6	82
60-74.8	2324	1662	23	22	151	5	195
664-4	2529	857	18	33	99	4	222
76-179.9	2465	1005	17	26	110	6	193
1966	2738	886	20	28	90	5	204
A23	4853	523	23	5	271	6	38
TR223	2882	855	20	29	111	5	204
TR6	2221	608	18	31	108	5	210

Negative values indicate less than the detection limit
LOI values less than 0.01% represent a Gain on Ignition

Adrienne I. Rittau, B.Sc., C.Chem
ICP Technical Manager

Sample TR6 corresponds to the sample TR6A in the text. Sample TR223 was collected from the same site as sample 1966, and only results for the sample 1966 are used in the text.

Table A.2. Activation Laboratories Ltd. Report on trace element analyses by the fusion-ICP/MS method (code 4B option 2, research).

Lithogeochem (Research Package) Job #: 16443 **Report#: 16221** **Customer: Vladimir Ispolatov**

Trace Element Values Are in Parts Per Million. Negative Values Equal Not Detected at That Lower Limit.

Sample ID:	V	Cr	Co	Ni	Cu	Zn	Ga	Ge	As	Rb	Sr	Y
397	193	172	18	78	29	65	15	1.6	27	225	674	21
613	242	225	32	78	89	34	17	1.6	28	321	723	27
658	84	92	13	46	17	41	17	1.3	-5	149	489	24
49-113.6	211	395	27	92	112	70	14	1.6	24	210	481	18
49-129.2	93	83	8.3	39	22	45	18	1.4	27	191	849	29
515-SP	152	69	11	30	17	20	16	1.2	16	210	557	22
515-X	248	797	17	109	132	57	20	1.6	10	318	854	17
55-62.7	140	99	11	31	18	49	18	1.5	36	267	1,344	22
57-166.2	78	130	6.5	42	32	21	18	1.3	7	208	705	22
57-174.1	81	78	7.5	40	17	29	18	1.5	9	203	728	23
60-74.8	191	111	19	44	11	94	17	1.7	14	247	1,683	24
664-4	220	268	29	82	15	55	16	1.9	16	147	893	20
76-179.9	188	339	26	82	71	81	14	1.3	31	297	1,030	19
1966	189	118	22	77	69	63	14	1.2	5	215	895	21
A23	38	33	3.5	64	-10	27	21	1.3	17	238	550	24
TR223	197	112	29	57	62	127	15	1.7	8	236	893	22
TR6	204	249	32	78	85	79	15	1.5	20	143	645	20
Blank	-5	-10	-0.5	-10	-10	-10	-1	-0.5	-5	-0.1	-0.01	-0.1
Standard STM1	-5	-10	0.6	-10	-10	234	36	1.5	-5	118	692	47
Certified STM1	**(8.7)**	**(4.3)**	**0.9**	**(3)**	**(4.6)**	**235***	**36***	**(1.4)**	**4.6**	**118***	**700***	**46***
Standard MAG1	139	95	21.1	60	26	103	22	1.7	15	149	140	28
Certified MAG1	**140***	**97***	**20.4***	**53***	**30***	**130***	**20.4***		**9.2**	**149***	**146***	**28***
Standard BIR1	316	373	51.2	161	126	75	15	1.4	-5	-0.1	107	16
Certified BIR1	**313***	**382***	**51.4***	**166***	**126***	**71***	**16**	**1.5**	**(0.4)**	**0.25***	**108***	**16***
Standard DNC1	153	280	56.7	246	103	71	15	1.3	-5	3.5	145	19
Certified DNC1	**148***	**285***	**54.7***	**247***	**96***	**66***	**15**	**(1.3)**	**(0.2)**	**(4.5)**	**145***	**18***
Standard W2	262	83	43.8	71	106	72	18	1.3	-5	19.6	194	23
Certified W2	**262***	**93***	**44***	**70***	**103***	**77***	**20***	**(1.0)**	**1.24**	**20***	**194***	**24***
Standard MRG1	525	434	85.6	191	132	190	18	1.4	-5	7.2	267	14
Certified MRG1	**526***	**430**	**87***	**193***	**134***	**191***	**17**		**0.73**	**8.5**	**266***	**14**
Standard SY3	47	-20	7.7	-20	-20	246	20	1.6	14	208	304	748
Certified SY3	**50**	**(11)**	**8.8**	**11**	**17**	**244***	**27***	**1.4**	**18.8**	**206***	**302***	**718***
Standard GXR1	81	-20	8.0	43	1,109	790	15	3.0	426	2.4	299	34
Certified GXR1	**80**	**12**	**8.2**	**41**	**1,110**	**760**	**13.8**		**427**	**(14)**	**275**	**32**

Table A.2. (Continued)

Sample ID:	Zr	Nb	Mo	Ag	In	Sn	Sb	Cs	Ba	La	Ce	Pr
397	148	10	0.4	-0.5	-0.1	1.8	6.29	11	3,889	45.8	110	10.41
613	151	13	2.6	-0.5	-0.1	2.3	2.92	18	3,010	69.7	154	14.04
658	170	17	0.5	-0.5	-0.1	1.6	0.70	6.9	5,227	49.9	114	10.23
49-113.6	109	7.1	4.0	-0.5	-0.1	1.5	3.76	13	2,234	48.1	109	10.10
49-129.2	252	18	3.4	-0.5	-0.1	2.2	7.71	2.4	2,933	63.1	145	13.09
515-SP	161	11	1.6	-0.5	-0.1	1.4	8.34	5.8	5,331	55.4	125	11.21
515-X	75	3.5	0.2	-0.5	-0.1	2.1	7.49	18	3,504	47.5	89.3	8.165
55-62.7	179	12	2.2	-0.5	-0.1	1.7	2.95	18	3,457	59.0	132	11.84
57-166.2	241	16	3.8	-0.5	-0.1	2.8	4.17	8.4	2,466	60.3	144	13.21
57-174.1	229	15	3.3	-0.5	-0.1	2.1	9.18	5.9	2,489	57.9	132	11.95
60-74.8	166	11	1.1	-0.5	-0.1	1.9	5.48	18	2,267	58.9	134	12.47
664-4	109	7.8	1.1	-0.5	-0.1	1.6	6.62	14	2,487	34.4	83.0	8.010
76-179.9	121	9.1	0.9	-0.5	-0.1	1.5	2.66	19	2,386	50.0	116	11.00
1966	109	8.4	-0.1	-0.5	-0.1	1.5	1.10	9.8	2,666	50.5	121	11.44
A23	304	25	0.3	-0.5	-0.1	2.4	1.52	2.5	4,502	64.9	149	13.51
TR223	123	9.0	0.7	-0.5	-0.1	2.0	1.58	12	2,841	50.6	121	11.43
TR6	123	8.7	0.3	-0.5	-0.1	21	4.42	6.3	2,263	40.1	95.8	9.151
Blank	-0.1	-0.5	-0.1	-0.5	-0.1	-0.5	-0.05	-0.1	-0.1	-0.01	-0.01	-0.005
Standard STM1	1,205	268	5.1	-0.5	-0.1	7.2	1.57	1.6	574	155	259	20.99
Certified STM1	**1210***	**268***	**5.2**	**0.079***	**(0.12)**	**6.8**	**1.66***	**1.54***	**560***	**150***	**259***	**19***
Standard MAG1	126	17	1.4	-0.5	-0.1	3.1	1.04	8.6	473	43.4	88.1	9.691
Certified MAG1	**126***	**12**	**1.6**	**0.08**	**(0.18)**	**3.6**	**0.96***	**8.6***	**479***	**43***	**88***	**9.3**
Standard BIR1	15	0.7	0.5	-0.5	-0.1	0.6	0.57	-0.1	6.7	0.73	2.12	0.384
Certified BIR1	**16**	**0.6**	**(0.5)**	**(0.036)**		**0.65**	**0.58**	**0.005**	**7**	**0.62***	**1.95***	**0.38***
Standard DNC1	37	1.6	0.1	-0.5	-0.1	2.4	0.88	0.2	105	3.98	10.58	1.320
Certified DNC1	**41***	**3**	**(0.7)**	**(0.027)**			**0.96***	**(0.34)**	**114***	**3.8***	**10.6**	**1.3**
Standard W2	95	7.8	0.4	-0.5	-0.1	2.1	0.66	0.9	171	11.0	23.9	3.037
Certified W2	**94***	**7.9**	**(0.6)**	**(0.046)**			**0.79**	**0.99***	**182***	**11.4***	**24***	**(5.9)**
Standard MRG1	106	21	0.8	-0.5	-0.1	3.6	0.53	0.6	47	9.68	27.1	3.717
Certified MRG1	**108***	**20**	**0.87**	**0.11**		**(3.6)**	**0.86**	**0.57**	**61**	**9.8***	**26**	**3.4**
Standard SY3	340	105	0.3	-1.0	-0.2	6.4	0.39	2.8	433	1,217	2,101	223
Certified SY3	**320**	**148**	**(1.0)**	**(1.5)**		**(6.5)**	**0.31**	**2.5**	**450**	**1340***	**2230***	**223***
Standard GXR1	27	1.7	18	31	0.8	54	122	2.9	790	7.8	16.4	2.014
Certified GXR1	**(38)**	**(0.8)**	**18**	**31**	**0.77**	**54**	**122**	**3**	**750**	**7.5**	**17**	

Table A.2. (Continued)

Sample ID:	Nd	Sm	Eu	Gd	Tb	Dy	Ho	Er	Tm	Yb	Lu	Hf
397	39.3	7.24	1.729	5.04	0.72	3.53	0.68	1.93	0.268	1.83	0.281	3.6
613	51.3	9.41	2.090	6.71	0.96	4.76	0.88	2.44	0.328	2.16	0.334	3.9
658	36.0	6.58	1.547	4.88	0.73	3.74	0.72	2.07	0.308	2.10	0.335	4.7
49-113.6	37.0	7.02	1.605	4.92	0.65	3.14	0.56	1.59	0.219	1.42	0.233	2.6
49-129.2	46.9	8.49	1.882	6.08	0.88	4.49	0.85	2.50	0.357	2.44	0.403	6.2
515-SP	40.1	7.37	1.821	5.21	0.75	3.68	0.68	1.96	0.282	1.87	0.314	3.8
515-X	29.8	5.67	1.609	4.16	0.59	2.97	0.54	1.48	0.204	1.37	0.231	2.1
55-62.7	41.0	7.30	1.775	5.20	0.74	3.62	0.70	1.97	0.275	1.90	0.309	4.1
57-166.2	46.6	8.42	1.890	5.95	0.82	4.11	0.77	2.24	0.329	2.21	0.368	6.6
57-174.1	42.0	7.39	1.652	5.28	0.78	3.74	0.70	2.00	0.291	2.01	0.324	5.8
60-74.8	45.5	8.37	1.907	5.94	0.82	4.11	0.76	2.17	0.301	1.92	0.315	3.9
664-4	30.2	5.90	1.389	4.38	0.65	3.28	0.63	1.83	0.255	1.67	0.275	2.8
76-179.9	40.5	7.47	1.711	5.29	0.72	3.42	0.60	1.71	0.219	1.43	0.229	3.1
1966	42.4	8.23	1.901	5.75	0.79	3.73	0.69	1.86	0.248	1.67	0.262	2.9
A23	46.1	7.89	1.852	5.54	0.80	3.92	0.73	2.19	0.317	2.18	0.361	7.9
TR223	42.9	8.24	1.924	5.83	0.80	3.89	0.70	1.95	0.262	1.74	0.274	3.2
TR6	34.6	6.67	1.521	4.78	0.67	3.37	0.64	1.81	0.253	1.69	0.271	3.0
Blank	-0.01	-0.01	-0.005	-0.01	-0.01	-0.01	-0.01	-0.01	-0.005	-0.01	-0.002	-0.1
Standard STM1	77.0	12.6	3.458	9.52	1.49	8.03	1.51	4.25	0.702	4.29	0.669	27.9
Certified STM1	**79***	**12.6***	**3.6***	**9.5***	**1.55***	**8.1***	**1.9**	**4.2***	**0.69**	**4.4***	**0.60**	**28***
Standard MAG1	38.4	7.40	1.450	5.78	0.95	5.14	0.98	3.00	0.428	2.55	0.395	3.6
Certified MAG1	**38***	**7.5***	**1.55***	**5.8***	**0.96***	**5.2***	**1.02***	**3**	**0.43***	**2.6***	**0.40***	**3.7***
Standard BIR1	2.49	1.09	0.502	1.68	0.36	2.50	0.56	1.73	0.268	1.63	0.260	0.6
Certified BIR1	**2.5***	**1.1***	**0.54***	**1.85***	**0.36***	**2.5***	**0.57***	**1.7***	**0.26***	**1.65**	**0.26***	**0.6***
Standard DNC1	4.79	1.45	0.592	1.98	0.41	2.75	0.62	2.02	0.333	2.07	0.330	1.0
Certified DNC1	**4.9***	**1.38***	**0.59***	**2**	**0.41***	**2.7**	**0.62**	**2***	**(0.33)**	**2.01***	**0.32***	**1.01***
Standard W2	13.7	3.33	1.104	3.52	0.64	3.79	0.78	2.39	0.361	2.05	0.305	2.5
Certified W2	**14**	**3.25***	**1.1***	**3.6***	**0.63**	**3.8***	**0.76***	**2.5**	**0.38**	**2.05***	**0.33***	**2.56***
Standard MRG1	19.1	4.59	1.430	4.00	0.58	2.98	0.51	1.30	0.154	0.78	0.120	3.7
Certified MRG1	**19.2***	**4.5***	**1.39***	**4**	**0.51***	**2.9**	**0.49***	**1.12**	**0.11**	**(0.6)**	**0.12**	**3.76***
Standard SY3	672	122	17.4	106	20.9	130	28.2	78.9	12.0	67.5	8.009	10.8
Certified SY3	**670**	**109**	**17***	**105***	**18**	**118**	**29.5***	**68**	**11.6***	**(62)**	**7.9**	**9.7**
Standard GXR1	16.2	3.10	0.632	4.01	0.83	4.99	0.99	2.93	0.431	2.30	0.337	0.8
Certified GXR1	**(18)**	**2.7**	**0.69**	**4.2**	**0.83**	**4.3**			**(0.43)**	**1.9**	**0.28**	**0.96**

Table A.2. (Continued).

Sample ID:	Ta	W	Tl	Pb	Bi	Th	U
397	0.48	12	3.11	22	0.40	18.0	4.53
613	0.53	3.9	2.75	11	1.32	21.1	7.67
658	0.94	2.7	1.60	21	0.90	24.9	6.68
49-113.6	0.31	15	1.60	14	0.40	17.7	5.50
49-129.2	0.90	24	2.09	28	0.57	27.5	5.96
515-SP	0.50	4.8	2.84	10	0.50	22.5	8.28
515-X	0.12	3.6	6.56	10	0.36	7.10	3.89
55-62.7	0.51	7.8	3.02	25	1.61	26.6	12.1
57-166.2	0.92	13	2.58	14	0.14	32.7	8.91
57-174.1	0.80	6.7	2.99	25	0.25	26.9	8.02
60-74.8	0.48	5.0	3.48	21	0.60	22.7	6.37
664-4	0.35	7.9	2.08	12	1.09	12.9	3.23
76-179.9	0.42	3.4	4.35	21	0.19	17.4	5.13
1966	0.41	1.4	1.93	25	0.17	16.2	4.60
A23	1.22	6.7	2.34	27	0.81	35.0	11.9
TR223	0.40	2.3	3.57	75	0.63	17.8	4.89
TR6	0.42	2.0	1.68	21	0.36	15.2	4.33
Blank	-0.01	-0.2	-0.05	-5	-0.05	-0.05	-0.05
Standard STM1	18.6	3.1	0.26	19	0.26	31.0	9.03
Certified STM1	**18.6***	**3.6***	**0.26**	**17.7***	**0.13**	**31***	**9.06***
Standard MAG1	1.14	1.4	0.30	15	-0.05	11.9	2.81
Certified MAG1	**1.1**	**1.4**	**(0.59)**	**24***	**0.34**	**11.9***	**2.7***
Standard BIR1	0.06	-0.2	-0.05	5	-0.05	0.12	-0.05
Certified BIR1	**0.04**	**0.07**	**(0.01)**	**3**	**(0.02)**	**0.03**	**0.01**
Standard DNC1	0.08	-0.2	-0.05	7	-0.05	0.31	0.08
Certified DNC1	**0.098***	**(0.2)**	**(0.026)**	**6.3**	**(0.02)**	**(0.2)**	**(0.1)**
Standard W2	0.45	0.3	0.08	7	-0.05	2.25	0.52
Certified W2	**0.5**	**(0.3)**	**(0.2)**	**9.3**	**(0.03)**	**2.2***	**0.53**
Standard MRG1	0.90	0.2	-0.05	6	0.17	0.84	0.30
Certified MRG1	**0.8***	**0.3**	**0.055**	**10**	**(0.13)**	**0.93**	**0.24**
Standard SY3	22.6	1.4	1.59	123	0.73	1,001	646
Certified SY3	**30***	**1.1***	**1.5**	**133***	**(0.8)**	**1003***	**650***
Standard GXR1	0.17	164	0.48	732	1,380	2.91	34.9
Certified GXR1	**0.175**	**164**	**(0.39)**	**730**	**1380**	**2.44**	**34.90**

NOTE: '*' = RECOMMENDED VALUES
'( )' = INFORMATION VALUES
ALL OTHER VALUES ARE PROPOSED

Certified By:

Date: ____________________

D. D'Anna, Dipl. T.
ICPMS Technical Manager, Activation Laboratories Ltd.

Unless otherwise instructed, samples will be disposed of 90 days from the date of this report.

Sample TR6 corresponds to the sample TR6A in the text. Sample TR223 was collected from the same site as sample 1966, and only results for the sample 1966 are used in the text.

Table A.3. A revised version of the report placed in Table A.2. The revision was conducted because of the error in the original report (Sn content for the sample TR6). Other than that , the two reports are identical.

Lithogeochem (Research Package) Job #: 16443 **Report#: 16221 REVISED** **Customer: Vladimir Ispolatov**

Trace Element Values Are in Parts Per Million. Negative Values Equal Not Detected at That Lower Limit.

Sample ID:	V	Cr	Co	Ni	Cu	Zn	Ga	Ge	As	Rb	Sr	Y
397	193	172	18	78	29	65	15	1.6	27	225	674	21
613	242	225	32	78	89	34	17	1.6	28	321	723	27
658	84	92	13	46	17	41	17	1.3	-5	149	489	24
49-113.6	211	395	27	92	112	70	14	1.6	24	210	481	18
49-129.2	93	83	8.3	39	22	45	18	1.4	27	191	849	29
515-SP	152	69	11	30	17	20	16	1.2	16	210	557	22
515-X	248	797	17	109	132	57	20	1.6	10	318	854	17
55-62.7	140	99	11	31	18	49	18	1.5	36	267	1,344	22
57-166.2	78	130	6.5	42	32	21	18	1.3	7	208	705	22
57-174.1	81	78	7.5	40	17	29	18	1.5	9	203	728	23
60-74.8	191	111	19	44	11	94	17	1.7	14	247	1,683	24
664-4	220	268	29	82	15	55	16	1.9	16	147	893	20
76-179.9	188	339	26	82	71	81	14	1.3	31	297	1,030	19
1966	189	118	22	77	69	63	14	1.2	5	215	895	21
A23	38	33	3.5	64	-10	27	21	1.3	17	238	550	24
TR223	197	112	29	57	62	127	15	1.7	8	236	893	22
TR6	204	249	32	78	85	79	15	1.5	20	143	645	20
Blank	-5	-10	-0.5	-10	-10	-10	-1	-0.5	-5	-0.1	-0.01	-0.1
Standard STM1	-5	-10	0.6	-10	-10	234	36	1.5	-5	118	692	47
Certified STM1	**(8.7)**	**(4.3)**	**0.9**	**(3)**	**(4.6)**	**235***	**36***	**(1.4)**	**4.6**	**118***	**700***	**46***
Standard MAG1	139	95	21.1	60	26	103	22	1.7	15	149	140	28
Certified MAG1	**140***	**97***	**20.4***	**53***	**30***	**130***	**20.4***		**9.2**	**149***	**146***	**28***
Standard BIR1	316	373	51.2	161	126	75	15	1.4	-5	-0.1	107	16
Certified BIR1	**313***	**382***	**51.4***	**166***	**126***	**71***	**16**	**1.5**	**(0.4)**	**0.25***	**108***	**16***
Standard DNC1	153	280	56.7	246	103	71	15	1.3	-5	3.5	145	19
Certified DNC1	**148***	**285***	**54.7***	**247***	**96***	**66***	**15**	**(1.3)**	**(0.2)**	**(4.5)**	**145***	**18***
Standard W2	262	83	43.8	71	106	72	18	1.3	-5	19.6	194	23
Certified W2	**262***	**93***	**44***	**70***	**103***	**77***	**20***	**(1.0)**	**1.24**	**20***	**194***	**24***
Standard MRG1	525	434	85.6	191	132	190	18	1.4	-5	7.2	267	14
Certified MRG1	**526***	**430**	**87***	**193***	**134***	**191***	**17**		**0.73**	**8.5**	**266***	**14**
Standard SY3	47	-20	7.7	-20	-20	246	20	1.6	14	208	304	748
Certified SY3	**50**	**(11)**	**8.8**	**11**	**17**	**244***	**27***	**1.4**	**18.8**	**206***	**302***	**718***
Standard GXR1	81	-20	8.0	43	1,109	790	15	3.0	426	2.4	299	34
Certified GXR1	**80**	**12**	**8.2**	**41**	**1,110**	**760**	**13.8**		**427**	**(14)**	**275**	**32**

Table A.3 (Continued)

Sample ID:	Zr	Nb	Mo	Ag	In	Sn	Sb	Cs	Ba	La	Ce	Pr
397	148	10	0.4	-0.5	-0.1	1.8	6.29	11	3,889	45.8	110	10.41
613	151	13	2.6	-0.5	-0.1	2.3	2.92	18	3,010	69.7	154	14.04
658	170	17	0.5	-0.5	-0.1	1.6	0.70	6.9	5,227	49.9	114	10.23
49-113.6	109	7.1	4.0	-0.5	-0.1	1.5	3.76	13	2,234	48.1	109	10.10
49-129.2	252	18	3.4	-0.5	-0.1	2.2	7.71	2.4	2,933	63.1	145	13.09
515-SP	161	11	1.6	-0.5	-0.1	1.4	8.34	5.8	5,331	55.4	125	11.21
515-X	75	3.5	0.2	-0.5	-0.1	2.1	7.49	18	3,504	47.5	89.3	8.165
55-62.7	179	12	2.2	-0.5	-0.1	1.7	2.95	18	3,457	59.0	132	11.84
57-166.2	241	16	3.8	-0.5	-0.1	2.8	4.17	8.4	2,466	60.3	144	13.21
57-174.1	229	15	3.3	-0.5	-0.1	2.1	9.18	5.9	2,489	57.9	132	11.95
60-74.8	166	11	1.1	-0.5	-0.1	1.9	5.48	18	2,267	58.9	134	12.47
664-4	109	7.8	1.1	-0.5	-0.1	1.6	6.62	14	2,487	34.4	83.0	8.010
76-179.9	121	9.1	0.9	-0.5	-0.1	1.5	2.66	19	2,386	50.0	116	11.00
1966	109	8.4	-0.1	-0.5	-0.1	1.5	1.10	9.8	2,666	50.5	121	11.44
A23	304	25	0.3	-0.5	-0.1	2.4	1.52	2.5	4,502	64.9	149	13.51
TR223	123	9.0	0.7	-0.5	-0.1	2.0	1.58	12	2,841	50.6	121	11.43
TR6	123	8.7	0.3	-0.5	-0.1	1.6	4.42	6.3	2,263	40.1	95.8	9.151
Blank	-0.1	-0.5	-0.1	-0.5	-0.1	-0.5	-0.05	-0.1	-0.1	-0.01	-0.01	-0.005
Standard STM1	1,205	268	5.1	-0.5	-0.1	7.2	1.57	1.6	574	155	259	20.99
Certified STM1	**1210***	**268***	**5.2**	**0.079***	**(0.12)**	**6.8**	**1.66***	**1.54***	**560***	**150***	**259***	**19***
Standard MAG1	126	17	1.4	-0.5	-0.1	3.1	1.04	8.6	473	43.4	88.1	9.691
Certified MAG1	**126***	**12**	**1.6**	**0.08**	**(0.18)**	**3.6**	**0.96***	**8.6***	**479***	**43***	**88***	**9.3**
Standard BIR1	15	0.7	0.5	-0.5	-0.1	0.6	0.57	-0.1	6.7	0.73	2.12	0.384
Certified BIR1	**16**	**0.6**	**(0.5)**	**(0.036)**		**0.65**	**0.58**	**0.005**	**7**	**0.62***	**1.95***	**0.38***
Standard DNC1	37	1.6	0.1	-0.5	-0.1	2.4	0.88	0.2	105	3.98	10.58	1.320
Certified DNC1	**41***	**3**	**(0.7)**	**(0.027)**			**0.96***	**(0.34)**	**114***	**3.8***	**10.6**	**1.3**
Standard W2	95	7.8	0.4	-0.5	-0.1	2.1	0.66	0.9	171	11.0	23.9	3.037
Certified W2	**94***	**7.9**	**(0.6)**	**(0.046)**			**0.79**	**0.99***	**182***	**11.4***	**24***	**(5.9)**
Standard MRG1	106	21	0.8	-0.5	-0.1	3.6	0.53	0.6	47	9.68	27.1	3.717
Certified MRG1	**108***	**20**	**0.87**	**0.11**		**(3.6)**	**0.86**	**0.57**	**61**	**9.8***	**26**	**3.4**
Standard SY3	340	105	0.3	-1.0	-0.2	6.4	0.39	2.8	433	1,217	2,101	223
Certified SY3	**320**	**148**	**(1.0)**	**(1.5)**		**(6.5)**	**0.31**	**2.5**	**450**	**1340***	**2230***	**223***
Standard GXR1	27	1.7	18	31	0.8	54	122	2.9	790	7.8	16.4	2.014
Certified GXR1	**(38)**	**(0.8)**	**18**	**31**	**0.77**	**54**	**122**	**3**	**750**	**7.5**	**17**	

Table A.3. (Continued)

Sample ID:	Nd	Sm	Eu	Gd	Tb	Dy	Ho	Er	Tm	Yb	Lu	Hf
397	39.3	7.24	1.729	5.04	0.72	3.53	0.68	1.93	0.268	1.83	0.281	3.6
613	51.3	9.41	2.090	6.71	0.96	4.76	0.88	2.44	0.328	2.16	0.334	3.9
658	36.0	6.58	1.547	4.88	0.73	3.74	0.72	2.07	0.308	2.10	0.335	4.7
49-113.6	37.0	7.02	1.605	4.92	0.65	3.14	0.56	1.59	0.219	1.42	0.233	2.6
49-129.2	46.9	8.49	1.882	6.08	0.88	4.49	0.85	2.50	0.357	2.44	0.403	6.2
515-SP	40.1	7.37	1.821	5.21	0.75	3.68	0.68	1.96	0.282	1.87	0.314	3.8
515-X	29.8	5.67	1.609	4.16	0.59	2.97	0.54	1.48	0.204	1.37	0.231	2.1
55-62.7	41.0	7.30	1.775	5.20	0.74	3.62	0.70	1.97	0.275	1.90	0.309	4.1
57-166.2	46.6	8.42	1.890	5.95	0.82	4.11	0.77	2.24	0.329	2.21	0.368	6.6
57-174.1	42.0	7.39	1.652	5.28	0.78	3.74	0.70	2.00	0.291	2.01	0.324	5.8
60-74.8	45.5	8.37	1.907	5.94	0.82	4.11	0.76	2.17	0.301	1.92	0.315	3.9
664-4	30.2	5.90	1.389	4.38	0.65	3.28	0.63	1.83	0.255	1.67	0.275	2.8
76-179.9	40.5	7.47	1.711	5.29	0.72	3.42	0.60	1.71	0.219	1.43	0.229	3.1
1966	42.4	8.23	1.901	5.75	0.79	3.73	0.69	1.86	0.248	1.67	0.262	2.9
A23	46.1	7.89	1.852	5.54	0.80	3.92	0.73	2.19	0.317	2.18	0.361	7.9
TR223	42.9	8.24	1.924	5.83	0.80	3.89	0.70	1.95	0.262	1.74	0.274	3.2
TR6	34.6	6.67	1.521	4.78	0.67	3.37	0.64	1.81	0.253	1.69	0.271	3.0
Blank	-0.01	-0.01	-0.005	-0.01	-0.01	-0.01	-0.01	-0.01	-0.005	-0.01	-0.002	-0.1
Standard STM1	77.0	12.6	3.458	9.52	1.49	8.03	1.51	4.25	0.702	4.29	0.669	27.9
Certified STM1	**79***	**12.6***	**3.6***	**9.5***	**1.55***	**8.1***	**1.9**	**4.2***	**0.69**	**4.4***	**0.60**	**28***
Standard MAG1	38.4	7.40	1.450	5.78	0.95	5.14	0.98	3.00	0.428	2.55	0.395	3.6
Certified MAG1	**38***	**7.5***	**1.55***	**5.8***	**0.96***	**5.2***	**1.02***	**3**	**0.43***	**2.6***	**0.40***	**3.7***
Standard BIR1	2.49	1.09	0.502	1.68	0.36	2.50	0.56	1.73	0.268	1.63	0.260	0.6
Certified BIR1	**2.5***	**1.1***	**0.54***	**1.85***	**0.36***	**2.5***	**0.57***	**1.7***	**0.26***	**1.65**	**0.26***	**0.6***
Standard DNC1	4.79	1.45	0.592	1.98	0.41	2.75	0.62	2.02	0.333	2.07	0.330	1.0
Certified DNC1	**4.9***	**1.38***	**0.59***	**2**	**0.41***	**2.7**	**0.62**	**2***	**(0.33)**	**2.01***	**0.32***	**1.01***
Standard W2	13.7	3.33	1.104	3.52	0.64	3.79	0.78	2.39	0.361	2.05	0.305	2.5
Certified W2	**14**	**3.25***	**1.1***	**3.6***	**0.63**	**3.8***	**0.76***	**2.5**	**0.38**	**2.05***	**0.33***	**2.56***
Standard MRG1	19.1	4.59	1.430	4.00	0.58	2.98	0.51	1.30	0.154	0.78	0.120	3.7
Certified MRG1	**19.2***	**4.5***	**1.39***	**4**	**0.51***	**2.9**	**0.49***	**1.12**	**0.11**	**(0.6)**	**0.12**	**3.76***
Standard SY3	672	122	17.4	106	20.9	130	28.2	78.9	12.0	67.5	8.009	10.8
Certified SY3	**670**	**109**	**17***	**105***	**18**	**118**	**29.5***	**68**	**11.6***	**(62)**	**7.9**	**9.7**
Standard GXR1	16.2	3.10	0.632	4.01	0.83	4.99	0.99	2.93	0.431	2.30	0.337	0.8
Certified GXR1	**(18)**	**2.7**	**0.69**	**4.2**	**0.83**	**4.3**			**(0.43)**	**1.9**	**0.28**	**0.96**

Table A.3. (Continued)

Sample ID:	Ta	W	Tl	Pb	Bi	Th	U
397	0.48	12	3.11	22	0.40	18.0	4.53
613	0.53	3.9	2.75	11	1.32	21.1	7.67
658	0.94	2.7	1.60	21	0.90	24.9	6.68
49-113.6	0.31	15	1.60	14	0.40	17.7	5.50
49-129.2	0.90	24	2.09	28	0.57	27.5	5.96
515-SP	0.50	4.8	2.84	10	0.50	22.5	8.28
515-X	0.12	3.6	6.56	10	0.36	7.10	3.89
55-62.7	0.51	7.8	3.02	25	1.61	26.6	12.1
57-166.2	0.92	13	2.58	14	0.14	32.7	8.91
57-174.1	0.80	6.7	2.99	25	0.25	26.9	8.02
60-74.8	0.48	5.0	3.48	21	0.60	22.7	6.37
664-4	0.35	7.9	2.08	12	1.09	12.9	3.23
76-179.9	0.42	3.4	4.35	21	0.19	17.4	5.13
1966	0.41	1.4	1.93	25	0.17	16.2	4.60
A23	1.22	6.7	2.34	27	0.81	35.0	11.9
TR223	0.40	2.3	3.57	75	0.63	17.8	4.89
TR6	0.42	2.0	1.68	21	0.36	15.2	4.33
Blank	-0.01	-0.2	-0.05	-5	-0.05	-0.05	-0.05
Standard STM1	18.6	3.1	0.26	19	0.26	31.0	9.03
Certified STM1	**18.6***	**3.6***	**0.26**	**17.7***	**0.13**	**31***	**9.06***
Standard MAG1	1.14	1.4	0.30	15	-0.05	11.9	2.81
Certified MAG1	**1.1**	**1.4**	**(0.59)**	**24***	**0.34**	**11.9***	**2.7***
Standard BIR1	0.06	-0.2	-0.05	5	-0.05	0.12	-0.05
Certified BIR1	**0.04**	**0.07**	**(0.01)**	**3**	**(0.02)**	**0.03**	**0.01**
Standard DNC1	0.08	-0.2	-0.05	7	-0.05	0.31	0.08
Certified DNC1	**0.098***	**(0.2)**	**(0.026)**	**6.3**	**(0.02)**	**(0.2)**	**(0.1)**
Standard W2	0.45	0.3	0.08	7	-0.05	2.25	0.52
Certified W2	**0.5**	**(0.3)**	**(0.2)**	**9.3**	**(0.03)**	**2.2***	**0.53**
Standard MRG1	0.90	0.2	-0.05	6	0.17	0.84	0.30
Certified MRG1	**0.8***	**0.3**	**0.055**	**10**	**(0.13)**	**0.93**	**0.24**
Standard SY3	22.6	1.4	1.59	123	0.73	1,001	646
Certified SY3	**30***	**1.1***	**1.5**	**133***	**(0.8)**	**1003***	**650***
Standard GXR1	0.17	164	0.48	732	1,380	2.91	34.9
Certified GXR1	**0.175**	**164**	**(0.39)**	**730**	**1380**	**2.44**	**34.90**

NOTE: '*' = RECOMMENDED VALUES
'( )' = INFORMATION VALUES
ALL OTHER VALUES ARE PROPOSED

Certified By:

Date: ____________________

D. D'Anna, Dipl. T.

ICPMS Technical Manager, Activation Laboratories Ltd.

Unless otherwise instructed, samples will be disposed of 90 days from the date of this report.

Sample TR6 corresponds to the sample TR6A in the text. Sample TR223 was collected from the same site as sample 1966, and only results for the sample 1966 are used in the text.

Table A.4. Activation Laboratories Ltd. (ACTLABS-SKYLINE) report on major and trace element analyses by fusion-ICP and fusion-ICP-MS methods (Code 4LITHORESEARCH)

REPORT 20602 CODE 4 LITHORES-MAJ ELEM FUS ICP

SAMPLE NUMBER	SiO2 %	Al2O3 %	Fe2O3 %	MnO %	MgO %	CaO %	Na2O %	K2O %	TiO2 %	P2O5 %	LOI %	TOTAL %
638-8	58.39	17.60	6.34	0.114	2.95	6.53	4.50	0.49	0.516	0.21	2.56	100.19
643-1	60.33	14.97	5.26	0.087	3.02	4.72	5.11	0.83	0.399	0.10	5.36	100.18
650-1	59.72	14.58	7.84	0.094	5.38	3.55	3.87	0.10	0.437	0.09	4.61	100.26
663.3	63.87	13.12	6.08	0.082	2.79	5.71	3.97	0.06	0.427	0.10	4.05	100.26
TR6-6	63.22	14.83	6.06	0.090	3.62	2.43	5.13	0.70	0.437	0.10	3.55	100.17
STANDARDS:												
SY3 CERT	59.62	11.75	6.49	0.32	2.67	8.26	4.12	4.23	0.15	0.54	1.16	
SY-3/A	59.62	11.77	6.47	0.324	2.63	8.34	4.12	4.34	0.149	0.54		
MRG-1 CERT	39.09	8.46	17.93	0.17	13.55	14.71	0.74	0.18	3.77	0.08	1.56	
MRG-1/A	39.09	8.48	17.97	0.169	13.46	14.62	0.73	0.17	3.769	0.06		
W-2 CERT	52.44	15.35	10.74	0.163	6.37	10.87	2.14	0.627	1.06	0.131	0.60	
W-2/A	52.75	15.32	10.75	0.164	6.28	10.80	2.19	0.64	1.040	0.13		
DNC-1 CERT	47.04	18.30	9.93	0.149	10.05	11.27	1.87	0.229	0.48	0.085	0.60	
DNC-1/A	47.06	18.47	9.93	0.146	10.15	11.29	1.93	0.29	0.473	0.07		
BIR-1 CERT	47.77	15.35	11.26	0.171	9.68	13.24	1.75	0.027	0.96	0.05		
BIR-1/A	47.77	15.41	11.37	0.171	9.58	13.24	1.83	0.04	0.940	0.02		
G-2 CERT	69.08	15.35	2.66	0.032	0.75	1.96	4.08	4.48	0.48	0.14		
G-2/A	69.79	15.37	2.66	0.032	0.76	1.97	4.09	4.49	0.474	0.14		
NBS 1633b CERT	49.24	28.43	11.13	0.020	0.799	2.11	0.271	2.26	1.32	0.53		
NBS 1633b/A	49.13	28.41	11.12	0.017	0.80	2.16	0.28	2.32	1.246	0.55		
STM-1 CERT	59.64	18.39	5.22	0.22	0.101	1.09	8.94	4.28	0.135	0.158		
STM-1/A	59.58	18.39	5.27	0.221	0.10	1.17	8.85	4.31	0.136	0.16		
IF-G CERT	41.20	0.15	55.85	0.042	1.89	1.55	0.032	0.012	0.014	0.063		
IF-G/A	40.70	0.18	55.85	0.037	1.93	1.54	0.05	0.03	0.014	0.07		
FK-N CERT	65.02	18.61	0.09	0.005	0.01	0.11	2.58	12.81	0.02	0.02		
FK-N/A	65.61	18.61	0.10	0.004	0.02	0.11	2.49	12.77	0.014	0.02		

SAMPLE NUMBER	Ba ppm	Sr ppm	Y ppm	Sc ppm	Zr ppm	Be ppm	V ppm	
638-8	338	1307	13	15	85	-1	142	
643-1	299	248	11	17	64	-1	122	
650-1	257	495	12	27	70	-1	162	
663.3	42	496	14	18	102	-1	158	
TR6-6	332	428	12	19	78	-1	132	
STANDARDS:								
SY3 CERT	450	302	718	6.8	320	20	50	syenite
SY-3/A	449	304	719	9	352	20	50	
MRG-1 CERT	61	266	14	55	108	0.61	526	gabbro
MRG-1/A	53	269	15	55	104	-1	526	
W-2 CERT	182	194	24	35	94	1.3	262	diabase
W-2/A	174	194	22	36	92	-1	263	
DNC-1 CERT	114	145	18	31	41	1	148	dolerite
DNC-1/A	105	141	18	31	40	-1	139	
BIR-1 CERT	7.7	108	16	44	22	0.58	313	basalt
BIR-1/A	7	107	14	44	24	-1	322	
G-2 CERT	1882	478	11	3.5	309	2.5	36	granite
G-2/A	1932	476	11	4	328	2	34	
NBS 1633b CERT	709	1041		41			296	fly ash
NBS 1633b/A	705	1019	88	40	232	12	290	
STM-1 CERT	560	700	46	0.61	1210	9.6 (8.7		syenite
STM-1/A	593	700	43	-1	1222	9	-5	
IF-G CERT	1.5	3	9	0.38	2.4	4.7	4	iron form sample
IF-G/A	10	6	12	1	16	4	-5	
FK-N CERT	200	39	0.3	0.05	13	1	3	K-feldspar
FK-N/A	204	38	3	-1	14	-1	-5	

Note: Certificate data underlined are recommended values; other values are proposed except those preceded by a "(" which are information values.

Note: The Fe2O3 for the standards is Total Fe2O3 and has not been adjusted for the FeO.

Note: Negative values indicate less than the reporting limit.

Note: LOI values less than -0.01% represent a Gain on Ignition.

Table A.4. (Continued)

REPORT 20602 CODE 4 LITHORES-TRACE ELEM FUS ICP/MS

Lithogeochem (Research Packa;

Trace Element Values Are in Parts Per Million. Negative Values Equal Not Detected at That Lower Limit.

Sample ID:	V	Cr	Co	Ni	Cu	Zn	Ga	Ge	As	Rb	Sr	Y
638-8	149	74	11	-20	18	-30	20	1.3	6	10	1,940	14.3
643-1	126	166	14	36	39	-30	15	0.9	5	29	259	10.1
650-1	169	421	29	82	-10	-30	14	1.1	-5	5	498	12.5
663.3	159	199	14	29	46	-30	13	1.1	-5	2	481	12.6
TR6-6	135	180	19	40	35	-30	15	1.0	-5	21	424	11.4
Control Material W2	261	90	41	67	111	55	18	1.2	-5	20	194	21.8
Certified W2	**262***	**93***	**44***	**70***	**103***	**77***	**20***	**(1.0)**	**1.2**	**20***	**194***	**24***
Control Material MRG	538	470	89	171	133	161	19	2.7	-5	8	275	13.6
Certified MRG-1	**526***	**430**	**87***	**193***	**134***	**191***	**17**		**0.7**	**8.5**	**266***	**14**
Blank	-5	-20	-1	-20	-10	-30	-1	-0.5	-5	-1	-2	-0.5
Calibration Standard M	144	102	24	30	28	127	23	2.0	13	152	143	28.0
Certified MAG1	**140***	**97***	**20.4***	**53***	**30***	**130***	**20.4***		**9.2**	**149***	**146***	**28***
Calibration Standard B	310	368	47	150	120	70	15	1.7	-5	-1	103	15.0
Certified BIR1	**313***	**382***	**51.4***	**166***	**126***	**71***	**16**	**1.5**	**(0.4)**	**0.25***	**108***	**16***
Calibration Standard D	157	291	58	249	105	68	14	1.7	-5	4	148	18.2
Certified DNC1	**148***	**285***	**54.7***	**247***	**96***	**66***	**15**	**(1.3)**	**(0.2)**	**(4.5)**	**145***	**18***
Calibration Standard G	57	43	10	-20	83		37	1.4	25	83	161	18.9
Certified GXR-2	**52**	**36**	**8.6**	**21**	**76**		**37**		**25**	**78**	**160**	**17**
Calibration Standard LI	81	82	34	35	34	156	15	1.4	29	74	246	30.1
Certified LKSD-3	**82**	**87**	**30**	**47**	**35**	**152**			**27**	**78**	**240**	**30**
Calibration Standard M	132	99	29	-20	-10	1,350	95	3.3	-5	2,210	5	48.5
Certified Mica Fe	**135***	**90***	**23***	**35***	**5***	**1300***	**95***	**3.2**	**3**	**2200***	**5***	**48***
Calibration Standard G	77	-40	8	54	1,110	718	12	5	425	4	271	29
Certified GXR1	**80**	**12**	**8.2**	**41**	**1,110**	**760**	**13.8**		**427**	**(14)**	**275**	**32**
Calibration Standard S'	54	-40	7	-40	-20	254	36	4	21	206	306	737
Certified SY3	**50**	**(11)**	**8.8**	**11**	**17**	**244***	**27***	**1.4**	**18.8**	**206***	**302***	**718***
Calibration Standard S'	-5	-20	-1	-20	-10	230	35	1.4	5	114	717	46.2
Certified STM-1	**(8.7)**	**(4.3)**	**0.9**	**(3)**	**(4.6)**	**235***	**36***	**(1.4)**	**4.6**	**118***	**700***	**46***
Calibration Standard IF	-5	-20	31	29	13	-30	-1	23.9	-5	-1	3	9.6
Certified IFG-1	**2**	**4**	**29***	**22.5**	**13***	**20***	**0.7**	**24**	**1.5**	**0.4**	**3**	**9***

NOTE: ' * ' = RECOMMENDED VALUES
' ( ) ' = INFORMATION VALUES
ALL OTHER VALUES ARE PROPOSED

Table A.4. (Continued)

REPORT 20602 CODE 4 LITHORES-TRACE ELEM FUS ICP/MS

Lithogeochem (Research Package)

Trace Element Values Are in Parts Per Million. Negative Values Equal Not Detected at That Lower Limit.

Sample ID:	Zr	Nb	Mo	Ag	In	Sn	Sb	Cs	Ba	La	Ce	Pr
638-8	80	2.3	-2	0.7	-0.1	-1	1.5	0.9	355	11.1	21.3	2.51
643-1	62	0.8	-2	-0.5	-0.1	-1	0.5	1.0	314	8.03	15.2	1.77
650-1	62	1.3	-2	-0.5	-0.1	-1	0.9	0.8	263	9.01	17.3	2.08
663.3	95	1.1	-2	-0.5	-0.1	-1	1.2	0.3	43	11.4	22.2	2.49
TR6-6	70	1.0	-2	-0.5	-0.1	-1	0.9	0.9	338	8.23	16.3	1.95
Control Material W2	95	7.2	-2	-0.5	-0.1	2	1.3	0.9	186	10.8	23.3	2.82
Certified W2	**94***	**7.9**	**(0.6)**	**(0.046)**			**0.79**	**0.99***	**182***	**11.4***	**24***	**(5.9)**
Control Material MRG	109	20.5	-2	-0.5	0.1	4	1.0	0.8	57	9.46	26.5	3.63
Certified MRG-1	**108***	**20**	**0.9**	**0.1**		**(3.6)**	**0.86**	**0.6**	**61.0**	**9.8***	**26**	**3.4**
Blank	-1	-0.2	-2	-0.5	-0.1	-1	-0.2	-0.1	-3	-0.05	-0.05	-0.01
Calibration Standard M	123	14.8	-2	-0.5	-0.1	3	1.1	8.7	530	42.3	87.0	9.47
Certified MAG1	**126***	**12**	**1.6**	**0.08**	**(0.18)**	**3.6**	**0.96***	**8.6***	**479***	**43***	**88***	**9.3**
Calibration Standard B	16	0.8	-2	-0.5	-0.1	-1	0.6	-0.1	7	0.70	2.08	0.39
Certified BIR1	**15.5**	**0.6**	**(0.5)**	**(0.036)**		**0.65**	**0.58**	**0.005**	**7**	**0.62***	**1.95***	**0.38***
Calibration Standard D	39	1.5	-2	-0.5	-0.1	2	1.2	0.3	115	3.79	9.05	1.15
Certified DNC1	**41***	**3**	**(0.7)**	**(0.027)**			**0.96***	**(0.34)**	**114***	**3.8***	**10.6**	**1.3**
Calibration Standard G	262	11.8	-2	16.6	-0.1	2	48.9	5.4	2,240	26.8	54.5	5.49
Certified GXR-2	**269**	**11**	**(2.1)**	**17**	**(0.252)**	**1.7**	**49**	**5.2**	**2,240**	**25.6**	**51.4**	
Calibration Standard L	157	7.1	-2	2.8	-0.1	3	1.4	2.3	706	48.2	90.9	11.1
Certified LKSD-3	**178**	**8**	**(<5)**	**2.7**		**3**	**1.3**	**2.3**	**680**	**52**	**90**	
Calibration Standard M	828	300	2	-0.5	0.6	70	1.1	174	165	202	444	48.9
Certified Mica Fe	**800***	**270***	**1.2**		**0.60**	**70***		**180***	**150***	**200***	**420***	**49***
Calibration Standard G	31	1.9	18	31	0.6	48	122	3.5	690	7.2	13.6	1.73
Certified GXR1	**(38)**	**(0.8)**	**18**	**31**	**0.77**	**54**	**122**	**3**	**750**	**7.5**	**17**	
Calibration Standard S	349	160	-4	-1	0.3	7	0.8	3.0	480	1,340	2,230	223
Certified SY3	**320**	**148**	**(1.0)**	**(1.5)**		**(6.5)**	**0.31**	**2.5**	**450**	**1340***	**2230***	**223***
Calibration Standard S	1,210	268	5	-0.5	0.1	7	1.8	1.6	603	149	258	24.1
Certified STM-1	**1210***	**268***	**5.2**	**0.079***	**(0.12)**	**6.8**	**1.66***	**1.54***	**560***	**150***	**259***	**19***
Calibration Standard IF	2	0.5	-2	-0.5	-0.1	-1	0.6	-0.1	2	2.97	4.10	0.44
Certified IFG-1	**1**	**0.1***	**0.7**		**0.2**	**0.3**	**0.63**	**0.06**	**1.5**	**2.8***	**4***	**0.4***

NOTE: '*' = RECOMMENDED VALUES
'( )' = INFORMATION VALUES
ALL OTHER VALUES ARE PROPOSED

Table A.4. (Continued)

REPORT 20602 CODE 4 LITHORES-TRACE ELEM FUS ICP/MS

Lithogeochem (Research Package)

Trace Element Values Are in Parts Per Million. Negative Values Equal Not Detected at That Lower Limit.

Sample ID:	Nd	Sm	Eu	Gd	Tb	Dy	Ho	Er	Tm	Yb	Lu	Hf
638-8	11.3	2.59	0.908	2.44	0.43	2.46	0.52	1.56	0.244	1.54	0.238	2.2
643-1	7.54	1.71	0.553	1.67	0.29	1.72	0.36	1.09	0.167	1.08	0.173	1.6
650-1	8.95	2.02	0.663	2.08	0.36	2.25	0.46	1.40	0.217	1.40	0.221	1.8
663.3	9.89	2.12	0.665	2.08	0.37	2.17	0.46	1.41	0.220	1.36	0.211	2.6
TR6-6	8.54	1.92	0.632	2.02	0.35	2.03	0.42	1.35	0.201	1.26	0.205	2.0
Control Material W2	12.5	3.12	1.06	3.57	0.66	3.79	0.82	2.07	0.334	2.01	0.310	2.6
Certified W2	**14.0**	**3.25***	**1.1***	**3.6***	**0.63**	**3.8***	**0.76***	**2.5**	**0.4**	**2.05***	**0.33***	**2.56***
Control Material MRG-	18.1	4.41	1.44	4.22	0.55	3.08	0.55	1.08	0.152	0.85	0.103	3.9
Certified MRG-1	**19.2***	**4.5***	**1.39***	**4.0**	**0.51***	**2.9**	**0.5**	**1.1**	**0.1**	**(0.6)**	**0.1**	**3.76***
Blank	-0.05	-0.01	-0.005	-0.01	-0.01	-0.01	-0.01	-0.01	-0.005	-0.01	-0.002	-0.1
Calibration Standard M	36.3	6.85	1.42	6.05	0.96	5.11	1.05	2.75	0.430	2.46	0.369	3.4
Certified MAG1	**38***	**7.5***	**1.55***	**5.8***	**0.96***	**5.2***	**1.02***	**3**	**0.43***	**2.6***	**0.40***	**3.7***
Calibration Standard B	2.48	1.07	0.495	1.83	0.39	2.48	0.58	1.69	0.250	1.58	0.251	0.7
Certified BIR1	**2.5***	**1.1***	**0.54***	**1.85***	**0.36***	**2.5***	**0.57***	**1.7***	**0.26***	**1.65**	**0.26***	**0.6***
Calibration Standard D	4.92	1.39	0.589	1.99	0.44	2.80	0.68	1.82	0.306	1.96	0.320	1.1
Certified DNC1	**4.9***	**1.38***	**0.59***	**2**	**0.41***	**2.7**	**0.62**	**2***	**(0.33)**	**2.01***	**0.32***	**1.01***
Calibration Standard G	20.7	3.67	0.751	3.30	0.48	3.13	0.68	1.63	0.291	1.85	0.294	7.0
Certified GXR-2	**(19)**	**3.5**	**0.81**	**(3.3)**	**0.48**	**3.3**			**(0.3)**	**2.04**	**(0.27)**	**8.3**
Calibration Standard L	42.1	7.79	1.39	6.18	0.92	4.97	1.05	2.50	0.419	2.65	0.405	4.4
Certified LKSD-3	**44**	**8.0**	**1.50**		**1.0**	**4.9**				**2.7**	**0.4**	**4.8**
Calibration Standard M	181	33.5	0.826	20.7	2.70	11.0	1.63	3.53	0.523	3.34	0.488	26.7
Certified Mica Fe	**180***	**33***	**0.7***	**21***	**2.7***	**11***	**1.6***	**3.8***	**0.48***	**3.5***	**0.5***	**26***
Calibration Standard G	8.2	2.73	0.61	3.95	0.8	4.47	0.95	2.27	0.40	2.07	0.287	0.8
Certified GXR1	**(18)**	**2.7**	**0.69**	**4.2**	**0.83**	**4.3**			**(0.43)**	**1.9**	**0.28**	**0.96**
Calibration Standard S	673	109	17.1	105	18.0	118	29.5	68.2	11.6	62.3	7.93	10.5
Certified SY3	**670**	**109**	**17***	**105***	**18**	**118**	**29.5***	**68**	**11.6***	**(62)**	**7.90**	**9.70**
Calibration Standard S	77.9	12.0	3.40	9.3	1.50	8.08	1.65	4.00	0.677	4.20	0.617	27.7
Certified STM-1	**79***	**12.6***	**3.6***	**9.5***	**1.55***	**8.1***	**1.9**	**4.2***	**0.69**	**4.4***	**0.60**	**28***
Calibration Standard IF	0.18	0.38	0.387	0.72	0.12	0.79	0.22	0.59	0.093	0.58	0.101	-0.1
Certified IFG-1	**0.2**	**0.4***	**0.39***	**0.74***	**0.11***	**0.8***	**0.2***	**0.63***	**0.09***	**0.6***	**0.09***	**0.04**

NOTE: ' * ' = RECOMMENDED VALUES
' ( ) ' = INFORMATION VALUES
ALL OTHER VALUES ARE PROPOSED

Table A.4. (Continued)

REPORT 20602 CODE 4 LITHORES-TRACE ELEM FUS ICP/MS

Lithogeochem (Research Package)

Trace Element Values Are in Parts Per Million. Negative Values Equal Not Detected at That Lower Limit.

Sample ID:	Ta	W	Tl	Pb	Bi	Sample II	Th	U
638-8	0.15	-0.5	0.12	38	0.5	638-8	1.34	0.52
643-1	0.12	0.5	0.14	27	0.4	643-1	1.32	0.50
650-1	0.16	-0.5	-0.05	12	0.2	650-1	2.26	0.68
663.3	0.19	0.5	-0.05	10	0.1	663.3	2.55	0.76
TR6-6	0.16	0.7	0.18	9	0.1	TR6-6	1.79	0.64
Control Material W2	0.50	-0.5	0.11	11	-0.1	Control M	2.08	0.50
Certified W2	**0.5**	**(0.3)**	**(0.2)**	**9**	**(0.03)**	**Certified**	**2.2***	**0.53**
Control Material MRG	0.85	-0.5	0.09	6	0.2	Control M	0.82	0.27
Certified MRG-1	**0.8***	**0.3**	**0.06**	**10**	**(0.13)**	**Certified**	**0.9**	**0.24**
Blank	-0.01	-0.5	-0.05	-5	-0.1	Blank	-0.05	-0.01
Calibration Standard M	1.16	1.3	0.36	17	0.3	Calibratio	11.1	2.61
Certified MAG1	**1.1**	**1.4**	**(0.59)**	**24***	**0.34**	**Certified**	**11.9***	**2.7***
Calibration Standard B	0.05	-0.5	-0.05	-5	-0.1	Calibratio	-0.05	0.02
Certified BIR1	**0.04**	**0.07**	**(0.01)**	**3**	**(0.02)**	**Certified**	**0.03**	**0.01**
Calibration Standard D	0.08	-0.5	-0.05	7	-0.1	Calibratio	0.24	0.07
Certified DNC1	**0.098***	**(0.2)**	**(0.026)**	**6.3**	**(0.02)**	**Certified**	**(0.2)**	**(0.1)**
Calibration Standard G	0.93	1.8	1.05	636	0.2	Calibratio	8.46	2.85
Certified GXR-2	**0.9**	**1.9**	**1.03**	**690**	**(0.69)**	**Certified**	**8.8**	**2.9**
Calibration Standard LI	0.66	0.7	0.54	25	0.1	Calibratio	11.0	4.32
Certified LKSD-3	**0.7**	**(<4)**		**29**		**Certified**	**11.4**	**4.6**
Calibration Standard M	33.2	8.5	16.0	19	1.4	Calibratio	158	80.1
Certified Mica Fe	**35***	**15**	**16**	**13***	**2**	**Certified**	**150***	**80***
Calibration Standard G	0.18	175	0.42	730	1,380	Calibratio	2.4	32.0
Certified GXR1	**0.175**	**164**	**(0.39)**	**730**	**1,380**	**Certified**	**2.44**	**34.9**
Calibration Standard S	25.7	1.8	1.60	111	1.0	Calibratio	1,000	651
Certified SY3	**30***	**1.1***	**1.50**	**133***	**(0.8)**	**Certified**	**1003***	**650***
Calibration Standard S	18.6	3.4	0.29	18	0.2	Calibratio	29.3	8.9
Certified STM-1	**18.6***	**3.6***	**0.26**	**17.7***	**0.13**	**Certified**	**31***	**9.06***
Calibration Standard IF	0.19	190	-0.05	-5	0.2	Calibratio	0.25	0.03
Certified IFG-1	**0.2**	**220**	**0.02**	**4**		**Certified**	**0.1**	**0.02**

NOTE: ' * ' = RECOMMENDED VALUES
' ( ) ' = INFORMATION VALUES
ALL OTHER VALUES ARE PROPOSED

NOTE: ' * ' = RECOMMENDED VALUES
' ( ) ' = INFORMATION VALUES
ALL OTHER VALUES ARE PROPOSED

Table A.5. Activation Laboratories Ltd. report on analyses for platinum group elements by Fire Assay-ICP-MS (Code1C Research)

PGE Job#17166	Report#: 17268	nt: Vlad Ispolatov		
Sample ID	weight, g	Pd, ppb	Pt, ppb	Au, ppb
515x	30	8.8	7.6	4
49-113.7	28.19	6.8	7.3	10
613	30	9.4	10	7
TR6	30	5.5	5.9	5
57-166.2	30	2.1	1.2	4

Certified by: D.D'Anna, Dipl. T.
ICPMS Technical Manager, Activation Laboratories Ltd.

Sample TR6 corresponds to sample TR6A in the text.
Detection limits, ppb: Au(1), Pt(0.1), Pd(0.1).

LITHOGEOCHEMISTRY FOR EXPLORATION AND RESEARCH

Actlabs has developed a revolutionary major oxide and trace element package for lithogeochemistry unique in the analytical industry. The package combines a fusion-ICP whole rock package (4B) with ICP/MS analysis for trace elements availabe in two grades of analysis (4B option 2, STANDARD or RESEARCH grade). This proprietary research grade ICP/MS option 2 provides the lowest detection limits for rare earth elements and some other trace elements available anywhere, at a price that is unbelievably low, yet with quality that is unsurpassed.

CODE-4B. WHOLE ROCK ANALYSIS - RESEARCH QUALITY FUSION-ICP

MAJOR OXIDES ALL WITH 0.01% DETECTION LIMITS

SiO_2 Al_2O_3 Fe_2O_3 MgO MnO CaO TiO_2 Na_2O K_2O P_2O_5

PLUS LOSS ON IGNITION (LOI)

PLUS TRACE ELEMENTS

Ba (2 ppm) Sr (2 ppm) Y (2 ppm) Zr (2 ppm) Sc (2 ppm) Be (1 ppm) V (5 ppm)

PRICE: (3 GRAMS REQUIRED)	CDN	US
1-10	$32.00	$27.00
11-500	$27.00	$22.50
500+	ON REQUEST	

CODE-4B OPTION 2-ADD ON (TOTAL) TRACE ELEMENT PACKAGE BY FUSION-ICP/MS

Elem. ppm	Standard	Research	Elem. ppm	Standard	Research	Elem. ppm	Standard	Research
*Ag	0.5	0.5	*Ni	10	10	La	0.1	0.01
*As	5	5	*Pb	5	5	Ce	0.1	0.01
Ba	1	0.1	Rb	0.5	0.1	Pr	0.05	0.005
*Bi	0.2	0.05	*Sb	0.1	0.05	Nd	0.1	0.01
*Co	0.5	0.5	*Sn	1	0.5	Sm	0.1	0.01
Cr	10	10	Sr	0.1	0.01	Eu**	0.05	0.005
Cs	0.5	0.1	Ta	0.05	0.01	Gd	0.1	0.01
*Cu	10	10	Th	0.1	0.05	Tb	0.1	0.01
Ga	1	1	Tl	0.1	0.05	Dy	0.1	0.01
Ge	1	0.5	U	0.1	0.05	Ho	0.1	0.01
Hf	0.2	0.1	V	5	5	Er	0.1	0.01
In	0.2	0.1	*W	0.5	0.2	Tm	0.05	0.005
*Mo	0.5	0.1	Y	1	0.1	Yb	0.1	0.01
Nb	1.0	0.5	*Zn	10	10	Lu	0.04	0.002
			Zr	0.5	0.1			

** Eu determinations are semiquantitative in samples having extremely high Ba concentrations.
This package is only available at the prices below with Pkg. 4B. Otherwise add $15.00CDN, or $12.00US. Package 4B Option 2 is intended primarily for unmineralized samples. Mineralized samples can be analyzed however data for elements with an * may be semi-quantitative. If quantitative numbers are required a surcharge of CDN $14 or US$10/sample will apply. Please indicate quantitative on your order.

PRICE	STANDARD		RESEARCH	
	CDN	US	CDN	US
1-10	$32.00	$27.00	$60.00	$51.00
11-500	$27.00	$22.50	$50.00	$42.50

Fig. A.1. Detection limits for CODE 4B and CODE 4B OPTION 2 analytical packages of Activation Laboratories Ltd.(a copy from the pricelist). Research quality was used for the trace element determination.

Lithogeochemistry for Exploration and Research

Code	INAA 4A-expl	INAA 4A-research	WRA-ICP 4B	Trace Element 4B2-std	WRA+trace 4Litho	Trace Element 4B2 -research	WRA+trace 4Lithoresearch	WRA-XRF 4C	XRF pressed pellet 4C1
SiO_2			0.01%		0.01%		0.01%	0.01%	
TiO_2			0.001%		0.001%		0.001%	0.01%	
Al_2O_3			0.01%		0.01%		0.01%	0.01%	
Fe_2O_3			0.01%		0.01%		0.01%	0.01%	
MnO			0.001%		0.001%		0.001%	0.01%	
MgO			0.01%		0.01%		0.01%	0.01%	
CaO			0.01%		0.01%		0.01%	0.01%	
Na_2O			0.01%		0.01%		0.01%	0.01%	
K_2O			0.01%		0.01%		0.01%	0.01%	
P_2O_5			0.01%		0.01%		0.01%	0.01%	
LOI			0.01%		0.01%		0.01%	0.01%	
Ag	5	2	(0.5+)	0.5	0.5	0.5	0.5		
As	2	1	(0.5++)	5 (0.5++)	5 (0.5++)	5 (0.5++)	5 (0.5++)		5
Au	5 ppb	2 ppb	(2 ppb++)	(2 ppb++)	(2 ppb++)	(2 ppb++)	(2 ppb++)		
Ba	100	20	3	3	3	3	3		5*
Be			1		1		1		
Bi			(10+)	0.4	0.4	0.1	0.1		5
Br	1	0.5	(0.5++)	(0.5++)	(0.5++)	(0.5++)	(0.5++)		
Ca	0.5%	0.2%							
Cd			(0.5+)	(0.5+)	(0.5+)	(0.5+)	(0.5+)		
Co	1	0.1	(1++)	1	1	1	1		5**
Cr	2	0.5	(5++)	20 (5++)	20 (5++)	20 (5++)	20 (5++)		5**
Cs	0.5	0.2	(1++)	0.5	0.5	0.1	0.1		
Cu			(1+)	10 (1+)	10 (1+)	10 (1+)	10 (1+)		5**
Fe	0.02%	0.005%		(0.01%++)		(0.01%++)			
Ga				1	1	1	1		5*
Ge				1	1	0.5	0.5		
Hf	0.5	0.2	(1++)	0.2	0.2	0.1	0.1		
In				0.2	0.2	0.1	0.1		
Ir	5 ppb	2 ppb	(5 ppb++)	(5 ppb++)	(5 ppb++)	(5 ppb++)	(5 ppb++)		
Mo	5	2	(5++)	2	2	2	2		
Nb				1	1	0.2	0.2		2*
Na	0.01%	0.001%		(0.01%++)		(0.01%++)			
Ni	100	50	(1+)	20 (1+)	20 (1+)	20 (1+)	20 (1+)		5**
Pb			(5+)	5	5	5	5		5**
Rb	20	10	(20++)	2	2	1	1		2*
S			(100+)	(100+)	(100+)	(100+)	(100+)		50
Sb	0.2	0.1	(0.2++)	0.5 (0.2++)	0.5 (0.2++)	0.2	0.2		
Sc	0.1	0.01	1	(0.1++)	1 (0.1++)	(0.1++)	1 (0.1++)		
Se	3	0.5	(3++)	(3++)	(3++)	(3++)	(3++)		
Sn				1	1	1	1		5
Sr	500	100	2	2	2	2	2		2*
Ta	1	0.3	(0.5++)	0.1	0.1	0.01	0.01		
Tl				0.1	0.1	0.05	0.05		
V			5	5	5	5	5		5**
W	3	1	(1++)	1	1	0.5	0.5		
Y			2	1	1	0.5	0.5		2*
Zn	40	10	(1+)	30 (1+)	30 (1+)	30 (1+)	30 (1+)		5**
Zr			4	5	5	1	1		5*
La	0.2	0.05	(0.5++)	0.1	0.1	0.05	0.05		
Ce	3	1	(3++)	0.1	0.1	0.05	0.05		
Pr		(†0.01)		0.05	0.05	0.01	0.01		
Nd	5	1	(5++)	0.1	0.1	0.05	0.05		
Sm	0.1	0.01	(0.1++)	0.1	0.1	0.01	0.01		
Eu	0.1	0.05	(0.2++)	0.05	0.05	0.005	0.005		
Gd		(†0.01)		0.1	0.1	0.01	0.01		
Tb	0.5	0.1	(0.5++)	0.1	0.1	0.05	0.01		
Dy		(†0.01)		0.1	0.1	0.01	0.01		
Ho		(†0.01)		0.1	0.1	0.01	0.01		
Er		(†0.01)		0.1	0.1	0.01	0.01		
Tm		(†0.01)		0.05	0.05	0.005	0.005		
Yb	0.1	0.05	(0.2++)	0.1	0.1	0.01	0.01		
Lu	0.05	0.01	(0.05++)	0.04	0.04	0.002	0.002		
U	0.5	0.1	(0.5++)	0.1	0.1	0.01	0.01		
Th	0.5	0.1	(0.2++)	0.1	0.1	0.05	0.05		
# samples 1-10	$21.00	$50.00	$27.00	$39.00	$54.00	$63.00	$78.00	$27.50	see Code 4C1 adjacent page
>11	$19.00	$47.00	$22.50	$34.50	$45.00	$54.50	$65.00	$25.00	

Elements are all in PPM except where noted.

Elements in brackets are optional - see notes, Page 15.

PAGE 14 International Pricelist Tel: +1.905.648.9611

Fig. A.2. Detection limits for the CODE 4-Lithoresearch analytical package of Activation Laboratories Ltd.(a copy from the pricelist).

Codes 4B, 4B2-STD, 4B2-RESEARCH, 4LITHO, 4LITHORESEARCH - Actlabs has developed a lithium metaborate/tetraborate fusion ICP Whole Rock Package Code 4B and a trace element ICP-MS package Code 4B2 which is unique for scope of elements and detection limits. The two packages are combined for Code 4Litho and Code 4Lithoresearch. The quality of whole rock data in Code 4B meets or exceeds quality of data by fusion XRF Code 4C, the old standard in whole rock analysis. The fusion process ensures total metals particularly for elements like REE in resistate phases. (This may not be the case for acid digestions, particularly for heavy rare earths and other elements contained in refractory minerals like zircon, sphene, monazite, chromite, gahnite and several other phases. If refractory minerals are not digested, a bias may occur for certain REE and HFSE with acid digestions). Quality of data is exceptional and can be used for the most exacting applications. The trace element package by ICP-MS, Codes 4B2-STD or 4B2-RESEARCH, on the fusion solution provides research quality data whether using standard or research detection limits. Eu determinations are semiquantitative in samples having extremely high Ba concentrations (greater than 1%). This package is intended primarily for unmineralized samples. Mineralized samples can be analyzed, however, data may be semiquantitative for chalcophile elements (Ag, As, Bi, Co, Cu, Mo, Ni, Pb, Sb, Sn, W and Zn). When quantitative values for the chalcophile elements are required on mineralized samples, please indicate as Code 4B2-STDQUANT, 4B2-RESEARCHQUANT, 4LITHOQUANT or 4LITHORESEARCHQUANT, and a surcharge of $12.00 per sample will apply. A minimum sample weight of 5g is required. Elements with (+) are available at an additional $6.25 (Code 4B1). Those indicated with (++) are available by INAA at an additional charge of $12.00 per sample (Code 4B-INAA). Please add 0.5 to 30g depending on sample size you prefer to analyze for Au with this option. Values on replicates and standards are provided at no cost, as are REE plots (see page 21).

Fig. A.3. A brief description for the CODE 4-Lithoresearch analytical package of Activation Laboratories Ltd. (a copy from the pricelist).

APPENDIX B

ELECTRON MICROPROBE DATA

Electron microprobe data are organized in 19 tables. Tables B.1 to B.9 contain data on mineral phases from alkalic intrusions. Tables B.9 to B.13 comprise data on hydrothermal phases. Tables B.14-B.16 contain results of analyses of mineral phases from granitoids. Tables B.17-B.19 summarize analyses of standard reference materials (SRM). Abbreviations: L=lamprophyre, SP=syenite porphyry, O=predominantly feldspathic segregation (ocellum) in lamprophyres, G(O)=Ordovician granite, G(S)=Silurian granite, G(D-C)=granite clast in Devonian-Carboniferous conglomerates.

Table B.1. Electron microprobe analyses of zoned biotite phenocrysts

probe run id	bio-49_113.7-3	bio-49_113.7-38	bio-49_113.7-32	bio-49_113.7-25	bio-49_113.7-23	bio-49_113.7-10	bio-49_113.7-14	bio-49_113.7-13
sample	49-113.7	49-113.7	49-113.7	49-113.7	49-113.7	49-113.7	49-113.7	49-113.7
rock name	L	L	L	L	L	L	L	L
zone	core	core	core	core	core	core	core	core
SiO_2	42.29	42.37	42.68	42.14	42.32	42.34	40.66	41.72
TiO_2	0.64	0.77	0.66	0.52	0.48	0.52	0.52	0.49
Al_2O_3	12.58	12.90	12.48	12.88	12.96	12.81	13.31	12.95
Cr_2O_3	0.52	0.07	0.20	0.49	0.44	1.00	1.10	1.15
MgO	23.59	23.58	24.35	23.94	22.44	24.29	20.05	20.51
CaO	0.02	0.06	0.00	0.01	0.01	0.02	0.01	0.03
MnO	0.05	0.04	0.00	0.00	0.03	0.02	0.22	0.13
FeO	5.65	6.50	4.71	5.34	7.12	4.39	13.79	9.30
BaO	0.22	0.22	0.29	0.22	0.20	0.15	0.21	0.18
Na_2O	0.07	0.06	0.00	0.00	0.04	0.00	0.06	0.04
K_2O	7.88	7.72	7.67	7.85	7.46	8.01	7.05	7.22
F	1.52	1.71	1.79	1.76	1.58	1.38	1.04	1.37
Cl	0.01	0.02	0.00	0.02	0.01	0.00	0.02	0.01
Total (uncorrected)	95.03	96.03	94.82	95.15	95.09	94.91	98.04	95.09
"-O=F,Cl"	0.64	0.73	0.75	0.75	0.67	0.58	0.44	0.58
Total (corrected)	94.39	95.31	94.06	94.40	94.42	94.33	97.59	94.51
Number of ions based on 24 O, F, Cl								
Si	6.509	6.466	6.536	6.464	6.526	6.491	6.302	6.509
Al	2.282	2.320	2.252	2.329	2.356	2.315	2.431	2.381
Ti	0.074	0.089	0.075	0.059	0.055	0.060	0.060	0.058
Cr	0.064	0.008	0.024	0.059	0.054	0.121	0.135	0.142
Mg	5.413	5.364	5.560	5.474	5.159	5.551	4.632	4.772
Ca	0.004	0.010	0.000	0.002	0.001	0.003	0.002	0.005
Mn	0.007	0.006	0.000	0.000	0.004	0.003	0.028	0.017
Fe	0.727	0.830	0.604	0.685	0.918	0.563	1.788	1.214
Ba	0.013	0.013	0.017	0.013	0.012	0.009	0.013	0.011
Na	0.021	0.019	0.000	0.000	0.013	0.000	0.017	0.011
K	1.548	1.503	1.498	1.535	1.468	1.566	1.393	1.437
F	0.737	0.827	0.867	0.854	0.772	0.668	0.509	0.676
Cl	0.003	0.006	0.001	0.005	0.001	0.001	0.006	0.002
Sum	17.399	17.459	17.434	17.479	17.340	17.348	17.317	17.235
mg#	0.88	0.87	0.90	0.89	0.85	0.91	0.72	0.80

Table B.1 (Continued)

probe run id	bio-49_113.7-12	bio-49_113.7-9	bio-49_113.7-1	bio-49_113.7-5	bio-49_113.7-8	bio-49_113.7-39	bio-49_113.7-21	bio-49_113.7-7
sample	49-113.7	49-113.7	49-113.7	49-113.7	49-113.7	49-113.7	49-113.7	49-113.7
rock name	L	L	L	L	L	L	L	L
zone	core	rim	rim	rim	rim	rim	rim	rim
SiO_2	42.84	41.68	41.30	41.38	41.53	39.65	40.94	40.66
TiO_2	0.58	0.53	0.68	0.47	0.45	1.21	0.67	0.63
Al_2O_3	13.14	13.01	13.32	13.46	12.96	14.78	13.94	13.34
Cr_2O_3	1.18	0.91	0.49	1.21	0.99	0.11	0.46	0.87
MgO	24.15	18.85	16.73	18.26	18.13	15.88	15.54	16.21
CaO	0.03	0.03	0.01	0.01	0.02	0.03	0.02	0.04
MnO	0.02	0.14	0.15	0.08	0.07	0.15	0.09	0.15
FeO	4.33	12.65	14.57	12.32	13.57	15.24	15.86	15.13
BaO	0.23	0.18	0.19	0.20	0.16	0.29	0.16	0.17
Na_2O	0.08	0.02	0.03	0.00	0.00	0.00	0.03	0.17
K_2O	7.90	7.62	6.74	6.93	7.43	7.26	6.64	7.58
F	0.96	0.00	1.11	1.06	0.91	0.86	1.05	0.96
Cl	0.01	0.02	0.00	0.01	0.02	0.04	0.03	0.03
Total (uncorrected)	95.44	95.63	95.30	95.38	96.23	95.50	95.44	95.95
"-O=F,Cl"	0.41	0.00	0.47	0.45	0.39	0.37	0.45	0.41
Total (corrected)	95.03	95.62	94.83	94.94	95.84	95.13	94.99	95.54
Number of ions based on 24 O, F, Cl								
Si	6.525	6.580	6.558	6.513	6.535	6.340	6.523	6.484
Al	2.358	2.420	2.492	2.497	2.404	2.784	2.618	2.507
Ti	0.066	0.063	0.081	0.055	0.053	0.146	0.080	0.076
Cr	0.141	0.113	0.061	0.151	0.123	0.014	0.058	0.110
Mg	5.483	4.436	3.960	4.284	4.253	3.785	3.692	3.855
Ca	0.005	0.005	0.001	0.001	0.004	0.005	0.004	0.008
Mn	0.003	0.018	0.020	0.011	0.009	0.021	0.012	0.020
Fe	0.551	1.670	1.934	1.622	1.785	2.037	2.114	2.018
Ba	0.014	0.011	0.012	0.013	0.010	0.018	0.010	0.011
Na	0.022	0.006	0.008	0.000	0.000	0.000	0.008	0.053
K	1.534	1.534	1.365	1.391	1.490	1.481	1.350	1.541
F	0.464	0.000	0.556	0.526	0.451	0.436	0.527	0.482
Cl	0.002	0.004	0.000	0.003	0.005	0.012	0.009	0.008
Sum	17.170	16.861	17.049	17.068	17.122	17.079	17.006	17.173
mg#	0.91	0.73	0.67	0.73	0.70	0.65	0.64	0.66

Table B.1 (Continued)

probe run id	bio-49_1292-7	bio-49_1292-32	bio-49_1292-17	bio-49_1292-4	bio-49_1292-3	bio-49_1292-15	bio-49_1292-24	bio-49_1292-29
sample	49-129.2	49-129.2	49-129.2	49-129.2	49-129.2	49-129.2	49-129.2	49-129.2
rock name	SP	SP	SP	SP	SP	SP	SP	SP
zone	core	core	core	core	core	core	core	core
SiO_2	40.54	40.71	42.52	41.34	42.16	41.67	42.52	41.90
TiO_2	1.27	0.55	0.63	0.48	0.54	0.65	0.55	0.68
Al_2O_3	13.63	12.77	12.59	12.95	13.16	12.67	12.93	12.80
Cr_2O_3	0.42	0.74	0.73	0.71	0.74	0.68	0.58	0.13
MgO	15.87	24.72	24.88	20.13	25.39	27.92	24.81	26.84
CaO	0.02	0.01	0.00	0.06	0.00	0.00	0.01	0.04
MnO	0.00	0.01	0.07	0.01	0.01	0.02	0.00	0.04
FeO	15.03	4.45	3.81	10.30	4.40	3.89	4.35	4.88
BaO	0.18	0.16	0.20	0.25	0.23	0.14	0.26	0.28
Na_2O	0.07	0.03	0.08	0.06	0.17	0.00	0.14	0.08
K_2O	8.58	10.63	8.60	8.44	9.55	8.66	8.49	8.57
F	3.16	0.00	3.39	2.55	3.47	0.00	3.27	2.92
Cl	0.04	0.02	0.00	0.03	0.00	0.01	0.01	0.01
Total (uncorrected)	98.80	94.80	97.52	97.29	99.84	96.30	97.92	99.15
"-O=F,Cl"	1.34	0.00	1.43	1.08	1.46	0.00	1.38	1.23
Total (corrected)	97.46	94.79	96.09	96.20	98.37	96.30	96.54	97.92
Number of ions based on 24 O, F, Cl								
Si	6.298	6.379	6.359	6.384	6.221	6.330	6.343	6.206
Al	2.495	2.358	2.220	2.356	2.289	2.267	2.274	2.235
Ti	0.149	0.064	0.071	0.056	0.059	0.074	0.062	0.076
Cr	0.052	0.092	0.087	0.087	0.087	0.081	0.068	0.015
Mg	3.677	5.774	5.547	4.635	5.585	6.323	5.518	5.926
Ca	0.004	0.001	0.000	0.009	0.000	0.000	0.001	0.007
Mn	0.000	0.001	0.009	0.001	0.001	0.003	0.000	0.005
Fe	1.952	0.583	0.476	1.330	0.543	0.494	0.543	0.605
Ba	0.011	0.010	0.012	0.015	0.014	0.008	0.015	0.016
Na	0.021	0.008	0.024	0.017	0.047	0.000	0.039	0.022
K	1.700	2.125	1.641	1.663	1.798	1.679	1.615	1.618
F	1.550	0.000	1.604	1.247	1.621	0.000	1.544	1.365
Cl	0.010	0.005	0.000	0.007	0.001	0.002	0.002	0.002
Sum	17.920	17.401	18.051	17.806	18.265	17.262	18.024	18.097
mg#	0.65	0.91	0.92	0.78	0.91	0.93	0.91	0.91

Table B.1 (Continued)

probe run id	bio-49_1292-28	bio-49_1292-9	bio-49_1292-8	bio-49_1292-5	bio-49_1292-2	bio-49_1292-6	bio-49_1292-18	bio-49_1292-19
sample	49-129.2	49-129.2	49-129.2	49-129.2	49-129.2	49-129.2	49-129.2	49-129.2
rock name	SP	SP	SP	SP	SP	SP	SP	SP
zone	core	core	rim	rim	rim	rim	rim	rim
SiO_2	41.75	41.77	41.00	38.52	41.22	40.81	41.23	40.51
TiO_2	0.73	0.57	0.51	2.41	0.63	0.70	0.53	1.48
Al_2O_3	13.15	12.69	12.94	13.78	13.07	13.20	12.29	13.02
Cr_2O_3	0.18	0.60	0.59	0.45	0.72	0.43	0.72	0.67
MgO	23.96	18.87	17.52	14.35	17.76	15.39	18.37	16.09
CaO	0.01	0.03	0.03	0.04	0.03	0.04	0.01	0.01
MnO	0.03	0.02	0.00	0.07	0.06	0.00	0.04	0.04
FeO	5.07	12.43	13.66	16.58	13.24	15.50	12.61	14.43
BaO	0.26	0.25	0.18	0.12	0.19	0.16	0.19	0.10
Na_2O	0.05	0.08	0.10	0.00	0.07	0.09	0.04	0.00
K_2O	8.78	7.60	7.67	9.06	8.26	8.28	7.34	7.80
F	2.89	2.64	2.64	2.12	2.37	2.11	2.42	0.00
Cl	0.03	0.02	0.02	0.06	0.02	0.06	0.01	0.02
Total (uncorrected)	96.88	97.55	96.85	97.54	97.64	96.76	95.80	94.17
"-O=F,Cl"	1.22	1.11	1.12	0.91	1.01	0.90	1.02	0.01
Total (corrected)	95.66	96.44	95.73	96.63	96.64	95.86	94.78	94.16
Number of ions based on 24 O, F, Cl								
Si	6.326	6.454	6.425	6.158	6.418	6.474	6.491	6.561
Al	2.348	2.311	2.389	2.597	2.399	2.469	2.280	2.485
Ti	0.083	0.066	0.060	0.289	0.074	0.083	0.063	0.180
Cr	0.022	0.074	0.073	0.056	0.088	0.053	0.089	0.086
Mg	5.413	4.347	4.094	3.420	4.121	3.641	4.313	3.885
Ca	0.001	0.004	0.004	0.007	0.004	0.007	0.002	0.002
Mn	0.003	0.002	0.000	0.010	0.007	0.000	0.005	0.005
Fe	0.643	1.606	1.790	2.216	1.724	2.056	1.660	1.955
Ba	0.015	0.015	0.011	0.007	0.012	0.010	0.012	0.006
Na	0.015	0.025	0.030	0.000	0.021	0.028	0.013	0.000
K	1.697	1.499	1.533	1.847	1.640	1.676	1.474	1.611
F	1.385	1.288	1.310	1.069	1.169	1.056	1.203	0.000
Cl	0.006	0.004	0.004	0.016	0.006	0.015	0.002	0.007
Sum	17.958	17.695	17.723	17.692	17.683	17.569	17.607	16.782
mg#	0.89	0.73	0.70	0.61	0.71	0.64	0.72	0.67

Table B.1 (Continued)

probe run id	bio-49_1292-23	bio-49_1292-26	bio-49_1292-27	bio-49_1292-1	bio-49_1292-33	bio-49_1292-31	bio-664_1-4	bio-664_1-8
sample	49-129.2	49-129.2	49-129.2	49-129.2	49-129.2	49-129.2	664-4	664-4
rock name	SP	SP	SP	SP	SP	SP	L	L
zone	rim	rim	rim	rim	rim	rim	core	rim
SiO_2	40.96	40.59	40.75	39.94	39.54	41.09	43.61	41.37
TiO_2	0.68	1.50	0.70	1.31	0.67	0.72	0.63	0.58
Al_2O_3	12.99	13.58	12.82	13.53	12.25	13.18	13.30	13.23
Cr_2O_3	0.61	0.17	0.14	0.73	0.74	0.15	0.59	1.04
MgO	16.89	16.37	18.23	16.19	17.67	17.87	23.99	17.48
CaO	0.03	0.02	0.03	0.02	0.03	0.02	0.00	0.01
MnO	0.00	0.00	0.00	0.04	0.04	0.00	0.01	0.20
FeO	14.02	15.00	13.24	14.63	13.15	13.86	4.98	14.22
BaO	0.18	0.28	0.32	0.10	0.16	0.25	0.18	0.14
Na_2O	0.00	0.00	0.05	0.14	0.04	0.77	0.00	0.05
K_2O	7.70	8.03	8.65	8.92	9.57	7.93	7.11	6.17
F	3.21	2.65	2.32	3.06	2.19	2.33	0.91	0.45
Cl	0.02	0.02	0.01	0.02	0.03	0.02	0.01	0.01
Total (uncorrected)	97.27	98.22	97.25	98.64	96.06	98.17	95.32	94.97
"-O=F,Cl"	1.36	1.12	0.98	1.29	0.93	0.98	0.39	0.19
Total (corrected)	95.92	97.10	96.27	97.34	95.13	97.19	94.93	94.77
Number of ions based on 24 O, F, Cl								
Si	6.399	6.323	6.391	6.233	6.339	6.379	6.609	6.570
Al	2.392	2.493	2.369	2.488	2.314	2.412	2.375	2.476
Ti	0.080	0.176	0.082	0.154	0.080	0.084	0.072	0.069
Cr	0.075	0.021	0.018	0.090	0.093	0.018	0.071	0.130
Mg	3.934	3.802	4.262	3.768	4.223	4.136	5.419	4.139
Ca	0.005	0.004	0.005	0.004	0.005	0.003	0.000	0.001
Mn	0.000	0.000	0.000	0.005	0.005	0.000	0.002	0.027
Fe	1.831	1.953	1.736	1.910	1.762	1.799	0.631	1.889
Ba	0.011	0.017	0.019	0.006	0.010	0.015	0.011	0.009
Na	0.000	0.000	0.014	0.041	0.013	0.233	0.000	0.016
K	1.533	1.596	1.730	1.775	1.958	1.570	1.374	1.250
F	1.583	1.305	1.151	1.511	1.109	1.142	0.436	0.228
Cl	0.006	0.006	0.004	0.005	0.008	0.004	0.002	0.002
Sum	17.849	17.697	17.782	17.991	17.920	17.796	17.002	16.807
mg#	0.68	0.66	0.71	0.66	0.71	0.70	0.90	0.69

Table B.1 (Continued)

probe run id	bio-664_1-3	bio-664_1-5
sample	664-4	664-4
rock name	L	L
zone	rim	rim
SiO_2	41.88	42.55
TiO_2	0.58	0.50
Al_2O_3	14.52	13.40
Cr_2O_3	0.53	0.51
MgO	16.73	17.58
CaO	0.07	0.01
MnO	0.13	0.16
FeO	14.70	14.00
BaO	0.18	0.23
Na_2O	0.00	0.00
K_2O	6.28	6.23
F	0.30	0.18
Cl	0.01	0.01
Total (uncorrected)	95.91	95.35
"-O=F,Cl"	0.13	0.08
Total (corrected)	95.78	95.27
Number of ions based on 24 O, F, Cl		
Si	6.573	6.694
Al	2.685	2.485
Ti	0.069	0.060
Cr	0.065	0.063
Mg	3.915	4.122
Ca	0.012	0.001
Mn	0.018	0.021
Fe	1.929	1.842
Ba	0.011	0.014
Na	0.000	0.000
K	1.258	1.249
F	0.150	0.091
Cl	0.003	0.003
Sum	16.688	16.645
mg#	0.67	0.69

Table B.1 (Continued[1])

probe run id	bio-49_113.7-11	bio-49_113.7-15	bio-49_113.7-16
sample	49-113.7	49-113.7	49-113.7
rock name	L	L	L
zone	core	rim	rim
SiO_2	40.91	40.79	38.43
TiO_2	0.54	0.60	1.00
Al_2O_3	12.44	14.01	15.08
Cr_2O_3	1.11	1.07	1.04
MgO	22.86	15.83	14.37
CaO	0.02	0.01	0.01
MnO	0.00	0.09	0.18
FeO	4.46	14.96	16.57
BaO	0.24	0.23	0.30
Na_2O	0.48	0.07	0.00
K_2O	7.98	7.14	8.39
F	1.41	8.37	6.95
Cl	0.02	0.02	0.07
Total (uncorrected)	92.48	103.18	102.38
"-O=F,Cl"	0.60	3.53	2.94
Total (corrected)	91.88	99.65	99.44
Number of ions based on 24 O, F, Cl			
Si	6.473	6.019	5.830
Al	2.321	2.436	2.695
Ti	0.065	0.066	0.114
Cr	0.139	0.125	0.124
Mg	5.392	3.483	3.250
Ca	0.004	0.002	0.002
Mn	0.000	0.011	0.024
Fe	0.591	1.845	2.103
Ba	0.015	0.013	0.018
Na	0.147	0.019	0.000
K	1.611	1.344	1.623
F	0.707	3.905	3.335
Cl	0.005	0.005	0.017
Sum	17.468	19.271	19.134
mg#	0.90	0.65	0.61

[1]The data used only for Figure 4.9.

Table B.2. Electron microprobe analysis of unzoned biotite phenocrysts

probe run id	bt-76-179.9-5	bt-76-179.9-2	bt-76-179.9-15	bt-76-179.9-4	bt-76-179.9-1	bt-76-179.9-6	bt-76-179.9-7	bt-76-179.9-8
sample	76-179.9	76-179.9	76-179.9	76-179.9	76-179.9	76-179.9	76-179.9	76-179.9
rock name	L	L	L	L	L	L	L	L
SiO_2	39.23	36.66	39.07	39.50	39.41	37.27	36.04	36.94
TiO_2	1.80	2.27	1.12	1.45	0.73	2.00	2.46	2.14
Al_2O_3	14.51	15.77	15.09	14.83	15.07	15.87	16.73	15.70
Cr_2O_3	0.37	0.11	1.52	1.42	0.75	0.39	0.09	0.09
MgO	13.83	12.38	13.27	13.51	14.36	12.78	11.82	12.35
CaO	0.09	0.07	0.09	0.09	0.00	0.11	0.04	0.01
MnO	0.02	0.05	0.05	0.01	0.04	0.06	0.03	0.05
FeO	16.33	17.91	15.58	15.82	15.67	17.68	17.90	17.93
NiO	0.00	0.04	0.01	0.04	0.02	0.02	0.03	0.02
BaO	0.14	0.65	0.15	0.12	0.23	0.00	0.90	0.53
Na_2O	0.06	0.05	0.07	0.07	0.14	0.53	0.07	0.05
K_2O	8.92	9.62	9.37	9.04	9.36	9.53	9.25	9.40
F	0.81	0.00	0.82	0.64	0.84	0.67	0.60	1.41
Cl	0.07	0.06	0.04	0.07	0.05	0.05	0.07	0.06
Total (uncorrected)	96.18	95.62	96.26	96.59	96.66	96.95	96.02	96.68
"-O=F,Cl"	0.36	0.01	0.35	0.28	0.36	0.29	0.27	0.61
Total (corrected)	95.82	95.61	95.90	96.30	96.29	96.65	95.75	96.07
Number of ions based on 24 O, F, Cl								
Si	6.328	6.076	6.306	6.340	6.324	6.053	5.946	6.033
Al	2.758	3.080	2.871	2.805	2.849	3.038	3.254	3.022
Ti	0.219	0.283	0.136	0.175	0.088	0.245	0.305	0.262
Cr	0.047	0.014	0.194	0.180	0.095	0.050	0.011	0.011
Mg	3.326	3.059	3.194	3.233	3.436	3.094	2.908	3.007
Ca	0.015	0.012	0.016	0.016	0.001	0.019	0.006	0.002
Mn	0.003	0.007	0.007	0.001	0.005	0.008	0.004	0.007
Fe	2.202	2.482	2.103	2.123	2.102	2.401	2.470	2.448
Ni	0.000	0.005	0.002	0.005	0.003	0.002	0.004	0.002
Ba	0.009	0.042	0.009	0.007	0.015	0.000	0.058	0.034
Na	0.019	0.015	0.020	0.023	0.044	0.167	0.023	0.016
K	1.836	2.033	1.929	1.851	1.916	1.974	1.948	1.959
F	0.414	0.000	0.417	0.323	0.424	0.342	0.311	0.727
Cl	0.018	0.016	0.011	0.018	0.013	0.015	0.020	0.017
Sum	17.194	17.126	17.214	17.100	17.314	17.407	17.268	17.547
mg#	0.60	0.55	0.60	0.60	0.62	0.56	0.54	0.55

Table B.2. (Continued)

probe run id	bt-76-179.9-9	bt-76-179.9-10	bt-76-179.9-11	bt-76-179.9-12	bt-76-179.9-13	bt-76-179.9-14	bt-76-179.9-3	57-166.2-14
sample	76-179.9	76-179.9	76-179.9	76-179.9	76-179.9	76-179.9	76-179.9	57-166.2
rock name	L	L	L	L	L	L	L	SP
SiO_2	35.74	36.06	37.00	38.84	37.29	36.76	35.92	39.20
TiO_2	2.15	2.29	2.05	2.18	2.22	2.25	2.01	1.90
Al_2O_3	15.58	15.96	16.15	15.63	15.58	15.82	15.98	14.76
Cr_2O_3	0.30	0.11	0.24	0.23	0.14	0.12	0.26	0.00
MgO	11.68	11.85	12.89	12.79	12.66	12.42	12.35	13.62
CaO	0.05	0.04	0.01	0.04	0.04	0.05	0.04	0.07
MnO	0.02	0.00	0.04	0.03	0.05	0.03	0.02	0.09
FeO	18.44	18.50	17.33	17.85	17.66	17.64	18.62	16.39
NiO	0.03	0.02	0.03	0.06	0.01	0.04	0.04	0.03
BaO	0.77	0.92	0.07	0.29	0.50	0.31	0.00	0.35
Na_2O	0.05	0.06	0.04	0.09	0.02	0.05	0.05	0.05
K_2O	9.64	9.37	10.10	6.94	9.48	9.90	9.84	9.34
F	0.69	0.60	0.63	0.74	0.00	0.57	0.65	0.81
Cl	0.07	0.08	0.05	0.08	0.07	0.06	0.05	0.04
Total (uncorrected)	95.21	95.88	96.63	95.79	95.71	96.03	95.82	96.65
"-O=F,Cl"	0.31	0.28	0.28	0.33	0.02	0.26	0.29	0.35
Total (corrected)	94.90	95.60	96.35	95.45	95.69	95.77	95.54	96.30
Number of ions based on 24 O, F, Cl								
Si	5.991	5.988	6.030	6.263	6.144	6.050	5.950	6.314
Al	3.078	3.123	3.103	2.971	3.024	3.068	3.119	2.801
Ti	0.271	0.286	0.251	0.264	0.275	0.278	0.251	0.230
Cr	0.039	0.014	0.031	0.029	0.018	0.016	0.034	0.000
Mg	2.917	2.934	3.132	3.074	3.110	3.048	3.050	3.271
Ca	0.008	0.007	0.002	0.007	0.006	0.009	0.007	0.013
Mn	0.003	0.001	0.005	0.004	0.007	0.004	0.002	0.012
Fe	2.585	2.569	2.362	2.407	2.433	2.428	2.580	2.208
Ni	0.004	0.003	0.004	0.008	0.001	0.006	0.005	0.004
Ba	0.051	0.060	0.004	0.018	0.032	0.020	0.000	0.022
Na	0.016	0.021	0.014	0.028	0.006	0.015	0.014	0.016
K	2.061	1.983	2.100	1.428	1.993	2.078	2.079	1.919
F	0.367	0.317	0.325	0.379	0.000	0.299	0.340	0.411
Cl	0.020	0.024	0.014	0.022	0.020	0.016	0.014	0.010
Sum	17.411	17.329	17.378	16.901	17.070	17.335	17.447	17.233
mg#	0.53	0.53	0.57	0.56	0.56	0.56	0.54	0.60

Table B.2. (Continued)

probe run id	57-166.2-13	57-166.2-12	57-166.2-11	57-166.2-10	57-166.2-9	57-166.2-8	57-166.2-7	57-166.2-6
sample	57-166.2	57-166.2	57-166.2	57-166.2	57-166.2	57-166.2	57-166.2	57-166.2
rock name	SP	SP	SP	SP	SP	SP	SP	SP
SiO_2	39.21	37.24	39.25	34.86	36.42	38.07	37.12	38.98
TiO_2	1.92	1.80	1.72	2.32	2.05	2.02	1.91	1.57
Al_2O_3	14.66	15.37	14.67	16.20	15.53	14.79	16.07	14.73
Cr_2O_3	0.30	0.22	0.39	0.04	0.00	0.03	0.02	1.63
MgO	13.71	12.74	13.70	11.43	12.39	13.32	12.93	12.91
CaO	0.05	0.03	0.02	0.08	0.12	0.06	0.15	0.09
MnO	0.05	0.02	0.07	0.12	0.05	0.02	0.07	0.08
FeO	16.58	17.61	16.11	18.73	18.43	17.23	17.77	15.88
NiO	0.01	0.04	0.03	0.01	0.01	0.02	0.06	0.03
BaO	0.21	0.80	0.28	1.63	0.09	0.12	0.17	0.24
Na_2O	0.05	0.16	0.13	0.09	0.04	0.06	0.44	0.05
K_2O	9.18	9.64	9.80	9.20	9.40	9.78	8.79	9.46
F	0.81	0.00	0.66	0.00	0.64	0.85	0.68	0.68
Cl	0.06	0.03	0.04	0.06	0.03	0.06	0.24	0.02
Total (uncorrected)	96.80	95.70	96.86	94.75	95.20	96.44	96.42	96.36
"-O=F,Cl"	0.36	0.01	0.29	0.01	0.28	0.38	0.35	0.29
Total (corrected)	96.45	95.69	96.58	94.74	94.92	96.07	96.07	96.07
Number of ions based on 24 O, F, Cl								
Si	6.303	6.161	6.321	5.916	6.047	6.196	6.048	6.309
Al	2.778	2.997	2.784	3.240	3.039	2.836	3.084	2.810
Ti	0.232	0.224	0.209	0.296	0.256	0.247	0.234	0.191
Cr	0.037	0.029	0.049	0.005	0.000	0.004	0.003	0.208
Mg	3.286	3.143	3.289	2.892	3.067	3.232	3.139	3.116
Ca	0.008	0.005	0.003	0.015	0.021	0.011	0.027	0.016
Mn	0.007	0.003	0.010	0.017	0.007	0.003	0.010	0.010
Fe	2.229	2.436	2.169	2.658	2.559	2.344	2.421	2.148
Ni	0.001	0.005	0.004	0.001	0.001	0.002	0.008	0.004
Ba	0.013	0.052	0.018	0.108	0.006	0.008	0.011	0.015
Na	0.015	0.052	0.040	0.029	0.014	0.020	0.138	0.015
K	1.882	2.035	2.013	1.992	1.990	2.031	1.826	1.954
F	0.412	0.000	0.334	0.000	0.335	0.439	0.350	0.349
Cl	0.015	0.009	0.010	0.017	0.009	0.017	0.067	0.006
Sum	17.219	17.150	17.253	17.185	17.352	17.391	17.365	17.152
mg#	0.60	0.56	0.60	0.52	0.55	0.58	0.56	0.59

Table B.2. (Continued)

probe run id	57-166.2-5	57-166.2-4	57-166.2-15	57-166.2-2	57-166.2-24	57-166.2-3	57-166.2-16	57-166.2-17
sample	57-166.2	57-166.2	57-166.2	57-166.2	57-166.2	57-166.2	57-166.2	57-166.2
rock name	SP	SP	SP	SP	SP	SP	SP	SP
SiO_2	36.85	39.04	39.76	40.00	40.61	36.54	39.66	40.07
TiO_2	2.35	2.15	1.82	2.00	1.31	2.10	1.74	1.72
Al_2O_3	15.55	14.71	14.46	13.91	14.23	15.57	14.72	14.54
Cr_2O_3	0.01	0.18	0.66	0.08	0.26	0.15	1.45	0.26
MgO	12.67	13.41	13.41	14.27	15.00	12.34	13.10	14.16
CaO	0.06	0.05	0.04	0.08	0.02	0.07	0.05	0.10
MnO	0.12	0.12	0.05	0.13	0.10	0.06	0.07	0.10
FeO	18.44	16.70	15.79	16.23	15.37	18.39	15.54	15.97
NiO	0.05	0.01	0.02	0.03	0.01	0.02	0.02	0.04
BaO	0.05	0.18	0.20	0.00	0.00	0.14	0.17	0.19
Na_2O	0.07	0.11	0.04	0.04	0.09	0.05	0.04	0.07
K_2O	9.77	9.34	9.22	8.89	8.92	9.91	9.11	8.04
F	0.58	1.08	0.00	0.00	1.19	0.56	0.00	4.43
Cl	0.05	0.08	0.03	0.05	0.04	0.07	0.05	0.09
Total (uncorrected)	96.61	97.17	95.49	95.69	97.12	95.95	95.71	99.77
"-O=F,Cl"	0.26	0.48	0.01	0.01	0.51	0.25	0.01	1.89
Total (corrected)	96.35	96.69	95.48	95.68	96.61	95.69	95.70	97.88
Number of ions based on 24 O, F, Cl								
Si	6.037	6.264	6.451	6.465	6.427	6.039	6.420	6.174
Al	3.002	2.782	2.765	2.649	2.653	3.032	2.808	2.640
Ti	0.289	0.259	0.222	0.244	0.156	0.261	0.212	0.199
Cr	0.001	0.023	0.085	0.010	0.033	0.020	0.186	0.032
Mg	3.094	3.208	3.243	3.437	3.539	3.040	3.161	3.252
Ca	0.010	0.008	0.007	0.014	0.003	0.012	0.008	0.016
Mn	0.017	0.016	0.007	0.017	0.013	0.009	0.010	0.012
Fe	2.526	2.241	2.143	2.194	2.033	2.541	2.103	2.058
Ni	0.006	0.001	0.003	0.004	0.001	0.003	0.002	0.005
Ba	0.003	0.011	0.013	0.000	0.000	0.009	0.011	0.012
Na	0.022	0.035	0.012	0.012	0.026	0.016	0.013	0.021
K	2.042	1.912	1.908	1.832	1.801	2.088	1.881	1.580
F	0.301	0.550	0.000	0.000	0.595	0.292	0.000	2.156
Cl	0.013	0.021	0.008	0.013	0.010	0.018	0.012	0.024
Sum	17.362	17.333	16.866	16.891	17.290	17.381	16.825	18.181
mg#	0.55	0.59	0.60	0.61	0.64	0.54	0.60	0.61

Table B.2. (Continued)

probe run id	57-166.2-18	57-166.2-19	57-166.2-20	57-166.2-21	57-166.2-1	57-166.2-23	57-166.2-25	57-166.2-26
sample	57-166.2	57-166.2	57-166.2	57-166.2	57-166.2	57-166.2	57-166.2	57-166.2
rock name	SP	SP	SP	SP	SP	SP	SP	SP
SiO_2	37.08	39.61	36.42	37.20	38.25	34.37	39.54	36.71
TiO_2	1.92	1.67	1.61	1.56	1.83	1.16	1.36	1.89
Al_2O_3	15.52	14.54	15.83	15.45	15.23	13.29	14.36	15.72
Cr_2O_3	0.19	0.95	0.45	0.23	0.01	0.13	0.61	0.00
MgO	12.98	13.35	12.89	13.12	13.40	12.65	13.99	12.82
CaO	0.00	0.03	0.03	0.04	0.11	10.81	0.03	0.02
MnO	0.07	0.08	0.07	0.07	0.09	0.16	0.06	0.11
FeO	17.58	15.73	18.45	17.60	16.84	13.75	16.02	18.24
NiO	0.01	0.03	0.00	0.01	0.03	0.03	0.04	0.01
BaO	0.06	0.07	0.00	0.00	0.53	0.00	0.06	0.04
Na_2O	0.00	0.06	0.03	0.05	0.06	0.00	0.05	0.06
K_2O	9.93	9.43	9.23	9.76	9.23	7.86	9.46	10.05
F	0.83	0.71	0.00	0.55	1.22	0.00	3.84	0.66
Cl	0.07	0.08	0.04	0.03	0.08	0.03	0.06	0.05
Total (uncorrected)	96.23	96.35	95.05	95.68	96.89	94.24	99.45	96.37
"-O=F,Cl"	0.37	0.32	0.01	0.24	0.53	0.01	1.63	0.29
Total (corrected)	95.86	96.03	95.04	95.44	96.35	94.23	97.82	96.08
Number of ions based on 24 O, F, Cl								
Si	6.072	6.379	6.051	6.120	6.177	5.839	6.170	6.030
Al	2.995	2.759	3.099	2.994	2.899	2.661	2.641	3.044
Ti	0.237	0.203	0.201	0.194	0.223	0.149	0.159	0.233
Cr	0.025	0.121	0.059	0.030	0.001	0.018	0.075	0.000
Mg	3.170	3.206	3.193	3.218	3.226	3.204	3.255	3.139
Ca	0.000	0.005	0.006	0.007	0.019	1.968	0.005	0.003
Mn	0.009	0.011	0.010	0.010	0.012	0.023	0.008	0.015
Fe	2.407	2.118	2.563	2.420	2.274	1.953	2.090	2.506
Ni	0.001	0.004	0.000	0.002	0.003	0.004	0.006	0.001
Ba	0.004	0.004	0.000	0.000	0.033	0.000	0.004	0.003
Na	0.000	0.017	0.009	0.014	0.018	0.000	0.016	0.019
K	2.073	1.937	1.955	2.048	1.903	1.703	1.882	2.107
F	0.431	0.359	0.000	0.287	0.625	0.000	1.892	0.343
Cl	0.019	0.022	0.011	0.009	0.021	0.008	0.016	0.013
Sum	17.443	17.146	17.157	17.354	17.433	17.529	18.217	17.455
mg#	0.57	0.60	0.55	0.57	0.59	0.62	0.61	0.56

Table B.2. (Continued)

probe run id	57-166.2-27	57-166.2-28	57-166.2-29	57-166.2-30	57-166.2-22	bio-56_158-1	bio-56_158-10	bio-56_158-15
sample	57-166.2	57-166.2	57-166.2	57-166.2	57-166.2	56-158.0	56-158.0	56-158.0
rock name	SP	SP	SP	SP	SP	L	L	L
SiO_2	36.91	39.09	38.92	38.27	37.04	38.42	38.83	37.18
TiO_2	1.99	2.12	1.80	1.68	1.54	2.83	2.14	2.36
Al_2O_3	15.45	14.10	14.57	14.84	15.81	15.95	15.62	15.92
Cr_2O_3	0.02	0.72	0.77	0.31	0.55	0.12	1.12	0.11
MgO	12.47	13.37	13.31	13.40	12.84	12.18	13.49	12.49
CaO	0.07	0.09	0.04	0.04	0.01	0.02	0.00	0.01
MnO	0.09	0.09	0.09	0.06	0.12	0.00	0.00	0.00
FeO	18.16	16.01	16.32	16.94	17.42	17.64	16.47	17.51
NiO	0.03	0.03	0.02	0.04	0.00	n.a.	n.a.	n.a.
BaO	0.07	0.11	0.24	0.06	0.00	1.17	0.52	1.10
Na_2O	0.02	0.05	0.04	0.03	0.06	0.04	0.00	0.00
K_2O	9.62	9.47	9.52	9.74	9.09	7.03	7.06	7.61
F	0.00	0.81	0.94	0.88	0.76	0.00	1.15	1.00
Cl	0.04	0.05	0.04	0.05	0.07	0.03	0.02	0.01
Total (uncorrected)	94.93	96.11	96.63	96.33	95.30	95.43	96.42	95.29
"-O=F,Cl"	0.01	0.35	0.41	0.38	0.34	0.01	0.49	0.42
Total (corrected)	94.91	95.76	96.23	95.95	94.96	95.42	95.93	94.87
Number of ions based on 24 O, F, Cl								
Si	6.139	6.334	6.287	6.222	6.091	6.257	6.202	6.099
Al	3.028	2.693	2.773	2.843	3.064	3.061	2.941	3.076
Ti	0.248	0.258	0.219	0.205	0.190	0.347	0.258	0.292
Cr	0.002	0.092	0.098	0.039	0.072	0.015	0.142	0.015
Mg	3.092	3.230	3.206	3.248	3.149	2.958	3.213	3.053
Ca	0.012	0.016	0.007	0.007	0.001	0.003	0.000	0.002
Mn	0.013	0.013	0.013	0.008	0.017	0.000	0.000	0.000
Fe	2.526	2.168	2.204	2.303	2.395	2.402	2.199	2.402
Ni	0.004	0.003	0.003	0.005	0.000	-	-	-
Ba	0.005	0.007	0.015	0.004	-	0.075	0.033	0.070
Na	0.007	0.017	0.014	0.009	0.018	0.013	0.000	0.000
K	2.042	1.956	1.961	2.019	1.906	1.461	1.438	1.591
F	0.000	0.413	0.482	0.453	0.396	0.000	0.581	0.519
Cl	0.012	0.014	0.011	0.015	0.021	0.008	0.006	0.003
Sum	17.129	17.216	17.292	17.379	17.321	16.599	17.012	17.120
mg#	0.55	0.60	0.59	0.59	0.57	0.55	0.59	0.56

Table B.2. (Continued)

probe run id	bio-56_158-16	bio-56_158-17	bio-56_158-20	bio-56_158-21	bio-56_158-22	bio-56_158-24	bio-56_158-3	bio-56_158-4
sample	56-158.0	56-158.0	56-158.0	56-158.0	56-158.0	56-158.0	56-158.0	56-158.0
rock name	L	L	L	L	L	L	L	L
SiO_2	37.94	39.56	38.10	37.61	38.02	39.53	39.42	41.37
TiO_2	2.01	1.96	2.45	2.41	1.81	1.39	1.89	0.43
Al_2O_3	15.94	14.70	15.88	16.16	16.30	15.05	15.79	13.75
Cr_2O_3	0.09	0.32	0.10	0.05	0.10	1.45	0.28	0.76
MgO	13.13	14.31	13.27	13.11	13.53	13.84	15.16	16.70
CaO	0.04	0.05	0.01	0.02	0.03	0.07	0.04	0.09
MnO	0.02	0.05	0.00	0.00	0.00	0.09	0.00	0.01
FeO	16.83	15.56	16.98	17.20	17.26	15.65	15.54	14.24
NiO	n.a.	n.a.	n.a.	n.a.	n.a.	n.a.	n.a.	n.a.
BaO	0.72	0.19	0.64	0.93	0.10	0.18	0.30	0.18
Na_2O	0.04	0.00	0.06	0.00	0.06	0.05	0.04	0.00
K_2O	7.45	7.60	8.11	7.82	7.78	7.25	7.70	7.50
F	0.00	1.25	0.00	0.38	0.79	1.03	1.25	1.45
Cl	0.02	0.01	0.02	0.03	0.02	0.03	0.02	0.03
Total (uncorrected)	94.25	95.55	95.61	95.72	95.78	95.58	97.43	96.49
"-O=F,Cl"	0.01	0.53	0.00	0.17	0.34	0.44	0.53	0.62
Total (corrected)	94.24	95.02	95.60	95.55	95.45	95.14	96.90	95.88
Number of ions based on 24 O, F, Cl								
Si	6.237	6.339	6.197	6.124	6.139	6.337	6.199	6.504
Al	3.088	2.776	3.044	3.101	3.101	2.842	2.926	2.547
Ti	0.249	0.237	0.299	0.295	0.220	0.167	0.223	0.051
Cr	0.012	0.040	0.012	0.007	0.013	0.184	0.035	0.094
Mg	3.218	3.419	3.217	3.183	3.257	3.307	3.553	3.914
Ca	0.007	0.008	0.002	0.004	0.005	0.011	0.007	0.016
Mn	0.003	0.006	0.000	0.000	0.000	0.012	0.000	0.001
Fe	2.313	2.085	2.310	2.341	2.331	2.097	2.043	1.872
Ni	-	-	-	-	-	-	-	-
Ba	0.047	0.012	0.041	0.060	0.006	0.011	0.018	0.011
Na	0.013	0.000	0.020	0.000	0.019	0.016	0.012	0.000
K	1.563	1.553	1.682	1.624	1.602	1.482	1.544	1.503
F	0.000	0.633	0.000	0.197	0.401	0.523	0.622	0.719
Cl	0.006	0.003	0.004	0.007	0.005	0.008	0.005	0.008
Sum	16.755	17.111	16.829	16.942	17.098	16.997	17.189	17.240
mg#	0.58	0.62	0.58	0.58	0.58	0.61	0.63	0.68

Table B.2. (Continued)

probe run id	bio-56_158-5	bio-56_158-6	bio-56_158-7	bio-56_158-8	bio-56_158-9	bio-58_583-1	bio-58_583-10	bio-58_583-12
sample	56-158.0	56-158.0	56-158.0	56-158.0	56-158.0	58-58.3	58-58.3	58-58.3
rock name	L	L	L	L	L	L	L	L
SiO_2	40.65	37.32	36.69	37.42	37.34	38.66	38.79	37.79
TiO_2	0.68	2.00	2.33	2.36	2.65	1.94	1.86	2.45
Al_2O_3	15.24	15.36	15.80	15.64	15.81	16.36	15.89	16.93
Cr_2O_3	1.58	1.20	0.05	0.73	0.08	0.07	0.06	0.02
MgO	14.71	12.57	13.05	15.24	12.78	13.94	15.77	13.40
CaO	0.02	0.04	0.01	0.02	0.02	0.01	0.05	0.05
MnO	0.06	0.00	0.02	0.06	0.00	0.09	0.02	0.09
FeO	14.39	17.09	17.37	17.13	17.01	15.57	15.84	16.21
NiO	n.a.	n.a.	n.a.	n.a.	n.a.	n.a.	n.a.	n.a.
BaO	0.21	0.53	1.31	0.93	1.45	0.61	0.02	0.91
Na_2O	0.00	0.04	0.06	0.04	0.06	0.03	1.37	0.03
K_2O	7.22	7.97	8.35	8.37	7.19	6.70	8.18	7.79
F	1.12	0.00	1.03	0.98	0.94	0.00	0.00	0.00
Cl	0.02	0.02	0.03	0.03	0.01	0.02	0.07	0.04
Total (uncorrected)	95.88	94.15	96.09	98.93	95.32	93.99	97.92	95.72
"-O=F,Cl"	0.47	0.01	0.44	0.42	0.40	0.01	0.02	0.01
Total (corrected)	95.41	94.14	95.65	98.51	94.92	93.99	97.90	95.71
Number of ions based on 24 O, F, Cl								
Si	6.434	6.192	6.014	5.935	6.109	6.283	6.126	6.117
Al	2.843	3.004	3.053	2.923	3.047	3.134	2.957	3.230
Ti	0.080	0.250	0.287	0.281	0.325	0.237	0.221	0.298
Cr	0.197	0.158	0.006	0.092	0.010	0.010	0.007	0.003
Mg	3.472	3.110	3.188	3.603	3.117	3.377	3.713	3.233
Ca	0.004	0.006	0.002	0.003	0.003	0.001	0.008	0.009
Mn	0.009	0.000	0.002	0.008	0.000	0.012	0.003	0.012
Fe	1.904	2.371	2.381	2.272	2.328	2.116	2.092	2.194
Ni	-	-	-	-	-	-	-	-
Ba	0.013	0.035	0.084	0.058	0.093	0.039	0.001	0.058
Na	0.000	0.012	0.018	0.012	0.018	0.009	0.419	0.009
K	1.457	1.686	1.745	1.693	1.500	1.389	1.648	1.608
F	0.559	0.000	0.533	0.492	0.487	0.000	0.000	0.000
Cl	0.005	0.006	0.008	0.007	0.003	0.006	0.018	0.012
Sum	16.976	16.829	17.321	17.379	17.040	16.611	17.214	16.783
mg#	0.65	0.57	0.57	0.61	0.57	0.61	0.64	0.60

Table B.2. (Continued)

probe run id	bio-58_583-13	bio-58_583-14	bio-58_583-15	bio-58_583-16	bio-58_583-17	bio-58_583-19	bio-58_583-20	bio-58_583-24
sample	58-58.3	58-58.3	58-58.3	58-58.3	58-58.3	58-58.3	58-58.3	58-58.3
rock name	L	L	L	L	L	L	L	L
SiO_2	36.82	37.71	37.25	37.90	38.29	37.49	35.51	40.66
TiO_2	2.06	1.91	2.04	1.97	2.05	2.42	2.81	1.91
Al_2O_3	16.51	16.45	16.80	16.58	16.74	17.05	17.08	14.80
Cr_2O_3	0.07	0.10	0.07	0.08	0.10	0.04	0.10	0.06
MgO	13.55	13.78	13.50	13.84	13.76	13.12	12.17	14.26
CaO	0.03	0.01	0.00	0.02	0.06	0.04	0.03	0.03
MnO	0.07	0.05	0.05	0.05	0.06	0.05	0.06	0.09
FeO	16.71	16.64	16.50	16.08	16.08	16.88	16.92	14.76
NiO	n.a.	n.a.	n.a.	n.a.	n.a.	n.a.	n.a.	n.a.
BaO	0.74	0.64	0.81	0.43	0.68	1.20	3.08	0.00
Na_2O	0.05	0.00	0.00	0.00	0.00	0.00	0.00	0.03
K_2O	8.51	8.67	8.56	7.01	6.92	7.29	7.17	8.26
F	0.41	0.36	0.30	0.46	0.52	0.00	0.00	0.72
Cl	0.06	0.04	0.05	0.04	0.05	0.02	0.05	0.04
Total (uncorrected)	95.59	96.35	95.93	94.45	95.31	95.59	94.96	95.63
"-O=F,Cl"	0.19	0.16	0.14	0.21	0.23	0.00	0.01	0.31
Total (corrected)	95.41	96.19	95.79	94.24	95.08	95.58	94.94	95.32
Number of ions based on 24 O, F, Cl								
Si	6.022	6.099	6.057	6.159	6.168	6.092	5.929	6.479
Al	3.183	3.136	3.219	3.174	3.178	3.264	3.362	2.780
Ti	0.254	0.232	0.249	0.241	0.249	0.296	0.353	0.229
Cr	0.009	0.013	0.008	0.010	0.013	0.006	0.013	0.008
Mg	3.303	3.323	3.272	3.352	3.304	3.177	3.028	3.388
Ca	0.005	0.002	0.001	0.003	0.010	0.008	0.005	0.005
Mn	0.010	0.007	0.007	0.006	0.008	0.006	0.008	0.012
Fe	2.285	2.251	2.243	2.184	2.166	2.293	2.362	1.967
Ni	-	-	-	-	-	-	-	-
Ba	0.047	0.041	0.052	0.027	0.043	0.076	0.201	0.000
Na	0.015	0.000	0.000	0.000	0.000	0.000	0.000	0.010
K	1.776	1.788	1.776	1.452	1.421	1.511	1.527	1.679
F	0.214	0.183	0.156	0.237	0.263	0.000	0.000	0.360
Cl	0.016	0.011	0.012	0.012	0.014	0.005	0.014	0.010
Sum	17.139	17.085	17.052	16.859	16.837	16.735	16.802	16.927
mg#	0.59	0.60	0.59	0.61	0.60	0.58	0.56	0.63

Table B.2. (Continued)

probe run id	bio-58_583-8	bio-58_583-9	bio-55_62.7-10	bio-55_62.7-13	bio-55_62.7-14	bio-55_62.7-5	bio-55_62.7-6	bio-57_1741-1
sample	58-58.3	58-58.3	55-62.7	55-62.7	55-62.7	55-62.7	55-62.7	57-174.1
rock name	L	L	SP	SP	SP	SP	SP	SP
SiO_2	40.47	41.99	39.18	39.02	37.90	38.24	37.27	36.74
TiO_2	1.14	0.48	1.37	1.69	1.54	1.48	1.39	2.30
Al_2O_3	15.45	14.24	15.66	15.96	16.45	16.03	16.43	15.84
Cr_2O_3	1.03	0.93	0.30	0.04	0.04	0.46	0.40	0.00
MgO	14.76	17.22	13.00	13.09	12.17	12.37	12.20	11.45
CaO	0.07	0.03	0.02	0.01	0.01	0.03	0.01	0.01
MnO	0.06	0.04	0.16	0.17	0.21	0.23	0.28	0.05
FeO	14.11	13.03	17.95	17.92	18.59	17.91	18.61	19.11
NiO	n.a.	n.a.	n.a.	n.a.	n.a.	n.a.	n.a.	n.a.
BaO	0.07	0.03	0.16	0.00	0.05	0.50	0.41	0.75
Na_2O	0.00	0.02	0.07	0.03	0.00	0.05	0.00	0.08
K_2O	7.20	6.52	7.57	6.88	7.37	7.08	7.09	7.62
F	0.57	0.69	0.00	0.00	0.32	0.36	0.00	0.66
Cl	0.05	0.02	0.06	0.05	0.05	0.07	0.06	0.04
Total (uncorrected)	94.99	95.25	95.50	94.85	94.70	94.79	94.14	94.64
"-O=F,Cl"	0.25	0.29	0.01	0.01	0.15	0.17	0.02	0.29
Total (corrected)	94.73	94.95	95.48	94.84	94.55	94.62	94.12	94.35
Number of ions based on 24 O, F, Cl								
Si	6.445	6.590	6.353	6.330	6.214	6.260	6.174	6.108
Al	2.900	2.634	2.993	3.051	3.179	3.092	3.207	3.105
Ti	0.137	0.057	0.167	0.207	0.190	0.182	0.173	0.287
Cr	0.130	0.115	0.038	0.005	0.005	0.059	0.052	0.000
Mg	3.505	4.028	3.143	3.165	2.975	3.018	3.014	2.838
Ca	0.012	0.005	0.004	0.002	0.001	0.004	0.002	0.001
Mn	0.007	0.006	0.022	0.023	0.029	0.032	0.040	0.007
Fe	1.878	1.711	2.433	2.431	2.549	2.451	2.578	2.656
Ni	-	-	-	-	-	-	-	-
Ba	0.005	0.002	0.010	0.000	0.003	0.032	0.026	0.049
Na	0.000	0.006	0.021	0.009	0.000	0.017	0.000	0.024
K	1.463	1.306	1.566	1.424	1.541	1.478	1.499	1.617
F	0.289	0.341	0.000	0.000	0.163	0.188	0.000	0.348
Cl	0.013	0.006	0.016	0.013	0.014	0.018	0.017	0.011
Sum	16.786	16.807	16.766	16.659	16.864	16.832	16.782	17.052
mg#	0.65	0.70	0.56	0.57	0.54	0.55	0.54	0.52

Table B.2. (Continued)

probe run id	bio-57_1741-10	bio-57_1741-4	bio-57_1741-6	bio-57_1741-7	bio-57_1741-8	bio-57_1741-9	bio-58_110-1	bio-58_110-2
sample	57-174.1	57-174.1	57-174.1	57-174.1	57-174.1	57-174.1	58-110.2	58-110.2
rock name	SP	SP	SP	SP	SP	SP	SP	SP
SiO_2	37.85	37.50	37.51	38.63	37.90	38.53	37.89	37.82
TiO_2	2.31	3.88	2.59	2.57	2.45	2.47	2.42	3.27
Al_2O_3	15.89	15.17	15.44	15.50	15.78	15.39	15.40	15.34
Cr_2O_3	0.03	0.02	0.06	0.03	0.01	0.03	0.30	0.13
MgO	13.01	12.15	12.03	12.88	15.50	12.87	12.27	12.72
CaO	0.05	0.02	0.02	0.02	0.03	0.00	0.02	0.02
MnO	0.02	0.01	0.00	0.06	0.00	0.01	0.10	0.03
FeO	17.90	18.33	18.51	17.58	18.29	18.12	18.32	17.50
NiO	n.a.	n.a.	n.a.	n.a.	n.a.	n.a.	n.a.	n.a.
BaO	0.13	0.00	0.75	0.57	0.12	0.00	0.17	0.29
Na_2O	0.00	0.00	0.05	0.00	0.04	0.00	0.04	0.05
K_2O	8.58	7.38	7.79	8.39	7.43	7.40	6.83	7.78
F	0.00	0.80	0.86	0.91	0.75	0.77	0.58	0.58
Cl	0.07	0.05	0.03	0.08	0.06	0.06	0.06	0.05
Total (uncorrected)	95.83	95.31	95.66	97.20	98.35	95.65	94.38	95.56
"-O=F,Cl"	0.02	0.35	0.37	0.40	0.33	0.34	0.26	0.26
Total (corrected)	95.81	94.96	95.28	96.80	98.02	95.31	94.12	95.30
Number of ions based on 24 O, F, Cl								
Si	6.166	6.115	6.148	6.198	5.989	6.233	6.223	6.152
Al	3.052	2.916	2.983	2.931	2.939	2.934	2.980	2.940
Ti	0.283	0.476	0.319	0.310	0.291	0.301	0.298	0.401
Cr	0.004	0.003	0.007	0.004	0.001	0.004	0.038	0.017
Mg	3.161	2.955	2.940	3.080	3.651	3.104	3.004	3.084
Ca	0.009	0.003	0.004	0.003	0.005	0.000	0.004	0.003
Mn	0.002	0.001	0.000	0.008	0.000	0.002	0.014	0.004
Fe	2.439	2.500	2.537	2.358	2.417	2.451	2.515	2.380
Ni	-	-	-	-	-	-	-	-
Ba	0.008	0.000	0.048	0.036	0.007	0.000	0.011	0.018
Na	0.000	0.000	0.017	0.000	0.013	0.000	0.013	0.015
K	1.783	1.534	1.628	1.716	1.498	1.528	1.430	1.614
F	0.000	0.410	0.447	0.460	0.372	0.394	0.303	0.299
Cl	0.018	0.015	0.009	0.022	0.017	0.017	0.016	0.014
Sum	16.924	16.929	17.088	17.124	17.200	16.967	16.850	16.940
mg#	0.56	0.54	0.54	0.57	0.60	0.56	0.54	0.56

Table B.2. (Continued)

probe run id	bio-58_110-4	bio-58_110-5	bio-58_110-8	bio-58_110-9	biot57-1741ph-2	biot57-1741ph-4	biot57-1741ph-6
sample	58-110.2	58-110.2	58-110.2	58-110.2	57-174.1	57-174.1	57-174.1
rock name	SP	SP	SP	SP	SP	SP	SP
SiO_2	37.51	38.45	37.73	37.38	36.84	36.05	37.32
TiO_2	2.24	2.37	2.30	2.52	2.52	3.19	2.30
Al_2O_3	15.76	15.87	16.00	15.82	15.02	14.74	14.71
Cr_2O_3	0.68	0.03	0.03	0.09	0.04	0.05	0.03
MgO	14.93	11.86	16.29	12.14	12.30	12.16	12.91
CaO	0.03	0.02	0.01	0.02	0.08	0.00	0.00
MnO	0.04	0.04	0.05	0.00	0.05	0.05	0.01
FeO	17.64	17.83	18.36	18.75	19.11	18.34	17.59
NiO	n.a.	n.a.	n.a.	n.a.	n.a.	n.a.	n.a.
BaO	0.05	0.27	0.22	0.30	0.02	0.15	0.45
Na_2O	0.02	0.06	0.01	0.05	0.07	0.06	0.04
K_2O	7.16	7.58	7.00	7.62	9.66	9.88	9.50
F	0.00	0.53	0.00	0.45	0.91	0.83	0.84
Cl	0.05	0.05	0.03	0.04	0.05	0.05	0.05
Total (uncorrected)	96.11	94.95	98.02	95.17	96.65	95.54	95.74
"-O=F,Cl"	0.01	0.24	0.01	0.20	0.39	0.36	0.37
Total (corrected)	96.09	94.71	98.01	94.97	96.26	95.18	95.37
Number of ions based on 24 O, F, Cl							
Si	6.052	6.275	5.977	6.137	6.047	5.997	6.146
Al	2.997	3.051	2.987	3.061	2.905	2.890	2.854
Ti	0.271	0.291	0.274	0.311	0.311	0.399	0.285
Cr	0.086	0.004	0.004	0.012	0.005	0.006	0.004
Mg	3.590	2.885	3.846	2.973	3.010	3.016	3.170
Ca	0.004	0.003	0.001	0.003	0.014	0.000	0.000
Mn	0.006	0.005	0.006	0.000	0.007	0.007	0.001
Fe	2.379	2.433	2.432	2.574	2.623	2.551	2.422
Ni	-	-	-	-	-	-	-
Ba	0.003	0.017	0.014	0.019	0.001	0.010	0.029
Na	0.005	0.018	0.002	0.015	0.022	0.018	0.013
K	1.473	1.577	1.414	1.597	2.023	2.097	1.997
F	0.000	0.275	0.000	0.232	0.472	0.434	0.435
Cl	0.014	0.014	0.009	0.010	0.013	0.014	0.015
Sum	16.882	16.849	16.966	16.942	17.452	17.438	17.370
mg#	0.60	0.54	0.61	0.54	0.53	0.54	0.57

Table B.3. Electron microprobe analyses of groundmass biotite

probe run id	biot397-1	biot397-2	biot397-3	biot397-4	bio-49_113.7-17	bio-49_113.7-18	bio-49_113.7-19	biot49-1137gr-1
sample	397	397	397	397	49-113.7	49-113.7	49-113.7	49-113.7
rock name	L	L	L	L	L	L	L	L
SiO_2	36.44	36.98	36.04	36.63	36.86	37.43	38.43	35.34
TiO_2	1.59	1.33	1.29	1.23	1.59	1.45	1.56	1.84
Al_2O_3	14.91	14.81	14.72	15.24	15.79	15.70	15.24	15.06
Cr_2O_3	0.03	0.04	0.10	0.12	0.10	0.26	0.05	0.04
MgO	12.55	13.19	13.08	12.74	12.51	13.26	13.99	13.06
CaO	0.25	0.01	0.02	0.01	0.01	0.03	0.00	0.29
MnO	0.20	0.11	0.15	0.18	0.17	0.15	0.09	0.14
FeO	19.08	19.13	19.06	19.45	18.52	18.56	17.40	18.53
BaO	0.88	0.56	0.42	0.43	1.22	0.53	0.63	0.97
Na_2O	0.06	0.03	0.05	0.03	0.00	0.04	0.00	0.05
K_2O	9.01	9.47	9.47	9.65	7.85	8.92	8.68	8.94
F	0.55	0.50	0.55	0.44	0.27	0.51	0.76	0.61
Cl	0.03	0.05	0.03	0.03	0.09	0.05	0.06	0.08
Total (uncorrected)	95.58	96.21	94.97	96.17	94.98	96.87	96.88	94.96
"-O=F,Cl"	0.24	0.22	0.24	0.19	0.14	0.23	0.33	0.28
Total (corrected)	95.34	95.98	94.73	95.98	94.84	96.64	96.54	94.68
Number of ions based on 24 O, F, Cl								
Si	6.081	6.117	6.054	6.076	6.125	6.098	6.202	5.945
Al	2.933	2.888	2.914	2.980	3.092	3.014	2.899	2.985
Ti	0.199	0.166	0.163	0.153	0.199	0.177	0.189	0.232
Cr	0.004	0.005	0.013	0.015	0.013	0.033	0.006	0.006
Mg	3.121	3.253	3.275	3.151	3.099	3.220	3.365	3.274
Ca	0.045	0.001	0.004	0.002	0.002	0.005	0.000	0.053
Mn	0.028	0.016	0.021	0.025	0.024	0.020	0.012	0.020
Fe	2.663	2.646	2.677	2.698	2.574	2.529	2.348	2.606
Ba	0.057	0.036	0.027	0.028	0.079	0.034	0.040	0.064
Na	0.020	0.008	0.015	0.010	0.000	0.014	0.000	0.016
K	1.918	1.998	2.028	2.043	1.664	1.854	1.787	1.919
F	0.288	0.262	0.293	0.229	0.143	0.263	0.387	0.324
Cl	0.010	0.015	0.010	0.008	0.025	0.014	0.016	0.024
Sum	17.369	17.411	17.493	17.418	17.039	17.273	17.252	17.468
mg#	0.54	0.55	0.55	0.54	0.55	0.56	0.59	0.56

Table B.3. (Continued)

probe run id	biot49-1137gr-2	biot49-1137gr-3	biot49-1137gr-4	biot49-1137gr-5	biot49-1137gr-6	biot56-158gr-1	biot56-158gr-2	biot56-158gr-3
sample	49-113.7	49-113.7	49-113.7	49-113.7	49-113.7	56-158.0	56-158.0	56-158.0
rock name	L	L	L	L	L	L	L	L
SiO_2	36.99	44.64	36.01	35.21	35.51	35.96	38.21	37.44
TiO_2	1.34	1.00	1.39	1.59	1.41	2.33	1.93	2.21
Al_2O_3	14.49	14.86	15.69	15.47	15.33	15.97	13.97	14.64
Cr_2O_3	0.02	0.13	0.03	0.13	0.04	0.11	0.05	0.18
MgO	13.67	12.78	12.64	12.65	12.49	12.37	14.64	14.31
CaO	0.04	0.18	0.01	0.03	0.02	0.00	0.00	0.08
MnO	0.12	0.06	0.15	0.15	0.17	0.00	0.00	0.00
FeO	18.06	12.29	19.36	19.37	19.20	17.84	16.33	15.08
BaO	0.00	0.00	1.31	1.07	0.78	0.76	0.00	0.30
Na_2O	0.04	2.49	0.06	0.06	0.05	0.03	0.05	0.06
K_2O	9.86	8.04	9.58	9.54	9.78	9.67	9.77	9.97
F	0.82	0.91	0.58	0.60	0.50	0.86	1.60	1.35
Cl	0.10	0.08	0.07	0.08	0.07	0.03	0.00	0.02
Total (uncorrected)	95.56	97.45	96.87	95.94	95.36	95.92	96.56	95.65
"-O=F,Cl"	0.37	0.40	0.26	0.27	0.23	0.37	0.67	0.58
Total (corrected)	95.18	97.05	96.61	95.67	95.12	95.55	95.89	95.07
Number of ions based on 24 O, F, Cl								
Si	6.123	6.876	5.972	5.905	5.978	5.952	6.181	6.112
Al	2.828	2.696	3.067	3.057	3.040	3.114	2.663	2.817
Ti	0.167	0.115	0.173	0.200	0.179	0.290	0.235	0.271
Cr	0.003	0.016	0.004	0.017	0.006	0.014	0.007	0.023
Mg	3.373	2.934	3.124	3.163	3.134	3.051	3.529	3.483
Ca	0.007	0.030	0.002	0.006	0.004	0.001	0.000	0.014
Mn	0.017	0.008	0.020	0.021	0.024	0.000	0.000	0.000
Fe	2.500	1.583	2.685	2.717	2.703	2.468	2.209	2.059
Ba	0.000	0.000	0.085	0.071	0.051	0.049	0.000	0.019
Na	0.013	0.743	0.021	0.020	0.015	0.009	0.016	0.019
K	2.082	1.579	2.027	2.041	2.099	2.041	2.017	2.076
F	0.431	0.445	0.303	0.319	0.268	0.450	0.816	0.699
Cl	0.027	0.021	0.021	0.022	0.021	0.008	0.001	0.006
Sum	17.571	17.047	17.505	17.558	17.522	17.448	17.674	17.597
mg#	0.57	0.65	0.54	0.54	0.54	0.55	0.62	0.63

Table B.3. (Continued)

probe run id	bio-58_583-3	biot58-583gr-1	biot58-583gr-2	biot58-583gr-3	biot58-583gr-4	biotTR223-1	biotTR223-2	biotTR223-3
sample	58-58.3	58-58.3	58-58.3	58-58.3	58-58.3	TR223	TR223	TR223
rock name	L	L	L	L	L	L	L	L
SiO_2	39.87	37.41	37.09	36.65	38.05	37.01	38.09	38.45
TiO_2	1.89	1.86	1.99	1.71	1.76	1.34	1.25	1.42
Al_2O_3	15.08	15.50	15.91	15.83	14.67	15.09	14.99	14.92
Cr_2O_3	0.01	0.07	0.06	0.65	0.01	0.01	0.03	0.02
MgO	15.13	13.89	13.87	13.91	14.86	13.32	13.47	13.36
CaO	0.05	0.03	0.06	0.02	0.03	0.01	0.00	0.04
MnO	0.01	0.02	0.04	0.10	0.02	0.17	0.24	0.18
FeO	14.97	16.32	16.22	15.92	15.21	17.70	17.59	17.68
BaO	0.00	0.43	0.72	0.00	0.00	0.00	0.03	0.06
Na_2O	0.05	0.04	0.06	0.07	0.03	0.04	0.00	0.04
K_2O	7.53	9.83	9.69	9.87	9.80	9.77	9.39	9.54
F	0.46	0.46	0.44	0.48	0.65	0.31	0.27	0.34
Cl	0.05	0.04	0.04	0.05	0.04	0.00	0.00	0.01
Total (uncorrected)	95.07	95.90	96.18	95.26	95.14	94.77	95.36	96.04
"-O=F,Cl"	0.20	0.20	0.19	0.21	0.28	0.13	0.11	0.14
Total (corrected)	94.87	95.69	95.98	95.05	94.85	94.64	95.25	95.89
Number of ions based on 24 O, F, Cl								
Si	6.380	6.118	6.057	6.027	6.213	6.156	6.260	6.277
Al	2.843	2.987	3.062	3.069	2.824	2.958	2.904	2.871
Ti	0.227	0.229	0.245	0.211	0.216	0.168	0.155	0.174
Cr	0.002	0.009	0.008	0.084	0.002	0.001	0.004	0.002
Mg	3.609	3.388	3.376	3.411	3.617	3.302	3.300	3.251
Ca	0.008	0.006	0.010	0.004	0.005	0.002	0.001	0.007
Mn	0.001	0.003	0.006	0.014	0.003	0.023	0.034	0.024
Fe	2.003	2.232	2.215	2.189	2.078	2.462	2.418	2.413
Ba	0.000	0.027	0.046	0.000	0.000	0.000	0.002	0.004
Na	0.014	0.013	0.019	0.023	0.011	0.012	0.001	0.013
K	1.536	2.051	2.018	2.070	2.041	2.074	1.969	1.987
F	0.231	0.240	0.227	0.249	0.338	0.165	0.139	0.174
Cl	0.013	0.010	0.011	0.014	0.010	0.001	0.001	0.003
Sum	16.868	17.312	17.300	17.364	17.357	17.322	17.186	17.201
mg#	0.64	0.60	0.60	0.61	0.64	0.57	0.58	0.57

Table B.3. (Continued)

probe run id	biotTR223-4	bio-49_1292-21	bio-49_1292-22	biot49-1292gr-1	biot49-1292gr-2	bio-55_62.7-2	bio-55_62.7-3	bio-55_62.7-4
sample	TR223	49-129.2	49-129.2	49-129.2	49-129.2	55-62.7	55-62.7	55-62.7
rock name	L	SP	SP	SP	SP	SP	SP	SP
SiO_2	37.86	39.19	36.63	36.40	37.30	38.77	39.12	37.99
TiO_2	1.38	2.32	5.22	2.03	2.95	1.22	1.34	0.94
Al_2O_3	14.89	13.78	13.71	14.31	13.68	15.23	15.08	15.03
Cr_2O_3	0.03	0.04	0.04	0.17	0.02	0.00	0.22	0.03
MgO	13.30	14.93	14.03	14.45	14.33	13.09	13.47	13.11
CaO	0.05	0.02	0.01	0.02	0.03	0.04	0.04	0.04
MnO	0.21	0.00	0.00	0.00	0.00	0.25	0.18	0.17
FeO	17.81	15.48	15.88	17.09	15.99	17.76	17.54	18.35
BaO	0.01	0.24	0.30	0.00	0.55	0.00	0.00	0.03
Na_2O	0.05	0.06	0.01	0.05	0.09	0.07	0.01	0.02
K_2O	9.60	9.11	9.38	9.99	9.87	8.40	7.91	8.29
F	0.27	2.92	2.23	2.77	2.95	0.55	0.50	0.54
Cl	0.00	0.05	0.05	0.05	0.05	0.04	0.03	0.04
Total (uncorrected)	95.45	98.15	97.50	97.32	97.80	95.41	95.43	94.59
"-O=F,Cl"	0.11	1.24	0.95	1.18	1.25	0.24	0.22	0.24
Total (corrected)	95.33	96.91	96.54	96.14	96.55	95.17	95.21	94.35
Number of ions based on 24 O, F, Cl								
Si	6.236	6.182	5.889	5.902	5.996	6.319	6.345	6.275
Al	2.891	2.562	2.598	2.733	2.591	2.926	2.882	2.925
Ti	0.170	0.275	0.632	0.247	0.356	0.150	0.164	0.117
Cr	0.003	0.005	0.005	0.021	0.002	0.000	0.028	0.004
Mg	3.266	3.512	3.362	3.492	3.434	3.182	3.256	3.229
Ca	0.010	0.003	0.002	0.003	0.006	0.006	0.007	0.007
Mn	0.029	0.000	0.000	0.000	0.000	0.034	0.024	0.024
Fe	2.454	2.042	2.135	2.317	2.149	2.420	2.379	2.534
Ba	0.000	0.015	0.019	0.000	0.035	0.000	0.000	0.002
Na	0.017	0.018	0.004	0.017	0.026	0.021	0.002	0.008
K	2.017	1.833	1.922	2.067	2.024	1.747	1.635	1.747
F	0.139	1.459	1.135	1.420	1.500	0.284	0.256	0.284
Cl	0.000	0.014	0.013	0.014	0.013	0.010	0.007	0.012
Sum	17.232	17.920	17.715	18.233	18.133	17.099	16.987	17.168
mg#	0.57	0.63	0.61	0.60	0.62	0.57	0.58	0.56

Table B.3. (Continued)

probe run id	bio-55_62.7-8	bio-55_62.7-9	biot55-627gr-1	biot55-627gr-2	biot55-627gr-3	biot57-1662gr-1	biot57-1662gr-2	biot57-1662gr-3
sample	55-62.7	55-62.7	55-62.7	55-62.7	55-62.7	57-166.2	57-166.2	57-166.2
rock name	SP	SP	SP	SP	SP	SP	SP	SP
SiO_2	38.48	37.55	39.18	37.74	37.55	38.06	38.39	36.97
TiO_2	1.22	0.03	1.16	1.38	1.18	1.69	1.88	1.91
Al_2O_3	15.35	21.81	14.35	15.07	15.43	14.64	14.68	14.57
Cr_2O_3	0.02	0.03	0.03	0.06	0.11	0.04	0.02	0.01
MgO	12.84	0.00	13.90	13.37	13.09	13.60	13.78	13.69
CaO	0.03	21.73	0.02	0.03	0.01	0.05	0.00	0.03
MnO	0.23	0.14	0.09	0.17	0.19	0.05	0.01	0.13
FeO	17.91	13.35	16.75	17.30	17.62	17.68	16.55	17.43
BaO	0.02	0.00	0.00	0.00	0.01	0.00	0.00	0.36
Na_2O	0.02	0.01	0.05	0.10	0.05	0.07	0.04	0.04
K_2O	8.67	0.10	9.67	9.96	9.97	9.94	9.98	9.60
F	0.49	0.00	0.61	0.52	0.52	0.95	1.07	0.86
Cl	0.06	0.00	0.05	0.07	0.06	0.06	0.04	0.07
Total (uncorrected)	95.33	94.75	95.85	95.76	95.79	96.83	96.43	95.65
"-O=F,Cl"	0.22	0.00	0.27	0.24	0.23	0.41	0.46	0.38
Total (corrected)	95.11	94.75	95.58	95.53	95.56	96.41	95.97	95.28
Number of ions based on 24 O, F, Cl								
Si	6.297	6.074	6.373	6.197	6.173	6.185	6.221	6.102
Al	2.960	4.158	2.750	2.915	2.989	2.804	2.804	2.834
Ti	0.150	0.004	0.142	0.170	0.146	0.206	0.229	0.237
Cr	0.003	0.004	0.004	0.008	0.014	0.006	0.002	0.001
Mg	3.132	0.000	3.371	3.273	3.208	3.295	3.329	3.368
Ca	0.006	3.766	0.004	0.005	0.002	0.009	0.000	0.005
Mn	0.032	0.019	0.013	0.023	0.026	0.007	0.002	0.018
Fe	2.450	1.806	2.278	2.375	2.422	2.402	2.243	2.406
Ba	0.001	0.000	0.000	0.000	0.001	0.000	0.000	0.024
Na	0.006	0.004	0.015	0.032	0.017	0.021	0.012	0.013
K	1.810	0.020	2.006	2.086	2.091	2.060	2.063	2.020
F	0.251	0.000	0.314	0.272	0.270	0.488	0.547	0.448
Cl	0.016	0.000	0.013	0.019	0.018	0.016	0.011	0.019
Sum	17.114	15.853	17.282	17.376	17.377	17.497	17.464	17.494
mg#	0.56	0.00	0.60	0.58	0.57	0.58	0.60	0.58

Table B.3. (Continued)

probe run id	biot57-1662gr-4	biot57-1741gr-1	biot57-1741gr-3	biot57-1741gr-5	biot58-110gr-1	biot58-110gr-2	biot58-110gr-3	biot58-110gr-4
sample	57-166.2	57-174.1	57-174.1	57-174.1	58-110.2	58-110.2	58-110.2	58-110.2
rock name	SP	SP	SP	SP	SP	SP	SP	SP
SiO_2	38.81	36.61	37.09	35.84	37.74	37.58	37.64	37.74
TiO_2	1.85	2.52	2.34	2.25	1.93	1.94	2.00	1.84
Al_2O_3	13.73	14.30	13.89	15.16	14.70	14.57	14.64	14.47
Cr_2O_3	0.01	0.00	0.02	0.04	0.04	0.03	0.02	0.08
MgO	14.61	12.33	12.76	12.83	13.86	13.95	13.89	13.68
CaO	0.05	0.05	0.28	0.05	0.04	0.24	0.04	0.04
MnO	0.05	0.00	0.02	0.04	0.00	0.00	0.01	0.07
FeO	15.99	17.81	17.18	18.21	17.03	16.58	16.08	17.05
BaO	0.00	1.04	0.49	0.32	0.00	0.01	0.00	0.00
Na_2O	0.02	0.07	0.08	0.06	0.06	0.06	0.05	0.08
K_2O	9.92	9.39	9.65	9.51	9.63	9.77	9.92	9.77
F	1.01	1.07	0.98	0.93	0.73	0.65	0.81	0.74
Cl	0.02	0.07	0.06	0.05	0.05	0.04	0.03	0.04
Total (uncorrected)	96.08	95.24	94.84	95.28	95.81	95.41	95.12	95.61
"-O=F,Cl"	0.43	0.47	0.43	0.40	0.32	0.28	0.35	0.32
Total (corrected)	95.64	94.78	94.41	94.87	95.49	95.12	94.77	95.29
Number of ions based on 24 O, F, Cl								
Si	6.298	6.109	6.181	5.969	6.173	6.172	6.184	6.196
Al	2.626	2.813	2.729	2.976	2.833	2.820	2.835	2.799
Ti	0.226	0.316	0.293	0.281	0.237	0.240	0.248	0.227
Cr	0.001	0.000	0.002	0.005	0.006	0.003	0.003	0.010
Mg	3.534	3.067	3.171	3.185	3.379	3.416	3.402	3.349
Ca	0.009	0.008	0.050	0.009	0.007	0.042	0.006	0.007
Mn	0.007	0.000	0.003	0.005	0.000	0.000	0.001	0.010
Fe	2.170	2.485	2.393	2.535	2.328	2.277	2.209	2.340
Ba	0.000	0.068	0.032	0.021	0.000	0.001	0.000	0.000
Na	0.008	0.023	0.025	0.019	0.018	0.018	0.017	0.026
K	2.054	1.999	2.051	2.021	2.008	2.048	2.079	2.046
F	0.518	0.563	0.516	0.489	0.375	0.339	0.421	0.386
Cl	0.006	0.018	0.017	0.015	0.015	0.010	0.009	0.010
Sum	17.455	17.470	17.465	17.531	17.379	17.384	17.413	17.406
mg#	0.62	0.55	0.57	0.56	0.59	0.60	0.61	0.59

Table B.3. (Continued)

probe run id	biot658-1	biot658-2	biot658-3
sample	658	658	658
rock name	SP	SP	SP
SiO_2	38.28	37.93	37.90
TiO_2	1.77	1.46	1.61
Al_2O_3	14.73	14.85	15.11
Cr_2O_3	0.02	0.11	0.13
MgO	12.91	13.25	13.31
CaO	0.01	0.19	0.04
MnO	0.16	0.04	0.09
FeO	18.13	18.14	17.71
BaO	0.00	0.00	0.03
Na_2O	0.03	0.03	0.08
K_2O	9.66	9.44	9.53
F	0.69	0.87	0.68
Cl	0.01	0.00	0.01
Total (uncorrected)	96.41	96.32	96.22
"-O=F,Cl"	0.30	0.37	0.29
Total (corrected)	96.11	95.96	95.93
Number of ions based on 24 O, F, Cl			
Si	6.244	6.192	6.184
Al	2.832	2.857	2.905
Ti	0.217	0.179	0.198
Cr	0.002	0.014	0.017
Mg	3.139	3.225	3.237
Ca	0.002	0.034	0.007
Mn	0.023	0.006	0.013
Fe	2.473	2.476	2.415
Ba	0.000	0.000	0.002
Na	0.010	0.010	0.025
K	2.011	1.965	1.984
F	0.358	0.447	0.349
Cl	0.003	0.000	0.002
Sum	17.313	17.405	17.337
mg#	0.56	0.57	0.57

Table B.4. Electron microprobe analyses of biotite from mafic enclaves

probe run id	biot56-158e-1	biot56-158e-2	biot56-158e-3	biot664-4e-1	biot664-4e-2	biot49-1292e-1	biot49-1292e-2	biot49-1292e-3
sample	56-158.0	56-158.0	56-158.0	664-4	664-4	49-129.2	49-129.2	49-129.2
rock name	L	L	L	L	L	SP	SP	SP
SiO_2	36.98	38.35	35.92	35.79	37.20	38.23	40.15	35.98
TiO_2	1.86	1.88	1.82	1.34	1.17	1.80	1.52	2.13
Al_2O_3	14.57	14.35	16.15	15.31	15.42	13.56	12.70	14.02
Cr_2O_3	0.60	0.62	0.19	0.13	0.07	0.36	0.06	0.07
MgO	14.51	14.60	13.14	13.17	13.35	15.76	18.24	14.24
CaO	0.01	0.03	0.04	0.02	0.05	0.04	0.08	0.03
MnO	0.04	0.00	0.00	0.20	0.16	0.02	0.00	0.01
FeO	16.21	15.97	17.94	18.29	18.35	15.61	11.38	17.28
BaO	0.00	0.00	0.50	0.60	0.07	0.00	0.00	0.23
Na_2O	0.05	0.03	0.05	0.06	0.09	0.05	0.04	0.03
K_2O	9.20	9.54	9.54	9.55	9.38	9.57	9.78	9.65
F	1.40	1.31	0.86	0.31	0.31	2.83	3.82	2.22
Cl	0.01	0.02	0.02	0.04	0.05	0.03	0.03	0.04
Total (uncorrected)	95.44	96.70	96.18	94.80	95.66	97.85	97.79	95.93
"-O=F,Cl"	0.59	0.56	0.37	0.14	0.14	1.20	1.62	0.94
Total (corrected)	94.85	96.15	95.81	94.66	95.52	96.65	96.17	94.98
Number of ions based on 24 O, F, Cl								
Si	6.054	6.178	5.917	6.014	6.133	6.083	6.248	5.932
Al	2.812	2.724	3.135	3.031	2.997	2.543	2.329	2.725
Ti	0.230	0.228	0.225	0.169	0.146	0.216	0.178	0.264
Cr	0.077	0.079	0.025	0.017	0.009	0.045	0.007	0.009
Mg	3.541	3.507	3.227	3.300	3.282	3.739	4.231	3.499
Ca	0.002	0.004	0.007	0.004	0.009	0.007	0.013	0.005
Mn	0.005	0.000	0.000	0.029	0.022	0.002	0.000	0.002
Fe	2.218	2.151	2.471	2.569	2.530	2.077	1.480	2.382
Ba	0.000	0.000	0.032	0.040	0.004	0.000	0.000	0.015
Na	0.017	0.010	0.014	0.020	0.028	0.017	0.013	0.011
K	1.921	1.961	2.005	2.048	1.972	1.942	1.941	2.030
F	0.726	0.669	0.447	0.163	0.160	1.423	1.882	1.155
Cl	0.002	0.004	0.006	0.012	0.013	0.008	0.008	0.011
Sum	17.605	17.515	17.514	17.415	17.305	18.102	18.329	18.041
mg#	0.61	0.62	0.57	0.56	0.56	0.64	0.74	0.59

Table B.4. (Continued)

probe run id	biot49-1292e-4	biot49-1292e-5	biot55-6272e-3	biot55-627e-1	biot55-627e-2	biot55-627e-4	biot55-627e-5	bt55-627e_rerun-1
sample	49-129.2	49-129.2	55-62.7	55-62.7	55-62.7	55-62.7	55-62.7	55-62.7
rock name	SP	SP	SP	SP	SP	SP	SP	SP
SiO_2	36.34	39.59	36.29	35.17	36.39	35.88	35.37	35.25
TiO_2	2.10	1.65	1.09	1.03	1.05	1.08	1.38	1.14
Al_2O_3	14.12	13.07	16.24	16.12	16.20	16.16	15.85	16.06
Cr_2O_3	0.10	1.44	0.27	0.29	0.26	0.26	1.13	0.20
MgO	13.94	16.30	12.53	12.50	12.58	12.54	11.74	12.67
CaO	0.05	0.06	0.03	0.04	0.01	0.02	0.01	0.02
MnO	0.06	0.01	0.19	0.23	0.20	0.16	0.21	0.20
FeO	17.26	13.58	19.14	18.69	18.94	19.19	19.01	17.85
BaO	0.69	0.00	0.24	0.33	0.35	0.34	0.60	0.35
Na_2O	0.05	0.07	0.08	0.06	0.06	0.04	0.07	0.03
K_2O	9.54	9.87	9.28	9.66	9.47	8.70	9.45	10.08
F	2.00	3.32	0.44	0.44	0.41	0.40	0.29	7.48
Cl	0.06	0.04	0.06	0.06	0.05	0.07	0.06	0.06
Total (uncorrected)	96.32	99.00	95.88	94.60	95.97	94.85	95.16	101.38
"-O=F,Cl"	0.86	1.41	0.20	0.20	0.18	0.19	0.14	3.16
Total (corrected)	95.46	97.59	95.68	94.40	95.79	94.67	95.03	98.22
Number of ions based on 24 O, F, Cl								
Si	5.979	6.176	6.008	5.931	6.023	5.997	5.953	5.519
Al	2.738	2.403	3.168	3.203	3.160	3.184	3.144	2.962
Ti	0.259	0.194	0.136	0.131	0.131	0.136	0.175	0.134
Cr	0.013	0.177	0.035	0.038	0.034	0.035	0.150	0.025
Mg	3.421	3.790	3.093	3.142	3.103	3.126	2.946	2.956
Ca	0.010	0.010	0.006	0.007	0.001	0.004	0.002	0.003
Mn	0.009	0.002	0.027	0.033	0.028	0.023	0.030	0.027
Fe	2.375	1.771	2.650	2.636	2.620	2.682	2.675	2.336
Ba	0.044	0.000	0.015	0.022	0.023	0.022	0.039	0.021
Na	0.016	0.020	0.025	0.021	0.020	0.014	0.022	0.009
K	2.003	1.964	1.960	2.077	1.999	1.854	2.028	2.013
F	1.042	1.638	0.228	0.235	0.215	0.214	0.154	3.703
Cl	0.016	0.010	0.018	0.016	0.013	0.019	0.016	0.015
Sum	17.925	18.157	17.369	17.492	17.372	17.308	17.335	19.724
mg#	0.59	0.68	0.54	0.54	0.54	0.54	0.52	0.56

Table B.4. (Continued)

probe run id	bt55-627e_rerun-2	biot57-1662e-1	biot57-1662e-2	biot57-1741e-1	biot57-1741e-2	biot57-1741e-3	biot58-1102e-1	biot58-1102e-2
sample	55-62.7	57-166.2	57-166.2	57-174.1	57-174.1	57-174.1	58-110.2	58-110.2
rock name	SP	SP	SP	SP	SP	SP	SP	SP
SiO_2	34.93	38.04	35.86	38.18	37.22	35.50	36.28	37.68
TiO_2	1.12	0.81	2.13	1.81	1.92	2.16	2.04	2.03
Al_2O_3	16.36	14.71	15.70	14.04	14.86	15.28	15.10	14.81
Cr_2O_3	0.81	1.13	0.04	0.40	0.32	0.09	0.07	0.05
MgO	12.20	13.50	11.93	14.13	12.88	12.49	12.93	13.71
CaO	0.04	0.03	0.03	0.06	0.06	0.03	0.02	0.00
MnO	0.21	0.02	0.00	0.07	0.04	0.01	0.08	0.03
FeO	18.22	16.89	19.07	17.05	18.09	18.72	18.37	17.08
BaO	0.40	0.39	1.13	0.07	0.17	0.38	0.00	0.00
Na_2O	0.06	0.05	0.03	0.04	0.05	0.05	0.04	0.05
K_2O	9.77	9.16	9.30	9.50	9.35	9.57	9.69	9.60
F	0.47	0.64	0.62	1.30	0.98	0.91	0.56	0.68
Cl	0.05	0.02	0.06	0.04	0.05	0.07	0.05	0.04
Total (uncorrected)	94.63	95.37	95.90	96.69	95.99	95.26	95.23	95.76
"-O=F,Cl"	0.21	0.27	0.27	0.55	0.42	0.40	0.25	0.29
Total (corrected)	94.42	95.10	95.62	96.14	95.56	94.86	94.98	95.46
Number of ions based on 24 O, F, Cl								
Si	5.892	6.253	5.980	6.190	6.115	5.937	6.035	6.165
Al	3.252	2.849	3.086	2.682	2.878	3.013	2.959	2.855
Ti	0.142	0.100	0.267	0.220	0.237	0.272	0.255	0.250
Cr	0.108	0.146	0.005	0.051	0.042	0.012	0.009	0.006
Mg	3.068	3.309	2.966	3.416	3.156	3.115	3.207	3.344
Ca	0.006	0.005	0.006	0.011	0.011	0.006	0.003	0.000
Mn	0.030	0.003	0.000	0.010	0.005	0.002	0.012	0.005
Fe	2.569	2.321	2.659	2.312	2.485	2.618	2.555	2.338
Ba	0.026	0.025	0.074	0.004	0.011	0.025	0.000	0.000
Na	0.019	0.016	0.010	0.014	0.016	0.017	0.013	0.017
K	2.101	1.921	1.977	1.965	1.961	2.041	2.057	2.004
F	0.251	0.334	0.324	0.665	0.507	0.481	0.296	0.350
Cl	0.015	0.005	0.017	0.010	0.013	0.021	0.015	0.010
Sum	17.480	17.287	17.371	17.549	17.436	17.559	17.416	17.344
mg#	0.54	0.59	0.53	0.60	0.56	0.54	0.56	0.59

Table B.5. Electron microprobe analyses of K-feldspar phenocrysts

run ID	fspTR223ph-6	fspTR223ph-5	ksp-491292-6	ksp-491292-4	ksp-491292-2	ksp-491292-3	ksp-491292-1	ksp-491292-5
rock type	L	L	SP	SP	SP	SP	SP	SP
sample	TR223	TR223	49-129.2	49-129.2	49-129.2	49-129.2	49-129.2	49-129.2
SiO_2	61.55	63.66	63.38	63.56	63.28	63.14	63.01	62.05
Al_2O_3	19.04	19.29	19.39	19.74	19.54	19.98	19.71	19.94
CaO	1.55	0.00	0.04	0.29	0.16	0.38	0.26	0.08
FeO	0.13	0.04	0.14	0.16	0.13	0.15	0.16	0.23
SrO	0.07	0.07	0.64	0.54	0.58	0.50	0.45	0.65
BaO	1.63	1.75	0.70	1.10	1.21	1.52	1.62	2.71
Na_2O	0.87	0.29	0.75	0.97	0.94	1.50	0.68	0.68
K_2O	15.70	15.83	15.39	14.87	15.04	13.91	15.29	14.79
Total	100.54	100.92	100.44	101.22	100.88	101.08	101.19	101.13
Number of ions on the basis of 32 O. All Fe recalculated as Fe^{3+}.								
Si	11.577	11.804	11.760	11.709	11.721	11.650	11.677	11.593
Al	4.222	4.216	4.241	4.287	4.268	4.347	4.307	4.392
Fe	0.020	0.006	0.022	0.025	0.020	0.024	0.025	0.036
Ca	0.312	0.000	0.008	0.057	0.032	0.075	0.052	0.016
Sr	0.007	0.007	0.069	0.057	0.062	0.053	0.049	0.071
Ba	0.120	0.127	0.051	0.079	0.088	0.110	0.117	0.198
Na	0.318	0.104	0.269	0.348	0.338	0.538	0.243	0.248
K	3.767	3.745	3.644	3.495	3.554	3.274	3.616	3.526
Sum	20.344	20.009	20.065	20.056	20.081	20.070	20.086	20.080
Ab	0.072	0.027	0.069	0.089	0.086	0.138	0.062	0.065
An	0.071	0.000	0.002	0.015	0.008	0.019	0.013	0.004
Or	0.857	0.973	0.929	0.896	0.906	0.842	0.924	0.930

run ID	ksp55627-3	ksp55627-5	ksp55627-4	ksp55627-10	ksp55627-2	ksp55627-11	ksp55627-1	ksp55627-9
rock type	SP	SP	SP	SP	SP	SP	SP	SP
sample	55-62.7	55-62.7	55-62.7	55-62.7	55-62.7	55-62.7	55-62.7	55-62.7
SiO_2	61.47	61.39	61.10	60.39	60.37	60.14	59.20	59.76
Al_2O_3	20.22	20.26	20.44	20.93	20.47	21.22	20.39	21.05
CaO	0.32	0.23	0.24	0.35	0.20	0.39	0.27	0.35
FeO	0.11	0.15	0.15	0.14	0.19	0.19	0.16	0.18
SrO	0.79	0.75	0.70	0.87	0.65	0.81	0.73	0.88
BaO	2.56	3.37	3.87	3.91	4.59	4.61	5.17	5.41
Na_2O	1.30	1.00	1.06	1.32	1.12	1.34	1.16	1.18
K_2O	13.56	13.66	13.49	13.07	13.26	12.84	12.83	12.35
Total	100.32	100.80	101.04	100.97	100.84	101.53	99.91	101.15
Number of ions on the basis of 32 O. All Fe recalculated as Fe^{3+}.								
Si	11.534	11.523	11.478	11.368	11.424	11.306	11.365	11.316
Al	4.473	4.483	4.528	4.644	4.566	4.702	4.613	4.699
Fe	0.017	0.024	0.023	0.023	0.029	0.030	0.026	0.028
Ca	0.064	0.045	0.047	0.070	0.041	0.079	0.056	0.072
Sr	0.086	0.081	0.076	0.095	0.072	0.088	0.081	0.096
Ba	0.188	0.248	0.285	0.288	0.340	0.340	0.389	0.401
Na	0.471	0.365	0.385	0.480	0.412	0.488	0.431	0.431
K	3.246	3.271	3.233	3.139	3.201	3.080	3.142	2.984
Sum	20.080	20.041	20.055	20.108	20.085	20.112	20.102	20.028
Ab	0.125	0.099	0.105	0.130	0.113	0.134	0.119	0.124
An	0.017	0.012	0.013	0.019	0.011	0.022	0.015	0.021
Or	0.858	0.889	0.882	0.851	0.876	0.845	0.866	0.856

Table B.5. (Continued)

run ID	ksp55627-7	ksp55627-6	fsp57-166.2-39	fsp57-166.2-14	fsp57-166.2-50	fsp57-166.2-30	fsp57-166.2-21	fsp57-166.2-1
rock type	SP	SP	SP	SP	SP	SP	SP	SP
sample	55-62.7	55-62.7	57-166.2	57-166.2	57-166.2	57-166.2	57-166.2	57-166.2
SiO_2	59.58	58.91	64.41	63.23	63.76	63.67	63.60	64.18
Al_2O_3	20.69	20.69	19.35	19.46	19.37	19.44	19.40	19.41
CaO	0.21	0.17	0.15	0.16	0.24	0.19	0.05	0.19
FeO	0.16	0.18	0.10	0.09	0.12	0.21	0.11	0.14
SrO	0.70	0.61	0.19	0.66	0.33	0.60	0.74	0.19
BaO	5.71	6.46	0.06	0.36	0.38	0.43	0.47	0.48
Na_2O	1.07	0.44	1.06	0.97	1.02	1.15	1.02	0.84
K_2O	12.68	12.88	15.50	15.07	15.18	14.92	15.12	15.52
Total	100.81	100.35	100.80	100.00	100.40	100.62	100.51	100.95
Number of ions on the basis of 32 O. All Fe recalculated as Fe^{3+}.								
Si	11.352	11.332	11.822	11.748	11.781	11.754	11.768	11.798
Al	4.648	4.693	4.186	4.263	4.220	4.231	4.233	4.207
Fe	0.026	0.030	0.015	0.014	0.018	0.033	0.016	0.022
Ca	0.043	0.035	0.029	0.031	0.048	0.037	0.010	0.038
Sr	0.077	0.068	0.020	0.071	0.036	0.064	0.080	0.020
Ba	0.427	0.487	0.004	0.026	0.028	0.031	0.034	0.035
Na	0.395	0.164	0.375	0.349	0.365	0.411	0.364	0.299
K	3.083	3.162	3.630	3.572	3.577	3.515	3.570	3.640
Sum	20.050	19.970	20.081	20.074	20.072	20.076	20.075	20.057
Ab	0.112	0.049	0.093	0.088	0.092	0.104	0.092	0.075
An	0.012	0.010	0.007	0.008	0.012	0.009	0.002	0.010
Or	0.876	0.941	0.900	0.904	0.897	0.887	0.905	0.915

run ID	fsp57-166.2-19	fsp57-166.2-12	fsp57-166.2-2	fsp57-166.2-38	fsp57-166.2-46	fsp57-166.2-10	fsp57-166.2-23	fsp57-166.2-28
rock type	SP	SP	SP	SP	SP	SP	SP	SP
sample	57-166.2	57-166.2	57-166.2	57-166.2	57-166.2	57-166.2	57-166.2	57-166.2
SiO_2	63.78	63.73	63.85	64.14	63.97	63.44	63.54	62.95
Al_2O_3	19.59	19.60	19.46	19.20	19.48	19.62	19.44	19.78
CaO	0.29	0.19	0.19	0.01	0.22	0.27	0.25	0.33
FeO	0.13	0.09	0.11	0.03	0.12	0.19	0.15	0.16
SrO	0.50	0.50	0.22	0.01	0.34	0.47	0.34	0.56
BaO	0.55	0.56	0.58	0.62	0.66	0.70	0.81	0.88
Na_2O	0.93	0.78	1.02	0.73	1.16	0.94	0.68	1.44
K_2O	15.24	15.41	15.25	15.94	14.91	15.17	15.45	14.12
Total	101.00	100.87	100.68	100.68	100.86	100.78	100.65	100.21
Number of ions on the basis of 32 O. All Fe recalculated as Fe^{3+}.								
Si	11.744	11.752	11.774	11.837	11.773	11.719	11.757	11.677
Al	4.252	4.261	4.231	4.178	4.228	4.272	4.240	4.326
Fe	0.019	0.014	0.017	0.004	0.018	0.029	0.023	0.025
Ca	0.058	0.037	0.038	0.002	0.044	0.053	0.050	0.066
Sr	0.053	0.054	0.023	0.001	0.036	0.050	0.036	0.061
Ba	0.040	0.040	0.042	0.044	0.048	0.050	0.058	0.064
Na	0.331	0.280	0.366	0.260	0.413	0.338	0.245	0.517
K	3.579	3.625	3.588	3.754	3.501	3.575	3.647	3.341
Sum	20.076	20.063	20.079	20.080	20.061	20.087	20.057	20.076
Ab	0.083	0.071	0.092	0.065	0.104	0.085	0.062	0.132
An	0.015	0.009	0.009	0.000	0.011	0.013	0.013	0.017
Or	0.902	0.920	0.899	0.935	0.885	0.901	0.925	0.851

Table B.5. (Continued)

run ID	fsp57-166.2-16	fsp57-166.2-7	fsp57-166.2-48	fsp57-166.2-29	fsp57-166.2-26	fsp57-166.2-18	fsp57-166.2-41	fsp57-166.2-9
rock type	SP	SP	SP	SP	SP	SP	SP	SP
sample	57-166.2	57-166.2	57-166.2	57-166.2	57-166.2	57-166.2	57-166.2	57-166.2
SiO_2	63.21	63.71	63.27	62.74	62.52	63.30	63.04	63.52
Al_2O_3	19.60	19.52	19.51	19.56	19.58	19.68	19.65	19.33
CaO	0.19	0.28	0.29	0.25	0.22	0.23	0.23	0.01
FeO	0.16	0.11	0.14	0.18	0.10	0.10	0.15	0.05
SrO	0.47	0.40	0.50	0.68	0.49	0.31	0.40	0.04
BaO	0.96	0.96	0.99	1.08	1.12	1.20	1.27	1.36
Na_2O	0.94	1.21	1.00	0.99	0.78	0.86	1.41	0.39
K_2O	14.97	14.41	14.80	14.71	14.96	15.18	14.20	16.12
Total	100.49	100.60	100.50	100.18	99.77	100.85	100.35	100.82
Number of ions on the basis of 32 O. All Fe recalculated as Fe^{3+}.								
Si	11.721	11.760	11.730	11.691	11.697	11.714	11.700	11.782
Al	4.283	4.249	4.264	4.298	4.318	4.293	4.300	4.228
Fe	0.025	0.018	0.022	0.027	0.015	0.015	0.023	0.008
Ca	0.038	0.054	0.057	0.050	0.045	0.045	0.046	0.003
Sr	0.051	0.043	0.053	0.073	0.053	0.033	0.043	0.004
Ba	0.070	0.070	0.072	0.079	0.082	0.087	0.093	0.099
Na	0.336	0.433	0.359	0.359	0.283	0.309	0.506	0.140
K	3.540	3.394	3.500	3.496	3.571	3.583	3.363	3.814
Sum	20.063	20.021	20.057	20.074	20.063	20.078	20.073	20.077
Ab	0.086	0.112	0.092	0.092	0.072	0.078	0.129	0.035
An	0.010	0.014	0.015	0.013	0.012	0.011	0.012	0.001
Or	0.905	0.874	0.894	0.895	0.916	0.910	0.859	0.964

run ID	fsp57-166.2-35	fsp57-166.2-5	fsp57-166.2-22	fsp57-166.2-51	fsp57-166.2-6	fsp57-166.2-32	fsp57-166.2-13	fsp57-166.2-47
rock type	SP	SP	SP	SP	SP	SP	SP	SP
sample	57-166.2	57-166.2	57-166.2	57-166.2	57-166.2	57-166.2	57-166.2	57-166.2
SiO_2	63.14	62.96	62.48	62.74	62.46	62.55	61.98	62.35
Al_2O_3	19.59	19.84	20.10	19.61	19.88	19.49	20.07	20.01
CaO	0.13	0.18	0.40	0.23	0.27	0.04	0.26	0.18
FeO	0.14	0.11	0.15	0.14	0.12	0.01	0.17	0.14
SrO	0.50	0.57	0.74	0.42	0.53	0.19	0.93	0.50
BaO	1.37	1.51	1.53	1.53	1.69	1.89	1.92	1.95
Na_2O	1.01	0.78	1.52	0.80	0.83	0.38	0.95	0.88
K_2O	14.86	15.06	13.44	14.96	14.81	15.86	14.46	14.52
Total	100.73	101.00	100.36	100.42	100.58	100.42	100.73	100.52
Number of ions on the basis of 32 O. All Fe recalculated as Fe^{3+}.								
Si	11.712	11.672	11.611	11.691	11.639	11.708	11.573	11.626
Al	4.284	4.336	4.403	4.308	4.366	4.301	4.419	4.398
Fe	0.022	0.017	0.024	0.021	0.019	0.002	0.026	0.022
Ca	0.026	0.036	0.080	0.046	0.053	0.009	0.051	0.037
Sr	0.053	0.061	0.079	0.046	0.057	0.021	0.100	0.054
Ba	0.099	0.110	0.111	0.112	0.124	0.139	0.141	0.142
Na	0.364	0.280	0.547	0.288	0.301	0.137	0.343	0.319
K	3.515	3.561	3.187	3.556	3.521	3.787	3.445	3.453
Sum	20.075	20.072	20.043	20.067	20.079	20.103	20.098	20.050
Ab	0.093	0.072	0.143	0.074	0.078	0.035	0.089	0.084
An	0.007	0.009	0.021	0.012	0.014	0.002	0.013	0.010
Or	0.900	0.919	0.836	0.914	0.909	0.963	0.897	0.907

Table B.5. (Continued)

run ID	fsp57-166.2-45	fsp57-166.2-11	fsp57-166.2-49	fsp57-166.2-43	fsp57-166.2-22a	fsp57-166.2-31	fsp57-166.2-36	fsp57-166.2-24
rock type	SP	SP	SP	SP	SP	SP	SP	SP
sample	57-166.2	57-166.2	57-166.2	57-166.2	57-166.2	57-166.2	57-166.2	57-166.2
SiO_2	62.59	61.99	61.88	61.82	61.42	61.41	61.64	61.99
Al_2O_3	19.87	20.01	20.02	19.79	19.82	19.93	20.13	19.96
CaO	0.09	0.28	0.37	0.12	0.21	0.06	0.28	0.18
FeO	0.17	0.09	0.13	0.16	0.14	0.12	0.20	0.13
SrO	0.70	0.82	0.59	0.57	0.88	1.01	0.88	0.41
BaO	2.02	2.04	2.07	2.10	2.27	2.43	2.44	2.56
Na_2O	1.08	0.97	0.93	0.77	0.82	0.76	1.57	0.99
K_2O	14.30	14.25	14.30	14.74	14.38	14.61	13.14	14.33
Total	100.81	100.46	100.28	100.06	99.94	100.32	100.27	100.55
Number of ions on the basis of 32 O. All Fe recalculated as Fe^{3+}.								
Si	11.646	11.595	11.587	11.619	11.584	11.568	11.549	11.603
Al	4.358	4.412	4.419	4.385	4.408	4.426	4.446	4.404
Fe	0.027	0.014	0.020	0.024	0.023	0.019	0.031	0.020
Ca	0.017	0.056	0.073	0.024	0.042	0.013	0.057	0.036
Sr	0.075	0.089	0.064	0.062	0.096	0.110	0.095	0.044
Ba	0.148	0.150	0.152	0.155	0.167	0.179	0.179	0.188
Na	0.388	0.353	0.338	0.281	0.300	0.278	0.570	0.357
K	3.393	3.400	3.417	3.533	3.460	3.511	3.142	3.423
Sum	20.052	20.069	20.071	20.084	20.080	20.103	20.069	20.075
Ab	0.102	0.093	0.088	0.073	0.079	0.073	0.151	0.094
An	0.004	0.015	0.019	0.006	0.011	0.003	0.015	0.009
Or	0.893	0.893	0.892	0.921	0.910	0.924	0.834	0.897

run ID	fsp57-166.2-33	fsp57-166.2-8	fsp57-166.2-15	fsp57-166.2-37	fsp57-166.2-42	fsp57-166.2-3	fsp57-166.2-40	fsp57-166.2-27
rock type	SP	SP	SP	SP	SP	SP	SP	SP
sample	57-166.2	57-166.2	57-166.2	57-166.2	57-166.2	57-166.2	57-166.2	57-166.2
SiO_2	62.21	61.02	61.04	60.28	60.23	59.13	59.47	59.97
Al_2O_3	20.02	19.90	20.09	20.48	20.49	20.73	20.63	20.39
CaO	0.20	0.02	0.06	0.41	0.33	0.46	0.39	0.29
FeO	0.14	0.18	0.07	0.21	0.14	0.13	0.20	0.18
SrO	0.49	0.83	0.98	1.06	1.11	0.79	0.83	0.72
BaO	2.60	3.06	3.14	3.57	3.70	4.16	4.43	4.44
Na_2O	1.60	0.66	0.77	1.25	1.51	1.08	1.08	0.93
K_2O	13.35	14.44	14.06	12.87	12.64	13.02	12.76	13.38
Total	100.61	100.09	100.20	100.11	100.15	99.50	99.78	100.30
Number of ions on the basis of 32 O. All Fe recalculated as Fe^{3+}.								
Si	11.602	11.554	11.540	11.421	11.414	11.330	11.363	11.414
Al	4.402	4.443	4.477	4.573	4.579	4.682	4.646	4.576
Fe	0.022	0.028	0.011	0.033	0.023	0.021	0.032	0.029
Ca	0.040	0.003	0.013	0.082	0.067	0.094	0.080	0.059
Sr	0.053	0.091	0.108	0.116	0.122	0.088	0.092	0.079
Ba	0.190	0.227	0.232	0.265	0.275	0.313	0.331	0.331
Na	0.577	0.241	0.280	0.458	0.556	0.401	0.402	0.342
K	3.177	3.487	3.391	3.111	3.056	3.183	3.109	3.250
Sum	20.063	20.075	20.052	20.060	20.091	20.110	20.054	20.080
Ab	0.152	0.065	0.076	0.125	0.151	0.109	0.112	0.094
An	0.010	0.001	0.004	0.023	0.018	0.026	0.022	0.016
Or	0.837	0.935	0.920	0.852	0.831	0.865	0.866	0.890

Table B.5. (Continued)

run ID	fsp57-166.2-4	fsp57-166.2-44	fsp57-166.2-17	fsp57-166.2-34	fsp57-166.2-25	fsp57-166.2-20	ksp-571741-6	ksp-571741-3
rock type	SP	SP	SP	SP	SP	SP	SP	SP
sample	57-166.2	57-166.2	57-166.2	57-166.2	57-166.2	57-166.2	57-174.1	57-174.1
SiO_2	60.00	60.22	58.82	58.92	58.86	59.03	63.92	64.19
Al_2O_3	20.74	20.13	20.76	20.85	20.80	20.64	19.46	19.58
CaO	0.48	0.09	0.52	0.49	0.33	0.25	0.33	0.19
FeO	0.17	0.16	0.18	0.25	0.12	0.15	0.17	0.20
SrO	0.78	0.66	0.92	0.93	0.92	0.93	0.35	0.61
BaO	4.54	4.65	5.14	5.22	5.37	5.52	0.32	0.54
Na_2O	0.99	0.77	0.95	1.12	0.95	1.08	1.84	0.95
K_2O	13.07	13.90	12.71	12.30	12.91	12.54	14.17	15.33
Total	100.77	100.58	100.01	100.09	100.26	100.13	100.55	101.59
Number of ions on the basis of 32 O. All Fe recalculated as Fe^{3+}.								
Si	11.366	11.461	11.290	11.284	11.292	11.328	11.758	11.757
Al	4.632	4.515	4.698	4.709	4.704	4.669	4.220	4.227
Fe	0.027	0.025	0.028	0.041	0.020	0.023	0.026	0.030
Ca	0.097	0.019	0.107	0.101	0.069	0.052	0.065	0.037
Sr	0.086	0.073	0.103	0.104	0.102	0.103	0.037	0.065
Ba	0.337	0.347	0.386	0.392	0.404	0.415	0.023	0.039
Na	0.364	0.282	0.355	0.417	0.352	0.400	0.655	0.336
K	3.159	3.375	3.112	3.004	3.160	3.071	3.325	3.582
Sum	20.066	20.097	20.079	20.052	20.102	20.061	20.109	20.073
Ab	0.101	0.077	0.099	0.118	0.098	0.114	0.162	0.085
An	0.027	0.005	0.030	0.029	0.019	0.015	0.016	0.009
Or	0.873	0.918	0.871	0.853	0.883	0.872	0.822	0.906

run ID	ksp-571741-1	ksp-571741-4	ksp-571741-7	ksp-571741-8	ksp-571741-2	ksp-571741-5	kspA23-12	kspA23-10
rock type	SP	SP	SP	SP	SP	SP	SP	SP
sample	57-174.1	57-174.1	57-174.1	57-174.1	57-174.1	57-174.1	A23	A23
SiO_2	63.26	63.02	62.75	61.88	61.07	60.36	63.27	64.06
Al_2O_3	19.75	19.70	19.85	19.80	19.98	20.20	19.23	19.53
CaO	0.30	0.16	0.10	0.00	0.23	0.09	0.00	0.04
FeO	0.13	0.23	0.12	0.07	0.15	0.23	0.19	0.06
SrO	0.56	0.61	0.72	0.24	0.73	1.07	0.04	0.60
BaO	1.31	1.91	2.17	2.57	3.29	4.02	0.69	0.81
Na_2O	1.24	0.73	0.84	0.55	0.61	0.75	0.24	1.00
K_2O	14.56	14.87	14.63	15.39	14.27	13.87	16.54	15.23
Total	101.11	101.22	101.17	100.49	100.33	100.60	100.20	101.35
Number of ions on the basis of 32 O. All Fe recalculated as Fe^{3+}.								
Si	11.684	11.681	11.657	11.624	11.542	11.456	11.780	11.772
Al	4.301	4.305	4.346	4.385	4.452	4.520	4.221	4.232
Fe	0.019	0.036	0.018	0.010	0.024	0.036	0.030	0.009
Ca	0.060	0.031	0.019	0.000	0.046	0.019	0.000	0.009
Sr	0.060	0.065	0.077	0.026	0.080	0.118	0.004	0.064
Ba	0.095	0.139	0.158	0.189	0.244	0.299	0.050	0.059
Na	0.442	0.264	0.304	0.200	0.225	0.277	0.088	0.357
K	3.431	3.516	3.467	3.688	3.440	3.357	3.930	3.570
Sum	20.092	20.038	20.046	20.123	20.052	20.083	20.103	20.071
Ab	0.112	0.069	0.080	0.051	0.061	0.076	0.022	0.091
An	0.015	0.008	0.005	0.000	0.012	0.005	0.000	0.002
Or	0.872	0.923	0.915	0.949	0.927	0.919	0.978	0.907

Table B.5. (Continued)

run ID	kspA23-1	kspA23-8	kspA23-7	kspA23-6	kspA23-9	kspA23-11	kspA23-2	kspA23-3
rock type	SP	SP	SP	SP	SP	SP	SP	SP
sample	A23	A23	A23	A23	A23	A23	A23	A23
SiO_2	63.96	63.98	63.72	63.92	60.61	62.67	62.81	62.78
Al_2O_3	19.11	19.47	19.15	19.42	19.32	19.58	19.54	19.14
CaO	0.01	0.00	0.00	0.01	0.00	0.02	0.00	0.00
FeO	0.17	0.13	0.00	0.14	0.26	0.16	0.14	0.41
SrO	0.38	0.07	0.07	0.32	0.13	0.52	0.28	0.17
BaO	0.86	0.87	0.97	1.35	1.85	2.11	2.14	2.35
Na_2O	0.45	0.21	0.32	0.44	0.43	0.86	0.42	0.68
K_2O	16.02	16.35	16.32	15.77	15.54	14.90	15.61	15.20
Total	100.97	101.08	100.54	101.37	98.13	100.83	100.95	100.74
Number of ions on the basis of 32 O. All Fe recalculated as Fe^{3+}.								
Si	11.820	11.796	11.825	11.784	11.626	11.682	11.704	11.728
Al	4.163	4.231	4.189	4.221	4.368	4.303	4.293	4.215
Fe	0.026	0.021	0.000	0.022	0.041	0.025	0.022	0.064
Ca	0.002	0.000	0.000	0.002	0.000	0.005	0.001	0.000
Sr	0.041	0.007	0.007	0.034	0.014	0.057	0.030	0.019
Ba	0.062	0.063	0.071	0.097	0.139	0.154	0.156	0.172
Na	0.163	0.075	0.113	0.157	0.161	0.311	0.153	0.247
K	3.777	3.845	3.863	3.710	3.802	3.543	3.711	3.621
Sum	20.055	20.038	20.068	20.027	20.151	20.080	20.071	20.066
Ab	0.041	0.019	0.029	0.041	0.041	0.081	0.040	0.064
An	0.001	0.000	0.000	0.000	0.000	0.001	0.000	0.000
Or	0.958	0.981	0.971	0.959	0.959	0.918	0.960	0.936

run ID	kspA23-4	kspA23-5
rock type	SP	SP
sample	A23	A23
SiO_2	61.51	61.90
Al_2O_3	19.64	19.79
CaO	0.00	0.00
FeO	0.32	0.26
SrO	0.28	0.32
BaO	3.46	3.51
Na_2O	0.78	0.66
K_2O	14.25	14.53
Total	100.24	100.98
Number of ions on the basis of 32 O. All Fe recalculated as Fe^{3+}.		
Si	11.611	11.611
Al	4.371	4.377
Fe	0.050	0.041
Ca	0.000	0.000
Sr	0.030	0.035
Ba	0.256	0.258
Na	0.286	0.241
K	3.432	3.476
Sum	20.037	20.039
Ab	0.077	0.065
An	0.000	0.000
Or	0.923	0.935

Table B.6. Electron microprobe analyses of plagioclase phenocrysts

run ID	plA23-12	plA23-9	plA23-6	plA23-2	plA23-1	plA23-11	plA23-4	plA23-5
rock type	SP	SP	SP	SP	SP	SP	SP	SP
sample	A23	A23	A23	A23	A23	A23	A23	A23
SiO_2	67.04	67.70	66.78	67.46	67.07	68.31	66.76	68.14
Al_2O_3	20.11	19.62	20.16	20.29	20.14	19.98	19.93	19.96
CaO	0.12	0.08	0.21	0.28	0.25	0.06	0.21	0.16
FeO	0.03	0.04	0.05	0.02	0.02	0.03	0.05	0.00
SrO	0.02	0.01	0.04	0.16	0.11	0.00	0.12	0.05
BaO	0.00	0.00	0.00	0.00	0.00	0.01	0.01	0.02
Na_2O	11.35	11.59	11.42	11.31	11.38	11.40	11.10	11.33
K_2O	0.09	0.07	0.10	0.08	0.11	0.14	0.31	0.09
Total	98.76	99.11	98.76	99.60	99.06	99.93	98.50	99.74
Number of ions on the basis of 32 O. All Fe recalculated as Fe^{3+}.								
Si	11.860	11.935	11.829	11.846	11.844	11.932	11.863	11.926
Al	4.194	4.078	4.210	4.200	4.193	4.114	4.175	4.119
Fe	0.004	0.006	0.007	0.003	0.003	0.004	0.007	0.000
Ca	0.023	0.015	0.040	0.053	0.047	0.011	0.040	0.030
Sr	0.002	0.001	0.004	0.016	0.011	0.000	0.012	0.005
Ba	0.000	0.000	0.000	0.000	0.000	0.001	0.001	0.001
Na	3.893	3.962	3.922	3.851	3.896	3.861	3.824	3.845
K	0.020	0.016	0.023	0.018	0.025	0.031	0.070	0.020
Sum	19.997	20.012	20.035	19.987	20.019	19.955	19.993	19.947
Ab	0.989	0.992	0.984	0.982	0.982	0.989	0.972	0.987
An	0.006	0.004	0.010	0.013	0.012	0.003	0.010	0.008
Or	0.005	0.004	0.006	0.005	0.006	0.008	0.018	0.005

run ID	plA23-3	plA23-7	plA23-10	plA23-8
rock type	SP	SP	SP	SP
sample	A23	A23	A23	A23
SiO_2	67.42	68.16	68.49	68.24
Al_2O_3	20.19	19.93	19.92	19.70
CaO	0.43	0.09	0.10	0.12
FeO	0.05	0.07	0.02	0.12
SrO	0.16	0.00	0.00	0.12
BaO	0.02	0.03	0.04	0.04
Na_2O	11.22	11.43	11.35	11.45
K_2O	0.13	0.09	0.11	0.18
Total	99.61	99.80	100.02	99.96
Number of ions on the basis of 32 O. All Fe recalculated as Fe^{3+}.				
Si	11.846	11.925	11.948	11.939
Al	4.182	4.111	4.097	4.063
Fe	0.007	0.010	0.003	0.018
Ca	0.081	0.017	0.019	0.022
Sr	0.016	0.000	0.000	0.012
Ba	0.001	0.002	0.003	0.003
Na	3.822	3.878	3.839	3.884
K	0.029	0.020	0.024	0.040
Sum	19.985	19.963	19.933	19.982
Ab	0.972	0.991	0.989	0.984
An	0.021	0.004	0.005	0.006
Or	0.007	0.005	0.006	0.010

Table B.7. Electron microprobe analyses of groundmass K-feldspar

run ID	fsp397gr-1	fsp397gr-2	fsp397gr-4	fsp397gr-3	fsp49-1137gr-3	fsp49-1137gr-2	fsp49-1137gr-4	fsp56-158gr-2	fsp56-158gr-1
rock type	397	397	397	397	49-113.7	49-113.7	49-113.7	56-158.0	56-158.0
sample	L	L	L	L	L	L	L	L	L
SiO_2	64.81	64.17	64.09	64.17	64.20	63.42	64.00	64.23	64.05
Al_2O_3	19.07	19.31	19.17	19.43	19.15	19.23	19.41	19.19	19.20
CaO	0.03	0.00	0.01	0.01	0.10	0.03	0.01	0.01	0.03
FeO	0.05	0.05	0.09	0.15	0.11	0.07	0.12	0.08	0.13
SrO	0.05	0.02	0.08	0.06	0.13	0.14	0.22	0.10	0.10
BaO	0.52	1.06	1.19	1.21	1.26	1.27	1.29	0.53	0.83
Na_2O	0.00	0.23	0.27	0.17	0.09	0.29	0.95	0.45	0.59
K_2O	16.77	16.50	16.39	16.48	16.40	15.95	15.90	16.37	15.83
Total	101.30	101.34	101.29	101.67	101.43	100.42	101.89	100.96	100.76
Number of ions on the basis of 32 O. All Fe recalculated as Fe^{3+}.									
Si	11.894	11.820	11.825	11.796	11.833	11.799	11.758	11.837	11.827
Al	4.126	4.194	4.171	4.211	4.161	4.218	4.205	4.169	4.179
Fe	0.008	0.008	0.014	0.023	0.018	0.011	0.018	0.012	0.020
Ca	0.006	0.000	0.002	0.001	0.019	0.006	0.001	0.002	0.007
Sr	0.005	0.002	0.009	0.006	0.014	0.016	0.023	0.011	0.011
Ba	0.037	0.077	0.086	0.087	0.091	0.093	0.093	0.038	0.060
Na	0.000	0.081	0.096	0.061	0.031	0.105	0.338	0.159	0.211
K	3.926	3.877	3.858	3.866	3.856	3.786	3.727	3.847	3.730
Sum	20.002	20.058	20.060	20.050	20.022	20.032	20.163	20.076	20.044
Ab	0.000	0.020	0.024	0.015	0.008	0.027	0.083	0.040	0.054
An	0.002	0.000	0.001	0.000	0.005	0.002	0.000	0.001	0.002
Or	0.998	0.980	0.975	0.984	0.987	0.972	0.917	0.960	0.945

run ID	fspTR223gr-10	fspTR223gr-8	fspTR223gr-9	fspTR6-2	fspTR6-3	fspTR6-1	fsp49-1292gr-2	fsp49-1292gr-1	fsp49-1292gr-3
rock type	TR223	TR223	TR223	TR6A	TR6A	TR6A	49-129.2	49-129.2	49-129.2
sample	L	L	L	L	L	L	SP	SP	SP
SiO_2	64.19	63.28	63.42	64.32	63.91	64.22	65.37	64.99	66.52
Al_2O_3	19.27	19.14	19.43	19.18	19.19	19.11	18.87	18.63	19.20
CaO	0.00	0.04	0.11	0.01	0.05	0.02	0.04	0.04	0.13
FeO	0.08	0.20	0.14	0.17	0.23	0.19	0.26	0.43	0.35
SrO	0.03	0.03	0.05	0.03	0.04	0.02	0.00	0.00	0.14
BaO	1.03	1.16	1.84	0.95	1.00	1.04	0.07	0.07	0.08
Na_2O	0.00	0.79	0.22	0.17	0.16	0.08	0.25	0.22	2.51
K_2O	16.58	16.47	16.05	16.52	16.45	16.44	16.65	16.93	12.52
Total	101.18	101.11	101.26	101.35	101.01	101.13	101.51	101.31	101.45
Number of ions on the basis of 32 O. All Fe recalculated as Fe^{3+}.									
Si	11.835	11.743	11.751	11.837	11.812	11.845	11.929	11.914	11.951
Al	4.189	4.187	4.245	4.162	4.182	4.156	4.058	4.026	4.067
Fe	0.013	0.031	0.022	0.025	0.035	0.030	0.039	0.066	0.053
Ca	0.000	0.008	0.022	0.002	0.009	0.004	0.008	0.008	0.025
Sr	0.003	0.003	0.005	0.003	0.004	0.002	0.000	0.000	0.015
Ba	0.074	0.084	0.134	0.069	0.072	0.075	0.005	0.005	0.006
Na	0.000	0.286	0.079	0.061	0.057	0.029	0.089	0.079	0.875
K	3.901	3.899	3.793	3.878	3.877	3.868	3.876	3.960	2.869
Sum	20.015	20.241	20.051	20.038	20.048	20.011	20.005	20.059	19.861
Ab	0.000	0.068	0.020	0.015	0.015	0.007	0.022	0.019	0.232
An	0.000	0.002	0.006	0.001	0.002	0.001	0.002	0.002	0.007
Or	1.000	0.930	0.974	0.984	0.983	0.991	0.976	0.979	0.761

Table B.7. (Continued)

run ID	fsp55-627gr-1	fsp55-627gr-2	fsp57-1662gr-2	fsp57-1662gr-3	fsp57-1662gr-4	fsp57-1741gr-3	fsp57-1741gr-2	fsp658gr-4	fsp658gr-1
rock type	55-62.7	55-62.7	57-166.2	57-166.2	57-166.2	57-174.1	57-174.1	658	658
sample	SP	SP	SP	SP	SP	SP	SP	SP	SP
SiO_2	64.51	64.73	64.71	64.61	71.44	63.64	64.61	64.63	64.70
Al_2O_3	18.85	19.10	18.85	18.74	15.04	18.45	18.95	18.95	19.08
CaO	0.00	0.09	0.03	0.03	0.22	0.65	0.08	0.01	0.01
FeO	0.13	0.19	0.10	0.14	0.17	0.21	0.28	0.10	0.02
SrO	0.05	0.06	0.00	0.01	0.00	0.01	0.03	0.01	0.04
BaO	0.36	0.81	0.09	0.13	0.20	0.13	0.27	0.56	0.56
Na_2O	0.25	1.54	0.16	1.56	0.22	0.00	0.05	0.19	0.29
K_2O	16.66	12.99	16.80	15.57	13.49	16.03	16.84	16.65	16.58
Total	100.82	99.51	100.74	100.78	100.77	99.12	101.11	101.11	101.28
Number of ions on the basis of 32 O. All Fe recalculated as Fe^{3+}.									
Si	11.894	11.925	11.913	11.878	12.784	11.898	11.877	11.890	11.880
Al	4.097	4.148	4.091	4.061	3.173	4.067	4.107	4.111	4.131
Fe	0.019	0.029	0.016	0.022	0.025	0.033	0.043	0.016	0.004
Ca	0.000	0.018	0.006	0.005	0.042	0.131	0.015	0.003	0.002
Sr	0.005	0.006	0.000	0.001	0.000	0.001	0.003	0.001	0.004
Ba	0.026	0.059	0.006	0.009	0.014	0.009	0.019	0.040	0.040
Na	0.090	0.549	0.055	0.556	0.076	0.000	0.019	0.068	0.102
K	3.920	3.053	3.947	3.652	3.080	3.824	3.950	3.906	3.883
Sum	20.053	19.787	20.034	20.184	19.194	19.964	20.033	20.034	20.046
Ab	0.023	0.152	0.014	0.132	0.024	0.000	0.005	0.017	0.026
An	0.000	0.005	0.002	0.001	0.013	0.033	0.004	0.001	0.000
Or	0.977	0.843	0.985	0.867	0.963	0.967	0.992	0.982	0.974

run ID	fsp658gr-2	fsp658gr-3	fspTR6en-4	fspTR6en-2	fspTR6en-3
rock type	658	658	TR6A	TR6A	TR6A
sample	SP	SP	O	O	O
SiO_2	64.45	64.07	64.33	63.04	63.35
Al_2O_3	19.13	19.15	19.21	19.15	19.35
CaO	0.00	0.01	0.03	0.05	0.19
FeO	0.04	0.03	0.12	0.00	0.11
SrO	0.05	0.02	0.05	0.07	0.05
BaO	0.87	0.98	0.98	1.31	1.40
Na_2O	0.16	0.05	0.28	0.20	0.20
K_2O	16.34	16.43	16.44	16.34	16.15
Total	101.03	100.74	101.43	100.16	100.79
Number of ions on the basis of 32 O. All Fe recalculated as Fe^{3+}.					
Si	11.872	11.852	11.833	11.785	11.763
Al	4.154	4.177	4.165	4.221	4.236
Fe	0.006	0.005	0.018	0.000	0.017
Ca	0.000	0.001	0.005	0.009	0.038
Sr	0.005	0.002	0.005	0.007	0.005
Ba	0.063	0.071	0.071	0.096	0.102
Na	0.056	0.017	0.101	0.074	0.070
K	3.839	3.878	3.857	3.897	3.826
Sum	19.996	20.003	20.054	20.090	20.058
Ab	0.014	0.004	0.025	0.018	0.018
An	0.000	0.000	0.001	0.002	0.010
Or	0.986	0.995	0.973	0.979	0.972

Table B.8. Electron microprobe analyses of groundmass plagioclase

run ID	fsp397gr-8	fsp397gr-6	fspTR223gr-1	fspTR223gr-3	fspTR6en-6	fspTR6en-7	fspTR6en-5	fspTR6-6	fspTR6-5
rock type	397	397	TR223	TR223	TR6A	TR6A	TR6A	TR6A	TR6A
sample	L	L	L	L	O	O	O	L	L
SiO_2	67.52	67.94	68.74	68.92	69.03	67.94	69.36	68.97	68.56
Al_2O_3	20.96	20.42	20.29	20.43	20.22	20.11	20.31	20.31	20.33
CaO	0.71	0.30	0.24	0.25	0.05	0.13	0.05	0.21	0.18
FeO	0.21	0.21	0.20	0.18	0.05	0.04	0.00	0.22	0.12
SrO	0.23	0.12	0.06	0.08	0.03	0.00	0.03	0.00	0.02
BaO	0.05	0.13	0.00	0.01	0.00	0.02	0.02	0.00	0.00
Na_2O	11.46	11.31	10.04	11.80	11.92	11.71	12.01	12.08	11.69
K_2O	0.20	1.22	0.06	0.06	0.16	0.23	0.07	0.13	0.19
Total	101.33	101.64	99.64	101.71	101.45	100.18	101.84	101.92	101.08
Number of ions on the basis of 32 O. All Fe recalculated as Fe^{3+}.									
Si	11.710	11.787	11.975	11.858	11.901	11.871	11.908	11.856	11.867
Al	4.285	4.178	4.168	4.145	4.109	4.142	4.110	4.116	4.148
Fe	0.030	0.030	0.030	0.025	0.007	0.006	0.000	0.031	0.017
Ca	0.131	0.056	0.045	0.046	0.010	0.024	0.009	0.039	0.034
Sr	0.023	0.012	0.006	0.007	0.003	0.000	0.003	0.000	0.002
Ba	0.003	0.009	0.000	0.000	0.000	0.001	0.001	0.000	0.000
Na	3.854	3.803	3.390	3.937	3.985	3.969	3.999	4.026	3.923
K	0.045	0.269	0.014	0.013	0.035	0.052	0.014	0.029	0.043
Sum	20.082	20.145	19.628	20.031	20.051	20.065	20.044	20.098	20.033
Ab	0.956	0.921	0.983	0.985	0.989	0.981	0.994	0.983	0.981
An	0.033	0.014	0.013	0.011	0.002	0.006	0.002	0.009	0.008
Or	0.011	0.065	0.004	0.003	0.009	0.013	0.004	0.007	0.011

run ID	fspTR6-7	fsp55-627gr-4	fsp55-627gr-3	fsp57-1662gr-6	fsp57-1741gr-8	fsp658gr-8	fsp658gr-5	fsp658gr-7	fsp658gr-6
rock type	TR6A	55-62.7	55-62.7	57-166.2	57-174.1	658	658	658	658
sample	L	SP	SP	SP	SP	SP	SP	SP	SP
SiO_2	68.61	68.53	68.18	65.93	69.51	68.69	68.96	69.00	68.79
Al_2O_3	20.26	20.26	20.17	19.21	19.94	20.26	20.41	20.36	20.12
CaO	0.18	0.30	0.25	2.18	0.43	0.24	0.21	0.12	0.26
FeO	0.23	0.19	0.22	0.13	0.13	0.17	0.08	0.02	0.05
SrO	0.03	0.08	0.07	0.07	0.03	0.08	0.07	0.05	0.08
BaO	0.04	0.01	0.03	0.00	0.01	0.00	0.01	0.02	0.02
Na_2O	11.65	11.69	9.91	10.93	11.66	11.81	11.57	11.88	10.25
K_2O	0.08	0.32	0.13	0.11	0.21	0.14	0.19	0.11	0.15
Total	101.07	101.38	98.95	98.54	101.92	101.38	101.48	101.55	99.71
Number of ions on the basis of 32 O. All Fe recalculated as Fe^{3+}.									
Si	11.874	11.852	11.968	11.785	11.936	11.865	11.882	11.885	11.991
Al	4.133	4.131	4.173	4.047	4.036	4.126	4.147	4.134	4.135
Fe	0.033	0.028	0.032	0.019	0.019	0.024	0.011	0.003	0.007
Ca	0.034	0.055	0.046	0.417	0.078	0.045	0.038	0.022	0.049
Sr	0.003	0.008	0.007	0.007	0.003	0.008	0.007	0.005	0.008
Ba	0.003	0.000	0.002	0.000	0.000	0.000	0.001	0.001	0.001
Na	3.909	3.918	3.374	3.787	3.883	3.955	3.865	3.969	3.464
K	0.019	0.069	0.029	0.024	0.046	0.030	0.041	0.024	0.033
Sum	20.007	20.062	19.631	20.087	20.002	20.053	19.992	20.043	19.687
Ab	0.987	0.969	0.978	0.896	0.969	0.981	0.980	0.988	0.977
An	0.009	0.014	0.013	0.099	0.020	0.011	0.010	0.005	0.014
Or	0.005	0.017	0.008	0.006	0.012	0.007	0.010	0.006	0.009

Table B.9. Electron microprobe analyses of amphibole from lamprophyres

probe run id	amph397-1	amph397-2	amph397-3	amph397-4	amph397-5	amphTR6e-1	amphTR6e-2	amphTR6e-3	amphTR6e-4	amphTR6e-5
sample	397	397	397	397	397	TR6A	TR6A	TR6A	TR6A	TR6A
rock name	L	L	L	L	L	O	O	O	O	O
SiO_2	54.15	54.80	54.11	55.03	52.59	52.64	52.79	55.17	54.78	54.72
TiO_2	0.04	0.06	0.03	0.01	0.03	0.01	0.03	0.03	0.02	0.00
Al_2O_3	1.46	1.70	1.78	1.61	2.41	2.05	2.49	0.69	0.39	1.35
MgO	16.84	16.40	15.92	16.17	15.62	14.57	14.71	15.16	13.77	15.28
CaO	12.35	12.11	12.19	12.33	11.94	12.34	12.43	12.59	12.47	12.55
MnO	0.26	0.25	0.31	0.29	0.27	0.34	0.34	0.29	0.22	0.32
FeO	12.32	12.61	12.89	12.76	13.74	14.42	14.04	14.27	16.32	14.30
Na_2O	0.30	0.37	0.40	0.36	0.48	0.18	0.22	0.06	0.04	0.12
K_2O	0.09	0.14	0.20	0.10	0.18	0.11	0.10	0.04	0.03	0.06
Total(true)	97.80	98.44	97.82	98.65	97.23	96.66	97.14	98.30	98.04	98.70
Number of ions on the basis of 23 O (H_2O-free). All Fe calculated as Fe^{2+}										
Si	7.777	7.812	7.790	7.834	7.664	7.738	7.706	7.933	7.971	7.845
Al	0.246	0.286	0.301	0.271	0.413	0.355	0.428	0.116	0.067	0.227
Ti	0.004	0.006	0.003	0.001	0.003	0.002	0.003	0.003	0.002	0.000
Mg	3.605	3.486	3.418	3.432	3.392	3.194	3.201	3.250	2.988	3.265
Ca	1.900	1.850	1.880	1.881	1.863	1.944	1.943	1.940	1.945	1.928
Mn	0.032	0.031	0.037	0.035	0.033	0.042	0.042	0.036	0.027	0.039
Fe^{2+}	1.480	1.503	1.552	1.519	1.674	1.773	1.714	1.716	1.985	1.714
Na	0.085	0.102	0.111	0.099	0.134	0.050	0.062	0.016	0.010	0.032
K	0.017	0.025	0.037	0.018	0.034	0.020	0.019	0.007	0.005	0.012
Cation distribution (cf. Yavuz, 1999)										
Si(T)	7.777	7.812	7.790	7.834	7.664	7.738	7.706	7.933	7.971	7.845
Al(T)	0.223	0.188	0.210	0.166	0.336	0.262	0.294	0.067	0.029	0.155
Al(C)	0.024	0.099	0.092	0.105	0.077	0.093	0.134	0.049	0.038	0.073
Ti(C)	0.004	0.006	0.003	0.001	0.003	0.002	0.003	0.003	0.002	0.000
Mg(C)	3.605	3.486	3.418	3.432	3.392	3.194	3.201	3.250	2.988	3.265
Fe2(C)	1.367	1.408	1.488	1.463	1.527	1.711	1.662	1.697	1.972	1.662
Mn(C)	0.000	0.000	0.000	0.000	0.000	0.000	0.000	0.000	0.000	0.000
Fe^{2+}(B)	0.113	0.094	0.064	0.056	0.146	0.061	0.052	0.019	0.013	0.052
Mn(B)	0.032	0.031	0.037	0.035	0.033	0.042	0.042	0.036	0.027	0.039
Ca(B)	1.900	1.850	1.880	1.881	1.863	1.944	1.943	1.940	1.945	1.928
Na(B)	0.000	0.025	0.018	0.028	0.000	0.000	0.000	0.006	0.010	0.000
Na(A)	0.085	0.077	0.093	0.071	0.134	0.050	0.062	0.010	0.000	0.032
K(A)	0.017	0.025	0.037	0.018	0.034	0.020	0.019	0.007	0.005	0.012
T	8	8	8	8	8	8	8	8	8	8
C	5	5	5	5	5	5	5	5	5	5
B	2.044	2.000	2.000	2.000	2.042	2.047	2.037	2.000	1.996	2.019
A	0.101	0.101	0.130	0.088	0.168	0.071	0.081	0.017	0.005	0.044
Sum	15.146	15.101	15.130	15.088	15.210	15.118	15.118	15.017	15.001	15.063
mg#	0.71	0.70	0.69	0.69	0.67	0.64	0.65	0.65	0.60	0.66

Table B.9. (Continued)

probe run id	amphTR6-1	amphTR6-2	amphTR6-3	amphTR6-4	amphTR6-5	hbl49-1137gr-1	hbl49-1137gr-2	hbl49-1137gr-4	px(?)49-113-1	px(?)49-113-2
sample	TR6A	TR6A	TR6A	TR6A	TR6A	49-113.7	49-113.7	49-113.7	49-113.7	49-113.7
rock name	L	L	L	L	L	L	L	L	L	L
SiO_2	54.37	52.90	52.29	54.85	54.58	54.80	55.27	54.56	53.14	52.92
TiO_2	0.02	0.05	0.05	0.05	0.02	0.04	0.03	0.03	0.05	0.12
Al_2O_3	1.28	2.75	2.52	2.26	1.93	1.32	1.42	1.52	2.60	2.83
MgO	16.71	15.36	14.12	16.23	15.22	16.64	16.04	16.59	16.04	16.44
CaO	12.66	12.34	12.04	11.88	12.28	12.92	12.49	12.90	12.73	12.58
MnO	0.31	0.32	0.31	0.35	0.32	0.27	0.27	0.23	0.20	0.24
FeO	12.28	13.46	15.03	12.44	13.81	11.69	12.10	11.79	11.20	10.61
Na_2O	0.12	0.25	0.24	0.16	0.14	0.21	0.24	0.23	0.40	0.48
K_2O	0.04	0.11	0.17	0.45	0.09	0.09	0.09	0.11	0.19	0.34
Total(true)	97.78	97.53	96.76	98.67	98.39	97.98	97.96	97.95	96.55	96.56
Number of ions on the basis of 23 O (H_2O-free). All Fe calculated as Fe^{2+}										
Si	7.807	7.667	7.699	7.796	7.824	7.833	7.894	7.807	7.709	7.666
Al	0.216	0.470	0.437	0.379	0.325	0.222	0.239	0.256	0.445	0.483
Ti	0.002	0.005	0.005	0.006	0.002	0.004	0.004	0.003	0.005	0.013
Mg	3.577	3.319	3.099	3.438	3.253	3.547	3.416	3.538	3.469	3.551
Ca	1.947	1.916	1.900	1.809	1.886	1.978	1.911	1.978	1.978	1.952
Mn	0.037	0.039	0.038	0.042	0.039	0.032	0.032	0.028	0.025	0.029
Fe^{2+}	1.475	1.631	1.850	1.479	1.655	1.397	1.445	1.411	1.359	1.285
Na	0.034	0.071	0.067	0.043	0.039	0.059	0.067	0.064	0.112	0.135
K	0.008	0.020	0.032	0.081	0.017	0.016	0.017	0.020	0.035	0.063
Cation distribution (cf. Yavuz, 1999)										
Si(T)	7.807	7.667	7.699	7.796	7.824	7.833	7.894	7.807	7.709	7.666
Al(T)	0.193	0.333	0.301	0.204	0.176	0.167	0.106	0.193	0.291	0.334
Al(C)	0.023	0.138	0.135	0.174	0.149	0.055	0.133	0.063	0.153	0.149
Ti(C)	0.002	0.005	0.005	0.006	0.002	0.004	0.004	0.003	0.005	0.013
Mg(C)	3.577	3.319	3.099	3.438	3.253	3.547	3.416	3.538	3.469	3.551
Fe2(C)	1.398	1.539	1.760	1.382	1.596	1.394	1.445	1.396	1.359	1.285
Mn(C)	0.000	0.000	0.000	0.000	0.000	0.000	0.003	0.000	0.013	0.002
Fe^{2+}(B)	0.077	0.092	0.090	0.097	0.059	0.003	0.000	0.014	0.000	0.000
Mn(B)	0.037	0.039	0.038	0.042	0.039	0.032	0.029	0.028	0.011	0.028
Ca(B)	1.947	1.916	1.900	1.809	1.886	1.978	1.911	1.978	1.978	1.952
Na(B)	0.000	0.000	0.000	0.043	0.016	0.000	0.059	0.000	0.010	0.020
Na(A)	0.034	0.071	0.067	0.000	0.022	0.059	0.008	0.064	0.102	0.115
K(A)	0.008	0.020	0.032	0.081	0.017	0.016	0.017	0.020	0.035	0.063
T	8	8	8	8	8	8	8	8	8	8
C	5	5	5	5	5	5	5	5	5	5
B	2.062	2.047	2.028	1.991	2.000	2.014	2.000	2.020	2.000	2.000
A	0.042	0.090	0.099	0.081	0.039	0.075	0.025	0.084	0.137	0.178
Sum	15.104	15.138	15.127	15.072	15.039	15.089	15.025	15.104	15.137	15.178
mg#	0.71	0.67	0.63	0.70	0.66	0.72	0.70	0.71	0.72	0.73

Table B.9. (Continued)

probe run id	px(?)49-113-3	px(?)49-113-4	px(?)49-113-5
sample	49-113.7	49-113.7	49-113.7
rock name	L	L	L
SiO_2	55.23	53.69	53.05
TiO_2	0.04	0.06	0.05
Al_2O_3	1.27	2.25	2.41
MgO	17.49	15.71	16.28
CaO	13.03	12.60	12.45
MnO	0.19	0.25	0.21
FeO	9.54	11.85	11.34
Na_2O	0.21	0.39	0.00
K_2O	0.07	0.17	0.17
Total(true)	97.07	96.97	95.96
Number of ions on the basis of 23 O (H_2O-free). All Fe calculated as Fe^{2+}			
Si	7.881	7.768	7.732
Al	0.214	0.384	0.414
Ti	0.004	0.007	0.005
Mg	3.721	3.388	3.537
Ca	1.992	1.953	1.944
Mn	0.023	0.031	0.026
Fe^{2+}	1.138	1.434	1.382
Na	0.058	0.109	0.000
K	0.013	0.031	0.032
Cation distribution (cf. Yavuz, 1999)			
Si(T)	7.881	7.768	7.732
Al(T)	0.119	0.232	0.268
Al(C)	0.094	0.151	0.146
Ti(C)	0.004	0.007	0.005
Mg(C)	3.721	3.388	3.537
Fe2(C)	1.138	1.434	1.312
Mn(C)	0.042	0.020	0.000
Fe^{2+}(B)	0.000	0.000	0.070
Mn(B)	0.000	0.011	0.026
Ca(B)	1.992	1.953	1.944
Na(B)	0.008	0.036	0.000
Na(A)	0.050	0.073	0.000
K(A)	0.013	0.031	0.032
T	8	8	8
C	5	5	5
B	2.000	2.000	2.040
A	0.063	0.104	0.032
Sum	15.063	15.104	15.072
mg#	0.77	0.70	0.72

Table B.10. Electron microprobe analyses of hydrothermal white mica

probe run id	fchs59-855-1	fchs59-855-2	fchs59-855-3	fchs59-855-4	mu547-1	mu547-10	mu547-2	mu547-3	mu547-4
sample	59-85.5	59-85.5	59-85.5	59-85.5	547	547	547	547	547
mineral	fuchsite	fuchsite	fuchsite	fuchsite	muscovite	muscovite	muscovite	muscovite	muscovite
assemblage	QSCP alteration	QSCP alteration	QSCP alteration	QSCP alteration	Au vein	Au vein	Au vein	Au vein	Au vein
SiO_2	50.26	49.05	49.64	49.77	46.22	45.20	43.82	44.88	45.70
TiO_2	0.59	0.70	0.52	0.65	0.06	0.02	0.15	0.03	0.07
Al_2O_3	30.74	30.24	30.46	30.67	34.11	32.56	33.24	31.77	32.07
Cr_2O_3	1.57	1.63	1.56	1.53	0.00	0.00	0.04	0.00	0.01
MgO	2.50	2.68	2.53	2.45	1.27	1.23	0.92	1.38	1.47
CaO	0.01	0.02	0.02	0.01	0.02	0.01	0.01	0.02	0.02
MnO	0.00	0.00	0.00	0.00	0.00	0.00	0.00	0.00	0.00
FeO	1.83	1.94	1.93	1.73	2.33	2.94	2.68	3.67	3.46
BaO	0.45	0.59	0.55	0.47	2.69	3.32	4.56	3.91	3.66
Na_2O	0.13	0.13	0.14	0.09	0.12	0.28	0.20	0.27	0.25
K_2O	9.69	8.95	9.60	9.96	9.64	9.68	9.03	9.03	8.77
F	0.70	0.54	0.80	0.65	0.03	0.23	0.12	0.25	0.25
Cl	0.00	0.00	0.01	0.00	0.00	0.01	0.01	0.01	0.00
Total (uncorrected)	98.48	96.47	97.75	97.99	96.48	95.48	94.76	95.20	95.74
"-O=F,Cl"	0.29	0.23	0.34	0.27	0.01	0.10	0.05	0.11	0.11
Total (corrected)	98.18	96.24	97.41	97.72	96.47	95.38	94.71	95.10	95.63
Number of ions based on 24 O, F, Cl									
Si	7.076	7.045	7.053	7.055	6.762	6.763	6.647	6.772	6.812
Al	5.101	5.118	5.101	5.123	5.881	5.741	5.942	5.649	5.634
Ti	0.062	0.075	0.056	0.070	0.007	0.002	0.017	0.003	0.008
Cr	0.175	0.185	0.175	0.171	0.000	0.000	0.005	0.000	0.001
Mg	0.525	0.575	0.535	0.518	0.276	0.275	0.208	0.310	0.327
Ca	0.001	0.002	0.003	0.001	0.003	0.001	0.001	0.003	0.004
Mn	0.000	0.000	0.000	0.000	0.000	0.000	0.000	0.000	0.000
Fe	0.215	0.233	0.229	0.205	0.285	0.368	0.340	0.463	0.431
Ba	0.025	0.033	0.030	0.026	0.154	0.194	0.271	0.231	0.214
Na	0.035	0.037	0.038	0.024	0.034	0.082	0.059	0.078	0.073
K	1.741	1.640	1.739	1.801	1.799	1.848	1.747	1.737	1.668
F	0.310	0.244	0.361	0.290	0.012	0.106	0.058	0.120	0.119
Cl	0.001	0.000	0.001	0.000	0.000	0.003	0.002	0.003	0.000
Sum	15.267	15.188	15.323	15.286	15.213	15.384	15.296	15.369	15.292
mg#	0.709	0.712	0.700	0.716	0.492	0.427	0.380	0.401	0.432

Table B.10. (Continued)

probe run id	mu547-5	mu547-6	mu547-7	mu547-8	mu547-9	src-579-1	src-579-10	src-579-11	src-579-13
sample	547	547	547	547	547	579	579	579	579
mineral	muscovite	muscovite	muscovite	muscovite	muscovite	sericite	sericite	sericite	sericite
assemblage	Au vein	Au vein	Au vein	Au vein	Au vein	Au vein	Au vein	Au vein	Au vein
SiO_2	44.73	46.20	45.30	48.69	44.66	52.18	51.72	51.89	51.76
TiO_2	0.07	0.05	0.10	0.07	0.01	0.00	0.38	0.36	0.93
Al_2O_3	33.07	33.08	32.21	34.40	32.95	35.30	31.74	31.99	32.31
Cr_2O_3	0.00	0.00	0.02	0.02	0.00	0.00	0.26	0.21	0.06
MgO	1.10	1.54	1.43	0.87	1.19	0.79	2.47	2.58	2.34
CaO	0.00	0.01	0.04	0.05	0.01	0.16	0.11	0.10	0.00
MnO	0.00	0.00	0.00	0.00	0.00	0.00	0.00	0.00	0.00
FeO	3.37	2.70	3.19	1.22	2.81	1.07	1.91	2.01	2.32
BaO	3.79	3.55	3.38	0.19	3.64	0.04	0.58	0.53	0.74
Na_2O	0.32	1.80	0.26	0.10	0.32	0.04	0.03	0.04	0.06
K_2O	9.15	9.22	9.02	10.28	9.24	7.71	7.58	6.08	6.17
F	0.26	0.25	0.11	0.16	0.17	0.22	0.55	0.51	0.57
Cl	0.00	0.00	0.01	0.01	0.01	0.02	0.01	0.01	0.01
Total (uncorrected)	95.86	98.40	95.08	96.07	95.01	97.53	97.34	96.31	97.27
"-O=F,Cl"	0.11	0.11	0.05	0.07	0.08	0.10	0.23	0.22	0.24
Total (corrected)	95.75	98.29	95.02	96.00	94.94	97.43	97.11	96.09	97.03
Number of ions based on 24 O, F, Cl									
Si	6.687	6.724	6.792	6.968	6.714	7.183	7.225	7.253	7.192
Al	5.827	5.672	5.692	5.803	5.838	5.727	5.226	5.270	5.291
Ti	0.008	0.005	0.011	0.008	0.001	0.000	0.040	0.038	0.097
Cr	0.000	0.000	0.002	0.002	0.000	0.000	0.029	0.023	0.007
Mg	0.245	0.334	0.319	0.186	0.267	0.162	0.514	0.538	0.485
Ca	0.000	0.002	0.006	0.008	0.002	0.024	0.016	0.015	0.000
Mn	0.000	0.000	0.000	0.000	0.000	0.000	0.000	0.000	0.000
Fe	0.422	0.328	0.400	0.146	0.353	0.123	0.223	0.235	0.270
Ba	0.222	0.202	0.199	0.010	0.215	0.002	0.032	0.029	0.040
Na	0.092	0.508	0.075	0.028	0.094	0.011	0.008	0.011	0.016
K	1.744	1.711	1.724	1.876	1.772	1.354	1.351	1.084	1.094
F	0.124	0.114	0.054	0.072	0.082	0.096	0.243	0.225	0.250
Cl	0.000	0.001	0.003	0.003	0.003	0.005	0.002	0.002	0.002
Sum	15.371	15.602	15.278	15.112	15.341	14.686	14.910	14.724	14.744
mg#	0.368	0.504	0.444	0.560	0.431	0.568	0.697	0.696	0.643

Table B.10. (Continued)

probe run id	src-579-14	src-579-15	src-579-2	src-579-3	src-579-5	src-579-6	src-579-7	src-579-8	src-59-708-12
sample	579	579	579	579	579	579	579	579	59-70.8
mineral	sericite	sericite	sericite	sericite	sericite	sericite	sericite	sericite	sericite
assemblage	Au vein	Au vein	Au vein	Au vein	Au vein	Au vein	Au vein	Au vein	Au vein
SiO_2	51.80	51.55	51.19	51.98	51.38	50.10	51.92	51.09	52.06
TiO_2	0.59	0.63	0.06	0.53	1.07	0.02	0.55	0.36	0.89
Al_2O_3	30.96	31.60	37.07	32.08	31.81	37.07	32.03	30.32	30.54
Cr_2O_3	0.48	0.19	0.02	0.50	0.79	0.03	0.03	0.70	0.07
MgO	2.62	2.64	0.68	2.56	2.23	0.45	2.24	2.94	2.47
CaO	0.09	0.02	0.09	0.01	0.07	0.11	0.04	0.02	0.06
MnO	0.00	0.00	0.00	0.00	0.00	0.00	0.00	0.00	0.00
FeO	3.59	2.08	0.76	2.42	2.60	0.82	2.49	2.78	4.43
BaO	0.61	0.72	0.02	0.60	0.78	0.05	0.68	0.60	0.37
Na_2O	0.05	0.05	0.03	0.08	0.04	0.05	0.05	0.06	0.03
K_2O	5.86	6.58	6.73	6.07	5.81	7.07	5.81	5.39	6.22
F	0.62	0.54	0.13	0.56	0.49	0.21	0.54	0.77	0.58
Cl	0.00	0.00	0.00	0.00	0.00	0.01	0.00	0.00	0.01
Total (uncorrected)	97.27	96.60	96.78	97.39	97.07	95.99	96.38	95.03	97.73
"-O=F,Cl"	0.26	0.23	0.05	0.24	0.21	0.09	0.23	0.32	0.25
Total (corrected)	97.01	96.37	96.73	97.15	96.86	95.90	96.15	94.71	97.48
Number of ions based on 24 O, F, Cl									
Si	7.236	7.226	7.048	7.212	7.172	6.983	7.259	7.263	7.262
Al	5.097	5.220	6.015	5.245	5.233	6.089	5.277	5.080	5.021
Ti	0.062	0.066	0.006	0.055	0.112	0.002	0.058	0.038	0.093
Cr	0.053	0.021	0.002	0.055	0.087	0.003	0.003	0.079	0.008
Mg	0.546	0.552	0.140	0.530	0.464	0.094	0.467	0.623	0.514
Ca	0.013	0.003	0.013	0.001	0.010	0.016	0.006	0.003	0.009
Mn	0.000	0.000	0.000	0.000	0.000	0.000	0.000	0.000	0.000
Fe	0.419	0.244	0.088	0.281	0.303	0.096	0.291	0.330	0.517
Ba	0.033	0.040	0.001	0.033	0.043	0.003	0.037	0.033	0.020
Na	0.014	0.014	0.008	0.022	0.011	0.014	0.014	0.017	0.008
K	1.044	1.177	1.182	1.074	1.034	1.257	1.036	0.977	1.107
F	0.274	0.239	0.057	0.246	0.216	0.093	0.239	0.346	0.256
Cl	0.000	0.000	0.000	0.000	0.000	0.002	0.000	0.000	0.002
Sum	14.792	14.801	14.560	14.753	14.687	14.651	14.687	14.790	14.817
mg#	0.565	0.694	0.615	0.654	0.605	0.495	0.616	0.653	0.499

Table B.10. (Continued)

probe run id	src-59-708-14	src-59-708-2	src-59-708-4	src-59-708-6	src-59-708-8	src-59-708-9	mu601-1	mu601-10	mu601-11
sample	59-70.8	59-70.8	59-70.8	59-70.8	59-70.8	59-70.8	601	601	601
mineral	sericite	sericite	sericite	sericite	sericite	sericite	muscovite	muscovite	muscovite
assemblage	Au vein	Au vein	Au vein	Au vein	Au vein	Au vein	Au vein	Au vein	Au vein
SiO_2	52.25	52.31	52.21	52.61	52.47	52.62	47.44	47.22	47.65
TiO_2	0.76	0.08	0.05	0.05	0.45	0.36	0.22	0.23	0.12
Al_2O_3	30.78	33.09	32.60	32.71	30.15	30.54	33.92	34.60	34.34
Cr_2O_3	0.06	0.00	0.00	0.00	0.06	0.07	0.00	0.02	0.01
MgO	2.59	2.41	2.72	2.68	2.78	2.79	0.98	0.71	1.23
CaO	0.02	0.02	0.01	0.04	0.13	0.05	0.02	0.02	0.01
MnO	0.00	0.00	0.00	0.00	0.00	0.00	0.00	0.00	0.01
FeO	4.48	1.32	2.05	1.68	3.69	3.33	3.09	3.25	1.78
BaO	0.32	0.33	0.74	0.61	0.39	0.38	1.06	0.71	0.94
Na_2O	0.05	0.03	0.04	0.05	0.02	0.04	0.57	0.63	0.35
K_2O	5.91	7.40	7.34	7.15	6.65	6.72	9.49	9.15	10.10
F	0.53	0.55	0.52	0.73	0.53	0.66	0.23	0.13	0.17
Cl	0.01	0.00	0.01	0.00	0.00	0.00	0.00	0.01	0.00
Total (uncorrected)	97.76	97.54	98.29	98.31	97.32	97.56	97.01	96.67	96.70
"-O=F,Cl"	0.23	0.23	0.22	0.31	0.22	0.28	0.10	0.06	0.07
Total (corrected)	97.53	97.31	98.07	98.00	97.10	97.28	96.91	96.61	96.63
Number of ions based on 24 O, F, Cl									
Si	7.268	7.228	7.212	7.233	7.338	7.327	6.833	6.798	6.850
Al	5.046	5.388	5.307	5.300	4.969	5.011	5.759	5.870	5.817
Ti	0.080	0.008	0.005	0.005	0.047	0.038	0.024	0.025	0.013
Cr	0.007	0.000	0.000	0.000	0.007	0.008	0.000	0.002	0.001
Mg	0.537	0.496	0.560	0.549	0.580	0.579	0.210	0.153	0.263
Ca	0.003	0.003	0.001	0.006	0.019	0.007	0.003	0.003	0.001
Mn	0.000	0.000	0.000	0.000	0.000	0.000	0.000	0.000	0.001
Fe	0.521	0.153	0.237	0.193	0.432	0.388	0.372	0.391	0.214
Ba	0.017	0.018	0.040	0.033	0.021	0.021	0.060	0.040	0.053
Na	0.013	0.008	0.011	0.013	0.005	0.011	0.158	0.177	0.098
K	1.049	1.304	1.293	1.254	1.186	1.194	1.744	1.681	1.852
F	0.233	0.240	0.227	0.317	0.234	0.291	0.105	0.060	0.078
Cl	0.002	0.000	0.002	0.000	0.000	0.000	0.000	0.003	0.000
Sum	14.775	14.846	14.896	14.904	14.840	14.873	15.267	15.202	15.241
mg#	0.508	0.765	0.703	0.740	0.573	0.599	0.361	0.281	0.552

Table B.10. (Continued)

probe run id	mu601-2	mu601-3	mu601-4	mu601-5	mu601-6	mu601-7	mu601-8	mu601-9	MuAD2-1
sample	601	601	601	601	601	601	601	601	AD2A
mineral	muscovite	muscovite	muscovite	muscovite	muscovite	muscovite	muscovite	muscovite	muscovite
assemblage	Au vein	Au vein	Au vein	Au vein	Au vein	Au vein	Au vein	Au vein	Au vein
SiO_2	45.77	45.93	47.29	46.03	47.21	48.35	46.94	48.78	46.52
TiO_2	0.36	0.38	0.29	0.20	0.30	0.12	0.20	0.13	0.00
Al_2O_3	34.30	33.94	33.91	33.71	34.38	35.84	34.75	35.03	34.77
Cr_2O_3	0.01	0.00	0.01	0.01	0.01	0.00	0.01	0.03	0.00
MgO	0.64	0.84	0.90	0.67	0.84	0.82	0.00	1.14	1.31
CaO	0.01	0.01	0.01	0.00	0.00	0.04	0.04	0.02	0.06
MnO	0.00	0.02	0.00	0.00	0.00	0.00	0.00	0.00	0.02
FeO	2.59	2.66	3.18	2.94	2.92	2.12	2.58	1.49	1.60
BaO	1.19	1.19	1.06	0.83	1.01	0.29	1.05	0.12	2.43
Na_2O	0.60	0.56	0.53	0.66	0.29	0.84	0.51	0.80	0.29
K_2O	9.76	9.43	9.63	9.70	9.82	9.25	9.26	9.22	9.44
F	0.18	0.05	0.08	0.11	0.24	0.21	0.15	0.16	0.40
Cl	0.00	0.01	0.00	0.00	0.00	0.02	0.00	0.01	0.02
Total (uncorrected)	95.42	95.01	96.88	94.87	97.02	97.90	95.48	96.92	96.84
"-O=F,Cl"	0.08	0.02	0.03	0.05	0.10	0.09	0.06	0.07	0.17
Total (corrected)	95.34	94.98	96.85	94.82	96.92	97.81	95.42	96.85	96.67
Number of ions based on 24 O, F, Cl									
Si	6.721	6.762	6.830	6.787	6.798	6.808	6.833	6.901	6.735
Al	5.937	5.888	5.772	5.859	5.835	5.947	5.962	5.841	5.932
Ti	0.040	0.042	0.031	0.022	0.032	0.013	0.021	0.013	0.000
Cr	0.002	0.000	0.001	0.002	0.001	0.000	0.001	0.003	0.000
Mg	0.141	0.184	0.195	0.147	0.180	0.172	0.000	0.241	0.283
Ca	0.002	0.001	0.001	0.000	0.000	0.007	0.006	0.003	0.010
Mn	0.000	0.003	0.000	0.000	0.000	0.000	0.000	0.000	0.002
Fe	0.318	0.327	0.384	0.363	0.351	0.250	0.314	0.176	0.194
Ba	0.069	0.069	0.060	0.048	0.057	0.016	0.060	0.006	0.138
Na	0.170	0.158	0.148	0.189	0.081	0.229	0.145	0.220	0.080
K	1.828	1.772	1.774	1.824	1.803	1.661	1.719	1.664	1.743
F	0.085	0.024	0.036	0.053	0.110	0.094	0.070	0.069	0.184
Cl	0.000	0.001	0.001	0.000	0.000	0.004	0.000	0.003	0.004
Sum	15.311	15.230	15.232	15.293	15.249	15.200	15.132	15.141	15.304
mg#	0.307	0.360	0.336	0.288	0.339	0.408	0.000	0.578	0.593

Table B.10. (Continued)

probe run id	MuAD2A-1	MuAD2A-2	MuAD2B-1	MuAD2B-2	mu532-1	mu532-10	mu532-11	mu532-12	mu532-2
sample	AD2A	AD2A	AD2B	AD2B	532	532	532	532	532
mineral	muscovite	muscovite	muscovite	muscovite	muscovite	muscovite	muscovite	muscovite	muscovite
assemblage	Au vein	Au vein	Au vein	Au vein	propylitic vein	propylitic vein	propylitic vein	propylitic vein	propylitic vein
SiO_2	46.94	47.05	47.71	47.57	47.64	46.58	46.87	47.23	47.78
TiO_2	0.01	0.28	0.00	0.01	0.25	0.42	0.18	0.22	0.32
Al_2O_3	34.26	33.64	34.29	33.19	28.67	28.37	28.65	28.87	28.61
Cr_2O_3	0.00	0.01	0.00	0.00	0.03	0.02	0.00	0.01	0.02
MgO	1.51	1.66	1.43	1.71	2.07	2.86	1.68	2.14	1.51
CaO	0.00	0.00	0.01	0.01	0.00	0.00	0.02	0.01	0.02
MnO	0.00	0.00	0.00	0.00	0.00	0.00	0.00	0.00	0.00
FeO	1.70	1.64	1.65	1.64	6.22	7.02	7.12	6.04	6.87
BaO	2.02	2.38	2.13	2.03	1.07	1.13	1.24	1.22	1.13
Na_2O	0.27	0.27	0.17	0.25	0.17	0.15	0.07	0.18	0.15
K_2O	9.94	9.91	9.71	9.91	10.53	10.15	10.08	10.16	10.18
F	0.46	0.45	0.94	0.49	0.09	0.04	0.10	0.01	0.00
Cl	0.00	0.00	0.01	0.00	0.00	0.01	0.00	0.00	0.00
Total (uncorrected)	97.10	97.28	98.06	96.79	96.74	96.75	96.00	96.10	96.59
"-O=F,Cl"	0.19	0.19	0.40	0.20	0.04	0.02	0.04	0.01	0.00
Total (corrected)	96.90	97.09	97.66	96.59	96.70	96.73	95.96	96.09	96.59
Number of ions based on 24 O, F, Cl									
Si	6.777	6.800	6.805	6.883	7.054	6.934	7.019	7.030	7.090
Al	5.829	5.729	5.765	5.659	5.002	4.977	5.056	5.063	5.002
Ti	0.001	0.030	0.000	0.001	0.028	0.046	0.020	0.025	0.036
Cr	0.000	0.001	0.000	0.000	0.003	0.003	0.000	0.002	0.003
Mg	0.324	0.358	0.305	0.368	0.458	0.635	0.374	0.476	0.334
Ca	0.001	0.000	0.002	0.002	0.000	0.000	0.004	0.002	0.002
Mn	0.000	0.000	0.000	0.000	0.000	0.000	0.000	0.000	0.000
Fe	0.205	0.198	0.197	0.198	0.770	0.873	0.891	0.752	0.853
Ba	0.114	0.135	0.119	0.115	0.062	0.066	0.073	0.071	0.066
Na	0.076	0.075	0.047	0.069	0.049	0.043	0.020	0.052	0.043
K	1.830	1.828	1.767	1.829	1.989	1.928	1.926	1.929	1.926
F	0.210	0.205	0.426	0.222	0.041	0.019	0.045	0.006	0.002
Cl	0.000	0.000	0.001	0.000	0.001	0.001	0.001	0.001	0.000
Sum	15.366	15.359	15.433	15.347	15.457	15.525	15.429	15.407	15.357
mg#	0.613	0.644	0.607	0.650	0.373	0.421	0.296	0.388	0.282

Table B.10. (Continued)

probe run id	mu532-3	mu532-4	mu532-5	mu532-6	mu532-7	mu532-8	mu532-9	fchs669-3-2	fchs669-3-4
sample	532	532	532	532	532	532	532	669-3	669-3
mineral	muscovite	muscovite	muscovite	muscovite	muscovite	muscovite	muscovite	fuchsite	fuchsite
assemblage	propylitic vein	propylitic vein	propylitic vein	propylitic vein	propylitic vein	propylitic vein	propylitic vein	fault zone	fault zone
SiO_2	47.41	48.07	46.55	48.09	46.14	47.01	48.20	48.61	48.90
TiO_2	0.24	0.29	0.43	0.16	0.30	0.24	0.28	0.07	0.10
Al_2O_3	28.82	29.12	28.58	29.19	28.48	29.58	28.35	36.99	35.46
Cr_2O_3	0.03	0.02	0.02	0.01	0.01	0.00	0.02	1.30	1.38
MgO	1.50	1.46	2.26	1.53	2.14	1.29	2.12	0.71	0.97
CaO	0.02	0.03	0.01	0.00	0.07	0.02	0.04	0.01	0.05
MnO	0.00	0.04	0.00	0.00	0.00	0.01	0.01	0.00	0.00
FeO	7.55	6.59	7.28	6.41	6.95	6.38	6.56	0.24	0.29
BaO	1.09	0.84	1.15	0.49	0.88	0.63	0.85	0.00	0.07
Na_2O	0.09	0.12	0.17	0.11	0.13	0.13	0.11	0.59	0.44
K_2O	9.85	9.80	9.96	10.30	10.18	10.30	9.56	8.78	8.75
F	0.00	0.06	0.06	0.05	0.02	0.08	0.00	0.10	0.07
Cl	0.00	0.00	0.00	0.01	0.01	0.00	0.00	0.01	0.00
Total (uncorrected)	96.59	96.43	96.45	96.34	95.30	95.67	96.10	97.41	96.48
"-O=F,Cl"	0.00	0.03	0.03	0.02	0.01	0.03	0.00	0.04	0.03
Total (corrected)	96.59	96.41	96.42	96.31	95.29	95.63	96.10	97.36	96.45
Number of ions based on 24 O, F, Cl									
Si	7.045	7.095	6.948	7.098	6.957	7.006	7.132	6.789	6.897
Al	5.047	5.065	5.026	5.077	5.062	5.196	4.944	6.088	5.894
Ti	0.026	0.032	0.048	0.018	0.034	0.027	0.032	0.008	0.011
Cr	0.004	0.003	0.002	0.001	0.001	0.000	0.002	0.143	0.154
Mg	0.332	0.320	0.502	0.336	0.480	0.286	0.468	0.147	0.203
Ca	0.003	0.005	0.001	0.000	0.012	0.002	0.006	0.001	0.008
Mn	0.000	0.004	0.000	0.000	0.000	0.002	0.001	0.000	0.000
Fe	0.938	0.813	0.909	0.791	0.876	0.795	0.811	0.028	0.034
Ba	0.063	0.048	0.067	0.028	0.052	0.037	0.049	0.000	0.004
Na	0.027	0.034	0.049	0.031	0.037	0.038	0.032	0.161	0.119
K	1.866	1.845	1.895	1.938	1.958	1.959	1.805	1.564	1.574
F	0.000	0.028	0.030	0.022	0.007	0.036	0.000	0.044	0.032
Cl	0.000	0.000	0.001	0.002	0.002	0.000	0.000	0.002	0.001
Sum	15.351	15.293	15.478	15.343	15.479	15.384	15.282	14.974	14.931
mg#	0.261	0.283	0.356	0.298	0.354	0.264	0.366	0.840	0.855

Table B.10. (Continued)

probe run id	fchs669-3-5	fchs675-2-1	fchs675-2-2	fchs675-2-3	fchs675-2-4	fchs675-2-5	fchs675-2-6	fchs675-2-6a	mu617-1
sample	669-3	675-2	675-2	675-2	675-2	675-2	675-2	675-2	617
mineral	fuchsite	fuchsite	fuchsite	fuchsite	fuchsite	fuchsite	fuchsite	fuchsite	muscovite
assemblage	fault zone	fault zone	fault zone	fault zone	fault zone	fault zone	fault zone	fault zone	barren vein
SiO_2	48.26	50.55	50.04	49.76	49.40	50.14	48.83	51.03	47.24
TiO_2	0.09	0.06	0.24	0.21	0.12	0.23	0.10	0.35	0.09
Al_2O_3	37.61	32.16	30.87	30.17	33.17	31.08	35.18	28.15	34.28
Cr_2O_3	1.12	0.71	1.00	1.60	1.58	1.72	1.70	2.49	0.01
MgO	0.39	2.04	1.89	2.50	1.24	2.06	0.82	2.97	0.20
CaO	0.01	0.00	0.00	0.00	0.01	0.01	0.01	0.01	0.02
MnO	0.00	0.01	0.01	0.00	0.00	0.00	0.00	0.00	0.00
FeO	0.11	2.08	3.37	3.50	2.45	2.87	1.07	3.10	2.13
BaO	0.04	0.10	0.09	0.16	0.03	0.10	0.01	0.11	0.00
Na_2O	0.78	0.20	0.23	0.03	0.32	0.04	0.38	0.07	0.25
K_2O	9.33	9.78	9.61	10.03	10.02	9.38	10.06	8.67	9.57
F	0.01	0.00	0.28	0.00	0.00	0.30	0.10	0.15	0.09
Cl	0.00	0.00	0.00	0.00	0.01	0.01	0.00	0.00	0.00
Total (uncorrected)	97.75	97.69	97.64	97.97	98.35	97.92	98.25	97.10	93.88
"-O=F,Cl"	0.00	0.00	0.12	0.00	0.00	0.13	0.04	0.06	0.04
Total (corrected)	97.74	97.69	97.52	97.97	98.35	97.79	98.21	97.04	93.85
Number of ions based on 24 O, F, Cl									
Si	6.739	7.130	7.120	7.100	6.969	7.095	6.851	7.281	6.921
Al	6.189	5.346	5.176	5.072	5.515	5.183	5.816	4.733	5.918
Ti	0.010	0.007	0.025	0.023	0.013	0.024	0.010	0.037	0.010
Cr	0.123	0.080	0.112	0.181	0.177	0.192	0.189	0.281	0.001
Mg	0.080	0.429	0.402	0.532	0.261	0.434	0.170	0.632	0.044
Ca	0.001	0.000	0.000	0.000	0.001	0.001	0.002	0.001	0.003
Mn	0.000	0.001	0.001	0.000	0.000	0.000	0.000	0.000	0.000
Fe	0.013	0.245	0.401	0.418	0.289	0.340	0.125	0.370	0.261
Ba	0.002	0.006	0.005	0.009	0.002	0.006	0.001	0.006	0.000
Na	0.212	0.056	0.065	0.007	0.089	0.011	0.104	0.020	0.070
K	1.662	1.759	1.745	1.825	1.804	1.693	1.800	1.577	1.789
F	0.003	0.000	0.128	0.000	0.000	0.135	0.043	0.067	0.040
Cl	0.001	0.000	0.000	0.001	0.001	0.002	0.000	0.000	0.001
Sum	15.035	15.058	15.179	15.167	15.119	15.114	15.111	15.007	15.059
mg#	0.864	0.636	0.501	0.560	0.474	0.561	0.577	0.631	0.144

Table B.10. (Continued)

probe run id	mu617-10	mu617-2	mu617-3	mu617-4	mu617-5	mu617-6	mu617-7	mu617-8	mu617-9
sample	617	617	617	617	617	617	617	617	617
mineral	muscovite	muscovite	muscovite	muscovite	muscovite	muscovite	muscovite	muscovite	muscovite
assemblage	barren vein	barren vein	barren vein	barren vein	barren vein	barren vein	barren vein	barren vein	barren vein
SiO_2	47.39	49.01	48.37	48.22	48.13	48.91	48.78	47.47	47.24
TiO_2	0.10	0.16	0.09	0.14	0.18	0.06	0.15	0.14	0.11
Al_2O_3	34.91	34.11	35.35	36.50	35.05	36.10	35.74	36.15	36.31
Cr_2O_3	0.02	0.00	0.01	0.03	0.00	0.00	0.00	0.02	0.01
MgO	0.28	1.11	0.37	0.31	0.42	0.71	0.61	0.45	0.31
CaO	0.01	0.02	0.00	0.01	0.00	0.05	0.02	0.01	0.05
MnO	0.01	0.00	0.01	0.00	0.00	0.01	0.00	0.04	0.00
FeO	2.74	2.76	2.53	1.87	2.13	1.79	2.16	1.84	1.96
BaO	0.07	0.06	0.23	0.20	0.20	0.11	0.14	0.05	0.10
Na_2O	0.28	0.26	0.21	0.23	0.31	0.34	0.25	0.22	0.17
K_2O	9.54	9.62	10.10	10.18	10.16	9.30	9.41	9.85	9.60
F	0.00	0.20	0.00	0.04	0.00	0.10	0.03	0.08	0.04
Cl	0.01	0.00	0.01	0.00	0.00	0.00	0.00	0.00	0.01
Total (uncorrected)	95.35	97.30	97.26	97.73	96.60	97.48	97.28	96.31	95.90
"-O=F,Cl"	0.00	0.09	0.00	0.02	0.00	0.04	0.01	0.03	0.02
Total (corrected)	95.35	97.21	97.26	97.71	96.60	97.44	97.27	96.28	95.88
Number of ions based on 24 O, F, Cl									
Si	6.861	6.949	6.878	6.804	6.885	6.873	6.885	6.783	6.773
Al	5.956	5.700	5.924	6.068	5.909	5.977	5.945	6.087	6.136
Ti	0.011	0.017	0.010	0.015	0.020	0.006	0.016	0.015	0.012
Cr	0.002	0.000	0.001	0.003	0.000	0.000	0.000	0.002	0.001
Mg	0.060	0.234	0.078	0.065	0.090	0.149	0.128	0.095	0.067
Ca	0.002	0.003	0.000	0.002	0.000	0.007	0.003	0.002	0.007
Mn	0.001	0.000	0.001	0.000	0.000	0.001	0.000	0.004	0.000
Fe	0.332	0.327	0.301	0.220	0.254	0.210	0.255	0.219	0.235
Ba	0.004	0.003	0.013	0.011	0.011	0.006	0.008	0.003	0.005
Na	0.078	0.071	0.058	0.063	0.087	0.094	0.070	0.060	0.046
K	1.763	1.739	1.831	1.831	1.855	1.667	1.694	1.794	1.756
F	0.001	0.091	0.000	0.019	0.000	0.046	0.013	0.036	0.019
Cl	0.001	0.000	0.001	0.000	0.001	0.000	0.000	0.001	0.001
Sum	15.071	15.135	15.095	15.102	15.112	15.036	15.015	15.102	15.059
mg#	0.154	0.418	0.205	0.228	0.262	0.415	0.334	0.302	0.222

Table B.10. (Continued)

probe run id	mu659-1	mu659-10	mu659-11	mu659-2	mu659-3	mu659-4	mu659-5	mu659-6	mu659-7
sample	659	659	659	659	659	659	659	659	659
mineral	muscovite	muscovite	muscovite	muscovite	muscovite	muscovite	muscovite	muscovite	muscovite
assemblage	barren vein	barren vein	barren vein	barren vein	barren vein	barren vein	barren vein	barren vein	barren vein
SiO_2	48.12	48.39	49.05	50.05	48.15	46.70	49.10	49.11	47.48
TiO_2	0.05	0.00	0.49	0.10	0.02	0.00	0.04	0.33	0.44
Al_2O_3	34.69	34.15	32.81	30.87	34.58	35.42	34.55	34.27	32.93
Cr_2O_3	0.01	0.00	0.01	0.00	0.03	0.00	0.00	0.04	0.00
MgO	1.22	1.51	1.94	2.50	1.21	0.90	1.27	1.63	2.00
CaO	0.03	0.00	0.01	0.00	0.03	0.02	0.02	0.00	0.04
MnO	0.00	0.01	0.00	0.00	0.00	0.00	0.04	0.02	0.00
FeO	1.30	1.52	1.79	2.44	1.34	0.97	1.43	1.42	1.98
BaO	0.76	0.60	0.29	0.58	0.74	0.73	0.56	0.34	0.36
Na_2O	0.24	0.19	0.25	0.00	0.21	0.66	0.23	0.26	0.23
K_2O	9.71	10.15	10.61	10.36	9.43	9.97	9.75	9.95	9.20
F	0.08	0.00	0.10	0.12	0.07	0.10	0.10	0.08	0.00
Cl	0.01	0.00	0.00	0.00	0.01	0.00	0.00	0.00	0.01
Total (uncorrected)	96.20	96.52	97.33	97.02	95.78	95.47	97.08	97.44	94.66
"-O=F,Cl"	0.04	0.00	0.04	0.05	0.03	0.04	0.04	0.03	0.00
Total (corrected)	96.16	96.52	97.28	96.97	95.75	95.43	97.03	97.41	94.66
Number of ions based on 24 O, F, Cl									
Si	6.898	6.930	6.986	7.167	6.918	6.767	6.961	6.940	6.917
Al	5.861	5.765	5.507	5.209	5.855	6.048	5.773	5.707	5.653
Ti	0.005	0.000	0.052	0.011	0.002	0.000	0.004	0.035	0.048
Cr	0.001	0.000	0.001	0.000	0.003	0.000	0.000	0.004	0.000
Mg	0.260	0.322	0.411	0.533	0.258	0.194	0.268	0.344	0.434
Ca	0.004	0.000	0.002	0.000	0.004	0.003	0.002	0.000	0.006
Mn	0.000	0.001	0.000	0.000	0.000	0.000	0.004	0.003	0.000
Fe	0.155	0.183	0.213	0.292	0.161	0.117	0.169	0.168	0.241
Ba	0.042	0.034	0.016	0.032	0.041	0.042	0.031	0.019	0.021
Na	0.068	0.051	0.068	0.000	0.057	0.187	0.062	0.072	0.064
K	1.775	1.855	1.927	1.893	1.729	1.843	1.764	1.794	1.709
F	0.037	0.000	0.046	0.053	0.030	0.047	0.046	0.034	0.000
Cl	0.001	0.000	0.000	0.000	0.003	0.000	0.000	0.000	0.001
Sum	15.107	15.140	15.229	15.191	15.060	15.247	15.085	15.119	15.095
mg#	0.626	0.638	0.659	0.646	0.617	0.624	0.614	0.672	0.643

Table B.10. (Continued)

probe run id	mu659-8	mu659-9
sample	659	659
mineral	muscovite	muscovite
assemblage	barren vein	barren vein
SiO_2	47.42	47.26
TiO_2	0.01	0.02
Al_2O_3	36.45	37.62
Cr_2O_3	0.00	0.02
MgO	0.63	0.32
CaO	0.00	0.01
MnO	0.00	0.00
FeO	0.71	0.54
BaO	0.78	0.99
Na_2O	0.30	0.33
K_2O	9.91	10.00
F	0.04	0.00
Cl	0.00	0.00
Total (uncorrected)	96.25	97.10
"-O=F,Cl"	0.02	0.00
Total (corrected)	96.23	97.10
Number of ions based on 24 O, F, Cl		
Si	6.782	6.708
Al	6.143	6.293
Ti	0.002	0.002
Cr	0.000	0.002
Mg	0.135	0.067
Ca	0.000	0.001
Mn	0.000	0.000
Fe	0.085	0.064
Ba	0.044	0.055
Na	0.082	0.091
K	1.808	1.811
F	0.018	0.000
Cl	0.000	0.000
Sum	15.099	15.093
mg#	0.612	0.510

Table B.11. Electron microprobe analyses of hydrothermal biotite

probe run id	btA23	btA23-10	btA23-11	btA23-12	btA23-13	btA23-14	btA23-2	btA23-3	btA23-4	btA23-5
sample	A23	A23	A23	A23	A23	A23	A23	A23	A23	A23
host rock	syenite	syenite	syenite	syenite	syenite	syenite	syenite	syenite	syenite	syenite
SiO_2	37.26	37.93	37.75	38.29	38.47	39.20	38.74	39.53	37.92	38.09
TiO_2	2.15	2.08	2.09	1.86	2.33	2.36	2.16	2.03	2.18	2.12
Al_2O_3	13.69	13.73	13.90	14.37	14.00	13.42	13.55	13.11	13.33	13.76
Cr_2O_3	0.01	0.18	0.24	0.07	0.00	0.00	0.04	0.04	0.10	0.08
MgO	13.93	14.29	13.88	14.54	14.57	15.11	14.71	15.18	14.17	13.68
CaO	0.01	0.02	0.02	0.02	0.01	0.03	0.03	0.03	0.03	0.09
MnO	0.18	0.11	0.09	0.06	0.12	0.15	0.17	0.11	0.11	0.14
FeO	16.28	16.24	16.31	15.65	15.26	14.92	16.00	14.94	16.24	16.36
BaO	0.00	0.00	0.00	0.00	0.00	0.00	0.00	0.00	0.00	0.00
Na_2O	0.05	0.10	0.07	0.06	0.06	0.05	0.07	0.05	0.03	0.05
K_2O	9.91	9.99	10.09	10.09	10.03	10.04	9.94	9.82	10.11	9.72
F	2.27	2.42	2.31	2.43	2.22	2.56	2.44	2.87	2.25	2.01
Cl	0.00	0.01	0.00	0.00	0.00	0.00	0.01	0.00	0.01	0.01
Total (uncorrected)	95.74	97.10	96.75	97.44	97.07	97.84	97.86	97.71	96.48	96.11
"-O=F,Cl"	0.96	1.02	0.97	1.02	0.93	1.08	1.03	1.21	0.95	0.85
Total (corrected)	94.78	96.08	95.78	96.42	96.14	96.76	96.83	96.50	95.53	95.26
Number of ions based on 24 O, F, Cl										
Si	6.105	6.119	6.118	6.125	6.165	6.217	6.178	6.265	6.163	6.197
Al	2.644	2.610	2.655	2.709	2.644	2.508	2.547	2.449	2.553	2.638
Ti	0.265	0.252	0.255	0.224	0.281	0.282	0.259	0.242	0.266	0.259
Cr	0.001	0.023	0.031	0.009	0.000	0.000	0.005	0.005	0.013	0.010
Mg	3.403	3.437	3.354	3.467	3.481	3.572	3.497	3.587	3.433	3.318
Ca	0.002	0.003	0.003	0.003	0.002	0.005	0.005	0.005	0.005	0.016
Mn	0.025	0.015	0.012	0.008	0.016	0.020	0.023	0.015	0.015	0.019
Fe	2.231	2.191	2.210	2.093	2.045	1.979	2.134	1.980	2.207	2.226
Ba	0.000	0.000	0.000	0.000	0.000	0.000	0.000	0.000	0.000	0.000
Na	0.016	0.031	0.022	0.019	0.019	0.015	0.022	0.015	0.009	0.016
K	2.071	2.056	2.086	2.059	2.050	2.031	2.022	1.985	2.096	2.017
F	1.176	1.234	1.184	1.229	1.125	1.284	1.230	1.438	1.156	1.034
Cl	0.000	0.003	0.000	0.000	0.000	0.000	0.003	0.000	0.003	0.003
Sum	17.939	17.974	17.930	17.946	17.829	17.913	17.925	17.986	17.920	17.754
mg#	0.604	0.611	0.603	0.624	0.630	0.644	0.621	0.644	0.609	0.599

Table B.11. (Continued)

probe run id	btA23-6	btA23-7	btA23-8	btA23-9	biot57-15675-1	biot57-15675-2	biot57-15675-3	biot57-15675-4	biot57-15675-5	biot57-15675-6
sample	A23	A23	A23	A23	57-156.75	57-156.75	57-156.75	57-156.75	57-156.75	57-156.75
host rock	syenite	syenite	syenite	syenite	sandstone	sandstone	sandstone	sandstone	sandstone	sandstone
SiO_2	37.43	37.17	38.94	37.60	39.08	39.44	40.89	40.03	38.62	39.27
TiO_2	1.99	1.70	2.16	2.49	1.26	1.33	1.22	1.34	1.32	1.33
Al_2O_3	13.83	13.84	13.28	13.89	14.50	13.91	13.87	14.69	14.59	14.17
Cr_2O_3	0.02	0.06	0.07	0.16	0.00	0.00	0.00	0.01	0.00	0.02
MgO	14.04	14.25	14.82	13.45	18.28	18.87	18.81	18.29	18.27	18.52
CaO	0.01	0.03	0.01	0.05	0.02	0.04	0.06	0.14	0.04	0.16
MnO	0.08	0.04	0.17	0.12	0.00	0.01	0.00	0.00	0.00	0.00
FeO	16.45	16.48	14.61	16.32	11.43	10.92	10.99	11.41	11.43	11.00
BaO	0.00	0.00	0.00	0.00	0.00	0.00	0.00	0.00	0.00	0.00
Na_2O	0.09	0.07	0.05	0.09	0.06	0.04	0.03	0.05	0.03	0.05
K_2O	10.12	10.15	9.97	10.08	9.56	9.78	9.56	9.63	9.80	9.41
F	2.34	2.44	2.82	2.03	1.58	1.59	1.70	1.46	1.49	1.46
Cl	0.00	0.01	0.00	0.01	0.03	0.03	0.01	0.01	0.01	0.00
Total (uncorrected)	96.40	96.24	96.90	96.29	95.78	95.95	97.14	97.05	95.59	95.39
"-O=F,Cl"	0.99	1.03	1.19	0.86	0.67	0.68	0.72	0.62	0.63	0.62
Total (corrected)	95.41	95.21	95.71	95.43	95.11	95.27	96.42	96.43	94.97	94.77
Number of ions based on 24 O, F, Cl										
Si	6.097	6.071	6.230	6.127	6.204	6.244	6.361	6.259	6.159	6.244
Al	2.655	2.664	2.504	2.668	2.712	2.596	2.544	2.706	2.741	2.656
Ti	0.244	0.209	0.260	0.305	0.151	0.158	0.143	0.158	0.158	0.159
Cr	0.003	0.008	0.009	0.021	0.000	0.000	0.000	0.001	0.000	0.003
Mg	3.410	3.470	3.535	3.268	4.326	4.453	4.364	4.262	4.343	4.389
Ca	0.002	0.005	0.002	0.009	0.003	0.007	0.010	0.023	0.007	0.027
Mn	0.011	0.006	0.023	0.017	0.000	0.002	0.000	0.000	0.000	0.000
Fe	2.241	2.251	1.954	2.224	1.517	1.445	1.430	1.492	1.524	1.462
Ba	0.000	0.000	0.000	0.000	0.000	0.000	0.000	0.000	0.000	0.000
Na	0.028	0.022	0.016	0.028	0.017	0.013	0.008	0.014	0.011	0.016
K	2.103	2.115	2.035	2.095	1.937	1.975	1.898	1.921	1.994	1.908
F	1.205	1.260	1.427	1.046	0.792	0.798	0.838	0.723	0.749	0.734
Cl	0.000	0.003	0.000	0.003	0.007	0.007	0.002	0.003	0.003	0.001
Sum	17.998	18.084	17.992	17.810	17.665	17.697	17.597	17.561	17.690	17.598
mg#	0.603	0.607	0.644	0.595	0.740	0.755	0.753	0.741	0.740	0.750

Table B.11. (Continued)

probe run id	biot57-15675-7	biot57-15675-8	biot57-15675-9
sample	57-156.75	57-156.75	57-156.75
host rock	sandstone	sandstone	sandstone
SiO_2	39.80	40.65	39.07
TiO_2	1.39	1.37	1.33
Al_2O_3	14.57	14.23	14.40
Cr_2O_3	0.03	0.01	0.00
MgO	18.04	18.66	18.30
CaO	0.04	0.08	0.07
MnO	0.00	0.00	0.00
FeO	11.54	11.28	11.37
BaO	0.00	0.00	0.00
Na_2O	0.03	0.05	0.05
K_2O	9.58	9.92	9.53
F	1.46	1.54	1.46
Cl	0.03	0.02	0.01
Total (uncorrected)	96.51	97.79	95.58
"-O=F,Cl"	0.62	0.65	0.62
Total (corrected)	95.88	97.14	94.97
Number of ions based on 24 O, F, Cl			
Si	6.262	6.307	6.214
Al	2.701	2.603	2.699
Ti	0.165	0.160	0.159
Cr	0.004	0.001	0.000
Mg	4.232	4.316	4.340
Ca	0.006	0.013	0.012
Mn	0.000	0.000	0.000
Fe	1.519	1.464	1.512
Ba	0.000	0.000	0.000
Na	0.009	0.014	0.015
K	1.924	1.963	1.933
F	0.725	0.753	0.736
Cl	0.009	0.006	0.002
Sum	17.555	17.599	17.621
mg#	0.736	0.747	0.742

Table B.12. Electron microprobe analysis of hydrothermal feldspar

run ID	ab-579-1	ab-579-3	ksp664-1-1	ksp664-1-2	ksp664-1-3	ksp664-1-4	ksp664-1-5	ksp664-1-6	ksp664-1-7	ksp664-1-8	ksp664-1-9
sample	579	579	664-1	664-1	664-1	664-1	664-1	664-1	664-1	664-1	664-1
mineral	Albite	Albite	K-fsp	K-fsp	K-fsp	K-fsp	K-fsp	K-fsp	K-fsp	K-fsp	K-fsp
assemblage	Au vein	Au vein	Au vein	Au vein	Au vein	Au vein	Au vein	Au vein	Au vein	Au vein	Au vein
SiO_2	69.07	69.50	63.56	64.29	63.99	64.34	65.01	64.33	64.34	64.31	64.15
Al_2O_3	20.11	20.14	19.11	18.99	19.03	19.09	18.88	18.97	19.00	18.96	18.83
CaO	0.11	0.05	0.02	0.00	0.00	0.02	0.00	0.00	0.00	0.02	0.00
FeO	0.12	0.24	0.03	0.00	0.00	0.00	0.02	0.00	0.00	0.03	0.02
SrO	0.09	0.05	0.06	0.02	0.03	0.03	0.03	0.01	0.03	0.06	0.04
BaO	0.04	0.00	0.72	0.65	0.35	0.67	0.28	0.10	0.37	0.51	0.55
Na_2O	11.69	11.84	0.27	0.23	0.22	0.22	0.21	0.17	0.26	0.25	0.23
K_2O	0.10	0.14	16.51	16.61	16.70	16.89	16.68	16.84	16.57	16.53	16.49
Total	101.33	101.96	100.27	100.77	100.31	101.27	101.11	100.41	100.58	100.65	100.31
Number of ions on the basis of 32 O. All Fe recalculated as Fe^{3+}.											
Si	11.919	11.921	11.819	11.876	11.861	11.851	11.929	11.888	11.882	11.880	11.893
Al	4.091	4.073	4.190	4.135	4.158	4.145	4.083	4.133	4.137	4.130	4.115
Fe	0.020	0.009	0.003	0.000	0.000	0.003	0.000	0.000	0.001	0.004	0.000
Ca	0.017	0.034	0.005	0.000	0.000	0.000	0.003	0.000	0.000	0.005	0.004
Sr	0.009	0.005	0.006	0.002	0.003	0.003	0.004	0.001	0.003	0.006	0.005
Ba	0.003	0.000	0.053	0.047	0.025	0.048	0.020	0.007	0.027	0.037	0.040
Na	3.911	3.938	0.099	0.082	0.077	0.080	0.075	0.060	0.093	0.089	0.084
K	0.022	0.031	3.916	3.915	3.950	3.969	3.904	3.970	3.904	3.895	3.900
Sum	19.993	20.010	20.091	20.055	20.074	20.101	20.018	20.060	20.048	20.045	20.040
Ab	0.989	0.990	0.025	0.020	0.019	0.020	0.019	0.015	0.023	0.022	0.021
An	0.005	0.002	0.001	0.000	0.000	0.001	0.000	0.000	0.000	0.001	0.000
Or	0.006	0.008	0.975	0.980	0.981	0.979	0.981	0.985	0.977	0.977	0.979

run ID	ksp664-1-10	ksp664-1-11	ksp664-1-12
sample	664-1	664-1	664-1
mineral	K-fsp	K-fsp	K-fsp
assemblage	Au vein	Au vein	Au vein
SiO_2	64.40	64.62	64.61
Al_2O_3	18.98	19.03	19.18
CaO	0.01	0.01	0.00
FeO	0.00	0.00	0.00
SrO	0.00	0.00	0.01
BaO	0.51	0.53	0.63
Na_2O	0.23	0.18	0.33
K_2O	16.42	16.68	16.25
Total	100.55	101.04	101.02
Number of ions on the basis of 32 O. All Fe recalculated as Fe^{3+}.			
Si	11.894	11.890	11.877
Al	4.132	4.128	4.157
Fe	0.002	0.001	0.000
Ca	0.000	0.000	0.000
Sr	0.000	0.000	0.001
Ba	0.037	0.038	0.045
Na	0.082	0.062	0.119
K	3.869	3.917	3.810
Sum	20.015	20.036	20.009
Ab	0.021	0.016	0.030
An	0.001	0.000	0.000
Or	0.979	0.984	0.970

Table B.13. Electron microprobe analysis of hydrothermal carbonate

probe run id	cc-579-1	cc-579-10	cc-579-11	cc-579-2	cc-579-3	cc-579-4	cc-579-5	cc-579-6	cc-579-7	cc-579-8	cc-579-9
sample	579	579	579	579	579	579	579	579	579	579	579
assemblage	Au vein	Au vein	Au vein	Au vein	Au vein	Au vein	Au vein	Au vein	Au vein	Au vein	Au vein
$Si(CO_3)_2$	0.07	0.05	0.27	0	0.04	0.08	0.03	0	0.05	0.08	0
$MgCO_3$	21.33	22.65	22.62	17.75	23.72	22.1	20.99	19.87	20.43	31.6	30.05
$CaCO_3$	50.59	54.56	49.96	49.1	49.17	51.98	52.77	51.14	50.05	52.07	50.98
$MnCO_3$	1.68	1.45	2.12	1.93	1.57	1.59	1.7	1.82	1.53	0.73	0.94
$FeCO_3$	25.89	22.5	28.15	30.82	24.28	23.98	25.14	27.5	28.02	16.58	17.73
$SrCO_3$	0.3	0.04	0.09	0.06	0.21	0.34	0.14	0.26	0.05	0.74	0.82
$BaCO_3$	0.04	0.02	0	0.04	0	0	0	0	0.02	0	0.01
Total	99.9	101.27	103.21	99.71	99	100.07	100.77	100.59	100.16	101.8	100.52
Total (without $Si(CO_3)_2$)	99.83	101.22	102.94	99.7	98.95	99.99	100.74	100.59	100.1	101.72	100.53

probe run id	cc-59-708-1	cc-59-708-10	cc-59-708-11	cc-59-708-12	cc-59-708-13	cc-59-708-14	cc-59-708-15	cc-59-708-16	cc-59-708-17	cc-59-708-18	cc-59-708-19
sample	59-70.8	59-70.8	59-70.8	59-70.8	59-70.8	59-70.8	59-70.8	59-70.8	59-70.8	59-70.8	59-70.8
assemblage	Au vein	Au vein	Au vein	Au vein	Au vein	Au vein	Au vein	Au vein	Au vein	Au vein	Au vein
$Si(CO_3)_2$	0.04	0.15	0.14	0.05	0.08	0.01	0	0.03	0.04	0.05	0.06
$MgCO_3$	28.24	28.92	27.05	27.41	27.26	29.35	29.12	28.82	19.82	28.87	28.87
$CaCO_3$	52.65	50.62	50.82	51.64	51.36	51.82	51.69	51.24	50.24	51.53	52.03
$MnCO_3$	0.26	0.9	1.15	1.15	1.04	0.63	0.62	0.58	1.11	0.68	1.14
$FeCO_3$	19.25	19.74	20.77	21.47	22.02	19.48	19.71	20.12	29.92	19.46	18.49
$SrCO_3$	0.78	0.31	0.13	0.09	0.23	0.79	0.94	0.77	0.09	0.8	0.37
$BaCO_3$	0	0	0	0	0.01	0.07	0	0.02	0	0	0.14
Total	101.22	100.64	100.05	101.81	101.99	102.15	102.09	101.57	101.22	101.39	101.09
Total (without $Si(CO_3)_2$)	101.18	100.49	99.92	101.76	101.92	102.14	102.08	101.55	101.18	101.34	101.04

Table B.13. Electron microprobe analysis of hydrothermal carbonate

probe run id	cc-59-708-2	cc-59-708-20	cc-59-708-3	cc-59-708-4	cc-59-708-5	cc-59-708-6	cc-59-708-7	cc-59-708-8	cc-59-708-9	cc49-113-1	cc49-113-3
sample	59-70.8	59-70.8	59-70.8	59-70.8	59-70.8	59-70.8	59-70.8	59-70.8	59-70.8	49-113.7	49-113.7
assemblage	Au vein	Au vein	Au vein	Au vein	Au vein	Au vein	Au vein	Au vein	Au vein	biotite alteration	biotite alteration
$Si(CO_3)_2$	0.08	0.05	0.09	0.02	0.06	0.07	0.05	0.02	0.22	0.03	0.1
$MgCO_3$	29.37	18.15	28.84	28.58	30.09	29.18	36.22	30.69	28.22	0.1	0.35
$CaCO_3$	52.39	51.34	52.3	51.75	52.58	52.71	52.84	52.42	51.73	99.29	100.4
$MnCO_3$	0.23	1.24	0.58	0.39	0.42	0.39	0.93	0.99	1.24	0.52	0.65
$FeCO_3$	18.73	30.52	19.6	20.03	18.15	18.63	10.85	16.92	18.35	0.14	0.41
$SrCO_3$	0.7	0.11	0.74	0.65	0.59	0.6	0.82	0.44	0.36	0.22	0.32
$BaCO_3$	0.01	0	0.06	0	0	0	0	0.09	0	0.04	0
Total	101.51	101.41	102.22	101.43	101.89	101.58	101.72	101.57	100.11	100.35	102.22
Total (without $Si(CO_3)_2$)	101.43	101.36	102.12	101.4	101.83	101.51	101.66	101.55	99.9	100.31	102.13

probe run id	cc49-113-4	cc49-1132	ccA23-2	ccA23-3	ccA23-4	ccA23-6	ccA23-7
sample	49-113.7	49-113.7	A23	A23	A23	A23	A23
assemblage	biotite alteration	biotite alteration	biotite alteration	biotite alteration	biotite alteration	biotite alteration	biotite alteration
$Si(CO_3)_2$	0.05	0.02	0.07	0.12	0.13	0.1	0.11
$MgCO_3$	0.48	0.14	1.11	1.04	0.87	0.92	0.9
$CaCO_3$	98.39	100.08	95.98	93.65	94.88	96.2	96.09
$MnCO_3$	1.11	0.71	2.3	2.01	1.98	2.23	2.13
$FeCO_3$	0.22	0.15	1.68	1.64	1.53	1.62	1.27
$SrCO_3$	0.25	0.22	0.53	0.74	0.66	0.62	0.48
$BaCO_3$	0	0	0	0	0	0.04	0.01
Total	100.5	101.33	101.67	99.2	100.07	101.72	100.99
Total (without $Si(CO_3)_2$)	100.45	101.3	101.6	99.08	99.92	101.63	100.88

Table B.14. (Continued)

run ID	ksp6261-11	ksp6261-2	ksp6261-5	ksp6261-12	ksp676-1	ksp676-3	ksp676-5	ksp676-9	ksp676-10	ksp676-2	ksp676-4
sample	626-1	626-1	626-1	626-1	676-1	676-1	676-1	676-1	676-1	676-1	676-1
rock type	G(S)	G(S)	G(S)	G(S)	G(D-C)	G(D-C)	G(D-C)	G(D-C)	G(D-C)	G(D-C)	G(D-C)
mineral	K-fsp	Albite[1]	Albite[1]	Albite[1]	K-fsp	K-fsp	K-fsp	K-fsp	K-fsp	Albite[1]	Albite[1]
SiO_2	64.02	68.57	69.27	67.23	65.00	64.51	64.51	64.89	63.66	67.16	68.16
Al_2O_3	19.02	20.26	20.26	20.94	18.77	18.74	18.89	18.75	18.76	20.86	19.96
CaO	0.04	0.26	0.14	0.68	0.04	0.00	0.01	0.09	0.02	0.77	0.15
FeO	0.00	0.00	0.02	0.06	0.07	0.02	0.13	0.01	0.20	0.08	0.25
SrO	0.05	0.02	0.01	0.05	0.02	0.00	0.00	0.02	0.02	0.00	0.01
BaO	0.05	0.01	0.03	0.01	0.00	0.06	0.01	0.04	0.06	0.02	0.00
Na_2O	0.26	11.77	11.85	11.58	0.25	0.18	0.25	0.27	0.24	11.40	11.87
K_2O	16.69	0.07	0.07	0.20	16.45	16.59	16.74	16.69	16.87	0.27	0.07
Total	100.13	100.95	101.65	100.75	100.60	100.10	100.54	100.75	99.82	100.56	100.46
Number of ions on the basis of 32 O. All Fe recalculated as Fe^{3+}.											
Si	11.865	11.879	11.912	11.712	11.949	11.935	11.897	11.935	11.858	11.720	11.878
Al	4.156	4.138	4.107	4.301	4.067	4.087	4.108	4.066	4.120	4.292	4.100
Fe	0.008	0.048	0.026	0.128	0.009	0.001	0.002	0.019	0.004	0.144	0.027
Ca	0.000	0.000	0.002	0.008	0.011	0.003	0.020	0.001	0.031	0.012	0.037
Sr	0.005	0.002	0.001	0.005	0.002	0.000	0.000	0.002	0.002	0.000	0.001
Ba	0.004	0.000	0.002	0.001	0.000	0.005	0.000	0.003	0.004	0.001	0.000
Na	0.094	3.952	3.951	3.911	0.090	0.064	0.088	0.097	0.087	3.857	4.010
K	3.945	0.014	0.016	0.045	3.859	3.915	3.937	3.916	4.009	0.059	0.014
Sum	20.076	20.035	20.017	20.111	19.987	20.009	20.052	20.038	20.115	20.086	20.067
Ab	0.023	0.984	0.989	0.958	0.023	0.016	0.022	0.024	0.021	0.950	0.990
An	0.002	0.012	0.007	0.031	0.002	0.000	0.000	0.005	0.001	0.035	0.007
Or	0.975	0.004	0.004	0.011	0.975	0.984	0.978	0.971	0.978	0.015	0.004

run ID	ksp676-7	ksp7002-1	ksp7002-5	ksp7002-6	ksp7002-10	ksp7002-11	ksp7002-2	ksp7002-4	ksp7002-9	ksp7002-12
sample	676-1	700-2	700-2	700-2	700-2	700-2	700-2	700-2	700-2	700-2
rock type	G(D-C)	G(O)	G(O)	G(O)	G(O)	G(O)	G(O)	G(O)	G(O)	G(O)
mineral	Albite[1]	K-fsp	K-fsp	K-fsp	K-fsp	K-fsp	Pl[1]	Pl[1]	Pl[1]	Pl[1]
SiO_2	68.01	65.14	65.10	65.04	63.69	64.37	61.04	61.94	61.59	59.75
Al_2O_3	20.29	19.06	18.92	19.10	19.17	19.23	25.33	24.52	25.16	26.25
CaO	0.12	0.05	0.00	0.02	0.05	0.02	5.93	4.90	5.59	6.96
FeO	0.00	0.06	0.14	0.08	0.09	0.09	0.11	0.17	0.18	0.21
SrO	0.03	0.12	0.08	0.14	0.11	0.13	0.13	0.13	0.14	0.14
BaO	0.01	0.07	0.13	0.20	1.18	0.80	0.01	0.00	0.02	0.00
Na_2O	11.97	0.57	0.44	0.42	0.74	0.48	8.15	8.87	8.41	7.53
K_2O	0.11	16.34	16.46	16.33	15.50	15.98	0.14	0.26	0.25	0.11
Total	100.54	101.42	101.28	101.33	100.53	101.10	100.85	100.79	101.34	100.94
Number of ions on the basis of 32 O. All Fe recalculated as Fe^{3+}.										
Si	11.846	11.897	11.913	11.895	11.811	11.843	10.765	10.918	10.812	10.559
Al	4.167	4.105	4.082	4.119	4.190	4.172	5.267	5.095	5.207	5.468
Fe	0.022	0.010	0.000	0.003	0.010	0.004	1.121	0.926	1.052	1.317
Ca	0.000	0.009	0.022	0.013	0.013	0.013	0.017	0.024	0.027	0.031
Sr	0.003	0.013	0.008	0.015	0.012	0.014	0.013	0.013	0.014	0.015
Ba	0.000	0.005	0.009	0.014	0.086	0.058	0.001	0.000	0.001	0.000
Na	4.042	0.202	0.155	0.150	0.267	0.170	2.787	3.032	2.863	2.580
K	0.025	3.808	3.844	3.810	3.667	3.750	0.032	0.058	0.055	0.024
Sum	20.104	20.050	20.034	20.019	20.055	20.024	20.003	20.067	20.031	19.994
Ab	0.989	0.050	0.039	0.038	0.068	0.043	0.707	0.755	0.721	0.658
An	0.005	0.002	0.000	0.001	0.002	0.001	0.285	0.231	0.265	0.336
Or	0.006	0.947	0.961	0.961	0.930	0.956	0.008	0.014	0.014	0.006

[1]Perthitic veinlets in K-feldspar. G(O)=Ordovician granite, G(S)=Silurian granite, G(D-C)=granite clast in conglomerates c(D-C).

Table B.14. (Continued)

run ID	ksp6261-11	ksp6261-2	ksp6261-5	ksp6261-12	ksp676-1	ksp676-3	ksp676-5	ksp676-9	ksp676-10	ksp676-2	ksp676-4
sample	626-1	626-1	626-1	626-1	676-1	676-1	676-1	676-1	676-1	676-1	676-1
rock type	G(S)	G(S)	G(S)	G(S)	G(D-C)	G(D-C)	G(D-C)	G(D-C)	G(D-C)	G(D-C)	G(D-C)
mineral	K-fsp	Albite[1]	Albite[1]	Albite[1]	K-fsp	K-fsp	K-fsp	K-fsp	K-fsp	Albite[1]	Albite[1]
SiO_2	64.02	68.57	69.27	67.23	65.00	64.51	64.51	64.89	63.66	67.16	68.16
Al_2O_3	19.02	20.26	20.26	20.94	18.77	18.74	18.89	18.75	18.76	20.86	19.96
CaO	0.04	0.26	0.14	0.68	0.04	0.00	0.01	0.09	0.02	0.77	0.15
FeO	0.00	0.00	0.02	0.06	0.07	0.02	0.13	0.01	0.20	0.08	0.25
SrO	0.05	0.02	0.01	0.05	0.02	0.00	0.00	0.02	0.02	0.00	0.01
BaO	0.05	0.01	0.03	0.01	0.00	0.06	0.01	0.04	0.06	0.02	0.00
Na_2O	0.26	11.77	11.85	11.58	0.25	0.18	0.25	0.27	0.24	11.40	11.87
K_2O	16.69	0.07	0.07	0.20	16.45	16.59	16.74	16.69	16.87	0.27	0.07
Total	100.13	100.95	101.65	100.75	100.60	100.10	100.54	100.75	99.82	100.56	100.46
Number of ions on the basis of 32 O. All Fe recalculated as Fe^{3+}.											
Si	11.865	11.879	11.912	11.712	11.949	11.935	11.897	11.935	11.858	11.720	11.878
Al	4.156	4.138	4.107	4.301	4.067	4.087	4.108	4.066	4.120	4.292	4.100
Fe	0.008	0.048	0.026	0.128	0.009	0.001	0.002	0.019	0.004	0.144	0.027
Ca	0.000	0.000	0.002	0.008	0.011	0.003	0.020	0.001	0.031	0.012	0.037
Sr	0.005	0.002	0.001	0.005	0.002	0.000	0.000	0.002	0.002	0.000	0.001
Ba	0.004	0.000	0.002	0.001	0.000	0.005	0.000	0.003	0.004	0.001	0.000
Na	0.094	3.952	3.951	3.911	0.090	0.064	0.088	0.097	0.087	3.857	4.010
K	3.945	0.014	0.016	0.045	3.859	3.915	3.937	3.916	4.009	0.059	0.014
Sum	20.076	20.035	20.017	20.111	19.987	20.009	20.052	20.038	20.115	20.086	20.067
Ab	0.023	0.984	0.989	0.958	0.023	0.016	0.022	0.024	0.021	0.950	0.990
An	0.002	0.012	0.007	0.031	0.002	0.000	0.000	0.005	0.001	0.035	0.007
Or	0.975	0.004	0.004	0.011	0.975	0.984	0.978	0.971	0.978	0.015	0.004

run ID	ksp676-7	ksp7002-1	ksp7002-5	ksp7002-6	ksp7002-10	ksp7002-11	ksp7002-2	ksp7002-4	ksp7002-9	ksp7002-12
sample	676-1	700-2	700-2	700-2	700-2	700-2	700-2	700-2	700-2	700-2
rock type	G(D-C)	G(O)	G(O)	G(O)	G(O)	G(O)	G(O)	G(O)	G(O)	G(O)
mineral	Albite[1]	K-fsp	K-fsp	K-fsp	K-fsp	K-fsp	Pl[1]	Pl[1]	Pl[1]	Pl[1]
SiO_2	68.01	65.14	65.10	65.04	63.69	64.37	61.04	61.94	61.59	59.75
Al_2O_3	20.29	19.06	18.92	19.10	19.17	19.23	25.33	24.52	25.16	26.25
CaO	0.12	0.05	0.00	0.02	0.05	0.02	5.93	4.90	5.59	6.96
FeO	0.00	0.06	0.14	0.08	0.09	0.09	0.11	0.17	0.18	0.21
SrO	0.03	0.12	0.08	0.14	0.11	0.13	0.13	0.13	0.14	0.14
BaO	0.01	0.07	0.13	0.20	1.18	0.80	0.01	0.00	0.02	0.00
Na_2O	11.97	0.57	0.44	0.42	0.74	0.48	8.15	8.87	8.41	7.53
K_2O	0.11	16.34	16.46	16.33	15.50	15.98	0.14	0.26	0.25	0.11
Total	100.54	101.42	101.28	101.33	100.53	101.10	100.85	100.79	101.34	100.94
Number of ions on the basis of 32 O. All Fe recalculated as Fe^{3+}.										
Si	11.846	11.897	11.913	11.895	11.811	11.843	10.765	10.918	10.812	10.559
Al	4.167	4.105	4.082	4.119	4.190	4.172	5.267	5.095	5.207	5.468
Fe	0.022	0.010	0.000	0.003	0.010	0.004	1.121	0.926	1.052	1.317
Ca	0.000	0.009	0.022	0.013	0.013	0.013	0.017	0.024	0.027	0.031
Sr	0.003	0.013	0.008	0.015	0.012	0.014	0.013	0.013	0.014	0.015
Ba	0.000	0.005	0.009	0.014	0.086	0.058	0.001	0.000	0.001	0.000
Na	4.042	0.202	0.155	0.150	0.267	0.170	2.787	3.032	2.863	2.580
K	0.025	3.808	3.844	3.810	3.667	3.750	0.032	0.058	0.055	0.024
Sum	20.104	20.050	20.034	20.019	20.055	20.024	20.003	20.067	20.031	19.994
Ab	0.989	0.050	0.039	0.038	0.068	0.043	0.707	0.755	0.721	0.658
An	0.005	0.002	0.000	0.001	0.002	0.001	0.285	0.231	0.265	0.336
Or	0.006	0.947	0.961	0.961	0.930	0.956	0.008	0.014	0.014	0.006

[1]Perthitic veinlets in K-feldspar. G(O)=Ordovician granite, G(S)=Silurian granite, G(D-C)=granite clast in conglomerates c(D-C).

Table B.15. Electron microprobe analyses of hornblende from Ordovician granites

probe run id	amph700-2-1	amph700-2-2	amph700-2-3	amph700-2-4
sample	700-2	700-2	700-2	700-2
SiO_2	47.22	47.53	54.16	47.95
TiO_2	1.40	1.11	0.30	1.10
Al_2O_3	6.93	6.61	2.39	6.30
MgO	14.21	13.27	17.97	13.78
CaO	10.74	11.41	12.09	11.56
MnO	0.58	0.46	0.61	0.53
FeO	14.19	15.13	9.86	14.52
Na_2O	1.67	1.28	0.58	1.27
K_2O	0.56	0.70	0.20	0.64
Total(true)	97.48	97.49	98.17	97.64
Number of ions on the basis of 23 O (H_2O-free). All Fe calculated as Fe^{2+}				
Si	6.971	7.047	7.679	7.077
Al	0.155	0.123	0.032	0.122
Ti	1.205	1.154	0.400	1.096
Mg	3.127	2.934	3.799	3.031
Ca	1.698	1.812	1.837	1.827
Mn	0.072	0.058	0.074	0.067
Fe^{2+}	1.751	1.875	1.170	1.792
Na	0.477	0.368	0.159	0.362
K	0.106	0.132	0.036	0.120
Cation distribution (cf. Yavuz, 1999)				
Si(T)	6.971	7.047	7.679	7.077
Al(T)	1.029	0.953	0.321	0.923
Al(C)	0.176	0.201	0.080	0.173
Ti(C)	0.155	0.123	0.032	0.122
Mg(C)	3.127	2.934	3.799	3.031
Fe2(C)	1.542	1.742	1.089	1.674
Mn(C)	0.000	0.000	0.000	0.000
Fe^{2+}(B)	0.210	0.133	0.080	0.118
Mn(B)	0.072	0.058	0.074	0.067
Ca(B)	1.698	1.812	1.837	1.827
Na(B)	0.020	0.000	0.009	0.000
Na(A)	0.457	0.368	0.150	0.362
K(A)	0.106	0.132	0.036	0.120
T	8	8	8	8
C	5	5	5	5
B	2.000	2.003	2.000	2.012
A	0.562	0.500	0.186	0.482
Sum	15.562	15.503	15.186	15.494
mg#	0.64	0.61	0.76	0.63

Table B.16. Electron microprobe analyses of biotite from Ordovician granites

probe run id	biot700-2-1	biot700-2-2	biot700-2-3	biot700-2-4
sample	700-2	700-2	700-2	700-2
SiO_2	35.92	36.49	37.49	37.69
TiO_2	3.78	3.66	3.93	3.42
Al_2O_3	13.46	13.57	13.73	13.57
Cr_2O_3	0.00	0.03	0.03	0.02
MgO	12.39	12.62	12.56	13.00
CaO	0.19	0.00	0.06	0.02
MnO	0.28	0.32	0.28	0.28
FeO	18.30	18.52	18.48	18.30
BaO	0.39	0.59	0.16	0.00
Na_2O	0.05	0.08	0.08	0.04
K_2O	9.27	8.97	9.32	9.69
F	0.81	0.84	0.89	0.96
Cl	0.06	0.05	0.05	0.04
Total (uncorrected)	94.91	95.74	97.06	97.01
"-O=F,Cl"	0.36	0.37	0.39	0.41
Total (corrected)	94.55	95.37	96.67	96.59
Number of ions based on 24 O, F, Cl				
Si	6.029	6.062	6.112	6.144
Al	0.478	0.457	0.482	0.419
Ti	2.662	2.656	2.638	2.606
Cr	0.000	0.003	0.004	0.003
Mg	3.101	3.126	3.053	3.159
Ca	0.033	0.000	0.010	0.003
Mn	0.040	0.045	0.039	0.038
Fe	2.568	2.572	2.519	2.494
Ba	0.026	0.039	0.010	0.000
Na	0.017	0.025	0.025	0.013
K	1.986	1.900	1.937	2.014
F	0.432	0.442	0.458	0.494
Cl	0.016	0.014	0.014	0.011
Sum	17.387	17.341	17.302	17.399
mg#	0.55	0.55	0.55	0.56

Table B.17. Summary of SRM analyses (amphiboles)

	Korath Kaersutite K1 (N=45)			Kakanui USNM 143965 Hornblende (N=39)		
	Mean	1σ	Accepted Value[1]	Mean	1σ	Accepted Value[2]
SiO_2	39.06	0.38	39.30	40.47	0.34	40.37
TiO_2	4.30	0.09	4.14	4.82	0.07	4.72
Al_2O_3	15.10	0.18	15.37	14.12	0.09	14.90
MgO	14.01	0.36	13.89	12.77	0.29	12.80
CaO	12.26	0.13	12.54	10.07	0.15	10.30
MnO	0.10	0.02	0.10	0.09	0.02	0.09
FeO	9.07	0.51	8.90	10.93	0.30	10.89
Na_2O	2.33	0.06	2.36	2.55	0.08	2.60
K_2O	1.26	0.03	1.36	2.12	0.05	2.05
H_2O[3]			1.38			0.94

[1]Donovan (pers. comm.)
[2]Jarosewich et al. (1980)
[3]Determined by stoichiometry

Table B.18. Summary of SRM analyses (biotite)

	Biotite-3 (N=20)		
	Mean	1σ	Accepted Value[1]
SiO_2	38.67	0.35	38.62
TiO_2	2.26	0.04	2.26
Al_2O_3	10.95	0.17	10.72
Cr_2O_3	0.02	0.01	
MgO	14.05	0.10	14.01
CaO	0.03	0.02	
MnO	0.91	0.04	0.95
FeO	18.24	0.32	18.13
Na_2O	0.61	0.07	0.69
K_2O	9.15	0.27	9.21
F	3.39	0.27	3.3
Cl	0.03	0.01	

[1]Kuehner, pers. comm.

Table B.19. Summary of SRM analyses (feldspars)

	UCB 305 Grass Valley Anorthite (N=12)			UCB 374 MAD-10 Orthoclase (N=32)			UCB 301 Cazadero Albite (N=12)		
	Mean	1σ	Accepted Value[1]	Mean	1σ	Accepted Value[1]	Mean	1σ	Accepted Value[1]
SiO_2	44.10	0.25	44.17	64.81	0.42	64.79	68.56	0.34	68.24
Al_2O_3	35.07	0.41	34.95	16.64	0.10	16.72	20.01	0.12	19.90
CaO	19.08	0.20	18.63				0.02	0.02	0.03
FeO	0.38	0.03	0.57	1.78	0.04	1.88			
SrO	0.08	0.03							
BaO				0.06	0.02				
Na_2O	0.58	0.05	0.79	0.96	0.03	0.91	11.79	0.17	11.94
K_2O	0.01	0.01	0.05	15.50	0.11	15.49	0.02	0.01	0.04

[1]Donovan (pers. comm.)

APPENDIX C

FUID INCLUSION DATA

This appendix contains seven tables. Table C.2 provides general information on samples that were characterized by fluid inclusion microthermometry and bulk trapped volatile analysis. Tables C.2, C.3, C.4, C.5, and C.6 present microthermometry data for fluid inclusions of types 1, 2, 3, 4, and 5, respectively. Table C.7 presents results of bulk trapped volatile (quadrupole mass spectrometer) analysis.

Table C.1. Summary of samples characterized by fluid inclusion microthermometry and bulk trapped volatile analysis

Sample ID	Au content[1]	Major ore minerals	Major gangue minerals[2]	Approximate location
			Au-bearing mineralized zones	
Drillcore, Buchuk area				
57-11.3	33.83	Py, Chp	Src, Cc	Buchuk
59-70.8	15.2	Py, Chp	Src, Cc	Buchuk
59-89.1	1.27	Py, Chp	Src, Cc	Buchuk
61-199.6	13.71	Py, Chp	Src, Cc	Buchuk
60-152.5	35.11	Py, Chp	Src, Cc	Buchuk
61-72.15	22.35	Py, Chp	Src, Cc	Buchuk
Surface samples				
Altyntor	Au	Py, Chp	Src, Cc	Altyntor
A	Au	Py, Chp	Src, Cc	Altyntor
579	Au	Py, Chp	Src, Cc, Ab	Altyntor
585	Au	Py, Chp	Src, Cc	Altyntor
587	Au	Py, Chp	Src, Cc	Altyntor
587-2	?	Sph, Py	Src, Cc	Altyntor
663-2	Au (?)	Py, Chp	Src, Cc	Buchuk
AD2	?	Py	Mu, Src, Cc	Buchuk (eastern part)
			Barren veins	
Propylitic veins (hosted by lamprophyres at flanks of the intrusive belt)				
TR6		Hm	Chl, Cc, Ep	to the west of Buchuk
TR223		Hm	Chl, Cc, Ep	to the east of Altyntor
Miscellaneous barren veins				
659			Mu, Cc, Chl	to the west of Altyntor, hosted by tO_2
669-2		Mt	Cc	to the southwest of Buchuk, hanging wall of the South Kumbel fault
TR223-s			K-fsp, Cc	to the east of Altyntor, barren vein in syenite (possibly, equivalent of propylitic veins)

[1]Numbers correspond to Au grades (g/t) for 1m-long core intervals (Newmont and Santa Fe exploration data), Au indicates occurrence of macroscopically visible native gold in hand samples

[2]Quartz is the main gangue mineral in all samples

Mineral symbols: Py=pyrite, Chp=chalcopyrite, Sph=sphalerite, Hm=hematite, Mt=magnetite, Ab=albite, Cc=carbonate; Chl=chlorite, Ep=epidote; K-fsp=K-feldspar, Mu=muscovite, Src=sericite

Table C.2. Microthermometric data for type 1 inclusions

sample	comp code	inclusion	origin	Tm	Th CO2(V-L)	Carb XCH4	Carb Density
663-2	1	1	uncertain	-57	18.4		
663-2	1	2	uncertain	-57.4	18.6	0.027	0.759
663-2	1	3	uncertain	-56.8	18.1	0.008	0.785
663-2	1	4	uncertain	-57.2	15.7	0.024	0.784
663-2	1	5	uncertain	-57.2	16.1	0.024	0.784
663-2	1	7	uncertain	-56.8	17.7	0.008	0.797
663-2	1	8	uncertain	-56.7	26.8	0.002	0.693
663-2	1	10	primary	-56.6	26.6	0	0.694
663-2	1	11	primary	-56.8	26.8	0.008	0.683
663-2	1	12	primary	-56.8	27.2	0.008	0.662
663-2	1	13	uncertain	-56.6	20.9	0	0.777
663-2	1	14	uncertain	-56.6	24.7	0	0.728
663-2	1	15	uncertain	-56.6	13.1	0	0.839
663-2	1	19	primary	-56.8	19.3	0.008	0.78
663-2	1	20	primary	-56.6	27.5	0	0.672
663-2	1	21	primary	-56.6	24.2	0	0.726
663-2	1	22	primary	-56.6	27.3	0	0.672
663-2	1	24	primary	-56.6	28.8		
663-2	1	27	uncertain	-56.9	15.1	0.01	0.806
663-2	1	28	uncertain	-56.9	17.8	0.01	0.793
663-2	1	29	uncertain	-56.5	28.8		
663-2	1	32	primary	-56.6	25.5	0	0.706
663-2	1	34	secondary	-57	22	0.015	0.75
663-2	1	37	primary	-56.9	15.6	0.011	0.805
663-2	1	41	primary	-56.7	30.2		
663-2	1	43	primary	-56.7	28.3	0.005769	0.649703
663-2	1	59	primary	-56.5	30.9		
585	1	89	primary	-59.9	9.1	0.129	0.704
585	1	90	uncertain	-61.2	12.6	0.206	0.495
585	1	91	uncertain	-60.1	4.8	0.135	0.737
585	1	92	primary	-59.8	6.6	0.126	0.734
A	1	105	primary	-56.9	15.2	0.01	0.806
587	1	110	secondary	-58	9.9	0.05	0.811
587	1	115	primary	-58.7	17	0.081	0.691
587	1	116	primary	-58.2	-0.6	0.053	0.874
587	1	117	primary	-59	5.2	0.089	0.785
579	1	120	secondary	-57	16	0.015	0.798
579	1	121	primary	-57.2	4.2	0.019	0.883
579	1	122	uncertain	-56.6	-3.6	0	0.942
579	1	123	uncertain	-56.7	15.5	0.002	0.811
579	1	125	primary	-56.8	6.6	0.008	0.878

V-L=vapor to liquid

Table C.3. Microthermometric data for type 2 fluid inclusions

sample	inclusion	origin	V non-aqueous	Volume estimate	Tm	Tm clath	Tm ice	Th CO2 (V-L)	Bulk XCO2	Carb XCH4	Carb Density	Wt% NaCl	Th (total)	Phases
663-2	6	uncertain	0.6	estimated	-56.7	9.1		16.3	0.328	0.015	0.798	1.810		
663-2	9	primary	0.95	estimated	-56.8	8.1		26.7	0.837	0.008	0.683	3.706		
663-2	25	primary	0.2	estimated	-56.7	6.9		28	0.063	0.006	0.659	5.855		
663-2	30	primary	0.21	calculated	-56.9	8		28.5	0.065	0.010	0.632	3.890	275.6	V-L
663-2	31	primary	0.2	estimated	-56.6	8.8		30.9	0.052	0.000	0.532	2.389		
663-2	35	uncertain	0.25	calculated	-56.5	8.2		30	0.076	0.000	0.596	3.521	338.8	V-L
663-2	36	primary	0.29	calculated	-56.5	8.2		30.1	0.091	0.000	0.591	3.521		
663-2	38	primary	0.28	calculated	-56.8	7.5		28.8	0.092	0.008	0.633	4.798	318	V-L
663-2	39	primary	0.26	calculated	-56.8	7.2		28.5	0.084	0.006	0.637	5.331	353	V-L
663-2	40	primary	0.32	calculated	-56.6	7.6		28.9	0.11	0.000	0.634	4.618		
663-2	42	primary	0.23	calculated	-56.6	7.5						4.798	321	V-L
663-2	44	primary	0.26	calculated	-56.5	7.2		28.2	0.086	0.000	0.652	5.331	355.4	V-L
663-2	45	primary	0.26	calculated	-56.6	7.8		27.8	0.087	0.000	0.661	4.256	312.8	V-L
663-2	46	primary	0.23	calculated	-56.6	6.6						6.371	338.2	V-L
663-2	57	primary	0.21	calculated	-56.6	7.7						4.438	309.4	V-L
663-2	58	primary	0.2	calculated	-57.2	7.8		30.3	0.057	0.021	0.596	4.256	321.8	V-L
663-2	60	primary	0.22	calculated	-57	7.5		31.8				4.798	323.1	V-L
587-2	69	uncertain	0.2	estimated	-56.4	2.2		29.3	0.06	0.000	0.622	12.941	386.7	V-L[1]
587-2	70	uncertain	0.15	estimated	-56.5	2.5		27.8	0.046	0.000	0.661	12.552		
587-2	71	primary	0.3	calculated	-56.5	2		29.1	0.1	0.000	0.628	13.196		
587-2	72	primary	0.27	calculated	-56.5	2.1		30.9	0.075	0.000	0.532	13.069		
A	104	uncertain	0.6	estimated		-1.9		6.5	0.353		0.887	17.391		
579	131	primary	0.4	estimated	-56.5		-20.8	26.8	0.159	0.000	0.681	22.888		

V-L=vapor to liquid; [1]leakage suspected

Table C.4. Microthermometric data for type 3 fluid inclusions

sample	type	inclusion	origin	V non-aqueous	Tm	Tm clath	Tm ice	Th CO2 (V-L)	Bulk XCO2	Carb Density	Wt% NaCl	Th(total)	Phases
663-2	3	16	secondary	0.1								225.4	V-L
663-2	3	18	secondary	0.1								253.6	V-L
663-2	3	26	uncertain	0.2		8.1					3.706		
663-2	3	33	secondary	0.2		7.6					4.618	269.3	V-L
663-2	3	47	secondary	0.07			-19.7				22.15		
663-2	3	48	secondary	0.05		-8.4					21.138	219.2	V-L
663-2	3	49	secondary	0.05		-9.6					21.387	297.6	V-L
663-2	3	50	secondary	0.7		-10.8					21.439	321	V-L
663-2	3	51	secondary	0.05		-8.9					21.259		
663-2	3	52	secondary	0.07		-10.3					21.439	316.7	V-L
663-2	3	53	secondary	0.1		-10.4					21.439	322.3	V-L
663-2	3	54	secondary	0.1		-8.5					21.164	217.8	V-L
663-2	3	64	secondary	0.15		-7					20.674	279	V-L
663-2	3	65	secondary	0.2		-10.8					21.439		
663-2	3	66	secondary	0.2		-6.6					20.507	263.2	V-L
663-2	3	67	secondary	0.25		-6.2					20.324	344.5	V-L
587-2	3	68	secondary	0.15	-56.5	2		25.1	0.049	0.71	13.1958		
587-2	3	73	secondary	0.9		1.8					13.446	97	V-L
587-2	3	74	uncertain	0.2		1.9		30.5	0.055	0.569	13.32161		
587-2	3	75	secondary	0.2		3		30.2	0.057	0.586	11.885	311.8	V-L
587-2	3	76	secondary	0.2		2.7		31.5			12.288		
587-2	3	77	secondary	0.03			-19.8				22.22	100.8	V-L
587-2	3	78	secondary	0.4		2.8		30.2	0.139	0.586	12.155		
587-2	3	79	secondary	0.1			-20.1				22.42	198	V-L
587-2	3	80	secondary	0.1			-22.2				23.5	179	V-L
587-2	3	81	secondary	0.1			-22.7				23.8	131	V-L
587-2	3	82	secondary	0.05			-22.4				23.6	121.6	V-L
587-2	3	83	secondary	0.03			-22				23.4	139	V-L
587-2	3	84	secondary	0.05			-22.5				23.7	158	V-L
585	3	85	secondary	0.2		2.5					12.552	190.1	V-L
585	3	86	secondary	0.1		0.2					15.314	208.6	V-L
585	3	88	secondary	0.2		0.9		18.7			14.527		
585	3	93	secondary	0.2		0.1					15.422	182.4	V-L
585	3	95	secondary	0.25		1.9					13.322	225	V-L
59-89.1	3	99	secondary	0.2		2.5					12.552	225	V-L
59-89.1	3	100	secondary	0.03		5.9					7.54	157.9	V-L
59-89.1	3	101	secondary	0.03		1.5					13.815		
59-89.1	3	102	secondary	0.2		3.2					11.611	232	V-L
59-89.1	3	103	secondary	0.2		4.3					10.037	203.8	V-L
A	3	106	secondary	0.03			-17.6				20.65	127	V-L
587	3	107	secondary	0.1		2.3					12.813	243	V-L
587	3	108	secondary	0.1		3.9					10.623		
587	3	109	secondary	0.1			-21.3				23		
587	3	111	secondary	0.2			-24.1				24.8		
587	3	112	secondary	0.2								235	V-L
587	3	113	secondary	0.05			-23.2				24	187	V-L
587	3	114	secondary	0.1			-20.4				22.62	196	V-L
579	3	124	secondary	0.2			-20.5				22.69	188	V-L
579	3	126	secondary	0.05			-21.3				23		
579	3	128	secondary	0.2								208	V-L
579	3	129	secondary	0.1			-19				21.66	106	V-L
579	3	130	secondary	0.1			-18.4				21.24	119	V-L
579	3	132	secondary	0.05		-11.4					21.439	183	V-L
579	3	133	secondary	0.05		-11.5					21.439	169	V-L
579	3	134	secondary	0.1			-20.4				22.62		

V-L=vapor to liquid

Table C.5. Microthermometric data for type 4 fluid inclusions

sample	type	inclusion	origin	V non-aqueous	Tm NaCl	Wt% NaCl	Th(total)	Phases
663-2	4	55	secondary	0.1	157.5	29.96	220.8	V-L
663-2	4	56	secondary	0.07	155.5	29.88	257.4	V-L
663-2	4	61	secondary	0.03	176.9	30.78	203.8	V-L
663-2	4	63	secondary	0.05	156.5	29.92	207.5	V-L
585	4	94	secondary	0.05	174.4	30.67	174.4	S-L
585	4	96	secondary	0.03	180.1	30.93	180.1	S-L
585	4	97	secondary	0.05	184.2	31.11	184.2	S-L
585	4	98	secondary	0.1	174.2	30.66	174.2	S-L
579	4	118	secondary	0.05	175.3	30.71	175.3	S-L
579	4	127	secondary	0.05	222	33.03	222	S-L

V-L=vapor to liquid; S-L=solid to liquid

Table C.6. Microthermometric data for type 5 fluid inclusions

sample	type	inclusion	host	origin	V non-aqueous	Tm ice	Tm NaCl	Wt% NaCl	Th(total)	Phases
TR223	5	135	qtz	secondary	0.05		199.1	31.83	199.1	S-L
TR223	5	136	qtz	secondary	0.1		234	33.71	234	S-L
TR223	5	137	qtz	secondary	0.05		218.8	32.86	218.8	S-L
TR223	5	138	qtz	secondary	0.05		219.7	32.9	219.7	S-L
TR223	5	139	qtz	secondary	0.05		225.3	33.21	225.3	S-L
TR223	5	140	qtz	secondary	0.07		245.7	34.41	245.7	S-L
TR223	5	141	qtz	secondary	0.03		220.7	32.96	220.7	S-L
TR223	5	142	qtz	secondary	0.03		264.4	35.61	264.4	S-L
TR223	5	143	qtz	secondary	0.07		204.5	32.1	204.5	S-L
TR223	5	144	qtz	secondary	0.05		446.5	52.83	446.5	S-L
TR223	5	145	qtz	secondary	0.05		222.7	33.07	222.7	S-L
TR6-2	5	146	qtz	secondary	0.05	-22.7		23.8	145	V-L
TR6-2	5	147	qtz	secondary	0.05	-14.2		17.94	166.2	V-L
TR6-2	5	148	qtz	secondary	0.1	-22.1		23.4	145.9	V-L
TR6-2	5	149	qtz	secondary	0.2	-20.7		22.82	156.5	V-L
TR6-2	5	150	qtz	secondary	0.01	-16.8		20.05	105.8	V-L
TR6-2	5	151	qtz	secondary	0.1	-23		23.9	150.9	V-L
TR6-2	5	152	qtz	secondary	0.05	-22.4		23.6	130.7	V-L
TR6-2	5	155	qtz	secondary	0.07	-17.8		20.8	194.7	V-L
TR6-2	5	156	qtz	secondary	0.2	-12.1		16.05	169.2	V-L
TR6-2	5	157	qtz	secondary	0.07	-18.4		21.24	150.5	V-L
TR6-2	5	158	qtz	secondary	0.05				152.9	V-L
TR6-2	5	159	qtz	secondary	0.07	-18.1		21.02	201.8	V-L
TR6-2	5	160	qtz	secondary	0.1	-18.6		21.38	196.8	V-L
TR6-2	5	161	qtz	secondary	0.05	-16.3		19.66	234.5	V-L
TR6-2	5	162	qtz	primary	0.3	-17.3		20.43	341.2	V-L
TR6-2	5	163	qtz	secondary	0.2	-13.5		17.33	179.8	V-L
TR6-2	5	164	cc	secondary	0.7	-18.4		21.24	159.5	V-L
TR6-2	5	165	cc	secondary	0.2	-15		18.62	145.6	V-L
TR6-2	5	166	cc	secondary	0.1	-15		18.62	150.5	V-L
TR6-2	5	167	cc	secondary	0.1	-15.8		19.27		
TR6-2	5	168	cc	primary	0.3	-13.2		17.07	162.4	V-L
TR6-2	5	169	cc	primary	0.3				143.2	V-L

V-L=vapor to liquid; S-L=solid to liquid

Sample	Phases	Crush	Counts	H_2	He	CH_4	H_2O	N_2	O_2	H_2S	Ar	CnHm	CO_2	SO_2	Volatiles excluding H_2O	CO_2/CH_4	N_2/Ar
59-199.6	Qtz	6521K	47495.5	0.21	0.006596	0.91	37.89	0.19	0.00	0.000000	0.000601	0.18	60.61	0.00241	62.12	66.68	322.67
59-199.6	Qtz	6521L	73739.46	0.15	0.007877	0.59	33.78	0.17	0.00	0.000092	0.000176	0.18	65.12	0.00248	66.22	110.58	995.76
59-199.6	Qtz	6521Q	161560.8	0.18	0.008933	1.04	36.47	0.18	0.00	0.000115	0.001060	0.17	61.95	0.00000	63.53	59.31	165.80
59-199.6	Qtz	6521R	216695.2	0.18	0.007752	1.65	34.80	0.20	0.00	0.000164	0.001303	0.20	62.96	0.00027	65.20	38.11	151.49
Altyntor	Qtz+Au	6465C	227454.7	0.06	0.001531	0.29	87.25	0.32	0.01	0.000015	0.001898	0.04	12.03	0.00055	12.75	41.89	169.41
Altyntor	Qtz+Au	6465D	216533	0.06	0.001729	0.36	82.84	0.34	0.01	0.000000	0.002236	0.05	16.33	0.00073	17.16	44.74	153.96
Altyntor	Qtz+Au	6465E	365903.5	0.05	0.001527	0.34	85.10	0.35	0.01	0.000000	0.001949	0.04	14.12	0.00069	14.90	41.34	179.23
Altyntor	Qtz+Au	6465F	376341.9	0.04	0.002499	0.38	86.01	0.33	0.01	0.000000	0.002117	0.04	13.18	0.00056	13.99	34.74	156.00
Altyntor	Qtz+Au	6465G	88050.68	0.15	0.001730	1.17	76.81	0.54	0.01	0.000000	0.002000	0.08	21.24	0.00090	23.19	18.12	271.21
Altyntor	Qtz+Au	6465H	146761.9	0.09	0.002021	0.63	79.78	0.46	0.01	0.000000	0.002341	0.06	18.96	0.00085	20.22	30.09	197.35
Altyntor	Qtz+Au	6465I	61037.17	0.17	0.002274	0.74	76.77	0.57	0.01	0.000000	0.002251	0.06	21.67	0.00051	23.23	29.38	253.04
AD2	Qtz	5947b	6910729	1.33	0.008017	0.43	90.32	2.47	0	0.000147	0.003821	0.01	5.43	0.00057	9.68	12.74	646.14
AD2	Qtz	5947c	7026301	1.33	0.005489	0.49	77.39	2.25	0	0.000215	0.004921	0.01	18.50	0.00080	22.61	37.66	457.80
AD2	Qtz	5947d	7250526	0.78	0.005193	0.41	80.39	1.85	0	0.000338	0.003729	0.02	16.54	0.00035	19.61	39.98	495.24
AD2	Qtz	5947e	12723480	0.61	0.013152	0.58	80.76	2.63	0	0.000337	0.004512	0.02	15.37	0.00045	19.24	26.31	583.61
AD2	Qtz	5947f	6242274	1.13	0.008463	0.46	75.73	1.42	0	0.000114	0.002434	0.02	21.23	0.00050	24.28	45.96	583.28
AD2	Qtz	5947g	17255670	0.46	0.012573	0.53	80.61	1.77	0	0.000408	0.003743	0.03	16.58	0.00028	19.39	31.47	474.04
AD2	Qtz	5947h	8548336	0.70	0.005562	0.51	81.17	1.92	0	0.000125	0.002530	0.02	15.67	0.00011	18.83	30.65	760.11
AD2	Qtz	5947i	3413726	1.69	0.003384	0.94	75.55	1.66	0	0.000000	0.002000	0.02	20.12	0.00006	24.45	21.34	830.02
Barren																	
669-2	Qtz	6519A	76165.41	0.49	0.000259	0.17	94.67	1.47	0.06	0.000000	0.006059	0.00	3.14	0.00005	5.33	18.97	242.30
669-2	Qtz	6519B	57781.71	0.51	0.000000	0.28	95.48	1.53	0.06	0.000000	0.007403	0.00	2.14	0.00000	4.52	7.70	207.25
669-2	Qtz	6519e	148909	0.15	0.000000	0.11	93.10	1.63	0.05	0.000000	0.004780	0.02	4.94	0.00023	6.90	45.77	340.78
669-2	Qtz	6519F	506673.1	0.06	0.000288	0.06	96.15	1.16	0.03	0.000000	0.003085	0.01	2.51	0.00004	3.85	39.22	377.61
669-2	Qtz	6519G	392877.5	0.08	0.000000	0.07	96.65	1.10	0.02	0.000000	0.002217	0.01	2.07	0.00013	3.35	31.36	497.13
669-2	Qtz	6519H	371517.9	0.08	0.000360	0.07	96.34	1.18	0.03	0.000000	0.003376	0.01	2.27	0.00011	3.66	33.98	350.98
669-2	Qtz	6519I	214806.1	0.11	0.000000	0.06	95.69	1.21	0.02	0.000000	0.002879	0.01	2.89	0.00011	4.31	46.39	420.81
669-2	Qtz	6519K	14900.49	0.91	0.000000	3.65	92.37	1.22	0.00	0.000000	0.000000	0.24	1.61	0.00042	7.63	0.44	-
669-2	Qtz	6519L	82351.73	0.18	0.000000	0.36	95.61	1.29	0.02	0.000000	0.003753	0.02	2.51	0.00000	4.39	6.89	342.97
669-2	Qtz	6519M	194939.3	0.11	0.000000	0.09	95.25	1.48	0.03	0.000000	0.003541	0.01	3.04	0.00010	4.75	35.33	418.12
TR 6-2	Qtz	6516A	10766.65	0.71	0.000000	0.35	97.59	0.67	0.00	0.000000	0.000000	0.03	0.65	0.00051	2.41	1.87	-
TR 6-2	Qtz	6516B	7698.089	0.76	0.000000	0.31	97.77	0.53	0.03	0.000000	0.003046	0.00	0.58	0.00000	2.23	1.86	175.47
TR 6-2	Qtz	6516C	8406.053	0.88	0.000000	0.12	97.06	0.90	0.00	0.001231	0.002274	0.02	1.02	0.00000	2.94	8.66	397.51
TR 6-2	Qtz	6516D	117189.8	0.28	0.000013	0.25	96.05	2.34	0.06	0.000000	0.007395	0.01	1.00	0.00000	3.95	3.98	316.20
TR 6-2	Qtz	6516E	33465.46	0.34	0.000000	0.21	96.97	1.23	0.00	0.000000	0.001805	0.01	1.25	0.00001	3.03	6.04	678.99
TR 6-2	Qtz	6516F	37045.52	0.30	0.000000	0.11	96.80	1.27	0.01	0.000043	0.002362	0.01	1.49	0.00023	3.20	13.28	537.92
TR 6-2	Qtz	6516G	30264.68	0.38	0.000000	0.16	97.07	1.00	0.00	0.000187	0.001390	0.01	1.38	0.00000	2.93	8.77	720.47
TR 6-2	Qtz	6516H	100907.1	0.23	0.000061	0.27	93.96	2.64	0.05	0.000000	0.007368	0.01	2.83	0.00000	6.04	10.62	358.44
TR223	Qtz	6518B	46455.19	0.18	0.000000	0.09	97.90	1.44	0.01	0.000000	0.005033	0.00	0.36	0.00007	2.10	3.86	285.26
TR223	Qtz	6518C	46026.39	0.23	0.001949	0.53	97.26	1.49	0.00	0.000000	0.003211	0.02	0.46	0.00000	2.74	0.86	465.50
TR223	Qtz	6518D	8035.241	0.45	0.003879	0.47	97.85	0.95	0.00	0.001806	0.004514	0.04	0.23	0.00097	2.15	0.48	210.76
TR223	Qtz	6518	10217.08	0.53	0.003621	0.70	96.61	1.40	0.00	0.000625	0.003190	0.06	0.69	0.00036	3.39	0.98	438.35
TR223	Qtz	6518F	34778.89	0.38	0.003551	1.38	95.28	1.83	0.01	0.000000	0.003991	0.10	1.01	0.00000	4.72	0.73	459.74
TR223	Qtz	6518G	33443.82	0.39	0.000000	1.46	95.60	2.03	0.00	0.000000	0.007147	0.10	0.42	0.00000	4.40	0.29	283.65
659	Qtz	6319b	226375	0.16	0.214695	0.34	93.56	1.94	0	0.000000	0.003441	0.00	3.78	0.00025	6.44	11.08	562.34
659	Qtz	6319c	730276	0.00	0.042672	0.28	96.17	1.14	0.01	0.000085	0.003867	0.00	2.35	0.00000	3.83	8.34	293.82
659	Qtz	6319d	251838	0.00	0.179103	0.24	96.79	1.16	0	0.000000	0.002742	0.00	1.63	0.00037	3.21	6.74	421.57
659	Qtz	6319e	515287.5	0.00	0.093884	0.42	92.85	3.01	0.01	0.000028	0.004039	0.01	3.61	0.00000	7.16	8.52	744.87
659	Qtz	6319f	264241.3	0.00	0.154881	0.38	95.64	1.70	0	0.000396	0.002847	0.00	2.11	0.00000	4.36	5.52	598.64
659	Qtz	6319g	844344.3	0.00	0.052765	0.25	96.18	1.18	0	0.000045	0.002874	0.00	2.32	0.00011	3.83	9.13	410.37
659	Qtz	6319h	696058.4	0.00	0.069730	0.40	95.58	1.32	0.01	0.000033	0.002463	0.00	2.62	0.00021	4.42	6.62	534.99
659	Qtz	6319I	1169852	0.00	0.048693	0.52	95.32	1.85	0	0.000132	0.002976	0.01	2.25	0.00009	4.69	4.37	622.82
659	Qtz	6319j	1390058	0.00	0.034616	0.43	95.72	1.66	0	0.000045	0.002637	0.00	2.14	0.00010	4.28	4.92	629.58
659	Qtz	6319k	1318328	0.00	0.035958	0.41	95.55	1.61	0	0.000003	0.002979	0.01	2.38	0.00012	4.46	5.79	541.87
659	Qtz	6319l	1493988	0.00	0.036380	0.34	96.03	1.58	0	0.000000	0.002435	0.00	2.00	0.00005	3.98	5.87	650.66
659	Qtz	6319m	3063698	0.00	0.013738	0.24	97.21	0.94	0	0.000015	0.001189	0.00	1.59	0.00008	2.79	6.70	792.10
659	Qtz	6319n	1551410	0.00	0.026620	0.37	96.16	1.49	0	0.000029	0.001927	0.00	1.94	0.00006	3.84	5.30	774.00
TR223-s	Qtz	6320a	2546669	0.00	0.021394	0.03	99.60	0.17	0	0.000020	0.000843	0.00	0.16	0.00000	0.40	4.63	204.63
TR223-s	Qtz	6320b	1549477	0.00	0.030666	0.04	99.54	0.19	0	0.000000	0.000549	0.00	0.19	0.00002	0.46	4.60	351.12
TR223-s	Qtz	6320c	471082.4	0.00	0.075571	0.02	99.57	0.16	0	0.000169	0.000365	0.00	0.17	0.00005	0.43	7.34	448.10
TR223-s	Qtz	6320d	1390636	0.00	0.031447	0.05	99.57	0.15	0	0.000007	0.000711	0.00	0.19	0.00000	0.43	3.88	207.46
TR223-s	Qtz	6320e	466296.2	0.00	0.086017	0.04	99.54	0.16	0	0.000000	0.000258	0.00	0.18	0.00001	0.46	4.50	607.46
TR223-s	Qtz	6320f	1098504	0.00	0.036175	0.08	99.38	0.24	0	0.000063	0.000455	0.00	0.27	0.00009	0.62	3.57	520.93
TR223-s	Qtz	6320g	215079.4	0.00	0.290695	0.44	98.79	0.25	0	0.000000	0.000266	0.00	0.23	0.00000	1.21	0.52	932.19
TR223-s	Kfsp	6321a	199098	0.00	0.226225	0.11	98.55	0.76	0.05	0.000064	0.005307	0.00	0.28	0.00005	1.45	2.50	143.67
TR223-s	Kfsp	6321b	219204.3	0.00	0.183230	0.23	98.08	1.02	0.05	0.000027	0.005601	0.00	0.44	0.00007	1.93	1.92	181.30
TR223-s	Kfsp	6321c	197003.9	0.00	0.205258	0.35	98.12	0.75	0.05	0.000000	0.006777	0.00	0.51	0.00000	1.89	1.45	110.96
TR223-s	Kfsp	6321d	396887	0.00	0.102049	0.21	98.13	0.95	0.06	0.000422	0.008727	0.00	0.53	0.00000	1.88	2.60	109.42
TR223-s	Kfsp	6321e	415686.9	0.00	0.117823	0.15	98.26	0.77	0.04	0.000076	0.007261	0.00	0.65	0.00000	1.74	4.32	105.99
TR223-s	Kfsp	6321f	476534.2	0.00	0.121614	0.21	98.12	0.93	0.04	0.000146	0.006546	0.00	0.57	0.00000	1.89	2.74	141.49
TR223-s	Kfsp	6321g	413753	0.00	0.118583	0.26	97.88	0.96	0.03	0.000000	0.006682	0.01	0.74	0.00001	2.13	2.87	143.26
TR223-s	Kfsp	6321h	353130.4	0.00	0.152459	0.52	97.51	1.10	0.05	0.000104	0.008263	0.01	0.64	0.00016	2.49	1.24	132.76
TR223-s	Kfsp	6321i	405985	0.00	0.132378	0.38	97.71	1.09	0.05	0.000000	0.007368	0.01	0.63	0.00000	2.30	1.65	147.55

Qtz=quartz, Qtz+Au=quartz intergrown with gold, Kfsp=K-feldspar

Sample	Phases	Crush	Counts	H_2	He	CH_4	H_2O	N_2	O_2	H_2S	Ar	CnHm	CO_2	SO_2	Volatiles excluding H_2O	CO_2/CH_4	N_2/Ar
59-199.6	Qtz	6521K	47495.5	0.21	0.006596	0.91	37.89	0.19	0.00	0.000000	0.000601	0.18	60.61	0.00241	62.12	66.68	322.67
59-199.6	Qtz	6521L	73739.46	0.15	0.007877	0.59	33.78	0.17	0.00	0.000092	0.000176	0.18	65.12	0.00248	66.22	110.58	995.76
59-199.6	Qtz	6521Q	161560.8	0.18	0.008933	1.04	36.47	0.18	0.00	0.000115	0.001060	0.17	61.95	0.00000	63.53	59.31	165.80
59-199.6	Qtz	6521R	216695.2	0.18	0.007752	1.65	34.80	0.20	0.00	0.000164	0.001303	0.20	62.96	0.00027	65.20	38.11	151.49
Altyntor	Qtz+Au	6465C	227454.7	0.06	0.001531	0.29	87.25	0.32	0.01	0.000015	0.001898	0.04	12.03	0.00055	12.75	41.89	169.41
Altyntor	Qtz+Au	6465D	216533	0.06	0.001729	0.36	82.84	0.34	0.01	0.000000	0.002236	0.05	16.33	0.00073	17.16	44.74	153.96
Altyntor	Qtz+Au	6465E	365903.5	0.05	0.001527	0.34	85.10	0.35	0.01	0.000000	0.001949	0.04	14.12	0.00069	14.90	41.34	179.23
Altyntor	Qtz+Au	6465F	376341.9	0.04	0.002499	0.38	86.01	0.33	0.01	0.000000	0.002117	0.04	13.18	0.00056	13.99	34.74	156.00
Altyntor	Qtz+Au	6465G	88050.68	0.15	0.001730	1.17	76.81	0.54	0.01	0.000000	0.002000	0.08	21.24	0.00090	23.19	18.12	271.21
Altyntor	Qtz+Au	6465H	146761.9	0.09	0.002021	0.63	79.78	0.46	0.01	0.000000	0.002341	0.06	18.96	0.00085	20.22	30.09	197.35
Altyntor	Qtz+Au	6465I	61037.17	0.17	0.002274	0.74	76.77	0.57	0.01	0.000000	0.002251	0.06	21.67	0.00051	23.23	29.38	253.04
AD2	Qtz	5947b	6910729	1.33	0.008017	0.43	90.32	2.47	0	0.000147	0.003821	0.01	5.43	0.00057	9.68	12.74	646.14
AD2	Qtz	5947c	7026301	1.33	0.005489	0.49	77.39	2.25	0	0.000215	0.004921	0.01	18.50	0.00080	22.61	37.66	457.80
AD2	Qtz	5947d	7250526	0.78	0.005193	0.41	80.39	1.85	0	0.000338	0.003729	0.02	16.54	0.00035	19.61	39.98	495.24
AD2	Qtz	5947e	12723480	0.61	0.013152	0.58	80.76	2.63	0	0.000337	0.004512	0.02	15.37	0.00045	19.24	26.31	583.61
AD2	Qtz	5947f	6242274	1.13	0.008463	0.46	75.73	1.42	0	0.000114	0.002434	0.02	21.23	0.00050	24.28	45.96	583.28
AD2	Qtz	5947g	17255670	0.46	0.012573	0.53	80.61	1.77	0	0.000408	0.003743	0.03	16.58	0.00028	19.39	31.47	474.04
AD2	Qtz	5947h	8548336	0.70	0.005562	0.51	81.17	1.92	0	0.000125	0.002530	0.02	15.67	0.00011	18.83	30.65	760.11
AD2	Qtz	5947i	3413726	1.69	0.003384	0.94	75.55	1.66	0	0.000000	0.002000	0.02	20.12	0.00006	24.45	21.34	830.02
Barren																	
669-2	Qtz	6519A	76165.41	0.49	0.000259	0.17	94.67	1.47	0.06	0.000000	0.006059	0.00	3.14	0.00005	5.33	18.97	242.30
669-2	Qtz	6519B	57781.71	0.51	0.000000	0.28	95.48	1.53	0.06	0.000000	0.007403	0.00	2.14	0.00000	4.52	7.70	207.25
669-2	Qtz	6519e	148909	0.15	0.000000	0.11	93.10	1.63	0.05	0.000000	0.004780	0.02	4.94	0.00023	6.90	45.77	340.78
669-2	Qtz	6519F	506673.1	0.06	0.000288	0.06	96.15	1.16	0.03	0.000000	0.003085	0.01	2.51	0.00004	3.85	39.22	377.61
669-2	Qtz	6519G	392877.5	0.08	0.000000	0.07	96.65	1.10	0.02	0.000000	0.002217	0.01	2.07	0.00013	3.35	31.36	497.13
669-2	Qtz	6519H	371517.9	0.08	0.000360	0.07	96.34	1.18	0.03	0.000000	0.003376	0.01	2.27	0.00011	3.66	33.98	350.98
669-2	Qtz	6519I	214806.1	0.11	0.000000	0.06	95.69	1.21	0.02	0.000000	0.002879	0.01	2.89	0.00011	4.31	46.39	420.81
669-2	Qtz	6519K	14900.49	0.91	0.000000	3.65	92.37	1.22	0.00	0.000000	0.000000	0.24	1.61	0.00042	7.63	0.44	-
669-2	Qtz	6519L	82351.73	0.18	0.000000	0.36	95.61	1.29	0.02	0.000000	0.003753	0.02	2.51	0.00000	4.39	6.89	342.97
669-2	Qtz	6519M	194939.3	0.11	0.000000	0.09	95.25	1.48	0.03	0.000000	0.003541	0.01	3.04	0.00010	4.75	35.33	418.12
TR 6-2	Qtz	6516A	10766.65	0.71	0.000000	0.35	97.59	0.67	0.00	0.000000	0.000000	0.03	0.65	0.00051	2.41	1.87	-
TR 6-2	Qtz	6516B	7698.089	0.76	0.000000	0.31	97.77	0.53	0.03	0.000000	0.003046	0.00	0.58	0.00000	2.23	1.86	175.47
TR 6-2	Qtz	6516C	8406.053	0.88	0.000000	0.12	97.06	0.90	0.00	0.001231	0.002274	0.02	1.02	0.00000	2.94	8.66	397.51
TR 6-2	Qtz	6516D	117189.8	0.28	0.000013	0.25	96.05	2.34	0.06	0.000000	0.007395	0.01	1.00	0.00000	3.95	3.98	316.20
TR 6-2	Qtz	6516E	33465.46	0.34	0.000000	0.21	96.97	1.23	0.00	0.000000	0.001805	0.01	1.25	0.00001	3.03	6.04	678.99
TR 6-2	Qtz	6516F	37045.52	0.30	0.000000	0.11	96.80	1.27	0.01	0.000043	0.002362	0.01	1.49	0.00023	3.20	13.28	537.92
TR 6-2	Qtz	6516G	30264.68	0.38	0.000000	0.16	97.07	1.00	0.00	0.000187	0.001390	0.01	1.38	0.00000	2.93	8.77	720.47
TR 6-2	Qtz	6516H	100907.1	0.23	0.000061	0.27	93.96	2.64	0.05	0.000000	0.007368	0.01	2.83	0.00000	6.04	10.62	358.44
TR223	Qtz	6518B	46455.19	0.18	0.000000	0.09	97.90	1.44	0.01	0.000000	0.005033	0.00	0.36	0.00007	2.10	3.86	285.26
TR223	Qtz	6518C	46026.39	0.23	0.001949	0.53	97.26	1.49	0.00	0.000000	0.003211	0.02	0.46	0.00000	2.74	0.86	465.50
TR223	Qtz	6518D	8035.241	0.45	0.003879	0.47	97.85	0.95	0.00	0.001806	0.004514	0.04	0.23	0.00097	2.15	0.48	210.76
TR223	Qtz	6518	10217.08	0.53	0.003621	0.70	96.61	1.40	0.00	0.000625	0.003190	0.06	0.69	0.00036	3.39	0.98	438.35
TR223	Qtz	6518F	34778.89	0.38	0.003551	1.38	95.28	1.83	0.01	0.000000	0.003991	0.10	1.01	0.00000	4.72	0.73	459.74
TR223	Qtz	6518G	33443.82	0.39	0.000000	1.46	95.60	2.03	0.00	0.000000	0.007147	0.10	0.42	0.00000	4.40	0.29	283.65
659	Qtz	6319b	226375	0.16	0.214695	0.34	93.56	1.94	0	0.000000	0.003441	0.00	3.78	0.00025	6.44	11.08	562.34
659	Qtz	6319c	730276	0.00	0.042672	0.28	96.17	1.14	0.01	0.000085	0.003867	0.00	2.35	0.00000	3.83	8.34	293.82
659	Qtz	6319d	251838	0.00	0.179103	0.24	96.79	1.16	0	0.000000	0.002742	0.00	1.63	0.00037	3.21	6.74	421.57
659	Qtz	6319e	515287.5	0.00	0.093884	0.42	92.85	3.01	0.01	0.000028	0.004039	0.01	3.61	0.00000	7.16	8.52	744.87
659	Qtz	6319f	264241.3	0.00	0.154881	0.38	95.64	1.70	0	0.000396	0.002847	0.00	2.11	0.00000	4.36	5.52	598.64
659	Qtz	6319g	844344.3	0.00	0.052765	0.25	96.18	1.18	0	0.000045	0.002874	0.00	2.32	0.00011	3.83	9.13	410.37
659	Qtz	6319h	696058.4	0.00	0.069730	0.40	95.58	1.32	0.01	0.000033	0.002463	0.00	2.62	0.00021	4.42	6.62	534.99
659	Qtz	6319I	1169852	0.00	0.048693	0.52	95.32	1.85	0	0.000132	0.002976	0.01	2.25	0.00009	4.69	4.37	622.82
659	Qtz	6319j	1390058	0.00	0.034616	0.43	95.72	1.66	0	0.000045	0.002637	0.00	2.14	0.00010	4.28	4.92	629.58
659	Qtz	6319k	1318328	0.00	0.035958	0.41	95.55	1.61	0	0.000003	0.002979	0.01	2.38	0.00012	4.46	5.79	541.87
659	Qtz	6319l	1493988	0.00	0.036380	0.34	96.03	1.58	0	0.000000	0.002435	0.00	2.00	0.00005	3.98	5.87	650.66
659	Qtz	6319m	3063698	0.00	0.013738	0.24	97.21	0.94	0	0.000015	0.001189	0.00	1.59	0.00008	2.79	6.70	792.10
659	Qtz	6319n	1551410	0.00	0.026620	0.37	96.16	1.49	0	0.000029	0.001927	0.00	1.94	0.00006	3.84	5.30	774.00
TR223-s	Qtz	6320a	2546669	0.00	0.021394	0.03	99.60	0.17	0	0.000020	0.000843	0.00	0.16	0.00000	0.40	4.63	204.63
TR223-s	Qtz	6320b	1549477	0.00	0.030666	0.04	99.54	0.19	0	0.000000	0.000549	0.00	0.19	0.00002	0.46	4.60	351.12
TR223-s	Qtz	6320c	471082.4	0.00	0.075571	0.02	99.57	0.16	0	0.000169	0.000365	0.00	0.17	0.00005	0.43	7.34	448.10
TR223-s	Qtz	6320d	1390636	0.00	0.031447	0.05	99.57	0.15	0	0.000007	0.000711	0.00	0.19	0.00000	0.43	3.88	207.46
TR223-s	Qtz	6320e	466296.2	0.00	0.086017	0.04	99.54	0.16	0	0.000000	0.000258	0.00	0.18	0.00001	0.46	4.50	607.46
TR223-s	Qtz	6320f	1098504	0.00	0.036175	0.08	99.38	0.24	0	0.000063	0.000455	0.00	0.27	0.00009	0.62	3.57	520.93
TR223-s	Qtz	6320g	215079.4	0.00	0.290695	0.44	98.79	0.25	0	0.000000	0.000266	0.00	0.23	0.00000	1.21	0.52	932.19
TR223-s	Kfsp	6321a	199098	0.00	0.226225	0.11	98.55	0.76	0.05	0.000064	0.005307	0.00	0.28	0.00005	1.45	2.50	143.67
TR223-s	Kfsp	6321b	219204.3	0.00	0.183230	0.23	98.08	1.02	0.05	0.000027	0.005601	0.00	0.44	0.00007	1.93	1.92	181.30
TR223-s	Kfsp	6321c	197003.9	0.00	0.205258	0.35	98.12	0.75	0.05	0.000000	0.006777	0.00	0.51	0.00000	1.89	1.45	110.96
TR223-s	Kfsp	6321d	396887	0.00	0.102049	0.21	98.13	0.95	0.06	0.000422	0.008727	0.00	0.53	0.00000	1.88	2.60	109.42
TR223-s	Kfsp	6321e	415686.9	0.00	0.117823	0.15	98.26	0.77	0.04	0.000076	0.007261	0.00	0.65	0.00000	1.74	4.32	105.99
TR223-s	Kfsp	6321f	476534.2	0.00	0.121614	0.21	98.12	0.93	0.04	0.000146	0.006546	0.00	0.57	0.00000	1.89	2.74	141.49
TR223-s	Kfsp	6321g	413753	0.00	0.118583	0.26	97.88	0.96	0.03	0.000000	0.006682	0.01	0.74	0.00001	2.13	2.87	143.26
TR223-s	Kfsp	6321h	353130.4	0.00	0.152459	0.52	97.51	1.10	0.05	0.000104	0.008263	0.01	0.64	0.00016	2.49	1.24	132.76
TR223-s	Kfsp	6321i	405985	0.00	0.132378	0.38	97.71	1.09	0.05	0.000000	0.007368	0.01	0.63	0.00000	2.30	1.65	147.55

Qtz=quartz, Qtz+Au=quartz intergrown with gold, Kfsp=K-feldspar

APPENDIX D

^{40}AR/^{39}AR DATA

The $^{40}Ar/^{39}Ar$ data are presented in four tables. Table D.1 presents results of step heating analyses of phyllosilicates and amphiboles. Table D.2 contains results of the UV laser in situ ablation analyses of magmatic and hydrothermal micas. Tables D.3 and D.4 report results of step-heating analyses of K-feldspars. Table D.3 contains data that were used for thermochronological modeling, whereas Table D.4 presents results of duplicate analyses.

Table D.1. $^{40}Ar/^{39}Ar$ data for step heating analyses (phyllosilicates and amphiboles)

ID	Temp (°C)	$^{40}Ar/^{39}Ar$	$^{37}Ar/^{39}Ar$	$^{36}Ar/^{39}Ar$ (x 10^{-3})	$^{39}Ar_K$ (x 10^{-15} mol)	K/Ca	Cl/K (x 10^{-3})	$^{40}Ar^*$ (%)	^{39}Ar (%)	Age (Ma)	±2s (Ma)
76-179.9 C1:80, biotite, 2.7 mg, J=0.003766949±0.09%, D=1.0052±0.00069, nm-80, Lab#=8565-01											
A	*600*	*305.8*	*0.3982*	*796.6*	*0.016*	*1.3*	*486.4*	*23.0*	*0.0*	*424.5*	*723.1*
B	*670*	*75.16*	*0.5620*	*182.3*	*0.583*	*0.91*	*119.5*	*28.4*	*0.4*	*139.4*	*12.6*
C	*750*	*60.05*	*1.528*	*35.55*	*3.97*	*0.33*	*29.1*	*82.7*	*3.1*	*309.6*	*1.9*
D	*830*	*66.84*	*1.936*	*17.84*	*4.18*	*0.26*	*23.8*	*92.3*	*5.9*	*377.4*	*1.8*
E	900	65.64	0.1797	2.565	35.7	2.8	8.7	98.8	29.7	394.5	1.6
F	970	65.06	0.0095	1.396	17.9	53.7	7.7	99.3	41.7	393.1	1.2
G	1020	65.35	0.0081	0.7259	16.2	62.9	7.3	99.6	52.6	395.8	1.2
H	1080	65.08	0.0049	0.6051	26.2	103.7	7.2	99.7	70.1	394.5	1.4
I	1140	65.36	0.0067	1.414	12.1	76.0	75.8	99.3	78.2	394.7	1.2
J	1200	65.38	0.0154	0.9354	18.8	33.1	7.9	99.5	90.7	395.6	1.1
K	*1300*	*64.61*	*0.1214*	*1.855*	*12.0*	*4.2*	*10.0*	*99.1*	*98.8*	*390.0*	*1.3*
L	*1650*	*91.35*	*0.0075*	*84.76*	*1.82*	*68.1*	*12.6*	*72.6*	*100.0*	*402.1*	*4.4*
total gas age			n=12		149.4	43.6				390.6	1.5
plateau			n=6	steps E-J	126.9	49.9			84.9	394.7	1.5
MSWD**		2.67									
57-174.1, D3:80, biotite, 3.92 mg, J=0.003684693±0.09%, D=1.0052±0.00069, nm-80, Lab#=8569-01											
A	*600*	*48.35*	*0.2615*	*120.8*	*0.808*	*2.0*	*98.2*	*26.2*	*0.3*	*82.3*	
B	*670*	*33.92*	*0.5473*	*33.87*	*0.700*	*0.93*	*26.0*	*70.5*	*0.6*	*152.5*	*4.5*
C	*750*	*56.53*	*0.3365*	*13.22*	*4.27*	*1.5*	*15.7*	*93.1*	*2.3*	*319.8*	*1.5*
D	*830*	*65.33*	*0.2351*	*6.920*	*6.58*	*2.2*	*10.0*	*96.9*	*4.9*	*378.2*	*1.4*
E	*860*	*65.53*	*0.0421*	*2.582*	*29.9*	*12.1*	*8.6*	*98.8*	*16.7*	*386.0*	*1.6*
F	900	64.23	0.0045	0.6480	34.4	112.9	8.3	99.7	30.4	382.1	1.5
G	970	63.74	0.0041	0.6023	31.5	124.1	8.2	99.7	42.8	379.5	1.2
H	1020	63.83	0.0064	0.8384	17.8	79.5	8.6	99.6	49.9	379.6	1.2
I	1080	64.16	0.0074	0.5168	23.0	68.8	7.8	99.7	59.0	381.9	1.3
J	1140	64.05	0.0082	0.6402	46.7	62.1	20.2	99.7	77.5	381.1	1.5
K	1200	64.22	0.0204	0.6507	23.4	25.0	14.0	99.7	86.8	382.0	1.5
L	*1300*	*64.45*	*0.1399*	*0.6399*	*30.6*	*3.6*	*8.5*	*99.7*	*98.9*	*383.4*	*1.3*
M	*1650*	*69.00*	*0.0113*	*19.73*	*2.71*	*45.0*	*10.6*	*91.5*	*100.0*	*377.4*	*2.9*
total gas age			n=13		252.4	59.0				379.2	1.4
plateau			n=6	steps F-K	176.9	80.7			70.1	380.9	1.7
MSWD**		3.30									
55-62.7, F2:80, biotite, 3.24 mg, J=0.003751531±0.09%, D=1.0052±0.00069, nm-80, Lab#=8580-01											
A	*600*	*43.92*	*0.2518*	*50.30*	*1.50*	*2.0*	*17.3*	*66.1*	*0.7*	*186.7*	*3.2*
B	*670*	*53.42*	*0.3691*	*7.799*	*3.15*	*1.4*	*7.9*	*95.7*	*2.2*	*316.6*	*1.5*
C	*750*	*63.26*	*0.2088*	*5.091*	*9.68*	*2.4*	*8.7*	*97.6*	*6.9*	*376.0*	*1.4*
D	*830*	*63.63*	*0.0605*	*1.015*	*21.7*	*8.4*	*8.6*	*99.5*	*17.3*	*384.5*	*1.3*
E	860	63.11	0.0146	0.1491	19.3	35.0	8.3	99.9	26.5	383.0	1.5
F	900	62.96	0.0196	0.0797	12.9	26.1	8.7	99.9	32.7	382.29	0.91
G	970	62.83	0.0777	0.2244	16.4	6.6	8.5	99.9	40.5	381.41	0.99
H	1020	62.95	0.0781	0.1724	24.1	6.5	8.5	99.9	52.1	382.1	1.2
I	1080	63.04	0.0172	0.4623	24.2	29.7	8.4	99.8	63.6	382.1	1.9
J	1140	63.17	0.0286	0.4630	30.2	17.9	8.5	99.8	78.1	382.9	1.3

ID	Temp (°C)	$^{40}Ar/^{39}Ar$	$^{37}Ar/^{39}Ar$	$^{36}Ar/^{39}Ar$ ($x 10^{-3}$)	$^{39}Ar_K$ ($x 10^{-15}$ mol)	K/Ca	Cl/K ($x 10^{-3}$)	$^{40}Ar*$ (%)	^{39}Ar (%)	Age (Ma)	±2s (Ma)
K	1200	63.36	0.1031	0.5156	21.0	4.9	8.7	99.7	88.2	383.9	1.5
L	*1300*	*63.68*	*0.2141*	*0.9253*	*14.7*	*2.4*	*8.9*	*99.6*	*95.2*	*385.0*	*1.1*
M	*1650*	*64.76*	*0.0256*	*3.511*	*9.96*	*19.9*	*8.8*	*98.4*	*100.0*	*386.6*	*1.5*
total gas age			n=13		208.9	14.8				380.4	1.3
plateau			n=7	steps E-K	148.1	17.8			70.9	382.3	0.9
MSWD		1.51									
57-166.2, D1:80, biotite, 3.61 mg, J=0.003746307±0.09%, D=1.0052±0.00069, nm-80, Lab#=8568-01											
A	600	50.59	0.3974	116.9	0.771	1.3	144.0	31.7	0.3	105.4	6.8
B	670	39.16	1.302	39.88	0.465	0.39	32.2	70.1	0.5	176.8	6.0
C	750	51.98	0.8831	12.56	4.78	0.58	13.0	93.0	2.7	300.3	1.6
D	830	64.26	0.8063	6.923	4.52	0.63	9.0	96.9	4.6	378.4	1.5
E	860	65.31	0.1406	2.269	25.3	3.6	7.2	99.0	15.8	391.2	1.3
F	900	65.37	0.0076	0.6227	29.3	66.9	6.9	99.7	28.8	394.1	1.3
G	970	65.49	0.0058	0.4705	28.2	88.0	6.6	99.8	41.2	395.0	1.4
H	1020	66.66	0.0073	0.4354	16.9	69.4	6.2	99.8	48.7	401.4	1.2
I	1080	66.13	0.0068	0.5450	24.1	75.6	6.0	99.7	59.3	398.3	1.4
J	1140	65.20	0.0061	0.4793	47.5	83.1	14.7	99.8	80.2	393.4	1.9
K	1200	65.45	0.0195	0.4617	26.8	26.1	12.2	99.8	92.1	394.8	1.2
L	1300	65.52	0.1433	0.8710	13.7	3.6	7.0	99.6	98.1	394.6	1.5
M	1650	70.03	0.0117	13.77	4.34	43.5	7.4	94.2	100.0	398.3	1.9
total gas age			n=13		226.8	54.8				391.2	1.4
58-58.3, D5:80, biotite, 4.05 mg, J=0.003725101±0.09%, D=1.0052±0.00069, nm-80, Lab#=8570-01											
A	600	60.68	0.1074	81.11	0.954	4.8	145.4	60.5	0.4	231.2	5.2
B	670	64.31	0.0518	20.67	0.723	9.9	64.4	90.5	0.7	353.9	4.8
C	750	63.98	0.0241	3.840	4.85	21.1	22.7	98.2	2.7	379.4	1.5
D	830	67.54	0.0039	3.011	6.33	132.2	9.9	98.7	5.3	400.0	1.5
E	860	67.31	0.0015	0.7009	33.3	341.4	7.2	99.7	19.1	402.4	1.3
F	900	64.95	0.0009	0.4303	22.1	543.8	7.2	99.8	28.3	390.1	1.4
G	970	65.72	0.0016	0.6974	16.6	322.0	7.4	99.7	35.1	393.9	1.7
H	1020	66.15	0.0015	0.6242	13.8	341.9	7.5	99.7	40.8	396.3	1.3
I	1080	65.85	0.0011	0.4915	26.8	474.5	6.7	99.7	51.9	394.9	1.7
J	1140	64.77	0.0012	0.4293	51.6	414.2	14.4	99.8	73.3	389.1	1.4
K	1200	65.17	0.0016	0.3991	27.9	311.8	15.7	99.8	84.8	391.3	2.5
L	1300	65.32	0.0014	0.4027	34.5	362.8	6.8	99.8	99.1	392.2	2.5
M	1650	70.02	0.0036	20.93	2.19	141.3	11.0	91.1	100.0	384.8	3.5
total gas age			n=13		241.7	372.5				392.4	1.8
56-158, C5:80, biotite, 3.35 mg, J=0.003728842±0.09%, D=1.0052±0.00069, nm-80, Lab#=8567-01											
B	670	134.0	0.2642	376.9	0.612	1.9	45.7	16.9	0.3	146.0	15.8
C	750	57.49	0.4181	24.90	3.80	1.2	11.5	87.2	2.0	309.3	1.6
D	830	64.87	0.4983	6.890	4.68	1.0	6.1	96.9	4.2	379.9	1.6
E	860	65.42	0.1236	2.001	24.0	4.1	4.5	99.1	15.2	390.6	1.2
F	900	64.57	0.0024	0.4039	26.5	214.2	3.8	99.8	27.3	388.4	1.5
G	970	63.87	0.0039	0.4646	28.2	132.1	3.9	99.8	40.3	384.5	1.2
H	1020	63.54	0.0064	0.4691	12.4	79.4	4.1	99.7	46.0	382.75	0.97
I	1080	64.17	0.0065	0.7239	20.3	78.1	3.7	99.6	55.3	385.8	1.3

ID	Temp (°C)	$^{40}Ar/^{39}Ar$	$^{37}Ar/^{39}Ar$	$^{36}Ar/^{39}Ar$ (x 10^{-3})	$^{39}Ar_K$ (x 10^{-15} mol)	K/Ca	Cl/K (x 10^{-3})	$^{40}Ar^*$ (%)	^{39}Ar (%)	Age (Ma)	±2s (Ma)
J	1140	63.22	0.0084	0.6114	34.2	60.4	19.3	99.7	71.0	380.8	1.4
K	1200	63.64	0.0253	0.4685	29.4	20.2	3.5	99.8	84.6	383.3	1.4
L	1300	63.41	0.0964	0.5543	30.9	5.3	3.6	99.7	98.8	381.9	1.3
M	1650	73.08	0.0051	35.60	2.70	99.3	4.7	85.6	100.0	378.2	2.8
total gas age			n=12		217.7	69.7				382.4	1.4

58-110.2, E4:80, biotite, 2.09 mg, J=0.003703385±0.09%, D=1.0052±0.00069, nm-80, Lab#=8573-01

ID	Temp (°C)	$^{40}Ar/^{39}Ar$	$^{37}Ar/^{39}Ar$	$^{36}Ar/^{39}Ar$ (x 10^{-3})	$^{39}Ar_K$ (x 10^{-15} mol)	K/Ca	Cl/K (x 10^{-3})	$^{40}Ar^*$ (%)	^{39}Ar (%)	Age (Ma)	±2s (Ma)
A	600	37.28	0.0953	30.34	0.973	5.4	8.0	75.9	0.6	179.8	3.8
B	670	47.68	0.2671	4.068	2.71	1.9	4.4	97.5	2.4	286.6	1.3
C	750	58.77	0.4007	2.546	6.79	1.3	5.5	98.7	6.7	351.3	1.2
D	830	61.51	0.3973	1.526	12.9	1.3	6.9	99.3	14.9	367.9	1.1
E	860	62.84	0.0792	0.6051	18.5	6.4	7.6	99.7	26.7	376.4	1.4
F	900	62.62	0.0034	0.3555	15.4	151.3	7.2	99.8	36.5	375.6	1.1
G	970	61.75	0.0051	0.4681	12.3	100.2	7.1	99.7	44.4	370.7	1.1
H	1020	61.71	0.0058	0.6393	11.2	88.7	6.7	99.7	51.5	370.19	0.98
I	1080	62.14	0.0046	0.1931	17.4	110.9	7.0	99.9	62.7	373.2	1.2
J	1140	61.68	0.0048	0.1706	24.1	106.0	7.0	99.9	78.1	370.8	1.2
K	1200	62.18	0.0107	0.5083	12.4	47.5	7.6	99.7	86.0	373.0	1.0
L	1300	63.15	0.0843	0.3081	19.0	6.1	8.0	99.8	98.1	378.6	1.6
M	1650	64.38	0.0100	8.897	3.02	50.9	7.6	95.9	100.0	371.4	1.9
total gas age			n=13		156.6	64.2				369.5	1.2

49-129.2, E10:80, zoned Fe-Mg mica, 3.05 mg, J=0.003720215±0.09%, D=1.0052±0.00069, nm-80, Lab#=8577-01

ID	Temp (°C)	$^{40}Ar/^{39}Ar$	$^{37}Ar/^{39}Ar$	$^{36}Ar/^{39}Ar$ (x 10^{-3})	$^{39}Ar_K$ (x 10^{-15} mol)	K/Ca	Cl/K (x 10^{-3})	$^{40}Ar^*$ (%)	^{39}Ar (%)	Age (Ma)	±2s (Ma)
A	600	23.51	0.1772	26.58	0.169	2.9	18.4	66.6	0.1	102.1	11.5
B	670	25.90	0.0462	3.475	0.408	11.0	8.9	96.0	0.3	159.6	4.7
C	750	75.05	0.0784	5.210	0.964	6.5	5.0	97.9	0.7	436.1	3.9
D	830	76.22	0.0079	3.981	2.53	64.3	4.9	98.4	1.9	444.1	1.7
E	860	72.88	0.0017	2.761	3.89	295.8	4.6	98.9	3.6	428.4	2.0
F	900	73.99	0.0009	2.150	8.35	570.9	3.7	99.1	7.5	435.2	1.5
G	970	74.35	0.0006	0.4380	19.0	906.5	2.8	99.8	16.2	439.8	1.4
H	1020	71.54	0.0008	0.6896	9.34	627.6	2.1	99.7	20.4	424.5	1.3
I	1080	73.12	0.0005	0.4679	10.5	1089.4	2.2	99.8	25.2	433.2	1.5
J	1140	73.39	0.0003	0.1958	21.5	1573.4	2.3	99.9	35.1	435.1	1.6
K	1200	73.60	0.0004	0.2427	19.8	1387.1	2.3	99.9	44.2	436.1	1.8
L	1300	75.08	0.0004	0.2430	56.4	1321.7	2.0	99.9	70.0	443.9	1.7
M	1650	76.94	0.0005	0.5873	65.5	1091.5	1.2	99.7	100.0	453.1	2.4
total gas age			n=13		218.3	1135.6				442.0	1.8

49-113.7 f1:80, zoned Fe-Mg mica, 2.43 mg, J=0.00376009±0.09%, D=1.0052±0.00069, nm-80, Lab#=8579-01

ID	Temp (°C)	$^{40}Ar/^{39}Ar$	$^{37}Ar/^{39}Ar$	$^{36}Ar/^{39}Ar$ (x 10^{-3})	$^{39}Ar_K$ (x 10^{-15} mol)	K/Ca	Cl/K (x 10^{-3})	$^{40}Ar^*$ (%)	^{39}Ar (%)	Age (Ma)	±2s (Ma)
A	600	165.0	0.0573	506.8	0.151	8.9	62.9	9.2	0.1	100.2	58.0
B	670	51.91	0.0438	33.62	0.690	11.7	19.6	80.8	0.5	264.3	4.2
C	750	58.34	0.0129	7.583	2.35	39.7	10.6	96.1	1.9	345.2	1.8
D	830	67.98	0.0051	6.196	3.10	99.7	10.1	97.3	3.8	400.6	1.8
E	860	71.84	0.0011	1.008	17.1	452.7	6.4	99.6	14.2	429.7	1.3
F	900	68.93	0.0010	0.5489	12.1	489.7	5.6	99.7	21.6	414.8	1.5
G	970	69.02	0.0015	0.6003	13.1	340.9	5.3	99.7	29.5	415.2	1.0
H	1020	69.30	0.0168	0.7346	11.3	30.4	5.7	99.7	36.4	416.5	1.3
I	1080	68.99	0.0209	0.2842	17.3	24.4	5.9	99.8	46.9	415.5	1.2

ID	Temp (°C)	$^{40}Ar/^{39}Ar$	$^{37}Ar/^{39}Ar$	$^{36}Ar/^{39}Ar$ (x 10^{-3})	$^{39}Ar_K$ (x 10^{-15} mol)	K/Ca	Cl/K (x 10^{-3})	$^{40}Ar^*$ (%)	^{39}Ar (%)	Age (Ma)	±2s (Ma)
J	1140	68.24	0.0042	0.2213	31.2	120.6	6.1	99.9	65.8	411.6	1.6
K	1200	67.56	0.0052	0.3089	24.4	98.4	6.7	99.8	80.6	407.8	1.5
L	1300	68.47	0.0084	0.1497	27.2	60.6	5.6	99.9	97.1	413.0	2.3
M	1650	68.94	0.0027	3.679	4.72	188.2	5.9	98.4	100.0	409.9	1.7
total gas age			n=13		164.8	170.1				412.3	1.6
TR6A, amphibole, 8.73 mg, J=0.01489866±0.10%, D=1.00644±0.00091, nm-116, Lab#=50781-01											
A	800	6.446	1.420	3.514	10.2	0.36	19.3	85.3	3.5	142.2	2.3
B	850	11.22	1.709	0.6954	40.7	0.30	2.3	99.2	17.3	277.16	0.94
C	950	11.04	0.1744	0.5207	36.5	2.9	1.6	98.5	29.7	270.84	0.87
D	1020	12.19	1.817	1.468	49.0	0.28	2.5	97.4	46.4	294.4	1.0
E	1080	13.06	5.861	2.435	45.1	0.087	2.0	98.0	61.8	316.0	1.2
F	1120	13.13	2.395	1.348	43.1	0.21	1.3	98.3	76.4	317.6	1.2
G	1160	11.83	2.775	1.568	24.5	0.18	5.0	97.8	84.8	287.4	1.1
H	1200	11.74	3.624	1.895	8.07	0.14	393.2	97.5	87.5	284.8	1.5
I	1300	12.29	5.129	2.011	29.4	0.099	6.0	98.4	97.5	299.9	1.3
J	1400	15.99	9.772	7.223	6.34	0.052	6.4	91.5	99.7	357.9	2.6
K	1650	27.67	69.86	65.02	0.907	0.007	20.1	51.2	100.0	361.9	17.4
total gas age			n=11		293.7	0.54				291.8	1.2
397, amphibole 5.05 mg, J=0.01494847±0.10%, D=1.00644±0.00091, nm-116, Lab#=50782-01											
A	800	13.40	9.351	8.356	12.8	0.055	22.7	87.1	9.2	292.0	1.9
B	850	14.67	4.569	2.687	13.3	0.11	7.8	97.0	18.8	348.8	1.4
C	950	14.14	1.239	1.124	15.9	0.41	7.2	98.2	30.2	340.5	1.2
D	1020	13.97	2.227	1.814	20.3	0.23	8.4	97.3	44.8	334.2	1.3
E	1080	14.94	7.362	3.056	20.6	0.069	10.3	97.8	59.6	358.2	1.5
F	1120	14.82	4.751	1.840	21.7	0.11	7.3	98.8	75.3	358.1	1.4
G	1160	14.84	2.072	1.332	20.5	0.25	6.9	98.3	90.1	356.4	1.2
H	1200	13.51	4.286	1.977	3.24	0.12	724.3	98.1	92.4	327.0	3.8
I	1300	12.88	7.110	2.783	8.03	0.072	16.6	97.9	98.2	313.1	1.7
J	1400	15.45	18.64	11.46	1.78	0.027	12.8	87.8	99.5	337.1	7.4
K	1650	32.47	86.92	88.84	0.714	0.006	43.8	41.1	100.0	347.5	21.9
total gas age			n=11		138.9	0.17				341.7	1.6
700-2 E:10:95, biotite, 6.18 mg, J=0.003962505±0.08%, D=1.00362±0.00105, NM-95, Lab#=9564-01											
A	600	46.28	0.1088	45.34	1.85	4.7	9.2	71.0	1.3	220.9	1.8
B	670	66.32	15.04	12.62	3.53	0.034	7.0	96.1	3.7	409.8	1.6
C	750	68.50	8.021	3.017	10.7	0.064	7.3	99.6	11.0	433.6	1.9
D	830	68.59	4.722	0.9256	18.6	0.11	7.4	100.1	23.7	435.3	2.1
E	860	67.81	4.532	0.7576	11.6	0.11	7.6	100.2	31.7	431.1	1.7
F	900	67.19	8.360	1.279	8.27	0.061	7.5	100.4	37.3	429.3	1.9
G	970	65.36	12.35	2.823	9.29	0.041	7.4	100.1	43.7	419.0	1.6
H	1020	65.85	8.724	2.832	11.2	0.058	7.1	99.7	51.4	419.3	1.9
I	1080	66.93	13.77	1.789	13.8	0.037	7.5	100.8	60.8	430.7	2.0
J	1140	68.30	8.674	1.306	19.0	0.059	7.4	100.4	73.7	435.7	1.7
K	1200	69.14	18.59	0.7045	19.5	0.027	8.0	101.7	87.1	448.3	2.4
L	1300	68.74	6.007	0.4603	18.3	0.085	7.6	100.4	99.5	437.8	2.6
M	1650	68.11	8.749	12.41	0.689	0.058	5.6	95.6	100.0	416.1	2.4

ID	Temp (°C)	$^{40}Ar/^{39}Ar$	$^{37}Ar/^{39}Ar$	$^{36}Ar/^{39}Ar$ (x 10^{-3})	$^{39}Ar_K$ (x 10^{-15} mol)	K/Ca	Cl/K (x 10^{-3})	$^{40}Ar^*$ (%)	^{39}Ar (%)	Age (Ma)	±2s (Ma)
total gas age			n=13		146.3	0.12				430.5	2.2
700-2, hornblende, 5.46 mg, J=0.003974663±0.08%, D=1.00362±0.00105, NM-95, Lab#=9565-01											
A	800	100.8	1.574	145.0	0.283	0.32	40.1	57.6	2.6	375.2	7.7
B	900	50.21	1.539	13.27	0.277	0.33	7.5	92.4	5.1	305.7	3.0
C	1000	66.97	8.117	12.04	0.663	0.063	37.1	95.7	11.2	411.6	2.1
D	1050	70.96	7.948	6.848	1.59	0.064	57.2	98.0	25.8	442.9	1.6
E	1080	70.79	7.660	4.071	3.57	0.067	62.6	99.2	58.6	446.3	1.7
F	1110	68.34	6.967	5.784	0.448	0.073	51.5	98.3	62.7	429.1	3.0
G	1130	67.73	7.670	2.938	0.303	0.067	49.7	99.6	65.5	430.9	3.7
H	1150	68.42	7.767	4.916	0.604	0.066	50.5	98.8	71.0	431.6	2.4
I	1180	71.00	7.557	4.246	1.56	0.068	53.9	99.1	85.3	447.1	1.8
J	1220	72.23	7.813	4.019	1.31	0.065	67.0	99.2	97.3	454.6	2.0
K	1300	78.21	9.834	9.620	0.097	0.052	71.9	97.4	98.2	480.3	10.8
L	1650	74.21	3.176	23.23	0.197	0.16	21.4	91.1	100.0	430.2	6.3
total gas age			n=12		10.9	0.081				437.5	2.2
59-85.5 E2 :80, sericite, 2.43 mg, J=0.00374505±0.09%, D=1.0052±0.00069, nm-80, Lab#=8572-01											
A	500	307.3	0.0554	984.3	0.063	9.2	21.6	5.3	0.0	107.4	192.2
B	550	39.91	0.0050	41.10	1.06	102.7	16.0	69.5	0.6	178.3	3.0
C	600	43.74	0.0047	6.153	0.909	109.7	8.6	95.8	1.1	263.0	2.8
D	625	46.91	0.0000	19.90	0.064	-	9.5	87.4	1.2	257.8	21.7
E	650	43.81	0.0172	4.282	1.91	29.7	2.5	97.1	2.3	266.6	1.4
F	675	44.83	0.0327	2.446	1.44	15.6	1.5	98.3	3.1	275.7	2.0
G	700	45.27	0.0435	3.286	2.13	11.7	1.0	97.8	4.3	276.8	1.5
H	725	46.07	0.0430	2.099	3.00	11.9	0.63	98.6	5.9	283.5	1.2
I	750	46.82	0.0410	2.088	3.65	12.4	0.42	98.6	8.0	287.8	1.1
J	800	47.49	0.0415	1.047	2.69	12.3	0.65	99.3	9.5	293.5	1.5
K	900	50.17	0.0094	0.8651	15.1	54.1	0.43	99.4	18.0	309.1	1.1
L	1000	54.10	0.0019	0.7428	51.9	268.2	0.34	99.6	47.2	331.5	1.3
M	1100	57.79	0.0014	0.4643	47.8	369.1	0.30	99.7	74.0	352.6	1.6
N	1200	57.68	0.0023	0.7563	21.3	220.1	0.24	99.6	86.0	351.5	1.2
O	1650	58.32	0.0198	0.9749	25.0	25.7	0.63	99.5	100.0	354.7	1.4
total gas age			n=15		178.0	214.3				335.4	1.4
62-115.2 e8 :80, sericite, 2.56 mg, J=0.00367855±0.09%, D=1.0052±0.00069, nm-80, Lab#=8576-01											
A	650	45.53	0.0030	47.44	2.09	171.9	4.3	69.2	1.1	197.8	2.3
B	700	42.37	0.0152	1.417	7.35	33.5	0.18	99.0	4.8	258.8	1.0
C	750	43.53	0.0164	0.9012	11.2	31.0	0.20	99.3	10.6	266.3	1.0
D	800	44.33	0.0007	1.109	5.89	721.9	0.16	99.2	13.6	270.54	0.94
E	840	45.40	0.0004	0.7265	22.3	1284.8	0.18	99.5	25.1	277.29	0.76
F	880	47.27	0.0001	0.8408	16.3	4033.8	0.20	99.4	33.4	287.69	0.95
G	920	49.52	0.0002	0.9243	13.6	2406.2	0.062	99.4	40.4	300.23	0.93
H	960	50.60	0.0002	1.024	20.7	2045.0	0.19	99.4	51.1	306.2	1.1
I	1000	52.62	0.0003	0.7231	24.1	1538.2	0.16	99.6	63.5	317.93	0.88
J	1040	54.93	0.0000	0.7101	9.86	14764.1	0.051	99.6	68.5	330.72	0.99
K	1080	56.63	0.0001	0.4183	23.4	3653.5	0.21	99.7	80.5	340.6	1.2
L	1120	56.35	0.0002	0.3554	20.9	2226.0	0.14	99.8	91.3	339.1	1.1

ID	Temp (°C)	$^{40}Ar/^{39}Ar$	$^{37}Ar/^{39}Ar$	$^{36}Ar/^{39}Ar$ (x 10^{-3})	$^{39}Ar_K$ (x 10^{-15} mol)	K/Ca	Cl/K (x 10^{-3})	$^{40}Ar*$ (%)	^{39}Ar (%)	Age (Ma)	±2s (Ma)
M	1160	55.67	0.0000	0.8380	7.03	-	0.025	99.5	94.9	334.6	1.1
N	1200	54.71	0.0000	2.808	1.69	-	-0.073	98.4	95.8	326.1	2.0
O	1650	56.30	0.0003	3.362	8.24	1505.6	0.29	98.2	100.0	334.0	1.1
total gas age			n=15		194.8	2579.8				307.3	1.0

59-85.5, Fine fuchsite 2.79 mg, J=0.003668547±0.09%, D=1.0052±0.00069, NM-80, Lab#=8575-01

ID	Temp (°C)	$^{40}Ar/^{39}Ar$	$^{37}Ar/^{39}Ar$	$^{36}Ar/^{39}Ar$ (x 10^{-3})	$^{39}Ar_K$ (x 10^{-15} mol)	K/Ca	Cl/K (x 10^{-3})	$^{40}Ar*$ (%)	^{39}Ar (%)	Age (Ma)	±2s (Ma)
A	650	49.93	0.0374	33.73	6.36	13.7	6.9	80.0	2.9	246.7	1.5
B	700	46.03	0.0790	2.038	4.52	6.5	1.1	98.7	5.0	278.0	1.0
C	750	47.40	0.0752	1.331	7.63	6.8	0.76	99.1	8.5	286.9	1.1
D	800	48.82	0.0648	1.444	5.32	7.9	0.65	99.1	10.9	294.8	1.2
E	840	50.48	0.0294	1.189	8.02	17.3	0.33	99.3	14.6	304.5	1.1
F	880	52.51	0.0067	0.8408	8.02	76.6	0.50	99.5	18.3	316.35	0.97
G	920	53.88	0.0040	1.248	13.4	128.6	0.42	99.3	24.4	323.2	1.2
H	960	55.63	0.0026	0.8651	19.9	198.7	0.21	99.5	33.6	333.6	1.3
I	1000	58.32	0.0020	0.9129	18.0	261.5	0.20	99.5	41.8	348.2	1.2
J	1040	59.83	0.0012	0.9660	33.2	419.9	0.11	99.5	57.0	356.3	1.3
K	1080	61.22	0.0010	0.8975	31.8	495.1	0.25	99.5	71.6	364.0	1.1
L	1120	61.81	0.0011	0.3496	32.9	476.6	0.12	99.8	86.7	368.0	1.2
M	1160	63.14	0.0019	0.7201	16.0	267.3	0.11	99.6	94.0	374.6	1.3
N	1200	62.56	0.0154	2.617	1.70	33.1	0.53	98.7	94.8	368.4	2.1
O	1300	60.34	0.0762	3.008	1.66	6.7	0.059	98.5	95.6	355.9	2.4
P	1650	62.85	0.0339	1.546	9.62	15.1	1.1	99.2	100.0	371.8	1.2
Q	1750	235.6	0.1128	402.2	0.031	4.5	-9.658	49.6	100.0	643.3	196.4
total gas age			n=17		217.9	280.6				344.4	1.2

AD2 C3 :80, muscovite, 2.54 mg, J=0.003695409±0.09%, D=1.0052±0.00069, nm-80, Lab#=8566-01

ID	Temp (°C)	$^{40}Ar/^{39}Ar$	$^{37}Ar/^{39}Ar$	$^{36}Ar/^{39}Ar$ (x 10^{-3})	$^{39}Ar_K$ (x 10^{-15} mol)	K/Ca	Cl/K (x 10^{-3})	$^{40}Ar*$ (%)	^{39}Ar (%)	Age (Ma)	±2s (Ma)
A	650	61.61	0.2966	63.66	0.865	1.7	86.8	69.5	0.4	264.9	5.6
B	700	53.73	0.2302	12.08	0.790	2.2	23.3	93.4	0.8	306.8	4.4
C	750	55.89	0.0971	7.265	1.69	5.3	12.6	96.1	1.7	326.8	2.0
D	800	59.04	0.0039	9.169	2.26	129.2	7.7	95.4	2.8	341.0	1.9
E	840	60.84	0.0028	5.836	4.55	181.6	3.8	97.1	5.2	356.4	1.5
F	880	62.25	0.0013	2.928	7.99	387.7	2.2	98.6	9.2	368.7	1.3
G	920	63.49	0.0008	1.344	16.8	646.7	0.78	99.3	17.8	378.0	1.2
H	960	63.56	0.0005	0.8055	27.7	999.0	0.27	99.6	31.9	379.2	1.6
I	1000	63.47	0.0005	0.7270	18.7	1127.5	0.26	99.6	41.4	378.9	1.5
J	1040	63.32	0.0004	0.6750	17.1	1360.8	0.20	99.7	50.1	378.1	1.3
K	1080	63.55	0.0006	0.6255	13.1	892.4	0.36	99.7	56.8	379.4	1.2
L	1120	63.72	0.0003	0.4823	17.9	1717.1	0.58	99.7	65.9	380.6	1.1
M	1160	64.11	0.0006	0.5709	16.5	863.0	37.9	99.7	74.3	382.6	1.3
N	1200	63.94	0.0005	0.2547	20.4	1059.3	0.59	99.8	84.7	382.2	2.0
O	1300	64.56	0.0009	0.9708	9.88	557.2	1.9	99.5	89.7	384.4	1.5
P	1650	65.55	0.0005	1.369	20.2	928.8	1.6	99.4	100.0	389.0	1.4
total gas age			n=16		196.5	965.4				378.3	1.4

AD2A, Muscovite 3.47 mg, J=0.003755053±0.09%, D=1.0052±0.00069, NM-80, Lab#=8571-01

ID	Temp (°C)	$^{40}Ar/^{39}Ar$	$^{37}Ar/^{39}Ar$	$^{36}Ar/^{39}Ar$ (x 10^{-3})	$^{39}Ar_K$ (x 10^{-15} mol)	K/Ca	Cl/K (x 10^{-3})	$^{40}Ar*$ (%)	^{39}Ar (%)	Age (Ma)	±2s (Ma)
A	650	89.69	0.4572	149.7	0.782	1.1	42.3	50.7	0.3	284.4	6.5
B	700	56.82	1.075	19.59	1.14	0.47	2.4	89.9	0.7	316.8	2.8
C	750	58.35	0.2474	14.61	2.18	2.1	0.69	92.6	1.5	333.3	2.1

ID	Temp (°C)	$^{40}Ar/^{39}Ar$	$^{37}Ar/^{39}Ar$	$^{36}Ar/^{39}Ar$ (x 10^{-3})	$^{39}Ar_K$ (x 10^{-15} mol)	K/Ca	Cl/K (x 10^{-3})	$^{40}Ar^*$ (%)	^{39}Ar (%)	Age (Ma)	±2s (Ma)
D	800	59.87	0.0102	11.17	2.89	49.9	-0.001	94.5	2.6	347.4	1.6
E	840	61.41	0.0041	7.911	6.42	125.2	0.27	96.2	5.0	361.3	1.3
F	880	62.41	0.0024	4.240	11.0	212.5	0.32	98.0	9.1	372.8	1.1
G	920	62.36	0.0012	2.583	24.1	417.8	0.084	98.7	18.1	375.3	1.2
H	960	62.24	0.0007	0.9867	37.5	752.6	0.12	99.5	32.1	377.2	1.6
I	1000	62.16	0.0005	0.8714	24.2	996.4	0.16	99.6	41.2	376.9	1.5
J	1040	62.08	0.0006	1.193	21.2	914.1	0.13	99.4	49.1	376.0	1.4
K	1080	62.33	0.0005	1.512	18.9	1092.8	0.043	99.2	56.2	376.8	1.2
L	1120	62.31	0.0004	1.625	24.1	1194.0	0.037	99.2	65.2	376.5	1.2
M	1160	62.78	0.0001	1.035	25.7	3430.4	0.13	99.5	74.8	380.1	1.3
N	1200	62.45	0.0001	0.6193	27.4	3489.3	0.060	99.7	85.0	378.9	1.1
O	1300	62.70	0.0006	0.6524	11.6	831.2	0.42	99.7	89.4	380.3	1.1
P	1650	63.32	0.0005	0.8151	28.5	1103.3	0.36	99.6	100.0	383.4	1.5
total gas age			n=16		267.6	1343.6				376.3	1.3

601 F:5:95, Muscovite 6.93 mg, J=0.003913398±0.08%, D=1.00362±0.00105, NM-95, Lab#=9569-01

ID	Temp (°C)	$^{40}Ar/^{39}Ar$	$^{37}Ar/^{39}Ar$	$^{36}Ar/^{39}Ar$ (x 10^{-3})	$^{39}Ar_K$ (x 10^{-15} mol)	K/Ca	Cl/K (x 10^{-3})	$^{40}Ar^*$ (%)	^{39}Ar (%)	Age (Ma)	±2s (Ma)
A	650	52.75	0.0038	16.42	4.68	133.7	4.0	90.8	2.5	309.8	1.3
B	700	54.24	0.0015	5.364	4.42	336.7	0.48	97.0	4.9	337.9	1.3
C	750	56.41	0.0013	5.229	7.04	378.8	0.69	97.2	8.7	350.8	1.3
D	800	58.53	0.0007	4.087	7.03	703.6	0.54	97.9	12.5	365.0	1.2
E	840	59.75	0.0007	2.114	15.2	746.9	0.38	98.9	20.6	375.3	1.7
F	880	60.31	0.0004	1.025	19.1	1254.9	0.18	99.5	30.9	380.4	1.6
G	920	60.63	0.0005	0.7180	20.5	1026.3	0.24	99.6	41.9	382.8	2.2
H	960	60.45	0.0004	0.9313	16.3	1301.6	0.27	99.5	50.7	381.3	1.2
I	1000	60.57	0.0003	0.8677	12.5	1823.0	0.29	99.5	57.4	382.1	2.0
J	1040	60.85	0.0004	1.048	13.8	1298.1	0.29	99.5	64.9	383.4	1.8
K	1080	61.10	0.0002	1.029	16.1	3253.2	0.28	99.5	73.6	384.9	2.3
L	1120	61.26	0.0003	0.7616	24.7	1887.6	0.092	99.6	86.8	386.3	1.3
M	1160	61.12	0.0002	0.4639	11.2	2321.3	0.025	99.7	92.9	386.0	1.6
N	1200	61.52	0.0000	0.3821	4.44	-	0.000	99.8	95.3	388.4	1.3
O	1300	61.87	0.0000	0.5748	2.23	-	0.26	99.7	96.5	390.0	1.7
P	1650	62.05	0.0002	1.002	6.52	2304.7	0.19	99.5	100.0	390.4	1.1
total gas age			n=16		185.7	1446.7				378.3	1.6

547 F:7:95, Muscovite 5.30 mg", J=0.003925119±0.08%, D=1.00362±0.00105, NM-95, Lab#=9570-01

ID	Temp (°C)	$^{40}Ar/^{39}Ar$	$^{37}Ar/^{39}Ar$	$^{36}Ar/^{39}Ar$ (x 10^{-3})	$^{39}Ar_K$ (x 10^{-15} mol)	K/Ca	Cl/K (x 10^{-3})	$^{40}Ar^*$ (%)	^{39}Ar (%)	Age (Ma)	±2s (Ma)
AA	650	55.91	0.0018	33.70	0.695	276.7	2.6	82.1	0.6	299.0	2.2
B	700	56.18	0.0012	17.59	0.785	428.7	0.12	90.7	1.2	328.9	1.7
C	750	58.67	0.0011	12.28	1.49	452.3	0.73	93.8	2.4	352.7	1.6
D	800	59.36	0.0004	4.933	2.75	1203.9	0.33	97.5	4.7	369.4	1.5
E	840	60.00	0.0004	0.9606	5.44	1327.2	0.27	99.5	9.1	379.7	1.4
F	880	60.75	0.0004	0.4382	8.66	1303.6	0.22	99.7	16.1	384.9	1.6
G	920	61.56	0.0003	0.2513	16.9	1595.4	0.040	99.8	29.8	389.9	2.2
H	960	61.06	0.0003	0.2837	14.0	1619.5	0.029	99.8	41.2	387.0	1.6
I	1000	60.73	0.0003	0.1761	9.07	1893.5	0.007	99.9	48.6	385.3	1.5
J	1040	61.15	0.0002	0.2414	8.87	2619.7	0.045	99.8	55.8	387.5	1.8
K	1080	60.82	0.0003	0.3127	8.58	1734.3	0.15	99.8	62.8	385.6	1.6
L	1120	61.24	0.0002	0.3168	10.2	2092.2	0.15	99.8	71.1	387.9	1.6
M	1160	61.53	0.0000	0.1836	12.2	11641.8	0.060	99.9	81.1	389.8	1.7

ID	Temp (°C)	$^{40}Ar/^{39}Ar$	$^{37}Ar/^{39}Ar$	$^{36}Ar/^{39}Ar$ (x 10^{-3})	$^{39}Ar_K$ (x 10^{-15} mol)	K/Ca	Cl/K (x 10^{-3})	$^{40}Ar*$ (%)	^{39}Ar (%)	Age (Ma)	±2s (Ma)
N	1200	61.39	0.0003	0.1035	8.44	1514.3	0.038	99.9	87.9	389.2	1.3
O	1300	62.01	0.0001	0.3122	2.86	4258.5	0.31	99.8	90.2	392.4	1.5
P	1650	61.68	0.0002	0.2740	12.0	2298.6	-0.044	99.8	100.0	390.5	1.8
total gas age			n=16		123.0	2799.9				386.0	1.6
532 F:1:95, Muscovite 5.14 mg, J=0.003952481±0.08%, D=1.00362±0.00105, NM-95, Lab#=9566-01											
A	650	51.59	0.0549	24.91	0.728	9.3	26.4	85.7	0.6	290.5	1.9
B	700	60.05	0.1693	6.653	0.759	3.0	2.3	96.7	1.2	372.8	1.7
C	750	61.24	0.0911	7.600	1.25	5.6	0.62	96.3	2.1	378.0	1.5
D	800	61.18	0.0167	3.684	2.10	30.6	0.53	98.2	3.8	384.3	1.5
E	840	61.59	0.0081	3.425	4.31	63.2	0.30	98.3	7.2	387.1	1.4
F	880	61.14	0.0037	0.9458	6.41	137.4	0.19	99.5	12.2	388.7	1.4
G	920	60.95	0.0015	0.5879	11.8	349.6	0.052	99.7	21.4	388.3	2.0
H	960	61.13	0.0008	0.3746	19.5	651.4	0.080	99.8	36.7	389.7	1.6
I	1000	61.21	0.0008	0.2553	10.6	668.3	0.097	99.8	45.0	390.3	2.0
J	1040	60.98	0.0006	0.3246	11.3	888.8	0.004	99.8	53.9	388.9	1.6
K	1080	61.16	0.0006	0.2947	11.2	849.1	0.098	99.8	62.6	390.0	1.8
L	1120	61.28	0.0004	0.2093	14.2	1254.0	0.014	99.9	73.8	390.8	2.4
M	1160	61.20	0.0004	0.2064	18.7	1181.1	0.014	99.9	88.4	390.3	1.9
N	1200	61.21	0.0005	0.2843	4.92	947.5	0.086	99.8	92.2	390.2	1.4
O	1300	61.95	0.0009	0.4067	1.86	571.1	0.46	99.8	93.7	394.3	1.5
P	1650	62.00	0.0005	0.7364	8.04	1023.0	0.14	99.6	100.0	394.0	1.7
total gas age			n=16		127.7	771.8				389.1	1.8
617 F:2:95, Muscovite 6.64 mg, J=0.003939931±0.08%, D=1.00362±0.00105, NM-95, Lab#=9567-01											
A	650	51.74	0.0024	22.38	3.96	210.9	27.8	87.2	3.0	295.1	1.2
B	700	54.75	0.0018	1.441	5.47	288.6	2.1	99.2	7.0	349.8	1.3
C	750	55.71	0.0013	1.506	6.92	406.6	1.2	99.2	12.2	355.2	1.7
D	800	56.40	0.0007	1.647	6.29	739.0	0.96	99.1	16.9	359.0	1.3
E	840	57.51	0.0007	1.290	9.83	756.1	0.63	99.3	24.2	366.1	1.4
F	880	58.62	0.0005	0.8371	11.7	1012.8	0.50	99.5	33.0	373.3	1.5
G	920	58.70	0.0006	0.6319	13.5	804.1	0.38	99.6	43.1	374.1	1.9
H	960	58.20	0.0010	0.6545	11.4	521.1	0.53	99.6	51.6	371.2	1.4
I	1000	58.56	0.0008	0.5180	9.43	659.0	0.46	99.7	58.6	373.5	1.7
J	1040	59.31	0.0007	0.4732	12.4	771.4	0.38	99.7	67.8	377.9	2.0
K	1080	59.76	0.0006	0.3822	16.6	895.5	0.26	99.8	80.2	380.6	1.6
L	1120	59.74	0.0006	0.3038	15.0	821.5	0.23	99.8	91.4	380.7	1.4
M	1160	59.97	0.0005	0.3581	7.99	943.9	0.17	99.8	97.4	381.9	1.6
N	1200	60.45	0.0012	0.4348	1.85	440.3	0.16	99.7	98.7	384.6	1.4
O	1300	61.30	0.0014	0.7592	0.872	352.4	0.37	99.6	99.4	388.9	1.8
P	1650	62.01	0.0015	3.197	0.812	350.1	0.53	98.4	100.0	388.8	2.5
total gas age			n=16		134.1	730.3				370.8	1.6
659 F:4:95, Muscovite 5.40 mg", J=0.003917367±0.08%, D=1.00362±0.00105, NM-95, Lab#=9568-01											
A	650	53.18	0.9664	22.32	1.28	0.53	5.1	87.7	0.8	302.9	1.9
B	700	55.54	0.3491	3.202	1.74	1.5	0.89	98.3	1.9	349.8	1.6
C	750	58.70	0.0140	3.586	3.13	36.5	0.55	98.2	3.9	367.2	1.4
D	800	60.26	0.0057	2.972	4.69	89.8	0.43	98.5	6.8	377.1	1.3

ID	Temp (°C)	$^{40}Ar/^{39}Ar$	$^{37}Ar/^{39}Ar$	$^{36}Ar/^{39}Ar$ (x 10^{-3})	$^{39}Ar_K$ (x 10^{-15} mol)	K/Ca	Cl/K (x 10^{-3})	$^{40}Ar^*$ (%)	^{39}Ar (%)	Age (Ma)	±2s (Ma)
E	840	60.76	0.0034	2.001	9.37	152.0	0.39	99.0	12.7	381.7	2.2
F	880	61.95	0.0011	0.8315	26.3	473.5	0.092	99.6	29.2	390.5	2.1
G	920	61.32	0.0012	0.5242	18.4	438.3	0.091	99.7	40.7	387.3	1.6
H	960	61.00	0.0012	0.7508	11.1	408.5	0.14	99.6	47.7	385.2	1.7
I	1000	60.84	0.0007	0.7249	10.2	694.3	0.013	99.6	54.1	384.3	1.8
J	1040	61.07	0.0006	0.6448	13.7	795.0	0.082	99.6	62.7	385.7	1.9
K	1080	61.34	0.0006	0.4813	13.6	831.3	0.040	99.7	71.3	387.6	1.5
L	1120	61.85	0.0005	0.6697	8.91	952.7	0.12	99.6	76.9	390.1	2.0
M	1160	61.87	0.0006	0.4830	9.67	920.1	-0.007	99.7	82.9	390.6	1.6
N	1200	61.54	0.0006	0.4157	8.90	837.9	0.11	99.8	88.5	388.8	2.4
O	1300	61.14	0.0008	0.3510	10.7	641.8	0.50	99.8	95.2	386.7	1.4
P	1650	62.64	0.0005	0.7065	7.63	1058.5	0.34	99.6	100.0	394.6	1.6
total gas age			n=16		159.3	603.1				386.0	1.8

57-157.5 -1biotite, 2.47 mg, J=0.01563256±0.10%, D=1.00707±0.0007, NM-122, Lab#=51182-01

A	*670*	*18.58*	*0.0217*	*17.25*	*42.9*	*23.5*	*64.3*	*72.4*	*4.7*	*344.5*	*5.5*
B	750	16.30	0.0042	0.1044	179.8	120.2	5.4	99.6	24.6	408.2	1.7
C	830	15.79	0.0030	0.0400	228.1	169.1	3.0	99.8	49.7	397.1	2.0
D	900	15.53	0.0027	0.0085	126.3	189.9	3.0	99.8	63.7	391.5	1.3
E	970	15.33	0.0033	0.0817	76.5	155.5	3.1	99.7	72.1	386.5	1.1
F	1020	15.60	0.0034	0.1722	48.2	151.2	4.1	99.5	77.5	391.9	1.8
G	1080	15.53	0.0040	0.2280	45.8	127.7	4.3	99.4	82.5	390.1	2.0
H	1140	15.51	0.0014	0.1236	55.4	356.9	77.8	99.6	88.6	390.1	1.4
I	1200	15.50	0.0013	-0.0222	50.8	384.8	5.9	99.9	94.2	390.9	1.2
J	1300	15.66	0.0030	0.2127	44.3	170.1	2.8	99.4	99.1	393.0	2.1
K	*1650*	*20.95*	*0.0820*	*5.383*	*7.92*	*6.2*	*7.4*	*92.3*	*100.0*	*476.5*	*3.7*
total gas age			n=11		906.1	173.4				394.2	1.8
plateau			n=9	steps B-J	855.3	182.5			94.4	391.9	7.5
MSWD**		65.96									

57-157.5 -2biotite, 4.53 mg, J=0.0157649±0.10%, D=1.00707±0.0007, NM-122, Lab#=51183-01

A	*670*	*15.52*	*0.1876*	*6.266*	*100.4*	*2.7*	*17.8*	*88.0*	*6.7*	*351.9*	*2.5*
B	750	15.69	0.0693	0.1114	208.2	7.4	3.2	99.7	20.5	397.5	2.0
C	830	15.46	0.0034	0.0745	284.4	149.1	2.5	99.7	39.4	392.5	1.2
D	900	15.26	0.0037	-0.1526	136.3	138.5	2.7	100.1	48.4	389.3	3.4
E	970	15.27	0.0048	-0.2674	90.2	106.7	3.0	100.3	54.4	390.3	2.8
F	1020	15.48	0.0046	-0.2514	73.8	111.8	3.6	100.3	59.3	395.1	2.2
G	1080	15.21	0.0026	-0.1917	110.5	198.0	3.0	100.2	66.7	388.5	2.5
H	1140	15.22	0.0018	-0.0425	159.4	284.8	33.3	99.9	77.2	387.7	1.2
I	1200	15.21	0.0011	-0.0442	157.9	454.2	3.6	99.9	87.7	387.4	1.6
J	1300	15.37	0.0018	0.1042	146.9	288.8	2.2	99.6	97.5	390.1	2.1
K	*1650*	*16.35*	*0.0167*	*1.306*	*38.0*	*30.6*	*4.5*	*97.5*	*100.0*	*404.5*	*3.9*
total gas age			n=11		1506.0	175.0				388.9	2.0
plateau			n=9	steps B-J	1367.6	191.6			90.8	390.6	3.8
MSWD**		14.96									

669-3 F:8:95, Fuchsite 7.45mg", J=0.003937669±0.08%, D=1.00362±0.00105, NM-95, Lab#=9571-01

A	650	46.66	0.0219	12.72	3.49	23.4	13.9	91.9	2.1	281.5	1.5

ID	Temp (°C)	$^{40}Ar/^{39}Ar$	$^{37}Ar/^{39}Ar$	$^{36}Ar/^{39}Ar$ (x 10^{-3})	$^{39}Ar_K$ (x 10^{-15} mol)	K/Ca	Cl/K (x 10^{-3})	$^{40}Ar^*$ (%)	^{39}Ar (%)	Age (Ma)	±2s (Ma)
B	700	58.66	0.0186	1.293	3.54	27.4	1.0	99.3	4.3	372.6	1.4
C	750	59.62	0.0091	0.9102	5.25	56.3	0.65	99.5	7.5	378.8	1.2
D	800	60.09	0.0037	0.9603	6.48	137.8	0.64	99.5	11.5	381.4	1.5
E	840	60.43	0.0006	0.5577	11.8	794.1	0.25	99.7	18.8	384.0	2.0
F	880	61.08	0.0005	0.3058	18.8	1060.4	0.081	99.8	30.3	388.2	1.7
G	920	60.49	0.0003	0.2602	19.9	1905.7	0.17	99.8	42.5	384.8	1.9
H	960	59.75	0.0004	0.2174	17.7	1223.1	0.066	99.9	53.4	380.7	2.4
I	1000	59.45	0.0004	0.2579	14.9	1188.1	0.031	99.8	62.6	378.9	1.7
J	1040	59.71	0.0005	0.2891	14.9	964.1	0.089	99.8	71.7	380.3	1.9
K	1080	60.47	0.0005	0.3290	12.1	1072.7	0.18	99.8	79.2	384.6	1.8
L	1120	60.75	0.0004	0.4558	9.53	1182.3	0.12	99.7	85.0	386.0	1.5
M	1160	61.89	0.0005	0.3711	9.71	1012.9	0.10	99.8	91.0	392.7	1.4
N	1200	62.49	0.0007	0.4945	6.82	728.1	0.31	99.7	95.2	395.9	1.3
O	1300	63.68	0.0011	1.175	4.22	483.3	1.1	99.4	97.8	401.5	1.8
P	1650	77.74	0.0017	6.565	3.62	307.5	5.9	97.5	100.0	471.1	1.8
total gas age			n=16		162.8	1010.7				384.3	1.7

669-3 F8:95 (rerun of previous sample), fuchsite, 5.65 mg, J=0.003937669±0.08%, D=1.00362±0.00105, NM-95, Lab#=9571-02

ID	Temp (°C)	$^{40}Ar/^{39}Ar$	$^{37}Ar/^{39}Ar$	$^{36}Ar/^{39}Ar$ (x 10^{-3})	$^{39}Ar_K$ (x 10^{-15} mol)	K/Ca	Cl/K (x 10^{-3})	$^{40}Ar^*$ (%)	^{39}Ar (%)	Age (Ma)	±2s (Ma)
A	650	46.93	0.0098	25.88	3.73	52.0	18.7	83.7	1.7	259.3	1.5
B	700	57.74	0.0036	1.858	5.22	140.4	1.4	99.0	4.1	366.3	1.3
C	750	59.82	0.0008	1.258	6.15	656.2	0.46	99.3	7.0	379.3	1.7
D	800	60.21	0.0009	1.296	11.1	589.6	0.52	99.3	12.1	381.5	1.2
E	840	60.50	0.0005	0.7824	15.0	1024.6	0.33	99.6	19.1	384.0	1.7
F	880	61.48	0.0005	0.4919	23.5	981.3	0.056	99.7	30.0	390.1	1.4
G	920	60.50	0.0006	0.4426	28.0	897.5	0.14	99.7	42.9	384.6	1.4
H	960	60.18	0.0005	0.4317	28.1	1011.7	0.16	99.7	56.0	382.8	1.9
I	1000	59.93	0.0003	0.3713	22.8	2009.8	0.100	99.8	66.5	381.5	1.4
J	1040	60.26	0.0004	0.4353	20.7	1150.3	0.11	99.7	76.1	383.3	1.5
K	1080	60.82	0.0005	0.4835	16.3	1005.2	0.25	99.7	83.6	386.4	1.4
L	1120	61.98	0.0008	0.6054	10.8	651.5	0.14	99.7	88.6	392.8	1.8
M	1160	62.09	0.0012	0.5757	9.42	422.8	0.36	99.7	93.0	393.5	1.2
N	1200	62.47	0.0014	0.3677	6.92	370.4	0.23	99.8	96.2	396.0	1.3
O	1300	64.99	0.0123	1.393	3.69	41.5	2.2	99.3	97.9	408.6	1.8
P	1650	76.77	0.2473	9.001	4.57	2.1	6.7	96.5	100.0	462.0	1.6
total gas age			n=16		216.0	941.0				384.9	1.5

675-2 F:10:95, Fuchsite 8.69 mg", J=0.003960233±0.08%, D=1.00362±0.00105, NM-95, Lab#=9572-01

ID	Temp (°C)	$^{40}Ar/^{39}Ar$	$^{37}Ar/^{39}Ar$	$^{36}Ar/^{39}Ar$ (x 10^{-3})	$^{39}Ar_K$ (x 10^{-15} mol)	K/Ca	Cl/K (x 10^{-3})	$^{40}Ar^*$ (%)	^{39}Ar (%)	Age (Ma)	±2s (Ma)
A	650	33.30	0.0395	6.985	5.04	12.9	6.4	93.7	3.9	210.30	0.98
B	700	56.78	0.0406	1.093	5.73	12.6	0.94	99.4	8.3	363.9	1.2
C	750	61.98	0.0207	0.5952	7.53	24.6	0.27	99.7	14.1	394.9	1.4
D	800	62.24	0.0019	0.4719	6.92	269.4	0.050	99.7	19.4	396.5	1.5
E	840	61.90	0.0012	0.3684	8.84	413.1	-0.002	99.8	26.2	394.8	1.7
F	880	62.65	0.0008	0.2585	8.89	655.5	-0.027	99.8	33.0	399.3	1.6
G	920	63.02	0.0006	0.2180	11.2	815.1	-0.046	99.9	41.6	401.5	1.6
H	960	63.51	0.0005	0.2140	15.3	967.7	-0.023	99.9	53.3	404.3	1.4
I	1000	64.32	0.0005	0.1782	15.9	1095.2	-0.081	99.9	65.5	408.9	2.8
J	1040	65.25	0.0005	0.2009	17.0	1048.6	0.029	99.9	78.6	414.2	2.1
K	1080	66.07	0.0006	0.2288	12.9	868.8	0.052	99.9	88.5	418.8	1.5

ID	Temp (°C)	$^{40}Ar/^{39}Ar$	$^{37}Ar/^{39}Ar$	$^{36}Ar/^{39}Ar$ (x 10^{-3})	$^{39}Ar_K$ (x 10^{-15} mol)	K/Ca	Cl/K (x 10^{-3})	$^{40}Ar^*$ (%)	^{39}Ar (%)	Age (Ma)	±2s (Ma)
L	1120	67.12	0.0009	0.3104	7.08	559.5	0.21	99.8	93.9	424.6	1.4
M	1160	67.71	0.0014	0.9349	2.50	352.8	0.43	99.6	95.8	426.9	1.6
N	1200	68.10	0.0037	1.507	0.870	139.5	1.4	99.3	96.5	428.1	2.1
O	1300	67.85	0.0026	1.034	2.06	193.7	1.2	99.5	98.1	427.5	1.9
P	1650	69.65	0.0023	3.513	2.51	221.3	2.1	98.5	100.0	433.5	1.8
total gas age			n=16		130.2	675.2				398.7	1.7

Isotopic ratios corrected for blank, radioactive decay, and mass discrimination, not corrected for interferring reactions.

Individual analyses show analytical error only; mean age errors also include error in J and irradiation parameters.

Analyses in italics are excluded excluded from mean age calculations.
Correction factors:

NM-80

(39Ar/37Ar)Ca = 0.00065±0.00005

(36Ar/37Ar)Ca = 0.00026±0.00002

(38Ar/39Ar)K = 0.0119

(40Ar/39Ar)K = 0.0210±0.0020

NM-95

$(^{39}Ar/^{37}Ar)_{Ca}$ = 0.00078±0.00003

$(^{36}Ar/^{37}Ar)_{Ca}$ = 0.00028±0.00001

$(^{38}Ar/^{39}Ar)_K$ = 0.0119

$(^{40}Ar/^{39}Ar)_K$ = 0.0240±0.0020

NM-116, NM-122

$(^{39}Ar/^{37}Ar)_{Ca}$ = 0.00071±0.00001

$(^{36}Ar/^{37}Ar)_{Ca}$ = 0.00028±0.00000

$(^{38}Ar/^{39}Ar)_K$ = 0.0119

$(^{40}Ar/^{39}Ar)_K$ = 0.0271±0.0001

Table D.2. Results of UV laser in situ ablation analyses

ID	$^{40}Ar/^{39}Ar$	$^{37}Ar/^{39}Ar$	$^{36}Ar/^{39}Ar$ (x 10^{-3})	$^{39}Ar_K$ (x 10^{-16} mol)	K/Ca	Cl/K (x 10^{-3})	$^{40}Ar^*$ (%)	^{39}Ar (%)	Age (Ma)	±2σ (Ma)
49-113.7-1 zoned biotite, J=0.01641202±0.10%, D=1.00644±0.00091, NM-107, Lab#=50334-01										
50334-01	16.89	0.2890	12.53	3.18	1.8	9.8	78.1	2.1	353.4	25.6
50334-02	23.90	0.0974	28.63	10.5	5.2	4.6	64.5	9.0	406.9	12.3
50334-03	19.06	0.1457	7.533	9.73	3.5	2.9	88.2	15.4	439.7	10.9
50334-04	94.57	0.0201	249.0	9.19	25.3	2.1	22.2	21.5	533.5	24.2
50334-05	21.11	0.0000	13.93	6.58	-	4.3	80.4	25.8	443.1	16.6
50334-06	26.75	0.0000	34.28	5.91	-	2.2	62.0	29.7	434.4	20.5
50334-07	22.56	0.0056	18.64	11.4	91.5	1.8	75.5	37.2	444.5	13.4
50334-08	47.12	0.1577	103.6	7.16	3.2	2.3	35.0	41.9	432.0	23.6
50334-09	25.62	0.1758	30.38	5.42	2.9	1.5	64.9	45.5	435.5	19.8
50334-10	144.1	0.0495	421.3	8.23	10.3	1.7	13.6	50.9	503.5	37.3
50334-11	28.27	0.1305	38.03	6.74	3.9	1.5	60.2	55.3	444.4	23.7
50334-12	21.00	0.0793	11.95	5.43	6.4	1.6	83.1	58.9	454.3	17.0
50334-13	63.82	0.1319	159.8	6.38	3.9	1.9	26.0	63.1	434.4	30.7
50334-14	30.27	0.0254	48.98	4.73	20.1	2.3	52.1	66.2	415.2	24.1
50334-15	77.00	0.2776	195.9	4.83	1.8	3.3	24.8	69.4	491.9	35.3
50334-16	187.2	0.3438	577.6	5.34	1.5	3.1	8.8	72.9	433.8	56.6
50334-17	27.81	0.1467	35.96	5.37	3.5	1.8	61.7	76.4	447.9	14.2
50334-18	19.01	0.2236	6.011	5.95	2.3	2.1	90.6	80.4	449.2	10.2
50334-19	19.53	0.2214	8.704	6.31	2.3	3.1	86.8	84.5	442.8	10.1
50334-20	18.63	0.0729	7.489	5.19	7.0	3.8	88.0	87.9	430.0	14.4
50334-21	23.03	0.0729	17.82	6.62	7.0	3.8	77.0	92.3	461.0	12.7
50334-22	16.18	0.0097	2.266	6.87	52.8	6.5	95.7	96.8	408.4	11.4
50334-23	15.72	0.1131	3.803	4.85	4.5	10.2	92.7	100.0	387.0	15.0
49-1137-2, zoned biotite, J=0.01641202±0.10%, D=1.00644±0.00091, NM-107, Lab#=50334-02										
50334-30	15.16	0.1387	1.872	3.79	3.7	6.8	96.2	6.2	387.3	14.0
50334-31	25.62	0.1208	30.36	4.35	4.2	3.8	64.9	13.2	435.5	15.7
50334-32	19.19	0.0956	7.971	4.66	5.3	2.6	87.6	20.8	439.7	12.2
50334-33	18.76	0.1601	7.575	4.31	3.2	1.9	88.0	27.8	432.7	12.8
50334-34	17.05	0.1649	5.554	3.30	3.1	4.5	90.3	33.2	406.3	17.2
50334-35	32.83	0.0547	54.47	5.27	9.3	2.1	50.9	41.7	437.2	14.8
50334-36	18.81	0.0185	7.186	5.19	27.5	2.2	88.6	50.1	436.1	11.3
50334-37	19.25	0.0669	9.914	4.82	7.6	2.3	84.7	58.0	427.6	12.3
50334-38	22.12	0.0000	19.73	3.31	-	0.54	73.5	63.4	426.9	21.1
50334-39	20.06	0.0000	11.43	5.03	-	1.3	83.0	71.5	436.1	14.1
50334-40	21.11	0.0000	11.24	4.21	-	-0.325	84.1	78.4	461.6	16.4
50334-41	20.91	0.0000	15.67	4.27	-	1.5	77.7	85.3	426.5	16.8
50334-42	17.38	0.0000	3.999	2.96	-	2.7	93.0	90.1	424.7	19.7
50334-43	16.72	0.0000	-0.1693	3.73	-	4.6	100.1	96.2	438.0	15.4
50334-44	14.59	0.0000	0.7461	2.35	-	6.3	98.3	100.0	381.2	24.3
49-129.2 zoned biotite, J=0.01634819±0.10%, D=1.00644±0.00091, NM-107, Lab#=50339-01										
50339-01	16.69	0.0000	-1.5116	7.33	-	4.6	102.5	6.4	444.8	10.0
50339-02	18.24	0.0000	-0.9034	7.69	-	1.5	101.3	13.2	476.2	10.3

ID	$^{40}Ar/^{39}Ar$	$^{37}Ar/^{39}Ar$	$^{36}Ar/^{39}Ar$ (x 10^{-3})	$^{39}Ar_K$ (x 10^{-16} mol)	K/Ca	Cl/K (x 10^{-3})	$^{40}Ar^*$ (%)	^{39}Ar (%)	Age (Ma)	±2σ (Ma)
50339-03A	23.04	0.0000	17.74	10.4	-	1.5	77.1	22.3	460.0	10.6
50339-04	18.48	0.0661	4.237	10.3	7.7	0.37	93.1	31.3	447.3	8.6
50339-05	18.40	0.0756	3.652	9.09	6.7	0.80	94.0	39.3	449.3	8.6
50339-06	18.44	0.0766	4.673	7.80	6.7	0.80	92.4	46.1	443.2	9.0
50339-07	18.10	0.0000	2.092	6.10	-	2.2	96.4	51.5	452.8	10.6
50339-08	17.81	0.0000	0.7221	8.24	-	1.3	98.6	58.7	455.6	8.0
50339-09	17.88	0.0000	1.197	8.15	-	1.9	97.9	65.9	453.9	8.2
50339-10	21.62	0.0000	14.18	5.34	-	2.5	80.5	70.6	451.7	12.6
50339-11	17.23	0.0380	-0.8338	5.06	13.4	1.8	101.3	75.0	452.9	11.6
50339-12	32.12	0.0534	50.55	5.41	9.6	1.1	53.4	79.8	446.2	16.2
50339-13	278.9	0.1464	892.1	6.29	3.5	3.4	5.5	85.3	401.2	86.9
50339-14	17.31	0.1018	1.138	6.04	5.0	2.0	97.9	90.6	441.3	10.2
50339-15	16.91	0.0631	0.7774	3.53	8.1	3.9	98.5	93.7	434.4	17.6
50339-16	15.64	0.0804	1.449	3.57	6.3	6.8	97.1	96.8	400.3	17.4
50339-17	15.89	0.1318	2.129	3.64	3.9	6.6	95.9	100.0	401.4	16.9
57-1662-1biotite, traverse 1, J=0.01640644±0.10%, D=1.00644±0.00091, NM-107, Lab#=50338-01										
50338-01	14.20	0.2865	1.727	2.65	1.8	7.7	96.4	6.1	365.4	17.4
50338-02	14.31	0.3742	1.923	1.32	1.4	9.4	96.1	9.1	367.0	32.7
50338-03	15.02	0.4166	1.020	3.29	1.2	8.5	98.0	16.6	390.6	14.0
50338-04	14.91	0.1131	0.5709	4.82	4.5	7.1	98.7	27.6	390.4	9.9
50338-05	16.86	0.0445	2.141	5.50	11.5	4.2	96.1	40.2	425.3	9.0
50338-06	16.14	0.1223	1.176	4.63	4.2	1.2	97.7	50.8	415.2	13.4
50338-07	17.76	0.1096	4.825	5.94	4.7	1.6	91.9	64.4	428.0	10.7
50338-08	16.77	0.0723	2.776	5.23	7.1	2.8	95.0	76.4	418.9	11.9
50338-09	18.40	0.1596	10.76	4.47	3.2	4.9	82.6	86.6	401.8	14.1
50338-10	14.93	0.0792	1.826	3.04	6.4	9.4	96.2	93.6	382.0	20.2
50338-11	14.48	0.4128	0.7599	2.81	1.2	7.5	98.5	100.0	379.4	21.4
57-166.2-1 biotite, traverse 2, J=0.01640644±0.10%, D=1.00644±0.00091, NM-107, Lab#=50338-02										
50338-20	14.61	0.5055	1.208	4.76	1.0	8.5	97.7	11.8	379.6	13.2
50338-21	15.07	0.4683	-0.4497	2.84	1.1	8.3	101.0	18.8	402.2	20.2
50338-22	15.65	0.6113	5.147	2.93	0.83	9.6	90.4	26.1	376.7	20.0
50338-23	17.60	0.0000	6.529	3.06	-	6.1	88.9	33.7	412.2	17.6
50338-24	16.45	0.0000	0.2493	5.35	-	4.4	99.4	47.0	428.6	9.9
50338-25	16.39	0.0000	1.631	5.47	-	4.8	96.9	60.5	417.7	9.6
50338-26	15.35	0.0000	1.865	5.73	-	6.9	96.2	74.7	391.5	12.4
50338-27	14.33	0.6154	-0.5129	2.83	0.83	8.1	101.2	81.8	385.3	22.6
50338-28	14.93	0.0000	0.7536	5.72	-	8.3	98.3	95.9	389.3	12.3
50338-30	18.09	0.0000	7.771	1.63	-	11.3	87.2	100.0	415.0	26.5
57-166.2-2 biotite, J=0.01640644±0.10%, D=1.00644±0.00091, NM-107, Lab#=50338-03										
50338-40	14.30	0.4030	4.260	6.64	1.3	8.2	91.2	5.0	350.1	10.4
50338-41	14.87	0.5124	3.625	5.88	1.00	9.2	92.9	9.5	368.6	10.2
50338-42	15.39	0.2766	3.428	6.45	1.8	7.8	93.4	14.4	382.0	9.8
50338-43	20.59	0.0128	16.47	6.06	39.9	5.1	76.2	19.0	413.4	9.5

ID	$^{40}Ar/^{39}Ar$	$^{37}Ar/^{39}Ar$	$^{36}Ar/^{39}Ar$ (x 10^{-3})	$^{39}Ar_K$ (x 10^{-16} mol)	K/Ca	Cl/K (x 10^{-3})	$^{40}Ar^*$ (%)	^{39}Ar (%)	Age (Ma)	±2σ (Ma)
50338-44	18.78	0.0000	7.490	6.69	-	4.2	88.1	24.1	433.1	9.1
50338-45	35.26	0.0000	60.59	6.62	-	2.8	49.1	29.1	451.3	16.2
50338-46	22.91	0.0354	21.26	5.87	14.4	3.1	72.5	33.6	434.6	11.0
50338-47	21.36	0.0663	17.03	10.6	7.7	3.2	76.3	41.7	427.7	7.9
50338-48	18.02	0.0836	6.110	6.71	6.1	3.1	89.9	46.8	425.1	8.4
50338-49	19.70	0.1028	10.87	11.4	5.0	3.6	83.6	55.4	431.5	8.1
50338-50	15.98	0.0595	-2.1059	4.67	8.6	4.8	103.8	58.9	434.0	9.5
50338-51	17.72	0.0842	2.057	4.63	6.1	2.9	96.5	62.5	446.0	9.9
50338-52	19.91	0.0601	7.996	10.5	8.5	2.1	88.0	70.5	456.0	7.2
50338-53	17.29	0.0380	4.006	4.26	13.4	1.2	93.0	73.7	422.4	15.1
50338-54	18.44	0.0246	8.416	6.59	20.7	2.3	86.4	78.7	418.7	10.5
50338-55	18.14	0.0372	8.537	8.79	13.7	4.1	86.0	85.4	411.0	8.8
50338-56	17.01	0.1125	6.750	10.8	4.5	8.3	88.2	93.6	396.9	10.3
50338-57	15.76	0.1038	3.716	8.40	4.9	7.9	92.9	100.0	388.5	12.9
601-1 muscovite, J=0.01621556±0.10%, D=1.00644±0.00091, NM-107, Lab#=50342-01										
50342-01	14.38	0.0224	-2.2798	3.51	22.8	1.3	104.5	7.2	393.5	13.9
50342-02	14.80	0.1092	-0.4835	4.02	4.7	1.8	100.8	15.5	391.0	12.7
50342-03	14.86	0.1196	1.030	4.88	4.3	-0.603	97.8	25.6	381.9	10.1
50342-04	15.05	0.0732	1.673	5.41	7.0	0.14	96.6	36.7	381.8	9.9
50342-05	14.44	0.0000	-0.0154	3.61	-	0.36	99.8	44.1	379.0	15.9
50342-06	14.91	0.0000	-0.1442	4.94	-	1.3	100.1	54.3	391.0	11.1
50342-07	15.28	0.0000	3.178	4.56	-	0.72	93.7	63.7	376.5	12.8
50342-08	14.84	0.0000	2.475	4.15	-	1.8	94.9	72.3	371.0	13.1
50342-09	14.54	0.0000	2.629	3.34	-	0.28	94.5	79.2	362.7	17.5
50342-10	15.08	0.0000	5.091	3.72	-	-0.053	89.8	86.8	358.3	16.3
50342-11	14.16	0.0000	1.470	3.55	-	1.2	96.7	94.1	361.9	16.8
50342-12	12.66	0.0000	1.968	2.84	-	0.000	95.2	100.0	322.0	20.8
601-2, muscovite, J=0.01621556±0.10%, D=1.00644±0.00091, nm-107, Lab#=50342-02										
50342-20	14.18	0.7574	7.126	0.285	0.67	2.4	85.4	2.5	323.6	20.7
50342-21	14.40	0.2956	2.822	0.807	1.7	0.62	94.2	9.4	358.7	7.7
50342-22	14.52	0.1507	2.585	1.17	3.4	0.56	94.6	19.5	363.0	5.9
50342-23	14.86	0.1117	1.914	1.28	4.6	0.79	96.1	30.6	375.8	4.8
50342-24	14.56	0.1098	0.9971	1.15	4.6	0.45	97.8	40.5	375.0	5.1
50342-25	14.54	0.1342	2.289	1.01	3.8	0.16	95.2	49.2	365.4	5.8
50342-26	14.50	0.1565	2.228	1.09	3.3	0.48	95.4	58.6	365.0	5.5
50342-27	14.44	0.0000	0.3687	1.12	-	0.23	99.1	68.2	376.2	4.8
50342-28	14.46	0.0000	-0.1329	1.03	-	-0.226	100.1	77.1	380.2	5.4
50342-29	14.67	0.0298	1.038	1.09	17.1	0.23	97.7	86.5	377.1	5.1
50342-30	14.53	0.0201	-0.6328	0.843	25.4	0.32	101.1	93.8	385.5	6.4
50342-31	14.48	0.0000	-1.3262	0.643	-	0.18	102.5	99.4	389.1	8.0
50342-32	12.82	0.0000	-11.7762	0.072	-	-4.310	126.9	100.0	422.5	66.7
AD2A, muscovite, J=0.01627381±0.10%, D=1.00644±0.00091, NM-107, Lab#=50343-01										
50343-20	14.54	0.2155	1.233	0.830	2.4	0.31	97.4	8.9	374.3	6.9

ID	$^{40}Ar/^{39}Ar$	$^{37}Ar/^{39}Ar$	$^{36}Ar/^{39}Ar$ (x 10^{-3})	$^{39}Ar_K$ (x 10^{-16} mol)	K/Ca	Cl/K (x 10^{-3})	$^{40}Ar*$ (%)	^{39}Ar (%)	Age (Ma)	±2σ (Ma)
50343-21	14.46	0.2051	0.5229	1.19	2.5	-0.060	98.9	21.7	377.3	6.4
50343-22	14.56	0.1535	0.6605	1.06	3.3	-0.374	98.6	33.1	378.7	5.9
50343-23	14.76	0.2409	0.3693	1.01	2.1	0.83	99.2	44.0	385.6	6.9
50343-24	14.35	0.0794	-0.1476	1.26	6.4	0.30	100.2	57.6	379.3	5.8
50343-25	14.84	0.1555	1.095	1.26	3.3	1.1	97.7	71.1	382.4	5.9
50343-26	14.31	0.1581	0.9039	1.06	3.2	0.57	98.0	82.6	370.9	6.4
50343-27	14.90	0.2119	3.000	1.07	2.4	0.51	94.0	94.2	370.4	6.6
50343-28	14.52	0.3659	2.451	0.540	1.4	14.1	95.0	100.0	365.5	11.7
532 Muscovite, J=0.01622227±0.10%, D=1.00644±0.00091, NM-107, Lab#=50341-01										
50341-01	16.00	0.5609	7.441	7.82	0.91	2.0	86.4	6.4	365.1	9.3
50341-02	16.61	0.3707	7.223	11.0	1.4	7.8	87.2	15.5	380.6	11.0
50341-03	15.69	0.1902	4.012	15.6	2.7	0.75	92.4	28.3	380.9	7.9
50341-04	15.78	0.0571	3.273	15.8	8.9	0.12	93.7	41.3	388.0	8.1
50341-05	14.77	0.0925	1.805	14.7	5.5	-0.233	96.3	53.4	374.3	8.4
50341-06	14.81	0.1009	1.690	6.62	5.1	-0.139	96.5	58.8	376.2	9.6
50341-07	15.03	0.0178	1.676	9.84	28.6	-0.036	96.5	66.9	381.4	7.0
50341-08	14.81	0.0385	1.464	10.2	13.3	-0.075	96.9	75.3	377.7	6.7
50341-09	14.61	0.0000	0.7118	9.55	-	0.069	98.4	83.1	378.0	6.1
50341-10	14.72	0.0000	1.079	8.18	-	-0.323	97.6	89.9	378.2	6.5
50341-11	14.81	0.0000	0.7152	6.55	-	0.56	98.4	95.3	382.9	7.6
50341-12	14.22	0.2201	2.155	5.19	2.3	1.5	95.5	99.5	359.1	10.2
50341-13	13.59	0.9388	19.68	0.568	0.54	7.9	57.6	100.0	215.7	91.0
547, muscovite, traverse 1, J=0.01621989±0.10%, D=1.00644±0.00091, NM-107, Lab#=50335-01										
50335-01	13.35	0.0000	-2.0109	4.63	-	0.71	104.2	2.1	367.2	12.1
50335-02	14.41	0.0000	-1.6011	3.89	-	0.51	103.1	3.8	389.4	13.9
50335-03	14.44	0.0000	-2.8319	2.99	-	-0.239	105.6	5.2	398.8	18.0
50335-04	14.41	0.0000	3.363	6.02	-	1.1	92.9	7.9	354.6	10.0
50335-05	14.91	0.0000	2.668	6.26	-	1.1	94.5	10.7	371.5	10.0
50335-06	14.66	0.0506	4.507	5.26	10.1	1.6	90.8	13.1	352.5	11.5
50335-07	14.26	0.0000	0.2665	4.57	-	-0.203	99.3	15.1	372.8	10.8
50335-08	14.38	0.0000	-1.0376	4.40	-	0.094	101.9	17.1	384.9	12.0
50335-10	14.60	0.0116	-1.4091	8.05	44.0	0.55	102.7	20.7	392.7	7.5
50335-11	14.54	0.0754	-0.8008	9.19	6.8	0.56	101.5	24.8	387.1	6.8
50335-12	14.56	0.0000	-1.4256	7.46	-	0.33	102.7	28.2	391.7	8.0
50335-13	14.39	0.0000	0.4604	8.85	-	0.44	98.9	32.2	374.7	6.7
50335-14	14.47	0.0184	0.9240	6.62	27.8	0.37	97.9	35.1	373.3	8.7
50335-15	14.67	0.0000	0.8203	7.26	-	-0.380	98.2	38.4	378.7	8.3
50335-16	14.39	0.0000	0.3843	6.72	-	-0.153	99.0	41.4	375.0	8.4
50335-17	16.04	0.0000	7.564	6.96	-	0.84	85.9	44.5	363.9	8.4
50335-18	14.42	0.0000	-0.7432	6.58	-	-0.445	101.3	47.5	383.6	8.0
50335-19	14.19	0.0121	0.4522	9.61	42.2	0.13	98.9	51.8	370.0	6.7
50335-20	14.20	0.0000	-0.6582	4.61	-	0.61	101.2	53.9	377.9	12.5
50335-21	14.70	0.0000	3.760	5.84	-	0.40	92.3	56.5	358.8	10.5
50335-22	13.80	0.0465	-0.6535	4.71	11.0	1.5	101.2	58.6	368.4	11.9

ID	$^{40}Ar/^{39}Ar$	$^{37}Ar/^{39}Ar$	$^{36}Ar/^{39}Ar$ (x 10^{-3})	$^{39}Ar_K$ (x 10^{-16} mol)	K/Ca	Cl/K (x 10^{-3})	$^{40}Ar^*$ (%)	^{39}Ar (%)	Age (Ma)	±2σ (Ma)
50335-23	14.05	0.0997	0.8557	5.87	5.1	0.83	98.1	61.2	363.9	9.9
50335-24	13.27	0.1232	1.851	5.57	4.1	1.4	95.7	63.7	338.1	10.7
50335-25	14.41	0.0000	-3.4186	7.12	-	-0.705	106.8	66.9	402.1	7.7
50335-26	14.67	0.0000	-0.2324	7.49	-	-0.480	100.3	70.3	386.0	7.3
50335-27	14.92	0.0000	-1.5639	4.96	-	0.68	102.9	72.5	401.3	10.6
50335-28	14.46	0.0000	-5.1118	2.91	-	7.5	110.3	73.8	409.8	22.0
50335-29	13.81	0.0000	-8.4993	1.77	-	11.1	118.0	74.6	417.9	35.6
50335-50	14.42	0.1093	0.0646	11.7	4.7	0.46	99.7	79.9	378.3	5.7
50335-51	14.51	0.1872	0.5118	11.1	2.7	0.29	98.9	84.9	377.4	6.0
50335-52	14.68	0.1828	0.7078	10.9	2.8	0.71	98.5	89.8	380.2	6.1
50335-53	14.52	0.0077	0.7157	11.1	66.3	0.35	98.4	94.8	375.8	5.4
50335-54	14.47	0.0000	-0.2907	11.6	-	0.22	100.4	100.0	381.9	5.0
547, muscovite, traverse 2, J=0.01621989±0.10%, D=1.00644±0.00091, nm-107, Lab#=50335-03										
50335-60	13.89	0.0000	0.4829	0.477	-	0.76	98.8	2.6	362.5	10.8
50335-61	14.17	0.0713	-0.3356	0.841	7.2	0.38	100.5	7.3	375.1	6.6
50335-62	13.94	0.0000	0.4446	1.08	-	0.53	98.9	13.2	364.0	5.4
50335-63	14.00	0.1347	2.278	1.15	3.8	0.43	95.1	19.6	352.7	5.1
50335-64	14.10	0.1794	2.448	1.15	2.8	0.76	94.8	25.9	354.1	5.1
50335-65	14.22	0.2402	2.978	1.17	2.1	0.54	93.8	32.4	353.3	5.0
50335-66	14.32	0.0000	-1.2665	1.15	-	-0.490	102.4	38.7	385.0	5.3
50335-67	14.44	0.0000	-1.6057	0.629	-	0.69	103.1	42.2	390.3	9.0
50335-68	14.44	0.0000	-1.2324	0.729	-	0.38	102.3	46.2	387.6	7.7
50335-69	14.85	0.0000	1.363	0.802	-	0.64	97.1	50.6	379.2	7.7
50335-70	14.43	0.0000	0.5479	0.942	-	0.23	98.7	55.8	375.0	6.4
50335-71	14.48	0.0588	0.0851	0.892	8.7	0.45	99.7	60.8	379.4	6.9
50335-72	17.18	0.0712	9.843	0.938	7.2	0.75	82.9	65.9	375.2	6.1
50335-73	14.51	0.1015	0.5958	0.929	5.0	0.21	98.7	71.1	376.7	5.6
50335-74	14.60	0.0635	1.422	0.889	8.0	0.34	97.0	76.0	372.9	6.4
50335-75	14.61	0.0000	0.8340	0.871	-	1.2	98.1	80.8	377.1	6.5
50335-76	14.48	0.0000	-0.3954	0.588	-	0.24	100.6	84.0	382.8	9.1
50335-77	14.42	0.0000	0.8510	0.784	-	0.79	98.1	88.3	372.6	7.2
50335-78	14.55	0.0756	-1.0324	0.728	6.7	0.43	102.0	92.3	388.9	8.1
50335-79	14.70	0.0000	-1.5666	0.730	-	0.044	103.0	96.4	396.1	8.2
50335-80	14.59	0.0000	-1.4486	0.657	-	0.35	102.7	100.0	392.7	9.4

Isotopic ratios corrected for blank, radioactive decay, and mass discrimination, not corrected for interferring reactions.

Individual analyses show analytical error only; mean age errors also include error in J and irradiation parameters.

Analyses in italics are excluded excluded from mean age calculations.

Correction factors:

$(^{39}Ar/^{37}Ar)_{Ca} = 0.00071 \pm 0.00001$

$(^{36}Ar/^{37}Ar)_{Ca} = 0.00028 \pm 0.00000$

$(^{38}Ar/^{39}Ar)_K = 0.0119$

$(^{40}Ar/^{39}Ar)_K = 0.0275 \pm 0.0004$

Table D.3. Results of step-heating analyses of K-feldspars used for MDD modeling

ID	Temp (°C)	Time	$^{40}Ar/^{39}Ar$	$^{37}Ar/^{39}Ar$	$^{36}Ar/^{39}Ar$ (x 10^{-3})	$^{39}Ar_K$ (x 10^{-15} mol)	K/Ca	Cl/K (x 10^{-3})	$^{40}Ar^*$ (%)	^{39}Ar (%)	Conventional age: Age (Ma)	Conventional age: ±2σ (Ma)	Age corrected for excess ^{40}Ar (Ma)	Model input: Age (Ma)	Model input: error (Ma)
A23 D:2:128, K-feldspar, 5.02 mg, J=0.01639256±0.09%, D=1.0069±0.0009999999, NM-128, Lab#=51531-02															
A	300	28.0	152.0	0.0435	306.5	1.17	11.7	24.4	40.4	0.1	1256.1	20.8	-	**200.0**	**50.0**
B	300	56.5	47.83	0.0591	106.2	0.309	8.6	8.4	34.4	0.1	430.5	37.2	-	**200.0**	**50.0**
C	350	26.2	23.88	0.0366	21.29	0.718	13.9	5.1	73.6	0.1	456.6	12.0	-	**200.0**	**50.0**
D	350	56.3	17.38	0.0656	25.98	0.692	7.8	2.5	55.7	0.1	265.7	13.5	-	**200.0**	**50.0**
E	400	21.1	28.21	0.0376	5.724	1.79	13.6	7.5	93.9	0.2	650.7	4.1	-	**200.0**	**50.0**
F	400	29.5	9.332	0.0127	5.264	1.49	40.3	1.3	83.1	0.3	215.8	5.9	-	**200.0**	**50.0**
G	450	21.5	19.66	0.0126	1.926	8.53	40.5	5.8	97.0	0.8	490.7	2.0	-	**200.0**	**50.0**
H	450	30.0	7.106	0.0083	1.047	6.61	61.6	0.71	95.3	1.1	189.9	1.4	-	189.92	0.70
I	500	21.4	12.47	0.0114	0.8520	23.2	44.6	2.9	97.8	2.3	328.7	1.3	-	**192.5**	**2.5**
J	500	29.8	7.118	0.0171	0.4117	14.2	29.9	0.47	98.0	3.0	195.26	0.90	-	195.26	0.45
K	550	21.8	11.35	0.0743	0.7040	31.3	6.9	2.2	98.0	4.6	302.2	1.1	-	**205.0**	**10.0**
L	550	30.1	7.832	0.1650	0.3429	16.3	3.1	0.20	98.6	5.4	214.97	0.82	-	214.97	0.41
M	600	11.6	11.84	0.1446	0.7254	20.1	3.5	2.0	98.1	6.5	314.5	1.3	-	**219.0**	**4.0**
N	600	21.7	8.138	0.0975	0.2765	16.8	5.2	0.21	98.8	7.3	223.35	0.91	-	223.35	0.45
O	650	11.5	10.62	0.0647	0.4621	22.8	7.9	1.6	98.5	8.5	285.6	1.2	-	**225.5**	**2.1**
P	650	21.6	8.298	0.0441	0.2487	18.4	11.6	0.32	98.9	9.4	227.62	0.79	-	227.62	0.40
Q	700	11.4	9.870	0.0273	0.4124	22.8	18.7	0.75	98.5	10.6	266.9	1.0	-	**230.0**	**2.0**
R	700	21.5	8.463	0.0183	0.2152	20.2	27.9	-0.077	99.0	11.6	232.1	1.0	-	232.12	0.52
S	750	11.7	8.878	0.0098	0.1270	22.4	51.9	0.40	99.3	12.8	243.52	0.94	-	**236.5**	**4.5**
T	750	21.7	8.812	0.0072	0.1856	21.8	70.4	0.18	99.1	13.9	241.36	0.99	-	241.36	0.50
U	800	11.6	8.975	0.0059	0.1517	23.0	85.9	0.031	99.2	15.1	245.83	0.99	-	245.83	0.50
V	800	21.6	8.943	0.0045	0.1735	25.5	112.5	0.23	99.2	16.4	244.84	0.90	-	244.84	0.45
W	850	11.8	9.082	0.0056	0.1409	29.2	91.0	0.23	99.3	17.9	248.68	0.88	-	248.68	0.44
X	850	21.9	8.954	0.0031	0.1672	33.5	167.2	0.22	99.2	19.6	245.17	0.89	-	245.17	0.45
Y	900	11.7	9.241	0.0058	0.1304	34.0	88.4	0.49	99.3	21.3	252.84	0.97	-	252.84	0.48
Z	900	21.7	9.368	0.0039	0.1755	39.3	129.4	0.57	99.2	23.3	255.77	0.79	-	255.77	0.39
ZA	950	11.9	10.24	0.0078	0.2720	45.7	65.5	1.3	99.0	25.7	277.29	0.86	-	277.29	0.43
ZB	950	21.9	10.76	0.0023	0.3416	60.7	220.7	1.6	98.8	28.8	289.87	0.89	-	289.87	0.44
ZC	1000	11.8	11.49	0.0060	0.3827	81.6	85.4	2.0	98.8	32.9	308.0	1.0	-	308.00	0.51
ZD	1000	21.8	11.53	0.0033	0.3382	94.3	154.1	1.8	98.9	37.7	309.2	1.1	-	309.23	0.53
ZE	1050	10.9	11.86	0.0046	0.3405	93.9	112.0	2.1	98.9	42.5	317.4	1.1	-	317.39	0.57
ZF	1050	16.0	11.80	0.0030	0.3036	64.4	168.4	1.9	99.0	45.8	316.23	0.99	-	316.23	0.49
ZG	1100	10.7	12.15	0.0032	0.3211	58.6	158.5	2.1	99.0	48.8	324.8	1.0	-	324.81	0.51
ZH	1100	25.8	12.68	0.0034	0.2992	72.4	149.3	2.1	99.1	52.5	338.0	1.1	-	338.01	0.54
ZI	1100	55.7	13.48	0.0018	0.3651	93.3	286.3	2.2	99.0	57.3	356.9	1.2	-	356.86	0.58
ZJ	1100	115.6	14.27	0.0019	0.5196	111.2	274.8	2.3	98.8	63.0	374.9	1.1	-	374.95	0.53
ZK	1100	235.7	14.92	0.0015	0.7245	127.7	330.5	2.5	98.4	69.5	389.1	1.0	-	389.09	0.52
ZL	1200	4.8	14.30	0.0038	0.4830	80.4	134.5	3.1	98.8	73.6	375.9	1.1	-	375.91	0.57
ZM	1250	5.1	15.22	0.0011	0.4897	362.0	482.8	2.8	98.9	92.1	397.7	1.3	-	397.73	0.67
ZN	1300	5.0	15.44	0.0027	0.4760	125.5	188.6	2.3	98.9	98.5	403.2	1.2	-	403.21	0.59
ZO	1700	4.9	15.75	0.0215	1.268	28.7	23.7	2.1	97.5	100.0	404.9	1.4	-	404.87	0.70
total gas age				n=41		1956.7	213.0				337.3	1.1			
49-129.2 D:4:95, K-feldspar, 2.60 mg, J=0.003916151±0.08%, D=1.00362±0.00105, NM-95, Lab#=9552-03															
A	500	12.3	94.58	0.0159	51.40	21.0	32.1	18.5	83.9	1.9	488.3	2.2	192.0	**192.0**	**2.2**
B	500	24.2	40.51	0.0294	8.605	5.87	17.4	3.6	93.7	2.5	249.9	2.0	189.1	**189.1**	**2.0**
C	550	14.6	76.41	0.0572	17.38	10.1	8.9	15.2	93.3	3.4	444.0	1.9	197.8	**197.8**	**1.9**
D	550	24.8	38.99	0.0802	6.079	4.37	6.4	2.8	95.3	3.8	245.2	1.6	198.0	**198.0**	**1.6**
E	600	14.6	60.02	0.0823	12.18	9.46	6.2	8.9	94.0	4.6	360.0	1.8	213.2	**213.2**	**1.8**
F	600	24.6	38.10	0.1027	5.721	5.11	5.0	1.9	95.5	5.1	240.4	1.5	207.4	**207.4**	**1.5**
G	650	15.0	55.27	0.0906	12.25	10.7	5.6	6.7	93.4	6.1	332.3	1.5	221.5	**221.5**	**1.5**
H	650	25.1	39.48	0.0252	3.354	6.89	20.3	1.0	97.4	6.7	253.2	1.4	235.7	**235.7**	**1.4**
I	700	4.9	46.36	0.0250	6.276	5.94	20.4	4.2	96.0	7.3	289.7	1.8	-	289.7	1.8
J	750	5.3	45.26	0.0170	4.847	13.0	30.1	2.5	96.8	8.4	285.6	1.3	-	285.6	1.3
K	800	5.3	44.22	0.0124	2.761	20.4	41.2	1.7	98.1	10.3	283.1	1.3	-	283.1	1.3
L	850	5.4	44.14	0.0093	2.023	28.9	55.1	1.2	98.6	12.9	283.9	1.1	-	283.9	1.1
M	900	5.2	44.18	0.0103	2.313	43.3	49.7	1.2	98.4	16.9	283.6	1.0	-	283.6	1.0
N	950	5.3	43.78	0.0116	2.106	58.9	44.1	1.8	98.5	22.3	281.6	1.2	-	281.6	1.2
O	1000	5.0	44.69	0.0085	2.189	73.5	59.7	2.7	98.5	29.0	286.9	1.1	-	286.9	1.1
P	1050	5.3	45.93	0.0081	2.209	95.2	62.8	2.8	98.5	37.6	294.3	1.1	-	294.3	1.1
Q	1100	5.0	46.48	0.0061	2.293	123.0	84.2	3.0	98.5	48.9	297.5	1.3	-	297.5	1.3
R	1100	25.0	49.10	0.0036	2.636	139.4	140.1	3.7	98.4	61.6	312.5	1.1	-	312.5	1.1
S	1100	55.0	52.44	0.0029	2.953	129.0	177.1	4.3	98.3	73.3	331.7	2.5	-	331.7	2.5
T	1100	115.0	54.67	0.0029	4.050	111.6	176.9	4.5	97.8	83.5	342.9	1.4	-	342.9	1.4

ID	Temp (°C)	Time	$^{40}Ar/^{39}Ar$	$^{37}Ar/^{39}Ar$	$^{36}Ar/^{39}Ar$ (x 10^{-3})	$^{39}Ar_K$ (x 10^{-15} mol)	K/Ca	Cl/K (x 10^{-3})	$^{40}Ar^*$ (%)	^{39}Ar (%)	Conventional age: Age (Ma)	Conventional age: ±2σ (Ma)	Age corrected for excess ^{40}Ar (Ma)	Model input: Age (Ma)	Model input: error (Ma)
U	1100	234.9	57.50	0.0032	5.011	93.5	157.9	4.5	97.4	92.1	357.7	1.6	-	357.7	1.6
V	1100	475.0	60.93	0.0045	9.997	52.7	112.7	4.7	95.1	96.9	369.0	1.2	-	369.0	1.2
W	1180	5.2	59.91	0.0032	2.903	9.83	157.7	4.5	98.5	97.8	375.2	1.8	-	375.2	1.8
X	1230	5.3	59.70	0.0040	2.913	17.3	129.0	4.2	98.5	99.3	374.0	1.6	-	374.0	1.6
Y	1280	5.4	60.52	0.0030	3.993	4.71	167.3	4.5	98.0	99.8	376.9	2.0	-	376.9	2.0
Z	1330	5.4	62.54	0.0027	8.048	0.999	188.8	4.3	96.2	99.9	381.6	5.5	-	381.6	5.5
ZA	1430	5.6	61.14	0.0056	11.04	1.11	90.5	5.9	94.6	100.0	368.4	5.5	-	368.4	5.5
ZB	1680	5.2	70.16	0.0110	76.54	0.436	46.2	8.0	67.7	100.0	307.9	14.7	-	307.9	14.7
total gas age				n=28		1096.3	107.0				320.7	1.4			
57-166.2 D:1:95, K-feldspar, 8.49 mg, J=0.003971759±0.08%, D=1.00362±0.00105, NM-95, Lab#=9550-01															
A	500	10.9	125.8	0.0109	28.10	39.6	47.0	28.1	93.4	1.4	690.8	2.9	195.5	**195.5**	**2.9**
B	500	23.2	45.12	0.0126	3.448	14.4	40.6	5.3	97.7	1.9	291.0	1.4	186.3	**186.3**	**1.4**
C	550	13.8	50.91	0.0241	3.046	18.0	21.1	7.1	98.2	2.5	326.7	1.4	188.4	**188.4**	**1.4**
D	550	24.1	40.88	0.0341	2.634	9.84	15.0	3.1	98.0	2.8	266.5	1.4	205.2	**205.2**	**1.4**
E	600	13.7	64.67	0.0505	3.503	19.5	10.1	9.3	98.4	3.5	406.4	1.7	230.6	**230.6**	**1.7**
F	600	23.7	41.98	0.0564	1.649	12.3	9.0	2.0	98.8	4.0	275.1	1.2	234.9	**234.9**	**1.2**
G	650	14.1	61.77	0.0564	2.398	22.2	9.0	7.2	98.8	4.7	391.6	1.5	255.6	**255.6**	**1.5**
H	650	24.2	46.00	0.0505	1.355	15.1	10.1	1.4	99.1	5.2	300.2	1.3	273.6	**273.6**	**1.3**
I	700	4.0	57.05	0.0475	1.121	10.2	10.8	4.5	99.4	5.6	366.4	1.7	-	**305.0**	**35.0**
J	750	4.7	59.54	0.0384	1.931	28.3	13.3	5.0	99.0	6.6	379.5	1.6	-	**305.0**	**35.0**
K	800	4.7	52.58	0.0227	0.9144	42.4	22.5	1.9	99.4	8.1	340.4	1.2	-	340.4	1.2
L	850	5.3	51.22	0.0145	0.6258	62.8	35.3	0.90	99.6	10.2	332.8	1.1	-	332.8	1.1
M	900	5.2	51.55	0.0107	0.3805	91.4	47.6	0.74	99.7	13.4	335.3	1.3	-	335.3	1.3
N	950	5.1	51.70	0.0094	0.4369	125.0	54.5	0.64	99.7	17.8	336.0	1.4	-	336.0	1.4
O	1000	4.9	51.00	0.0105	0.4595	149.6	48.8	0.80	99.7	23.0	331.8	1.3	-	331.8	1.3
P	1050	5.0	49.69	0.0108	0.6343	148.3	47.5	1.5	99.6	28.1	323.7	1.4	-	323.7	1.4
Q	1100	4.8	51.11	0.0093	0.9386	186.6	54.9	2.6	99.4	34.6	331.6	1.6	-	331.6	1.6
R	1100	24.8	52.63	0.0077	0.9120	305.4	66.5	3.0	99.4	45.2	340.7	1.3	-	340.7	1.3
S	1100	54.6	54.12	0.0074	0.6765	235.1	68.7	2.6	99.6	53.4	350.0	1.7	-	350.0	1.7
T	1100	114.6	56.02	0.0066	0.7644	205.5	77.8	2.6	99.6	60.5	361.0	1.9	-	361.0	1.9
U	1100	234.5	58.44	0.0059	1.172	187.3	86.2	3.1	99.4	67.0	374.4	1.6	-	374.4	1.6
V	1100	474.6	60.57	0.0054	2.164	192.2	94.7	3.4	98.9	73.7	385.1	2.0	-	385.1	2.0
W	1180	4.9	59.38	0.0081	1.110	24.1	62.9	4.2	99.4	74.5	380.0	1.5	-	380.0	1.5
X	1230	5.2	60.30	0.0062	0.7491	140.2	82.9	4.7	99.6	79.4	386.0	1.8	-	386.0	1.8
Y	1280	5.3	61.82	0.0051	0.5011	307.9	99.6	3.6	99.7	90.1	395.1	2.6	-	395.1	2.6
Z	1330	5.4	62.23	0.0060	0.5831	150.6	84.7	3.2	99.7	95.3	397.4	1.4	-	397.4	1.4
ZA	1430	5.5	61.38	0.0068	0.6430	90.8	74.8	2.8	99.7	98.5	392.4	1.5	-	392.4	1.5
ZB	1680	5.3	61.41	0.0079	2.500	43.5	65.0	2.4	98.8	100.0	389.4	1.3	-	389.4	1.3
total gas age				n=28		2878.3	68.1				364.3	1.6			
57-174.1 F:11:95, K-feldspar, 6.46 mg, J=0.003964202±0.08%, D=1.00362±0.00105, NM-95, Lab#=9573-01															
A	500	11.9	155.7	0.0156	40.96	6.34	32.8	22.7	92.2	1.5	813.0	3.6	165.4	**165.4**	**3.6**
B	500	23.8	52.70	0.0283	3.700	1.34	18.0	5.6	97.9	1.9	335.7	4.7	151.2	**151.2**	**4.7**
C	550	14.5	47.95	0.0666	1.347	1.71	7.7	1.8	99.1	2.3	311.5	3.6	252.7	**160.0**	**9.0**
D	550	24.6	41.21	0.0955	2.325	1.04	5.3	1.7	98.3	2.5	268.7	6.0	214.3	**160.0**	**9.0**
E	600	14.0	51.82	0.1094	1.604	2.03	4.7	5.1	99.1	3.0	334.2	3.5	168.5	**168.5**	**3.5**
F	600	24.2	38.08	0.1047	3.788	1.28	4.9	0.76	97.0	3.3	246.6	4.7	221.7	**221.7**	**4.7**
G	650	14.8	51.20	0.1025	2.376	2.66	5.0	4.3	98.6	4.0	329.1	2.9	190.8	**190.8**	**2.9**
H	650	25.0	37.94	0.0943	0.7523	1.73	5.4	1.7	99.4	4.4	251.3	3.7	196.4	**196.4**	**3.7**
I	700	4.8	48.62	0.0722	-0.9005	1.43	7.1	2.6	100.5	4.7	319.5	5.1	-	**230.0**	**40.0**
J	750	5.1	48.38	0.0469	0.3628	3.42	10.9	2.5	99.7	5.5	315.8	2.4	-	**230.0**	**40.0**
K	800	5.3	43.82	0.0327	0.5294	5.10	15.6	1.3	99.6	6.8	287.9	1.8	-	287.9	1.8
L	850	5.4	42.03	0.0189	0.2832	6.70	27.0	0.65	99.7	8.4	277.4	1.6	-	277.4	1.6
M	900	5.1	42.49	0.0151	0.6999	8.52	33.8	0.80	99.5	10.4	279.4	1.5	-	279.4	1.5
N	950	5.1	43.42	0.0142	0.6885	11.1	36.0	1.0	99.5	13.1	285.1	1.1	-	285.1	1.1
O	1000	4.9	45.97	0.0144	0.9680	14.6	35.5	1.3	99.3	16.6	300.1	1.4	-	300.1	1.4
P	1050	4.9	49.07	0.0078	1.359	22.8	65.7	2.3	99.1	22.2	318.1	1.2	-	318.1	1.2
Q	1100	5.0	51.43	0.0055	1.426	44.8	92.8	2.9	99.1	33.0	332.1	1.2	-	332.1	1.2
R	1100	25.0	52.38	0.0040	1.127	54.1	127.6	2.3	99.3	46.0	338.2	1.3	-	338.2	1.3
S	1100	54.9	54.50	0.0028	1.745	34.8	183.4	2.3	99.0	54.4	349.7	1.4	-	349.7	1.4
T	1100	115.0	58.48	0.0022	3.674	30.3	230.4	2.2	98.1	61.7	369.7	1.2	-	369.7	1.2
U	1100	235.0	61.91	0.0030	6.727	27.4	172.5	2.8	96.8	68.3	384.4	1.4	-	384.4	1.4
V	1100	475.0	66.54	0.0027	15.48	24.8	185.8	3.1	93.1	74.3	396.2	1.6	-	396.2	1.6
W	1180	5.3	58.99	0.0061	0.8124	3.16	84.0	3.0	99.6	75.1	377.6	2.7	-	377.6	2.7
X	1230	5.2	60.06	0.0036	0.5745	20.0	139.9	3.2	99.7	79.9	384.2	1.2	-	384.2	1.2
Y	1280	5.5	62.99	0.0020	0.6786	70.6	257.7	3.2	99.6	96.9	400.9	1.5	-	400.9	1.5
Z	1330	5.2	61.83	0.0028	1.237	5.66	182.4	3.2	99.4	98.3	393.3	2.1	-	393.3	2.1

											Conventional age		Age corrected for excess ^{40}Ar	Model input	
ID	Temp	Time	$^{40}Ar/^{39}Ar$	$^{37}Ar/^{39}Ar$	$^{36}Ar/^{39}Ar$	$^{39}Ar_K$	K/Ca	Cl/K	$^{40}Ar^*$	^{39}Ar	Age	±2σ		Age	error
	(°C)				(x 10^{-3})	(x 10^{-15} mol)		(x 10^{-3})	(%)	(%)	(Ma)	(Ma)	(Ma)	(Ma)	(Ma)
ZA	1430	5.5	61.76	0.0050	0.6395	4.74	102.8	3.6	99.7	99.4	393.9	2.2	-	393.9	2.2
ZB	1680	5.0	61.37	0.0058	16.76	2.31	88.4	2.0	91.9	100.0	364.0	3.8	-	364.0	3.8
total gas age				n=28		414.4	144.8				361.4	1.5			
626-1 E:1:95, K-feldspar, 6.93 mg, J=0.003973641±0.08%, D=1.00362±0.00105, NM-95, Lab#=9558-01															
A	500	12.6	183.0	0.0194	94.00	5.53	26.3	55.5	84.8	1.3	866.5	5.9	150.2	**150.2**	**5.9**
B	500	24.4	49.02	0.0361	14.16	1.45	14.1	10.0	91.4	1.6	295.7	5.6	142.9	**142.9**	**5.6**
C	550	14.8	48.93	0.0784	6.853	1.81	6.5	6.3	95.8	2.0	308.3	4.8	214.1	**214.1**	**4.8**
D	550	24.9	38.20	0.0726	8.671	0.942	7.0	2.8	93.2	2.2	238.9	7.9	195.9	**195.9**	**7.9**
E	600	14.7	104.3	0.0146	25.48	16.5	35.0	26.9	92.8	6.0	586.6	2.4	216.2	**216.2**	**2.4**
F	600	24.8	37.17	0.0044	3.652	1.51	116.5	0.96	97.0	6.4	241.6	4.4	227.1	**227.1**	**4.4**
G	650	15.0	44.21	0.0062	7.507	2.83	82.4	6.2	94.9	7.0	278.2	2.9	183.7	**183.7**	**2.9**
H	650	25.1	34.71	0.0000	1.320	1.94	-	1.6	98.8	7.5	230.5	3.6	205.7	**205.7**	**3.6**
I	700	4.9	35.54	0.0000	0.0550	1.41	-	1.9	99.9	7.8	238.1	4.7		238.1	4.7
J	750	5.5	38.18	0.0027	2.121	3.95	188.8	2.6	98.3	8.7	250.8	2.3		250.8	2.3
K	800	5.4	34.05	0.0037	1.640	5.57	138.3	1.3	98.5	10.0	225.7	1.7		225.7	1.7
L	850	5.4	33.69	0.0041	1.842	6.49	124.8	1.3	98.3	11.5	223.1	1.6		223.1	1.6
M	900	5.5	33.17	0.0034	0.9488	7.50	149.8	0.63	99.1	13.2	221.4	1.3		221.4	1.3
N	950	5.2	34.39	0.0047	1.548	8.33	109.1	1.6	98.6	15.1	228.0	1.3		228.0	1.3
O	1000	5.1	35.71	0.0032	1.108	9.34	158.2	2.4	99.0	17.2	237.2	1.3		237.2	1.3
P	1050	5.2	38.54	0.0041	2.350	11.1	123.8	3.7	98.1	19.8	252.6	1.3		252.6	1.3
Q	1100	5.3	42.71	0.0056	3.044	14.4	91.5	5.1	97.8	23.1	277.1	1.1		277.1	1.1
R	1100	25.3	47.85	0.0051	4.997	24.8	100.2	6.5	96.9	28.8	305.0	1.1		305.0	1.1
S	1100	54.9	52.84	0.0048	6.419	25.7	105.5	7.1	96.4	34.7	332.4	1.5		332.4	1.5
T	1100	114.9	56.35	0.0053	10.07	31.6	97.1	7.9	94.7	42.0	346.9	1.5		346.9	1.5
U	1100	234.9	59.57	0.0069	13.43	37.5	73.6	8.7	93.3	50.6	360.0	1.5		360.0	1.5
V	1100	474.9	62.16	0.0102	21.17	42.5	49.9	10.0	89.9	60.3	361.7	1.7		361.7	1.7
W	1180	5.2	57.97	0.0124	10.09	2.05	41.2	12.9	94.8	60.8	356.4	3.8		356.4	3.8
X	1230	5.4	59.72	0.0313	16.60	18.2	16.3	21.0	91.8	65.0	355.4	1.7		355.4	1.7
Y	1280	5.7	57.61	0.0041	7.474	78.6	123.9	9.0	96.1	83.0	358.8	1.3		358.8	1.3
Z	1330	5.4	58.98	0.0034	6.837	61.0	152.3	6.2	96.5	97.1	367.9	1.1		367.9	1.1
ZA	1430	5.6	60.46	0.0078	9.270	9.37	65.3	7.8	95.4	99.2	372.4	1.7		372.4	1.7
ZB	1680	5.1	66.43	0.0141	20.97	3.45	36.2	3.9	90.6	100.0	387.0	3.7		387.0	3.7
total gas age				n=28		435.4	99.5				350.2	1.6			
676-2 D:8:95, K-feldspar, 10.77 mg, J=0.003935777±0.08%, D=1.00362±0.00105, NM-95, Lab#=9555-01															
A	500	9.8	171.3	0.0114	82.34	11.5	44.7	74.7	85.8	1.7	823.4	3.9	195.6	**195.6**	**3.9**
B	500	22.5	69.90	0.0115	24.06	4.94	44.4	22.3	89.8	2.4	398.3	3.0	185.8	**185.8**	**3.0**
C	550	13.4	72.67	0.0226	18.89	9.48	22.6	23.5	92.3	3.8	422.6	1.9	201.8	**201.8**	**1.9**
D	550	23.7	48.41	0.0552	11.58	4.08	9.2	9.2	92.9	4.4	294.0	2.3	204.6	**204.6**	**2.3**
E	600	13.1	79.02	0.0396	21.89	24.0	12.9	27.8	91.8	7.9	453.1	1.8	193.1	**193.1**	**1.8**
F	600	23.1	50.79	0.0892	10.00	5.59	5.7	9.8	94.1	8.7	311.1	2.2	216.3	**216.3**	**2.2**
G	650	13.8	51.65	0.0508	10.93	9.53	10.0	11.7	93.7	10.1	314.6	1.8	201.3	**201.3**	**1.8**
H	650	24.1	39.64	0.0267	6.008	5.14	19.1	4.3	95.5	10.9	250.5	1.9	208.1	**208.1**	**1.9**
I	700	3.7	49.29	0.0158	8.090	5.23	32.3	9.9	95.1	11.6	305.5	2.2	305.5	305.5	2.2
J	750	4.6	45.47	0.0119	7.099	11.0	42.7	7.8	95.3	13.3	284.2	1.4	284.2	284.2	1.4
K	800	4.2	37.00	0.0125	2.656	10.9	40.9	2.7	97.8	14.9	240.2	1.1	240.2	240.2	1.1
L	850	4.8	35.55	0.0118	1.926	12.6	43.3	1.9	98.3	16.7	232.6	1.0	232.6	232.6	1.0
M	900	4.7	35.17	0.0082	1.731	16.0	61.8	1.9	98.5	19.0	230.5	1.0	230.5	230.5	1.0
N	950	5.1	36.70	0.0057	2.921	19.7	89.1	3.5	97.6	21.9	237.9	1.0	237.9	237.9	1.0
O	1000	4.8	39.32	0.0054	5.251	31.5	94.6	5.6	96.0	26.5	249.9	1.0	249.9	249.9	1.0
P	1050	5.0	40.79	0.0046	5.358	55.9	111.7	6.5	96.1	34.7	258.73	0.99	258.73	258.73	0.99
Q	1100	4.8	41.74	0.0047	5.379	71.8	109.2	6.9	96.1	45.2	264.55	0.92	264.55	264.55	0.92
R	1100	24.8	43.42	0.0041	4.781	84.3	125.8	7.0	96.7	57.6	275.9	1.2	275.9	275.9	1.2
S	1100	54.7	46.96	0.0034	4.776	64.7	148.8	7.3	96.9	67.1	297.4	1.1	297.4	297.4	1.1
T	1100	114.7	49.63	0.0034	6.699	62.2	150.8	7.7	96.0	76.2	309.9	1.3	309.9	309.9	1.3
U	1100	234.8	51.17	0.0033	8.040	60.6	152.7	8.4	95.3	85.0	316.8	1.3	316.8	316.8	1.3
V	1100	474.8	51.17	0.0033	8.040	60.6	152.7	8.4	95.3	93.9	1108.9	113.7	1108.9	**316.8**	**1.3**
W	1180	4.6	51.26	0.0000	4.718	4.03	-	9.2	97.2	94.5	323.1	2.7	323.1	323.1	2.7
X	1230	5.0	50.99	0.0012	4.801	23.9	439.4	8.8	97.2	98.0	321.4	1.4	321.4	321.4	1.4
Y	1280	5.4	51.84	0.0002	5.193	7.51	3217.9	7.9	97.0	99.1	325.8	1.7	325.8	325.8	1.7
Z	1330	5.3	51.83	0.0000	0.4204	1.85	-	7.7	99.7	99.4	334.0	3.5	334.0	334.0	3.5
ZA	1430	5.7	51.30	0.0000	6.504	2.92	-	6.9	96.2	99.8	320.3	2.5	320.3	320.3	2.5
ZB	1680	5.2	61.08	0.0000	25.21	1.38	-	9.3	87.8	100.0	345.4	5.1	345.4	345.4	5.1
total gas age				n=28		682.9	155.1				302.1	1.3			
700-1 E:7:95, K-feldspar, 9.88 mg, J=0.003915359±0.08%, D=1.00362±0.00105, NM-95, Lab#=9562-01															
A	500	12.6	203.4	0.0131	64.21	33.0	39.1	3.9	90.7	1.1	980.3	3.5	-	**198.0**	**3.5**

ID	Temp (°C)	Time	$^{40}Ar/^{39}Ar$	$^{37}Ar/^{39}Ar$	$^{36}Ar/^{39}Ar$ (x 10^{-3})	$^{39}Ar_K$ (x 10^{-15} mol)	K/Ca	Cl/K (x 10^{-3})	$^{40}Ar^*$ (%)	^{39}Ar (%)	Conventional age: Age (Ma)	Conventional age: ±2σ (Ma)	Age corrected for excess ^{40}Ar (Ma)	Model input: Age (Ma)	Model input: error (Ma)
B	500	24.2	30.58	0.0102	3.010	23.8	50.2	-0.051	97.0	1.8	198.25	0.76	-	198.25	0.76
C	550	14.7	35.15	0.0105	1.951	38.7	48.4	-0.022	98.3	3.1	228.87	0.82	-	**201.0**	**3.0**
D	550	24.9	30.94	0.0099	1.133	28.6	51.3	0.004	98.8	4.0	204.01	0.82	-	204.01	0.82
E	600	14.7	40.43	0.0095	2.141	49.1	53.5	0.20	98.4	5.6	261.11	0.99	-	**208.0**	**4.0**
F	600	24.8	32.17	0.0088	0.6231	34.0	58.3	0.14	99.4	6.7	212.75	0.86	-	212.75	0.86
G	650	15.1	37.83	0.0089	1.763	53.1	57.5	0.19	98.6	8.4	245.81	0.97	-	**213.0**	**1.0**
H	650	25.0	32.37	0.0079	0.5727	38.8	64.6	-0.109	99.4	9.7	214.07	0.82	-	214.07	0.82
I	700	4.8	40.57	0.0079	2.612	29.4	64.2	0.079	98.0	10.6	261.09	0.92	-	**219.0**	**5.0**
J	750	5.3	37.37	0.0085	1.345	66.3	59.9	-0.024	98.9	12.8	243.73	0.86	-	**225.0**	**2.0**
K	800	5.2	34.72	0.0088	1.001	90.4	57.9	0.053	99.1	15.7	228.0	1.0	-	228.0	1.0
L	850	5.6	33.95	0.0097	0.8094	101.0	52.7	-0.022	99.2	19.0	223.49	0.88	-	223.49	0.88
M	900	5.3	34.34	0.0104	1.130	99.5	49.3	-0.053	99.0	22.2	225.39	0.94	-	225.39	0.94
N	950	5.2	35.36	0.0127	1.488	102.9	40.3	-0.102	98.7	25.5	231.03	0.77	-	231.03	0.77
O	1000	5.0	37.50	0.0122	1.628	117.6	42.0	0.044	98.7	29.3	244.05	0.95	-	244.05	0.95
P	1050	5.2	40.88	0.0099	2.115	151.3	51.6	0.078	98.4	34.2	263.91	0.90	-	263.91	0.90
Q	1100	5.2	44.47	0.0085	2.542	226.8	60.3	0.28	98.3	41.6	284.9	1.2	-	284.9	1.2
R	1100	25.3	47.51	0.0077	2.271	339.3	65.9	0.23	98.5	52.6	303.7	1.7	-	303.7	1.7
S	1100	54.9	50.79	0.0081	1.765	244.6	62.7	0.23	98.9	60.5	324.0	1.5	-	324.0	1.5
T	1100	115.0	53.68	0.0068	1.654	209.3	74.8	0.36	99.0	67.3	341.2	1.6	-	341.2	1.6
U	1100	234.9	56.68	0.0058	1.895	201.9	88.4	0.40	99.0	73.8	358.2	1.6	-	358.2	1.6
V	1100	474.8	58.75	0.0048	2.901	201.5	106.6	0.42	98.5	80.3	368.4	2.1	-	368.4	2.1
W	1180	5.2	59.42	0.0071	2.298	27.0	71.8	0.77	98.8	81.2	373.3	1.4	-	373.3	1.4
X	1230	5.4	60.30	0.0049	2.246	202.8	103.6	0.73	98.9	87.8	378.5	1.6	-	378.5	1.6
Y	1280	5.7	61.78	0.0019	1.637	276.4	263.2	0.67	99.2	96.7	388.0	1.9	-	388.0	1.9
Z	1330	5.4	59.13	0.0146	3.125	37.9	34.8	0.94	98.4	97.9	370.3	1.4	-	370.3	1.4
ZA	1430	5.7	63.33	0.0269	4.455	22.1	19.0	1.1	97.9	98.7	392.0	1.3	-	392.0	1.3
ZB	1680	5.3	59.10	0.0068	4.988	41.6	74.8	0.54	97.5	100.0	366.9	1.2	-	366.9	1.2
total gas age				n=28		3088.9	84.5				314.7	1.4			
700-2 E:8:95, K-feldspar, 12.83 mg, J=0.003928266±0.08%, D=1.00362±0.00105, NM-95, Lab#=9563-01															
A	500	11.8	428.9	0.0801	60.20	20.9	6.4	15.6	95.8	0.6	1734.2	6.4	191.6	**191.6**	**22.0**
B	500	23.9	36.30	0.0600	4.497	15.1	8.5	0.25	96.3	1.0	232.1	1.2	194.1	**194.1**	**22.0**
C	550	14.5	47.11	0.0759	2.953	26.3	6.7	0.52	98.1	1.8	301.0	1.1	223.6	**223.6**	**50.0**
D	550	24.7	34.94	0.0928	2.032	20.8	5.5	0.36	98.2	2.4	228.17	0.97	171.60	**171.60**	**0.97**
E	600	14.4	53.54	0.1014	3.416	36.2	5.0	0.63	98.1	3.4	338.4	1.3	245.9	**175.0**	**5.0**
F	600	23.8	33.52	0.1080	1.010	21.4	4.7	0.15	99.1	4.1	221.20	0.89	198.67	**180.0**	**5.0**
G	650	14.3	44.49	0.1146	1.838	39.7	4.5	0.46	98.7	5.2	287.2	1.1	217.6	**185.0**	**5.0**
H	650	24.4	33.73	0.1142	0.6014	32.2	4.5	0.22	99.4	6.1	223.27	0.90	189.85	**189.8**	**1.0**
I	700	4.1	50.11	0.1152	2.852	28.6	4.4	0.43	98.3	7.0	319.1	1.3	-	**203.0**	**14.0**
J	750	5.3	47.08	0.1254	2.300	68.5	4.1	0.42	98.5	9.0	302.0	1.1	-	**215.0**	**12.0**
K	800	5.2	39.01	0.1433	1.221	78.3	3.6	0.12	99.0	11.2	254.95	0.96	-	228.0	13.0
L	850	5.4	36.24	0.1630	1.258	78.1	3.1	0.23	98.9	13.5	237.75	0.82	-	237.7	0.8
M	900	5.3	37.16	0.1812	1.583	82.7	2.8	0.17	98.7	15.9	242.9	1.0	-	242.9	1.0
N	950	5.1	38.92	0.1884	1.976	85.8	2.7	0.29	98.5	18.3	253.0	1.1	-	253.0	1.1
O	1000	4.9	41.33	0.1728	1.666	91.1	3.0	0.26	98.8	21.0	268.4	1.0	-	268.4	1.0
P	1050	5.1	47.62	0.0968	1.585	116.7	5.3	0.41	99.0	24.4	306.5	1.1	-	306.5	1.1
Q	1100	5.1	56.59	0.0409	1.750	222.5	12.5	0.47	99.0	30.8	359.0	1.4	-	359.0	1.4
R	1100	25.0	57.89	0.0234	1.375	414.2	21.8	0.50	99.3	42.8	367.2	2.1	-	367.2	2.1
S	1100	55.0	58.22	0.0226	0.8912	327.0	22.6	0.45	99.5	52.2	369.9	1.9	-	369.9	1.9
T	1100	115.0	60.64	0.0204	0.8779	275.1	25.0	0.48	99.5	60.2	383.8	2.1	-	383.8	2.1
U	1100	234.9	63.86	0.0195	1.100	293.1	26.2	0.52	99.5	68.6	401.9	2.1	-	401.9	2.1
V	1100	474.9	66.83	0.0192	1.753	285.6	26.6	0.57	99.2	76.9	417.5	2.0	-	417.5	2.0
W	1180	5.2	72.15	0.0378	0.9791	70.5	13.5	0.96	99.6	78.9	448.5	1.5	-	448.5	1.5
X	1230	5.5	71.88	0.0288	0.7664	267.3	17.7	0.85	99.7	86.7	447.3	2.1	-	447.3	2.1
Y	1280	5.6	69.66	0.0191	0.5649	203.3	26.7	0.69	99.7	92.5	435.3	2.2	-	435.3	2.2
Z	1330	5.4	71.62	0.0917	2.456	51.2	5.6	1.3	99.0	94.0	443.1	1.4	-	443.1	1.4
ZA	1430	5.6	73.03	0.0857	1.174	130.1	6.0	0.99	99.5	97.8	453.1	2.4	-	453.1	2.4
ZB	1680	5.1	72.59	0.0399	1.932	77.1	12.8	0.82	99.2	100.0	449.3	1.9	-	449.3	1.9
total gas age				n=28		3459.5	16.7				378.6	1.8			
664-1 E:5:95, K-feldspar, 6.54 mg, J=0.003914337±0.08%, D=1.00362±0.00105, NM-95, Lab#=9561-01															
A	500	12	132.5617	0.0002	32.1025	62.870	2139.77	9.65	92.8	2.5	709.3	3.1	-	**220.0**	**20.0**
B	500	24	33.4735	0.0003	1.9383	39.694	1793.31	0.89	98.2	4.1	218.40	0.80	-	218.40	0.80
C	550	15	34.2954	0.0000	1.4098	45.559	11465.13	1.02	98.7	5.9	224.51	0.86	-	224.51	0.86
D	550	25	34.5969	0.0000	1.1479	28.408	-	0.87	99.0	7.0	226.87	0.89	-	226.87	0.89
E	600	15	35.3105	0.0000	0.9048	41.178	-	0.66	99.2	8.6	231.75	0.78	-	231.75	0.78
F	600	25	33.8426	0.0000	0.8897	32.371	-	0.51	99.2	9.9	222.64	0.77	-	222.64	0.77
G	650	15	34.2448	0.0000	0.7015	44.603	-	0.57	99.3	11.6	225.50	0.73	-	225.50	0.73

ID	Temp	Time	$^{40}Ar/^{39}Ar$	$^{37}Ar/^{39}Ar$	$^{36}Ar/^{39}Ar$	$^{39}Ar_K$	K/Ca	Cl/K	$^{40}Ar*$	^{39}Ar	Conventional age: Age	Conventional age: ±2σ	Age corrected for excess ^{40}Ar	Model input: Age	Model input: error
	(°C)				(x 10^{-3})	(x 10^{-15} mol)		(x 10^{-3})	(%)	(%)	(Ma)	(Ma)	(Ma)	(Ma)	(Ma)
H	650	25	33.9076	0.0000	0.6289	34.232	38676.58	0.42	99.4	13.0	223.53	0.75	-	223.53	0.75
I	700	5	34.6728	0.0000	0.6918	20.343	-	0.88	99.3	13.8	228.18	0.83	-	228.18	0.83
J	750	5	39.1450	0.0001	1.7755	47.168	4633.03	1.05	98.6	15.7	253.83	0.83	-	253.83	0.83
K	800	5	35.9423	0.0000	0.7672	53.431	-	0.96	99.3	17.8	235.92	0.86	-	235.92	0.86
L	850	6	36.9440	0.0000	0.6507	54.533	-	0.45	99.4	19.9	242.33	0.86	-	242.33	0.86
M	900	5	37.1678	0.0000	0.3992	48.354	-	0.46	99.6	21.8	244.17	0.84	-	244.17	0.84
N	950	5	39.0973	0.0000	0.4451	52.946	-	0.56	99.6	23.9	255.95	0.81	-	255.95	0.81
O	1000	5	41.3371	0.0000	0.6606	59.973	23625.62	0.72	99.5	26.3	269.24	0.97	-	269.24	0.97
P	1050	5	44.6482	0.0000	0.9257	69.265	-	0.75	99.3	29.0	288.8	1.1	-	288.8	1.1
Q	1100	5	48.9509	0.0001	1.3194	78.982	6048.51	0.76	99.2	32.2	313.8	1.1	-	313.8	1.1
R	1100	25	53.9475	0.0001	1.8579	112.031	4386.90	0.93	98.9	36.6	342.3	1.5	-	342.3	1.5
S	1100	55	58.2735	0.0002	2.7751	115.887	2574.88	1.08	98.6	41.2	365.8	1.3	-	365.8	1.3
T	1100	115	61.2835	0.0001	3.6113	139.692	5238.45	1.11	98.2	46.7	381.7	1.2	-	381.7	1.2
U	1100	235	62.0057	0.0002	4.0633	151.234	3263.38	1.06	98.0	52.6	385.0	1.7	-	385.0	1.7
V	1100	477	62.4727	0.0002	4.9580	173.730	3279.41	1.16	97.6	59.5	386.2	1.7	-	386.2	1.7
W	1180	5	61.6699	0.0000	2.5543	17.068	-	0.90	98.7	60.2	385.7	1.6	-	385.7	1.6
X	1230	5	61.6370	0.0002	2.1624	103.847	3399.79	0.85	98.9	64.3	386.1	1.5	-	386.1	1.5
Y	1280	5	61.5806	0.0002	2.8260	200.644	2103.38	1.17	98.6	72.2	384.7	1.8	-	384.7	1.8
Z	1330	6	60.8081	0.0003	3.6690	646.865	1595.32	1.39	98.2	97.8	378.9	1.9	-	378.9	1.9
ZA	1430	6	60.0657	0.0005	3.4807	51.998	1006.85	1.85	98.2	99.8	374.9	1.3	-	374.9	1.3
ZB	1680	5	33.7208	0.0000	26.4062	4.593	-	11.63	76.8	100.0	174.2	3.0	-	174.2	3.0
total gas age				n=28		2531.501	3959.38				348.3	1.5			

Isotopic ratios corrected for blank, radioactive decay, and mass discrimination, not corrected for interferring reactions.
Individual analyses show analytical error only; mean age errors also include error in J and irradiation parameters.
Analyses in italics are excluded excluded from mean age calculations.
Correction factors:

NM-95

$(^{39}Ar/^{37}Ar)_{Ca}$ = 0.00078±0.00003
$(^{36}Ar/^{37}Ar)_{Ca}$ = 0.00028±0.00001
$(^{38}Ar/^{39}Ar)_K$ = 0.0119
$(^{40}Ar/^{39}Ar)_K$ = 0.0240±0.0020

NM-128

$(^{39}Ar/^{37}Ar)_{Ca}$ = 0.00070±0.00005
$(^{36}Ar/^{37}Ar)_{Ca}$ = 0.00028±0.00000
$(^{38}Ar/^{39}Ar)_K$ = 0.0119
$(^{40}Ar/^{39}Ar)_K$ = 0.0250±0.0003

Table 4. Resutls of step heating analyses of K-feldspar (duplicates)

ID	Temp (°C)	$^{40}Ar/^{39}Ar$	$^{37}Ar/^{39}Ar$	$^{36}Ar/^{39}Ar$ (x 10^{-3})	$^{39}Ar_K$ (x 10^{-15} mol)	K/Ca	Cl/K (x 10^{-3})	$^{40}Ar^*$ (%)	^{39}Ar (%)	Age (Ma)	±2σ (Ma)	Time (sec)
49-129.2 E11:80, Kspar, 2.11 mg, J=0.003740714±0.09%, D=1.0052±0.00069, nm-80, Lab#=8578-01												
A	550	143.4	0.0324	85.88	1.80	15.7	34.8	82.3	0.8	659.8	5.0	13.33
B	550	45.03	0.0372	15.08	0.862	13.7	6.7	90.1	1.1	254.8	2.8	17.47
C	600	85.26	0.0727	15.85	2.09	7.0	15.7	94.5	2.0	475.2	2.4	12.24
D	600	46.75	0.1369	10.04	0.994	3.7	5.1	93.6	2.4	273.6	3.0	17.45
E	650	107.5	0.1371	25.74	2.87	3.7	20.5	92.9	3.6	572.9	2.8	12.71
F	650	45.74	0.2828	13.14	1.06	1.8	6.0	91.5	4.0	262.5	2.8	17.97
G	700	91.06	0.3094	19.71	2.17	1.6	17.3	93.6	4.9	499.4	2.6	11.83
H	700	44.47	0.5733	7.204	1.43	0.89	4.0	95.3	5.5	265.5	2.0	17.89
I	750	61.41	0.5804	7.718	2.53	0.88	9.6	96.3	6.6	360.8	1.8	13.13
J	750	40.11	0.2181	5.809	1.41	2.3	2.3	95.7	7.2	242.1	1.6	18.20
K	800	45.87	0.0674	4.004	2.05	7.6	4.7	97.4	8.0	278.8	1.6	10.73
L	850	44.82	0.0242	3.535	3.38	21.0	3.4	97.6	9.5	273.5	1.2	10.73
M	900	42.68	0.0131	1.860	4.53	39.0	1.8	98.7	11.3	263.91	0.92	10.48
N	950	42.66	0.0094	1.672	6.13	54.3	1.0	98.8	13.9	264.11	0.92	10.85
O	1000	43.09	0.0090	1.802	6.81	56.5	0.92	98.7	16.8	266.40	0.91	10.06
P	1050	44.02	0.0120	1.883	10.4	42.5	1.7	98.7	21.1	271.69	0.86	9.27
Q	1100	45.79	0.0108	1.772	13.9	47.3	2.4	98.8	26.9	282.08	0.82	8.74
R	1150	47.16	0.0067	1.646	21.4	76.6	2.9	98.9	35.8	290.2	1.1	11.06
S	1150	48.23	0.0048	2.444	17.8	107.3	2.7	98.5	43.3	295.01	0.98	28.00
T	1150	49.75	0.0050	2.711	13.6	103.0	3.2	98.3	48.9	303.3	1.1	57.97
U	1150	53.05	0.0046	5.888	12.0	110.4	3.6	96.7	53.9	316.7	1.1	118.07
V	1150	56.92	0.0047	10.90	10.9	108.4	4.0	94.3	58.5	330.1	1.0	237.97
W	1150	60.36	0.0049	19.15	11.2	104.1	4.5	90.6	63.2	335.7	1.2	478.02
X	1250	53.93	0.0079	2.577	14.0	64.8	4.4	98.6	69.0	327.1	1.0	10.76
Y	1300	57.41	0.0046	3.336	41.0	111.0	5.7	98.2	86.1	345.4	1.5	11.40
Z	1350	59.22	0.0041	3.408	30.4	123.2	5.5	98.3	98.8	355.3	1.4	11.55
ZA	1400	62.57	0.0186	6.566	1.65	27.4	5.2	96.9	99.5	368.7	2.7	11.59
ZB	1500	64.83	0.1030	13.78	1.10	5.0	4.6	93.7	100.0	369.4	3.2	11.60
ZC	1750	218.5	0.0241	514.6	0.104	21.2	2.7	30.4	100.0	400.1	78.6	11.30
total gas age			n=29		239.5	83.7				323.6	1.3	
57-174.1 E5:80, Kspar, 2.11 mg, J=0.003682886±0.09%, D=1.0052±0.00069, nm-80, Lab#=8574-01												
A	550	307.0	0.0383	61.91	1.41	13.3	50.3	94.0	0.6	1306.5	6.0	11.44
B	550	54.98	0.0393	6.499	0.570	13.0	4.5	96.5	0.9	321.9	3.5	17.59
C	600	83.82	0.0678	6.034	1.26	7.5	9.5	97.9	1.4	476.2	2.9	12.33
D	600	59.56	0.1606	6.787	0.622	3.2	4.8	96.6	1.7	346.8	3.4	17.40
E	650	132.7	0.1604	7.295	2.29	3.2	17.9	98.4	2.7	708.4	3.0	12.81
F	650	56.55	0.3704	4.338	0.744	1.4	2.9	97.7	3.0	334.3	2.8	17.87
G	700	106.1	0.2530	7.419	2.06	2.0	11.9	97.9	3.9	584.4	2.4	11.87
H	700	48.63	0.3586	5.834	1.04	1.4	2.5	96.5	4.4	287.6	2.5	17.82
I	750	70.13	0.2461	3.012	2.60	2.1	6.4	98.7	5.5	409.8	1.6	13.17
J	750	43.33	0.1663	4.572	1.20	3.1	2.2	96.9	6.1	259.3	2.3	18.22
K	800	49.68	0.0706	3.229	1.85	7.2	2.2	98.0	6.9	297.7	1.9	11.05
L	850	46.15	0.0244	1.888	3.12	20.9	1.0	98.7	8.2	279.9	1.1	10.79
M	900	44.79	0.0139	1.046	4.58	36.7	0.63	99.3	10.3	273.6	1.0	10.76

ID	Temp (°C)	$^{40}Ar/^{39}Ar$	$^{37}Ar/^{39}Ar$	$^{36}Ar/^{39}Ar$ (x 10^{-3})	$^{39}Ar_K$ (x 10^{-15} mol)	K/Ca	Cl/K (x 10^{-3})	$^{40}Ar^*$ (%)	^{39}Ar (%)	Age (Ma)	±2σ (Ma)	Time (sec)
N	950	44.94	0.0105	0.8242	6.51	48.4	0.69	99.4	13.1	274.8	1.1	11.00
O	1000	46.08	0.0110	0.8495	6.75	46.2	0.46	99.4	16.1	281.3	1.1	10.05
P	1050	48.15	0.0126	0.9081	10.2	40.6	0.91	99.4	20.6	292.88	0.83	9.20
Q	1100	51.34	0.0077	0.9435	15.5	65.9	1.6	99.4	27.4	310.78	0.90	8.97
R	1150	53.83	0.0062	1.017	27.6	82.5	2.3	99.4	39.5	324.5	1.1	11.04
S	1150	54.83	0.0046	0.8771	22.8	109.9	1.7	99.5	49.6	330.3	1.0	28.07
T	1150	56.88	0.0036	1.377	16.4	141.4	1.6	99.2	56.8	340.76	0.99	57.88
U	1150	60.50	0.0030	5.234	11.2	169.6	2.1	97.4	61.7	354.4	1.3	117.86
V	1150	62.81	0.0033	6.183	11.9	154.4	2.1	97.1	67.0	365.4	1.0	237.81
W	1150	65.67	0.0034	11.01	11.6	150.2	2.3	95.0	72.1	373.2	1.3	477.84
X	1250	62.31	0.0042	0.7054	12.9	120.9	2.6	99.6	77.7	371.5	1.1	10.71
Y	1300	64.34	0.0036	0.4968	26.6	141.4	3.0	99.7	89.4	382.7	1.2	11.41
Z	1350	65.32	0.0023	0.4570	18.4	222.0	3.1	99.8	97.5	388.1	1.3	11.63
ZA	1400	64.57	0.0042	1.898	1.94	120.1	2.4	99.1	98.4	381.8	2.0	11.53
ZB	1500	64.54	0.0038	1.816	3.00	133.1	2.5	99.1	99.7	381.7	1.6	11.80
ZC	1750	91.88	0.0054	101.8	0.738	95.2	3.3	67.2	100.0	369.9	6.9	11.34
total gas age			n=29		227.4	110.2				355.1	1.2	

57-166.2 F4:80, Kspar, 2.52 mg, J=0.00370623±0.09%, D=1.0052±0.00069, nm-80, Lab#=8581-01

ID	Temp (°C)	$^{40}Ar/^{39}Ar$	$^{37}Ar/^{39}Ar$	$^{36}Ar/^{39}Ar$ (x 10^{-3})	$^{39}Ar_K$ (x 10^{-15} mol)	K/Ca	Cl/K (x 10^{-3})	$^{40}Ar^*$ (%)	^{39}Ar (%)	Age (Ma)	±2σ (Ma)	Time (sec)
A	550	179.5	0.0114	47.16	1.86	44.9	43.6	92.2	0.7	863.0	4.2	11.18
B	550	43.85	0.0093	3.115	1.03	54.9	5.8	97.9	1.0	266.2	2.6	17.53
C	600	135.7	0.0157	5.716	2.36	32.5	30.2	98.7	1.9	727.5	2.8	12.17
D	600	55.41	0.0364	2.375	0.735	14.0	6.9	98.7	2.1	333.0	3.3	17.31
E	650	133.8	0.0429	4.612	2.77	11.9	34.6	99.0	3.1	720.4	3.2	12.84
F	650	51.72	0.1199	4.241	0.698	4.3	4.1	97.6	3.3	309.3	3.3	17.84
G	700	103.7	0.0779	5.141	2.09	6.5	22.9	98.5	4.1	579.5	2.5	11.77
H	700	47.10	0.0957	5.173	0.951	5.3	2.7	96.7	4.4	281.5	2.2	17.70
I	750	59.92	0.0815	5.031	1.63	6.3	6.6	97.5	5.0	353.6	2.0	12.97
J	750	45.37	0.0569	6.732	0.956	9.0	1.6	95.6	5.3	268.9	2.5	18.01
K	800	54.16	0.0430	14.89	1.81	11.9	3.2	91.8	6.0	305.2	2.1	13.00
KA	800	46.46	0.0239	4.778	1.34	21.3	0.66	96.9	6.5	278.5	1.9	17.89
L	850	48.60	0.0182	4.040	2.26	28.1	1.6	97.5	7.3	291.9	1.4	12.70
LA	850	48.38	0.0115	3.323	2.60	44.2	0.93	97.9	8.2	291.9	1.4	17.77
M	900	49.22	0.0107	1.562	3.70	47.8	0.90	99.0	9.5	299.5	1.3	10.73
N	950	49.81	0.0102	1.231	6.80	49.9	1.2	99.2	11.9	303.4	1.1	10.88
O	1000	49.39	0.0097	0.7463	8.38	52.6	1.2	99.5	14.9	301.9	1.1	10.03
P	1050	50.38	0.0110	0.9059	13.2	46.2	2.0	99.4	19.5	307.25	0.93	9.27
Q	1100	52.98	0.0078	0.8571	18.9	65.5	3.7	99.5	26.2	321.9	1.2	8.95
R	1150	55.54	0.0071	0.9836	25.3	71.9	4.9	99.4	35.2	336.0	1.1	11.01
S	1150	56.20	0.0059	1.086	23.9	86.2	4.1	99.4	43.6	339.5	1.3	28.06
T	1150	58.60	0.0054	1.655	19.8	95.1	3.6	99.1	50.7	351.8	1.1	57.99
U	1150	62.33	0.0049	4.968	16.3	103.2	4.0	97.6	56.4	366.85	0.98	117.98
V	1150	64.98	0.0047	7.025	12.7	109.3	4.6	96.8	60.9	378.0	1.6	178.99
W	1150	81.71	0.0053	61.74	7.16	96.6	5.0	77.6	63.5	381.0	1.9	146.19
WW	1150	69.62	0.0053	19.22	5.48	96.5	5.1	91.8	65.4	383.6	1.7	126.68
X	1150	70.07	0.0051	18.36	11.5	99.1	5.0	92.2	69.5	387.4	1.4	329.34
Y	1250	64.40	0.0053	0.3940	16.8	97.0	5.7	99.8	75.4	385.4	1.5	10.74

ID	Temp (°C)	$^{40}Ar/^{39}Ar$	$^{37}Ar/^{39}Ar$	$^{36}Ar/^{39}Ar$ (x 10^{-3})	$^{39}Ar_K$ (x 10^{-15} mol)	K/Ca	Cl/K (x 10^{-3})	$^{40}Ar^*$ (%)	^{39}Ar (%)	Age (Ma)	±2σ (Ma)	Time (sec)
Z	1300	64.47	0.0049	0.4387	40.2	103.4	5.2	99.8	89.7	385.7	1.3	11.44
ZA	1350	65.63	0.0040	0.5244	20.2	127.8	5.1	99.7	96.8	391.9	1.6	11.56
ZB	1400	65.75	0.0085	1.520	5.45	59.8	4.8	99.3	98.8	390.9	1.6	11.72
ZC	1500	66.56	0.0073	5.476	2.50	69.9	4.2	97.5	99.7	389.0	2.2	11.81
ZD	1750	83.64	0.0000	61.63	0.959	-	3.3	78.2	100.0	391.6	4.5	11.23
total gas age			n=33		282.2	82.9				366.9	1.4	
57-166.2 G:5:107, K-feldspar, 12.49 mg, J=0.01631909±0.10%, D=1.0069±0.0009999999, NM-107, Lab#=50336-01												
A	300	1976.8	273.5	5127.9	0.944	0.002	251.9	24.5	0.0	4292.9	127.8	28.01
B	300	69.76	0.0000	166.9	0.309	-	29.2	29.3	0.0	518.8	44.6	56.47
C	350	69.40	187.1	42.14	0.641	0.003	76.5	104.2	0.0	1549.4	452.9	26.12
D	350	30.45	0.0000	39.12	0.622	-	21.5	62.0	0.0	484.2	13.4	56.29
E	400	68.27	0.0000	15.00	1.95	-	77.1	93.5	0.1	1287.3	5.8	21.02
F	400	17.86	68.14	7.581	1.23	0.007	17.6	118.6	0.1	559.3	363.6	29.51
G	450	33.03	12.64	3.841	6.78	0.040	36.3	99.6	0.2	781.1	58.2	21.33
H	450	10.28	8.688	1.549	4.90	0.059	5.9	102.2	0.3	287.3	100.7	29.91
I	500	22.06	3.902	1.919	21.3	0.13	23.1	98.8	0.8	550.2	21.0	21.30
J	500	9.099	3.766	0.9490	11.6	0.14	3.1	100.0	1.0	250.4	43.0	29.76
K	550	20.82	0.0000	1.247	33.4	-	20.5	98.1	1.6	519.0	1.5	21.68
L	550	9.571	0.0000	0.4518	13.9	-	2.6	98.3	1.9	257.7	1.0	30.07
M	600	22.26	0.0000	1.220	22.5	-	21.5	98.3	2.4	550.7	1.8	11.60
N	600	10.30	0.0000	0.4261	13.7	-	2.6	98.5	2.6	276.5	1.1	21.67
O	650	16.89	3.432	0.7254	22.1	0.15	11.9	100.2	3.1	441.1	24.2	11.50
P	650	10.77	0.7863	0.3526	16.3	0.65	2.1	99.4	3.4	290.6	33.3	21.61
Q	700	13.01	7.177	0.4481	21.6	0.071	4.7	103.3	3.8	359.4	23.2	11.36
R	700	11.10	0.0000	0.2034	21.5	-	0.98	99.2	4.2	298.1	1.2	21.47
S	800	12.61	1.923	0.2958	77.5	0.27	2.9	100.3	5.8	339.1	8.2	11.51
T	900	12.07	0.6188	0.1345	277.9	0.82	0.98	99.9	11.2	324.2	3.5	21.66
U	1000	12.04	0.0000	0.1508	350.7	-	1.4	99.4	18.1	321.8	1.5	11.74
V	1100	12.69	0.0000	0.2238	990.1	-	3.8	99.3	37.6	337.2	2.2	20.66
W	1200	13.90	0.0000	0.1435	1281.0	-	4.2	99.5	62.8	367.2	3.2	11.84
X	1230	14.70	0.7496	0.1163	859.1	0.68	3.8	100.0	79.7	388.0	3.5	11.79
Y	1280	14.97	0.0000	0.1111	761.2	-	3.6	99.6	94.7	392.9	1.5	27.03
Z	1330	14.78	13.62	0.1925	67.3	0.037	2.8	107.0	96.0	417.8	12.7	4.97
ZA	1430	14.73	4.958	0.1221	138.8	0.10	2.4	102.3	98.8	398.1	6.2	5.25
ZB	1690	14.78	8.688	0.4475	62.2	0.059	1.9	103.7	100.0	405.1	10.8	4.84
total gas age			n=28		5080.9	0.32				368.1	3.8	
A23, D1, NM-128, K-feldspar, 1.38 mg, J=0.01639256±0.09%, D=1.006±0.0014, NM-128, Lab#=51531-01												
A	600	25.37	2.187	5.454	9.77	0.23	7.7	94.3	1.7	597.4	2.9	9.56
B	700	15.28	0.1026	1.426	17.2	5.0	3.6	97.1	4.8	393.0	1.5	4.73
C	750	10.48	0.1178	0.5233	12.6	4.3	1.6	98.4	7.0	281.9	1.2	5.70
D	800	9.402	0.0540	0.4307	7.72	9.4	1.0	98.4	8.4	254.8	1.5	4.48
E	850	9.047	0.0273	0.3190	12.2	18.7	0.75	98.7	10.6	246.5	1.2	5.32
F	900	8.532	0.0215	0.3301	12.5	23.8	0.16	98.6	12.8	233.0	1.1	5.32
G	950	8.506	0.0215	0.1532	14.2	23.7	0.28	99.2	15.3	233.7	1.1	5.39
H	1000	8.543	0.0703	0.2482	16.8	7.3	0.47	98.9	18.3	234.1	1.1	5.29

ID	Temp (°C)	$^{40}Ar/^{39}Ar$	$^{37}Ar/^{39}Ar$	$^{36}Ar/^{39}Ar$ (x 10^{-3})	$^{39}Ar_K$ (x 10^{-15} mol)	K/Ca	Cl/K (x 10^{-3})	$^{40}Ar^*$ (%)	^{39}Ar (%)	Age (Ma)	±2σ (Ma)	Time (sec)
I	1050	8.859	0.0289	0.3882	19.6	17.6	0.53	98.4	21.8	241.1	1.1	5.41
J	1100	9.836	0.0079	0.3558	27.9	64.6	1.3	98.7	26.8	266.4	1.2	5.31
K	1150	10.90	0.0425	0.4063	42.2	12.0	1.9	98.7	34.3	292.9	1.2	4.74
L	1200	11.18	0.0267	0.4218	45.9	19.1	2.1	98.7	42.5	299.9	1.2	5.56
M	1250	11.93	0.0123	0.3712	60.9	41.4	2.3	98.9	53.3	318.9	1.2	5.85
N	1300	14.02	0.0067	0.4906	119.7	76.7	2.5	98.8	74.6	369.2	1.8	5.92
O	1350	14.95	0.0099	0.5145	111.0	51.7	2.1	98.8	94.4	391.3	1.8	5.87
P	1400	14.71	0.1131	0.5577	15.4	4.5	2.2	98.8	97.1	385.5	1.5	5.79
Q	1750	15.27	3.064	8.161	16.2	0.17	3.7	85.7	100.0	351.3	2.0	5.71
total gas age			n=17		561.8	39.6				335.1	1.5	

Isotopic ratios corrected for blank, radioactive decay, and mass discrimination, not corrected for interferring reactions.
Individual analyses show analytical error only; mean age errors also include error in J and irradiation parameters.
Analyses in italics are excluded excluded from mean age calculations.

Correction factors:
NM-80
$(^{39}Ar/^{37}Ar)_{Ca} = 0.00065 \pm 0.00005$
$(^{36}Ar/^{37}Ar)_{Ca} = 0.00026 \pm 0.00002$
$(^{38}Ar/^{39}Ar)_K = 0.0119$
$(^{40}Ar/^{39}Ar)_K = 0.0210 \pm 0.0020$
NM-107, NM-128
$(^{39}Ar/^{37}Ar)_{Ca} = 0.00070 \pm 0.00005$
$(^{36}Ar/^{37}Ar)_{Ca} = 0.00028 \pm 0.00000$
$(^{38}Ar/^{39}Ar)_K = 0.0119$
$(^{40}Ar/^{39}Ar)_K = 0.0250 \pm 0.0003$